JSR A

JOURNAL OF
SCIENTIFIC REPORTS A

JOURNAL OF SCIENTIFIC REPORTS A - SEPTEMBER 2022 - NUMBER 50

gate of
science

Journal of Scientific Reports-A started its publication life in 2000 as name of Journal of Science and Technology of Dumlupınar University and is a national peer-reviewed journal published regularly twice a year in June and December. The language of the journal is English. Articles submitted to the journal are evaluated by at least two referees who are experts in the subject and selected by the editorial board. All articles submitted to the journal are evaluated by the double-blind method. Articles submitted to our journal for review should not be previously published, accepted for publication and in the process of being evaluated for publication in another journal. All responsibility for the articles published in the journal belongs to the author(s).

The journal aims to share scientific studies carried out in the fields of science and engineering at national and international level with scientists and the public. Original research articles, review articles and short notes in science and engineering disciplines are accepted for the journal. Original research articles are expected to contain theoretical and experimental results and should not be published in other journals. In the review articles, it is expected that scientific, technological and current developments on a specific subject are reflected by using an extensive bibliography and made a satisfying evaluation of these. Short notes should be brief writings prepared to announce the first findings of an original study.

Editorial Policy
The journal is open access and the article evaluation period is between 1-2 months.

Advisory Board

JOURNAL OF SCIENTIFIC REPORTS-A
E-ISSN: 2687-6167

CONTENTS

RESEARCH ARTICLES

RESEARCH ARTICLE

PERFORMANCE EVALUATION of STAGED ORC POWER PLANT SOURCED by WASTE HEAT

İlyas CEYLAN[1]*, Oğuz ARSLAN[2]

[1]Bilecik Şeyh Edebali University, Faculty of Engineering, Departement of Mechanical Engineering, Bilecik, ilyasceylan1995@gmail.com, ORCID: 0000-0001-5404-1551
[2]Bilecik Şeyh Edebali University, Faculty of Engineering, Departement of Mechanical Engineering, oguz.arslan@bilecik.edu.tr, ORCID: 0000-0001-8233-831X

ABSTRACT

Organic Rankine Cycle (ORC) is a power cycle in which energy can be produced without extra heating. The basic logic is to generate energy with the help of special fluids that can change phase at low temperatures. In this study, one, two and three stage ORC sourced by waste heat was designed and analyzed in view point of different working fluids. In this aim, it was aimed to investigate the stage and fluid effects on the performance of the system. As a result of the study, it was determined that the efficiency increases with increase of the number of stages. It was also determined that the used fluid type was effective on the performance of the staged system. The energy and exergy efficiency of the three-staged ORC was determined as 31% and 49%, respectively.

Keywords: *Energy, Exergy, Staged ORC, Waste heat.*

1. INTRODUCTION

As known, Rankine cycle is a thermodynamic cycle that converts heat energy into work, and water is used as the working fluid of the cycle for many years. Water is a traditional liquid in the Rankine cycle and is the first choice for generating electricity in large and medium power plants. Although it is preferred as a working fluid due to its safety, environmental protection, and high heat transfer properties, it also has some disadvantages. Some of the disadvantages are high abrasiveness and high freezing temperature [1]. In recent years, hydrocarbon-based fluids with a higher molecular weight and lower boiling temperature are used instead of water in the Rankine cycle called as organic Rankine Cycle (ORC). ORCs are sourced by low temperature resources such as waste heat, solar energy and geothermal energy. ORCs have become one of the most common power generation processes depending on the parameters such as climate change, rising oil prices and environmental problems. In this regard, ORC sourced by waste heat is the cleanest and most reliable way for power generation.

In the literature, many studies were conducted about performance of ORCs [2-5], optimization of ORCs [6-10] and heat sources of ORCs [11-13].The waste heat is one the most preferred energy sources in ORC power plants. Varga et al. [13] investigated the partial replacement of an air cooler to

observe the waste heat behaviour during the temperature decreasing from 140 °C to 45 °C. In this study, they determined that 32 MW of heat released to the environment. Chen et al. [14], developed a mathematical model for the integration of ORC with the circulating heat transfer fluid as an intermediate fluid for the waste heat recovery. In this aim, an ORC-integrated superstructure was proposed that considers all possible heat exchange couplings between waste heat process streams, circulating heat transfer fluid, and ORC. Arslan et al. [15] designed a multiple generation system including electricity generation, domestic hot water and H_2 production for waste recovery of a 150 MW coal-fired power plant. A high-temperature electrolyzer is integrated into the existing system to produce H_2. The second product of O_2 from the electrolyzer was used to enrich the combustion process. The power required for the electrolyzer was obtained from the bottom organic Rankine cycle (ORC). In this context, a supercritical ORC was designed using cyclopentane as the working fluid. An increase of 15.78%−16.53% was achieved in energy efficiency. This increase was achieved in exergy efficiency by 20.43-21.16%. In another study of Arslan [16], supercritical ORC with R601 was investigated. The ORC was sourced by waste heat. The energy and exergy efficiencies of the ORC were recorded as 15.59% and 32.93%, respectively. The kind of the used working fluid is also much important for the system performance of ORC power plants. Arslan et al. [17], investigated s1 type supercritical ORC power plant with an installed capacity of 64.2 MW. They used R744 as the working fluid in the system. They parametrically analyzed the designed system for different temperature and pressures. For the most profitable design, T_{1b}, T_{2a} and P_{2a} were determined as 80 °C, 130 °C and 12 MPa, respectively. Tzu-Chen Hung [18], investigated various working fluids such as Benzene (C6H6), Toluene (C7H8), p-Xylene (C8H10), R113, and R123. Among the studied working fluids, p-Xylene has the highest efficiency and Benzene has the lowest efficiency. The study also showed that irreversibilities strongly depend on the type of heat source.

Literature reviews have shown that double loop, triple loop, and multi-loop ORC has better performance in comparison to the single ORC for the recovery of waste heat. Studies showed that using multi-staged ORCs can significantly improve thermal efficiency and heat source utilization rate. One of the most effective ways to improve ORC's performance is to increase the ORC's cycle count. Double-loop ORC (DL-ORC) has shown great potential in thermodynamic and economic performance. In addition, DL-ORC has a low carbon footprint and high CO_2 emission reduction [19,20]. Braimakis et al. [21] investigated the thermo-economic optimization of the ORC-ORC combined power system. They optimized the use of ORC-ORC for waste heat recovery. The researchers aimed to explore the increasing potential of the exergy efficiency for the ORC-ORC combined power system in comparison to a single-stage ORC. The heat source temperature ranging between 100 and 300 °C were investigated. They concluded that the power output and exergy efficiency can be increased by ORC-ORC in comparison to single-stage cycles at the same these operating conditions. Xia et al. [22] performed the working fluid selection for double-loop ORC (DL-ORC) using multi-objective optimization. The targets for optimization are the payback period, annual emission reduction and exergy efficiency. Study results showed that cyclohexane/butane was the most suitable working fluid amongst the 18 candidate working fluid pairs.

In this study, ORC with three loops, sourced by the waste heat of a ceramic production process was performed parametrically. The designed systems were thermodynamically analyzed by energy and exergy methods. In the analyses, EES software was used. Finally, the best designed system was determined in terms of turbine inlet temperature and pressure, and kind of working fluids.

2. MATERIAL AND METHOD

In the most industrial applications, waste heat is discharged to the environment. Especially in the cement and iron and steel industries, a significant amount of waste heat is lost in the form of flue gases at temperatures of 200-300 °C. These temperature levels are not high enough to recover this waste heat through conventional steam Rankine cycles. For this reason, ORC applications are widely used in industrial waste heat recovery applications. In this study, the waste heat of stack gases of the ceramic production process was evaluated in an ORC with tree loops. The data of waste is given in Table 1 [23].

Table 1. Waste heat data used in the study [23].

Flow rate (m^3/h)	16939		
Gas velocity (m/min)	7.4		
Humidity (%)	5.2		
Pressure (kPa)	92.2		
Flow rate(Nm^3/h)	10817		
Dry cond. Flow rate (Nm^3/h)	10258		
	Measurement 1	Measurement 2	Measurement 3
Gas Temp. (°C)	116.0	115.0	117.0
Dust (kg/h)	0.0014	0.0014	0.0015
CO (kg/h)	0.1432	0.1512	0.1751
SO_2 (kg/h)	0.0000	0.0000	0.0182
NO (kg/h)	0.1364	0.1449	0.1535
NO_2 (kg/h)	0.2092	0.2222	0.2353

The type of fluid directly affects the dryness of the steam at the turbine outlet. The slope of the saturated vapour curve of the fluid used in the Rankine cycle is given by ξ value. In this term, the fluid is classified as wet type when ξ value is less than zero. It is named as dry type when ξ value is greater than zero. It is classified as isentropic type when ξ value is equal to zero. In Table 2, the used fluids and its slopes are given.

Table 2. The properties of used refrigerants [24-28].

Fluid	Molecular Weight (g)	Critical Temperature (K)	Critical Pressure (kPa)	ODP	GWP	ξ	Type
R-134a	102.03	374.21	4059	0	1430	-0.39	Wet
R-13	104.46	301.88	3879	1	14400	-3.39	Wet
R-22	86.47	369.3	4990	0.05	1810	-1.33	Wet
R-123	152.93	456.83	3668	0.02	77	0.26	Dry
R-290	44.10	369.83	4200	0	3	-0.79	Wet
R-600	58.12	425.13	3796	0	4	1.03	Dry
R-	58.12	425.17	3800	0	3	1.03	Dry

Fluid	Molecular Weight (g)	Critical Temperature (K)	Critical Pressure (kPa)	ODP	GWP	ξ	Type
600A							
R-245fa	134.05	427.20	3651	0	1030	0.19	Isentropic

2.1. System Discription

In the purpose of the evaluating the waste heat, the ORC with three loops were designed. The flow diagram and *T-s* diagrams of the proposed system are given in Fig. 1 and Fig. 2, respectively.
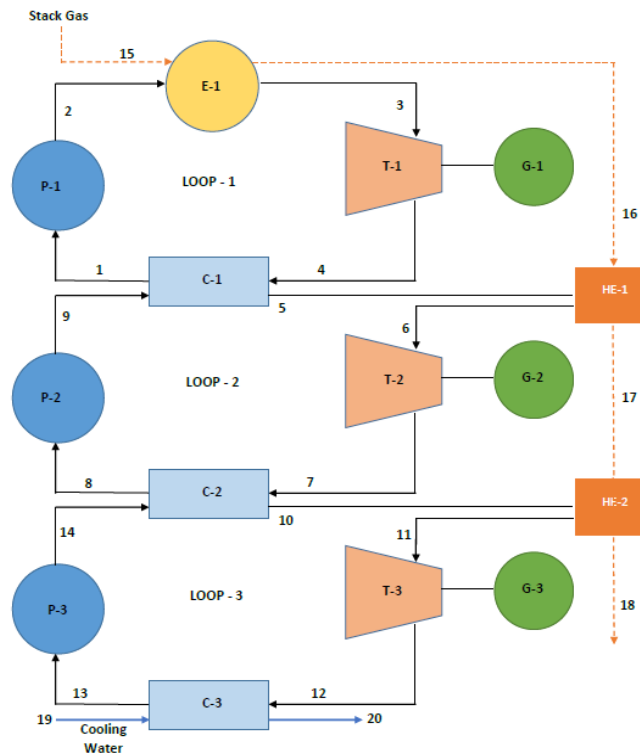
Figure 1. Flow diagram of designed system.

According to Fig 1, the working fluid enters pump 1 (P-1) of the first loop as saturated liquid at point 1 and leaves the pump at point 2. It enters the evaporator 1 (E-1) at the compressed liquid phase, where it draws heat energy from the waste heat source and becomes saturated liquid, then exits E-1. At point 3, the fluid entering the turbine 1 (T/G-1) leaves the T/G-1 as liquid-steam mixture, saturated steam or superheated steam at point 4, depending on the operating conditions. The fluid entering the condenser (C-1) condenses by giving its heat to the fluid in the lower loop.

In the second loop, the fluid enters P-2 as a saturated liquid at point 8 and leaves P-2 at point 9. It enters the condenser of the 1st loop, which is accepted as the pre-heater for the 2nd loop, and takes the waste heat, and enters the heat exchanger 1 (HE-1). In HE-1, the fluid takes the waste heat and leaves

the HE-1 in the saturated vapour phase at point 6. Fluid entering T/G-2 as saturated vapour leaves as superheated steam at point 7. The fluid entering C-2 condenses by giving its heat to the fluid in the 3rd loop, and enters P-2 again as a saturated liquid.

In the third loop, the fluid enters P-3 as a saturated liquid at point 13 and leaves P-3 at point 14. It enters the condenser of the 2nd loop, which is accepted as the pre-heater for the 3rd loop, and takes the waste heat, and enters to HE-2. In HE-2, the fluid takes the waste heat from and leaves the HE-2 in the saturated vapour phase at point 11. The fluid that enters T/G-3 as saturated vapour leaves as superheated vapour. The fluid entering the C-3 condenses by giving its heat to the cooling water.
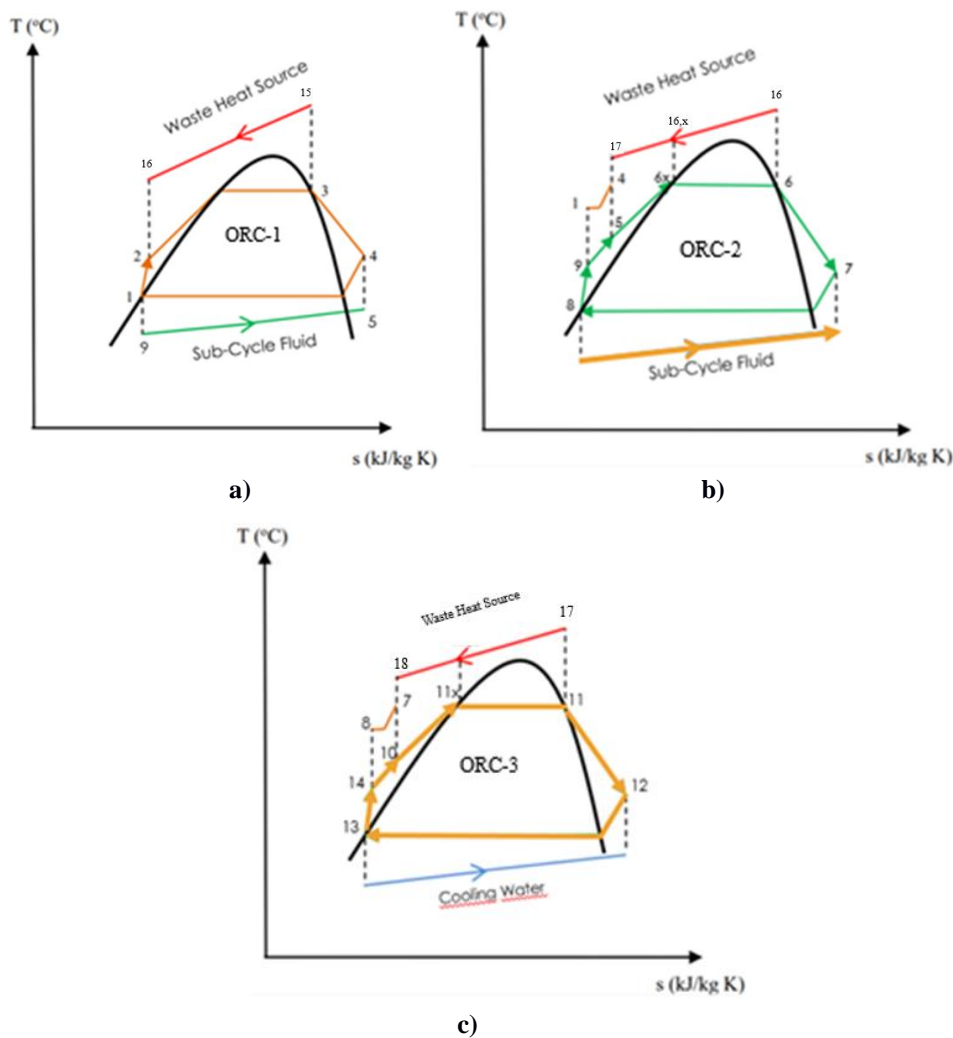
Figure 2. T-s graph of single loop (a) dual loop (b), and triple loop (c).

2.2. Energy Analysis

The conservation of mass and energy is the base of energy analysis. The mass balance, energy balance and energy efficiency equations are given as follows [29]:

$$\sum \dot{m}_{in} = \sum \dot{m}_{out} \tag{1}$$

$$\dot{Q} + \dot{W} = \sum \dot{m}_{out}\dot{h}_{out} - \sum \dot{m}_{in}\dot{h}_{in} \tag{2}$$

$$n_{th} = \frac{\dot{W}_{net}}{\dot{Q}_{net}} \tag{3}$$

The energy balances of the components of the proposed system are given in Table 3.

Table 3. The mass. energy and efficiency equations of the proposed system.

Component	Mass balance	Energy balance	Energy efficiency
E-1	$\dot{m}_2 = \dot{m}_3$ $\dot{m}_{15} = \dot{m}_{16}$	$\dot{Q}_{E-1} = \dot{m}(h_3 - h_2)$	$n_{E-1} = \dfrac{h_3}{h_2}$
T/G-1	$\dot{m}_3 = \dot{m}_4$	$\dot{W}_{T-1} = \dfrac{\dot{m}(h_3 - h_4)}{n_{T-1}}$	$n_{T-1} = \dfrac{h_4}{h_3}$
C-1	$\dot{m}_4 = \dot{m}_1$ $\dot{m}_9 = \dot{m}_5$	$\dot{Q}_{C-1} = \dot{m}(h_4 - h_1)$	$n_{C-1} = \dfrac{h_1}{h_4}$
P-1	$\dot{m}_1 = \dot{m}_2$	$\dot{W}_{P-1} = \dfrac{\dot{m}(h_2 - h_1)}{n_{P-1}}$	$n_{P-1} = \dfrac{h_2}{h_1}$
Loop-1	-	$(\dot{Q}_{E-1} - \dot{Q}_{C-1}) - (\dot{W}_{T-1} - \dot{W}_{P-1}) = 0$	$n_{th} = \dfrac{\dot{W}_{T-1} - \dot{W}_{P-1}}{\dot{m}(h_3 - h_2)}$
HE-1	$\dot{m}_{16} = \dot{m}_{17}$ $\dot{m}_5 = \dot{m}_6$	$\dot{Q}_{HE-1} = \dot{m}(h_6 - h_5) + \dot{m}(h_{17} - h_{16})$	$n_{HE-1} = \dfrac{h_6 + h_{17}}{h_5 + h_{15}}$
T/G-2	$\dot{m}_6 = \dot{m}_7$	$\dot{W}_{T-2} = \dfrac{\dot{m}(h_6 - h_7)}{n_{T-2}}$	$n_{T-2} = \dfrac{h_7}{h_6}$
C-2	$\dot{m}_7 = \dot{m}_8$ $\dot{m}_{14} = \dot{m}_{10}$	$\dot{Q}_{C-2} = \dot{m}(h_7 - h_8)$	$n_{C-2} = \dfrac{h_8}{h_7}$

P-2	$\dot{m}_8 = \dot{m}_9$	$\dot{W}_{P-2} = \dfrac{\dot{m}(h_9 - h_8)}{n_{P-2}}$	$n_{P-2} = \dfrac{h_9}{h_8}$
Loop-2	-	$(\dot{Q}_{HE-1} - \dot{Q}_{C-2}) - (\dot{W}_{T-2} - \dot{W}_{P-2}) = 0$	$n_{th} = \dfrac{\dot{W}_{T-2} - \dot{W}_{P-2}}{\dot{m}(h_6 - h_5)}$
HE-2	$\dot{m}_{17} = \dot{m}_{18}$ $\dot{m}_{10} = \dot{m}_{11}$	$\dot{Q}_{HE-2} = \dot{m}(h_{11} - h_{10})$	$n_{HE-2} = \dfrac{h_{11} + h_{18}}{h_{10} + h_{17}}$
T/G-3	$\dot{m}_{11} = \dot{m}_{12}$	$\dot{W}_{T-3} = \dfrac{\dot{m}(h_{11} - h_{12})}{n_{T-3}}$	$n_{T-3} = \dfrac{h_{12}}{h_{11}}$
C-3	$\dot{m}_{13} = \dot{m}_{12}$ $\dot{m}_{19} = \dot{m}_{20}$	$\dot{Q}_{C-3} = \dot{m}(h_{13} - h_{12})$	$n_{C-3} = \dfrac{h_{13}}{h_{12}}$
P-3	$\dot{m}_{13} = \dot{m}_{14}$	$\dot{W}_{P-3} = \dfrac{\dot{m}(h_{14} - h_{13})}{n_{P-3}}$	$n_{P-3} = \dfrac{h_{14}}{h_{13}}$
Loop-3	-	$(\dot{Q}_{HE-2} - \dot{Q}_{C-3}) - (\dot{W}_{T-3} - \dot{W}_{P-3}) = 0$	$n_{th} = \dfrac{\dot{W}_{T-3} - \dot{W}_{P-3}}{\dot{m}(h_{11} - h_{10})}$
Overall	-	$[(\dot{Q}_{E-1} + \dot{Q}_{HE-2} + \dot{Q}_{HE-3}) - (\dot{Q}_{C-1} + \dot{Q}_{C-2} + \dot{Q}_{C-3})]$ $-[(\dot{W}_{T-1} + \dot{W}_{T-2} + \dot{W}_{T-3}) - (\dot{W}_{P-1} + \dot{W}_{P-2} + \dot{W}_{P-3})] = 0$	n_{th} $= \dfrac{(\dot{W}_{T-1} + \dot{W}_{T-2} + \dot{W}_{T-3}) - (\dot{W}_{P-1} + \dot{W}_{P-2} + \dot{W}_{P-3})}{\dot{m}(h_{15} - h_{18})}$

In the analysis % is the efficiencies of the pumps, turbines and all heat exchangers were included in to calculations as 85%, 85% and 98%, respectively [11].

2.3. Exergy Analysis

Where the first law deals with energy balance, second law deals with irreversibility, entropy generation, and further exergy analysis. The exergy balance and exergy efficiency of the kth component is given as follows [29]:

$$\dot{E}x_{d.k} = \dot{E}x_k^Q + \dot{E}x_k^W + \sum \dot{m}_k \psi_i - \sum \dot{m}_k \psi_{out} \tag{4}$$

where $\dot{E}x_k^Q$. $\dot{E}x_k^W$ and ψ_i respectively indicate the exergy of heat exergy. exergy of work and specific flow exergy. They are given as follows [29]:

$$\dot{Ex}_k^Q = \sum (1 - \frac{T_0}{T})\dot{Q} \qquad (5)$$

$$\dot{Ex}_k^W = \sum \dot{W} \qquad (6)$$

$$\psi_i = (h_i - h_0) - T_0(s_i - s_0) \qquad (7)$$

$$\varepsilon_k = 1 - \frac{\dot{Ex}_{d.k}}{\dot{Ex}_{in.k}} \qquad (8)$$

The exergy balances of the components of the proposed system are given in Table 4.

Table 4. The exergy balance equations of the proposed system.

Component	Exergy balance	Exergy efficiency
E-1	$\dot{Ex}_{d.E-1} = (\dot{m}_2\psi_2 + \dot{m}_{15}\psi_{15}) - (\dot{m}_3\psi_3 + \dot{m}_{16}\psi_{16} + \sum \dot{Q}_{E-1}\left(1 - \frac{T_0}{T}\right))$	$n_{E-1} = \dfrac{\dot{E}_3 - \dot{E}_2}{\dot{E}_{15} - \dot{E}_{16}}$
T/G-1	$\dot{Ex}_{d.T/G-1} = (\dot{m}_3\psi_3) - (\dot{m}_4\psi_4 + \sum \dot{W}_{k,T/G-1})$	$n_{T/G-1} = \dfrac{\dot{W}_{T/G-1}}{\dot{E}_3 - \dot{E}_4}$
C-1	$\dot{Ex}_{d.C-1} = (\dot{m}_4\psi_4 + \dot{m}_9\psi_9) - (\dot{m}_5\psi_5 + \dot{m}_1\psi_1)$	$n_{C-1} = \dfrac{\dot{E}_1 - \dot{E}_4}{\dot{E}_9 - \dot{E}_5}$
P-1	$\dot{Ex}_{d.P-1} = \dot{m}_1\psi_1 - \dot{m}_2\psi_2 + \sum \dot{W}_{k,P-1}$	$n_{P-1} = \dfrac{\dot{E}_1 - \dot{E}_2}{\dot{W}_{P-1}}$
Loop-1	$\dot{Ex}_{d.E-1} + \dot{Ex}_{d.T/G-1} + \dot{Ex}_{d.C-1} + \dot{Ex}_{d.P-1}$	$n_{th} = \dfrac{\dot{W}_{T/G-1} - \dot{W}_{P-1}}{\dot{E}_{15} - \dot{E}_{16}}$
HE-1	$\dot{Ex}_{d.HE-1} = (\dot{m}_{16}\psi_{16} + \dot{m}_5\psi_5) - (\dot{m}_{17}\psi_{17} + \dot{m}_6\psi_6) + \sum \dot{Q}_{HE-1}\left(1 - \frac{T_0}{T}\right)$	$n_{HE-1} = \dfrac{\dot{E}_6 - \dot{E}_5}{\dot{E}_{17} - \dot{E}_{16}}$
T/G-2	$\dot{Ex}_{d.T/G-2} = (\dot{m}_6\psi_6) - (\dot{m}_7\psi_7 + \sum \dot{W}_{k,T/G-2})$	$n_{T/G-2} = \dfrac{\dot{W}_{T/G-2}}{\dot{E}_6 - \dot{E}_7}$
C-2	$\dot{Ex}_{d.C-2} = (\dot{m}_{14}\psi_{14} + \dot{m}_7\psi_7) - (\dot{m}_8\psi_8 + \dot{m}_{10}\psi_{10})$	$n_{C-2} = \dfrac{\dot{E}_8 - \dot{E}_7}{\dot{E}_{14} - \dot{E}_{10}}$
P-2	$\dot{Ex}_{d.P-2} = \dot{m}_8\psi_8 - \dot{m}_9\psi_9 + \sum \dot{W}_{k,P-2}$	$n_{P-2} = \dfrac{\dot{E}_8 - \dot{E}_9}{\dot{W}_{P-2}}$
Loop-2	$\dot{Ex}_{d.HE-2} + \dot{Ex}_{d.T/G-2} + \dot{Ex}_{d.C-2} + \dot{Ex}_{d.P-2}$	$n_{th} = \dfrac{\dot{W}_{T/G-2} - \dot{W}_{P-2}}{\dot{E}_{16} - \dot{E}_{17}}$
HE-2	$\dot{Ex}_{d.HE-2} = (\dot{m}_{17}\psi_{17} + \dot{m}_{10}\psi_{10}) - (\dot{m}_{18}\psi_{18} + \dot{m}_{11}\psi_{11}) + \sum \dot{Q}_{HE-1}\left(1 - \frac{T_0}{T}\right)$	$n_{HE-2} = \dfrac{\dot{E}_{11} - \dot{E}_{10}}{\dot{E}_{18} - \dot{E}_{17}}$

T/G-3	$\dot{Ex}_{d.T/G-3} = (\dot{m}_{11}\psi_{11}) - (\dot{m}_{12}\psi_{12} + \sum \dot{W}_{k,T/G-3})$	$n_{T/G-3} = \dfrac{\dot{W}_{T/G-3}}{\dot{E}_{11} - \dot{E}_{12}}$
C-3	$\dot{Ex}_{d.C-3} = (\dot{m}_{19}\psi_{19} + \dot{m}_{12}\psi_{12}) - (\dot{m}_{13}\psi_{13} + \dot{m}_{20}\psi_{20})$	$n_{C-3} = \dfrac{\dot{E}_{13} - \dot{E}_{12}}{\dot{E}_{19} - \dot{E}_{20}}$
P-3	$\dot{Ex}_{d.P-3} = \dot{m}_{13}\psi_{13} - \dot{m}_{14}\psi_{14} + \sum \dot{W}_{k,P-3}$	$n_{P-3} = \dfrac{\dot{E}_{13} - \dot{E}_{14}}{\dot{W}_{P-3}}$
Loop-3	$\dot{Ex}_{d.HE-3} + \dot{Ex}_{d.T/G-3} + \dot{Ex}_{d.C-3} + \dot{Ex}_{d.P-3}$	$n_{th} = \dfrac{\dot{W}_{T/G-3} - \dot{W}_{P-3}}{\dot{E}_{17} - \dot{E}_{18}}$
Overall	$\dot{Ex}_d = \sum \dot{Ex}_{d,k}$	$n_{th} = \dfrac{\sum \dot{W}_{T/G} - \sum \dot{W}_P}{\dot{E}_{15} - \dot{E}_{18}}$

3. RESULT

The parametric analyses were conducted to evaluate the performance of the proposed system. The used parameters are given in Table 5.

Table 5. The design parameters of the proposed system.

Fixed values	Temperature of waste heat	185 °C – 207 °C
	Coolant Temperature	27 °C
	Condenser Inlet Pressure	900 kPa
Independent variables	Organic Fluids	R290, R22, R123,R134a,R13,R245fa;R600,R600a
	Turbine Inlet Pressure Range	1200 kPa to 2500kPa
	Turbine Inlet Temperature Range	65°C to 80 °C

3.1. The Results of Energy Analysis

The selected fluids were analyzed by energy method. The obtained results are given in Table 6. In Table 6, the fluids were evaluated to determine the available selections as the first decision.

Table 6. Energy efficiency values of the proposed system for the first decision stage.

Temp.	R134A	R13	R22	R123	R245FA	R290	R600	R600a
65 °C	21.45%	0.83%	12.51%	19.97%	19.39%	14.48%	19.62%	19.60%
67 °C	23.06%	0.86%	14.35%	20.04%	19.45%	18.70%	19.70%	19.69%
68 °C	24.46%	0.89%	18.49%	20.12%	19.51%	20.44%	19.78%	19.77%
70 °C	25.69%	0.92%	20.10%	20.19%	19.57%	21.98%	19.86%	19.85%
72 °C	26.67%	0.95%	21.54%	20.26%	19.64%	23.35%	19.93%	19.93%
73 °C	27.73%	0.98%	22.85%	20.33%	19.70%	24.58%	20.01%	20.01%
75 °C	28.57%	1.91%	24.03%	20.40%	19.76%	25.69%	20.09%	20.09%
77 °C	29.32%	3.34%	25.11%	20.48%	19.82%	26.68%	20.16%	20.17%

Temp.	R134A	R13	R22	R123	R245FA	R290	R600	R600a
78 °C	28.95%	4.66%	26.10%	20.55%	19.88%	27.57%	20.24%	20.25%
80 °C	20.34%	5.89%	27.00%	20.62%	19.94%	28.38%	20.32%	20.33%

According to Table 6, the calculations were made for various organic fluids and the three most efficient were selected for analysis of looped system. These fluids were determined as R290, R13, and R123.

3.2. The Case of R290 Use in Each Cycle

In the first stage of the analysis, the calculations were made by using the most efficient fluid of R290 in single, dual, and triple looped cases. First, the ORC with single loop is evaluated. Then, dual and triple looped cases were handled. For the turbine inlet temperature, a temperature difference of 5 $^{\circ}$C was taken into account for each loop. The inlet pressure was taken as 2500 kPa. Fig. 3 shows the cycle efficiencies according to the variation of the turbine inlet temperature (T_3).
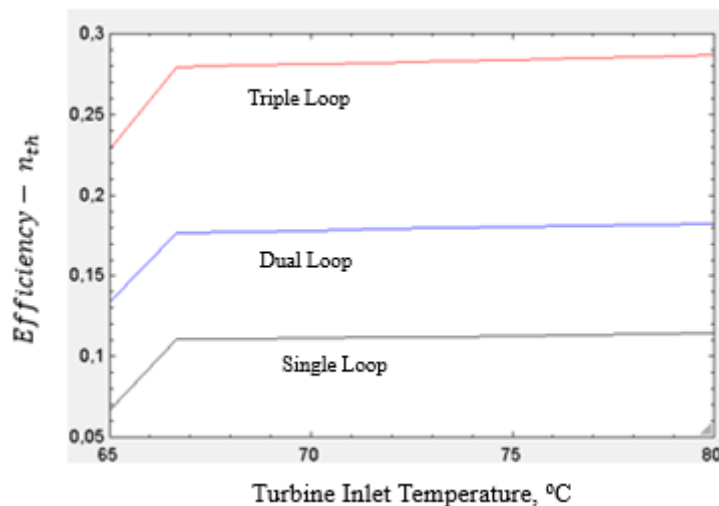
Figure. 3. Variation the energy efficiency versus Turbine-1 inlet temperature for R290.

According to Fig. 3, the efficiency ranges between 6% and 11% for the single looped system. It ranges between 13.5% and 18% for dual looped system where it ranges between 23% and 28% for triple looped system. According to the obtained results, the optimum configuration was determined for 66.5 $^{\circ}$C where a sharp breaking point was observed considering the economical factors. Fig. 4 shows the cycle efficiencies according to the variation of the turbine inlet pressure (P_3).
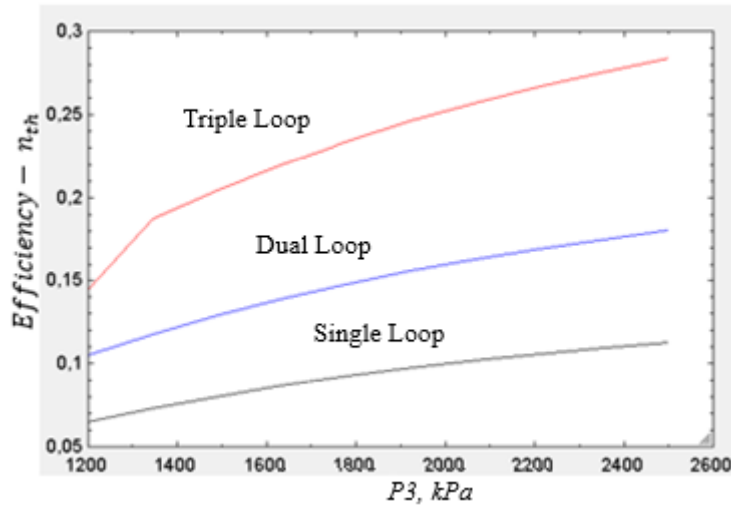
Figure. 4. Variation the energy efficiency versus P_3 for R290 (T_3=80 ^{o}C).

According to Fig. 4, the efficiency ranges between 6.5% and 11% for the single looped system. It ranges between 10.5% and 17.0% for dual looped system where it ranges between 14.5% and 28.4% for triple looped system. According to the obtained results, the optimum configuration was determined for 2500 kPa which is the available maximum.

3.3. The Case of Using R290 in the First Cycle and R22 in the Second and Third Cycles
In the second stage of the analysis, the calculations were made by using the most efficient fluid of R290 in single, and R22 dual and triple looped cases. First, the ORC with single loop is evaluated. Then, dual and triple looped cases were handled. For the turbine inlet temperature of the loops, a temperature difference of 5 ^{o}C was taken into account. The inlet pressure was taken as 2500 kPa. Fig. 5 shows the cycle efficiencies according to the variation of the turbine inlet temperature (T_3).
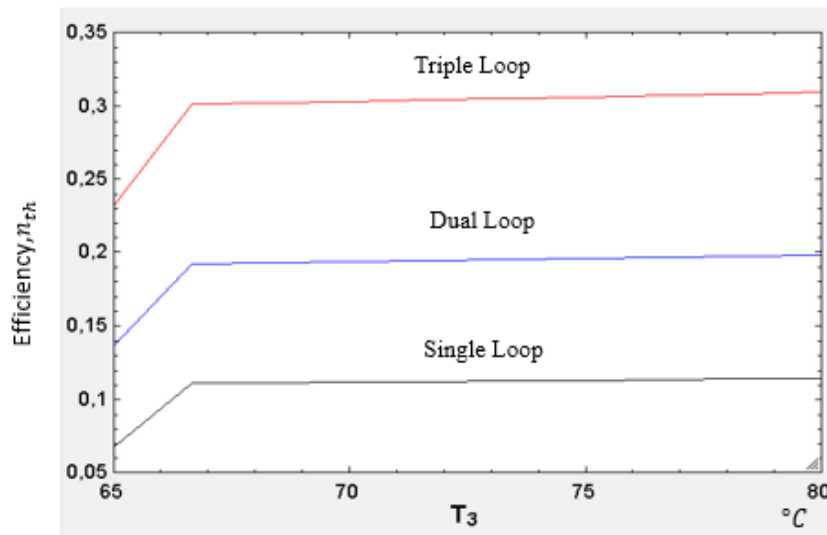
Figure 5. Variation the energy efficiency versus T_3 for fluid of R290 single loop and fluid of R22 dual and triple loop.

According to Fig. 5, the efficiency ranges between 7% and 11% for the single looped system. It ranges between 14% and 19% for dual looped system where it ranges between 23.5% and 30.5% for triple looped system. According to the obtained results, the optimum configuration was determined for 66.8 °C again where a sharp breaking point was observed considering the economical factors. Fig. 6 shows the cycle efficiencies according to the variation of the turbine inlet pressure (P_3).
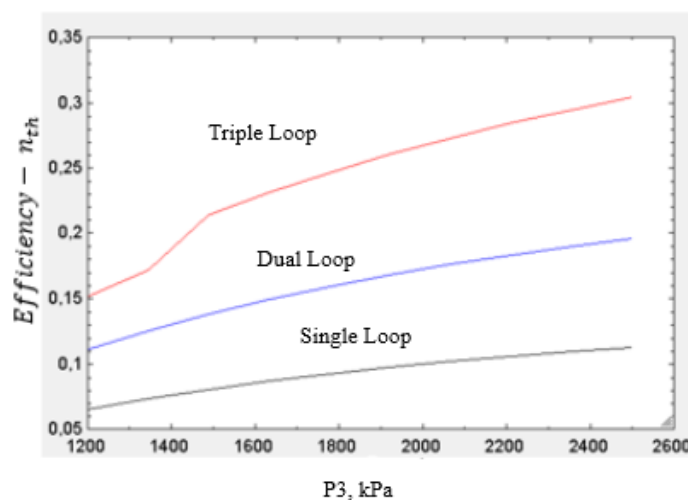
Figure 6. Variation the energy efficiency versus P_3 for single loop R290 and fluid of R22 for dual and triple loop (T_3=80 °C).

According to Fig. 6, the efficiency ranges between 6.5% and 11% for the single looped system. It ranges between 11% and 17% for dual looped system where it ranges between 15% and 30.5% for triple looped system. According to the obtained results, the optimum configuration was determined for 2500 kPa which is the handle maximum.

3.4. The Case of Using R290 in the First Cycle, R22 in the Second Cycle, and R123 in the Third Cycle

In the final stage of the analysis, the calculations were made by using the most efficient fluid of R290 in single, R22 in dual and f R123 in triple looped cases. First, the ORC with single loop is evaluated. Then, dual and triple looped cases were handled again. The inlet pressure was taken as 2500 kPa. Fig. 7 shows the cycle efficiencies according to the variation of the turbine inlet temperature (T_3).
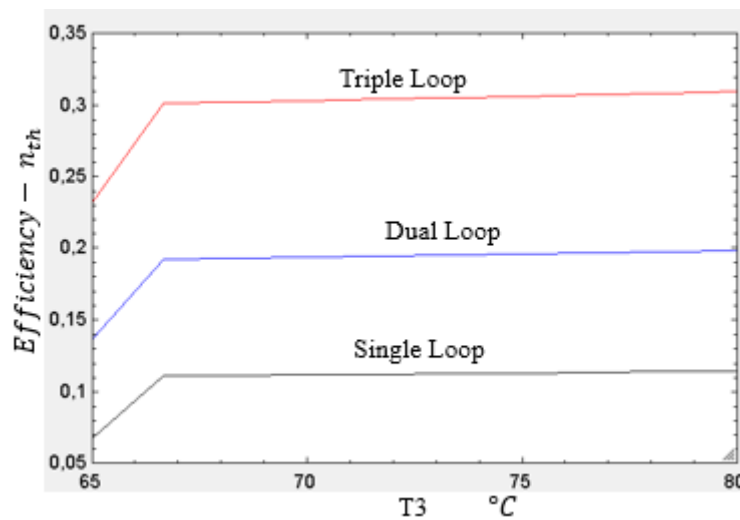
Figure 7. Graphic of the calculation results for three different fluid and parametric temperatures

According to Fig. 7, the efficiency ranges between 7% and 11.5% for the single looped system. It ranges between 14% and 20% for dual looped system where it ranges between 23.5% and 31% for triple looped system. According to the obtained results, the optimum configuration was determined for 66.8 ^{o}C where a sharp breaking point was observed considering the economical factors as in the other cases. Fig. 8 shows the cycle efficiencies according to the variation of the turbine inlet pressure (P_3).
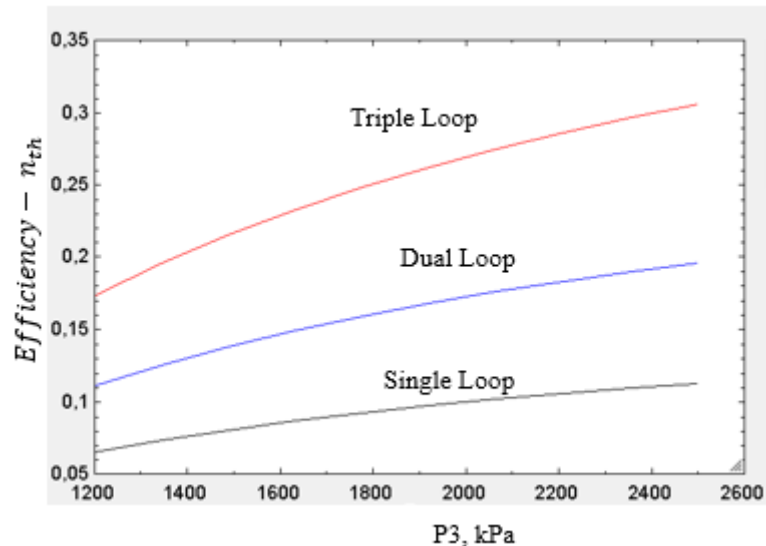
Figure 8. Graphic of the calculation results in three different fluid and parametric pressure conditions.

According to Fig. 8, the efficiency ranges between 6.5% and 11% for the single looped system. It ranges between 11% and 18% for dual looped system where it ranges between 17.5% and 31% for triple looped system. According to the obtained results, the optimum configuration was determined for 2500 kPa which is the handle maximum.

Although simple one-cycle Rankine cycles are the most frequently used systems, the use of two or more cycle systems has increased recently. As can be seen in this study, when the number of cycles increased to two as a result of the analyzes made with the EES software. the efficiency increased significantly. Since the cost of each cycle is significant, the decision should be made after the economic evaluation for two or three looped systems. One of the main aims of the study is to understand the effect of the fluids used on efficiency. When the same fluid (R290) is used in each cycle, the maximum efficiency is 29% for parametric temperature and pressure. When two different fluids are used, it is 30%. Finally for the different fluids in each loop, it is 31%. The thermo-physical properties of the best design are given in Table7.

Table 7. Thermo-physical properties of the best ORC design.

Points	Fluid	m (kg/s)	T (^{o}C)	P (kPa)	h (kJ/kg)	S (kJ/)kgK	ψ	Ex
0	Stack gases	-	25	100	309.3	6.839	-	-
0	R290	-	25	100	630.8	2.849	-	-
0	R22	-	25	100	429.3	1.984	-	-
0	R123	-	25	100	226.2	1.091	-	-
0	Water	-	25	100	104.8	0.3669	-	-
1	R290	6.55	27	925	271	1.226	1392	58089
2	R290	6.55	28.2	2758	387.8	1.75	3023	126153

3	R290	6.55	80	2500	691.9	2.408	5169	215707
4	R290	6.55	48.34	971.6	644.3	2.408	4629	193172
5	R22	15.44	22	1960	226.6	1.129	1144	572447
6	R22	15.44	80	2500	448.8	1.709	2975	1488663
7	R22	15.44	33.43	596.2	422.4	1.709	2594	1298014
8	R22	15.44	20	584.3	225.4	1.026	8596	430136
9	R22	15.44	21.59	2000	229.7	1.217	1402	701548
10	R123	61.08	18	980	219.2	1.204	1362	2261032
11	R123	61.08	75	2500	285.9	1.242	1481	2458581
12	R123	61.08	10.48	369.5	276.1	1.242	140	2324115
13	R123	61.08	10	362.1	210.8	1.011	8205	1362097
14	R123	61.08	12.5	1000	213.3	1.014	8357	1387331
15	Stack gases	32.61	207	120	495.5	3.496	2566	975080
16	Stack gases	32.61	148.5	120	433.7	3.282	2201	836380
17	Stack gases	32.61	119.3	120	401	7.033	1211	460180
18	Stack gases	32.61	89.7	120	381	6.99	1066	405080
19	Water	6.18	-5	100	-343.4	-1.259	-4076	-1223615
20	Water	6.18	7	100	301.8	0.01066	-929	-278886

According to values given in Table 7, the results of exergy analysis on the component basis are given in Table 8.

Table 8. Exergy analysis results of the best ORC design.

Components	Q (kW)	W	Eg	Ec	Exg	Exc	Exd	η (%)	E (%)
E-1	1991.62	-	485066.92	733256.02	331980.37	562488.74	171821.53		
T/G-1	-	265.01	733256.02	674942.56	562488.74	504175.28	49571.93		
C-1	1680.07	-	674942.56	291567.28	504175.28	291567.28	166045.09		
P-1	-	25.43	291567.28	485066.92	291567.28	331980.37	34622.38		
Loop-1	311.55	239.58						**11%**	**12%**
HE-1	994.11		1505180.00	1485420.00	830680.00	460180.00	-387789.82		
T/G-2		346.47	571367.40	521855.04	389383.13	339739.08	42138.18		
C-2	47.86		521855.04	272976.40	339739.08	113193.69	22333.24		
P-2		30.88	272976.40	352380.54	113193.69	184617.91	69676.80		
Loop-2	946.24	315.6						**31%**	**44%**
HE-2	1029.52		1485420.00	1428040.00	454100.00	402800.00	-78901.05		
T/G-3		508.80	119788.02	116293.11	64437.39	60986.17	2951.89		
C-3	152.71		116293.11	88683.33	60986.17	35844.67	2284.80		
P-3		152.7	88683.33	89382.31	35844.67	36508.70	338.31		
Loop-3	876.81	356.1						**34%**	**48%**
Overall	2134.6	911.28						**23%**	**34%**

According to Table 8, the highest exergy destruction was occurred in E-1 with a value of 1991.62 kW in Loop-1; P-2 with a value of 30.88 kW in LOOP-2 and T/G-3 with a value of 508.8 kW in LOOP-3. The energy and exergy efficiencies of Loop-1 were determined as %11 and %12 respectively. The energy and exergy efficiencies of Loop -2 were determined as %31 and %44, respectively. The energy and exergy efficiencies of Loop -3 were determined as %34 and %48. For the overall system, the energy and exergy efficiencies were determined as % 23 and %34 respectively.

4. CONCLUSION

In this study the organic Rankine cycle with multi-loop was analyzed by energy and exergy method. EES software was used in the calculations. The waste heat of a ceramic factory was evaluated for this purpose to reduce energy costs.

One of the main aims of the study is to understand the effect of the fluids used on efficiency. In the analysis, the maximum efficiency is 29% when the same fluid (R290) is used in each cycle. It is 30% if two different fluids are used. It is 31% if different types of fluids are used in each loop. This means that using different types of fluid in each loop gives the most efficient result.

The results obtained showed that the efficiency increases with the increase of loop number. However, it is issue that the initial investment cost of each loop corresponds to significant amounts. So, it is necessary to handle an economic evaluation.

ACKNOWLEDGMENT

REFERANCES

[1] Tchanche, B., Lambrinos, G., Frangoudakis, A. and Papadakis, G. (2011), Low-Grade Heat Conversion Into Power Using Organic Rankine Cycles-A Review of Various Applications Renewable and Sustainable Energy Reviews vol 15 no 8 pp 3963-3979.

[2] Arslan, O., Ozgur, M.A. and Kose, R. (2012), Electricity generation ability of Simav geothermal field: A technoeconomic approach. Energy Sources, Part A, 34: 1130– 1144.

[3] Boukelia, T.E., Arslan, O., Bouraoui, A., (2021), Thermodynamic performance assessment of a new solar tower-geothermal combined power plant compared to the conventional solar tower power plant, Energy, Volume 232, 121109.

[4] Arslan, O., Erbas, O., Ozgur, M.A. and Kose, R. (2012), ANN based optimization of b2 and b3 types of ORC-Binary geothermal power plant: Simav case study. Energy Education Science and Technology Part A: Energy Science and Research, 28(2): 1039–1050.

[5] Arslan, O. (2015), ANN Approximation of Geothermal Aided Power Cycles Energy Sci. and Tech. Vol. 9: Geothermal and Ocean Environment, Chapter 7., pp: 163-188. Studium Press LLC, USA.

[6] Arslan, O. and Yetik, O. (2014), ANN modelling of ORC-binary geothermal power plant: Simav case study. Energy Sources, Part A, 36: 418–428.

[7] Arslan, O. , Ergenekon Arslan, A. and Şentürk Acar, M. (2019), Multi-Criteria Making-Decision Modeling of b-type ORC-Binary Geothermal Power Plant: EATWOS Analysis . Bilecik Şeyh Edebali Üniversitesi Fen Bilimleri Dergisi , 6 (1) , 29-48 . DOI: 10.35193/bseufbd.561668.

[8] Arslan, A.E., Arslan, O. and Kandemir, S.Y. (2021), AHP–TOPSIS hybrid decision-making analysis: Simav integrated system case study. J Therm Anal Calorim 145, 1191–1202

[9] Arslan, A.E, Senturk, M.A, Arslan, O. (2018), Effectiveness analysis of orc-binary geothermal power plant using data enveloping. Proceedings of International Congress ON Afro-Eurasian Research IV, pp: 109-117, April 27-29, 2018, Budapest, Hungary.

[10] Arslan, A.E, Senturk, M. A, Arslan, O. (2018), Data enveloping based effectiveness analysis of integrated geothermal system: Simav case study. Proceedings of International Congress ON Afro-Eurasian Research IV, pp: 118-124, April 27-29, 2018, Budapest, Hungary.

[11] Arslan,, O., Kılıç D., (2021), Concurrent optimization and 4E analysis of organic Rankine cycle power plant driven by parabolic trough collector for low-solar radiation zone, Sustainable Energy Technologies and Assessments, Volume 46, 101230.

[12] Erikgenoğlu, D., Arslan O., (2021), Artificial neural network modelling of parabolic trough types solar thermal power plant, Turkish Journal of Electromechanics and Energy Vol 6, No 3

[13] Varga, Z., Varga, R., Istvan, C. and Farkas C., (2012), Waste Heat Recovery with Organic Rankine Cycle in the Petroleum Industry Researchgate

[14] Chen, C., Li, P., Le, S., (2016), Organic Rankine Cycle for Waste Heat Recovery in a Refinery American Chemical Society

[15] Arslan, O., Acıkkalp, E., Genç, G.,(2022), A multi-generation system for hydrogen production through the high-temperature solid oxide electrolyzer integrated to 150 MW coal-fired steam boiler Fuel, Volume 315, 123201, ISSN 0016-2361.

[16] Arslan, O., (2021), Performance analysis of a novel heat recovery system with hydrogen production designed for the improvement of boiler effectiveness, International Journal of Hydrogen Energy, Volume 46, Issue 10, 7558-7572.

[17] Arslan, O., Yetik, O., (2011), ANN based optimization of supercritical ORC-Binary geothermal power plant: Simav case study, Applied Thermal Engineering , 2011 , 31 , 17-18 , 3922-3928

[18] Hung, T. (2001), Waste heat recovery of organic Rankine cycle using dry fluids, Energy Conversion and Management, Volume 42, pp:539-553

[19] Ouyang, T., Su, Z., Huang, G., Zhao, Z., Wang, Z., Chen, N. and Huang, H., (2019), Modeling and Optimization of a Combined Cooling Cacaded Power and Flue Gas Purification System in Marine Diesel Engines. Energy Conversion and Management,151, pp:286-295.

[20] Sciubba, E., Tocci, L., Toro, C., (2016), Thermodynamics Analysis of a Rankine Dual Loop Waste Thermal Energy Recovery System, Energy Conversion and Management,122, pp: 109-118, 2016.

[21] Braimakis, K. and Karellas, S., (2018), Exergetic Optimisation of double stage Organic Rankine Cycle (ORC), Energy,2018. doi: 10.1016/j.energy.2018.02.044.

[22] Xia, X., Wang, Z., Zhou, N., Hu, Y., Zhang, J. and Chen, Y., (2020), Working Fluid Selection of Dual-Loop Organic Rankine Cycle Using Multi-Objective Optimization and Improved Grey Relational Analysis, Applied Thermal Engineering,171.

[23] Ceylan, I. (2022), Design and Optimization of Staged ORC Power Plant by Waste Heat. Unpublished Master's Thesis, University of Bilecik Şeyh Edebali, Turkey.

[24] Kavasoğulları. B. and Han. E. (2015), Organik Rankine Çevrimi (ORC) ile Birlikte Çalışan Buhar Sıkıştırmalı Bir Soğutma Çevriminin Ekserji Analizi. Tesisat Mühendisliği. P.150.

[25] He, C., Liu, C., Gao, H., Xie, H., Li, Y., Wu, S., (2012), The optimal evaporation temperature and working fluids for subcritical organic Rankine cycle. Energy, 38,136-143.

[26] Lai, N.A, Wendland, M, Fischer J., (2011), Working fluids for high-temperature organic Rankine cycles. Energy, 36, 199-211.

[27] Sauret, E, Rowlands, A.S., (2011), Candidate radial-inflow turbines and high-density working fluids for geothermal power systems. Energy,36,4460-4467.

[28] Nouman, J. (2012), Comporative studies and analyses of working fluids for Organic Rankine Cycle-ORC, KTH Industrial Engineering and Management, Master of Science Thesis, Stockholm, pp 83-87, 2012

[29] Çengel, Y. and Boles, M. (2012), Thermodynamics: An Engineering Approach 5 Edition.

NOMENCLATURE

C-1 : Condenser-1
C-2 : Condenser-2
C-3 : Condenser-3
E : Exergy Efficiency
E-1 : Evaporator-1

Ec	**:**	Energy outlet			
Eg	**:**	Energy inlet			
EES	**:**	Engineering Equation Solver			
Exc	**:**	Exergy outlet			
Exd	**:**	Exergy			destruction
Exg	**:**	Exergy inlet			
GWP	**:**	Global	Warming		Potential
h	**:**	Enthalpy			
HE-1	**:**	Heat Exchanger-1			
HE-2	**:**	Heat Exchanger-2			
ODP	**:**	Ozone Depletion Potential			
P	**:**	Pressure			
P-1	**:**	Pump-1			
P-2	**:**	Pump-2			
P-3	**:**	Pump-3			
Q	**:**	Heat Energy			
s	**:**	Entropy			
T	**:**	Temperature			
T/G-1	**:**	Turbine/Generator-1			
T/G-2	**:**	Turbine/Generator-2			
T/G-3	**:**	Turbine/Generator-3			
W	**:**	Work			
η	**:**	Efficiency			

RESEARCH ARTICLE

INVESTIGATION of ACTIVITIES ENZYME PROLIDASE (PRO) and GLUTATHIONE S-TRANSFERASE (GST) in POLYCYSTIC OVARY SYNDROME (PCOS) PATIENTS

Kazım UÇKAN[1,*], Halit DEMİR[2], Yusuf BAŞKIRAN[3], Canan DEMİR[4]

[1]Van Yüzüncü Yıl University, Medical Faculty, Van, druckan65@hotmail.com, ORCID: 0000-0002-5576-6789
[2]Van Yüzüncü Yıl University, Medical Faculty, Van, halitdemir@yyu.edu.tr, ORCID: 0000-0001-5598-2601
[3]SBU Van Regional Training and Research Hospital, Van, yusufbaskiran1@gmail.com, ORCID: 0000-0003-1123-6062
[4]Van Yüzüncü Yıl University, Vocational School of Health Services, Van, canandemir@yyu.edu.tr, ORCID: 0000-0002-4204-9756

ABSTRACT

This study investigated serum antioxidant enzyme activity (Glutathione-S-transferase) and Prolidase in patients with PCOS.

A total of 42 patients with PCOS and 43 healthy control subjects were enrolled. Serum Prolidase and Glutathione-S-transferase (GST) activities were measured spectrophotometrically.

Age, TSH, fT4, Prolactin, Estradiol, FSH, systolic and diastolic blood pressure parameters were not statistically significant between PCOS group and healthy control group. BMI, weight, height, waist-hip ratio, menstrual cycle, FGS, FPG, LH, Insulin, androstenedione, SHBG, total testosterone parameters were statistically significantly increased in the PCOS group compared to the healthy control group. The serum glutathione-S-transferase was significantly decreased ($p < 0.05$) in patients with PCOS, compared with control subjects. Prolidase (Pro) activity has been found to be significantly higher in women with PCOS than in the control group.

Antioxidant enzyme GST activity has found to be decreased in PCOS patient group. Prolidase (Pro) enzyme is a candidate to be a leading parameter in the elucidation of the disease. In conclusion, the activities of glutathione-S-transferase and Prolidase (Pro) enzymes may be precursors in the etiopathogenesis of PCOS. This study has done in the literature for the first time. In addition, more work should be done in this area.

Keywords: *PCOS, Prolidase, Glutathione-s-transferase (GST)*

1. INTRODUCTION

Polycystic ovary syndrome (PCOS), which affects fertile women, is known as one of the endocrine disorders. This extended disorder of unknown aetiology is characterized by three fundamental properties: chronic anovulation, hyperandrogenism and ultrasonographic evidence of polycystic

ovaries [1, 2]. In metabolism, antioxidants may decrease if oxidative stress increases. [3]. There are many different types of antioxidants [4,5]. Collagen is a very large component of extracellular matrix (ECM) [6]. The Glutathione-S-transferase (GST) has first described in 1961 by Booth et al. [7].Glutathione-s-transferase neutralizes electrophilic xenobiotics. Also, it is the dimeric enzymes that provide the excretion from the body [8,9] . Thanks to its antioxidant effects, the GST family is effective in the destruction of harmful reactive oxygen derivatives formed in the case of oxidative stress. It has been reported that changes in the genetic or structural structure of GST enzymes may cause many diseases, especially PCOS, in women [10]. Prolidase (E.C. 3.4.13.9) is involved in collagen synthesis and recovery of proline for cell growth, and also acts as an interface between protein nutrition and matrix breakdown [11]. Prolidase enzyme activity has been studied in various disorders, such as chronic liver disease; diabetic neuropathy, renal cell carcinoma, acute hemorrhagic stroke, osteoporosis, osteoarthritis, uremia and helicobacter pylori infection [12-19]. Collagen and extracellular matrix proteins are powerful in the regulation of cellular events, tissue stabilization and prevention of invasion. Matrix metalloproteinases (MMP) break down collagen, leading to the spread of diseases. Prolidase is active in matrix remodeling and collagen turnover, as it is a member of the MMP family [20]. It has stated in the study conducted by Wilk et al. that that increased prolidase levels in parallel with the abnormalities in collagen metabolism are associated with malignant diseases. It was determined that the microenvironment of the tumor was reorganized and its invasiveness increased thanks to the increased prolidase levels [21]. In a study conducted in endometrial cancers, it has found that prolidase levels increased and it could be associated with focal invasion [22]. Our aim is to reveal the relationship between enzymatic glutathione-S-transferase (GST) and prolidase (Pro) in PCOS.

2. SUBJECTS and METHODS
The study cases were enrolled from patients and healthy individuals presenting to the gynecology department in Van Training and Research Hospital.This study was performed on 42 (mean age of 24.2±5.9) women patients with PCOS and 43 (mean age of 23.7±4.4) healthy women volunteers with no history of PCOS. We received ethics committee approval for laboratory studies.

Blood of both patient and control groups were taken. Sera were obtained by separating them in a centrifuge at 5,000 rpm for 10 minutes. It was then stored at -85˚C.Determination of activity enzyme prolidase (Pro). Prolidase activity was performed according to the method developed by Myara et al. [23] . The definition of pcos is made according to the Rotterdam Criteria. These criteria include hyperandrogenism, oligoanovulation, and ultrasound image compatible with polycystic ovary morphology.[24]

2.1. Determination of Glutathione-S-transferase Activity (GST).
Glutathione S transferase activity (GST) has determined accordingto Habig et al., [25].

2.2. Statistical Analysis
Comparisons were made between groups. T-test was performed in the normal distribution condition was fulfilled. The Mann Whitney U test was performed when it was not meet the normal distribution condition. The Pearson correlation coefficient was calculated. Also, Spearman's rank correlation coefficient was measured. Significance level $p<0.05$ was considered significant. The data analysis was made in the SPSS (ver: 13) package program.

3. RESULTS

Age, TSH, fT4, Prolactin, Estradiol, FSH, systolic and diastolic blood pressure parameters were not statistically significant between PCOS group and healthy control group. BMI, weight, height, waist-hip ratio, menstrual cycle, FGS, FPG, LH, Insulin, androstenedione, SHBG, total testosterone parameters were statistically significantly increased in the PCOS group compared to the healthy control group.

The serum Glutathione-s-transferase (GST) was significantly decreased (p<0.05) in patients with PCOS, compared with control subjects. Prolidase (Pro) activity has been found to be significantly higher in women with PCOS than in the control group.

Table 1. Parameters biochemical Glutathione-s-transferase and Prolidase (Pro).

	Control group (n=43)	PCOS group (n=42)	P value
Age(year)	23.7±4.4	24.2±5.9	0.311
BMI (kg/m2)	22.63±4.10	27.98±2.78	0.001
Weight(kg)	64.23±5.52	75.13 ±4.56	0.001
Height(cm)	165.34±6.43	160.23 ±4.10	0.001
Waist-hip ratio(cm)	0.66±0.17	0.78±0.15	0.001
SBP (mmHg)	115.12±11.33	122.20 ±6.60	0.324
DBP (mmHg)	75.10±4.46	78.13 ±4.12	0.231
Menstruel cycle (day)	22.11±6.2	66.45 ±14.16	0.001
FGS	5.67 ±1.01	12.17±5.34	0.001
TSH (uIu /dl)	1.54±0.77	1.76±1.21	0.546
T4(ng/dl)	14.4±1.28	15.7±1.47	0.332
E2(pg/ml)	47.23±9.23	48.6±11.34	0.340
FPG (mg/dl)	84.13±7.65	127.45±11.67	0.001
FSH (mu /ml)	5.2±1.68	4.8±0.98	0.237
LH (mu /ml)	4.56±1.45	8.45±1.96	0.001
Insulin (U/ml)	5.35±1.22	9.54±1.34	0.001
Androstenedion(ng/ml)	1.55±0.72	4.32±1.11	0.001
SHBG (nmol/l)	132.13±9.21	66.32±11.34	0.001
Total Testosteron (ng/ml))	1.29±0.48	4.45±1.35	0.001
Prolactin (ng/ml)	16.80±2.45	21.9±3.6	0.538
Pro(U/L)	58.616 ± 2.991	149.679 ± 30.591	0.001
GST(U/L)	0.0291 ± 0.0146	0.0044 ± 0.0028	0.001

Table 2. Correlation between parameters in patient with PCOS.

	Prolidase	GST	Androstenedion	BMI	E2	FGS	FSH	LH	Prolaction	Total Testesteron	TSH	Whr	Age
Prolidase(U/L)	1												
GST(U/L)	0,064	1											
Androstenedion(ng/ml)	-0,067	0,093	1										
BMI(kg/m2)	-0,051	0,204	-0,154	1									
E2(pg/ml)	0,241	-0,066	0,211	-0,041	1								
FGS	0,114	-0,149	0,019	0,171	**0,420****	1							
FSH(mu/ml)	0,141	-0,023	**0,330***	0,021	0,106	**0,300***	1						
LH(mu/ml)	0,017	**0,343***	0,03	0,265	0,012	0,186	-0,147	1					
Prolaction(ng/ml)	-0,092	0,099	-0,026	-0,117	**-0,309***	**-0,302***	0,068	**-0,308***	1				
Total Testesteron(ng/ml)	0,038	0,12	**0,619****	0,178	0,193	0,079	**0,313***	-0,115	-0,143	1			
TSH(ulu/dl)	-0,122	0,077	0,062	0,083	-0,006	0,088	-0,1	**0,286***	**-0,283***	0,141	1		
Whr	0,022	-0,108	0,133	0,071	0,202	0,25	0,061	0,015	-0,213	0,021	0,268	1	
Age	-0,097	0,068	-0,122	**0,461****	0,128	0,252	-0,205	0,262	**-0,318***	0,004	0,151	-0,036	1

*Corelation is significant at the 0.05 level (2tailed)

**Corelation is significant at the 0.01 level (2tailed)

34% between GST and LH, 33% between Androstendion and Fsh, 62% between Androstendion and Testesterone, 46% between BMI and age, 42% between E2 and FGS, 30% between FGS and Fsh,%31 between Fsh and Testesterone, 29% between LH and TSH positive, 31% between E2 and Prolactin, 30% between FGS and Prolactin, 31% between LH and Prolactin, 28% between Prolactin and TSH, 32% between Prolactin and age negative and statistically significant a significant correlation was found (p <0.05).
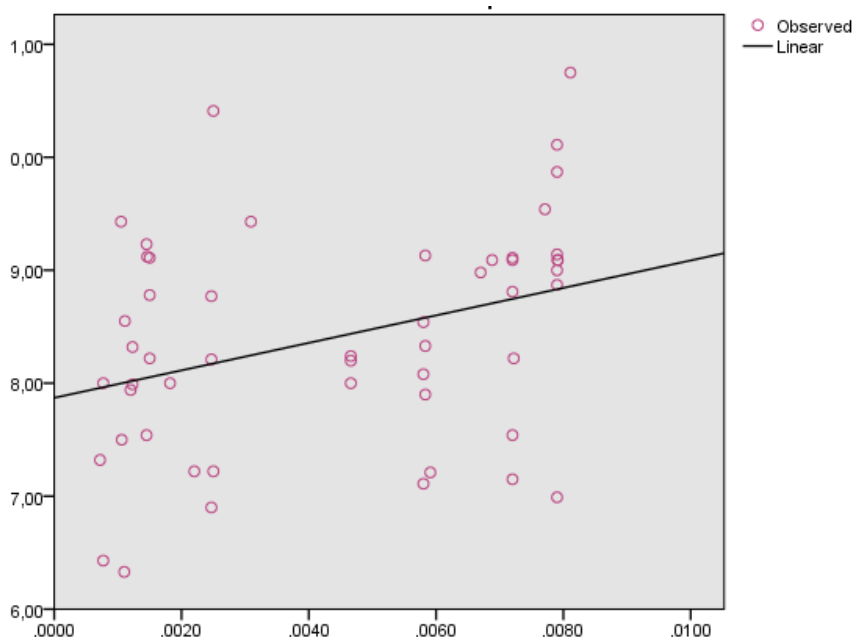
Figure 1. Correlation between LH and GST in patients with PCOS.

4. DISCUSSION

PCOS is an important problem especially for women between the ages of 15-45. This syndrome has the effect of causing DM, hypertension, infertility and cancer later in life.[26]. The exact cause of this disease, which has a complex pathophysiology, is still unclear. It has many causes such as insulin resistance, oxidative stress, metabolic syndromes and hyperandogenism. Today, the diagnosis and correct management of this disease is very important to prevent negative situations that may occur in the future.[27,28]. Although the place of oxidative stress in the pathophysiology of PCOS has been shown in many studies, this relationship between them has not been clarified yet [29]. In this study, we aimed to research the relationship of two parameters that contribute to the oxidative stress mechanism, such as prolidase and gst, with PCOS. PCOS is a very common disease in women [30,31].The definition of oxidative stress is the deterioration of the balance between oxidant and antioxidant [32].The level of oxidative stress have been increased in many studies and in different diseases [33].In patients with PCOS, oxidative stress increases and affects egg follicles [34].It has been suggested that oxidative stress parameters may be important in women with PCOS [35]. In case of difference in amount between oxidant and antioxidant molecules, an increase in harmful structures called reactive oxygen species (ROS) occurs. The occurrence of ROS has been found to be associated

with many ailments in women, especially PCOS, infertility and abortion. [36,37]. Due to the excessive amount of ROS in the body, irregularity may occur in the amount of cellular calcium ions. Due to this unbalanced situation, mitochonrial membranes and ATP metabolism are adversely affected, and in this case, it may contribute to menstrual irregularities and follicle development disorders in women.[38]. In contrast, cells have molecules called antioxidants that prevent these reactions by donating an electron to free radicals before they become unstable. Thanks to these important antioxidant enzymes, including GST, tissue damage is prevented in case of excessive ROS production in the cell [39]. The relationship between oxidative stress (OS) and PCOS has studied by Desai et al. In a study of 25 non-obese PCOS and 25 healthy women. treatment has been found to be effective in preventing the progression of the disease [40]. In the study performed by Rahsepar et al., in which the relationship between vitamin D level and OS in women with PCOS was investigated, a total of 150 patients between the ages of 20 and 40 were included in the study. In this study, no significant difference was observed between the two groups in terms of serum 25(OH)D levels and oxidative stress [41]. The association of OS with malignant diseases in women has investigated in PCOS patients. It has been stated that ROS disrupts the DNA structure, causes point mutations and affects the basic mechanism of the body by affecting tumor suppressor genes. In the study conducted by Zuo et al., it has determined that there is a relationship between OS and DNA methylation and damage [42]. It has been shown that there is a clear association between women with PCOS and metabolic syndromes, and it has been stated that the risk increases especially as the BMI increases. It has been determined that increased fasting insulin level and BMI contribute to androgen production in the ovaries in patients with PCOS [43]. In our study, a significant difference was observed between the two groups in terms of BMI and Fasting Insulin levels. Looking at the literature, one of the studies investigating the links between PCOS and hyperandrogenism has conducted by Dunaif A et al. In our study, a significant difference was observed between the two groups in terms of SHBG, testosterone and androstenedione levels [44]. Glutathione - S - Transferase (GST) is a group of multiproteins hepatic and electrophilic chemicals that potentially remove harmful hydrophilic compounds from blood. Glutathione transferase (GST) detoxifies xenobiotics and free radicals, but also plays a role in catalyzing the conjugation of different endogenous substrates, including steroids andprostaglandins. Also, In addition, GST functions as binding proteins for steroid hormones, bile acids and neurotransmitters [45].As a result of hyperandrogenemia, it has been reported that the increase of free radical production in the development of PCOS [46,47].The serum glutathione-s-transferase was significantly decreased all $(p < 0.05)$ in patients with PCOS, compared with control subjects. In this study, a positive correlation was also observed between GST and LH. In a study by Shenta et al., in which the effect of Gst on pcos patients has studied, it has found that GST levels, known for its antioxidant effect, were lower in pcos patients. [48]. In a study by Alves et al, in which GSTgen polymorphism has investigated and 201 patients participated, it has stated that there was no significant difference in terms of GST polymorphism between pcos patients and the control group [49]. In another study investigating the relationship between pcos and GST in the literature, lower GST levels have found in pcos patients. [50].

Prolidase (Pro)(EC.3.4.13.9) is a metalloprotease group [13]. It has a special requirement for manganese and ion (Mn+2) activates the enzyme [51].The final stage of collagen degradation is done by prolidasee [52].Prolidase has a unique role in all cell types .Prolidase enzyme activity has been suggested to be a speed limiting factor in the regulation of collagen biosynthesis [53].Prolidase enzyme activity has been found in erythrocytes and organ [54]. Prolidase plays an important role in many mechanisms for the regular functioning of cellular events. Thanks to the disintegrating feature of prolidase, proline or hydroxyproline, which plays an important role in intracellular communication, is formed. Prolidase is a ligand of human epidermal growth factor receptor 2 (HER2) and contributes

greatly to regeneration processes in case of tissue injury or infection under normal conditions. In particular, nuclear factor κβ (NF-κβ) contributes to the formation of an inflammatory response by affecting the transcription factor [55]. Prolidase enzyme activity has been studied in many diseases such as preeclampsia[56] postmenopausal osteoporos[57] ,early pregnancy loss [58], infertility and erectile dysfunction [59] and ovarian cancer [60]. Tuncay et al. 116 covid and 46 healthy patients participated in a study investigating the relationship between covid 19 and prolidase, which has recently emerged. As a result of this study, prolidase levels have found to be lower as a reflection of increased inflammatory mechanisms in covid patients and have associated with the inflammatory process [61].

In a study investigating the effects of oxidative stress factors and prolidase on unexplained infertility, prolidase levels have found to be higher in the patient group and it has stated that it has a place in pathophysiology [62]. There are few studies on prolidase in patients PCOS. In a study conducted by Hilali et al, which included 61 patients, it was found that serum Prolidase activity and oxidative stress levels were increased in women with PCOS compared to normal healthy group. Prolidase activity and oxidative stress level increased in PCOS patients [63].In another study performed by Bhatnager et al, Prolidase levels have significantly higher in patients with PCOS.Also, İt has found a significant correlation between increasing Prolidase level and ovarian cyst count. In our study, prolidase levels were found to be statistically significantly higher in the PCOS group compared to the control group [64].

As a result, antioxidant enzyme GST activity has found to be decreased in PCOS patient group. Prolidase (Pro) enzyme is a candidate to be a leading parameter in the elucidation of the disease. The activities of glutathione-S-transferase and Prolidase (Pro) enzymes may be precursors in the etiopathogenesis of PCOS. This study has done in the literature for the first time. In addition, more work should be done in this area.

ACKNOWLEDGEMENT

REFERENCES

[1] Zhang, W., Huang, G., Wei, J. and Yan, D. (2013). Gemini micellar enhanced ultrafiltration (GMEUF) process for the treatment of phenol wastewater. Desalination, 311, 31-36.

[2] Bako, A. U., Morad, S. and Atiomo, W. A. (2005). Polycystic ovary syndrome: an overview. Reviews in Gynaecological practice, 5(2), 115-122.

[3] Jiménez, P., Piazuelo, E., Sánchez, M. T., Ortego, J., Soteras, F. and Lanas, A. (2005). Free radicals and antioxidant systems in reflux esophagitis and Barrett's esophagus. World journal of gastroenterology: WJG, 11(18), 2697.

[4] Seres, I., Bajnok, L., Harangi, M., Sztanek, F., Koncsos, P. and Paragh, G. (2010). Alteration of PON1 activity in adult and childhood obesity and its relation to adipokine levels. Paraoxonases in Inflammation, Infection, and Toxicology, 129-142.

[5] Roszkowski, K. (2014). Oxidative DNA damage-the possible use of biomarkers as additional prognostic factors in oncology. Frontiers in Bioscience-Landmark, 19(5), 808-817.

[6] Sell, D. R. and Monnier, V. M. (1990). End-stage renal disease and diabetes catalyze the formation of a pentose-derived crosslink from aging human collagen. The Journal of clinical investigation, 85(2), 380-384.

[7] Hayes, J. D., and Pulford, D. J. (1995). The glut athione S-transferase supergene family: regulation of GST and the contribution of the lsoenzymes to cancer chemoprotection and drug resistance part I. Critical reviews in biochemistry and molecular biology, 30(6), 445-520.

[8] Ketterer, B., Harris, J. M., Talaska, G., Meyer, D. J., Pemble, S. E., Taylor, J. B. and Kadlubar, F. F. (1992). The human glutathione S-transferase supergene family, its polymorphism, and its effects on susceptibility to lung cancer. Environmental health perspectives, 98, 87-94.

[9] Yildiz, A., Demirbag, R., Yilmaz, R., Gur, M., Altiparmak, I. H., Akyol, S. and Erel, O. (2008). The association of serum prolidase activity with the presence and severity of coronary artery disease. Coronary artery disease, 19(5), 319-325.

[10] Chatterjee, A., Gupta, S. (2018). The multifaceted role of glutathione S-transferases in cancer. Cancer letters, 433, 33-42.

[11] Sienkiewicz, P., Palka, M. and Palka, J. (2004). Oxidative stress induces IGF-I receptor signaling disturbances in cultured human dermal fibroblasts. A possible mechanism for collagen biosynthesis inhibition. Cell Mol Biol Lett, 9(4A), 643-50.

[12] Gejyo, F., Kishore, B. K. and Arakawa, M. (1983). Prolidase and prolinase activities in the erythrocytes of patients with chronic uremia. Nephron, 35(1), 58-61.

[13] Myara, I., Myara, A., Mangeot, M., Fabre, M., Charpentier, C. and Lemonnier, A. (1984). Plasma prolidase activity: a possible index of collagen catabolism in chronic liver disease. Clinical chemistry, 30(2), 211-215.

[14] Erbağcı, A. B., Araz, M., Erbağcı, A., Tarakçıoğlu, M. and Namıduru, E. S. (2002). Serum prolidase activity as a marker of osteoporosis in type 2 diabetes mellitus. Clinical Biochemistry, 35(4), 263-268.

[15] Altindag, O., Erel, O., Aksoy, N., Selek, S., Celik, H. and Karaoglanoglu, M. (2007). Increased oxidative stress and its relation with collagen metabolism in knee osteoarthritis. Rheumatology international, 27(4), 339-344.

[16] Aslan, M., Nazligul, Y., Horoz, M., Bolukbas, C., Bolukbas, F. F., Aksoy, N. and Erel, O. (2007). Serum prolidase activity and oxidative status in Helicobacter pylori infection. Clinical biochemistry, 40(1-2), 37-40.

[17] Pirinçci, N., Kaba, M., Geçit, İ., Güneş, M., Yüksel, M. B., Tanık, S. and Demir, H. (2016). Serum prolidase activity, oxidative stress, and antioxidant enzyme levels in patients with renal cell carcinoma. Toxicology and industrial health, 32(2), 193-199.

[18] Endo, F., Tanoue, A., Nakai, H., Hata, A., Indo, Y., Titani, K. and Matsuda, I. (1989). Primary structure and gene localization of human prolidase. Journal of Biological Chemistry, 264(8), 4476-4481.

[19] Hu, M., Cheng, Z. and Zheng, L. (2003). Functional and molecular characterization of rat intestinal prolidase. Pediatric research, 53(6), 905-914.

[20] Yoon, S. O., Park, S. J., Yun, C. H. and Chung, A. S. (2003). Roles of matrix metalloproteinases in tumor metastasis and angiogenesis. BMB Reports, 36(1), 128-137.

[21] Wilk, P., Wątor, E., and Weiss, M. S. (2021). Prolidase–A protein with many faces. Biochimie, 183, 3-12.

[22] Arioz, D. T., Camuzcuoglu, H., Toy, H., Kurt, S., Celik, H. and Aksoy, N. (2009). Serum prolidase activity and oxidative status in patients with stage I endometrial cancer. International Journal of Gynecologic Cancer, 19(7).

[23] Myara, I., Charpentier, C. and Lemonnier, A. (1982). Optimal conditions for prolidase assay by proline colorimetric determination: application to iminodipeptiduria. Clinica Chimica Acta, 125(2), 193-205.

[24] Eshre, R., (2004), Consensus on diagnostic criteria and long-term health risks related to polycystic ovary syndrome (PCOS). ASRM-Sponsored PCOS Consensus Workshop Group. Human Reproduction (Oxford, England), 19(1), 41-47.

[25] Habig, W., Pabst, M. J., Jakoby, W. B. (1974). The first enzymatic step in mercapturic acid formation. Glutathione-S-transferase. J. Biol. Chem, 249, 7130-7139.

[26] Conway, G., Dewailly, D., Diamanti-Kandarakis, E., Escobar-Morreale, H. F., Franks, S., Gambineri, A. and Yildiz, B. O. (2014). The polycystic ovary syndrome: a position statement from the European Society of Endocrinology. European journal of endocrinology, 171(4), P1-P29.

[27] Rocha, A. L., Oliveira, F. R., Azevedo, R. C., Silva, V. A., Peres, T. M., Candido, A. L. and Reis, F. M. (2019). Recent advances in the understanding and management of polycystic ovary syndrome. F1000Research, 8.

[28] Ozgokce, C., Elci, E. and Yildizhan, R. (2020). C-Reactive Protein, Fibrinogen, Leptin, and Adiponectin Levels in Women with Polycystic Ovary Syndrome. The Journal of Obstetrics and Gynecology of India, 70(6), 490-496.

[29] Zuo, T., Zhu, M. and Xu, W. (2016). Roles of oxidative stress in polycystic ovary syndrome and cancers. Oxidative medicine and cellular longevity, 2016.

[30] Norman, R. J., Dewailly, D., Legro, R. S. and Hickey, T. E. (2007). Polycystic ovary syndrome. The Lancet, 370(9588), 685-697.

[31] Valkenburg, Olivier. Polycystic Ovary Syndrome. Diss. Erasmus MC: University Medical Center Rotterdam, 2015.

[32] Asker, S., Asker, M., Sarikaya, E., Sunnetcioglu, A., Aslan, M. and Demir, H. (2015). Oxidative stress parameters and their correlation with clinical, metabolic and polysomnographic parameters in severe obstructive sleep apnea syndrome. International journal of clinical and experimental medicine, 8(7), 11449.

[33] Dandona, P., Thusu, K., Cook, S., Snyder, B., Makowski, J., Armstrong, D. and Nicotera, T. (1996). Oxidative damage to DNA in diabetes mellitus. The Lancet, 347(8999), 444-445.

[34] González, F., Rote, N. S., Minium, J. and Kirwan, J. P. (2006). Reactive oxygen species-induced oxidative stress in the development of insulin resistance and hyperandrogenism in polycystic ovary syndrome. The Journal of Clinical Endocrinology and Metabolism, 91(1), 336-340.

[35] Macut, D., Bjekić-Macut, J. and Savić-Radojević, A. (2013). Dyslipidemia and oxidative stress in PCOS. Polycystic Ovary Syndrome, 40, 51-63.

[36] Sekhon,H., Gupta,L., Kim, S. Y. and Agarwal, A. (2010). Female infertility and antioxidants. Current Women's Health Reviews, 6(2), 84-95.

[37] Rizzo, A., Roscino, M. T., Binetti, F. and Sciorsci, R. L. (2012). Roles of reactive oxygen species in female reproduction. Reproduction in Domestic Animals, 47(2), 344-352.

[38] Rashidi, B., Haghollahi, F., Shariat, M., and Zayerii, F. (2009). The effects of calcium-vitamin D and metformin on polycystic ovary syndrome: a pilot study. Taiwanese Journal of Obstetrics and Gynecology, 48(2), 142-147.

[39] Al-Gubory, K. H., Fowler, P. A. and Garrel, C. (2010). The roles of cellular reactive oxygen species, oxidative stress and antioxidants in pregnancy outcomes. The international journal of biochemistry and cell biology, 42(10), 1634-1650.

[40] Desai, V., Prasad, N. R., Manohar, S. M., Sachan, A., Narasimha, S. R. P. V. L. and Bitla, A. R. R. (2014). Oxidative stress in non-obese women with polycystic ovarian syndrome. Journal of clinical and diagnostic research: JCDR, 8(7), CC01.

[41] Rahsepar, M., Mahjoub, S., Esmaelzadeh, S., Kanafchian, M. and Ghasemi, M. (2017). Evaluation of vitamin D status and its correlation with oxidative stress markers in women with polycystic ovary syndrome. International journal of reproductive biomedicine, 15(6), 345.

[42] Zuo, T., Zhu, M. and Xu, W. (2016). Roles of oxidative stress in polycystic ovary syndrome and cancers. Oxidative medicine and cellular longevity, 2016.

[43] Stepto, N. K., Cassar, S., Joham, A. E., Hutchison, S. K., Harrison, C. L., Goldstein, R. F. and Teede, H. J. (2013). Women with polycystic ovary syndrome have intrinsic insulin resistance on euglycaemic–hyperinsulaemic clamp. Human reproduction, 28(3), 777-784.

[44] Dunaif, A., Segal, K. R., Futterweit, W. and Dobrjansky, A. (1989). Profound peripheral insulin resistance, independent of obesity, in polycystic ovary syndrome. Diabetes, 38(9), 1165-1174.

[45] Hayes, J. D. and Strange, R. C. (2000). Glutathione S-transferase polymorphisms and their biological consequences. Pharmacology, 61(3), 154-166.

[46] Savić-Radojević, A., Mažibrada, I., Djukić, T., Stanković, Z. B., Plješa-Ercegovac, M., Sedlecky, K., and Macut, D. (2018). Glutathione S-transferase (GST) polymorphism could be an early marker in the development of polycystic ovary syndrome (PCOS)—an insight from non-obese and non-insulin resistant adolescents. Endokrynologia Polska, 69(4), 366-374.

[47] Sienkiewicz, P., Palka, M. and Palka, J. (2004). Oxidative stress induces IGF-I receptor signaling disturbances in cultured human dermal fibroblasts. A possible mechanism for collagen biosynthesis inhibition. Cell Mol Biol Lett, 9(4A), 643-50.

[48] Shenta, A., Saud, K. and Al-Shawi, A. (2020). Assessment the Correlations of Hormones, Lipid Profiles, Oxidative Stress, and Zinc Concentration in Iraqi Women with Polycystic Ovary Syndrome. Reports of Biochemistry and Molecular Biology, 9(3), 270.

[49] Alves, M. M. C., Almeida, M., Oliani, A. H., Breitenfeld, L. and Ramalhinho, A. C. (2020). Women with polycystic ovary syndrome and other causes of infertility have a higher prevalence of GSTT1 deletion. Reproductive BioMedicine Online, 41(5), 892-901.

[50] Kurdoglu, Z., Ozkol, H., Tuluce, Y. and Koyuncu, I. (2012). Oxidative status and its relation with insulin resistance in young non-obese women with polycystic ovary syndrome. Journal of Endocrinological Investigation, 35(3), 317-321.

[51] Mock, W. L. and Green, P. C. (1990). Mechanism and inhibition of prolidase. Journal of Biological Chemistry, 265(32), 19606-19610.

[52] Surazynski, A., Miltyk, W., Palka, J. and Phang, J. M. (2008). Prolidase-dependent regulation of collagen biosynthesis. Amino acids, 35(4), 731-738.

[53] Namiduru ES. Prolidase.Bratisl Lek Listy. 2016;117(8):480-5.

[54] Liu, G., Nakayama, K., Awata, S., Tang, S., Kitaoka, N., Manabe, M. and Kodama, H. (2007). Prolidase isoenzymes in the rat: their organ distribution, developmental change and specific inhibitors. Pediatric research, 62(1), 54-59.

[55] Misiura, M. and Miltyk, W. (2020). Current understanding of the emerging role of prolidase in cellular metabolism. International Journal of Molecular Sciences, 21(16), 5906.

[56] Pehlivan, M., Ozün Ozbay, P., Temur, M., Yılmaz, O., Verit, F. F., Aksoy, N. And Üstünyurt, E. (2017). Is there any role of prolidase enzyme activity in the etiology of preeclampsia?. The Journal of Maternal-Fetal and Neonatal Medicine, 30(9), 1108-1113.

[57] Verit, F. F., Geyikli, I., Yazgan, P. and Celik, A. (2006). Correlations of serum prolidase activity between bone turnover markers and mineral density in postmenopausal osteoporosis. Archives of Gynecology and Obstetrics, 274(3), 133-137.

[58] Toy, H., Camuzcuoglu, H., Camuzcuoglu, A., Celik, H. and Aksoy, N. (2010). Decreased serum prolidase activity and increased oxidative stress in early pregnancy loss. Gynecologic and obstetric investigation, 69(2), 122-127.

[59] Pirinççi, N., Yildirim, S., Taş, A., Kuşcu, Y., Ozan, T., Fırdolaş, F., and Karakeci, A. (2018). Evaluation of Prolidase Activity, Oxidative Stress, and Antioxidant Enzyme Levels in Testicular and Penile Tissues after Human Chorionic Gonadotropin Treatment in Rats by Predicting Infertility and Erectile Dysfunction. Medical Principles and Practice, 27, 217-221.

[60] Camuzcuoglu, H., Arioz, D. T., Toy, H., Kurt, S., Celik, H. and Aksoy, N. (2009). Assessment of preoperative serum prolidase activity in epithelial ovarian cancer. European Journal of Obstetrics and Gynecology and Reproductive Biology, 147(1), 97-100.

[61] Ergin Tuncay, M., Neselioglu, S., Asfuroglu Kalkan, E., Inan, O., Sena Akkus, M., Ates, I. and Erel, O. (2022). Modified Proline Metabolism and Prolidase Enzyme in COVID-19. Laboratory Medicine.

[62] Isbilen, E., Kulaksizoglu, S., Kirmizioglu, M., Karuserci Komurcu, O. and Tabur, S. (2022). Role of prolidase activity and oxidative stress biomarkers in unexplained infertility. International Journal of Gynecology and Obstetrics, 156(3), 430-435.

[63] Hilali, N., Vural, M., Camuzcuoglu, H., Camuzcuoglu, A. and Aksoy, N. (2013). Increased prolidase activity and oxidative stress in PCOS. Clinical endocrinology, 79(1), 105-110.

[64] Bhatnager, R., Nanda, S. and Dang, A. S. (2018). Plasma prolidase levels as a biomarker for polycystic ovary syndrome. Biomarkers in Medicine, 12(6), 597-606.

RESEARCH ARTICLE

OPTIMIZATION of PLATINUM BATHS USED in JEWELRY INDUSTRY in TURKEY

Elif Simay ERTÜRK[1]*, Burcu Didem ÇORBACIOĞLU[2], Zehra Gülten YALÇIN[3]

[1]Yıldız Teknik University,Faculty of Chemistry-Metelurgy, Departement of Chemical Engineering, İstanbul,
erturk.s@hotmail.com,ORCID: 000-0003-3858-7428
[2]Yıldız Teknik University,Faculty of Chemistry-Metelurgy, Departement of Chemical Engineering, İstanbul,
bcorbaci@yildiz.edu.tr, ORCID: 0000-0002-8156-6094
[3]Karatekin University, Faculty of Engineering, Departement of Chemical Engineering, Çankırı, zaltin@karatekin.edu.tr,
ORCID: 0000-0001-5460-289X

ABSTRACT

Platinum group metals are used a lot in fields such as jewellery, electronics and health due to being precious metals and their brightness, corrosion resistance, thermal resistance and electrical conductivity. With the excessive increase in the prices of gold and rhodium, which are the most used in the jewelry sector, a tendency towards the more affordable platinum metal has begun. In this study, the optimization of baths used in the jewelry industry, which is one of the areas where platinum coating is used most, is discussed. The conditions required for the re-coating of the platinum bath, which is used and separated as waste in jewelry workshops, were investigated experimentally. A waste bath was taken from a jewelry plating workshop in the Grand Bazaar, and the content of the bath was determined by ICP-OES analysis and IR Spectroscopy. Later, on this waste platinum bath, a few substances, which are used as brighteners in the market, and which show parallel diffraction with the original bath in FTIR analysis were added and the effects of temperature, current and time parameters on the coating were investigated. L*a*b values were measured with PCE Instruments Colorimeter device by making platinum coating on brass-coated plates using the waste bath to which brighteners were added. As a result of the study, the brighteners and color properties of the coated surfaces and the reference coating properties were compared.

Keywords: *Platinum, Metal coating, brightness*

1. INTRODUCTION

Rhodium, platinum and palladium of Groups 9 and 10 in the periodic table which are considered to be precious metals are called platinum group elements (PGM). These metals have high corrosion resistance and good thermal properties in pure form, and they are mostly good conductors [1]. Thanks to the characteristics they demonstrate, PGMs have a wide range of uses in the automotive industry, chemistry industry, electronic parts, ceramics, glass industry as well as some aviation components [2], and jewelry. Since these metals are precious metals, they can demonstrate the same properties with a lower consumption amount when the coating technique is applied. Table 1 shows the platinum consumption by industry within the last three years. When the amount is analyzed, it is seen that the

largest use of platinum within the last three years was in automotive and jewelry industry. They are used in converters, filters and electronic parts in the automotive industry. As for jewelry, platinum coatings are made on decorative products and jewelry [3].

Table 1. Platinum consumption by industry within the last three years [4].

SECTORAL DEMAND (tonnes)	2019	2020	2021
Automotive	89	71.2	90.5
Chemical	20.8	19.9	19.7
Electronics	7.2	7.5	8.7
Glass	13.7	14.1	16
Investment	35.1	31.8	9.6
Jewelry	64.2	53.1	55.9
Medical ve biomedical	7.5	6.7	7.2
Petroleum	8	9.4	5.4
Other	18.3	14.3	16.8
Total gross demand	**263.8**	**228**	**229.8**

1.1. Coating

Surface coatings, which are obtained by applying a material to the surface of another either by overlaying or precipitating with the purpose of protecting the material from the effects of the environment as well as improving its appearance and properties [5]. Gaseous state, solution state and molten/semi-molten state processes are used in metallic coatings.

The most common plating method in the jewelry industry is the electrolytic plating method. This method is carried out by depositing a metal on the surface with the help of an electric current [6]. In the electroplating device, the part to be coated becomes the cathode. A high conductivity metal is used as anode. The anode and cathode placed in the electrolyte containing the material to be coated are connected to a power source. When the current is applied, reduction occurs and metal ions accumulate on the coated material [7].

The success of a coating process depends on initial surface preparation which includes removing burrs and filing. Prior to coating, some other processes are applied to the surface for cleaning. They are essential since they affect the properties and quality of the coating. For this reason, in order to make the surface appropriate for the coating process, some processes such as removing impurities, improving the surface roughness and activating the surface to be coated are performed by chemical, electrochemical or mechanical means.

The brightness of the surface is a desired feature in the metal plating process. The glossy surface determines that the reflection is smooth. As for rough surfaces, it would be difficult to achieve gloss since the reflection will not be smooth. In chemical and electrochemical processes to improve the roughness of the surface, some additives called brighteners are added to the electrolyte. These additives are classified into two categories; namely, carrier brighteners and brightening additives. Carrier brighteners, also known as primary brighteners, are given below.

- Sulfonamides
- Sulfonimides

- Benzene sulfonic acids (mono-di or trisulfonic acids)
- Alkyl sulphonic acids
- Sulfinic acids
- Arylsulfonsulfanates

The use of these brighteners alone is not enough. Additional additives are used to provide a brighter appearance. These additives are given below [7];

- Thiourea
- Acylthiourea
- Mercaptoalkylsulfonic acid
- Bis(sulfoalkyl) acid amide
- Thiocarboxylic acid amine
- Thiocarbozone
- Thiosemicarbozone
- Thiohaydantoin

Figure 1 shows a laboratory-scale mechanism of a catalytic coating. The ionic solution is called the electrolyte. Although electrolytes are generally in liquid form, they may also be gases.
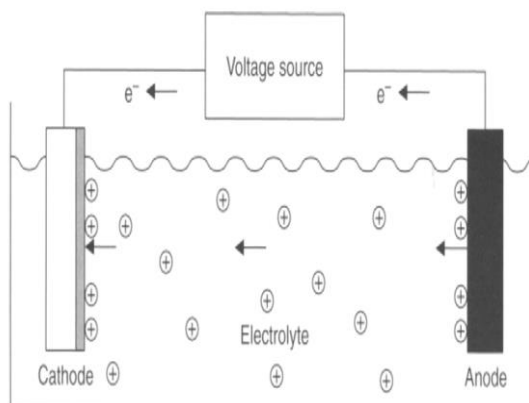
Figure 1. Laboratory-scale mechanism of a catalytic coating.

While the most convenient salt of the metal is mainly used in an electrolyte, impurities may also contribute to the bath processes.

The anode is the positively charged electrode used to coat the material. While there is deposition at the cathode, the anode is only for ionization reactions, so no disposition occurs.

The cathode is the negative-ended electrode on which the coating process is performed. For flow coating, the material, which has undergone the necessary pre-cleaning processes, is immersed in the solution and the coating is performed because of the required contact. Reactions 1 and 2 [7] show the fundamental reactions occurring at the cathode and the anode.

$$Me^{n+} + n^{e-} \longrightarrow M \quad \text{(cathodic reaction)} \tag{1}$$

$$Me^0 \longrightarrow Me^{n+} + n^{e-} \quad \text{(anodic reaction)} \tag{2}$$
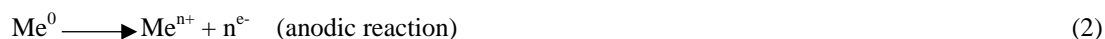
Electric current is delivered by a power supply. Furthermore, there is also a temperature sensor and stirrer available in electroplating devices.

Since current is used in electrolytic coating, high current and low current zones are formed on the metal surface. High flow zones occurring on uneven surfaces will lead to inhomogeneous coating. The material to be coated must be prepared for pre-treatment.

For the deposition thickness to be the same in every region of the surface, the current density must be the same at all points of the cathode. This is possible only if the distance between the closest point of the anode and every point of the cathode is the same. The current-related resistance between different points of the anode and cathode is different, and therefore the current density at these points varies [8].

The coating can be divided into two stages as surface preparation and surface coating processes. Burr cleaning and filing are the physical processes to be performed. Prior to preparing the surface, it must initially undergo a cleaning phase which includes hot degreasing, electrolytic degreasing, and acidic cleaning. Then the coating is performed and followed by quality control Water rinsing process is performed at each step.

The first cleaning phase is through hot degreasing. The material should be free from chemicals used during preparation, lubrication through touching as well as environmental dirt and oxides. Then the acidic cleaning is performed. Even if the parts are lubricated, they are subject to some corrosion. Baths with 20-50% acid content are used to remove the rust. During acidic cleaning, an inhibitor should be used to prevent the iron from corroding because of the acid and contaminating the bath. Examples of acid solutions used in surface cleaning and the processing conditions of these solutions are given in Table 2.

In electrolytic degreasing, although the surface of the part is flat, it should not be ignored that there are micro pits on the surface. Electrolysis with water is conducted to clean the remaining oil in these pits. As a result of hydrolysis, the released hydrogen molecules take the oil in the micro pits and bring it to the surface.

Table 2. Acid types and concentrations used in surface cleaning [5].

No	Acid Solution	Concentration	Work Conditions
1	Hydrochloric acid (HCl)	%20-85	Room temperature
2	Sulfuric acid (H_2SO_4)	%5-15	Under inhibitor conditionss and at 50-80 °C
3	Sulfuric acid (H_2SO_4)	%4-6	At 50-65 °C and at 3.2-6.5 A/dm²
4	Hydrochloric acid (HCl) Nitric acid (HNO_3)	%20-85 %1-5	Room temperature
5	Sulfuric Asid (H_2SO_4) Potassium nitrate (KNO_3)	22.5 g/l 22.5 g/l	At 70 °C

Table 3. The most commonly used coating baths [5].

Metal	Bath type	Anode	Cathode current density (A/dm²)	Temperature (°C)	Current efficiency (%)
Gold	Cyanide	Au	0.1-0.5	60-80	70-90
Copper	Asid-Sulfate	Cu	1-4	25-50	97-100
	Alkali Cyanide	Cu	0.3-1.5	35-40	30-60
Zinc	Sulfate	Zn	1-3	20-30	99
	Sulfate (Hot)	Zn	8-10	50-60	
	Chloride	Zn	4-10	20-40	
	Alkali Cyanide	Zn	0.8-2	40-50	85-90
Iron	Chloride	Fe	10-18	90-100	90-98
	Couple Sulfate	Fe	2-3	20-30	95-98
Silver	Cyanide	Ag	0.3-0.8	15-25	98-100
Cadmium	Alkali Cyanide	Cd	1-5	20-30	
Tin	Alkali Stannite	Sn	1	50	
	Alkali Stannate	Sn	0.5-1.5	60	70-95
Cobalt	Sulfate	Co	3-17	20-30	95-98
Chromium	Chromic Acid +Sulfate	Pb	10-30	40-50	12-20
Lead	Fluoroborate	Pb	0.5-2	20-30	20-93
	Perchlorate	Pb	2-3	20-30	95
Nickel	Sulfate	Ni	0.5-2	20-30	94-98
Sulfate	Sulfate Chloride	Ni	1.5-5	50	94-98
Palladium	Chloride	Pd	1		98-100
Platinum	Phosphate	Pt	0.1	70	
Alloy	Cyanide	Cu-Zn	0.2-0.3	32-45	80

Only a few of these brighteners, which provide a bright appearance, are used in the coating industry. The major reason for this is the necessity of optimizing the appropriate temperature and current density in order to make the coatings [7].

Afterwards, degreasing and acidic cleaning processes are performed. After the coating is completed, the surface is made ready for use by rinsing and drying, respectively [9], [10].

The plating bath basically contains the salts of the metal to be coated. However, conductivity enhancers, brighteners, surface wetting agents and buffer solutions can be added to increase the coating quality and facilitate the process [7], [11].

There are multiple factors for the effectiveness of a coating. Among these are current density, current efficiency, pH, temperature, concentration, dispersion power, and surface properties [8], [12], [13].

2. MATERIALS AND METHODS

This study was carried out in the chemical engineering laboratory of Yıldız Technical University. A jewelry workshop in the Grand Bazaar provided a bath solution which was used before and separated as waste since it was not functioning any more. The parts to be coated were pre-treated, polished, degreased and cleaned, and made ready for the experiments. As a result of the literature review and market research, 2 different brighteners were determined and obtained to be used in the experiments. For the electrolysis setup, a regulator (Yıldırım Electronic Devices Ind. Trd. Ltd. Co.), connection cables, a heater (Yellowline MSC Basic C) were used. In addition, Perkin Elmer Spectrum Two FTIR and PCE Instruments Colorimeter devices were used. ICP-OES analysis was conducted in the Metallic Analysis Laboratory in Başakşehir. The experimental setup used for the electroplating is given in Figure 2.

Figure 2. Electrolytic coating mechanism.

The platinum bath used by the jewelers was analyzed both before it was used and in its waste condition to be used in the experiments using the ICP-OES 4200MP-AES model device to determine the amount of platinum it contained, and the difference in their chemical structures was checked by FTIR analysis in Figure 3. In the experiments, Saccerete Clear and Triton-x 100 brighteners were added to the waste solution taken from the workshop, whose ICP results are given in Table 4.

Triton-x 100 is a nonionic surfactant with a hydrophilic polyethylene oxide chain and an aromatic hydrocarbon lipophilic or hydrophobic group. It is used in industrial (metal plating) processes [14].

By adding certain amounts of brighteners, coating was made at a temperature range of 35 °C, 45 °C and 55 °C, with a current of 2.5 A/dm^2 in a processing time of 1 minute. Coating was done under the

same conditions as the original coating bath, and the waste bath was optimized to achieve the desired brightness and color properties of the coating.

Table 4. ICP-OES analyses results for the original bath and waste bath.

Sample Name	Test Method	Test materiel	Result
Original Pt Bath	ICP-OES-MP-AES	Pt	4.001 g/lt
Waste Pt Bath	ICP-OES-MP-AES	Pt	2.065 g/lt
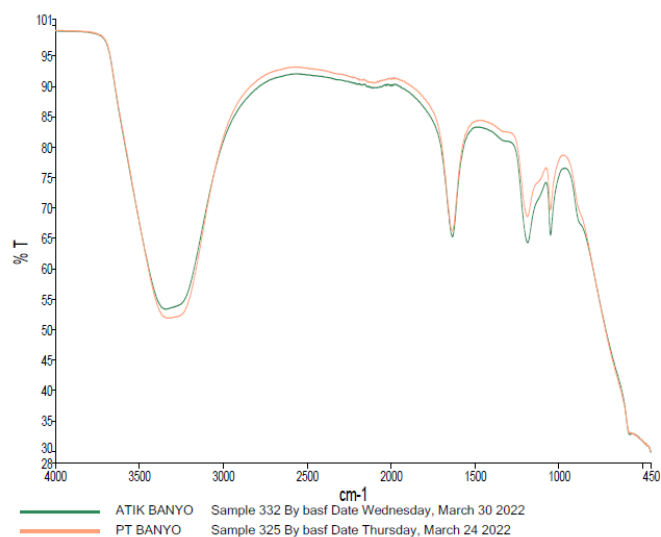
Figure 3. Comparative FTIR graphs of original bath and waste bath.

After coating processes, L, a, b values were measured using the PCE Instruments Colorimeter device. Measurement results represent points within a three-dimensional color system, as shown in Figure 4. The L value on the vertical axis can be defined as brightness. Regarding the L value ranging between 0-100, zero represents black while a hundred represents white. The a and b values on the horizontal axis represent the yellow, blue, red, and green tones of the color. "b" is the yellow/blue axis with b (+) indicating the yellow hue while b (-) indicating the blue hue. Likewise, in the "a" axis representing the red/green colors, a (+) indicates the red hue, while a indicates that the green hue increases in the (-) direction [15].
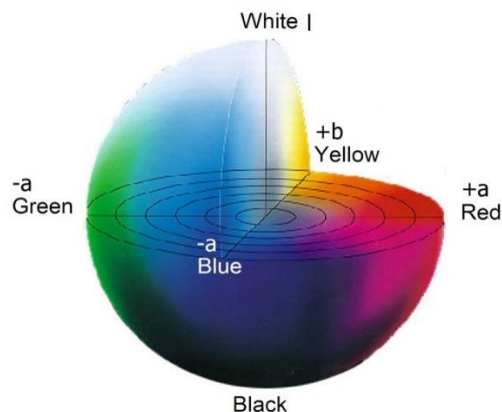
Figure 4. L*a*b color graph [16].

3. RESEARCH RESULTS

The ICP-OES analysis revealed that the amount of Pt in the waste bath, which was separated by the workshop as it did not yield sufficient brightness, was reduced to approximately half. Since it is known that it does the coating in half the amount but does not reach sufficient brightness, the coating processes were carried out by adding the brightening agents Saccerete Clear and Triton-x 100. Under the same conditions, coatings were also made with the original bath which had a Pt content of 4 g/lt. L*a*b measurements were made for three different areas for each coating with the PCE Instruments Colorimeter device and the results are given in Table 5, Table 6, Table 7 and Table 8.

Table 5. L*a*b results of the original bath containing 4 g/L of Pt and the coatings at 35 °C, 45 °C and 55 °C.

		2.5 A (7-8 V)		
		L	**a**	**b**
4 g/l Original Pt bath	35 °C	93.7	1.91	6.84
		93.87	2.23	6.89
		92.98	2.1	7.18
	45 °C	95.04	1.81	7
		94.85	2.05	7.07
		93.52	2.26	6.67
	55 °C	95.42	1.78	5.17
		94.31	1.68	5.74
		94.59	1.83	5.72

Table 6. L*a*b results of coatings at 35°C with the filtered waste bath containing 2.065 g/L of Pt.

		35 °C		
		L	a	b
Waste bath	2.5 A (7-8 V)	72.59	1.79	6.77
		72.32	1.83	6.56
		74.49	2.66	7.43
Saccerete Clear 0.5 ml additional	2.5 A (7-8 V)	87.48	2.33	6.09
		89.96	2.62	7.0
		89.06	2.72	6.36
Triton-x 0.25 ml additional	2.5 A (7-8 V)	74.6	3.24	6.89
		77.82	3.32	6.4
		76.22	4.24	8.02

Table 7. L*a*b results of the filtered waste bath containing 2.065 g/L of Pt and the coatings at 45 °C.

		45 °C		
		L	a	b
Waste bath	2.5 A (7-8 V)	77.21	2.6	8.85
		78.73	2.99	8.95
		78.4	2.24	8.27
Saccerete Clear 0.5 ml additional	2.5 A (7-8 V)	84.06	3.58	8.6
		84.45	3.46	8.75
		86.78	2.5	7.63
Triton-x 0.25 ml additional	2.5 A (7-8 V)	85.33	4.22	7.78
		83.91	4.34	8.51
		83.06	4.35	8.87

Table 8. L*a*b results of the filtered waste bath containing 2.065 g/L of Pt and the coatings at 45 °C.

		55 °C		
		L	a	b
Waste bath	2.5 A (7-8 V)	78.49	3.65	11.7
		74.71	3.18	11.51
		79.75	3.97	12.24
Saccerete Clear 0.5 ml additional	2.5 A (7-8 V)	88.39	2.4	7.36
		87.41	2.46	7.18

			86.73	2.6	7.54
Triton-x 0.25 ml additional		2.5 A (7-8 V)	72.29	4.64	13.39
			73.57	4.42	13.19
			71.88	4.49	13.21

4. DISCUSSION

Electrolysis of platinum dates back to ancient times. In 1989, Matthey described a new bath in his patent. In this bath, based on the tetrammineplatinum (II) solution, the coating process is achieved at Pt (NH$_3$)]$^+$, low concentration, aqueous buffer at a pH range of 10.0-10.6, operating at the recommended operating temperature range between 91 and 95°C.

Skinner [3] used a new bath in his study, and as a result, it is seen that this study made a high performance platinum coating with a smooth surface at low current density.

In various coating studies, in the thesis study of Bakan [7], the effect of different pH values on the brightness of the silver coating was investigated, and when the effect of the additives on the coating color was examined, it was observed that the ethylene glycol additive alone gave the color closest to the reference silver sample.

In a study conducted by Satpathy et al., it was stated that silver coatings were made with the environmentally friendly thiosulfate-based silver electroplating method using agalvanic bath and brightness was achieved [17].

5. CONCLUSION

As seen in Table 6, the effect of the addition of Saccerete Clear at 35 °C on the L, a, b values of the prepared bath is seen. An L value of 89.96 stands for brightness and it is seen that a is measured as 2.62 while b is 7. According to the color scale in Figure 4, it is seen that the b value is obtained as a color close to green. Again, in Figure 4, it is seen that the a value is close to red.

According to Table 6, when Triton -x 100 is used, it has been observed that L, a, b values decrease and foam occurs in the solution. For this reason, it has been determined that it causes a negative effect on the coating. As seen in Table 7, increasing the bath temperature from 35°C to 45°C increased the L, a, b values in the filtered waste bath, while the addition of 0.5 ml of Saccerete Clear at 45°C dropped the L, a, b values of the bath. Additions of Triton- x 100 at 45°C increased the L, a, b values. In Table 8, although it is expected that there will be a positive effect on bath efficiency with an increase in temperature by 55°C, a decrease was observed in the other brightener except for Saccerete Clear. The revelation of high a, b values as a result of the brightener addition indicate a deviation from the original bath. As seen in Table 5, it was determined that the L, a, b values were not satisfactory. In addition, comparative FTIR graphs of the original bath and the waste bath are given in Figure 3. According to this graph, a big difference is not observed in the spectra.

In this study, the waste bath used in the jewelry industry was filtered as a pre-treatment to get rid of sediments and by adding 0.5 ml of Saccerete Clear and Triton-x 0.25 ml brighteners to this bath, 2.5 A (7-8 V) current density coatings were made.

It is known that approximately 2.5 kg of coating was made with the original 4 g/L Pt bath. In the same experimental conditions, L, a, b values on the color scale of the original bath were also examined.
It is seen that the L, a, b values were found to be 95.42, 1.78, and 5.17, respectively, at 55 °C, which gives the best brightness in the original Pt bath. In the study, in which brighteners have been added at 55°C, it is seen that the expected increase in L, a, b values could not achieve the brightness of the original bath. Only with the addition of 0.5 ml of Saccerete Clear, L, a, b values of 89.96, 2.62, 7.0 indicates an achievement of a bit of brightness at 35°C which is still not the desired brightness of the original bath.

Both of the brighteners used could not provide the desired brightness in the bath. It was concluded that it is not suitable for use as a commercial product.

ACKNOWLEDGMENT

REFERENCES

[1] Morcalı, M. H., (2014), Nikel Sülfür Ateş Analizi Metodu ile Katalitik Konvertörlerdeki Platin, Paladyum ve Rodyum Metallerinin Tayini ve Metodun Optimizasyonu. Yüksek Lisans Tezi, İstanbul Teknik Üniversitesi, Fen Bilimleri Enstitüsü, İstanbul, 136p.

[2] Skinner, P.E., (1989), Platinum Metals Reviews. (33),102.

[3] Hagelüken, C., (2012), Recycling the Platinum Group Metals: A European Perspective. Platinum Metals Reviews. (56) pp. 29-35.

[4] Cowley, A., (2021), PGM Market Report. Johnson Matthey.

[5] Uyanık, M., (2012), Sic Nanopartikül İlaveli Asitli Çinko Kaplama Banyolarında Yapılan Kaplamaların Malzemenin Korozyon Direnci ve Mekanik Özelliklerine Etkisinin Araştırılması. Yıldız Teknik Üniversitesi, Fen Bilimleri Enstitüsü, Yüksek Lisans Tezi, İstanbul.

[6] Giurlani, W., Zangari, G., Gambinossi, F., Passaponti, M., Salvietti, E., Benedetto, F. D., Caporali S. and Innocenti, M., (2018), Electroplating for Decorative Applications: Recent, Coatings, Vol 260, no. 8.

[7] Bakan, E., (2011), Elektrolitik Parlak Gümüş Kaplama Banyolarının Geliştirilmesi. Yüksek Lisans Tezi, İstanbul Teknik Üniversitesi, Fen Bilimleri Enstitüsü, İstanbul. 151p.

[8] Elektrometal Kaplamanın Temel Prensipleri, Ders 2, Elektrometal Kaplama Tekniği.

[9] Çakar, H., (2010), Elektrokimyasal Yöntemle Üretilen Ni-B Esaslı Kaplamaların NaCl Ortamındaki Korozyonu. Yüksek Lisans Tezi, Sakarya Üniversitesi, Fen Bilimleri Enstitüsü, Sakarya. 105p.

[10] Dikici, T., (2009), Çelik Malzeme Yüzeyine Elektrolitik Yolla Kaplanan Zn-Ni-Co Alaşımının Mekanik ve Yapısal Özelliklerinin İncelenmesi. Yüksek Lisans Tezi, Dokuz Eylül Üniversitesi, Fen Bilimleri Enstitüsü, İzmir. 125p.

[11] Kanani, N., (2004), Elektroplating, Basic Principles, Procesesses and Practice, Elsevier Science.

[12] Sönmez, S., (2006), Metal Kaplama Sanayi Atık Sularından Perlit Minerali ile Toplam Krom Gideriminin İncelenmesi. Yüksek Lisans Tezi, Sakarya Üniversitesi, Fen Bilimleri Enstitüsü, Sakarya. 106p.

[13] Ellwood, W. B., (7 November 1961). Rhodium Plating. New York Patent: 3,007,855.

[14] [Online]. Available: https://en.wikipedia.org/wiki/Triton_X-100. [Reached: April 2022].

[15] [Online]. Available: https://www.lovibond.com/tr. [Reached: April 2022].

[16] [Online]. Available: https://en.wikipedia.org/wiki/CIELAB_color_space. [Reached: April 2022].

[17] Bangmaya, S., Sambedan, J., Siddhartha, D., Karabi, D., (2021), A comparative study of electrodeposition routes for obtaining silver coatings from a novel and environment-friendly thiosulphate-based cyanide-free electroplating bath. Surface & Coatings Technology. (424). 127680.

RESEARCH ARTICLE

COMPARISON of the DISTRIBUTION of ENVIRONMENTALLY HAZARDOUS ELEMENTS in COAL with KRIGING and IDW METHODS (TEKİRDAĞ-MALKARA COALFIELD)

Cevdet Bertan GÜLLÜDAĞ[1], Neslihan ÜNAL KARTAL[2*]

[1]Akdeniz University, Vocational School of Technical Science, Department of Construction Technology, Antalya, bgulludag@akdeniz.edu.tr, ORCID: 0000-0001-5777-1808
[*2]Burdur Mehmet Akif Ersoy University, Gölhisar School of Applied Sciences, Department of Land Registry and Cadastre, Burdur, nunal@mehmetakif.edu.tr, ORCID: 0000-0002-3684-9984

ABSTRACT

Coal is a fossil fuel that can have negative impacts on the environment and human health during extraction, transportation, and burning. In this study, samples were collected from eight boreholes in the Tekirdağ-Malkara coalfield and the major-trace element analysis was performed. Lithology data obtained from boreholes constitute well logs. Interpolation forms the basis of log correlation. The study aimed to determine the local areas that may pose a risk after selecting the interpolation method that provides the most accurate results directly in the study area. Among the elements, those that may cause environmental and human health problems were selected and divided into four groups according to their hazard class. The distributions in the whole field were estimated by Kriging and Inverse Distance Wighting (IDW) interpolation methods. These two interpolation methods were evaluated with a selected test probe and the Kriging method was determined to provide the most accurate results. With this method, the accuracy of results obtained with the elements in the hazard class were as follows: Hg and Cr 100%, Se 98.86%, Cd 75%, As 66.2%. After determining Kriging as the method to be applied, a re-classification analysis was carried out, and estimates made in the field were compared with coal from Turkey, the US, China, and the average upper continental crust. As a result of this comparison, the elements with the highest rate of distribution in all averages were determined as Be, Cu, V, and the elements with the lowest distribution rate were Mn, Mo, P, Sb.

Keywords: *Major-trace element, IDW, Kriging, Coal, Interpolation*

1. INTRODUCTION

Different methods are used in mineral exploration with the development of technology [1]. By processing the lithological data obtained from mineral exploration drillings with various software, many analyses such as minefield reserve, seam continuity, and the tectonic effect can be performed [2]. In addition, the distribution estimates in the minefield can be made by processing the laboratory test results applied to the samples taken from the boreholes in this software. One of them is the results obtained by major-trace element analyses. It is possible to create risk areas at the mining site in cases where the elements are above the limit values. Interpolation forms the basis of all these estimation methods. Interpolation, with a simple definition, is the determination of unknown values using known

values. It can be expressed as the estimation of empty spaces with the help of existing numerical values in cases where the data are scattered or heterogeneous. IDW (Inverse Distance Weighted) is an interpolation technique used to determine cell values of non-sampled points with the help of values of known sample points, and points are detected in unknown areas by going further away from the known point. Since it is an estimation method, the further away and the greater the distance, the less the effect on the cell value calculation will be. Kriging can be defined as the interpolation method used to estimate the measurements of unknown points by using the measured values in proportion to their weight. The measured points and the points to be predicted are determined depending on the distance. An adjustment is made within the whole field based on the regional variation theory. Therefore, it has been observed that the Kriging method is generally used in earth sciences [3]. These two methods were used in the study, and it was aimed to determine which method obtained more accurate borehole sample results.

Spatial surface modeling, groundwater, precipitation, mining and geology studies were carried out to compare different interpolation methods. For the estimation of element distributions in rocks, additions can be made to Geographic Information System (GIS) software with different purpose-oriented software tools. As a result, three results can be derived. The first of these is the derivation of major-trace element interpolation maps and the establishment of structural relationships, the second is the generation of lithological maps in which the geochemical diagrams of the rocks and the main element data are based on geostatistical interpolation, and the third is the questioning of certain parameter estimation by creating interpolation maps [4]. Potential coal sites can be determined with bivariate statistical approaches at mining fields [5]. The Kriging interpolation method has shown realistic results in determining lignite reserves and the amount of stripping [6]. Kriging, IDW, Spline techniques can be used to estimate the distribution of elements such as As, Pb, which are environmentally hazardous elements, and the volume of the cover layer to be removed from these areas can be determined by 3D modeling [7]. In the comparison of three-dimensional stratigraphic models with Kriging, IDW and closest neighbor methods, the closest neighbor model was observed as the most suitable method in stratigraphic modeling, and Kriging was observed as the closest model in three-dimensional prediction [8]. The reason why the accuracy is lower than the numerical tests in the comparisons made in the application of Spline, IDW, Kriging methods in the coal may be the position differences of the lattice center points of the surfaces whose points are simulated [9]. Estimation methods are also used in water resources. It has been determined that the fuzzy Kriging method exhibits less error than the ordinary Kriging, IDW, and Theissen polygons in cases that vary over time such as a groundwater table [10]. Interpolation methods used to estimate the transparency of water resources from data obtained from satellite data have yielded highly accurate results [11]. While the results are limited in the estimation of seawater mixing with groundwater, the results on the quality degradation elements of the water are more accurate [12]. Precipitation estimates were compared using IDW and Kriging methods, and as a result of the study, it was determined that the estimates obtained by the IDW method gave better results [13]. Although precipitation estimates using Kriging, IDW, Spline support the new method, these have significant differences and are unsatisfactory [14]. In another study conducted in earth sciences, the most suitable landfill site in a province was determined by using the Kriging interpolation method and Multi-Criteria Decision Analysis (MCDA) [15].

2. GEOLOGICAL SETTING

The study area is located in the Thrace press in the Thrace Sub-region of the Marmara Region of Turkey (Figure 1). The Thrace basin is an intermountain Tertiary basin containing Middle Eocene-Pliocene aged units [16, 17]. Thrace basin is particularly important in terms of coal potential as well

as hydrocarbon potential. Eocene aged sediments consisting of conglomerate, sandstone, siltstone, claystone, shale, tuffite and limestone units overlie the basement rocks in the basin (Figure 2). Oligocene deposits begin with the Mezardere Formation, which consists of sandstone containing claystone and tuffite in places. It continues upwards with the Osmancık Formation, which consists of sandstone, and ends with the Danişmen Formation, which includes layers of shale, claystone, sandstone, conglomerate, and coal. On the outskirts of Istranca, where there are no formations of Osmancık and Mezardere, the Danişmen formation unconformably overlies older units in regions [17]. Over the Danişmen formation respectively Miocene aged volcanics, sandstone, siltstone and limestone deposits, Pliocene aged conglomerate and claystone overlie unconformably.
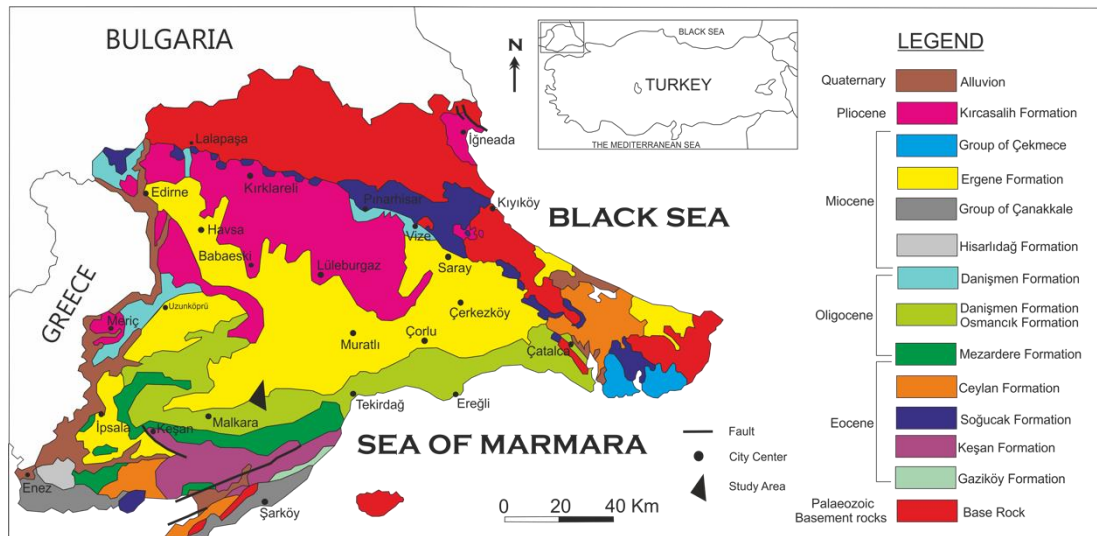

Figure 1. Geological map of Thrace Basin (Modified from [17-20]).

AGE	FORMATION		THICKNESS (m)	LITHOLOGY	DESCRIPTIONS	SEDIMENTARY AREA
PLIOCENE	KIRCASALİH		500		Conglomerate, Claystone	Fluvial
MIOCENE	ERGENE		100-1400		Sandstone, Siltstone, Claystone	Near Shore Lake Fluvial
	HİSARLIDAĞ		800		Volcanite	Volcanism
OLIGOCENE	GROUP OF YENİMUHACIR	DANİŞMEN	300-1000 100		MEMBER OF ARMUTBURNU — Siltstone, Conglomerate, Sandstone / Limestone, Sandstone, Tuffite, Siltstone, Coal / MEMBER OF PINARHİSAR / MEMBER OF TAŞLISEKBAN	Delta Plain
		OSMANCIK	400-800		Sandstone	Delta Front
		MEZARDERE	500-2000 100-400		Sansstone with Siltstone,Tuffite	Pro Delta
EOCENE	KEŞAN	CEYLAN	400-1000		Marl, Siltstone, Tuffite	Turbidites
		SOĞUCAK	40-400		Limestone	Shallow-Deep Marine
		KOYUNBABA	10-100		Sandstone-Siltstone,Claystone	Shallow Marine
	GAZİKÖY	HAMITABAT	2000-3000		Conglomerate-Shale Sandstone-Shale, Sandstone,Shale, Siltstone	Turbidites Delta Fluvial
PALEOZOIC, MESOZOIC	BASE ROCK					

Figure 2. Generalized stratigraphic section of the Thrace Tertiary Basin (Modeified from [21]).

Deltaic and lacustrine environments were formed in the Oligocene with regression in the basin. Coals of the Thrace Basin are also included in the units deposited in these environments [22]. Coal-bearing units that are the subject of the study are found in the Oligocene aged Danişmen formation. Three members have been defined within the Danişmen Formation: Taşlısekban member consisting of conglomerate, sandstone, and marl, Pınarhisar member consisting of limestone and Armutburnu member consisting of conglomerate, sandstone, and claystone. The formation represents the delta plain facies which is at the top unit of the declining delta system. It consists of lake, swamp, flood plain and fluvial sediments [17]. The thickness of the formation reaches 1000 m in places. Different researchers have assigned different ages to the formation: Early Oligocene [23], Middle Oligocene [24-26], Late Oligocene [27, 28], Late Oligocene-Early Miocene [29, 30].

When the loggings from the eight boreholes in the study are examined, Coal seams were detected that are cutting sandstone, siltstone, claystone intercalation. These levels are like the general features of the Oligocene aged Danişmen Formation. The type of coal is lignite, and it is partially clayey. Organically dyed lignite fragments and fossils may be present within the siltstone, sandstone and claystone levels at the bottom and ceiling of lignite veins. Lignite veins start at 25 meters and continue to a depth of 550 meters. The thicknesses of lignite veins vary between 25-100 centimeters.

3. MATERIALS AND METHODS

The study area is located in Malkara, Suleymanpasa, and Hayrabolu districts of Tekirdag province. The area is 15 km^2 and is represented by a triangular polygon. There are 8 boreholes [TD-155 (x:45 34 442 y:05 05 038 z:95), TD-147 (x:45 34 580 y:05 06 670 z:132), TD-151 (x:45 34 398 y:05 07 727 z:157), TD-152 (x:45 34 535 y:05 08 240 z:160), TD-153 (x:45 32 990 y:05 08 120 z:168), TD-133 (x:45 35 960 y:05 07 745 z:90), TD-129 (x:45 37 155 y:05 07 785 z:90), TD-131 (x:45 37 507 y:05 07 817 z:104)] in total in the study area. Borehole selection was made in north-south and east-west section lines to represent the field (Figure 3).
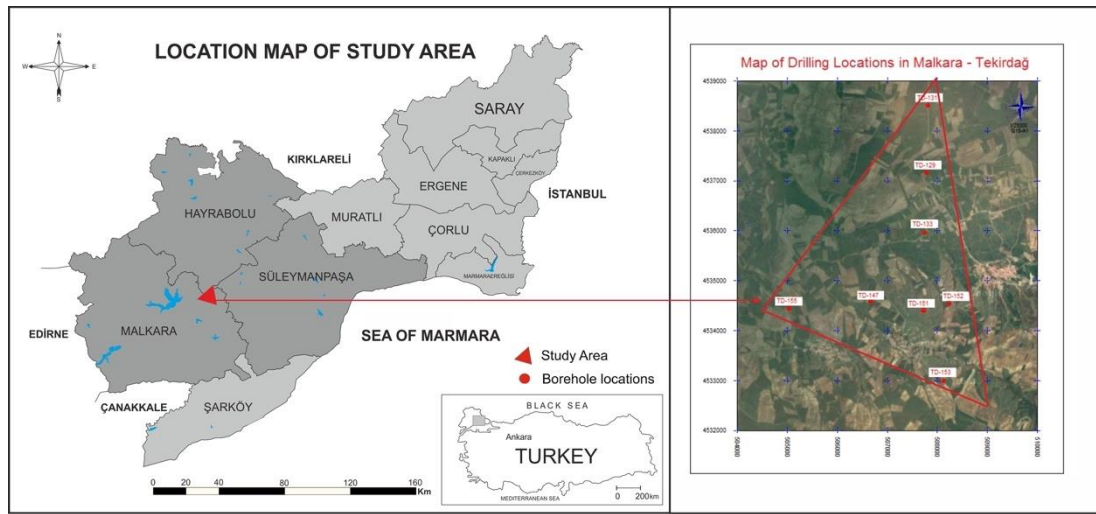

Figure 3. Location map of study area and boreholes.

Well logs were created from the lithological data obtained from eight exploration boreholes in the study area. Since Kriging is the most used interpolation method in earth sciences, NetPro/Mine, which is a correlation software that creates these logs with Kriging, was preferred.

In this study, it was aimed to calculate the proximity values of the actual results obtained from the borehole samples and the results obtained as a result of interpolation. The following method was used in the study. Numerical variables are presented with descriptive statistics such as mean and standard deviation.

Average value change amount = (Maximum value - Minimum value) / Number of class intervals
Difference = Approximate value range average - Actual value
Error Rate = (Difference / Average change amount) * Total number of class intervals
Prediction Accuracy Rate = 100 - Error Rate

If the actual value is lower than the minimum value in the boreholes, then these operations were not performed, and the following formula was used for the difference. The rest of the calculations were made in the same way.

Difference = Minimum borehole value - Actual value

The reason for calculating the difference in this way is that when interpolated, the minimum and the maximum borehole value range is taken as a basis. For example, while the minimum class range value in As study is 5.98 ppm, the actual value is 3.15 ppm. Since it is impossible to obtain this value, it is more logical to calculate how close it is to the minimum borehole value in a similar situation.

Major-trace element analysis was performed on the samples taken in the ACME analytical laboratory (Canada). Major oxides were determined by the ICP-AES method and trace elements were determined by ICP-MS method. The same procedure was applied to each sample and standardization was achieved. As a result of the analyses, the rates of the elements available in the samples were determined. Borehole averages were calculated from the results obtained for each element. Precision and relative standard deviation (RSD) values were calculated for the quality control elements. (Table 1).

Table 1. The average presence of environmentally hazardous elements in the borehole samples (those marked with * are given in %, other values are given in ppm).

Element Group	Elements	TD-129 (n=8)	TD-131 (n=7)	TD-133 (n=7)	TD-147 (n=9)	TD-151 (n=5)	TD-152 (n=7)	TD-153 (n=4)	TD-155 (n=7)	RSD %
Group 1	As	11.52	9.13	7.97	11.10	3.15	5.93	14.35	6.18	
	Cd	0.20	0.25	0.23	0.20	0.15	0.17	0.20	0.20	
	Cr*	0.01	0.01	0.01	0.02	0.01	0.01	0.02	0.03	12.86
	Hg	0.09	0.05	0.09	0.11	0.07	0.06	0.11	0.06	
	Se	1.58	1.40	1.40	1.10	0.50	1.70	6.00	1.15	
Group 2A	Mn*	0.03	0.02	0.02	0.03	0.03	0.02	0.03	0.03	
	Mo	2.46	2.10	1.17	1.93	0.55	0.97	1.10	1.13	
	Ni	92.20	69.00	105.33	145.25	122.00	83.00	219.00	87.50	5.94
	Pb	10.50	9.53	8.80	10.50	15.00	8.00	14.90	7.30	
Group 2B	Be	2.00	3.67	4.00	2.50	1.50	2.00	2.50	2.75	12.86
	Cu	31.28	33.13	30.77	36.75	27.85	55.50	42.10	38.10	
	P*	0.08	0.01	0.02	0.02	0.01	0.02	0.02	0.02	
	Th	6.50	5.73	5.00	6.83	9.05	4.70	7.65	4.70	
	U	5.24	2.97	5.00	4.70	2.75	2.50	5.80	3.40	0.92
	V	76.00	102.00	135.00	123.75	113.50	126.67	150.50	90.00	2.12
	Zn	35.60	34.67	33.33	51.50	50.50	39.33	65.50	32.25	
Group 3	Ba	291.80	249.00	234.67	228.75	310.50	268.00	276.50	215.25	1.19
	Co	9.54	12.20	17.73	20.95	15.50	16.67	25.05	14.78	2.32
	Sb	0.38	0.20	0.83	0.35	0.20	0.23	0.50	0.45	
	Sn	1.00	1.00	1.33	1.50	2.00	1.00	1.50	1.25	
	Ti*	0.16	0.18	0.21	0.23	0.28	0.21	0.29	0.18	

Environmentally important elements can be examined in four parts as Group 1, Group 2A, Group 2B, and Group 3 [31]. The most hazardous of these element classes in terms of environmental and human health is Group 1 (Arsenic, Cadmium, Chromium, Mercury, Selenium), and the other element classes from the most to the least hazardous are Group 2A (Boron, Chlorine, Fluorine, Manganese, Molybdenum, Nickel, Lead), Group 2B (Beryllium, Copper, Phosphorus, Thorium, Uranium,

Vanadium, Zinc), and Group 3 (Barium, Cobalt, Antimony, Tin, Titanium), respectively. Distribution maps of elements evaluated in four different hazard groups as a result of major-trace element analysis were created with Quantum GIS, an open source GIS software.

These element values are known at the borehole points. However, the values of these elements are not known in the areas that are in between and are not borehole. Since the field represents a local area, it is possible to estimate these gaps from the data obtained by boreholes. The interpolation method is used for this purpose. In this study, two interpolation methods were applied and compared. It was aimed to determine the most suitable method for coal element values. IDW and Krigging methods were applied. TD-151, which is located at the intersection of north-south and east-west section lines, was used for testing purposes. Both interpolation methods were used without taking into account the TD-151 borehole samples. Since the element values in this borehole are known beforehand, it was tried to determine which method gave the most accurate value.

After using Kriging as the interpolation method, the maps obtained were converted to Raster data format. With this technique expressed in cells, the range of values each pixel corresponds to was determined using the Reclass (reclassification) technique. The diagram showing the flow of the study is given in Figure 4.
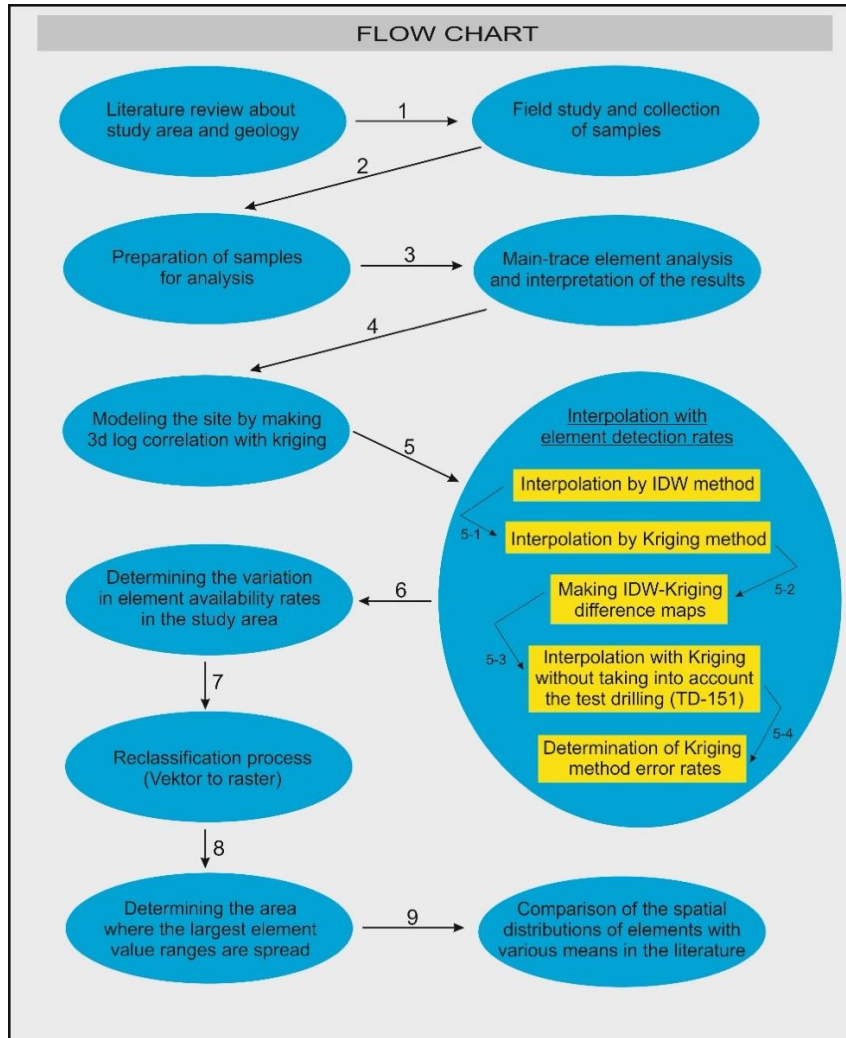
Figure 4. Flow chart of the study.

4. RESULTS AND DISCUSSION

The correlation formed according to the lithology data processed in the NetPro/Mine software was compared with the strut sections. Two section lines were examined on the east-west (Figure 5) and north-south (Figure 6) lines. In the software, similar results were obtained in both section lines, with ceiling lignite at the top, floor lignite at the bottom, and a layer of clayey lignite in between. The accuracy of these findings was tested by comparing them with the seams in the strut sections. Highly accurate results were observed for both section lines. The increase in the number of coal seams on the north-south section line from south to north shows that tectonism has an effect on coal formation in the north of the study area. While the clayey lignite layer was not found in the south of the study area, it was observed that it was formed gradually towards the north. There are more stable deposition

conditions where tectonism has less effect on the east-west line. It was found that the clayey lignite seam disappeared to the east of this section line.
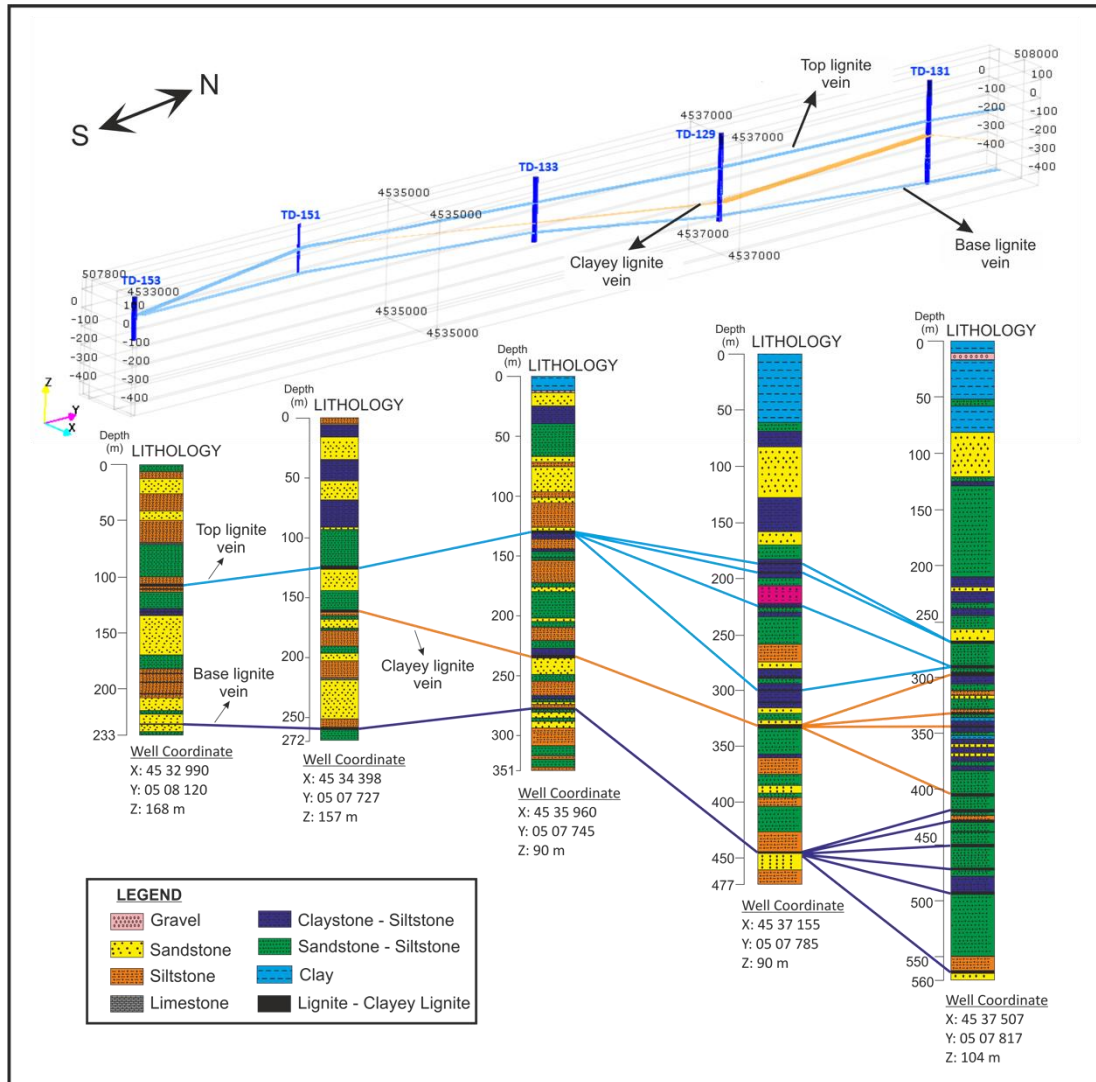

Figure 5. North-south line created with Kriging and strut sections (ceiling, bottom coal lode and clayey lignite lode).
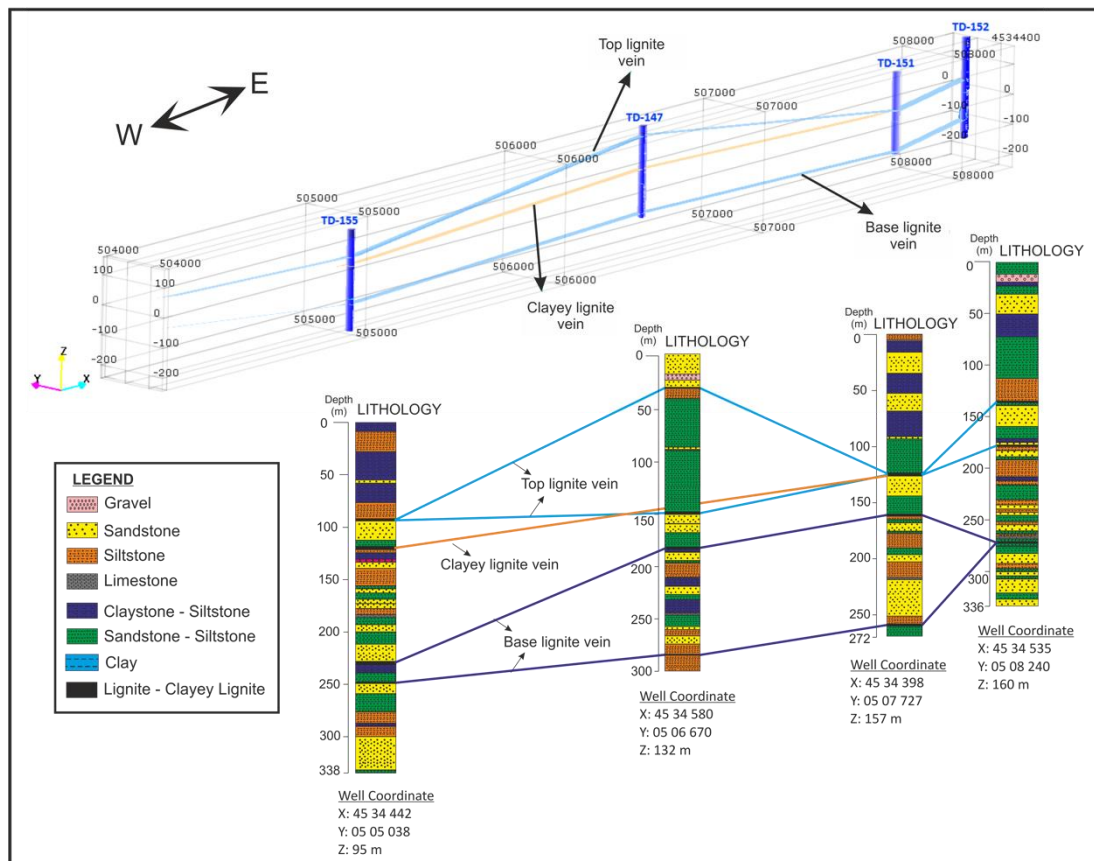
Figure 6. East-west line created with Kriging and strut sections (ceiling, bottom coal lode and clayey lignite lode).

4.1. Estimating Element Distributions

The spatial spread estimates were made by applying IDW and Kriging interpolation methods of the elements. The study was conducted for all element classes including Group 1, Group 2A, Group 2B, and Group 3, and similar results were observed. The spatial spread estimates of Group 1 (the most hazardous element class) elements of As (Figure 7), Cd (Figure 8), Cr (Figure 9), Hg (Figure 10), Se (Figure 11) were made by IDW and Kriging methods.
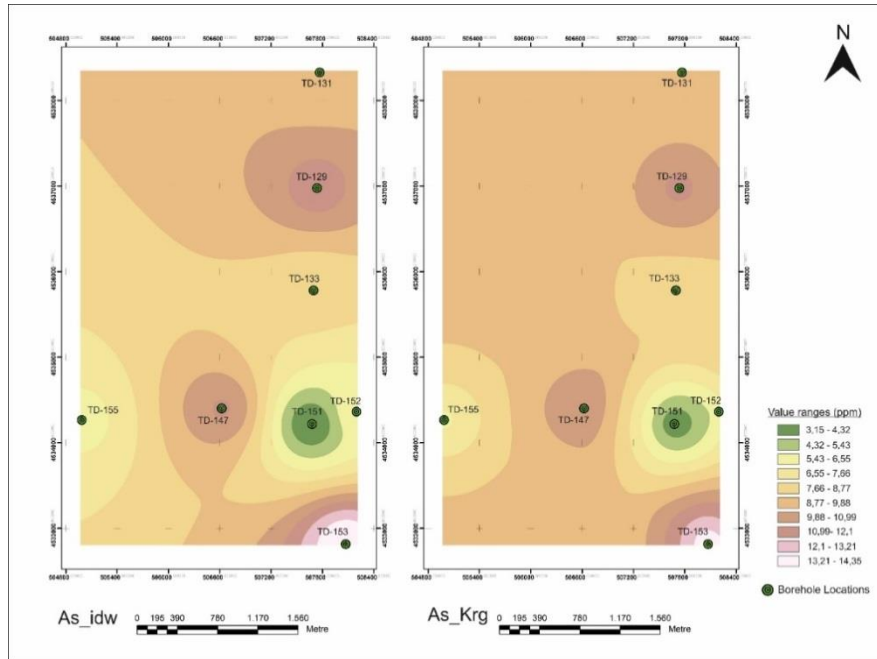
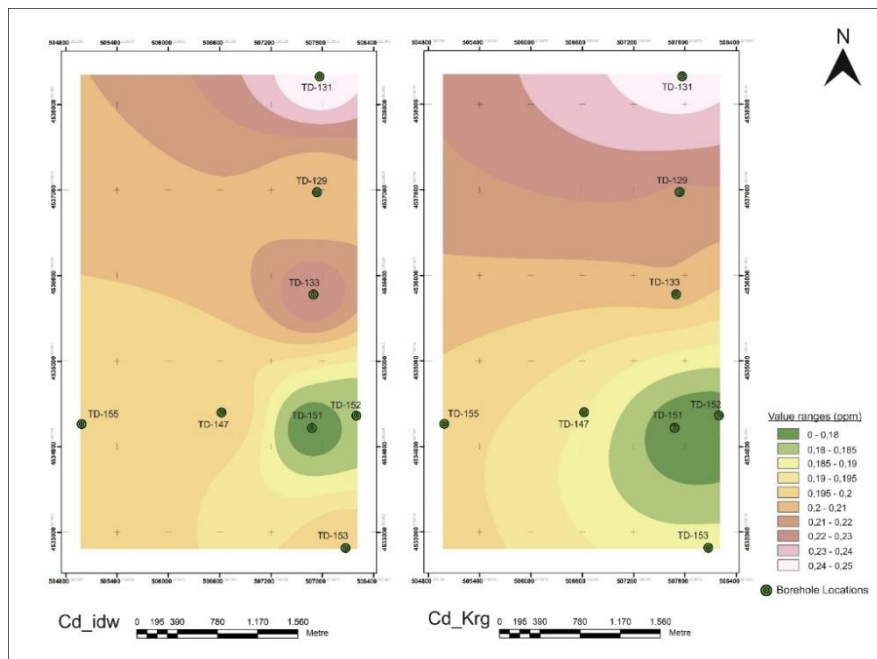**Figure 7.** Areal spreading of As by Kriging and IDW.

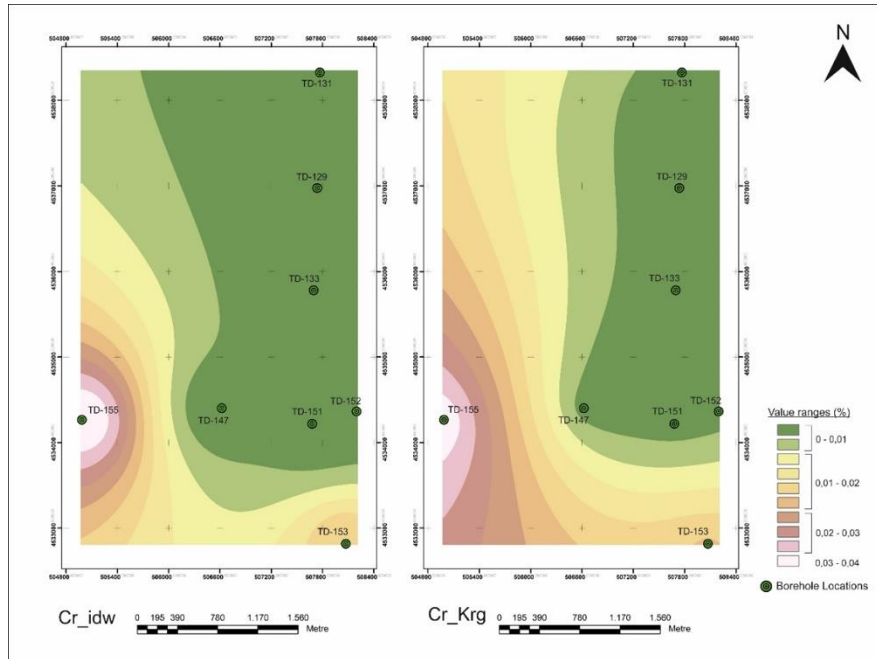**Figure 8.** Areal spreading of Cd by Kriging and IDW.

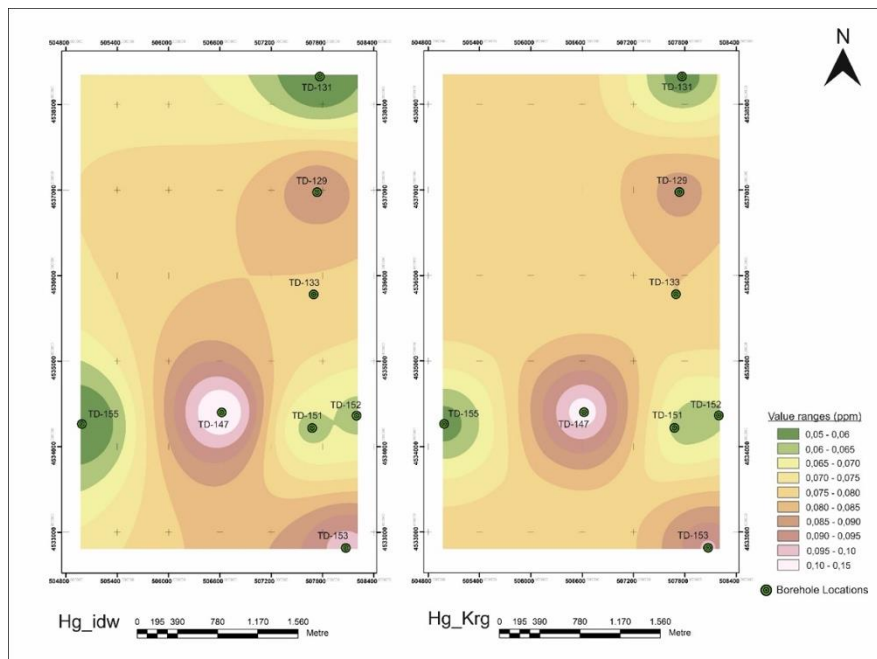**Figure 9.** Areal spreading of Cr by Kriging and IDW.

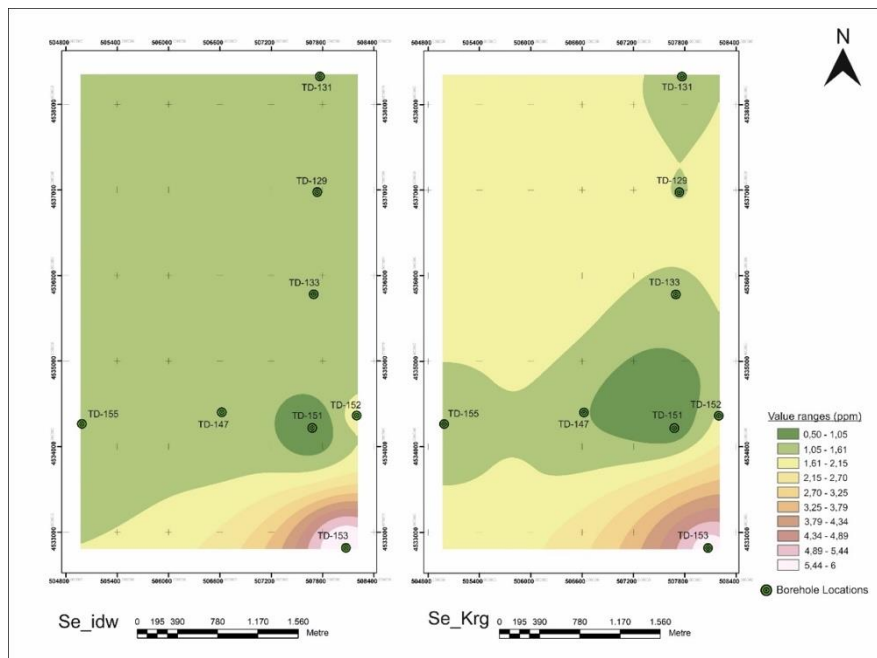**Figure 10.** Areal spreading of Hg by Kriging and IDW.

Figure 11. Areal spreading of Se by Kriging and IDW.

In line with the differences considered, the areas that gave the same result in both methods are white and in shades of white. This is why the spots where there are boreholes are white or in shades of white. The places that are completely different as a result of the two methods are in black. The fact that the changing colors (gray and its shades) are close to black or white also determines the degree of this difference. The results obtained from the difference maps can also be interpreted as the light-colored places are the most accurate while the accuracy decreases as the color gets darker. In addition, another result that can be inferred is that the accuracy increases as the black color decreases.

When the analysis is made on the basis of elements, it can be said that As is the most accurate estimate because the results were less accurate in two small local areas in the west and east of the study area but similar results were obtained in the remaining area. Cd was observed to be dark in the east of the study area, in the part covering the area of TD-151 and TD-152, and around the TD-129. For Cr, it was determined that there are local differences in the south-west and north-west of the study area. Hg was determined to be dark in two local areas in the south-west of the study area, around the TD-151, and in a single local area in the north-east. Se also differs in two different areas. It was concluded that it was dark and different in a large area in the north-west of the study area and a small local area in the south-east (Figure 12).
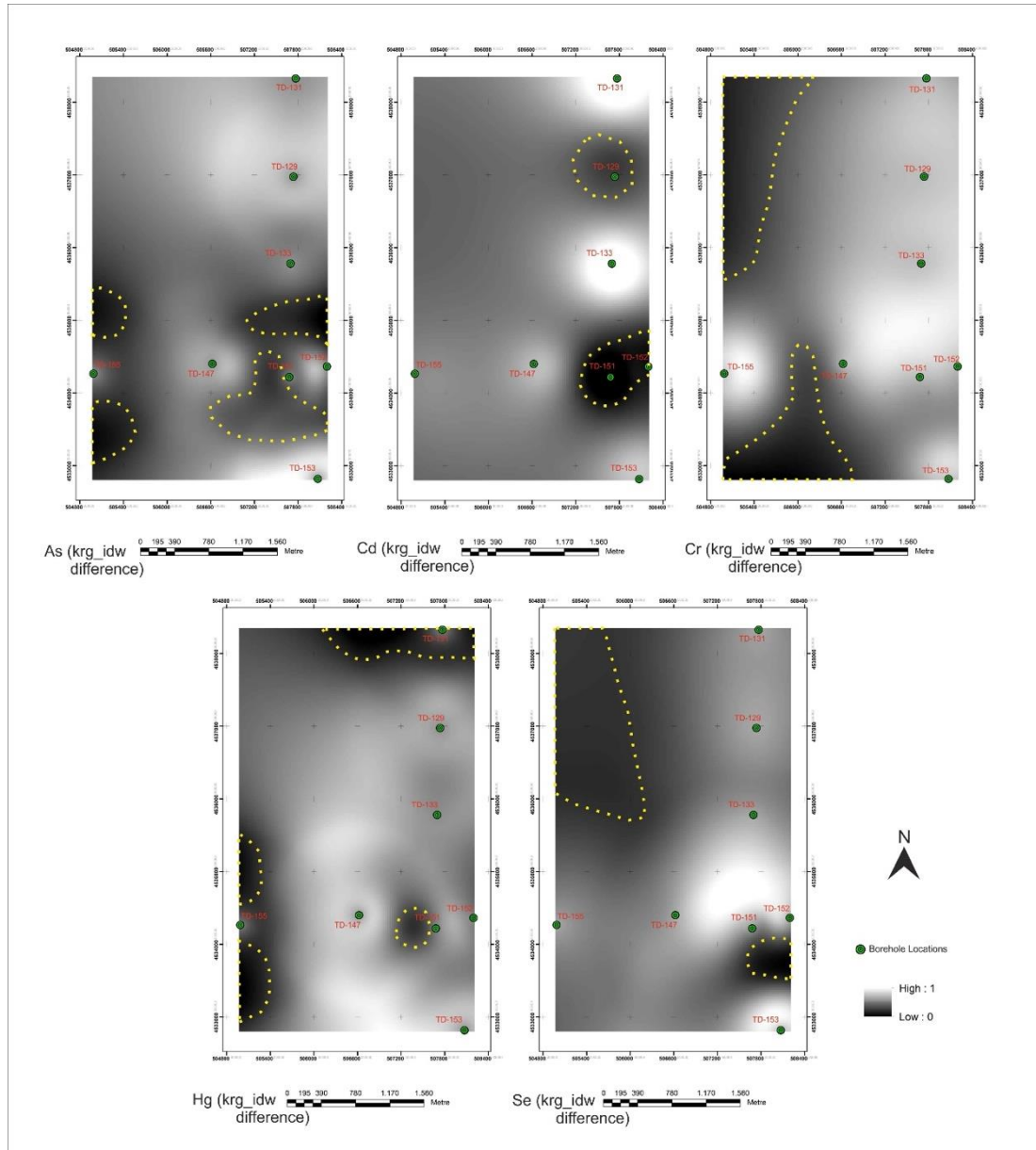
Figure 12. The display of the areas where the group 1 elements were found to differ as a result of two methods (Kriging and IDW).

The well numbered TD-151 was chosen for testing purposes as it is the borehole located on the north-south and east-west section line of the study area. Interpolation was performed for the Group 1 elements over the remaining 7 boreholes. Kriging was chosen as the method. An example map of the element As is given in Figure 13. The same procedures were applied to other elements.

As a result of the interpolation performed with the Kriging method without adding the TD-151, the value in TD-151 was estimated and compared with the actual value. As a result, the margin of error was determined. Error rates for Group 1 elements are given in Table 2. Cr and Hg gave exact results because the values determined with the actual values coincided with the exact range. 96.86% correct results were obtained in Se and 75% in Cd. The margin of error in As was higher than the other elements, and the accuracy rate of the prediction was determined as 66.2%. The true value of the elements As, Cd, Se is lower than the minimum value in the boreholes. The second evaluation method was used to calculate the differences among these three elements in order to achieve accuracy in interpolation.

Table 2. Error and prediction accuracy rates of Group 1 elements of TD-151 borehole site made by the Kriging method.

Elements	Error rate (%)	Accuracy of estimates (%)
As	33,8	66,2
Cd	25	75
Cr	0	100
Hg	0	100
Se	9,14	90,86
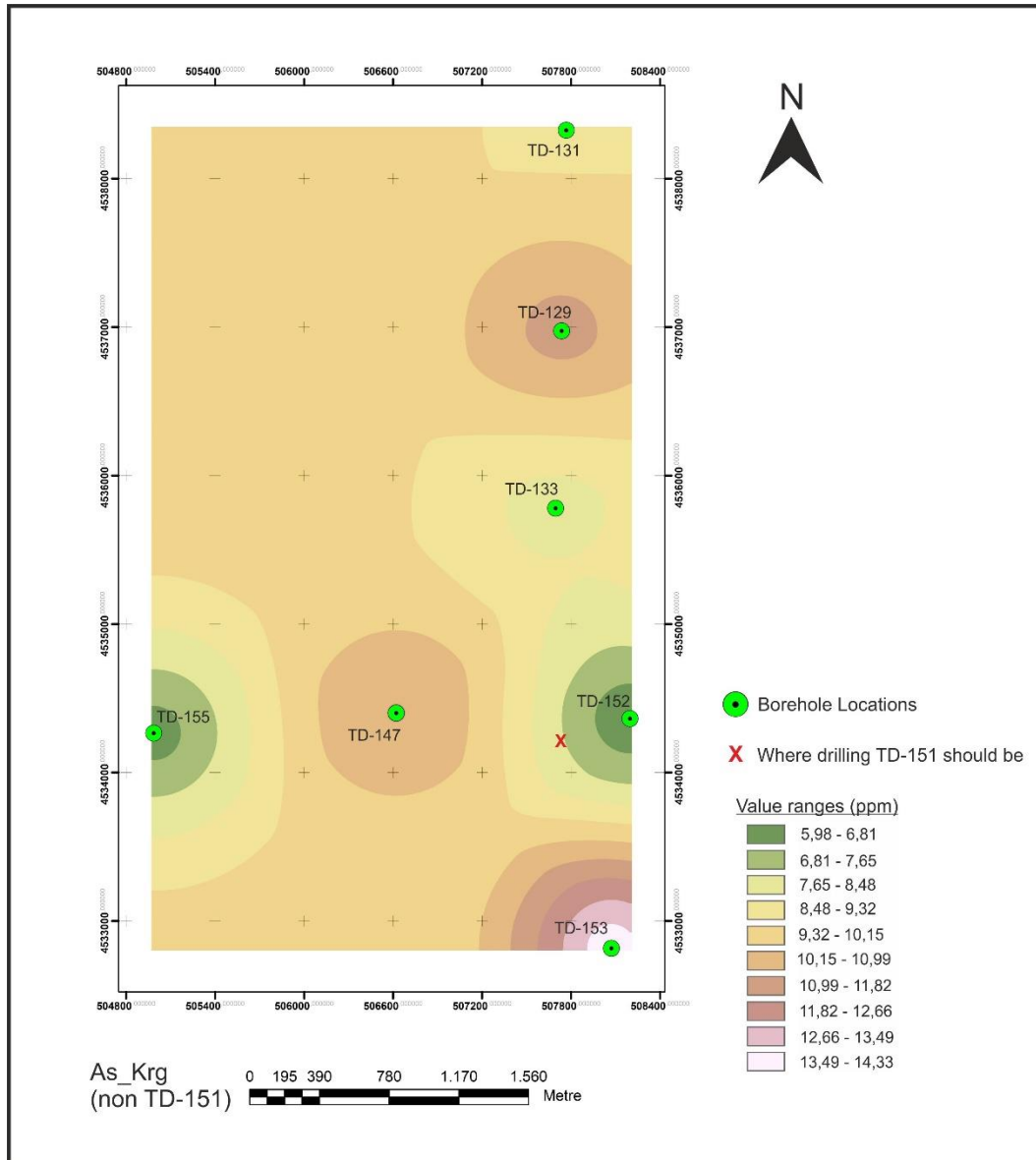
Figure 13. Kriging interpolation method of As without adding TD-151 borehole.

4.2. Determination of Environmentally Sensitive Element Distributions with Kriging Method

The average values of the element concentrations of 54 samples taken for a total of 8 boreholes were taken. It is very important to carry out this study especially for the 25 environmentally sensitive elements. The individual average values of the samples taken from each borehole were examined for environmentally sensitive elements. The elements examined in 4 groups were classified as Group 1, Group 2A, Group 2B, and Group 3.

Cr, As, Cd, Hg, Se are in the 1st group and are considered the most hazardous class. When the average values on the basis of boreholes were examined, it was determined that the Cr, Cd, and Hg elements did not show a great change and were in close concentration in 8 boreholes. It was determined that Se and As varied in borehole averages. It was observed that the As gave the lowest value in the average of the TD-155, which is located in the farthest part of the study area, and the highest value in the average of the TD-153 located in the south of the north-south section line. Although the values for the Se element also varied, it was determined that the lowest borehole value average was in the TD-151, and the highest average value of the borehole was in the TD-153 located to the south of the north-south section line.

Group 2A consisted of less hazardous elements than Group 1 and was examined in terms of Mn, Mo, Pb, Ni. It was determined that the Mn gave the lowest borehole average value in the TD-133 and the highest average value in the TD-151. The lowest borehole average value for Mo was in the TD-151 and the highest average value was in the TD-129. When the Pb was examined, the lowest average value of the borehole was seen in the TD-152, located at the intersection of the north-south and east-west section lines, and the highest average value was seen in the TD-153 located to the south of the north-south section line. Ni gave the lowest average value in the TD-155, located in the far west of the study area, and the highest average value in the TD-153, located in the south of the north-south section line.

Group 2B did not vary in the borehole averages and gave close values in 8 boreholes. Be gave the lowest average value of the borehole in the TD-152, located at the intersection of the north-south and east-west lines, and the highest average value in the TD-147. Th gave the lowest average borehole value in the TD-152 and the highest value in the TD-153. It was determined that the Mn gave the lowest borehole average value in the TD-133 and the highest average value in the TD-151. V gave the lowest borehole average value in the TD-155 in the west of the study area and the highest value in the TD-131 at the far north of the study area. Cu gave the lowest borehole average value in the TD-133, and the highest average value in the TD-153. Zn gave the lowest borehole average value in the TD-152 and the highest average value in the TD-153.

Group 3, which is environmentally sensitive but the least hazardous compared to other group elements, consists of Ti, Ba, Co, Sn, Sb. Ti gave the lowest average value in boreholes TD-152 and TD-155, and the highest average value in the TD-153. Ba gave the lowest borehole average value in the TD-155 and the highest average value in the TD-147. Co gave the lowest borehole average value in the TD-129 and the highest average value in the TD-152. Sn gave the lowest borehole average value in TD-152 and the highest average value in the TD-147. It was determined that the Sb gave the lowest borehole average value in the TD-151 and the highest average value in the TD-133.

According to these results, local concentrations of environmentally sensitive elements in the study area were determined. According to the findings, the TD-153 had the highest concentration average in the field in terms of As, Cu, Ni, Pb, Se, Th, Ti, Zn elements. When the averages of the TD-147 were examined, Be, Ba, Sn elements had the highest value. Mo and U elements gave the highest value in the average values of the TD-129. In the other four boreholes, one element had the highest value in each. It was determined that the highest concentration of Mn was in the TD-151, V in the TD-131, Co in the TD-152, and Sb in the TD-133.

When the lowest value concentrations were examined, the averages of the TD-153, TD-147, and TD-131 did not give the lowest value in any borehole. TD-152 is the borehole with the lowest

concentration of elements. Pb, Be, Th, U, Zn, Ti, Sn elements gave the lowest value according to the borehole averages in this borehole. As, Ni, V, Ti, Ba had the lowest mean value in the TD-155. It was determined that TD-151 had the lowest value for Mo, Se, Sb, TD-133 for the Cu and Mn, TD-129 for Co.

According to all these findings, an increase was observed in As, Cu, Ni, Pb, Se, Th, Ti, Zn values in the southernmost of the study area. It was determined that the concentrations of Co, Sb Mo and U increased, respectively, further towards the north on the north-south section line. It was determined that the V element concentration value was high in the northernmost part of the study area. Mn value increased further from east to west on the east-west section, and Be, Ba, Sn increased gradually.

The lowest environmentally sensitive element values in the study area show that these areas are less hazardous. When examined from this point of view, Pb, Be, Th, U, Zn, Ti, Sn elements at the intersection point of north-south and east-west section lines gave the lowest value in the whole field. It was determined that the Mn and Cu gave the lowest value further north from this point, and Co in a little further north. It was determined that further towards the west from the same intersection, primarily Se, Mo, Sb, and As, Ni, V, Ti, Ba element concentrations at the farthest point gave the lowest value compared to the field average (Figure 14).
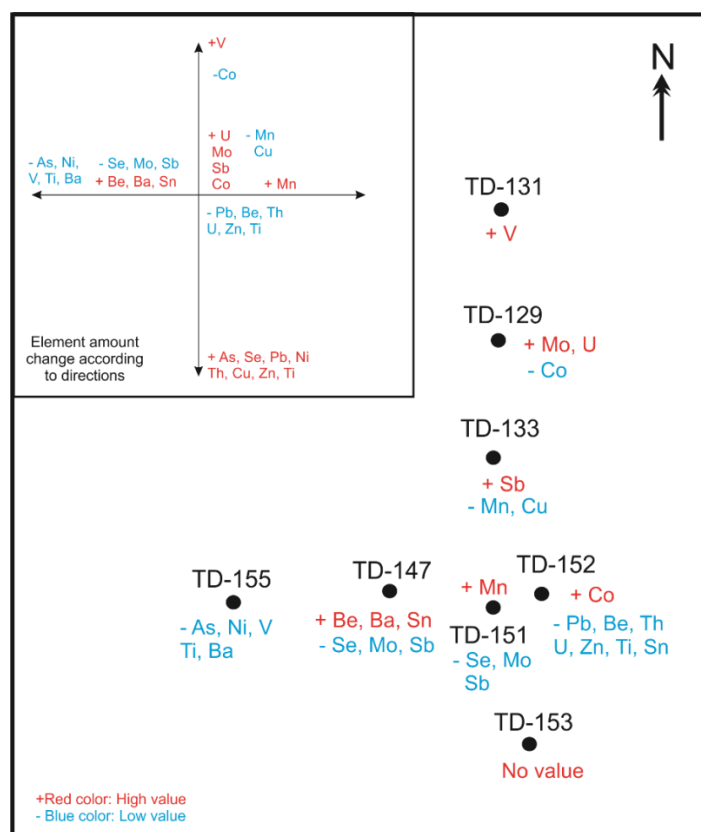

Figure 14. Change of elemental presence rates according to borehole locations.

4.3. Spatial Spread of Element Distributions

Based on the fact that the total area is the same in each map, it was determined how many square meters each value range (color) covered (Figure 15). The list of methods applied to environmentally important elements in groups is included in Table 3 below.

	Pixel Count	Area (m²)
1	97,00000000000	291
2	277,00000000000	831
3	458,00000000000	1374
4	825,00000000000	2475
5	3094,00000000000	9282
6	13253,00000000000	39759
7	1586,00000000000	4758
8	242,00000000000	726
9	98,00000000000	294
10	50,00000000000	150
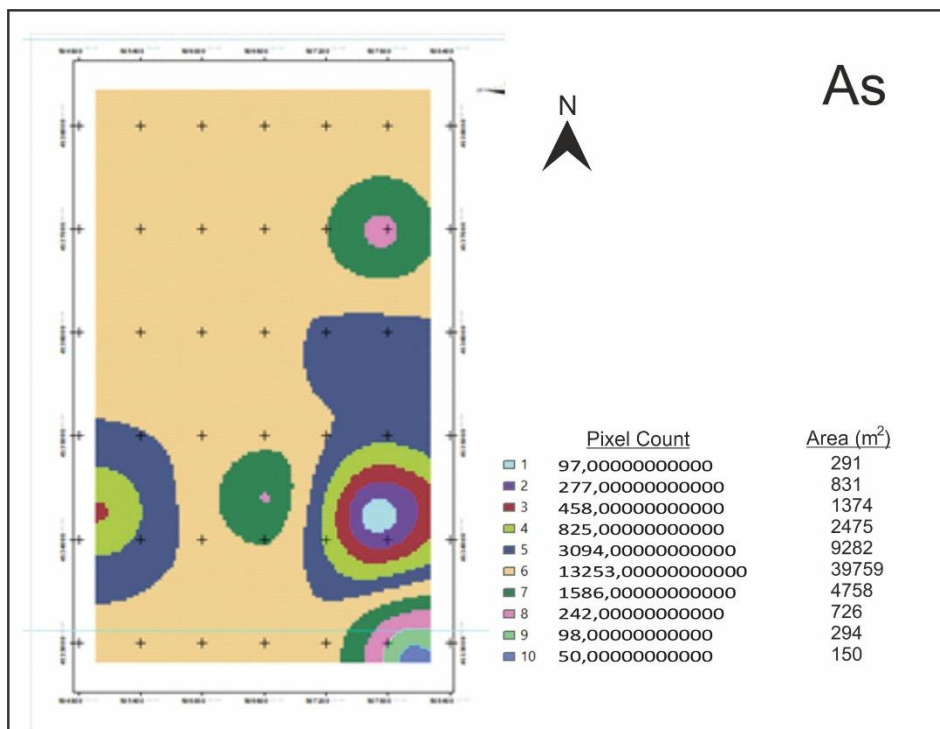
Figure 15. A sample reclassification study of As.

Table 3. The largest area spread by the elements according to their value range (those marked with * are given in %, other values are given in ppm for value range column).

Element	Largest Area (m²)	Value range	Group
As	39759	8.77-9.88	Group 1
Cd	9183	0.19-0.20	
Cr*	18900	0-0.01	
Hg	34815	0.075-0.08	
Se	35814	1.61-2.15	
Mn*	33636	0.02-0.03	Group 2A
Mo	10344	1.30-1.40	
Ni	16650	92.55-101.68	
Pb	21867	7-7.5	
Be	54612	2.50-2.74	Group 2B
Cu	54129	36.15-38.83	
P*	37089	0.01-0.015	

Th	54297	6.01-6.43	
U	30258	4.15-4.48	
V	16398	105.96-113.37	
Zn	27870	32.25-37.1	
Ba	53493	229-236	
Co	11088	14.21-15.76	
Sb	37158	0.35-0.40	Group 3
Sn	53928	1.31-1.41	
Ti*	14760	0.17-0.19	

Results of the values obtained as a result of calculations were compared with the average values of Turkey, the US, China coals, and the average upper continental crust. The evaluation was made on 21 elements. Figure 16 contains the percentage values of the areas above the average value. Be, Cu, V remained completely above all limit values in the study area. It was observed that Mn, Mo, P, Sb were completely below all limit values in the study area. Be, Cu and V are associated with organic matter in coal. However, Be is associated with quartz and clay minerals [32], V is associated with clay minerals [33-35] and Cu is associated with sulfides [35-37].

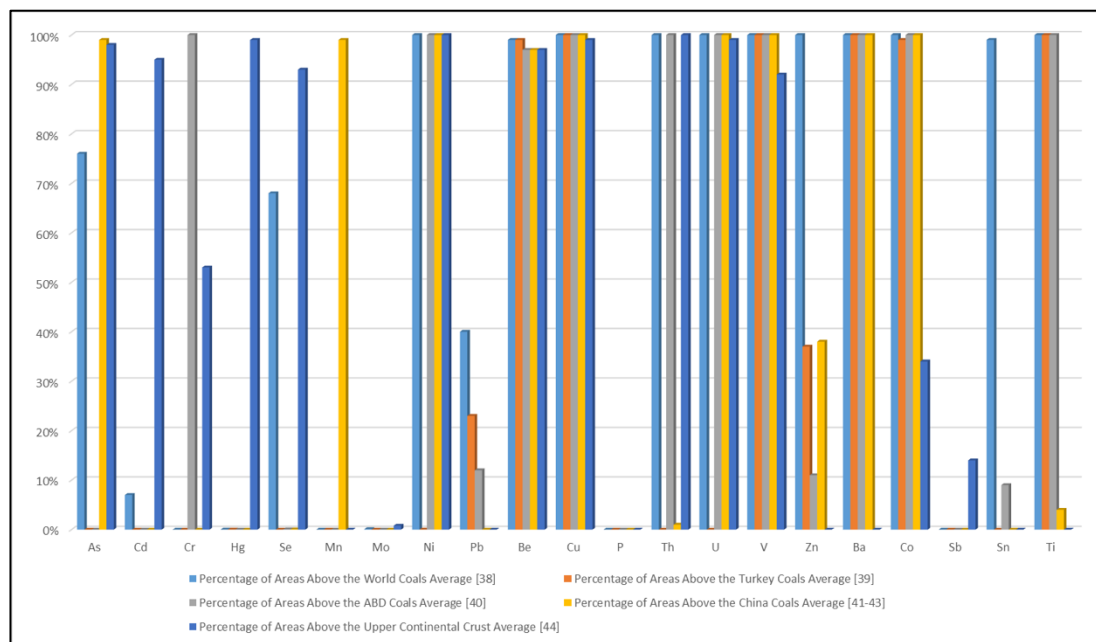**Figure 16.** The comparison of areal extent of the elements with world, Turkey, USA, China and the upper continental crust.

5. CONCLUSION

The difference between methods IDW and Kriging methods was determined by maps. It was determined that the method that gave the most accurate result to the test borehole TD-151 was Kriging. According to the results obtained from the elements of the most hazardous class Group 1, the

accuracy of Cr and Hg was 100%, that of Se was 90.86%, Cd was 75%, and As was 66.2%. Class ranges determined by Kriging interpolation method were re-mapped and converted into Raster (cellular) data format. As a result of the comparison of values in each cell with the average values of the world, Turkey, USA, China, and the upper continental crust, it was determined that Be, Cu, V elements were completely above the limit values, and Mn, Mo, P, Sb elements were completely below the limit values. Applying the same method with different interpolation methods in different coalfields and other mines other than coal will contribute to the literature.

ACKNOWLEDGEMENTS

REFERENCES

[1] Paraskevis, N., Roumpos, C., Stathopoulos, N., and Adam, A., (2019), Spatial analysis and evaluation of a coal deposit by coupling AHP and GIS techniques. International Journal of Mining Science and Technology, 29, 943–953.

[2] Kiš, I.M., (2016), Comparison of Ordinary and Universal Kriging interpolation techniques on a depth variable (a case of linear spatial trend), case study of the Šandrovac Field. The Mining-Geology-Petroleum Engineering Bulletin, 31(2), 41-58.

[3] Qi, A., Kang, W., Zhang, G., and Lei, H., (2019), Coal Seam Thickness Prediction Based on Transition Probability of Structural Elements. Applied Sciences, 9(6), 1144.

[4] Fiannacca, P., Ortolano, G., Pagano, M., Visalli, R., Cirrincione, R., and Zappala, L., (2017), IG-Mapper: A new ArcGIS (R) toolbox for the geostatistics-based automated geochemical mapping of igneous rocks. Chemical Geology, 470, 75-92.

[5] Sütçü, E., Paker, S., Nurlu, Y., Kumtepe, P., and Cengiz, T., (2009), Bivariate statistical approach to determine potential coalfield areas with using gis methods in Tekirdag-Malkara Basin. International Geographical Information Systems Congress, Nov. 2–6, 2009, Izmir, Turkey. İzmir.

[6] Cengiz, T., Nurlu, Y., Kumtepe, P., and Sütçü., E., (2009), Rezerv ve dekapaj miktarlarının coğrafi bilgi sistemleri kullanılarak tespiti ve diğer yöntemlerle karşılaştırılması: Sivas-Kangal-Kalburçayırı linyit yatağı örneği. International Geographical Information Systems Congress, Nov. 2–6, 2009, İzmir, Turkey.

[7] Boente, C., Gallego J.R., Rodriguez-Valdez, E., Sierra, C., and Menendez-Aguado, J., (2016), Geostatistical approach to the 3d-distribution of hazardous waste and polluted soil in a brownfield. 16th International Multidisciplinary Scientific Geoconference (SGEM 2016), Albena, Bulgaria.

[8] Wei, W.X., Quan, T., Wang, Y., Wang, H., and Li, P.Z. (2014), Application of three-dimensional interpolation methods in contaminated site evaluation. 8th International Conference on Waste Management and Technology (ICWMT 8), Shanghai, Peoples R China, 878, 782-790.

[9] Yue, T. X., Du, Z. P., Song, D. J., and Gong, Y., (2007), A new method of surface modeling and its application to DEM construction. Geomorphology, 91, 161-172.

[10] Masoumi, Z., Rezaei, A., and Maleki, J. (2019), Improvement of water table interpolation and groundwater storage volume using fuzzy computations. Environmental Monitoring and Assesment, 191, 401.

[11] Jaskula, J., and Sojka, M., (2019), Application of remote sensing and gis to water transparency estimation in reservoirs. Carpathian Journal of Earth and Environmental Sciences, 14, 353-366.

[12] Momejian, N., Abou Najm, M., Alameddine, I., and El-Fadel, M., (2019), Groundwater Vulnerability Modeling to Assess Seawater Intrusion: a Methodological Comparison with Geospatial Interpolation. Water Resources Management, 33, 1039-1052.

[13] Taylan, D. E., and Damçayırı, D., (2016), Isparta bölgesi yağış değerlerinin IDW ve Kriging Enterpolasyon Yöntemleri ile Tahmini. Teknik Dergi/Technical Journal of Turkish Chamber of Civil Engineers, 459, 7551-7559.

[14] Zhao, N., Yue, T.X., Chen, C.F., Zhao, M.W., and Fan, Z., (2018), An improved statistical downscaling scheme of tropical rainfall measuring mission precipitation in the Heihe River basin, China. International Journal of Climatology, 38, 3309-3322.

[15] Aksoy, E., and San, B. T. (2019), Geographical information systems (GIS) and multi-criteria decision analysis (MCDA) integration for sustainable landfill site selection considering dynamic data source. Bulletin of Engineering Geology and the Environment, 78(2), 779-791.

[16] Keskin, C., (1974), Stratigraphy of the Northern Thrace Basin. Turkey Second Petroleum Congress Proceedings Book, 137-163.

[17] Perinçek, D., Ataş, N., Karatut, Ş., and Erensoy, E. (2015), Geological factors that controls the potential of lignite layers in Danişmen Formation, Trakya Basin. Journal of Mineral Research and Exploration, 150, 79-110.

[18] Kasar, S., Bürkan, K., Siyako, M., and Demir, O., (1983), Tekirdag-Sarkoy-Keşan-Enez geology and hydrocarbon possibilities of the region. TPAO Research Group, Report no: 1771, Ankara.

[19] Türkecan, A. and Yurtsever A., (2002), Istanbul map, 1: 500 000 scale geological map series of Turkey. General Directorate of Mineral Research and Exploration, Ankara.

[20] Siyako, M., (2006), Lithostratigraphy units of the Thrace Region (Tertiary section). Stratigraphy Committee, Lithostratigraphy Units Series-2. Publication of General Directorate of Mineral Research and Exploration, Ankara.

[21] Siyako, M., (2006), Lignite sandstones of the Thrace Basin. Mineral Research and Exploration Journal, 132, 63-73.

[22] Şenguler, İ., (2013), Geology and coal potential of Ergene (Thrace) Basin. MTA Natural Resources and Economy Bulletin, 16, 109-114.

[23] Saraç, G., (1987), Mammal paleo-fauna of Edirne-Kırklareli-Saray-Çorlu-Uzunköprü Derekebir regions at North Trakya District, Ankara Uni., Institute of Science and Technology, Department of Geological Engineering, Postgraduate Thesis, Ankara.

[24] Umut, M., İmik, M., Kurt, Z., Özcan, İ., Sarıkaya H. and Saraç, G. (1983), Geology of Tekirdağ, Silivri (Istanbul), Pınarhisar districts. General Directorate of Mineral Research and Exploration Report No: 7349, Ankara.

[25] Umut, M., İmik, M., Kurt, Z., Özcan, İ., Ateş, M., Karabıyıkoğlu M. and Saraç, G. (1984), Geology of Edirne – Kırklareli – Lüleburgaz – Uzunköprü neighborhoods. General Directorate of Mineral Research and Exploration Report No: 7604, Ankara.

[26] Sümengen, M., Terlemez, İ., Şentürk, K., Karaköse, C., Erkan, E.N., Ünay, E., Gürbüz, M. and Atalay, Z. (1987), Stratigraphy of the Gelibolu Peninsula and southwestern Thrace Tertiary basin, sedimentology and tectonics. General Directorate of Mineral Research and Exploration, Technical Report: 8218, Ankara.

[27] Kasar, S. and Eren, A. (1986), Geology of Kırklareli – Saray – Kıyıköy district. TPAO Investigation Group Report No: 2208, Ankara.

[28] Batı, Z., Alişan, C., Ediger, V.Ş., Teymur, S., Akça, N., Sancay, H., Ertuğ, K., Kirici, S., Erenler, M. and Aköz, Ö., (2002)., Palinomorph, foraminiferal and nanoplankton biostratigraphy of Northern Trakya Basin. Turkey Stratigraphy Committee Workshop (Lithostratigraphic Notorious of Trakya District) Abstracts, p. 14.

[29] Alişan, C., (1985), Palinostratigraphy of sheared formations and evaluation of sedimented environments of Umurca-1, Kaynarca-1, Delen-1 boreholes at Trakya "I" district. TPAO Investigation Group Report No: 386, Ankara.

[30] Gerhard, J.E. and Alişan, C., (1987), Palynostratigraphy, paleoecology, and visual organic geochemistry Turgutbey-2, Değirmencik-3 and Pancarköy-1, Thrace Basin, Turkey. TPAO Investigation Group Report No: 983, Ankara.

[31] Swaine, D.J., and Goodarzi, F., (1995), Environmental aspects of trace elements in coal. Springer Science and Business Media, Netherlands, 322p.

[32] Singh, R.M., Singh, M.P. and Chandra, D., (1983), Occurence, distribution and probable source of trace elements in Ghugas coals, Wardha Valley, district chandrapur and Yeotmal, Maharashtra, India. International Journal of Coal Geology, 2, 371-381.

[33] Querol, X., Cabrera, Ll., Pickel, W., Fernandez-Turıel, J.L., Hagemann, H.W. and Lopez-soler, A., (1996), Controls on the quality of the Mequinenza Coal Deposit, NE Spain. International Journal of Coal Geology, 29, 67-91.

[34] Finkelman, R.B. and Grosss, P.M.K., (1999), The types of data needed for assessing the environmental and human health impacts of coal. International Journal of Coal Geology, 40, 91-101.

[35] Goodarzi, F., (2002), Mineralogy, elemental composition and modes of occurrence of elements in Canadian feed-coals. Fuel, 81, 1199-1213.

[36] Querol, X., Finkelman, R.B., Alastuey, A., Huerta, A., Palmer, C.A., Mroczkowski, S., Kolker, A., Chenery, S.N.R., Robinson, J.J., Juan, R. and Lopez-soler, A., (1998), Quantitative determination of modes of occurrence of major, minor and trace elements in coal: Comparison of results from different methods. AIE 8th Australian Coal Science Conference, Proceedings, pp. 51-56.

[37] Swaine, D.J., (1990), Trace Elements in Coal. Butterwarh, London, 278 p.

[38] Ketris, M.P., and Yudovich, Y.E., (2009), Estimations of clarkes for carbonaceous biolithes: world averages fortrace element contents in black shales and coals. International Journal of Coal Geology, 78, 135-148.

[39] Palmer, C.A., Tuncalı, E., Dennen, K.O., Coburn, T.C., and Finkelman R.B., (2004), Characterization of Turkishcoals: a nation wide perspective. International Journal of Coal Geology, 60, 85-115.

[40] Finkelman, R.B., (1993), Trace and minor elements in coal. In: Organic Geochemistry (ed. M.H. Engel, S.A. Macko) (Ed.). New York, Plenum.

[41] Dai, S.F., Zhou, Y.P., Ren, D.Y., Wang, X.B., Li, D., and Zhao, L., (2007), Geochemistry and mineralogy of the Late Permian coals from the Songzao Coalfield, Chongqing, southwestern China. Science in China Series D: Earth Science, 50, 678-688.

[42] Dai, S.F., Li, D., Chou, C.-L., Zhao, L., Zhang, Y., Ren, D.Y, Ma, Y.W., and Sun, Y.Y., (2008), Mineralogy and geochemistry of boehmite-richcoals: new insights from the Haerwusu Surface Mine, Jungar Coalfield, Inner Mongolia, China. International Journal of Coal Geology, 74:185-202.

[43] Dai, S.F., Ren, D.Y., Chou, C.L., Finkelman, R.B., Seredin, V.V., and Zhou, Y.P., (2012), Geochemistry of trace elements in Chinese coals: A review of abundances, genetic types, impacts on human health, and industrial utilization. International Journal of Coal Geology, 94, 3-21.

[44] Rudnick, R.L., and Gao, S., (2003), Treatise on Geochemistry Volume 3. In: The Cust (ed. H.D. Holland, K.K. Turekian). Elsevier-Pergamon, Oxford.

RESEARCH ARTICLE

THE EFFECT of OMEGA 3, 6,9 and STEARIC ACID on TRACE ELEMENTS in ISCHEMIA/REPERFUSION-INDUCED HEART TISSUE in a RAT HIND LIMB MODEL

Tuğba GÜR[1]*

[1]Yüzüncü Yıl University, Vocational School of Health Services, Van, tugbagur@yyu.edu.tr, ORCID: 0000-0001-7220-0210

ABSTRACT

In this study, the effect of omega fatty acids (3, 6, 9) and stearic acid on some trace elements (Cu, Mn and Zn) in heart tissue, which is a distant organ, by creating ischemia/reperfusion in the hind legs of rats was investigated. Animals were divided into ten groups: Control (C), I/R, I/R+Omega 3, I/R+Omega 6, I/R+Omega 9, I/R+stearic acid, omega 3, omega 6, omega 9 and stearic acid groups. I/R was applied to the right hind legs of I/R, I/R+omega 3, I/R+omega 6, I/R+omega 9 and I/R+stearic acid groups under anesthesia. In this study, the levels of Cu, Mn and Zn elements were studied in samples obtained from heart tissue in animal models divided into ten groups using an inductively coupled plasma optical emission spectroscopy (ICP-OES) device. Compared to the control group, heart tissue's Cu and Zn levels were low, Mn levels were high but not important in the ischemia group ($p > 0.05$). When ischemia and omega 3, 6, 9 and stearic acid applied groups were compared with the ischemia group, heart tissue's Cu level was found to be low and Mn level was higher, but this result was not important ($p > 0.05$). Compared to the ischemia group, heart tissue's Zn levels were found to be notably higher in omega 6+IR, omega 9+IR and stearic acid groups ($p < 0.05$). As a result, I/R application changes trace element levels in heart tissue, which is a distant organ. In the case of I/R, omega fatty acids and stearic acid treatment may provide a protective effect by improving trace element levels.

Keywords: *Omega fatty acids, Stearic acid, Heart tissue, Rat, Trace elements*

1. INTRODUCTION

The term ischemia/reperfusion (I/R) is described as the restoration of blood circulation to certain organs after blood supply has been impaired for a certain period of time. IR injury is a common and important clinical problem affecting many organs, especially the brain (stroke and head injury), heart (myocardial infarction) and skeletal muscle. Skeletal muscle has high metabolic activity and is for this reason sensitive to reperfusion damage after ischemia. I/R damage to skeletal muscle can cause severe injury to the extremities, including severe necrosis major to amputation and severe life-threatening necrosis [1]. Inflammatory variables seen in patients under chronic ischemia and surgical treatment may change the concentrations of macro and trace elements in the blood [2]. While copper (Cu) is necessary to maintain the structure and function of some proteins and antioxidants, it also affects the development of atherosclerosis. Marginal copper intake or deficiency has been suggested as a risk factor for cardiovascular illnesses, and serum copper concentration has been found to increase in

atherosclerosis obliterans [3]. Zinc (Zn) is one of the most abundant trace elements in our organism. In addition to growth, improvement, differentiation, immune response and receptor activity, Zn functions as a component of more than 300 enzymes [4]. Disruption of Zn homeostasis, which is a necessary trace element required for normal cellular structure and functions, is associated with various health problems including cardiovascular diseases. Both exogenously and endogenously released zinc may be effective in cardiac protection after ischemia/reperfusion injury [5]. Trace elements are necessary for the proper function of living organisms. Some elements may have a preservative impact on target organs during ischemia and reperfusion [6-11] and have a favorable role in stabilizing organ protection solutions [12-14]. Manganese (Mn) has important roles in protein, polysaccharide and cholesterol metabolism, fetal development and lactation, as well as hydrolases, transferases and kinases [15]. It is an integral compound of Mn-SOD, an antioxidant enzyme that converts the superoxide radical to hydrogen peroxide (H_2O_2). Therefore, manganese superoxide dismutase has protective properties especially against oxidative stress. Manganese deficiency causes respiratory system diseases, nervous system diseases and infertility in humans (16). In a study, it was revealed that the increase in Mn-SOD activation mediated by free radical production during hyperthermia is important in providing early phase and late phase cardio preservation against ischemia/reperfusion damage in rats [17].

Polyunsaturated fatty acids (PUFAs) are necessary for many biochemical cases. Although omega-3 and omega-6 fatty acids come from the same origin, they have opposite physiological effects. A-linolenic acid (ALA), docosahexaenoic acid (DHA), and eicosapentaenoic acid (EPA) are essential omega-3 fatty acids. Dietary DHA deficiency results in elevated levels of zinc in the hippocampus and overexpression of the putative zinc transporter ZnT3 in the rat brain [18].

Ischemia causes devastating health and economic burdens brought about by disorders characterized by reduced organ-specific blood flow. Mechanisms and treatments underlying tissue damage caused by ischemia have been studied for many years to reduce these. Therefore, in our work, we wanted to determine the effects of omega 3, omega 6, omega 9 and stearic acid (SA) fatty acids on some trace element levels in heart tissue after experimental limb ischemia reperfusion. Our aim in the study is to examine the possible usability of some elements in rats with hind limb ischemia reperfusion model.

2. MATERIALS and METHODS

2.1. Animal Material
67 Wistar albino female rats (200-250 gr and 6-7 months old) were obtained from Experimental Animals Production Center. It was housed in standard conditions with a 12-hour light-dark cycle and free access to water and food was provided. All experimental studies were started in line with the animal ethics committee guidelines and after the approval of the Van Yüzüncü Yıl University Experimental Animals Local Ethics Committee (YÜHADEK) dated 28/04/2022 and numbered 2022/04-05.

2.2. Experimental Procedures
Rats were separated into ten different groups in accordance with the procedures to be performed. Fatty acids (omega 3, 6, 9) and stearic acid were given to rats orally daily for 14 days in the amount of 300 mg/kg [19]. Two hours of ischemia-2 hours of reperfusion was performed over the leg (quadriceps muscle) under anesthesia in rats that underwent ischemia-reperfusion procedure [20].

Rats divided into 10 different groups were arranged as follows: 1. Group: Control group: The rats in this group were fed normally (standard rat pellet food and water) for 14 days without any treatment. 2.Group: Ischemia-reperfusion group: At the end of the 14-days ad libitum feeding with standard rat pellet food and water, 2 hours of reperfusion under anesthesia was applied to the leg (quadriceps muscle) with a tourniquet after 2 hours of ischemia. 3. Group: Omega-3 group: Daily 300 mg/kg Omega 3 (O-3) was given by gastric gavage for 14 days. 4.Group: Omega-6 group: Daily 300 mg/kg Omega 6 (O-6) was given by gastric gavage for 14 days. 5. Group: Omega-9 group: 300 mg/kg Omega -9 (O-9) was given daily for 14 days by gastric gavage. 6. Group: Stearic acid group: 300 mg/kg stearic acid (SA) was given daily by gavage for 14 days. 7. Group: Omega-3+ischemia-reperfusion group: 300 mg/kg Omega-3 (O-3) was given daily for 14 days by gavage. At the end of the 14th day, 2-hour ischemia-2 hours reperfusion under anesthesia was administered to the rats on the leg (quadriceps muscle). 8.Group: Omega-6+ischemia-reperfusion group: 300 mg/kg O6 per day was given by gavage and ischemia reperfusion was applied on the 14th day. 9. Group: Omega-9+ischemia-reperfusion group: 300 mg/kg Omega-9 (O-9) was given daily for 14 days by gavage. At the end of the 14th day, 2 hours ischemia-2 hours reperfusion under anesthesia was applied to the rats on the leg (quadriceps muscle). 10. Group: Stearic acid+ischemia-reperfusion group: 300 mg/kg stearic acid (SA) was given daily by gavage for 14 days. At the end of the 14th day, 2-hour ischemia-2 hours reperfusion under anesthesia was administered to the rats on the leg (quadriceps muscle).

2.3. Preparation of Tissues

After the procedures applied for 14 days, the rats were euthanized and their heart tissues were surgically separated and placed in ziplock bags and stored in the freezer at -80°C until experimental studies were conducted. Tissue samples taken from the hearts of rats were dried at 105°C for 1 hour and weighed correctly and placed in 25 mL experimental tubes. Then, nitric acid and perchloric acid were added in a 1:1 ratio to dissolve the solid form. The solution was digested thoroughly using a microwave digestion oven. After digestion, the samples were cooled at room temperature. 1 ml of the cooled samples was taken and diluted by adding 9 ml of distilled water. Analysis of Cu, Mn and Zn elements in digested samples was carried out. The analyzes were measured using the ICP-OES (ICP-OES, Thermo ICAP 6300 DUO Scientific) device at Van Yüzüncü Yıl University Science Application Center. The device was calibrated using standard solutions.

2.4. Statistical Analysis

All data were given as mean±standard error and statistical analysis was performed with SPSS 20.00 (SPSS Inc, Chicago, IL) package program. Groups were compared by using one-way analysis of variance followed by post hoc Tukey Test.

3. RESULTS

In the study, the levels of Cu, Mn and Zn elements were determined in the heart tissues of rats fed with different fatty acids for 14 days.

Table 1. Heart tissue Cu, Mn and Zn levels of all groups.

	Cu (ppm)	Mn (ppm)	Zn (ppm)
Control	0,122±0,082 [a, b]	0,020±0,007 [a,b]	0,687±0,107 [c]
Ischemia	0,141±0,086 [a]	0,014±0,004 [b,c]	0,713±0,063 [c]
Omega3+IR	0,053±0,020 [c]	0,016±0,004 [a,b,c]	0,691±0,042 [c]
Omega6+IR	0,080±0,034 [a, b,c]	0,016±0,002 [a,b,c]	1,176±0,484 [a]

Omega9+IR	0,101±0,021 [a, b,c]	0,016±0,004 [a,b,c]	1,010±0,255 [a, b]
SA +IR	0,069±0,012 [a, b,c]	0,021±0,004 [a]	1,194±0,457 [a]
Omega3	0,079±0,035 [a, b,c]	0,012±0,003 [c]	0,774±0,150 [b, c]
Omega6	0,047±0,015 [c]	0,015±0,004 [a,b,c]	0,749±0,074 [b, c]
Omega9	0,113±0,060 [a, b,c]	0,016±0,004 [a,b,c]	0,734±0,045 [c]
SA	0,069±0,012 [b,c]	0,014±0,001 [c]	0,822±0,149 [b, c]

*, different letters in the same line denote statistical significance
Note: Different characters in the same column indicate statistical significance.

The heart tissue Cu level in the ischemia group was higher than all groups, but it was found to be significant only when compared with the omega 6, Omega 3+IR and Stearic acid groups ($p<0.05$). The heart tissue Cu level of the control group was found to be remarkably higher than that of the omega 6 group ($p<0.05$).

Heart tissue Mn levels in the control group and stearic acid+IR group were found to be significantly higher than omega 3 and stearic acid groups ($p<0.05$). The heart tissue Mn level in the stearic acid+IR group was found to be significantly higher than the ischemia group ($p<0.05$). While the heart tissue Mn level in the ischemia group was lower than the control group, this decrease was not significant ($p>0.05$)

Although the heart tissue Zn level in the ischemia group was higher than the control group, this was not significant ($p>0.05$). The heart tissue Zn level in the ischemia group was found to be significantly lower than the Omega 6+IR, Omega 9+IR and stearic acid+IR groups ($p<0.05$). While the heart tissue Zn level was higher in the omega 3, omega 6, omega 9 and stearic acid groups than in the control and ischemia groups, this elevation was not meaningful ($p>0.05$).

4. DISCUSSION

Ischemia is described as insufficient systemic blood providing to a local tissue because of occlusion of the vascular system in that tissue; these cases are among the most widespread reasons of heart attack and stroke in humans [22–24]. Reperfusion is described as restoring blood flow to a previously absent tissue; restoration of nutritional reinforcement to previously starved areas underlies many important pathogenic manifestations [23]. Thanks to ischemia-reperfusion studies in experimental animals, it has become easier to understand the molecular and physiological changes accompanying stroke and heart attack [26, 21–25]. Although IR can occur in every tissue, its harmful effect on skeletal muscle is much more severe compared to other body tissues due to devastating systemic complications [27].

Polyunsaturated fatty acids (DHA), are essential for human metabolism but cannot be produced *de novo*. Therefore, people have to take these fatty acids from the diet [28]. The levels and composition of these substances can be determined directly by diet or by dietary intake of fatty acid precursors. Fatty acid precursors are converted endogenously into physiologically active long chain polyunsaturated fatty acids by extension and desaturation by fatty acid desaturase enzymes. Reports have shown that dietary DHA supplementation has a protective effect on retinal ischemia damage and oxidative damage after post-ischemic oxidative stress in fetal rat brain [21, 22]. Evidence of interaction between trace elements and essential fatty acid (EFA) metabolism has been revealed in studies [29]. For example, it has been shown that zinc may be needed as a cofactor in desutarase 6 (Δ6) enzyme activity in rats [30]. According to the data obtained in a study, especially plasma EFA

composition shows that plasma zinc, calcium and magnesium levels are related [31]. EFAs are significant in the absorption of zinc, calcium or magnesium. Therefore, trace elements appear to make an important contribution to fatty acid metabolism [32, 33].

Zinc is very plentiful trace element in the body system after iron and involved in many physiological processes such as neuronal death, immunity and cancer [34]. In animal studies, it has been shown that Zn deficiency causes atherosclerosis by causing the release of proatherogenic factors in mice [35]. It has been shown that ischemic stroke increases the serum Zn level [36]. Some studies suggest that although zinc is not the initiator of damage, changes in its levels can lead to the damage process [37]. Other studies have suggested that it may cause excessive zinc release from neurons in stroke, as in irregularities occurring in neurotoxicity [38, 39]. De Paula et al., [40] stated that massive and transient zinc accumulation during cerebral ischemia is importantly related in brain injury by promoting neuronal apoptotic death, and therefore they suggested that zinc removal may be a way to reduce ischemic brain injury. Akçıl et al., [41] showed that the plasma zinc level of wistar albino rats increased significantly who underwent ischemia with 30 minutes clamping of the superior mesenteric artery followed by 20 minutes of reperfusion when compared to the control group. It has been demonstrated that the increase in plasma Zn concentration can be attributed to severe tissue damage and peroxidant and antioxidant properties of Zn, considering the size of the affected area after ischemia-reperfusion. In another study, it was shown that serum Zn level decreased in the I/R group when compared to the control group [42]. Zn is also very significant in cell viability as it has antioxidant, antiapoptotic and anti-inflammatory effects. The increase in plasma zinc level after ischemia may be the result of its anti-atherogenic properties preventing vascular endothelial derangements and its role in signaling pathways involved in apoptosis. The role of Zn in ischemia as a cytoprotective by reducing the formation of oxygen radicals has also been suggested [43]. In the present study, although the heart tissue Zn level in the ischemia group was higher than the control group, this highness was not significant ($p>0.05$). The heart tissue Zn levels of the groups in which ischemia was induced and omega 6, omega 9 and steraic acid were applied were found to be higher than the ischemia group, but only omega 6+IR and stareic acid+IR groups were found to be significantly higher ($p<0.05$). In our study, a significant increase was observed in rat heart tissue Zn levels with omega 6, omega 9 and stearic acid treatment and subsequent ischemia application to rats. It can be said that this treatment protects the tissues by increasing the antioxidant, antiapoptotic and anti-inflammatory properties of Zn.

Copper is an essential element for biological systems. The redox cycle between Cu^{+1} and Cu^{+2} catalyzes the production of highly toxic hydroxyl radicals [42]. Cu is also a metal cofactor of various enzymes. When rats with superior mesenteric artery I/R were compared with the control group, it was indicated that the plasma copper level increased significantly. Increased plasma copper level may be the cause of excessive tissue damage and a prooxidant characteristic [34]. In experimental animal studies, it has been shown that copper levels increase due to oxidative stress in I/R models [44,42]. Increased Cu concentration in serum in lower extremity ischemia may result from the acute phase response [43]. In the presented study, the heart tissue Cu level in the ischemia group was seen to be higher than in all other groups, but it was found to be significantly higher only in the omega 6 and omega 3+IR groups ($p<0.05$). Ischemia and the application of omega 3, omega 6, omega 9 and stearic acid treatment caused a decrease in the heart tissue Cu level. The increase in copper level in the ischemia group may have increased the acute phase reaction and the treatment may have prevented the acute phase response. According to the data obtained, it can be concluded that omega 3, omega 6, omega 9 and staeric acid applications may be beneficial in ischemic conditions.

Manganese superoxide dismutase (Mn-SOD) is an enzyme that protects mitochondria, an important organelle for cellular respiration, from reperfusion damage and limits mitochondria-associated apoptosis. It has been shown that plasma Mn levels increase after I/R injury, but this increase is not significant [41]. In one study, they observed that rised activity of mitochondrial Mn-SOD during I/R damage is important in mitochondrial protection and reduction of apoptosis [45]. In another study, Mn-SOD activity was seen to be significantly reduced by I/R administration to the kidney of rats that underwent 45 minutes of ischemia followed by 3 hours of reperfusion [46]. It has been described that changes in the calcium, potassium, magnesium, sodium, and phosphorus content of the liver in rats undergoing hepatic ischemia-reperfusion are associated with injury to cell membranes, which can be confirmed by the quantity of diene conjugates produced [47]. In rats undergoing a liver ischemia/reperfusion model, pretreatment of all-trans retinoic acid (atRA) has been demonstrated to reduce liver I/R injury by inhibiting malondialdehyde (MDA) release and increasing the activity of manganese superoxide dismutase (Mn-SOD) [48]. In the present study, the heart tissue Mn level of the ischemia group was found to be significantly lower than the control group ($p < 0.05$). Performing ischemia and applying omega 3, omega 6, omega 9 and stearic acid treatment caused an increase in the heart tissue Mn level, and the heart tissue Mn level in the group that was treated only with stearic acid was seen to be significantly higher than the ischemia group ($p < 0.05$). The treatments applied may have caused an increase in the antioxidant level due to the increase in the heart tissue Mn level.

These results show that ischemia/reperfusion injury causes significant changes in trace element concentrations in heart tissue, which is a distant organ. In line with the data we have obtained, it can be concluded that trace element levels can be corrected with omega fatty acids and stearic acid applications in case of ischemia.

ACKNOWLEDGEMENT

REFERENCES

[1] Huang, T., Wang, W., Tu, C., Yang, Z., Bramwell, D. and Sun, X., (2015), Hydrogen-rich saline attenuates ischemia–reperfusion injury in skeletal muscle, Journal of Surgical Research, 194(2),471-480.

[2] Iskra, M., Barałkiewicz, D., Majewski, W. and Pioruńska-Stolzmann, M., (2005), Serum magnesium, copper and zinc concentration changes in lower limb ischemia and postoperative treatment, Magnesium Research, 18(4), 261-267.

[3] Iskra, M. and Patelski, J., (1993), Concentrations of calcium, magnesium, zinc and copper in relation to free fatty acids and cholesterol in serum of athe-rosclerotic men, Trace Element Analytical Chemistryin Medicine and Biology, 6, 261.

[4] De Mel, D. and Suphioglu, C., (2014), Fishy business: effect of omega-3 fatty acids on zinc transporters and free zinc availability in human neuronal cells, Nutrients, 6(8), 3245-3258.
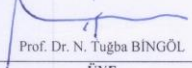
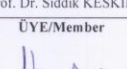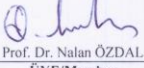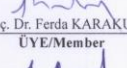[5] Xu, Z. and Zhou, J., (2013), Zinc and myocardial ischemia/reperfusion injury, Biometals, 26(6), 863-878.

[6] Korb, S.M., Albornoz, G. and Light, J.A., (1990), Selenium addition to the flush/preservation solution protects kidneys against oxidative stress during warm and cold ischemia, Transplant Proc, 22(2),452–454.

[7] Treska, V., Kuntscher, V., Molacek, J., Kobr, J., Racek, J. and Trefil, L., (2003), Can ischemia-reperfusion syndrome in transplanted kidneys procured from non-heart-beating donors be influenced by adding selenium into the reperfusion solution? An experimental study, Transplant Proc, 35(8),3125–3127.
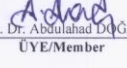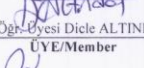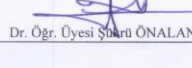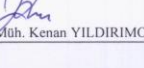
[8] Soncul, H., Kaptanoglu, M., Öz, E., Halit, V., Bilgehan, A., Çaycı, B., Gökgöz, L., Turkozan, N. and Ersoz, A., (1994), The role of selenium added to pulmonary preservation solutions in isolated guinea pig lungs, J Thorac Cardiovasc Surg, 108(5),922–927.

[9] Lymbury, R., Venardos, K. and Perkins, A.V., (2006), Effect of sodium selenite-enriched reperfusion solutions on rat cardiac ischemia–reperfusion injury, Biol Trace Elem Res Winter, 114(1–3),197–206.

[10] Cheng, Y., Liu, Y. and Liang, J., (2002), Zinc is a potent heat shock protein inducer during liver cold preservation in rats, Chin Med J, 115(12),1777–1779.

[11] Gałecka, E., Jacewicz, R., Mrowiska, M., Florkowski, A. and Gałecki, P., (2008), Antioxidative enzymes—structure, properties, functions, Pol Merk Lek, XXV(147), 266.

[12] Ostróżka-Cieślik, A., Ryszka, F. and Dolińska, B., (2008), Characteristic of the solutions used for perfusion and preservation of organs, Ann Acad Med Siles, 62(1),70–75.

[13] Dolińska, B., Ostróżka-Cieślik, A., Caban, A., Cierpka, L. and Ryszka, F., (2012), Comparing the effect of Biolasol and HTK solutions on maintaining proper homeostasis, indicating the kidney storage efficiency prior to transplantation, Ann Transplant, 17(2),74–78.

[14] Ryszka, F., Dolińska, B., Caban, A., Ostróżka-Cieślik, A., Budziński, G., Krzysztofik, M., Oczkowicz, G. and Cierpka, L., (2011), Hepatoprotective effect of prolactin and cysteine contained in perfusion and preservation solutions on porcine liver stored in simple hypothermia, Transplant Proc, 43(8),2882–2886.

[15] Soetan, K.O., Olaiya, C.O. and Oyewole, O.E., (2010), The importance of mineral elements for humans, domestic animals and plants: A review, African Journal of Food Science, 4(5), 200-222.

[16] Aswathanarayana, U., Professor (1994), Trace Substances Environment and Health, Science Reviews, 222-3.

[17] Yamashita, N., Hoshida, S., Taniguchi, N., Kuzuya, T. and Hori, M., (1998), Whole-body hyperthermia provides biphasic cardioprotection against ischemia/reperfusion injury in the rat, Circulation, 98(14), 1414-1421.

[18] Jayasooriya, A.P., Ackland, M.L., Mathai, M.L., Sinclair, A.J., Weisinger, H.S., Weisinger, R.S., Halver, J.E., Kitajka, K. and Puskás, L.G., (2005), Perinatal omega-3 polyunsaturated fatty acid supply modifies brain zinc homeostasis during adulthood, Proc Natl Acad Sci, USA, 102, 7133–7138.

[19] Meganathan, M., Madhana Gopal, K., Sasikala, P., Mohan, J., Gowdhaman, N., Balamurugan, K., Nirmala, P., Santhakumari, S. and Samuel, V., (2011), Evaluation of Hepatoprotective Effect of Omega 3-Fatty Acid against Paracetamol Induced Liver Injury in Albino Rats, Global Journal of Pharmacology, 5 (1), 50-53.

[20] Konukoğlu, D., (2008), Omega-3 ve omega-6 yağ asitlerinin özellikleri, etkileri ve kardiyovasküler hastalıklar ile ilişkileri, Türk Aile Hek Derg, 12(3), 121-129.

[21] Glozman, S., Green, P. and Yavin, E., (1998), Intraamniotic ethyl docosahexaenoate administration protects fetal rat brain from ischemic stress, J Neurochem, 70,2484–2491.

[22] Miyauchi, O., Mizota, A., Adachi-Usami, E. and Nishikawa, M., (2001), Protective effect of docosahexaenoic acid against retinal ischemic injury: an electroretinographic study, Ophthalmic Res, 33,191–195.

[23] Lopez-Neblina, F., Toledo, A.H. and Toledo-Pereyra, L.H., (2005), Molecular biology of apoptosis in ischemia and reperfusion, J Invest Surg, 18,335–350.

[24] Bell, R.D., and Zlokovic, B.V., (2009), Neurovascular mechanisms and the blood–brain barrier disorder in Alzheimer's disease, Acta Neuropathol, 118,103–113.

[25] Bazan, N.G., Marcheselli, V.L. and Cole-Edwards, K., (2005), Brain response to injury and neurodegeneration: endogenous neuroprotective signaling, Ann N Y Acad Sci, 1053,137–147.

[26] Bazan, N.G., (2009), Cellular and molecular events mediated by docosahexaenoic acid-derived neuroprotectin D1 signaling in photoreceptor cell survival and brain protection, Prostaglandins Leukot Essent Fat Acids, 81,205–211.

[27] Gillani, S., Cao, J., Suzuki, T. and Hak, D. J., (2012), The effect of ischemia reperfusion injury on skeletal muscle, Injury, 43(6), 670-675.

[28] Bezard, J., Blond, J., Bernard, A. and Clouet, P., (1994), Themetabolism and availability of essential fatty acids in animal and human tissues, Reprod Nutr Dev, 34 (6), 539–568.

[29] Huang, Y.S., Cunnane, S.C., Horrobin, D.F. and Davignon, J., (1982), Most biological effects of zinc deficiency corrected by γ-linolenic acid (18:3w6) but not by linoleic acid (18:2w6), Atherosclerosis, 41 (2–3), 193–207.

[30] Horrobin, D.F., (1981), Loss of delta-6-desaturase activity as a key factor in aging, Med Hypotheses, 7 (9), 1211–1220.

[31] Sfar, S., El Heni, J., Laporte, F., Braham, H., Jawed, A., Amor, S., Sfar M.T. and Kerkeni, A. (2012), Trace element status and fatty acids metabolism during healthy ageing: An example of a population from the Tunisian eastern coast, Experimental gerontology, 47(3), 243-249.

[32] Djurhuus, M.S., Klitgaard, N.A., Pedersen, K.K., Blaabjerg, O., Altura, B.M., Altura, B.T. and Henriksen, J.E., (2001), Magnesium reduces insulin-stimulated glucose uptake and serum lipid concentrations in type 1 diabetes, Metabolism, 50 (12), 1409–1417.

[33] Kruger, M.C. and Horrobin, D.F., (1997), Calcium metabolism, osteoporosis and essential fatty acids: a review, Prog Lipid Res, 36 (2–3), 131–151.

[34] Plum, L. M., Rink, L., and Haase, H., (2010), The essential toxin: impact of zinc on human health, Int J Environ Res Public Health, **7**(4), 1342-1365.

[35] Reiterer, G., MacDonald, R., Browning, J.D., Morrow, J., Matveev, S.V., Daugherty, A., Smart, E., Toborek, M., and Hennig, B., (2005), Zinc deficiency increases plasma lipids and atherosclerotic markers in LDL-receptor-deficient mice, J Nutr, 135(9),2114-2118.

[36] Bhatt, A., Farooq, M.U., Enduri, S., Pillainayagam, C., Naravetla, B., Razak, A., Safdar, A., Hussain, S., Kassab, M., and Majid, A., (2010), Clinical significance of serum zinc levels in cerebral ischemia, Stroke research and treatment.

[37] Cuajungco, M. P. and Lees, G. J. (1997), Zinc metabolism in the brain: relevance to human neurodegenerative disorders, Neurobiol Dis, 4(3-4),137-169.

[38] Koh, J. Y., Suh, S.W., Gwag, B.J., He, Y.Y., Hsu, C. Y. and Choi, D. W. (1996), The role of zinc in selective neuronal death after transient global cerebral ischemia, Science, 272(5264), 1013-1016.

[39] Shuttleworth, C. W. and Weiss, J. H., (2011), Zinc: new clues to diverse roles in brain ischemia, Trends Pharmacol Sci, 32(8), 480-486.

[40] De Paula, R. C., Aneni, E.C., Costa, A.P., Figueiredo, V.N., Moura, F.A., Freitas, W.M., Quaglia, L.A., Santos, S.N., Soares, A.A., Nadruz, W., Blaha, Jr., M., Blumenthal, R., Agatston, A., Nasir, K. and Sposito, A.C., (2014), Low zinc levels is associated with increased inflammatory activity but not with atherosclerosis, arteriosclerosis or endothelial dysfunction among the very elderly, BBA Clin, 2, 1-6.

[41] Akçil, E., Tuğ, T. and Döşeyen, Z., (2000), Antioxidant enzyme activities and trace element concentrations in ischemia-reperfusion, Biological trace element research, 76(1), 13-17.

[42] Sırmalı, M., Uz, E., Sırmalı, R., Kılbaş, A., Yılmaz, H.R., Altuntaş, İ., Nazıroğlu, M., Delibaş, N. and Vural, H., (2007), Protective effects of erdosteine and vitamins C and E combination on ischemia–reperfusion-induced lung oxidative stress and plasma copper and zinc levels in a rat hind limb model, Biological trace element research, 118(1), 43-52.

[43] Iskra, M. and Majewski, W., (1999), Oxidase activity of ceruloplasmin and concentrations of copper and zinc in serum in chronic arterial occlusion of the lower limbs, Journal of trace elements in medicine and biology, 13(1-2), 76-81.

[44] Aydemir, O., Nazıroğlu, M., Celebi, S., Yılmaz, T. and Kükner, A.S., (2004), Antioxidant effects of alpha-gamma- and succinate-tocopherols in guinea pig retina during ischemia-reperfusion injury, Pathophysiology, 11(3), 167-171.

[45] Suzuki, K., Murtuza, B., Sammut, I. A., Latif, N., Jayakumar, J., Smolenski, R. T., Kaneda, Y., Sawa, Y., Matsuda, H. and Yacoub, M. H., (2002), Heat shock protein 72 enhances manganese superoxide dismutase activity during myocardial ischemia-reperfusion injury, associated with mitochondrial protection and apoptosis reduction, Circulation, 106(12_suppl_1), I-270.

[46] Korkmaz, A., Kolankaya, D., (2010), Protective effect of rutin on the ischemia/reperfusion induced damage in rat kidney, Journal of surgical research, 164(2), 309-315.

[47] Váli, L., Stefanovits-Bányai, É., Szentmihályi, K., Fébel, H., Sárdi, É., Lugasi, A., Kocsis, İ. and Blázovics, A., (2007), Liver-protecting effects of table beet (*Beta vulgaris var. rubra*) during ischemia-reperfusion, Nutrition, 23(2), 172-178.

[48] Rao, J., Zhang, C., Wang, P., Lu, L. and Zhang, F., (2010), All-trans retinoic acid alleviates hepatic ischemia/reperfusion injury by enhancing manganese superoxide dismutase in rats, Biological and Pharmaceutical Bulletin, 33(5), 869-875.

ATTACHMENTS

	VAN YÜHADYEK VAN YÜZÜNCÜ YIL ÜNİVERSİTESİ Hayvan Deneyleri Yerel Etik Kurulu	

ÇALIŞMA ONAY BELGESİ

VAN YUZUNCU YIL UNIVERSITY (TURKEY) ANIMAL RESEARCHES LOCAL ETHIC COMMITTEE APPROVAL CERTIFICATE

Araştırmanın Adı: **Research Title:**	Şıçan arka bacak iskemi/reperfüzyona bağlı indüklenen kalp dokusunda eser elementler üzerine omega 3, 6,9 ve stearik asitlerin etkisi Effect of omega 3, 6,9 and stearic acids on trace elements in rat hind limb ischemia/reperfusion-induced heart tissue.	
Araştırıcı(lar): *Investigator(s)*	Yürütücü / *Chief investigator:*	Dr. Öğr. Üyesi Tuğba Gür
	Yardımcı Araştırıcı(lar) / *Co-investigator(s):*	

Araştırmada kullanılacak hayvanlar / *Animals to be used in the research:*

Tür / species: *Rat*	Sayı / *Numbers:* 67
Yaş /*Age: 8-12 hafta/weeks*	Cinsiyet / *Sex: Dişi/Female*

Araştırmanın Öngörülen Başlama Tarihi / *Proposed Research Starting Date:01.05.2021*

Araştırmanın Öngörülen Bitiş Tarihi / *Proposed Research Completion Date:02.06.2022*

Karar:
Yukarıda bilgileri verilen planlanan araştırma projesi için Hayvan Deneyleri Etik Kurul Onayı gerekmemektedir.
Tarih: 28/04/2022 Karar No: 2022/04-05
Decision:
The proposed research project detailed above does not need Animal Researches Ethic Committee Approval. Date:. 28/04/2022 Decision number: 2022/04-05

BAŞKAN/CHAIR		
	Prof. Dr. Semiha DEDE	
ÜYE/Member	ÜYE/Member	ÜYE/Member
Prof. Dr. N. Tuğba BİNGÖL	Prof. Dr. Sıddık KESKİN	Prof. Dr. Nalan ÖZDAL
ÜYE	ÜYE/Member	ÜYE/Member
Prof. Dr. Atilla DURMUŞ	Doç. Dr. Ferda KARAKUŞ	Doç. Dr. Yıldıray BAŞBUĞAN
ÜYE/Member	ÜYE/Member	ÜYE/Member
Doç. Dr. Canser Yılmaz DEMİR	Doç. Dr. Abdulahad DOĞAN	Dr. Öğr. Üyesi Dicle ALTINDAL
ÜYE/Member	ÜYE/Member	ÜYE/Member
Dr. Öğr. Üyesi Şükrü ÖNALAN	Vet. Hek. İsmail Hakkı BEHÇET	Zir.Müh. Kenan YILDIRIMOĞLU

RESEARCH ARTICLE

SYNTHESIS and CHARACTERIZATION of MECHANICAL ACTIVATION ASSISTED BORON CARBIDE (B4C) PRECURSOR POWDERS

Hediye AYDIN[1,2*], Elif TUNCER[3]

[1]Kütahya Dumlupınar University, Department of Metallurgy and Material Engineering, Kütahya
[2]Kütahya Dumlupınar University Advanced Technologies Design Research Development and Application Center (ILTEM), Kütahya, hediye.aydin@dpu.edu.tr, ORCID: 0000-0003-2164-6129
[3]Kütahya Dumlupınar University, Graduate Education İnstitute, Kütahya, tuncerelif43@gmail.com, ORCID: 0000-0002-3547-9010

ABSTRACT

The study carries out the synthesis and characterization of the precursor to be converted to boron carbide (B_4C). For this purpose, starting materials are boric acid (H_3BO_3) and sodium citrate ($C_6H_5Na_3O_7$). Both starting materials' reactions formed a complex structure (precursor) consisting of B-O-C-Na elements. Phase and microstructure analyses and bond characteristics of the precursor powders perform using X-ray diffraction (XRD), scanning electron microscopy (SEM/EDS), and Fourier spectroscopy (FT-IR) methods, respectively. As a result, the heat treatment carried out at relatively low temperatures (1000 ^{o}C) and under an inert gas atmosphere resulted in XRD patterns of the B_4C phase. This study also investigated the possible reaction mechanism of the formation of the boron carbide phase and the effect of mechanical activation on the phase formation.

Keywords: *Boric Acid (H_3BO_3), Sodium Citrate ($C_6H_5Na_3O_7$), Boron carbide (B_4C), mechanical activation*

1. INTRODUCTION

In parallel with the rapidly advancing technology, the place and importance of advanced technology products are increasing daily [1]. Since the beginning of the 80s, developments in some sectors have increased the need for structural materials exposed to high temperatures and stresses at these temperatures, aerospace, space and satellite vehicles, advanced engines, and are resistant to temperature and radiation. The mechanical (strength, elastic modulus, hardness) and physical (density, electrical and electronic structure) properties of boron carbide (B_4C) have increased the choice of this material and expanded its usage area. Boron carbide can be used as an anode material in the nuclear field with its neutron absorption feature, in ballistics and automobile industries with its high strength, low specific gravity, and high elastic modulus, and also in supercapacitors due to its energy storage property [2-4].

63 % of the world's boron reserves, the primary raw material of boron carbide used in different advanced technology fields, are in our country. Therefore, studies on B_4C, a boron-based high-tech ceramic family member, are essential. An alternative method for producing boron carbide is by magnesiothermic reduction of boron oxide in the presence of carbon. The reaction products (boron

carbide) are processed by aqueous methods to remove them from magnesium oxide. Carbide still contains magnesium borides formed as stable compounds. This reduction technique is very suitable for manufacturing sintered products and produces fine amorphous powder [5-7].

The synthesis of boron carbide from the elements is uneconomical due to the high cost of elemental boron. Therefore, it is only used for special applications such as B10 enriched or pure boron carbide. Boron and carbon are mixed well, turned into pellets, and reacted at high temperatures for the synthesis of elements. B_4C production is carried out with boron-loaded organic compounds such as carburan, triphenylborane, polyvinyl pentaborane, and borazines [8-9]. Generally, this process is carried out in a vacuum or inert atmosphere in the temperature range of 1000-1500°C. Boron carbide is traditionally prepared by carbothermal reduction of boric acid. Carbon is used as a reducing agent. This process is carried out in electric arc or graphite resistance furnaces. The reaction temperature is > 2000 °C, and the boron carbide yield is low due to the evaporation of boron oxide. The production process is endothermic and requires 16800 kJ / mol of energy. Therefore, the disadvantages of this method are; high-temperature requirement, high energy requirement, low efficiency, and low homogeneity due to uneven temperature distribution in the reaction zone [10]. Synthesis of precursor powders (starting material that will turn into boron carbide) used in the production of B_4C is one of the alternative methods. The precursor elements are mixed homogeneously at the atomic scale offers many advantages. These; are due to short diffusion distance phase formation at low temperatures, high efficiency, low energy demand, prevention/reduction of the evaporation of components, and accordingly control of stoichiometry, small grain size, and poor agglomeration and high purity. Therefore, selecting and controlling the powder production process, which determines the starting powder properties for controllable properties and high performance in the final product, is a critical step [11-14]. The aim of this study is the synthesis and characterization of a precursor powder with conversion to boron carbide (B_4C) using native boric acid (H_3BO_3) and sodium citrate ($C_6H_5Na_3O_7$).

2. MATERIAL and METHOD

2.1. Preparation of Precursor Xerogel Powders

The starting chemicals used in synthesizing B_4C powders and their properties are given in Table 1. Sodium citrate synthesized compounds that homogeneously mixed boron, carbon, sodium, hydrogen, and oxygen (B-C-Na-H-O) elements were at the atomic level by forming a clamp/chelate with boric acid. Another task of sodium citrate is to provide a carbon source to take part in carbothermal reactions. Acetone was used as an anti-solvent "agent to precipitate the water-soluble compound formed between sodium citrate and boric acid.

Table 1. Starting chemicals used in boron carbide synthesis.

Chemical	Chemical Formula	Aim of usage	Purity
Boric acid	H_3BO_3	Boron source	%98
Sodium Citrate	$C_6H_5Na_3O_7.2H_2O$	Carbon source	≥ %98
Acetone	C_3H_6O	Anti-solvent	+%99

Sodium citrate (S) and boric acid (B) were used in two different molar ratios (S/B ratio 1:1 and 1:1.3). In Table 2, sample codes, mole ratios of components, and applied procedures are in table 2. While preparing xerogel precursor powders for B_4C synthesis, sodium citrate and boric acid were first added to 100 ccs distilled water, respectively, and mixed until a clear and homogeneous solution was obtained.

Table 2. Sample codes, mole ratios of components, and applied processes.

Sample Code	$C_6H_5Na_3O_7.2H_2O$ [mole]	H_3BO_3 [mole]	Applied Process
BC1	1	1	As synthesized
BC2	1	1.3	As synthesized
BC1-A	1	1	Mechanical activation
BC2-A	1	1.3	Mechanical activation

In order to concentrate the obtained solution, it is heated in a Heidolp brand rotary dryer device in a water pool with a temperature of 80 ^{o}C for approximately 90 minutes with a rotation speed of 137 cycles/min. During this time, 400 mbar vacuum pressure water was evaporated. 25 ml of acetone at -80 ^{o}C was added to the concentrated solution and mixed with a glass baguette stick, thus allowing a gel structure to precipitate from the solution. Xerogel was obtained by separating the gel part from the liquid it was in with the help of centrifugation and drying it completely in an oven at 80 ^{o}C for 48 hours. The characterization of the powder passed through a 125 μm sieve was made. This received product is defined as "precursor powder" in the following parts of the study.

2.1.1. Mechanical activation of precursor powders

Mechanical activation is the term applied to a powder synthesising method in which chemical reactions and phase transformations occur due to application of mechanical energy. In mechano-chemical synthesis, ball milling assistes the reaction in a mixture of reactive powders [15]. Mechanical activation was applied to the synthesized precursor powders with a Retsch PM 200 brand planetary mill. Powder and balls were placed in stainless steel crucibles under an argon atmosphere for this process. Mechanical activation parameters are given in Table 3.

Table 3. Parameters of mechanical activation.

Parameter	
Rotation speed of vial (rpm)	500
Milling Time (h)	2
Vial material	Stainless steel
Capacity of vial (ml)	125
Ball material	ZrO_2
Diameter of balls (mm)	5
Powder/ball ratio	1/20
Powder amount (g)	5

2.1.2. Heat treatment of precursor powders

For the purpose of improve formation of B_4C, the milled synthesized precursor powders were subjected to a heat treatment. Protherm brand high-temperature furnace was used for the heat

treatment of the precursor powders. The prepared powders were placed in a graphite crucible and placed in an alumina tube furnace, and heat treatment was applied for 1 hour at a heating rate of 5 ^{o}C/min at temperatures of 800 – 1000 ^{o}C.

2.2. Characterization of Synthesis Powders

For the phase analysis of the powders, images were taken in Cu-Kα radiation at a scanning speed of 2 ^{o}/min using the Panalytical Empyrean brand X-ray device located in Kütahya Dumlupınar University Advanced Technologies Design Research Development and Application Center (ILTEM). FEI / NOVA NANOSEM 650 scanning electron microscope (SEM) was used to analyze the microstructure and elemental composition of the powders. Bruker brand Fourier Transform Infrared Spectroscopy (FT-IR) device was used to define the bonds within the atomic structure. The bandgap between 350 and 4000 cm^{-1} was examined in FT-IR analysis. The absorbance spectrum of the components in the solutions used to synthesize the precursor powders were determined with the SpectroStar nano UV-VIS spectrophotometer device. Quartz cuvettes with an optical path length of 2 mm were used for the measurements. Mettler Toledo brand instrument was used to measure the pH of the solutions. The instrument was calibrated before use. The pH value of the boric acid solution was measured as 3.97, and sodium citrate was 8.31. The pH value of the boric acid-sodium citrate solution is 7.5, and the pH measured after 2 hours at 80 ^{o}C is 7.9. When the pH of BC2 was measured, values close to those of the BC1 solution were obtained. According to the pH measurement results, the pH values of boric acid - sodium citrate solutions support the formation of a compound between these two chemicals.

3. RESULTS AND DISCUSSION

3.1. Wavelength of Solutions – Optical Density Results

Figure 1 – 3 shows the absorption characteristics corresponding to the wavelength of the solutions obtained with boric acid, sodium citrate, and boric acid - sodium citrate solution (boric acid: sodium mole ratio 1:1). The x-axis wavelength (nm); the y-axis represents the optical density (OD). The optical density of each solution measured at different wavelengths, that is, the measure of light absorption, will be other. Here, the UV-VIS spectrophotometer technique is used to observe the formation of a compound due to a sodium citrate-boric acid reaction. When the boric acid solution was examined, it was determined that while a high absorption value was obtained at low wavelengths, absorption decreased with increasing wavelength.

The wavelength-absorption relationship was obtained similarly for sodium citrate, and mixture solutions measured the highest absorbance value as 0.13 for the boric acid solution, 3 for sodium citrate, and 2.8 for boric acid - sodium citrate solution, respectively. 2.8 absorbance value obtained in boric acid – sodium citrate solution; It can be said that a new structure is formed as a result of the reaction of these two components (boric acid and sodium citrate) and affects the optical properties of the solution [1].
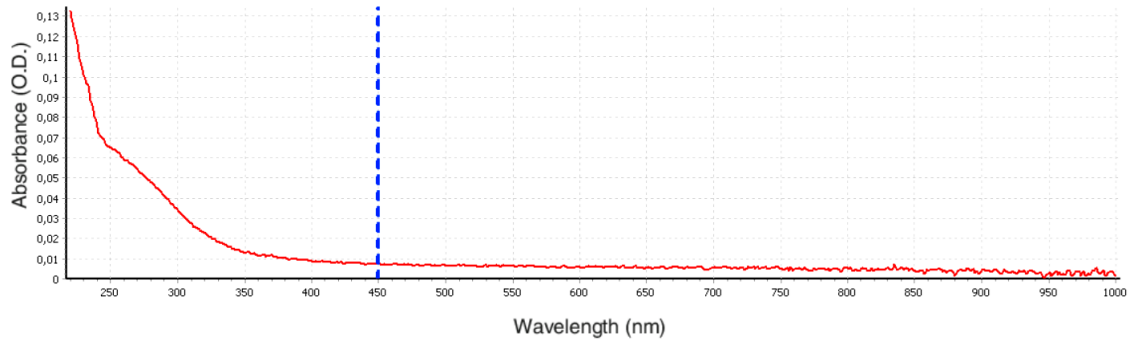
Figure 1. UV-Vis optical density graph of the boric acid solution prepared for the production of BC1 coded powder [1].
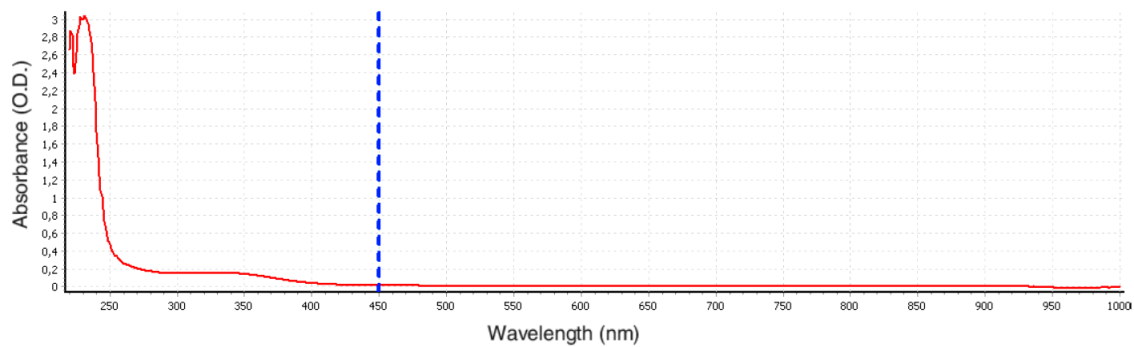

Figure 2. UV-Vis optical density graph of sodium citrate solution prepared for the production of BC1 coded powder [1].
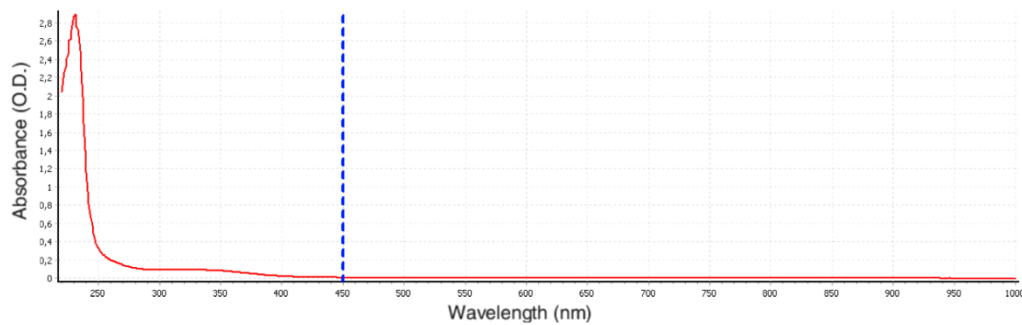

Figure 3. UV-Vis optical density graph of the boric acid-sodium citrate solution prepared for the production of BC1 coded powder [1].

Figures 4 - 6 show the absorption characteristics corresponding to the wavelength of the solutions obtained by boric acid, sodium citrate, and boric acid - sodium citrate solution (mole ratio of boric acid: sodium citrate 1:1.3). We measured the highest absorbance value as was 0.095 for the boric acid

solution, 2.8 for sodium citrate, and 2.6 for boric acid - sodium citrate solution, respectively. Similarly, it can state that a new structure is formed by the reaction (chelation) of these two components in boric acid and sodium citrate solution [1].
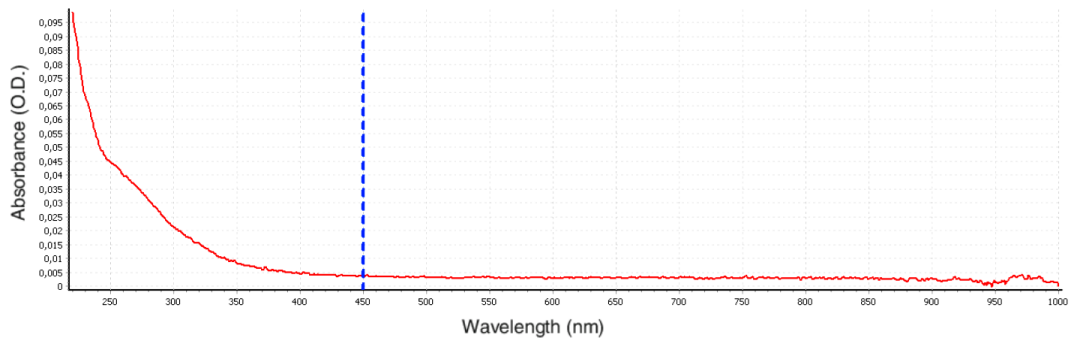

Figure 4. UV-Vis optical density graph of the boric acid solution prepared for the production of BC2 coded powder [1].
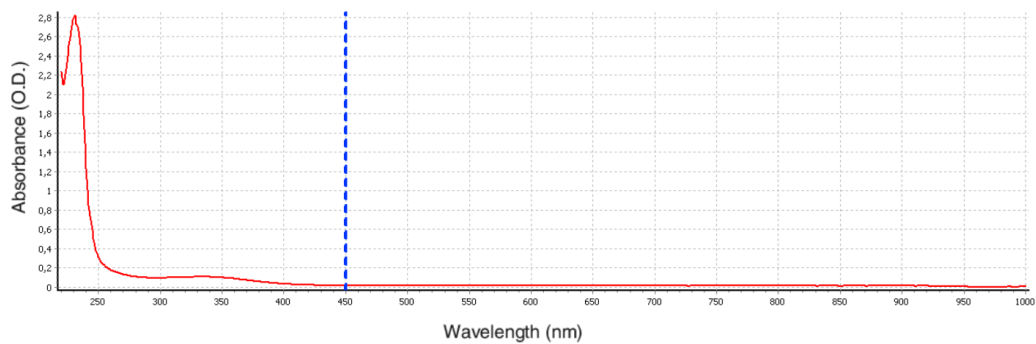

Figure 5. UV-Vis optical density graph of sodium citrate solution prepared for the production of BC2 coded powder [1].
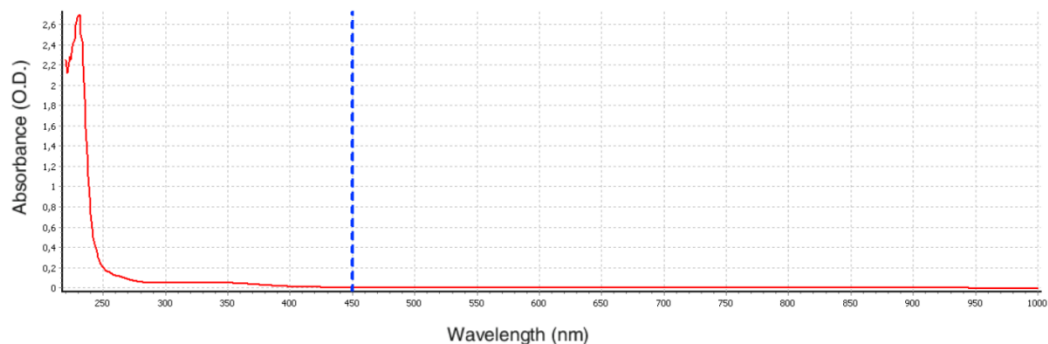

Figure 6. UV-Vis optical density graph of the boric acid-sodium citrate solution prepared for the production of BC2 coded powder [1].

Sodium citrate and boric acid were dissolved in distilled water at room temperature. The resulting solution was stirred at 80 $^{\circ}$C, and the water evaporated. Then, 25 ml of acetone was added to the solution at -80 $^{\circ}$C. As a result of this process, it was observed that a gelled phase precipitated. This event resulted in a water-soluble compound formed between sodium citrate and boric acid, and this compound precipitates with the addition of acetone. According to this result, acetone acted as an anti-solvent. The images of the precipitated phase with the addition of acetone and dried at 90 $^{\circ}$C and ground in agate mortar are given in Figure 7, respectively [1].

Figure 7. The gel product precipitated by the addition of acetone and the precursor powder obtained by drying the gel product [1].

3.2. Phase (XRD), Microstructure (SEM/EDS) and Bond Characteristic (FT-IR) Analysis Results of Powders

XRD phase analysis results of BC1 coded raw powders (as-synthesized) were given in Figure 8. When the mole ratio of sodium citrate: boric acid was 1:1, peaks of sodium and sodium borate-based compounds were observed. These phases are; disodium dodecahydroxo-dodecaborate tetrahydrate (indexed #1), disodium tecto-octaborate (#2), and trisodium heptaborate (#3). It was also observed in the diffraction of the aqueous sodium hydroxide (#4) phase. The formation of single-phase compounds of Na and B elements has been interpreted as the homogeneous coexistence of these elements at the atomic level [1].
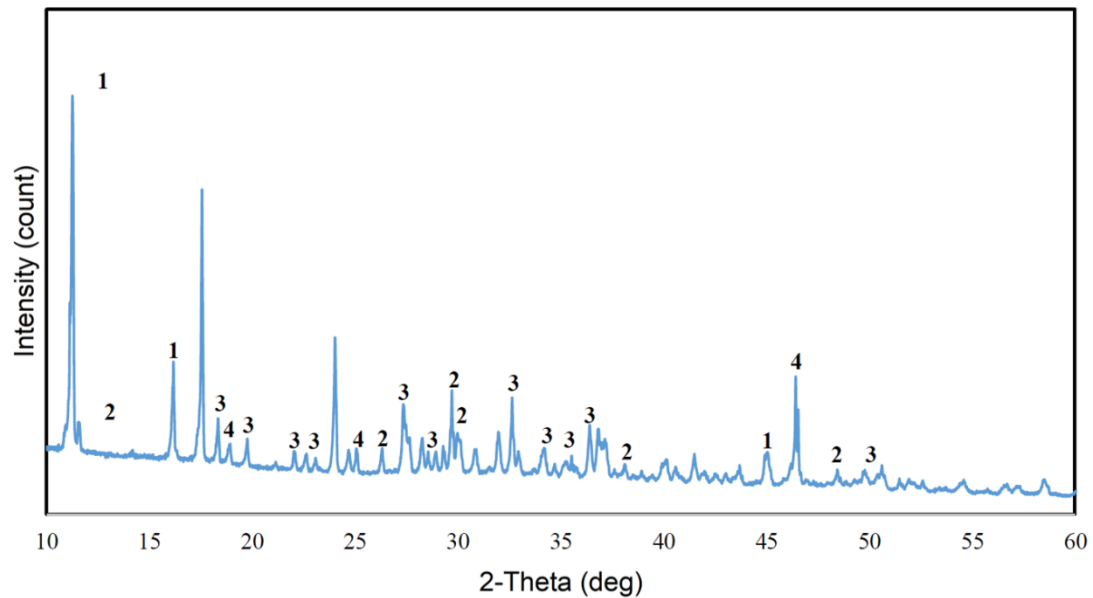
Figure 8. XRD diffraction pattern of BC1 coded powder [1].

In Figure 9, the phase contents of BC2 coded raw powders (as-synthesized) were obtained by X-ray diffraction. In the case where the mole ratio between sodium citrate: and boric acid is 1:1.3, the amount and intensity of the crystalline phase in the structure decreases, while it was observed that the powder has an irregular (amorphic) phase content. Observed sodium-boron-based phases; trisodium heptaborate (#1) and disodium octaborate (#2). It was also observed in the diffraction of the aqueous sodium hydroxide (#3) phase. Due to the amorphic structure of the powder, it may turn into a crystalline structure at relatively lower temperatures [1].
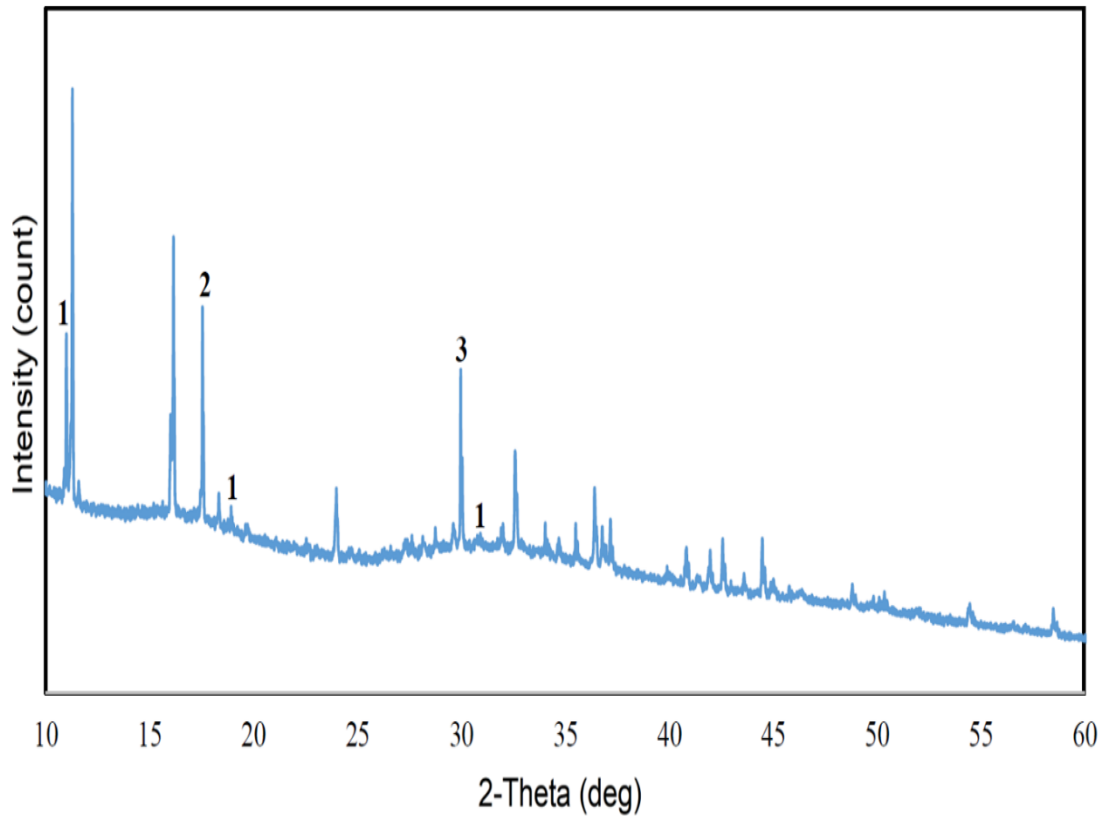
Figure 9. XRD diffraction pattern of BC2 coded powder [1].

FT-IR analysis results of BC1 and BC2 coded powders are given in Figures 10 and 11, respectively. The FT-IR spectrum characteristics obtained from both powders are similar. According to FT-IR analysis; peaks of 1071.47 cm^{-1}, 1296.98 cm^{-1} and 1527.22 cm^{-1} belong to B-C, 1632.98 cm^{-1} B-OH, 2413.33 cm^{-1} C-C, 2986.85 cm^{-1} O-H bonds determined as peaks. Here, the B-C bond, boron, and carbon coexist at the atomic scale, and the boron carbide phase is thought to occur in the formation reactions.

Figure 10. FT-IR spectrum of BC1 coded powder [1].

Figure 11. FT-IR spectrum of BC2 coded powder [1].

Figure 12-a and b show microstructure images of BC1 coded powder obtained from a scanning electron microscope (SEM). SEM microstructure images showed that the powder size has a wide
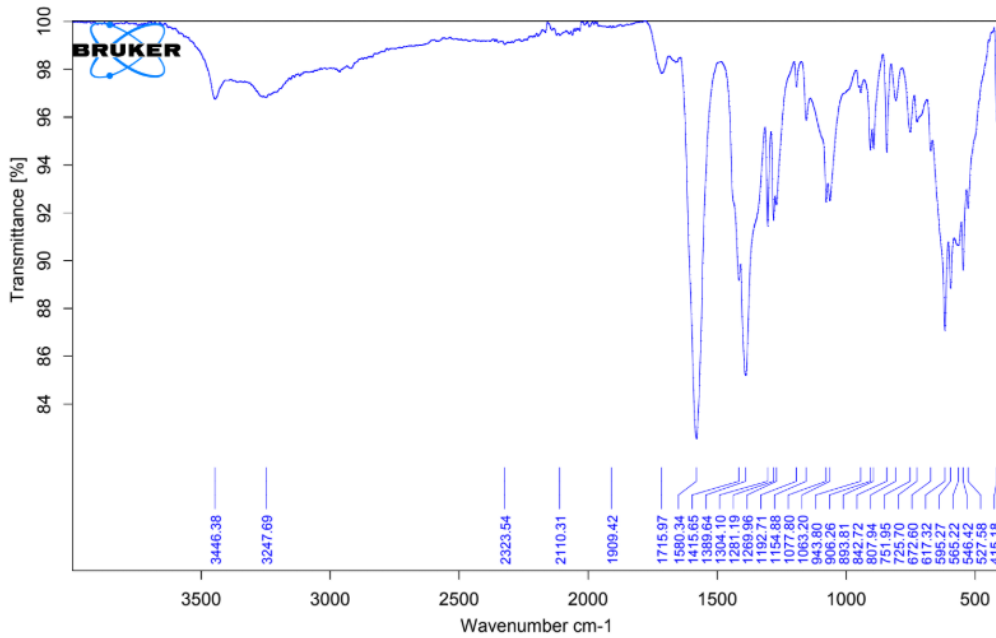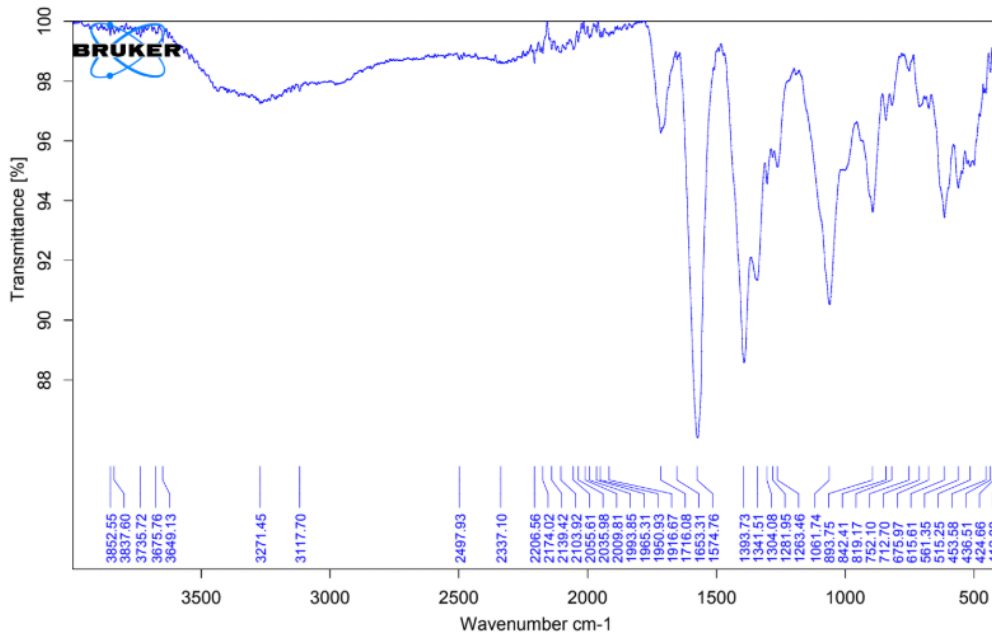
range (~50 μm – nano level). The powders were generally irregular and observed broken shapes with sharp corners. In addition, the particles are dense and do not contain pores [1].
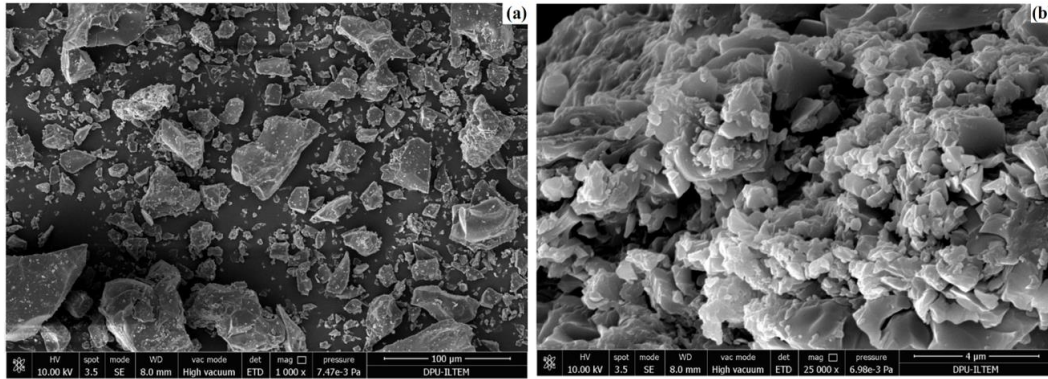
Figure 12. SEM microstructure images of BC1 coded powder (a) X 1000, (b) X 25000 [1].

Microstructure images of BC2 coded powder obtained from scanning electron microscope (SEM) were given in Figure 13-a and b. Compared to the BC1 coded powders, coarser grains were observed. The structure does not have a homogeneous size distribution. It has been determined that small-sized grains come together to form coarse and irregular powder agglomerations [1].
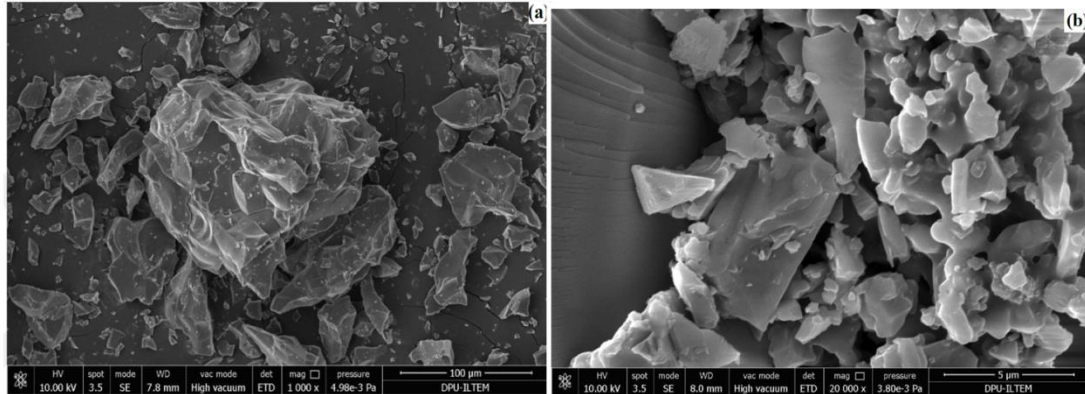
Figure 13. SEM microstructure images of BC2 coded powder (a) X 1000, (b) X 25000 [1].

XRD phase analyses of mechanically activated and heat-treated BC2 powders are shown in Figure 14. In general, when the phase analysis results of the powders obtained after both processes are examined, it is seen that there is no significant difference. In the powder heat-treated only at 1000 $^{\circ}$C, the peaks are sharper and of higher intensity, suggesting better crystallization. However, characteristic diffractions of B_4C were found at 2θ:23.4 and 34 angles [1].
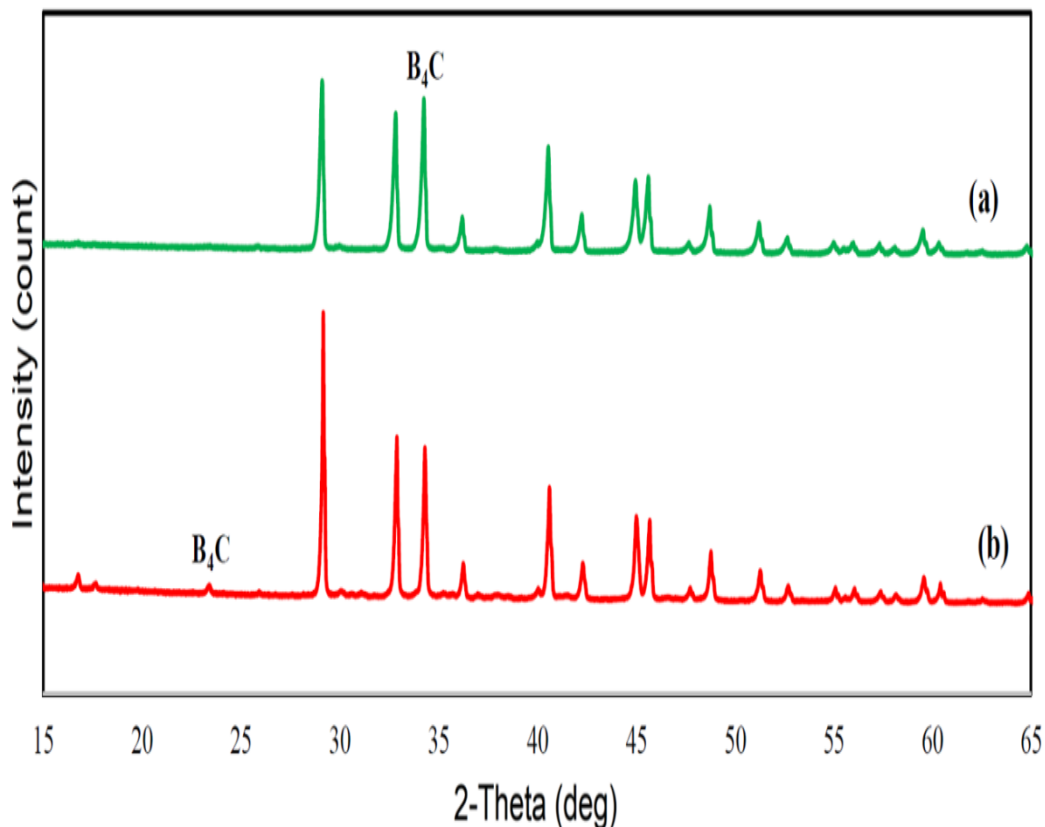
Figure 14. XRD pattern of BC2 coded powders (a) mechanical activation and heat treatment at 1000 $^{\circ}$C, (b) heat treatment at 1000 $^{\circ}$C [1].

The result of FT-IR analysis of the BC2 coded powder raw (as ground), heat-treated at 1000 $^{\circ}$C, and heat-treated after activation was given in Figure 3.15. The peaks observed in 1061 - 675 cm^{-1} bands were defined as B-C bonds, 1575 - 1304 cm^{-1} B-O-C bonds, 2200 - 1900 cm^{-1} C-C bonds, and 3270 - 3117 cm^{-1} bands were defined as O-H bonds. According to the FT-IR results, the B-C bonds will be the precursors for the nucleation of the B$_4$C phase by heat treatment. In addition, the presence of C-C bonds indicates that there is a free carbon phase in the structure [1].
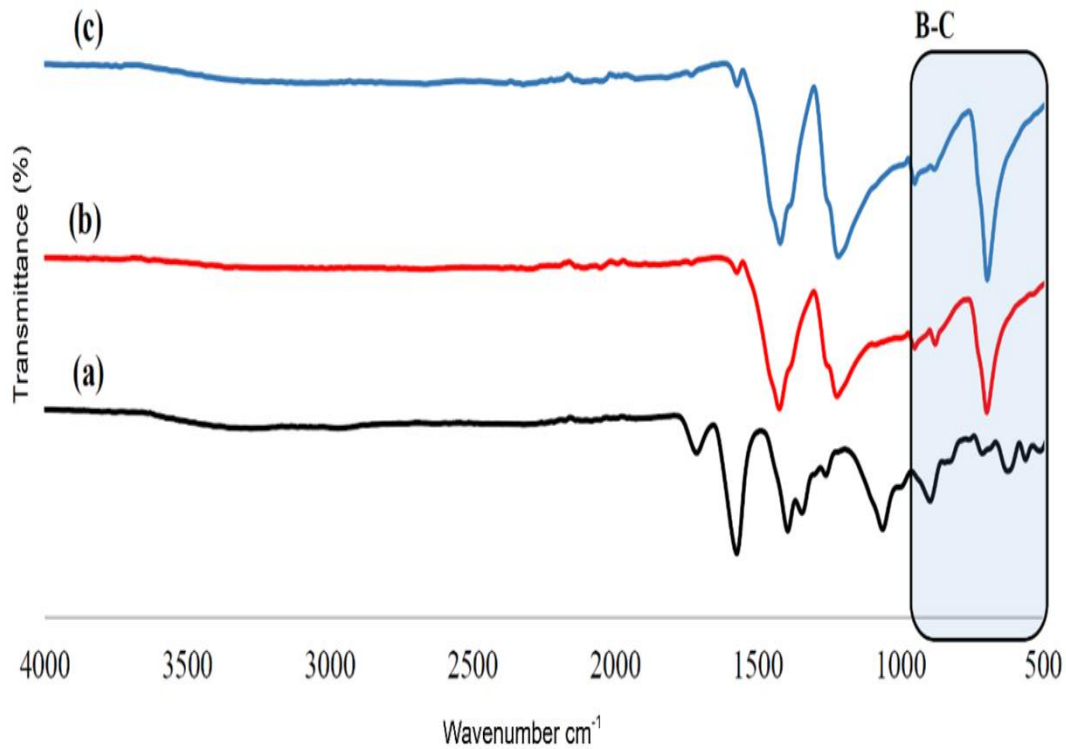
Figure 15. FT-IR spectrum graph of BC2 coded powders (a) raw powder, (b) powder heat-treated at 1000 ^{o}C, (c) activated and heat-treated powder [1].

The microstructure images obtained from a scanning electron microscope (SEM) of BC1 coded powder heat-treated at 1000 ^{o}C are given in Figure 3.16. It was observed that the size distribution in the powder mass varies in the range of ~ five μm – nanoscale. In addition, the grains exhibit a morphology close to spherical. It is thought that the dust lumps formed in the structure are created by the melting of the oxide components consisting of sodium - oxygen (Na-O) or sodium - boron - oxygen (Na-B-O) elements and bonding the grains together. For this reason, the powders need to be removed by dissolving these molten phases by washing them with pure water, which has weak acidic properties, after the heat treatment.
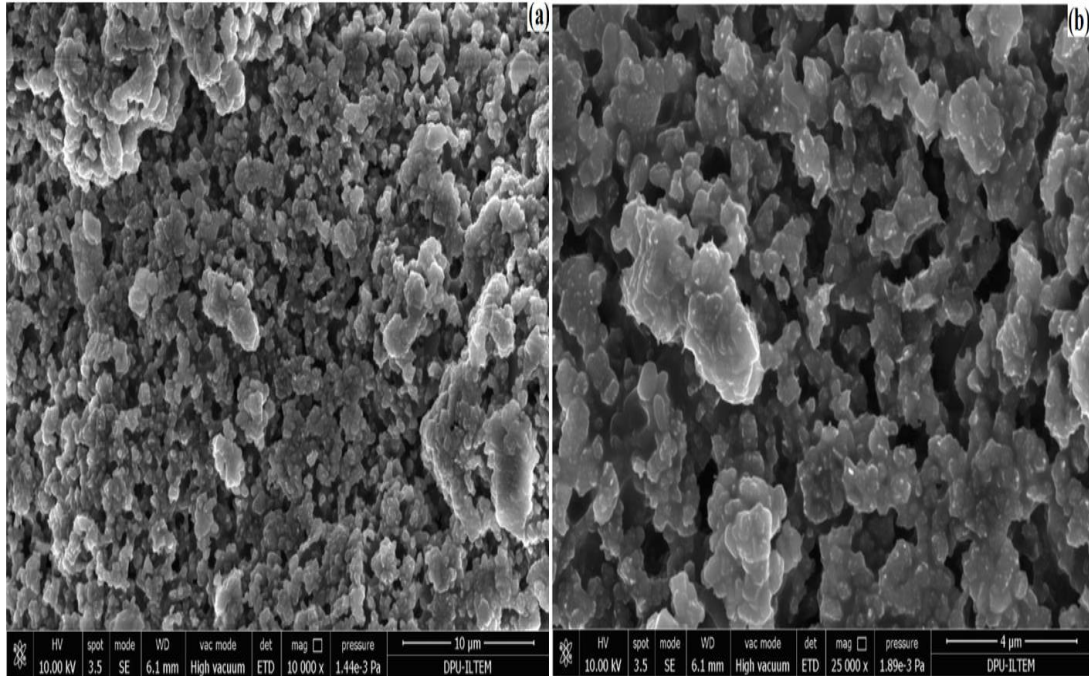
Figure 16. SEM microstructure images of BC1 coded powder heat treated at 1000 ^{o}C (a) X 10000, (b) X 50000 [1].

Figure 17 shows the SEM/EDS analysis results of the BC1 coded powder heat-treated at 1000 ^{o}C. Boron (B), carbon (C), nitrogen (N), oxygen (O) and sodium (Na) elements in the structure were analysed according to the EDS results on different regions. Boron content varies between 12.02 – 7.99 wt.%, carbon 10.93 – 6.73 wt.%, nitrogen 1.53 – 0.91 wt.%, oxygen 39.32 – 32.40 wt.% and sodium content between 47.55 – 40.66 wt.%. The results support the formation of boron-based (BxCy, BxNayOz) oxide and non-oxide phases and sodium-based (NaxOy, NaxByOz) oxide phases. Soluble phases can be removed from the structure by washing with pure water with weak acidic properties [1].
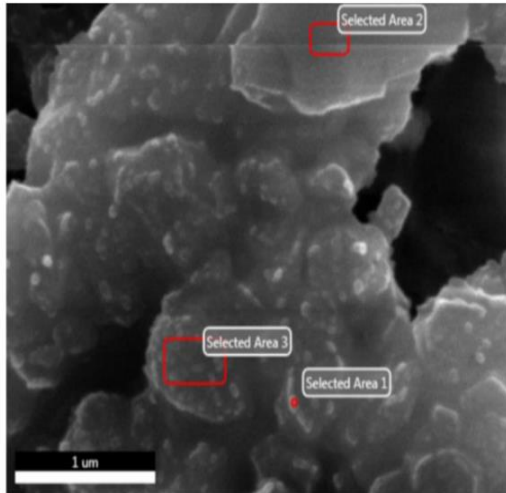
Element	Zone 1		Zone 2		Zone 3	
	Weight %	Atomic %	Weight %	Atomic %	Weight %	Atomic %
B	11,76	18,17	7,99	12,70	12,02	18,42
C	6,73	9,37	10,83	15,49	10,93	15,07
N	1,53	1,83	1,23	1,50	0,91	1,07
O	39,32	41,07	32,40	34,78	33,68	34,86
Na	40,66	29,56	47,55	35,52	42,46	30,58

Figure 17. SEM/EDS analysis of BC1 coded powder heat treated at 1000 $^{\circ}$C [1].

Microstructure images obtained from scanning electron microscope (SEM) of BC2 coded powder heat-treated at 1000 $^{\circ}$C were given in Figure 18, and SEM/EDS analysis results were shown in Figure 19. Dense grains with rod-like morphology and ~1 μm in size were observed in the powder mass. Observed Boron (B), carbon (C), nitrogen (N), oxygen (O), and sodium (Na) elements in the SEM/EDS analysis performed on different regions of these grains. Boron content is 14.89 – 12.44 wt.%, carbon is 3.91 – 3.32 wt.%, nitrogen is 2.11 – 1.94 wt.%, oxygen is 49.45 wt.% and sodium is 32.67 – 29.83 wt.%. The results support the formation of boron-based (BxCy, BxNayOz) oxide and non-oxide phases and sodium-based (NaxOy, NaxByOz) oxide phases.
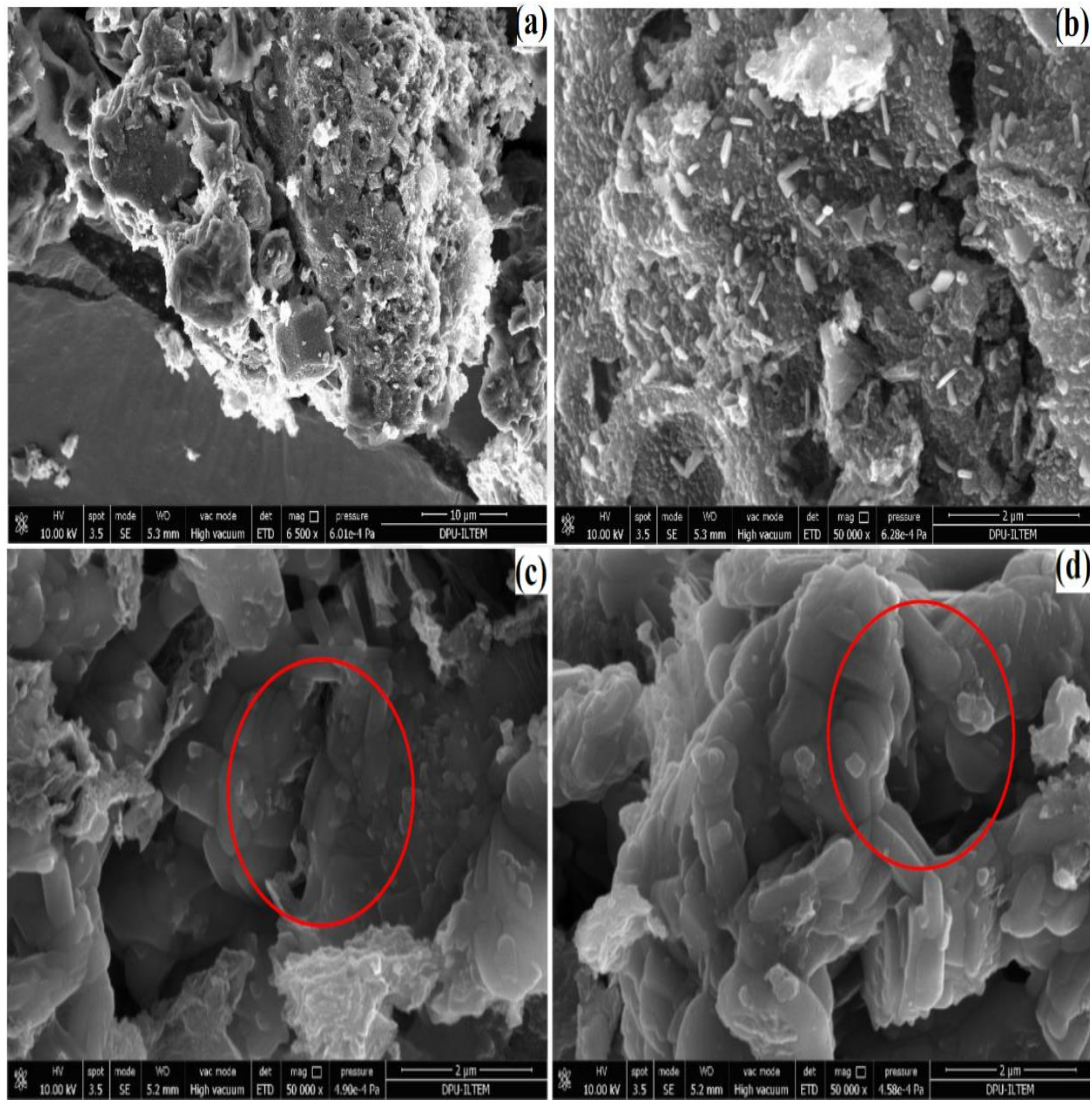
Figure 18. SEM microstructure images of BC2 coded powder heat treated at 1000 $^{\circ}$C (a) X 6500, (b) X 50000, (c) X 50000, (d) X 50000 [1].
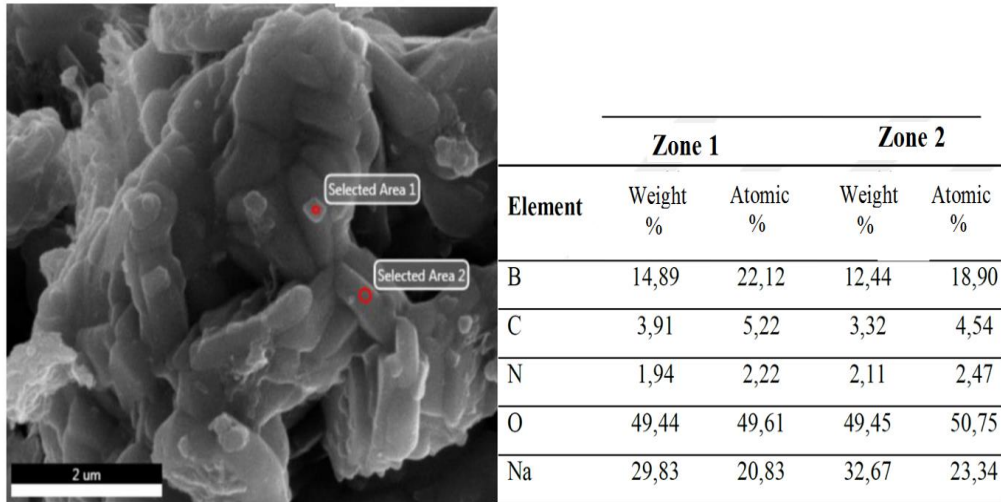
Figure 19. SEM/EDS analysis of BC2 coded powder heat treated at 1000 $^\circ$C [1].

	Zone 1		Zone 2	
Element	Weight %	Atomic %	Weight %	Atomic %
B	14,89	22,12	12,44	18,90
C	3,91	5,22	3,32	4,54
N	1,94	2,22	2,11	2,47
O	49,44	49,61	49,45	50,75
Na	29,83	20,83	32,67	23,34

A complex structure consisting of B-O-C-Na elements occurs between boric acid (H_3BO_3) and sodium citrate ($C_6H_5Na_3O_7$). This structure is the precursor that will later be converted to boron carbide (B_4C) by heat treatment. With increasing temperature, sodium reacted with oxygen and boron and formed oxide phases. At high temperatures, these oxide components melted to form a liquid phase. This liquid phase triggered B_4C nucleation by reducing the diffusion distance and allowing the boron (B) and carbon (C) to react at low temperatures. Possible reactions to the interaction of B-O-C-Na elements are given below [1].

$$x \text{ mole Na} + y \text{ mole O} \rightarrow Na_xO_y \qquad \text{(oxide phase)} \qquad (1)$$

$$x \text{ mole Na} + y \text{ mole B} + z \text{ mole O} \rightarrow Na_xB_yO_z \qquad \text{(oxide phase)} \qquad (2)$$

$$C + O_2 \rightarrow CO_2 \qquad \text{(gas phase)} \qquad (3)$$

$$X \text{ mole B} + y \text{ mole C} \rightarrow z \text{ mole } B_4C \qquad \text{(Nucleation of the } B_4C \text{ phase)} \qquad (4)$$

4. CONCLUSION

B_4C phase nucleation was observed by the anti-solvent precipitation method using sodium citrate and boric acid.

Sodium citrate was used as a source of sodium and carbon. Sodium (Na) acted as the mineralizer that would allow the designed phase to form at low temperatures. In other words, the liquid B_4C phase formed by sodium with oxygen created an environment that allowed nucleation at relatively low temperatures (1000 $^\circ$C). These soluble oxide compounds must be removed from the structure by washing.

Scanning electron microscopy (SEM) analyses showed micron-level, agglomerated particles that did not exhibit a specific morphology.

The optical density values of the solutions at different wavelengths are characterized. Different absorbance (OD) values were obtained depending on the solutions' light diffraction and absorption characteristics; different absorbance (OD) values were obtained.

After the BC2 coded sample @ 1000 ^{o}C heat treatment, regions with dense grains were observed. The SEM/EDS chemical analysis carried out in this region showed that the B-O-N-Na elements exhibited a homogeneous distribution. Low-intensity diffraction of B_4C nucleation was observed in XRD analysis.

ACKNOWLEDGEMENT

REFERENCES

[1] Tuncer, E., (2021). 'Synthesis and Characterization of Precursor Powders for Boron Carbide (B_4C) Ceramics' Kütahya Dumlupınar University, Graduate Education Institute, Department of Materials Science and Engineering, Kütahya, Türkiye.

[2] Subramanian, C., Suri, A. K., (2004). Development of boron based neutron absorber materials. Met. Mater. Process, 16(1), 39-52.

[3] Vijay, S. K., Prabhu, R. K., Annie, D., Chandramouli, V., Anthonysamy, S., Jain, A., (2020). Microwave-assisted preparation of precursor for the synthesis of nanocrystalline boron carbide powder. Transactions of the Indian Ceramic Society, 79(4), 244-250.

[4] Avcioglu, S., Buldu, M., Kaya, F., Ustundag, C.B., Kam, E., Menceloglu, Y.Z., Kaya, C., (2020). Processing and properties of boron carbide (B_4C) reinforced LDPE composites for radiation shielding. Ceramics International, 46(1), 343-352.

[5] Aghaie, A., Falamaki, C., Yekta, B.E., Afarani, M.S., (2002). Effect of seeding on the synthesis of B_4C by the magnesiothermic reduction route. Industrial Ceramics, 22(2), 121-125.

[6] Asgarian, P., Nourbakhsh, A., Amin, P., Ebrahimi-Kahrizsangi, R., MacKenzie, K.J., (2014). The effect of different sources of porous carbon on the synthesis of nanostructured boron carbide by magnesiothermic reduction. Ceramics International, 40(10), 16399-16408.

[7] Domnich, V., Reynaud, S., Haber, R.A., Chhowalla, M., (2011). Boron carbide: structure, properties, and stability under stress. Journal of the American Ceramic Society, 94(11), 3605–3628.

[8] Kakiage, M., Tahara, N., Watanabe, R., Yanase, I., Kobayashi, H., (2013). Microstructure in precursor formed by controlling composition of condensed boric acid-poly (vinyl alcohol) product for low-temperature synthesis of boron carbide powder. Journal of the Ceramic Society of Japan, 121(1409), 40-44.

[9] Murray, P., (2010). Low Temperature Synthesis of Boron Carbide Using a Polymer Precursor Powder Route. Master Thesis, University of Birmingham, United Kingdom, 88s.

[10] Khanra, A., (2007). Production of boron carbide powder by carbothermal synthesis of gel material. Bulletin of Material Science, 30(22), 93-96.

[11] Chen, X. W., Dong, S. M., Kan, Y. M., Zhou, H. J., Hu, J. B., Ding, Y. S., (2016). Effect of glycerine addition on the synthesis of boron carbide from condensed boric acid–polyvinyl alcohol precursor. RSC Advances, 6(11), 9338-9343.

[12] Karaahmet, O., Cicek, B., (2022). Effect of mechanically modification process on boron carbide synthesis from polymeric precursor method. Ceramics International, 48 (9), 11940-11952.

[13] Fathi, A., Ehsani, N., Rashidzadeh, M., Baharvandi, H., Rahimnejad, A., (2012). Synthesis of boron carbide nano particles using polyvinyl alcohol and boric acid. Ceramics-Silikaty, 56(1), 32-35.

[14] Kosanović, D., Milovanović, L., Milovanović, S., Šaponjić, A., (2007). Low-temperature Synthetic route for boron carbide powder from boric acid-citric acid gel precursor. In Materials Science Forum, (555), 255-260.

[15] Rabiezadeh, A., Hadian, A.M., Ataie, A., (2012). Preparation of alumina/titanium diboride nano-composite powder by milling assisted sol–gel method. Int. Journal of Refractory Metals and Hard Materials, 31, 121-124.

RESEARCH ARTICLE

PREDICTION of POWER SYSTEMS HARMONIC USING FUZZY LOGIC

Ersen KURU[1,*], Leyla TEKIN[2]

[1]Düzce University, Engineering Faculty, Mechatronics Engineering, Duzce, ersenkuru@duzce.edu.tr,
ORCID:0000-0003-1102-7295
[2]Düzce Üniversity, Engineering Faculty, Computer Engineering, Duzce, leylakuru@duzce.edu.tr,
ORCID:0000-0001-7198-1000

ABSTRACT

This paper presents a new approach for predicting the Voltage Total Harmonic Distortion (THD_V) in power systems. We benefit from a power system with nonlinear dynamic load belonging to an Iron and Steel Industry. In this power system the nonlinear load consist of DC motor drives, high frequency welding machine, thyristor controlled AC chopper, rectifier and invertor. Especially high frequency machines used in heating and welding process in an iron and steel industry are playing rol in voltage distortions. Basic relationships about harmonics, effects of the harmonics and ways for the THD_V measurement are described in the firstly and prediction of THD_V using Fuzzy Inference Systems (FIS) are examined in the secondly part of the paper. Power Factor (PF), and 3rd phase current (IL3) values are measured for an example system. After FIS is designed for prediction of THD_V and method is tested using both FIS simulation and field measurements, the proposed fuzzy prediction approach is successfully applied to predict THD_V

Keywords: *Harmonic, Fuzzy Inference System, Power Factor, Active Filter, Distortion Factor*

1. INTRODUCTION

Today, in industrial facilities that make serious contributions to the economy; It is aimed to operate the equipment in the safest environment, especially the continuity of production. While establishing an industrial facility, it first seeks to investigate whether the energy need, which is the basic infrastructure needs, can be met. The next step is to increase the quality of the energy to be received. Industrial facilities can connect to distribution or transmission networks depending on power and generation. In addition to providing continuous and uninterrupted energy, it is among the biggest goals of the relevant transmission and distribution network operators to provide quality energy and to prevent all kinds of disruptive effects from the facilities [1].

Non-linear loads cause current and voltage waveforms to form far from sinusoidal forms on the system. Elements such as power electronics, transformers, converters and arc furnaces are commonly known as nonlinear loads. Energy losses on the system, defects in insulation and heating problems in materials are the harbingers of harmonics. Active and passive filtering systems have been developed in order to prevent the negativities that may occur on the network due to harmonics such as these.

These systems aim to eliminate the disruptive effects in the event of harmonics or by staying on continuously.

Active filters are divided into series active filters, shunt active filters, combined power quality regulators, while passive filters are divided into series passive filters and shunt passive filters. Active filters based on advanced power electronics are more costly than passive filters. Active filters can eliminate harmonics by destroying frequencies other than the fundamental frequency. The working principle of the active filter is to apply the current other than the fundamental component that the non-linear load will draw to the load in a suitable phase. Passive filters consist of a series-connected capacitor and an inductance block. If necessary, ohmic resistor can be added to this block. The working principle of passive filters is to ensure that the harmonic waveform, which is the multiple of the fundamental component, is connected to the ground over L and C values without applying it to the load. In order to eliminate each harmonic component, L and C values must be determined separately [2].

Today, it is aimed to predict and intervene the harmonics that create a disruptive effect on the networks before a certain period of time. With the estimation studies, the filtering systems, which are constantly in operation, will be activated during the times when harmonics will occur, which will provide significant gains in terms of cost and equipment life [3].

This paper presents THD_V method was used for harmonic analysis instead of FIS based studies. In this study, the differences between normal and abnormal harmonics and particularly high level harmonics in a power system with nonlinear dynamic loads are determined using a new technic that uses Fuzzy Inference Systems.

2. MATERIAL AND METHOD

2.1. Harmonics in Power Systems

In power networks, non-linear load means load that has no relationship between current and voltage. The voltage and current curves that are the load source are not sinusoidal. According to Fourier analysis, these non-sinusoidal terms are called harmonics. In energy distribution systems, when a sinusoidal voltage source is applied to a non-linear load such as an arc furnace, transformer, sinusoidal waveform distortions will occur. The reason for the distortion of the current waveform, which should be in the sine form or close to the sinus form, is the sine waves that occur outside the basic network frequency. These currents in the form of other sinuses originating from the non-linear load other than the network frequency (50 Hz) are called harmonics [4].

The presence of harmonics in the system requires a redefinition of their electrical magnitude. Below are some definitions necessary to determine the quality of power systems. The smaller these values are, the higher the quality of the energy drawn by the consumers from the power plants and the closer to the sinusoidal waveform.
.

Effective current (I) and Current Total Harmonic distortion (THD_1) are described as below;

$$I = \sqrt{\left(\frac{1}{T}\int_0^T i^2(t).dt\right)} = (I_0^2 + I_1^2 + I_2^2 + \cdots)^{1/2} \qquad (1)$$

$$\text{THD}_I = \frac{\sqrt{\sum_{n=2}^{\infty} I_n^2}}{I_1} \tag{2}$$

2.2. Effects Of Harmonics on Power Factor (PF)

The use of parallel capacitors reduces voltage shape distortions and increases the power factor. It also has a significant effect on harmonic levels. Capacitors do not generate harmonics but provide grid networks for possible resonance conditions. If the added capacitors are tuned to a harmonic frequency in the system voltage or current, in the resonant frequency range, large currents or voltages will occur. This may lead to dielectric failure or capacitor breakdown. Fuse blows in capacitors are a symptom of the harmonic problem. The resonance frequency of capacitor banks with a low voltage system can be found as follows [5].

Active Power, Power Factor and Apparent Power are represented as P, PF, S.
Active power calculation is given at below:

$$P = P_1 = VI_1 cos\varphi_1 \tag{3}$$

The angle between voltage and load current is shown as φ1. When the average power is examined, it consists of current and voltage.

$$S = VI \tag{4}$$

Power Factor (PF):

$$PF = \frac{P}{S} = \frac{VI_1|cos\varphi_1|}{VI} = \frac{I_1||cos\varphi_1|}{\sqrt{\sum_{n=1}^{K} I_n^2}} \tag{5}$$

The distortion factor is expressed as I_1 / I. When the power factor is rearranged;

$$PF = |cos\varphi_1| * DF \tag{6}$$

The baseline distortion factor must be less than 1 possible. The more sinusoidal the waveforms, the closer the power factor value is to 1.

3. RESULTS

Fuzzy logic is a model that enables the use and representation of human knowledge. Fuzzy logic represents information in a simpler way than the interpretation of the human brain, which has the ability to interpret information at an advanced level [7, 8]. An important issue, especially in the electrical energy sector, is the analysis of power quality [6].

In this study, we benefit from a power system with nonlinear dynamic load belonging to an Iron and Steel Industry. Figure 1. In this power system the nonlinear load consist of DC motor drives, high frequency welding machine, thyristor controlled AC chopper, rectifier and invertor. Especially high frequency machines used in heating and welding process in an iron and steel industry are playing role

in voltage distortions. Therefore this plant is very suitable for our study. Firstly, Power Factor (PF), $\cos\varphi$, 3rd phase Current (IL3) and THD_V values must be measured. This values are measured from the busses illustrade in Figure 3. The results of these measuremnets are shown respectively in Figure 5, Figure 6 ve Figure 7.

This study introduces a system design that can achieve the target between power factor and other electrical parameters.

Figure 1. Nonlinear loods in Iron and Steel Factory.

Figure 2. High frequency welding machinery.

There are four inputs and one output in total in the system. Inputs of system are Power Factor (PF), $\cos\varphi$, difference (D), 3rd Phase Current (IL3), Output of system is THD_V. Fuzzy Logic Toolbox on the Matlab platform was used to design this system. The system design is highly estimated THD_V with high accuracy.

Figure 4, 5 and 6 show output membership functions (MFs), According to the figures, it was decided to create one MF for each of the inputs and 3 MFs for THD_V. Table 1 shows the value ranges for MFs. By means of Mamdani fuzzy inference, the fuzzy space includes 15 (5 MFs x 3 MFs) parts.
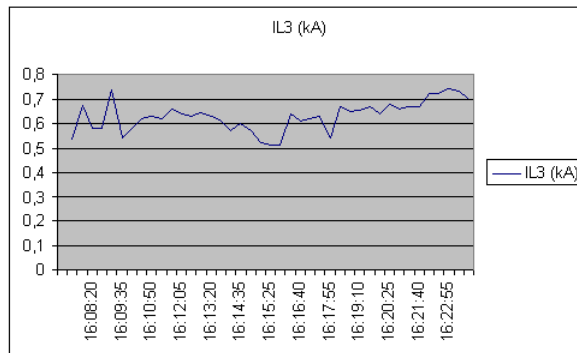
Figure 3. Measurement point.

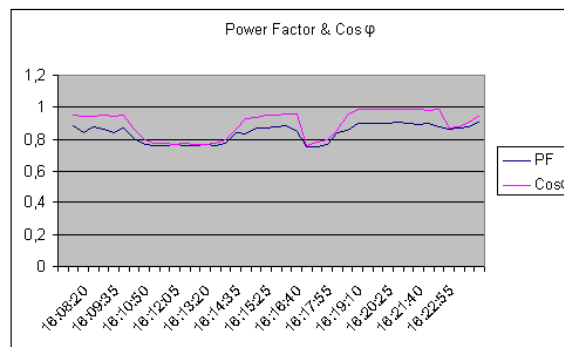**Figure 4.** Real time current measurement values.

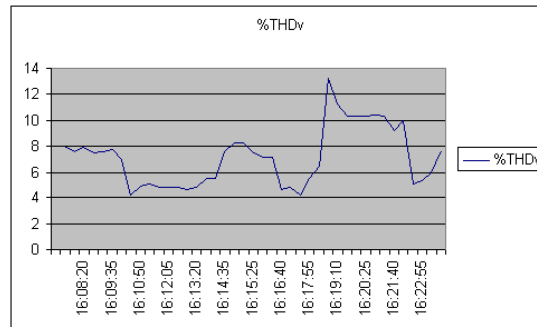**Figure 5.** Real time power factor and cosφ measurement values.

Figure 6. Real time harmonic measurement values.

MFs of input and output variables are designed according to Figures 4, 5 and 6. THD_V values vary between 4.2 and 13.2. In the membership function, these values are divided into three parts and named "LOW", "NORMAL" and "HIGH". Power factor, $\cos\varphi$, membership functions are named as "LOWLOW", "LOW" and "NORMAL". The current membership functions in Figure 4 consist of three parts as "LOW", "NORMAL" and "HIGH". Membership function range values are given in Table 1.

Table 1. Membership Function Intervals.

PF	Cos	D	IL3	%THD$_v$
0,751-0,88	0,764 0,905	0-0,031	540-740	0-6,5
0,805-0,915	0,865-0,955	0,06-0,108	510-735	6,5-10
0,88-0,905	0,977-0,991	0,08-0,110	640-680	10-13,2

After the FIS design, the rules within the method had to be tested. The FIS Test was performed with the real harmonic measurements in Table 1. The measurement of the actual data was taken at 15 sec intervals. It also means that it includes voltage harmonics under varying load conditions. In this way, real THD_V estimations, which are the output of the system, can be made.

An increase in the difference between PF and $\cos\varphi$ causes an increase in THD_V. Within the scope of the application, it is seen that there is an increase in the harmonic level with the decrease in the power factor. Figure 7 shows the FIS architecture, which establishes a relationship between PF and harmonics.
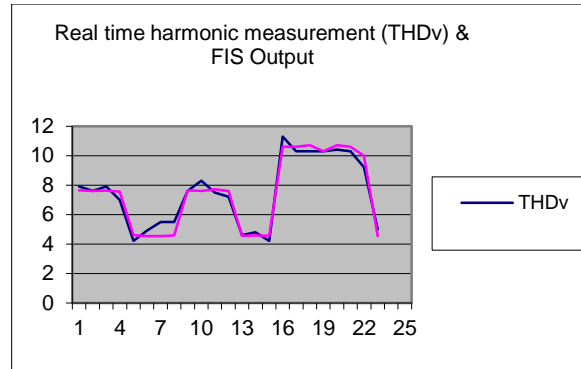
Figure 7. Real time harmonic measurement and FIS Output.

4. CONCLUSION

In this study, it is seen that fuzzy logic systems for THD_V extraction are quite successful. The proposed fuzzy logic inference method has achieved quite peaceful results in estimating THD_V. In this way, cosφ, power factor and phase current values can be estimated with very little error. FIS structures in THD_V systems can make accurate predictions. With the proposed method, an effective method in harmonic analysis is used in real time. At the same time, this fuzzy logic based harmonic filter design seems to be more economical.

ACKNOWLEDGEMENTS

REFERENCES

[1] Yiğit, E., Özkaya, U., Öztürk, Ş., Singh, D., Gritli, H. (2021), Automatic detection of power quality disturbance using convolutional neural network structure with gated recurrent unit. Mobile Information Systems, 2021.

[2] Fang Z. P. (2001), Harmonic Sources and Filtering Approaches. IEEE Industry Applications Magazine, 18-25.

[3] Probabilistic Aspects Task Force of the Harmonics Working Group Subcommittee of the Transmission and Distribution Committee, Time-Varying Harmonics:Part I – Characterizing Measured Data, IEEE Transactions on Power Delivery, 13(3), 1998, 938-944.

[4] Janik, P., Lobos, T. (2006), Automated classification of power-quality disturbances using SVM and RBF networks. IEEE Transactions on Power Delivery, 21(3), 1663-1669.

[5] Yılmaz, A., Küçüker, A., Bayrak, G. (2022), Automated classification of power quality disturbances in a SOFC&PV-based distributed generator using a hybrid machine learning method with high noise immunity. International Journal of Hydrogen Energy, 47(45), 19797-19809.

[6] Wang, J., Zhang, D., Zhou, Y. (2022), Ensemble deep learning for automated classification of power quality disturbances signals. Electric Power Systems Research, 213, 108695.

[7] Zadeh L.A. (1965), Fuzzy sets. Information Control, 8, 338-353.

[8] Hung T. N., Elbert A.W. (2000), A first Course in Fuzzy Logic, Chapman and Hall / CRC .

[9] Fuzzy Logic Toolbox User's Guide (2013), The MathWorks, Inc., Massachusetts, USA.

[10] Mamdani E.H., Assilian S. (1975), An experiment in linguistic synthesis with a fuzzy logic controller. International Journal of Man-Machine Studies, 7(1), 1-13.

RESEARCH ARTICLE

AUTOMATED PSYCHIATRIC DATA ANALYSIS from SINGLE CHANNEL EEG with SIGNAL PROCESSING and ARTIFICIAL INTELLIGENCE METHODS

Ali Berkan URAL[1]*, Uğur ERAY[2]

[1] Kafkas University, Department of Electrical Electronics Engineering, Kars, berkan.ural@kafkas.edu.tr, ORCID:0000-0001-5176-9280

[2] Kars Harakani State Hospital, Department of Psychiatry, Kars, drugureray@gmail.com, ORCID:0000-0001-5417-3394

ABSTRACT

Artificial Intelligence (AI) methods have been generally used in neuroimaging data to identify patients with psychiatric problems/disorders. Schizophrenia (SZ) is generally defined as a mental problem that affects the thinking ability and memory. Manual assessment of SZ participants is sometimes difficult and susceptible to diagnostic mistakes. Thus, we achieved a Computer Aided Diagnosis (CAD) algorithm to analyze and interpretate SZ patients successfully using single channel measurement Electroencephalogram (EEG) signals with Signal Processing and Artificial Intelligence methods. First, the EEG signals of participants were pre-processed (signal enhancement, filtering, noise removal), Then, signals were disseminated into windowing/segmentation process. Then, the EEG signals are separated with wavelet decomposition via seven sub-bands. Next, the feature extraction process was achieved and specific feature parameters were obtained by summing the numerical values of the processed signals. Then, Feature ranking process was achieved to identify the obtained features of the normal and schizophrenia groups. After ranking process, features are fed to AI (SVM), We have obtained the highest accuracy of 99.31% using SVM with five fold and take off one cross validations.

Keywords: *Schizophrenia (SZ), Single Channel EEG, Computer Aided Diagnosis (CAD), Artificial Intelligence, Feature Extraction*

1. INTRODUCTION

The brain's main function is controlling the work of the entire body and the problems might affect normal/common activities. The common thing of the mental disorder is that any mental disease may impact the human body, also thinking and other important functions. The schizophrenia (SZ) could be a complex, inveterate mental wellbeing clutter characterized by a extend of indications counting daydreams, mental trips, disorganized discourse or conduct, and impeded cognitive capacities. Yet, the exact and ultimate treatment is not available. Objectives within the treatment of schizophrenia incorporate soothing side effects, avoiding backslide, and expanding versatile working so that the persistent can be reintegrated into society. The early and successful location of SZ is fundamental since it influences the quality of living.

In psychiatry, mental diseases are investigated using physiological signals and some questionnaire methods. Nowadays, electroencephalogram (EEG) signals are chosen as a common way to study brain-related disorders. Indeed, these signals are easy for multi-channel acquisition and also more economical. The radiological imaging techniques (MRI and CT) are costly and take more time for obtaining the result. With using these EEG signals, different types of disorders can be easily interpretated. One type of the disease is commonly Parkinson's disease [1], sleep disorders [2, 3], dementia, Alzheimer's disease and other mental disorders [4-8].

Some insights can be provided by recent studies about computer based SZ classification using EEG signals. Kim et al. (2015) worked on EEG signals according to the 10-20 international positioning standard [9]. They gotten completely five recurrence groups and they computed the control parameter with utilizing Fast Fourier Transform (FFT), The accuracy was obtained as approximately 62%. Indeed, Dvey-Aharon studied about EEG signals with using Stockwell approach and Time-frequency transformation was applied to these signals [10]. For five electrodes, the accuracy was obtained as approximately 92%. Santos-Mayo et al. (2016) utilized brain vision equipments for obtaining the single-channel EEG signals, then they used EEG-LAB interface for pre-processing [11]. Totally 16 features were obtained for each electrode and these were classified with Multi-Layer Perceptron (MLP) and Support Vector Machine (SVM), Finally, the accuracy was obtained as 93.42% for MLP and 92.23% for SVM classification. Also, Ibanez-Molina et al. (2018) investigated a study which was about the EEG-based SZ assessments [12]. The resting state EEGs were chosen and used and they were obtained via specific amplifiers. The analyzing process was achieved with using a sliding window over the whole EEG recording. Next, Lempel-Ziv complexity (LZC) was computed from the signal [13]. According to 80 EEG segments the final multiscore LZC score was obtained. Moreover, Oh et al. (2019) observed a system with Deep Learning for classification EEG signals of SZ patients [14]. They used Convolutional Neural Network (CNN) with specific parameters and according to ten-fold cross validation the accuracy was obtained as approximately 98%. Vicnesh et al. (2019) studied on a CAD system for classifying two groups of patients from EEG segments [15]. The accuracy was obtained as 93% with using SVM classifier with 12 features. Sharma et al. (2021) studied on automated detection of SZ from EEG segments with using KNN classifier [16]. They were reported the accuracy as 99.21% from a single channel EEG.

Our proposed system was given in Figure 1. The EEG recordings were pre-processed (signal enhancement, filtering/noise removal), Then, signals were disseminated into windowing/segmentation into 25 epochs according to the World Health Organization (WHO) sleep recording analysis criteria. Then, the EEG signals are disseminated into the wavelet decomposition via seven sub-bands. Next,

the feature extraction process was achieved and some feature parameters (Linear features as EEG asymmetry, amplitude, frequency, I_1 norm value; nonlinear features as Energy, Spectral Energy Density, Shannon Entropy, Spectral Entropy, Correlation, Fractal Dimension (FD), Higher Order Spectra (HOS), Hurst's Exponent, Detrented Fluctuation Analysis (DFA)) were obtained by summing the numerical values of the sub-bands. For Feature Extraction process, only signal's I_1 norm value was computed from itself and 6 subbands of Cz channel. The other features were computed from only the processed Cz-channel. At that point, Feature ranking was accomplished to distinguish and rank the centrality of the extricated features. The profoundly positioned features are encouraged to AI (SVM), The five-fold cross validation strategy is for the most part utilized to prepare and select the finest classifier, which accomplishes tall classification accuracy with least number of highlights. The most highlights of proposed think about are as takes after.

1. We have accomplished a single-channel EEG based CAD framework while a few of the existing considers given in Table 6 are utilized numerous channels [15, 16, 17]. Therefore, our sytem is simple and easy to use for patients.

2. In this study, we used a lot of important features for discriminating the EEG recordings. This study can be explained as a complex but according to the usage, the system is very portable.

3. In the proposed study, we have used some novel features for signals in detail such as Linear features as EEG asymmetry, amplitude, frequency, I_1 norm value; nonlinear features as Energy, Spectral Energy Density, Shannon Entropy, Spectral Entropy, Correlation, Fractal Dimension (FD), Higher Order Spectra (HOS), Hurst's Exponent, Detrented Fluctuation Analysis (DFA), These salient features were fed into AI.

4. Simulation results reveals that the proposed method has important AUC values and the accuracy of 99.31% for SVM using only the Cz-EEG channel.

5. In the proposed work, we have created a novel ideal multiple-band orthogonal channel bank, so channels are ideally gotten and localized within the frequency space.

6. To ensure the system's performance stability and avoiding possible overfitting problems, we used 5-fold cross validation and hold out validation.
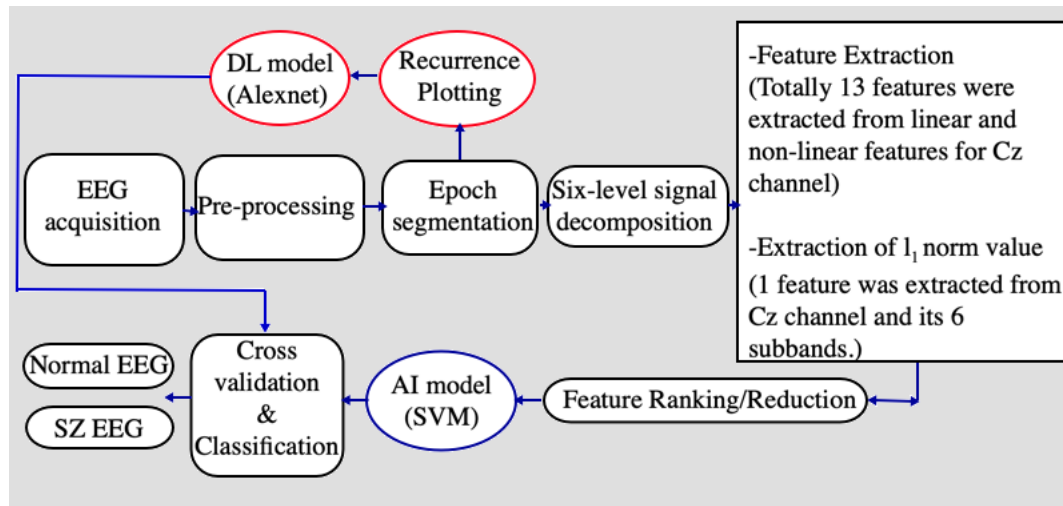
Figure 1. Proposed system flow diagram (and future implementation with Deep Learning-AlexNet model),

2. MATERIAL and METHODS

2.1. Data Set

36 SZ patients (18 females-18 males) and 36 normal members were utilized with a normal age of 35.3 ± 4.1 and 33.9 ± 3, separately. Open access information was obtained from the Research Facility for Neurophysiology Interfacing from Moscow State University-Faculty of Science. The EEG signals were recorded on a multichannel with a testing frequency of 128 Hz. All electrodes were utilized as T4, T6, Fp2, F8, Fp1, F7, F4, Fz, T3, T5, O1, O2, C4, P4, P3, F3, C3, Cz and Pz. The inspecting frequency of EEG signals is chosen 128 Hz for digitizing the EEG recordings. The duration of each epoch is 60s; hence, each epoch contains 7680 samples. Figure 2 and 3 shows the EEG signal from Cz-channel of two groups of patient. Table 1 moreover incorporates the points of interest of the data-set. 16-channel EEG signals comparing to the normal and SZ classes are given in Figure 4 and 5, individually.
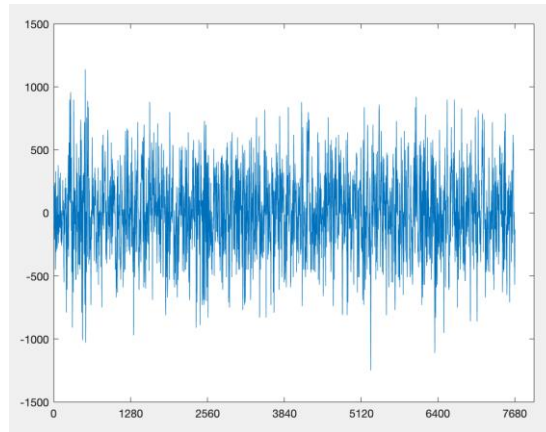
Figure 2. Random EEG signal of acquired from Cz-channel of normal participant.
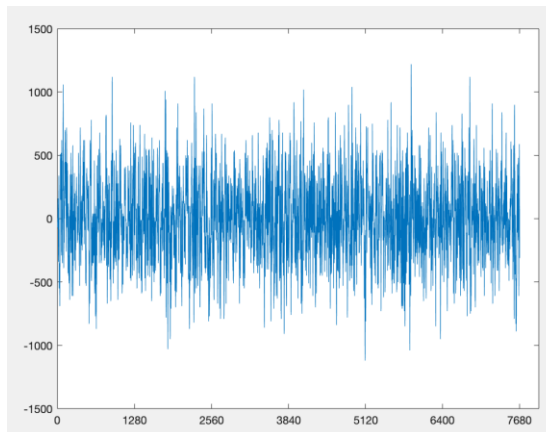
Figure 3. Random EEG signal of acquired from Cz-channel of SZ participant.

Table 1. Details of used dataset.

Type	Number of Participants	Average age value of male and female
Normal	36(18M+18F)	$35.3 \pm 4.1, 33.9 \pm 3.1$
SZ	36(18M+18F)	$35.3 \pm 4.1, 33.9 \pm 3.1$
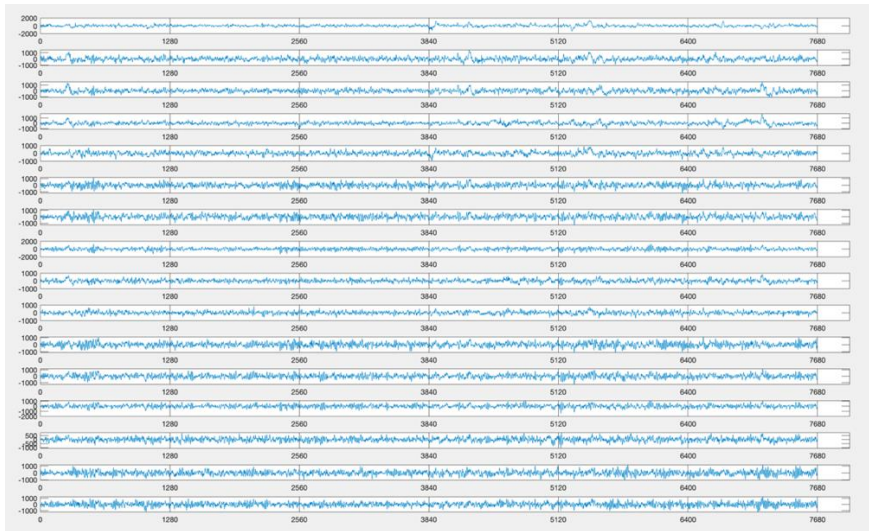
Figure 4. EEG subsignals of a normal participant. Y-axis represents F7, F3, F4, F8, T3, C3, Cz, C4, T4, T5, P3, Pz, P4, T6, O1, O2, respectively.

X-axis represents number of samples at sampling frequency 128 Hz.
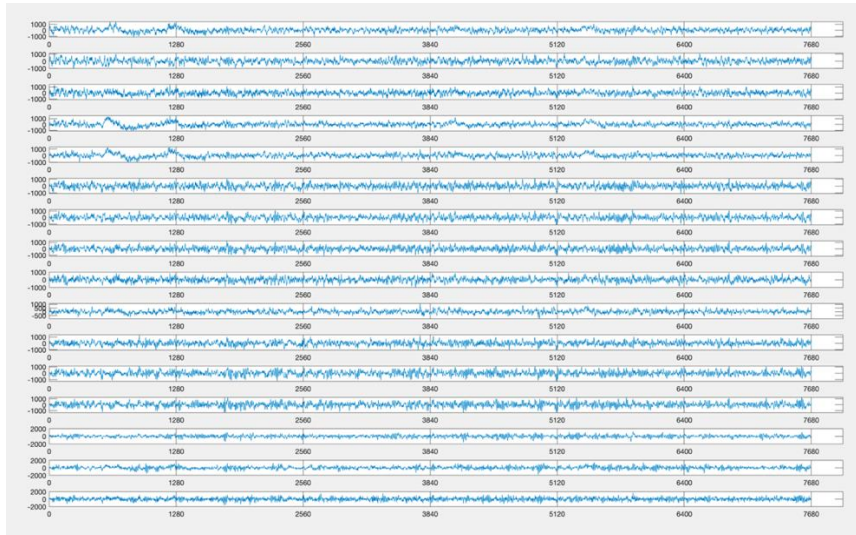
Figure 5. EEG subsignals of a SZ participant. X-axis represents number of samples at sampling frequency 128 Hz.

2.2. Proposed Method

For this study, EEG signals were sampled at 128 Hz. Firstly, these signals were pre-processed by filtering with sixth-order Butterworth filter and signal enhancement methods. The specific details are given in Table 1.

2.2.1. Pre-processing (optimal filter design and filtering), epoch segmentation and six-level-signal decomposition

Because of being time-varying and non-stationary, the Fourier Transform (FT) can sometimes not be effective for the analysis of signals in detail [18]. Then, this problem can be eliminated by using Fast Fourier Transform (FFT) by analyzing the signal into windows and then the whole information is gathered from these slices. It is important that for FFT, specific details of the signals have to be obtained in both frequency spaces. Wavelet is called the significant device that gives the data around almost a signal in both spaces [19, 20]. The wavelet primarily disseminates the signal into little windows in arrange that the specified data can be gotten from scaling and moving forms. For this ponder, for signal investigation, a two-orthogonal-channel was in a general sense utilized. For getting ideal comes about, the mean-squared-frequency-spread of the channels was utilized for planning the limited orthogonal wavelet banks. The ideal channels utilized in this think about have ideal and least recurrence spread and the effective number of zero moments. Without a doubt, frequency localization can be communicated as an imperative quality in planning ideal channels. Moreover, cut-off frequencies regarding to the stop passbands do not be required and instead of this situation, the RMS bandwidth can be considered for this issue because this bandwidth is related to the entire spectrum of the signal [21]. The whole filter coefficients of low pass filter for using in wavelet decomposition are given in Table 2, respectively.

Table 2. Coefficients of optimal LPF filter.

Number	Coefficient value
1	0.1225
2	0.4996
3	0.7622
4	0.3252
5	-0.2126
6	-0.1197
7	0.0997
8	0.0248
9	-0.0295
10	0.00077
11	0.00455
12	-0.0015

2.2.2. Feature extraction

In this section, some specific parameters called as features were computed from EEG signals. For this phase, totally 13 features were extracted from linear and non-linear features for Cz channel of the EEG signals. Indeed, 1 extra feature as l_1 norm values was extracted from Cz channel and its 6 sub-bands. In Figure 7, sample bispectrum magnitude plots of the sample EEG signals given in Figure 2 for normal and Figure 3 for SZ patient.
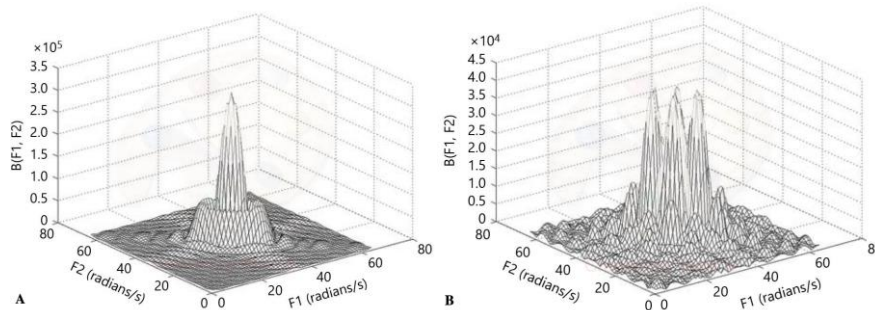
Figure7. Sample bispectrum magnitude plots of Figure 2 (normal participant) and Figure 3. (SZ patient),

Non-linear features obtained from signals;

o   Energy [22]:
In signal processing, the energy E of s continuous time signal x(t) can be expressed in Eq. (2);

$$E = \int_{-\infty}^{\infty} |X(t)|^2 dt \tag{1}$$

Indeed, the energy E of the discrete time signal $x[n]$ can be expressed in Eq. (3);

$$E = \sum_{-\infty}^{\infty} |x[n]|^2 \tag{2}$$

o   Spectral Energy Density [23]:
The spectral energy density of the signal X(t) is given in Eq. (4);

$$E(f) = |X(f)|^2 \tag{3}$$

Where X(f) is the Fourier Transform of X(t),

o   Shannon Entropy [24]:
Information entropy S is defined as:

$$S_{en} = - \sum_{i=!}^{N} p(xi) log_a^{p(xi)} \quad (a>1) \tag{4}$$

where p(xi) are probabilities of acknowledgment by the arbitrary variable x values xi. Shannon entropy is clarified by a degree of vulnerability related with the event of the result. At long last, a better esteem of the entropy gives a more questionable result and it is said that it is more troublesome to anticipate.

o   Spectral Entropy [25]:
Spectral entropy primarily employments the Fourier change strategy and the power spectral density (PSD) can be gotten. The PSD speaks to the dispersion of control as a work of recurrence. So, normalization of P(f) yields a likelihood thickness work. Utilizing the definition of Shannon's entropy, spectral entropy can be characterized as:

$$\text{Sp}_{en} = \sum_{i=flow}^{fhigh} p(i)\log(pi) \tag{5}$$

Spectral entropy is usually normalized $\text{Sp}_{en}/ \log N_f$, where N_f is the number of frequency components in the range $[f_{low}, f_{high}]$.

o   Correlation [26]:
First, we have to express defining a convolution between two continuous time signals x(t) and a(t) is given by;

$$y(t) = \int_{-\infty}^{\infty} x(T)a(t-T)dT \tag{6}$$

Then, we have to express defining a convolution between two discrete time signals x[n] and a[n] is given by;

$$y[n] = \sum_{i=-\infty}^{i=\infty} x[i]a[n-i] \tag{7}$$

The correlation between the same two signals given above can be expressed as;

$$c(t) = x(t) * a(t) = x(t) \otimes h(-t) \tag{8}$$

Where $\otimes$ operand i represents the convolution operation. For discrete time signals, the correlation between the same two signals can be expressed as

$$c[n] = \sum_{i=-\infty}^{i=\infty} x[i]a[i-n] \tag{9}$$

o   Fractal Dimension [27]:
Fractal Measurements (FD) are one of the prevalent measures utilized for characterizing signals. They have been utilized as complexity measures of signals in different areas counting discourse and biomedical applications. The fractal measurement has been calculated by utilizing the DWT and this will be gotten by the taking after condition:

$$\text{level}_{max} = \log(n) / \log(2) \tag{10}$$

where n is the number of focuses of each considered window/signal [28]. After the DWT is connected, two vectors, x[n] and y[n] were produced [28, 29]. Once the vectors are decided, the fractal measurement can be calculated concurring to Eq. (12):

$$D = 2 - \left|\frac{\beta-1}{2}\right| \tag{11}$$

where, β is the point of the normal line given by the vectors x[.] (length of each leaf) and y[.] (energy of each leaf), by implies of the least squares method [28, 29].

o   Higher Order Spectra (HOS) [30]:
HOS comprises of higher-order moment spectra, which is characterized for deterministic signals, and cumulant   spectra.   In common there   are   three inspirations behind   the utilize of

HOS investigation in signal preparing: First, to smother Gaussian noise and fluctuation within the range of location and parameter estimation issues. Second, to reproduce the stage and the size reaction of signals/systems. Third, to detect and characterize nonlinearities within the information.

$$C(w1,w2) = \sum_{r1=-L}^{L} \quad \sum_{r2=-L}^{L} C(T1, T2) \, e^{-j(w1T1+w2T2)} W(T1, T2 < \theta). \tag{12}$$

where L < M -1, and W(Tl, T2) is a two dimensional window, used to smooth out edge effects.

o   Hurst's Exponent [31]:
The Hurst exponent is alluded to as the "file of reliance" or "record of long-range reliance". It explores the relative inclination of a time arrangement. A esteem H within the run 0.5–1 shows a time arrangement with long-term positive autocorrelation. This in differentiate to the ordinarily control law rot for the 0.5 < H < 1 and < H < 0.5 cases. The Hurst exponent, H, is characterized in terms of a time arrangement as follows;

$$C_n^H = E(R(n)/S(n)) \quad (n \rightarrow \infty), \tag{13}$$

where; R(n) is the run of the primary n total deviations from the cruel, S(n) is the series (whole) of the primary n standard deviations, E|x| is the anticipated esteem, n is the time span of the perception (number of data points in a time arrangement), C could be a constant.

o   Detrented Fluctuation Analysis [32]:
For DFA, it is useful for analyzing time series that appear to be long-memory processes or 1/f noise. It isn't always the case that the scaling exponents are independent of the scale of the system. In the case depends on the power extracted from;

$$F_q(n) = \sqrt[q]{(\frac{1}{N} \sum_{t=1}^{N} (X_t - Y_t)^q} \tag{14}$$

Linear features obtained from signals;

o   Asymmetry [33]:
This feature regards to measure symmetry by taking any suitable norm on the signals. For example the symmetry of f(x) can be measured as;

$$s[f] = \|f+\| / (\|f+\| + \|f-\|) \tag{15}$$

$$\|f\| = \sqrt{\int_R f(x)^2 dx} \tag{16}$$

which ranges from 0 (fully asymmetric) to 1 (fully symmetric),

o   Amplitude:
This feature regards to the peak-to-peak value of the signal. This value is obtained from the signals and used in Feature Extraction part.

o   Frequency:

This feature regards to the frequency value (f=1/period) of the signal. This value is obtained from the signals and used in Feature Extraction part.

o l_1 Norm Value [34]:

The l1 standard highlight of subbands has been computed in this work. The l1 standard can be basically calculated as;

$$l_1(x) = \sum_{n \in Z} |X(n)| \tag{17}$$

where n is the index of the sequence x(n) and Z denotes the set of integers.

2.2.3. Feature ranking/reduction:

Feature/Variable Ranking is the method of requesting the features by the esteem of a few scoring work, which ordinarily measures feature-relevance. A straightforward strategy for highlight determination using variable ranking is to choose the k-highest positioned highlights concurring to signal.

2.2.4. Classification with aı model via cross validation [35]:

All these calculated numerical feature vectors were first fed into Support Vector Machine (SVM), which is a classical Artificial Intelligence (AI) method, and the system learned it. Classification can be mainly defined as distinguishing and identifying situations or objects with similar characteristics from those with other different characteristics.

2.2.4.1. Support vector machines (svms)

SVM is fundamentally used as an effective AI method for classification processes. The SVM algorithm allows to work on small and large data sets in order to extract important information from data sets [36]. The main purpose in the SVM algorithm is to create a learning task with a given finite number of training data. The SVM learning method is achieved with an optimally separated hyperplane that maximizes the margin (the shortest distance to the data point.

2.2.5. Training, testing and validation

In this think about, the information set utilized was obtained from 16 channels. For each EEG age, seven l1 standard highlights and completely 10 direct and nonlinear highlights were computed. Firstly, each channel have tried independently and we took all highlights 16 channel EEG signal for classification utilizing five fold cross-validation. The channel (Cz) was utilized with take off one validation and hold out endorsement. In TOCV, 35 subjects out of 36 were utilized to plan the illustrate, and the remaining one utilized for testing the illustrate. We as well performed hold-out endorsement for the Cz channel that gave the foremost great execution utilizing the five-fold CV [35, 36]. In this technique, from 10% to 50% hold-outs are utilized, respectively.

3. RESULTS

We arranged the proposed CAD utilizing Macbook Pro 13 inch 16.0 GB and 64-bit working system and MATLAB R2019a adaptation was utilized. The highlight extraction time has been generally 3 seconds. Highlights were situated utilizing t-test and t-test was utilized to evaluate the estimations of the assortment. The t-value illustrates whether the two classes were assorted or not. The typical time taken for planning and testing is 5.75 p. The classification was accomplished with SVM (with Feature

Extraction) for the Cz channel utilizing the five-fold CV is given in Table 3. Figure 8 appears recipient working characteristic (ROC) comparing to the Cz channel when the classification is performed utilizing all highlights and SVM with five-fold CV.

Table 3. Five fold CV results.

CF	CA	CS	CSF	F1 value
With SVM	98.4%	99.53%	99.10%	99.18%

CF:classifier, CA: classification accuracy, CS: classification sensitivity, CSF: classification specificity

The classification accuracy of the adjusted subset has been found to be 98.4% for SVM.
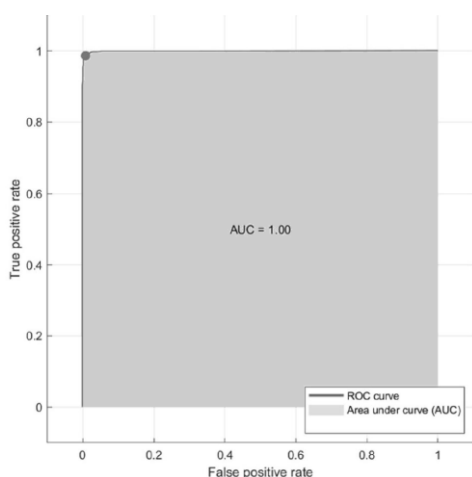
Figure 8. ROC analysis results using SVM with five fold CV.

In arrange to guarantee over-fitting, we utilized TOCV for the classification models utilizing Cz channel. For this demonstrate, the accuracy of 99.31% and F1-score of 99.52% accomplished for SVM with TOCV. In fact, the accuracy of 99.61 with TOCV. The disarray framework and classification come about for holdout approval with SVM classifier were appeared in Tables 4 and 5, separately. The leading classification accuracy is 99.82% for 30% holdout validation.

Table 4. Confusion matrix using Cz channel.

Holdout value (%)	True negative	False positive	False negative	True positive
10	51	1	0	62
20	102	3	0	124
30	156	0	2	187
40	205	2	2	246
50	254	5	3	311

Table 5. Results obtained using Cz channel.

Holdout value (%)	Accuracy	Sensitivity	Specificity	F1 value
10	99.22	99.98	98.34	99.05
20	98.88	99.12	98.31	98.64
30	99.82	99.45	99.37	99.45
40	98.92	98.65	99.20	98.89
50	98.62	98.86	98.46	98.60

4. DISCUSSION

Filtering was achieved with the optimal filter bank for wavelet decomposition. After filtering with max seven decomposition levels, l_1 norm value was computed for each wavelet and also linear and non-linear features were computed for the whole EEG processed signal epochs. Indeed, it was found that the features correspond to the sixth level gave the best performance metrics to us. After classification with the AI model using five-fold CV, we obtained the best accuracies of 99.31% and 99.68% for Cz-channel of EEG signals, respectively. Table 6 gives detailed information about the studies with distinguishing normal and SZ EEg signals.

Table 6. Comparison of our results for SZ detection in literatüre.

Study	Method	Number of participants	Dataset	CA (%)	Used electrodes
Johannesen et al. (2016)	SVM	Normal:12 Abnormal:40	VACHS, Yale	Model 1:84 Model 2:87	Cz, Fz, Oz
Santos-Mayo et al. (2016)	MIFS or DISR	Normal:31 Abnormal:16	Dep. of EEE University of Vallodolid	MLP: 93.42 SVM: 92.23	C3, C4, Cz, F3, F4, F7, F8, Fp1, Fp2, Fz, O1, O2, P3, P4, Pz, T5, T6
Oh et al. (2019)	11-layered CNN	Normal:14 Abnormal:14	Inst. of Neurology, Warsaw, Poland	81.26	Fp1, Fp2, F7, F3, Fz, F4, F8, T3, C3, Cz, C4, T4, T5, P3, Pz, P4, T6, O1, O2
Vicnesh et al. (2019)	SVM, KNN, LD, PNN, DT	Normal:14 Abnormal:14	Inst. of Neurology, Warsaw, Poland	92.91	Fp1, Fp2, F7, F3, Fz, F4, F8, T3, C3, Cz, C4, T4, T5, P3, Pz, P4, T6, O1, O2

Sharma et al. (2021)	l_1 norm, ES-KNN	Normal:14 Abnormal:14	Inst. of Neurology, Warsaw, Poland	97.2	Fp1, Fp2, F7, F3, Fz, F4, F8, T3, C3, Cz, C4, T4, T5, P3, Pz, P4, T6, O1, O2
Our proposed method	l_1 norm, linear and nonlinear features, SVM	Normal:36 Abnormal:36	Laboratory for Neurophysiology and Neuro-computer Interfaces from Moscow State University	SVM:99.31	F7, F3, F4, F8, T3, C3, Cz, C4, T4, T5, P3, Pz, P4, T6, O1, O2

According to the table given above, our proposed system can efficiently distinguish normal and SZ classes from EEG signal epochs. Moreover, with using AI model of SVM, advanced and optimal features were chosen and used optimally in the Feature Extraction part and classification was achieved successfully. Thus, according to the table, our system has better performance results than the other related studies from literature.

Main advantages of our proposed method are:

1. Obtained successful and high accuricies of 99.31 for SVM using only Cz channel of EEG signals with LOCV and five-fold cross validation. Furthermore, the system is more accurate and efficient.

2. Obtained high classification performance results are also important.

3. With using complex and detailed features, features were calculated and also one feature was calculated from seven subbands of the signal via wavelet decomposition. Finally, Feature extraction was achieved for AI model successfully and robust.

4. Developed and more efficient wavelet based decomposition system (filter bank)

In near future, the system can be improved and will be used in the pre-diagnosis CAD systems for detecting some important EEG, Polisomnograpghy (PSG) based disorders, so life will become easier via these CAD systems.

5. CONCLUSION

Methods that help and facilitate the diagnosis of mental illnesses are attracting attention. In this study, a unique methodology for successful detection of schizophrenia using specific complex features via Feature Extraction from single case/channel Cz EEG signals. Indeed, for this study, optimized orthogonal wavelet filters are developed for accurate detection of schizophrenia. Then, 13 specific features were calculated from signals and it is important that one of the features was calculated from seven subbands of EEG signals and the other features were calculated from whole processed EEG signals of participants. In this work, for AI, SVM model was used and highest classification results were obtained. Also, we achieved detailed comparable analysis and classification with EEG signals in

this study with using TOCV and five-fold CV. The methods are mainly less expensive than the existing methods. With using our proposed methods, we obtained important higher classification performance results. The proposed model can be developed to different areas in Biomedical Engineering for online monitoring of schizophrenia. In the future, the main aim will be testing this system with some other diverse and big databases with different EEG based mental disorders.

ACKNOWLEDGEMENT

REFERENCES

[1] Zayrit S., Belhoussine D. T., Nsiri B., Korkmaz Y., Ammoumou A., (2021), The detection of Parkinson disease using the genetic algorithm and SVM classifier, Applied Acoustics 171, 107528.

[2] Jarchi D, Andreu-Perez J, Kiani M, Vysata O, Kuchynka J, Prochazka A, Sanei S., (2020), Recognition of Patient Groups with Sleep Related Disorders using Bio-signal Processing and Deep Learning, Sensors, 20(9):2594. https://doi.org/10.3390/s20092594

[3] Ipsit V.V., Zachary K., Chen-Yu H., Brent P.F., Patrick M., Rose M., Katherine H., Usman M., Kreshnik H., Dina K., (2020), Radio Signal Sensing and Signal Processing to Monitor Behavioral Symptoms in Dementia: A Case Study, The American Journal of Geriatric Psychiatry, 28(8):820-825.

[4] Geman O., Chiuchisan I., Covasa M., Konstantinos E., Saeid S., Jonni G.F.M., Ronney A.M.B., (2016), Joint EEG — EMG signal processing for identification of the mental tasks in patients with neurological diseases, 2016 24th European Signal Processing Conference (EUSIPCO), 1598-1602. doi: 10.1109/EUSIPCO.2016.7760518.

[5] [5] Bone D., Lee C., Chaspari T., Gibson J. and Narayanan S., (2017), Signal Processing and Machine Learning for Mental Health Research and Clinical Applications [Perspectives], IEEE Signal Processing Magazine, 34(5):196-195. doi: 10.1109/MSP.2017.2718581.

[6] Faro A., Giordano D., Pennisi M., Scarciofalo G., Spampinato C., Tramontana F., (2005), Transcranial Magnetic Stimulation (TMS) to Evaluate and Classify Mental Diseases Using Neural Networks, In: Miksch S., Hunter J., Keravnou E.T. (eds) Artificial Intelligence in Medicine. AIME 2005, Lecture Notes in Computer Science 3581. https://doi.org/10.1007/11527770_43

[7] Valenza G., Garcia R.G., Citi L., Scilingo E.P., Tomaz C.A. and Barbieri R., (2015), Nonlinear digital signal processing in mental health: characterization of major depression using instantaneous entropy measures of heartbeat dynamics, Front. Physiol, 6:74. doi: 10.3389/fphys.2015.00074

[8] Zung, W.W. (1965), A self-rating depression scale. Arch. Gen. Psychiatry, 12:63–70. doi: 10.1001/archpsyc.1965.01720310065008

[9] Kim J.W., Lee Y.S, Han D.H., Min K.J., Lee J., Lee K., (2015), Diagnostic utility of quantitative EEG in un-medicated schizophrenia, Neurosci Lett, 589:126–131.

[10] Dvey-Aharon Z., Fogelson N., Peled A., Intrator N., (2015), Schizophrenia detection and classification by advanced analysis of EEG recordings using a single electrode approach, PLoS ONE, 10(4):e0123033.

[11] Santos-Mayo L., San-Jose-Revuelta L.M., Arribas J., (2016), A computer-aided diagnosis system with EEG based on the p3b wave during an auditory odd-ball task in schizophrenia, IEEE Trans Biomed Eng, 64(2):395–407.

[12] Iba n˜ez-Molina A.J., Lozano V., Soriano M.F., Aznarte J.I., Go mez-Ariza C.J., Bajo M., (2018), Eeg multiscale complexity in schizophrenia during picture naming, Front Physiol, 9:1213

[13] Abásolo D., Hornero R., Gómez C., García M., López M., (2006), Analysis of EEG background activity in Alzheimer's disease patients with Lempel–Ziv complexity and central tendency measure, Medical Engineering and Physics, 28(4): 315-322.

[14] Oh S.L., Vicnesh J., Ciaccio E.J., Yuvaraj R., Acharya U.R., (2019), Deep convolutional neural network model for automated diagnosis of schizophrenia using EEG signals, Appl Sci, 9(14):2870.

[15] Vicnesh J., Oh S.L., Rajinikanth V., Ciaccio E., Cheong K., Arunkumar Acharya U.R., (2019), Automated detection of schizophrenia using nonlinear signal processing methods, Artif Intell Med 100:101698.

[16] Sharma M., Acharya U.R., (2021), Automated detection of schizophrenia using optimal wavelet-based $l1$ norm features extracted from single-channel, EEG. Cogn Neurodyn, 15, 661–674. https://doi.org/10.1007/s11571-020-09655-w

[17] Moulin P., Anitescu M., Kortanek K.O., Potra F.A., (1997), The role of linear semi-infinite programming in signal-adapted qmf bank design, IEEE Trans Signal Process, 45(9):2160–2174.

[18] Meignen, S., Pham D.H., Colominas M.A., (2021), On the use of short-time fourier transform and synchrosqueezing-based demodulation for the retrieval of the modes of multicomponent signals, Signal Processing, 178:107760.

[19] Li Y.M., Wei D., Zhang L., (2021), Double-encrypted watermarking algorithm based on cosine transform and fractional Fourier transform in invariant wavelet domain, Information Sciences, 551:205-227.

[20] Gannouni S., Aledaily A., Belwafi K., Aboasamh H., (2021), Emotion detection using electroencephalography signals and a zero-time windowing-based epoch estimation and relevant electrode identification, Sci Rep, 11, 7071. https://doi.org/10.1038/s41598-021-86345-5

[21] Biswas S., Maniruzzaman M. and Bairagi R.N., (2021), Noise Removing from ECG Signal Using FIR Filter with Windowing Techniques, 2021 International Conference on Electronics, Communications and Information Technology (ICECIT), 1-4, doi: 10.1109/ICECIT54077.2021.9641381.

[22] Yu-xing L., Shang-bin J., Xiang G., (2021), A novel signal feature extraction technology based on empirical wavelet transform and reverse dispersion entropy, Defence Technology, 17(5): 1625-1635.

[23] Yong L., Gang C., Chang L., (2021), Research on bearing fault diagnosis based on spectrum characteristics under strong noise interference, Measurement, 169:108509.

[24] Havryliuk V., (2019), The Wavelet Based Detecting of the Signalling Relay Armature Defects, 2019 IEEE 2nd Ukraine Conference on Electrical and Computer Engineering (UKRCON),

[25] Borowska M., (2015), Entropy-Based Algorithms in the Analysis of Biomedical Signals, Studies in Logic, Grammar and Rhetoric.

[26] Kaya Y., Kuncan M., Kaplan K., Minaz M.R. and Ertunç H.M., (2021), A new feature extraction approach based on one dimensional gray level co-occurrence matrices for bearing fault classification. Journal of Experimental and Theoretical Artificial Intelligence, 33(1):161-178, Doi: 10.1080/0952813x.2020.1735530

[27] Ribeiro M., Henriques T., sa Castro L., Souto A., s Antunes L., Costa-Santos C., Teixeira A., (2021), The Entropy Universe, Entropy.

[28] Yunqiang Z. Guoquan R., Dinghai W., Huaiguang W., (2021), Rolling bearing fault diagnosis utilizing variational mode decomposition based fractal dimension estimation method, Measurement, 181: 109614.

[29] Humairani A., Atmojo B.S., Wijayanto I., Hadiyoso S., (2021), Fractal based Feature Extraction Method for Epileptic Seizure Detection in Long Term RRG Recording, J. Phys. Conf. Ser., 1844 012019.

[30] Petropulu A.P., (1994), Higher-Order Spectra in Biomedical Signal Processing, IFAC Proceedings Volumes.

[31] Baygin M., Dogan S., Tuncer T., Prabal D.B., Oliver F., Arunkumar N., Enas W.A., Elizabeth E.P., Acharya U.R., (2021), Automated ASD detection using hybrid deep lightweight features extracted from EEG signals, Computers in Biology and Medicine, 134:104548.

[32] Kavitha N., Soundar R., Kumar T., (2021), An Improved DFA Based Kernel Ensemble Learning Machine Using Local Feature Representations for Face Recognition, Journal of IntelligentandFuzzy Systems, 1203 – 1216.

[33] Jian L., Zijian Q., Xiaojian D., Bing H., Chuanlai Z., (2021), Stochastic resonance induced weak signal enhancement over controllable potential-well asymmetry, Chaos, Solitons and Fractals, 146:110845.

[34] Yuanhang S., Jianbo Y., (2022), Adaptive adjacent signal difference lasso for bearing fault detection, Measurement, 190:110652.

[35] Ural A.B., Eray U., (2022), Psychiatric Data Analysis And Interpretation With Artificial Intelligence, Machine Learning And Deep Learning, ISPEC Publication New Horizons İn The Health Sciences, 231-256.

[36] Ural A.B., (2021), Deep Computer Based Pre-Diagnosis From Chest CTs of COVID-19 Patients, 2021 13th International Conference on Electrical and Electronics Engineering (ELECO), 229-233. doi: 10.23919/ELECO54474.2021.9677723

RESEARCH ARTICLE

EFFECTS of LOW REACTION RATE on ZNO THIN FILMS PRODUCED by a CHEMICAL BATH DEPOSITION METHOD

Metehan ÖNAL[1*], Barış ALTIOKKA[2]

[1]Bilecik Şeyh Edebali University, Vocational School, Bilecik, metehan.onal@bilecik.edu.tr,
ORCID:0000-0001-7128-7123
[2]Bilecik Şeyh Edebali University, Vocational School, Bilecik, baris.altiokka@bilecik.edu.tr,
ORCID0000-0001-8891-973X

ABSTRACT

In the presented study, while ZnO thin films were deposited onto glass substrates, chemical bath deposition method was used and $Na_2S_2O_3$ was used as an inhibitor to reduce the reaction rate. Four different samples were produced using 0, 4, 8 and 16mM $Na_2S_2O_3$, respectively. The images obtained from the scanning electron microscope showed that the amount of nano flowers on the film surfaces decreased due to the increase in the amount of inhibitor. The X-ray diffraction results were consistent with the ASTM card and showed that all the films were crystallized in a hexagonal structure. UV measurements showed that the absorbance value of the sample obtained without the use of inhibitor was up to four times higher than the other samples. It was observed that the energy band gaps of the films increased up to 4.24 eV depending on the amount of inhibitor. Visual analysis showed that all films adhered very well to the glass surface.

Keywords: *ZnO, Thin film*, *Chemical bath deposition*, *Inhibitor*

1. INTRODUCTION

Thin films, which have an important place for scientific and industrial studies due to their wide application areas, attract the attention of researchers, while zinc oxide (ZnO) thin films get their share of this interest. Zinc oxide is a non-toxic, low-cost and easily accessible [1]. Showing n-type semiconductor properties due to the presence of oxygen vacancies, ZnO has an energy band gap of 3.37 eV and an exciton binding energy of 60 meV at room temperature [2–4]. Application areas of ZnO thin films include many applications such as optoelectronic devices, photo-catalysts, and ultraviolet laser diodes, cathode ray tubes, gas sensors and piezoelectric transducers [5–8]. ZnO thin films are used as conductive and optical cover layers of large-area solar cells [9].

ZnO crystallizes in a hexagonal wurtzite structure [10, 11]. Many techniques are used to produce zinc oxide thin films. These techniques include magnetron sputtering, electro deposition, pulsed laser deposition (PLD), thermal oxidation, spray pyrolysis, chemical vapor deposition (CVD), sol-gel techniques, and chemical bath deposition (CBD) [12–18]. In the present study, the chemical bath deposition technique was chosen to deposit ZnO thin films due to its advantages such as simplicity of the required equipment, ability to be deposited at relatively low temperatures, and low cost.

While producing compound semiconductors with CBD, many properties that can be changed and controlled such as solution temperature, mixing speed, pH value, complex agent type and amount, deposition time have been investigated by researchers [8, 9, 19, 20]. However, no study was found in which Sodium thiosulfate ($Na_2S_2O_3$) was used as an inhibitor in the precipitation of ZnO thin films. In addition, in a study, it was reported that the reaction rate was reduced by using Sodium sulfite (Na_2SO_3) while producing ZnO thin films. In that study, the use of inhibitor significantly affected the crystallite dimensions and increased the energy band gaps 1.03V more than the previous value [21].

In this study, the reaction rate was reduced by using $Na_2S_2O_3$ in three different molarities as inhibitor. $Na_2S_2O_3$ was used for the first time in the literature for ZnO precipitation by chemical bath deposition method. It has been observed that the absorbance values of the films produced by using inhibitor during ZnO production were quite low, and in parallel with this, their transmittance values were quite high. The energy band gap values of the films were 3.89 eV when no inhibitor was used. When the inhibitor was used, it ranged from 4.13 eV to 4.24 eV. Analyzes using SEM images magnified 1000 times and 20000 times showed that as the amount of $Na_2S_2O_3$ increased, the nano-flowers on the film surfaces decreased.

2. EXPERIMENTAL DETAILS

ZnO thin films were deposited on glass substrates using the chemical bath deposition method. Before starting the deposition process, glass substrates were washed with acetone and rinsed with deionized water. While the first sample labeled S0 was produced, 60 mM $ZnCl_2$ and 8 mM EDTA were dissolved in 100 ml of deionized water without using an inhibitor, and ammonia (NH_3) was added with a dropper until the pH value of the solution was 9.5. While producing the samples labeled S1, S2 and S3, 4, 8 and 16 mM $Na_2S_2O_3$ were added to the final solution, respectively. While all samples were being fabricated, the solution temperature was kept at 85 ± 2 °C and mixed at 600 rpm. The deposition process was continued for 20, 25, 30 and 35 minutes, respectively, depending on the amount of inhibitor. When the deposition process was completed, the films were rinsed by using deionized water, labeled and left to dry at room conditions. Experimental conditions were tabulated and given in Table 1.

Table 1. Experimental conditions for ZnO deposited by chemical bath deposition method.

Experiments	$ZnCl_2$ (mM)	EDTA (mM)	Temp. (°C)	Ph	$Na_2S_2O_3$ (mM)	Deposition time (min)
S0	60	8	85±2	9.5	0	20
S1	60	8	85±2	9.5	4	25
S2	60	8	85±2	9.5	8	30
S3	60	8	85±2	9.5	16	35

The thickness of ZnO thin films was calculated using the Gravimetric method which has been given in Eq. 1 [22].

$$t = \frac{m}{\rho A} \tag{1}$$

In this equation, t is the film thickness, m is the mass of the film, ρ is the density, and A is the surface area. The bulk density value for ZnO is 5.675 g/cm^3 [23].

The thickness of the films named S0 and S1 was calculated as 480 nm on average. Moreover, the thickness of the sample named S2 was approximately 400 nm, and the thickness of S3 was approximately 380 nm. These results showed that the thickness of the produced samples decreased as the amount of $Na_2S_2O_3$ used increased.

A PANalytic Empyrean XRD was used to perform structural analyzes of ZnO films, a AandE lab with single-beam UV-vis spectrometer and a Zeiss SUPRA 40VP SEM to determine their optical and morphological properties, respectively.

3. RESULT AND DISCUSSION

3.1. Structural analysis of ZnO Films

In Figure 1, XRD diffraction patterns are given for ZnO thin films obtained depending on the amount of $Na_2S_2O_3$ added to the solution. When Figure 1 was examined, it was seen that all the films were formed in a hexagonal structure and all of the matched the ASTM card no 98-005-7478. Preferred orientations of the films were determined by using the TC (Texture coefficient) given in Eq. 2. [24].

$$TC = \frac{I_{(hkl)}/I_{0(hkl)}}{\frac{1}{N}\sum_N(\frac{I_{(hkl)}}{I_{0(hkl)}})} \tag{2}$$

Table1. Calculated Texture Coefficients of ZnO films.

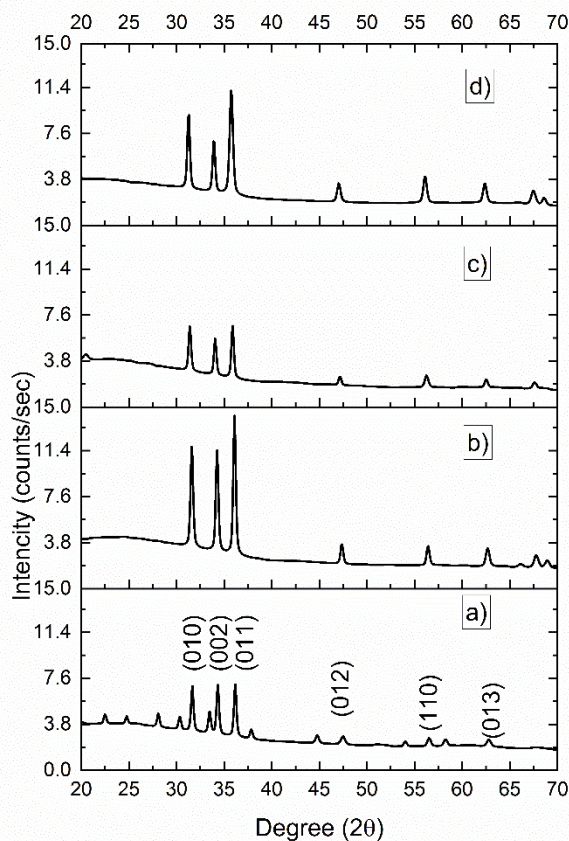| Experiments	S0	S1	S2	S3
T.C.(010)	0.92	0.95	0.85	0.85
T.C.(002)	0.68	0.79	0.85	1.00
T.C.(011)	1.39	1.25	1.30	1.25

Figure1. Diffraction patterns of XRD for ZnO obtained using different molarities of inhibitor. a) 0 mM, b) 4 mM, c) 8 mMand d) 16 mM of $Na_2S_2O_3$.

In this equation, I (hkl) is the measured relative intensity of a (hkl) plane and I_0 (hkl) is the standard intensity of the (hkl) plane given in ASTM card. Preferred orientation values calculated using Equation 2 are given in Table 2. When Figure 1 and Table 2 are examined together, it can be said that the films obtained in S0, S1 and S2 have (011) preferential orientation. On the other hand, the film obtained S3 exhibits two preferred orientations such as (011) and (002),

The Debye Scherrer formula used to calculate the crystallite size was given in Eq. 3 and the calculated values were presented in Table 3.

$$cs = \frac{0.089 * 180 * \lambda}{314 * \beta cos\theta_C} nm$$
$$\lambda = 1.54056 \text{ Å} \tag{3}$$

It is denoted by the crystal size cs, the wavelength of X-ray radiation λ, the full width half maximum β, and the maximum center $2\theta_C$ [25]. In Table 3, crystallite sizes are given. It can be understand from Table 3 that the average crystallite sizes range from 255 to. 292 nm

Table2. The crystallite size and energy band gaps of the ZnO films.

Experiments	cs (nm) (010)	cs (nm) (002)	cs (nm) (011)	cs(nm) Average	BandGap (eV)
S0	292	287	288	289	3.89
S1	270	275	280	275	4.22
S2	285	303	288	292	4.24
S3	272	275	220	255	4.13

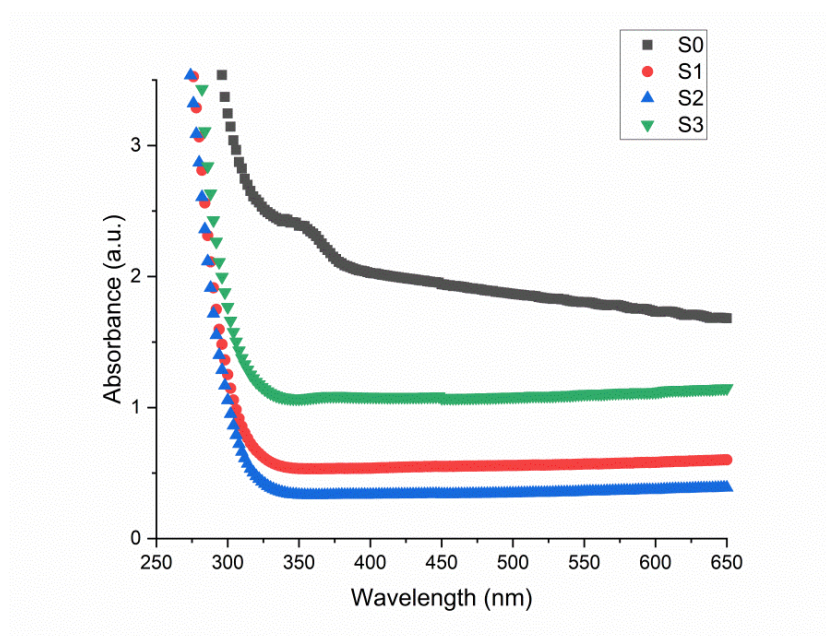## 3.2. Optical Properties of The ZnO films

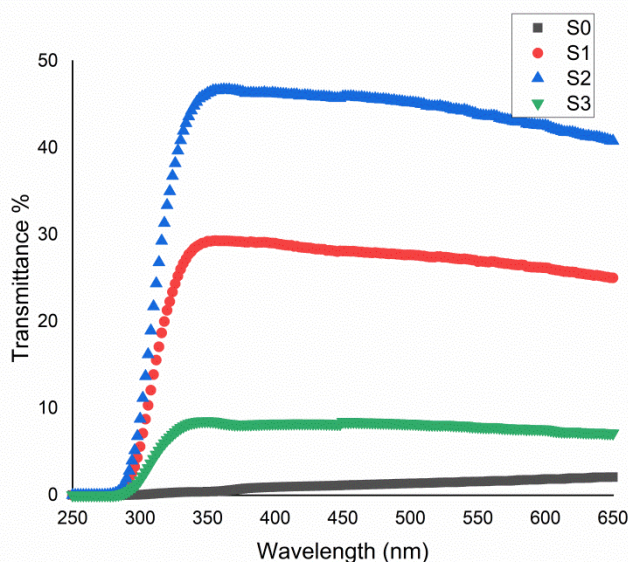**Figure 2.** Absorbance measurements of ZnO thin films.

Figure 3. Transmittance plots of ZnO thin films.

Optical absorbance values of ZnO thin films were measured with a UV-Vis spectrometer at wavelengths between 650 and 300 nm and they were shown in Figure 2. Figure 2 shows that the absorbance value of the sample produced without using the inhibitor is 2 to 4 times higher than the samples produced using $Na_2S_2O_3$. This means tha the transmittance values of the samples named S1 and S2 increase. Low absorbance and there for e high transmittance values are preferred for window layers of solar cells. Transmittance graphs were given in Figure 3.

The Tauc equation is used to calculate the optical energy band gap of thin films and is shown in Eq. 4.

$$(\alpha h\upsilon)^2 = A(h\upsilon - E_g)^n \tag{4}$$

In this equation, α is the absorption coefficient, $h\upsilon$ is the photon energy, A is the constant, and Eg is the energy band gap of the films. In direct band gap semiconductors, n is 1/2, in indirect band gap semiconductors it is 2 [26, 27]. ZnO is a direct band gap semiconductor[28]. Eg band gap value is obtained from the $(\alpha h\upsilon)^2 \sim h\upsilon$ graph. The point where the line drawn from the upper part of the curve formed in this graph to the $h\upsilon$ axis intersects the axis gives the band gap value[29]. The energy band gap of thin films is given in Figure 4. Figure 4 shows that the energy band gaps of the films vary between 3.89 eV and 4.24 eV .It is thought that these values may be due to film thicknesses, crystal sizes and surface roughness. It has been observed in the literature that the energy band gaps of ZnO thin films are 3.37 eV[3].
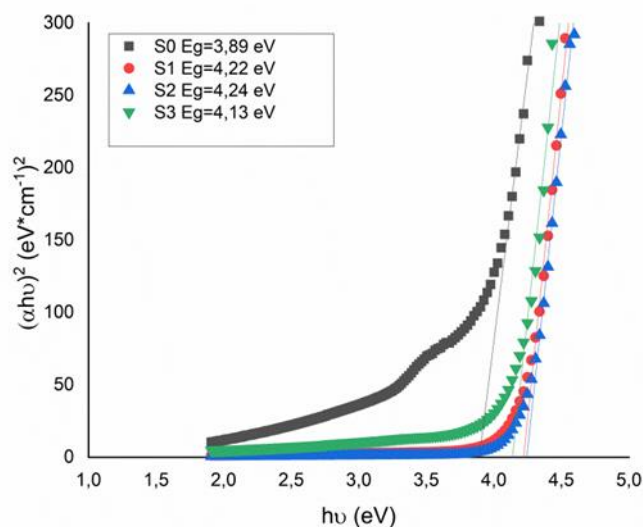
Figure 3. Energy band gaps and Tauc plots of ZnO thin films.

3.3. SEM Analysis of The ZnO films

Scanning electron microscope was used to examine the surface morphology of the produced ZnO thin film samples. Surface images of ZnO films magnified 1000 times and 20000 times were given in Figure 5 and Figure 6 respectively.

In both magnifications, it was observed that nano flowers did not form on the surface of the sample labeled S0, but the entire surface was completely covered. When the surfaces of the samples named S1, S2, and S3were examined, it is seen that nano flowers were seen on all surfaces, but nano flowers decrease due to the increase in the amount of inhibitor used. It is thought that this situation may be due to the decrease in the reaction rate and the prolongation of the precipitation time due to the use of inhibitor. It can be stated that the surface morphology of the films changes significantly depending on the amount of inhibitor used.

Table 3. Surface roughness values changing depending on the amount of $Na_2S_2O_3$.

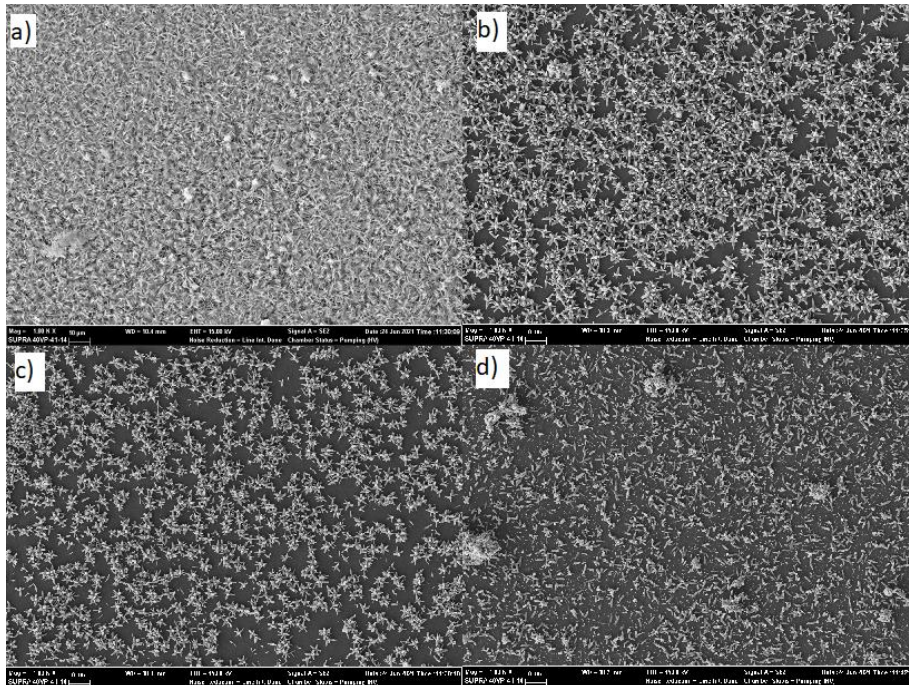| Experiments	$Na_2S_2O_3$ (mM)	Ra (nm)	Rq (nm)
S0	0	42	55
S1	4	56	67
S2	8	54	63
S3	16	51	60

Figure 4. SEM images of ZnO films at 1,000 times magnification.
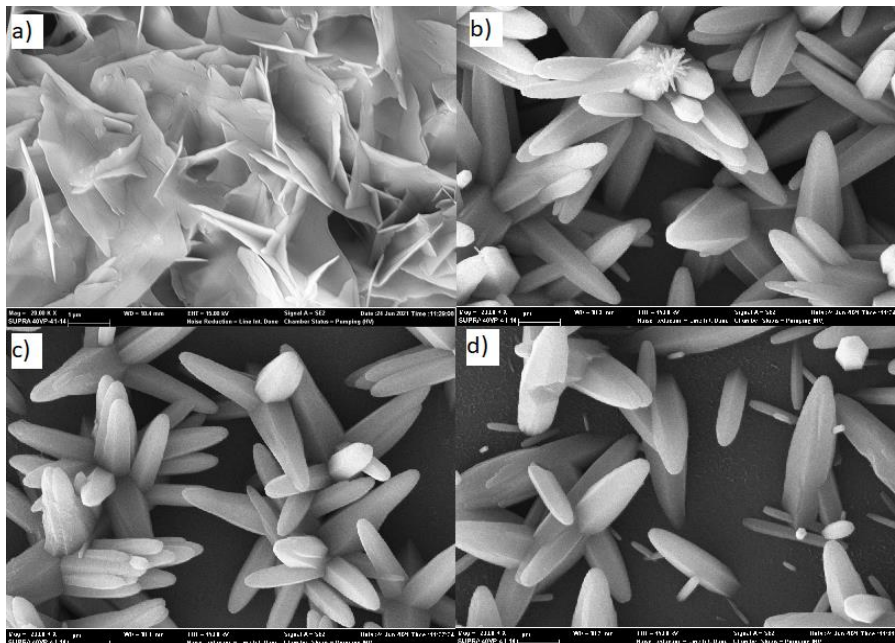

Figure 5. SEM images of ZnO films at 20,000 times magnification.

SEM images used to analyze the surface roughness of the samples were processed with version 1.53c of ImageJ software. The surface roughness images obtained using this software were given in Figure 7 and the calculated average (Ra) and root mean square (Rq) surface roughness values were given in Table 4. When the values given in Table 4 were examined, it was seen that the roughness values of the films produced using inhibitor were relatively high. Due to the high surface roughness values of the films produced using inhibitors, these films are thought to could be a suitable material for gas sensors.
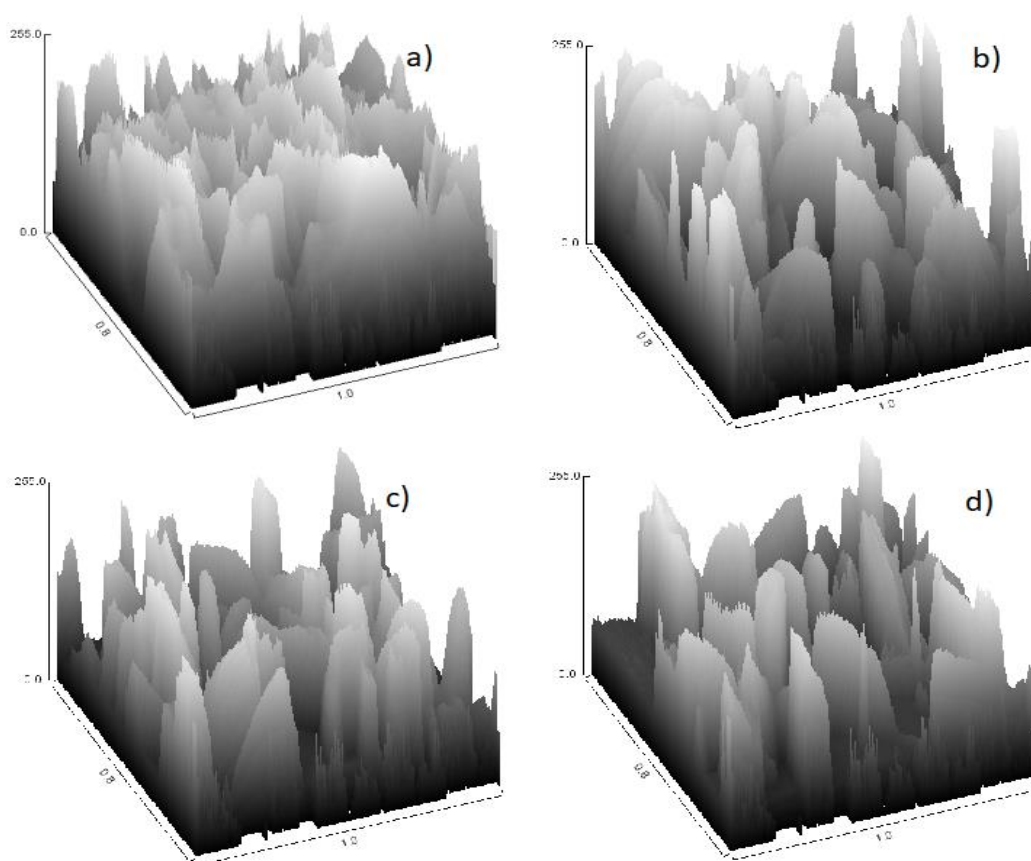

Figure 6. Surface roughness plots of ZnO films.

3.4. Photos of The ZnO Thin Films

Photographs of all ZnO films are shown in Figure 8. All films adhere quite well to the glass substrate surface and the film surfaces appear very compact. However, there was a tonal difference in the image of S0 compared to other films.
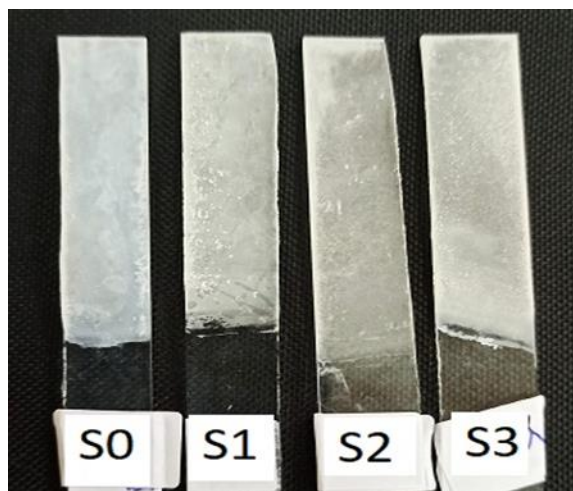
Figure 8. The photographs of the ZnO films.

4. CONCLUSIONS

Thin films of ZnO were precipitated by the chemical bath deposition method and the optical and morphological effects of the amount of $Na_2S_2O_3$ used as an inhibitor on thin films were investigated in this study. Samples were named depending on the amount of inhibitor used. Namely S0- ZnO film produced from the electrolyte without $Na_2S_2O_3$, S1- ZnO film fabricated from the electrolyte with 4 mM $Na_2S_2O_3$, S2- ZnO film deposited from the electrolyte with 8 mM $Na_2S_2O_3$ and S4- ZnO film grown from the electrolyte with 16 mM $Na_2S_2O_3$. Optical analyzes of the films were made, and it was observed that the point where the absorbance increased in the sample named S0 corresponds to a wavelength of 375 nm. It was determined that the absorbance of the other samples increased around 300 nm. At the same time, it was observed that the absorbance values of two samples named S1 and S2 decreased significantly compared to S0 and S3, and the transmittance values increased 20 times. Low absorbance and high transmittance values allow these samples to be utilized as a window layer in thin film solar cells.

The band gap of the samples was calculated using tauc plots. These calculations showed that the energy band gaps of the samples named S0-S1-S2-S3 were 3.89 eV, 4.22 eV, 4.24 eV and 4.13 eV, respectively. According to these results, the use of $Na_2S_2O_3$ as an inhibitor while producing ZnO thin films caused a significant increase in the energy band gaps of the produced thin films.

According to the XRD results, it is seen that all of the films obtained are in hexagonal crystal structure. However, the XRD graph obtained from the sample named S0 shows that there are impurities other than ZnO in the sample. When the XRD graphics of the other samples were examined, it was concluded that the use of $Na_2S_2O_3$ as an inhibitor removed the impurities in the crystal structure.

The surface morphology of the films was examined with a Scanning electron microscope (SEM), SEM images showed that the nano flowers on the film surfaces decreased as the amount of inhibitor

used increased. When the amount of $Na_2S_2O_3$ used was 4 mM and 8 mM, it was observed that the film surfaces were completely covered with nano flowers.

ACKNOWLEDGEMENT

REFERENCES

[1]   Temel, S., Gokmen, F. O., and Yaman, E., (2017), Effects of Deposition Time on Structural and Morphological Properties of Synthesized ZnO Nanoflowers Without Using Complexing Agent, European Scientific Journal, ESJ, 13(27), 28

[2]   Wang, J. X., Sun, X. W., Yang, Y., Kyaw, K. K. A., Huang, X. Y., Yin, J. Z., … Demir, H. V., (2011), Free-standing ZnO–CuO composite nanowire array films and their gas sensing properties, Nanotechnology, 22(32), 325704.

[3]   Shukla, V., and Patel, A., (2020), Effect of doping concentration on optical and electrical properties of intrinsic n-type ZnO (i-ZnO) and (Cu , Na and K) doped p-type ZnO thin films grown by chemical bath deposition method, Nanosystems Physics Chemistry Mathematics, 11(4), 391–400.

[4]   Saraç, U., and Baykul, M. C., (2021), The influence of seed layer electroplating time on structural properties, optical energy bandgap, diameter, growth orientation and surface roughness of ZnO nanorods, Journal of Materials Science: Materials in Electronics, 32(22), 26578–26587.

[5]   Wang, H., Liu, Y., Li, M., Huang, H., Xu, H., and Shen, H., (2011), Fabrication of three-dimensional ZnO with hierarchical structure via an electrodeposition process, Applied Physics A, 25, 463–466.

[6]   Edinger, S., (2017), Comparison of chemical bath-deposited ZnO films doped with Al , Ga and In, Journal of Materials Science, 52(16), 9410–9423.

[7]   Of, O., (2013), Structural Properties of ZnO Thin Films Obtained by Chemical Bath Deposition Technique, Journal of Nano- and Electronic Physics, 5(1), 4–7.

[8]   Önal, M., and Altıokka, B., (2020), Effect of stirring on chemically deposited ZnO thin films, Acta Physica Polonica A, 137(6), 1209–1213.

[9]   Kumar, S., Kang, H. C. J. T. W., Seth, R., Panwar, S., and Shinde, S. K., (2019), Variation in chemical bath pH and the corresponding precursor concentration for optimizing the optical , structural and morphological properties of ZnO thin films, Journal of Materials Science: Materials in Electronics, (0123456789),

[10] Fortunato, M., Chandraiahgari, C. R., Bellis, G. De, Ballirano, P., Soltani, P., Kaciulis, S., … Sarto, M. S., (2018), Piezoelectric Thin Films of Grown by Chemical Bath Deposition, IEEE Transactions on Nanotechnology, 17(2), 311–319.

[11] Janotti, A., and Walle, C. G. Van De, (2009), Fundamentals of zinc oxide as a semiconductor, Reports on progress in physics, (December),

[12] I, T. S., and Brien, P. O., (1995), Deposition and characterisation of ZnO thin films grown by chemical bath deposition, Thin solid films, 271, 35–38.

[13] Ramamoorthy, K., Arivanandhan, M., Sankaranarayanan, K., and Sanjeeviraja, C., (2004), Highly textured ZnO thin films : a novel economical preparation and approachment for optical devices , UV lasers and green LEDs, , 85, 257–262.

[14] Avila-garcı, A., and Ortega-lo, M., (2003), Improved efficiency of the chemical bath deposition method during growth of ZnO thin films, Materials Research Bulletin, 38, 1241–1248.

[15] Masuda, S., Kitamura, K., Okumura, Y., Miyatake, S., Tabata, H., and Kawai, T., (2003), Transparent thin film transistors using ZnO as an active channel layer and their electrical properties, Journal of Applied Physics, 93(3), 1624–1630.

[16] Drici, A., Djeteli, G., Tchangbedji, G., Derouiche, H., Jondo, K., Napo, K., … Gbagba, M., (2004), Structured ZnO thin films grown by chemical bath deposition for photovoltaic applications, Physica status solidi (a), 1536(7), 1528–1536.

[17] Ouerfelli, J., Regragui, M., Morsli, M., Djeteli, G., and Jondo, K., (1954), Properties of ZnO thin films deposited by chemical bath deposition and post, Journal of Physics D: Applied Physics, 1954.

[18] Bundesanstalt, P. T., (2008), Electrodeposition of ZnO nanorods for device, Applied Physics A, 599(3), 595–599.

[19] Yuan, Z., (2015), Low-Temperature Growth of Well-Aligned ZnO Nanorod Arrays by Chemical Bath Deposition for Schottky Diode Application, Journal of Electronic Materials, 44(4), 1187–1191.

[20] Önal, M., and Altıokka, B., (2020), Optimization of EDTA – Ammonia Ratio for Chemically Deposited Layers of ZnO Nanoparticles, Crystallography Reports, 65(7), 1237–1241.

[21] Yildizay, H., (2022), Effects of inhibitor on chemically deposited ZnO thin films, Emerging Materials Research, Volume 11(1),

[22] Mohammed, I. M. S., Gubari, G. M. M., Sonawane, M. E., Kasar, R. R., Patil, S. A., Mishra, M. K., … Sharma, R., (2021), Influence of pH on the physical properties of CdS thin film and its photosensor application, Applied Physics A: Materials Science and Processing, 127(8), 1–10.

[23] Jambure, S. B., Patil, S. J., Deshpande, A. R., and Lokhande, C. D., (2014), A comparative study of physico-chemical properties of CBD and SILAR grown ZnO thin films, Materials Research Bulletin, 49(1), 420–425.

[24] Shaikh, S. K., Inamdar, S. I., Ganbavle, V. V., and Rajpure, K. Y., (2016), Chemical bath deposited ZnO thin film based UV photoconductive detector, Journal of Alloys and Compounds, 664, 242–249.

[25] Bhowmik, R., Murty, M. N., and Srinadhu, E. S., (2008), Magnetic modulation in mechanical alloyed Cr1.4Fe0.6O3oxide, PMC Physics B, 1(1),

[26] Rahul, Verma, A. K., Tripathi, R. S. N., and Vishwakarma, S. R., (2012), Electrical and optical characterization of electron beam evaporated indium antimonide thin films, National Academy Science Letters, 35(5), 367–372.

[27] Bal, I., Baykul, M. C., and Saraç, U., (2021), The effect of solution temperature on chemically manufactured cds samples, Chalcogenide Letters, 18(1), 1–10.

[28] Berruet, M., and Va, M., (2010), Materials Science in Semiconductor Processing Electrodeposition of single and duplex layers of ZnO with different morphologies and electrical properties, Materials science in semiconductor processing, 13, 239–244.

[29] Khan, Z. R., Khan, M. S., Zulfequar, M., and Shahid Khan, M., (2011), Optical and Structural Properties of ZnO Thin Films Fabricated by Sol-Gel Method, Materials Sciences and Applications, 02(05), 340–345.

RESEARCH ARTICLE

DESIGN OPTIMIZATION of a BRACKET PLATE for an AMMUNITION FEED MECHANISM of a MEDIUM CALIBER CANNON

Cihan TURAN [1,2*], Hacı Abdullah TAŞDEMİR[3]

[1]Istanbul Technical University, Mechanical Engineering, Istanbul,
[2]Aselsan Inc., Ankara, turanc21@itu.edu.tr , ORCID: 0000-0003-2849-8368
[3]Istanbul Technical University, Mechanical Engineering, Istanbul, tasdemirh@itu.edu.tr,
ORCID: 0000-0002-2836-5488

ABSTRACT

Topology optimization has been one of the major concerns for mechanical engineers over the years. With increasing utilization of the finite element method, mechanical analyses can be done easily these days and their results are quite reliable. In weapon systems, high loads act on system components. Due to high loads, every component must be designed to operate without any failure. While designing them, attention must be given in order to avoid excessive weights. So, topology optimization is needed in weapon system components. In this study, design with topology optimization of a bracket plate of an ammunition feed mechanism were investigated using the finite element method. By utilizing topology optimization concept, the dimensions, material and the number of mounting holes of the bracket plate of an ammunition feed mechanism were changed to see their effects on the elemental Von-Mises stress and nodal displacement values. The results show that the increase in mounting hole number and the thickness of the material with selecting a material having higher strength properties decreases the elemental Von-Mises stress and nodal displacement values. According to the results, a safer bracket plate for an ammunition feed mechanism was designed to operate in the given working conditions without any failures.

Keywords: *Ammunition feed mechanism, Weapon turret, Topology optimization, Finite element method, Design*

1. INTRODUCTION

In the life of human beings, some tools have always been used for hunting, defensing and building. For defensing purposes, some primitive items such as animal teeth and wooden sticks were used as weapons [1]. Different from the past, today, weapon systems are complex systems and contain various auxiliary components such as ammunition feed mechanisms, weapon turrets, pneumatic and hydraulic systems, etc. [2]. In terms of loads, working conditions of ammunition feed mechanisms are quite tough. Also, depending on the types of weapons, various ammunition feed mechanisms can be designed and used [3].

The finite element method is extensively used for structural analyses. In order to simulate physical phenomena, the finite element method gives quite good results [4]. These results are close to physical

testing results generally. Especially for complicated systems that analytical solutions are impossible, one can utilize numerical method called finite element method [4]. In some cases, analytical solutions are not even close to real results [5]. By specifying the inputs and goal of the problem clearly, more reliable and high-quality results can be obtained [6]. The finite element method can be utilized for almost every case such as linear, nonlinear, transient and steady cases [7]. Also, many problems such as fluid flow and thermal, can be solved by using the finite element method [8].

In addition, topology optimization is used commonly in mechanics. Topology optimization is a process that determines the shape, location and number of features such as holes and ribs to make parts more reliable [9]. Specifically, for components carrying high loads, topology optimization is quite beneficial. Results of classical topology optimization methods are not suitable for classical machining processes generally [10]. Therefore, in this study, classical topology optimization methods were not used because solid geometry was required and the plate was intended to be produced by conventional machining processes like CNC milling. In fact, if one has limited design experience, manual topology optimization can be troublesome. For that applications commercial software can be more beneficial [11].

In this study, due to high loads acting on it, a bracket plate which connects an ammunition feed mechanism to a weapon turret wall was designed and topologically optimized manually by utilizing the finite element method. The design and optimization processes were done by using Siemens NX and NX Nastran software, respectively.

2. SYSTEM CHARACTERISTICS AND THEORETICAL MODEL

The bracket plate, which is colored as yellow in the figure 1, is used for assembling the ammunition feed mechanism to the weapon turret wall. Figure 1 shows the bracket plate, ammunition feed mechanism and weapon turret wall. Also, the plate has the dimensions of 500 mm width and 220 mm height.
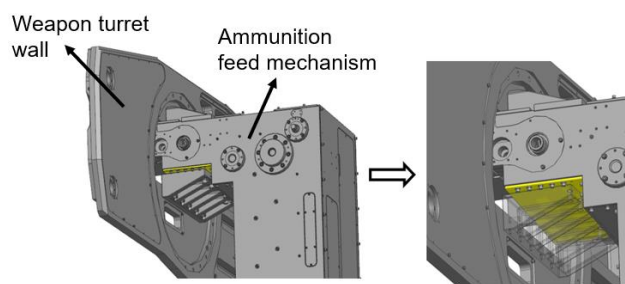
Figure 1. General view of the assembly.

In order to achieve optimization and make the bracket plate safer, various changes were made such as changing the thickness, material, hole numbers and hole locations on it. According to the changes, a new analysis was run and the part was topologically optimized. Two iterations were conducted in total and they were explained in this paper.

The bracket plate is mainly responsible from mounting of the ammunition feed mechanism to the weapon turret wall by using bolts. Due to the assembly, various forces act on the bracket plate. These

forces can be classified into 2 cases since they act on the bracket plate in separate situations. In the first case, only the operational forces of the weapon turret act on the bracket plate; however, in the second case, only the transportation loads act on the plate. Tables 1 and 2 show the loads of the two cases.

Table 1. Loading case-1.

Rotational torque of the elevation	77.5 Nm (along +y axis)	Acts on the COG of the mechanism
Centrifugal force of the elevation	40 N (on +z axis)	Acts on the COG of the mechanism
Rotational torque of the ring gear	246.8 Nm (along +z axis)	Acts on the COG of the mechanism
Centrifugal force of the ring gear	131.5 N (on -y axis)	Acts on the COG of the mechanism
Mass of the feed mechanism	400 kg (on +z axis)	Acts on the COG of the mechanism

Table 2. Loading case-2.

Transportation load	1.4 x mg (on the 3 axes simultaneously)	Acts on the COG of the mechanism

3. ANALYSES

3.1. First Iteration

For the initial iteration of the optimization, a rough geometry with 7050-T7451 Aluminum material was designed. An initial thickness of 10 mm with 6 side holes were given to the bracket plate. The diameter of the side holes is 6.6 mm and they are used for mounting the bracket plate to the ammunition feed mechanism. The side holes can be seen in red balloons in the figure 3. In addition, table 3 shows some mechanical properties of 7050-T7451 Aluminum. Then, finite element method was applied.

Table 3. Some mechanical properties of 7050-T7451 Aluminum.

Ultimate Tensile Strength	524 MPa
Tensile Yield Strength	469 MPa
Elongation at Break	11 %
Modulus of Elasticity	71.7 GPa

3D tetrahedral CTETRA (10) mesh with 5 mm element size was created. Then, the forces, mass and torques were applied to the center of gravity (center of gravity = COG) of the feed mechanism. The COG of the feed mechanism was connected to the bracket plate by a deformable connection element, namely RBE3. RBE3 element is generally used for transmission of distant loads. Also, the components between the bracket plate and the COG of the feed mechanism behave as deformable. Figure 2 shows the given mesh and COG of the feed mechanism, where the loads act. Also, 6 fixed

holes with 10.3 mm diameter can be seen as orange-colored in the figure 2. These holes fixate the plate to the weapon turret wall bracket; so, they were modelled as fixed.
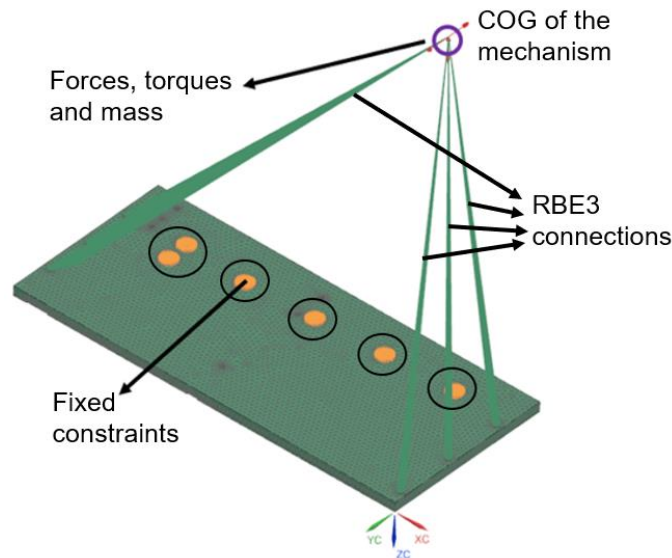
Figure 2. The mesh, loads, fixed constraints, RBE3 connections and COG of the mechanism for the first iteration.

Moreover, since this bracket plate is assembled to the feed mechanism with 6 bolts at the side holes, 1D rigid connection element, namely RBE2 was given to that 6 side holes as in the following figure 3. RBE2 connection element is a rigid element. Since the bolts are much stiffer than the bracket plate, the holes of the bolts were modelled as rigid. This yields more conservative results than the common hole modelling methods. In weapon systems, staying at the safer side is better.
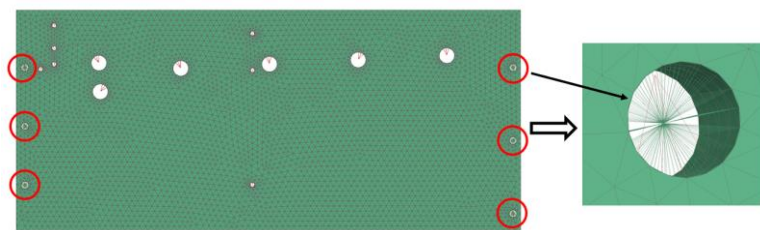
Figure 3. RBE2 connections for the bolts.

After that, loading cases were applied.

3.1.1. Loading case-1 of the first iteration
In the first run, loading case-1 was applied which was stated in the table 1. The rotational torque of the elevation, the centrifugal force of the elevation, the rotational torque of the ring gear, the centrifugal force of the ring gear and the mass of the feed mechanism were given to the COG of the feed

mechanism. For the boundary conditions, fixed constraints were given to the 6 mounting holes on which the plate is mounted to the turret wall. Figure 2 shows the fixed constraints as orange-colored holes. Table 1 and figure 2 show the magnitudes of the forces, torques, mass and the graphical representation of them, respectively. After completing that step, analysis was done and the results were given in the "Results" section. According to the results, there was no need to apply the loading case-2 for the first iteration as explained in the "Results" section.

3.2. Final Iteration

For the final iteration, the loading case-1 and 2 were applied separately, and 5 fixed mounting holes were used for the boundary conditions. Also, the number of side holes for mounting the bracket plate to the feed mechanism was 9 in this iteration, so the stress was wanted to be distributed around the side holes. Similarly, COG of the mechanism was connected to the side holes with RBE3 connections and the bolts at the side holes were modelled with RBE2 connections as in the first iteration. Figure 4 shows the modelled structure. Also, the material was Hardox 450 tool steel with 14 mm thickness in this iteration. Table 4 shows some mechanical properties of Hardox 450 steel.

Table 4. Some mechanical properties of Hardox 450 tool steel.

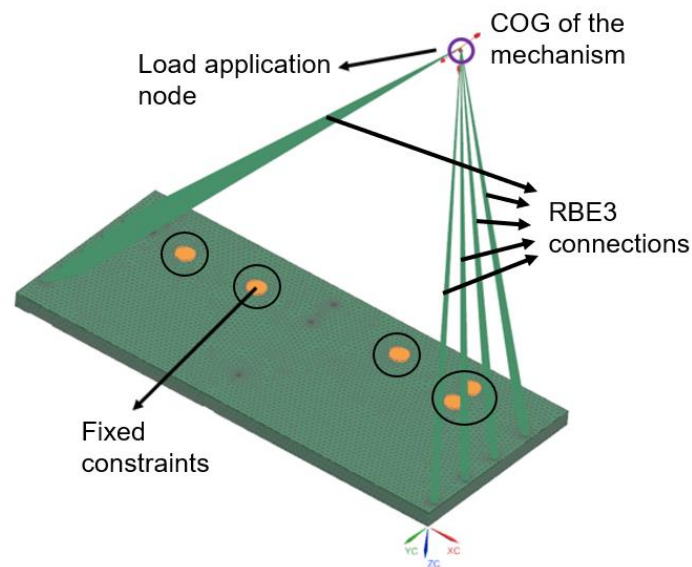|	
Ultimate Tensile Strength	1400 MPa
Tensile Yield Strength	1200 MPa
Elongation at Break	10 %
Modulus of Elasticity	200 GPa

Figure 4. The mesh, loads, fixed constraints, RBE3 connections and COG of the mechanism for the final iteration.

Similarly, 3D tetrahedral CTETRA (10) mesh with 5 mm element size was created and the loads of loading case-1 and 2 were applied to the COG of the mechanism.

3.2.1. Loading case-1 of the final iteration

After completing the preparation steps, the loads of loading case-1, which are the rotational torque of the elevation, the centrifugal force of the elevation, the rotational torque of the ring gear, the centrifugal force of the ring gear and the mass of the feed mechanism, were given to the COG of the mechanism similar to the first iteration. Then, the analysis was done and the results were given in the "Results" section.

3.2.2. Loading case-2 of the final iteration

Different from the loading case-1 of this iteration, this time, the loads of loading case-2, which are the transportation loads, were given to the COG of the mechanism. After that, the analysis was done and the results were given in the "Results" section.

4. RESULTS

4.1. First Iteration
4.1.1. Loading case-1 of the first iteration

As stated previously, only the loading case-1 was applied for the first iteration. Also, fixed boundary conditions were applied as shown in the figure 2. The elemental Von-Mises stress and nodal displacement values were adequate to examine in this paper. The following figures 5 and 6 show the elemental Von-Mises stress and displacement values, respectively.

Figure 5. Elemental Von-Mises stress values of the loading case-1 of the first iteration.

Figure 6. Nodal displacements of the loading case-1 of the first iteration.

As can be seen from the figures 5 and 6, the maximum elemental Von-Mises stress and nodal displacement values are 376.54 MPa and 1.396 mm, respectively. These values are quite high for the easier situation which is the loading case-1. Also, we can understand from the figure 5 that the stresses are concentrated near the side holes as expected.

Since the loading case-2 is much tougher than the loading case-1, there is no need to apply the loading case-2. The plate is nearly safe for the loading case-1 and it is apparent that it cannot withstand the loading case-2. So, optimization was needed and a new iteration was done.

4.2. Final Iteration
As stated previously, for the final iteration, the loading case-1 and 2 were applied separately and fixed boundary conditions were applied as in the figure 4.

4.2.1. Loading case-1 of the final iteration
Figures 7 and 8 show the elemental Von-Mises stress and displacement values for the loading case-1, respectively.
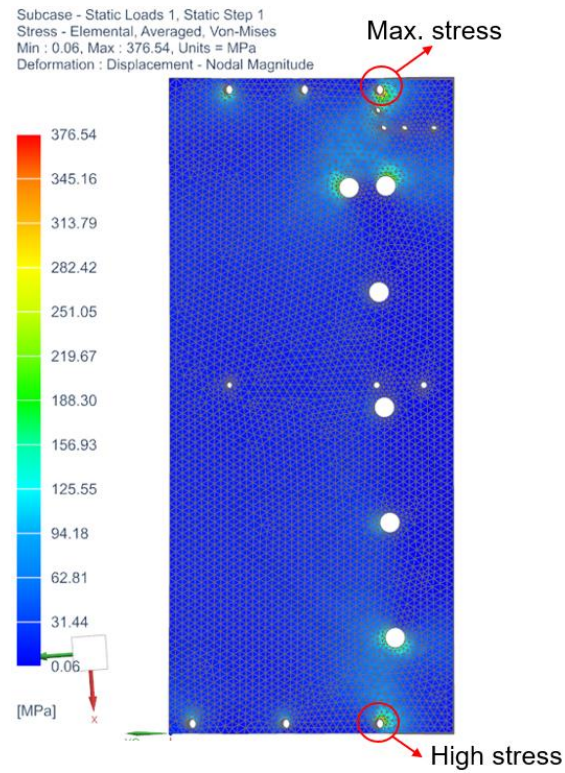

Figure 7. Elemental Von-Mises stress values of the loading case-1 of the final iteration.
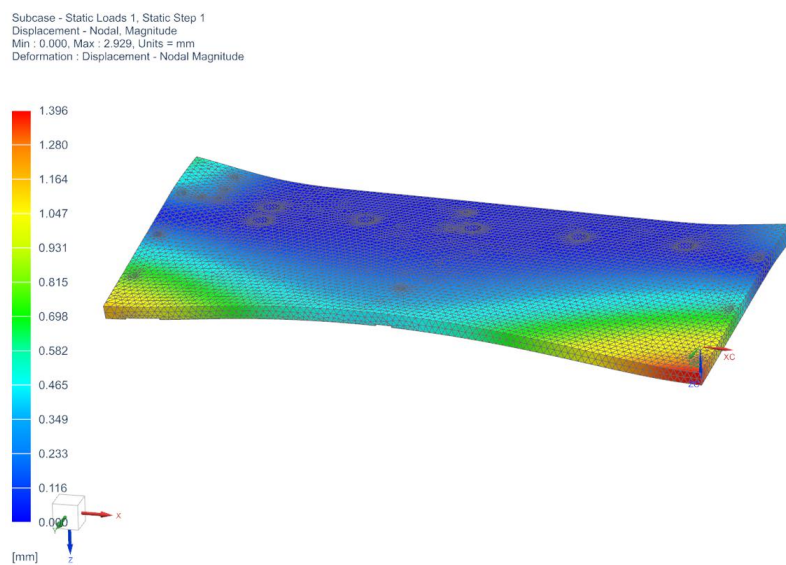
Figure 8. Nodal displacements of the loading case-1 of the final iteration.

As can be seen from the figures 7 and 8, the maximum elemental Von-Mises stress and nodal displacement values are 205.26 MPa and 0.191 mm, respectively. These values are quite acceptable since the tensile yield strength of Hardox 450 tool steel, which is 1200 MPa, is much higher than 205.26 MPa, and the maximum nodal displacement value is quite low.

4.2.2. Loading case-2 of the final iteration
According to the stress and displacement values above, the bracket plate is adequately safe in loading case-1. So, the loading case-2 can be applied now, and the elemental Von-Mises stress and displacement values can be seen for the loading case-2 in the figures 9 and 10, respectively.
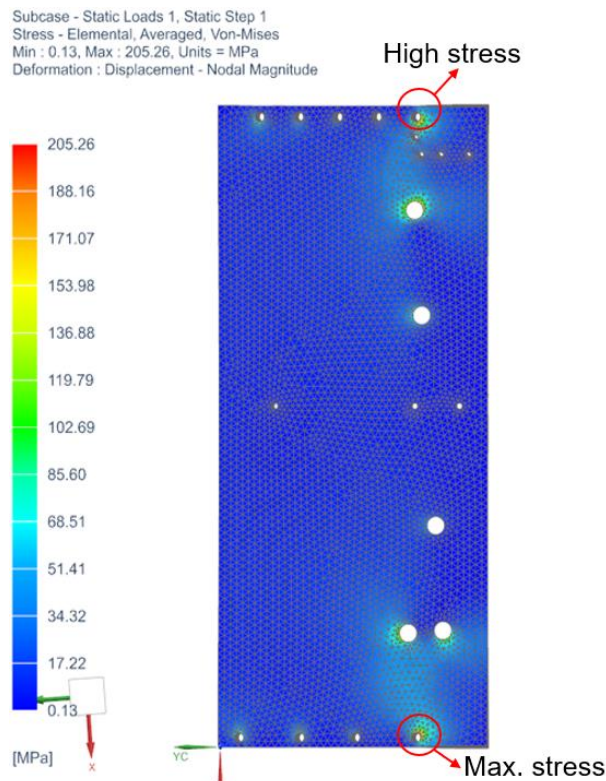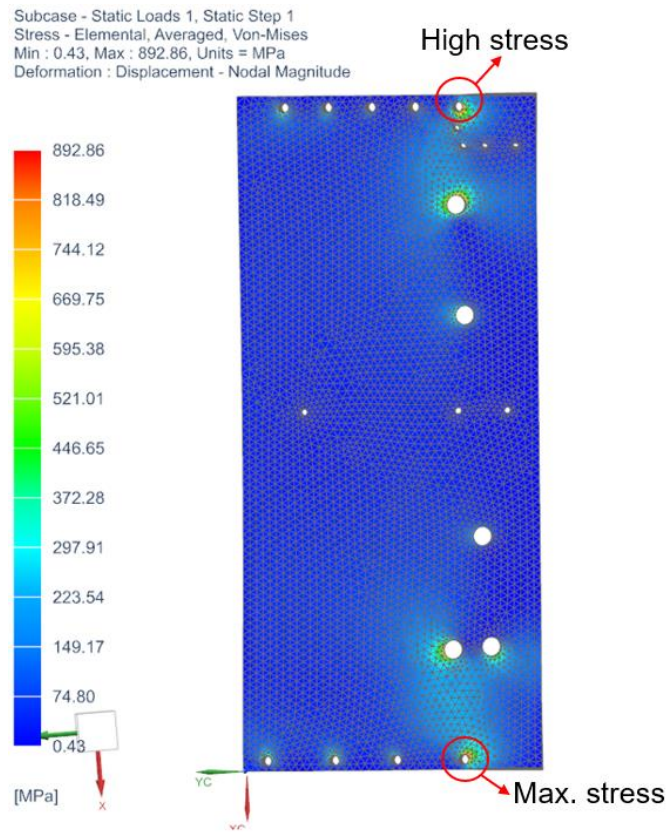
Figure 9. Elemental Von-Mises stress values of the loading case-2 of the final iteration.
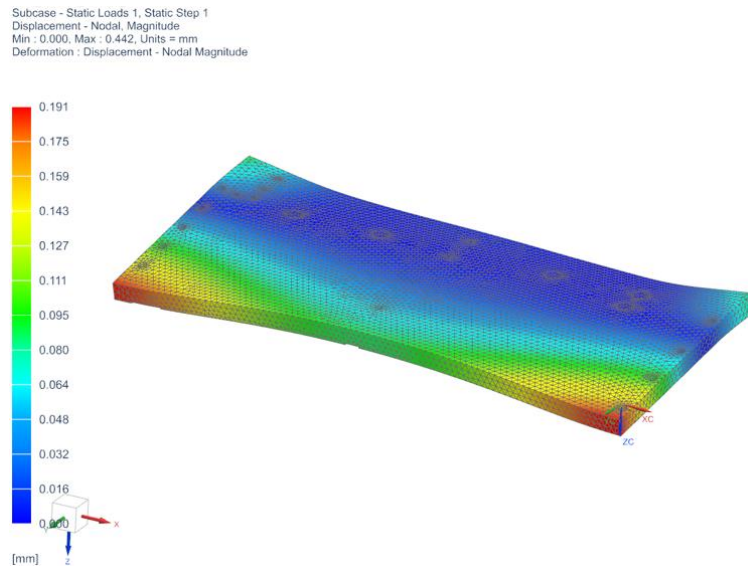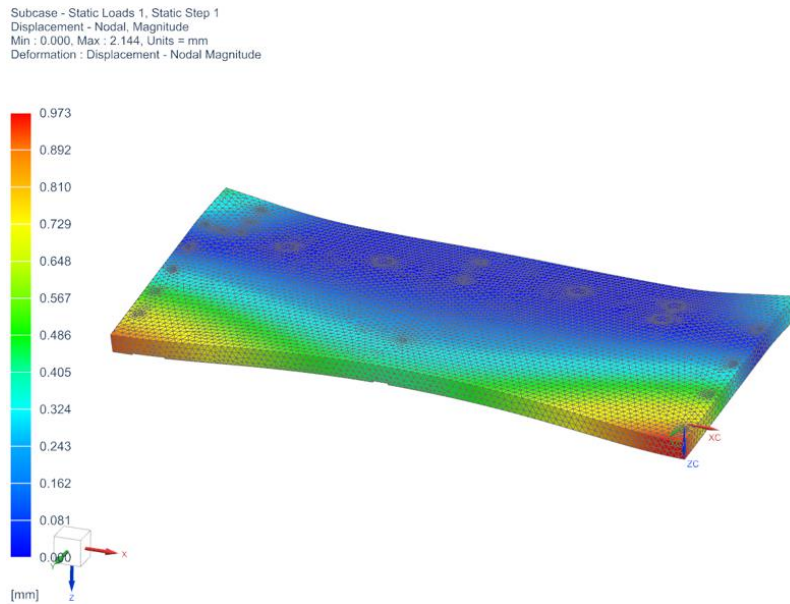
Figure 10. Nodal displacements of the loading case-2 of the final iteration.

As can be seen from the figures 9 and 10, the maximum elemental Von-Mises stress and nodal displacement values are 892.86 MPa and 0.973 mm, respectively. These values are quite acceptable again since the tensile yield strength of Hardox 450 tool steel, which is 1200 MPa, is much higher than 892.86 MPa, and the maximum nodal displacement value is quite low.

Table 5 summarizes the results clearly.

Table 5. Comparison of the results for the two iterations.

Iterations	Maximum Elemental Von-Mises Stress Value [MPa]	Maximum Displacement [mm]	Nodal Value
First Iteration – Loading Case 1	376.54	1.396	
Final Iteration – Loading Case 1	205.26	0.191	
Final Iteration – Loading Case 2	892.86	0.973	

As can be seen from the table 5, for the loading case-1, approximately 45% decrease in the maximum elemental Von-Mises stress value was achieved. In addition, the maximum nodal displacement value was decreased approximately 86%. These were achieved by changing the before-mentioned design parameters.

5. DISCUSSION

In order to see the effects of loads on components during design stage, the finite element method is quite beneficial for engineers. By utilizing the finite element method, critical stress concentration regions can be seen and they are minimized by changing the design of the part. For that purpose, in this study, topology optimization procedure was followed by utilizing the finite element method, and Von-Mises stress and nodal displacement values were reduced to make the bracket plate safer. Also, manual topology optimization process was followed in this study different from the topology optimization processes that use classical methods. Due to the manual process, all iterations and design changes were done manually. For future work, different finite element models for bolts can be applied and their results can be compared. Also, if non-conventional manufacturing methods, such as additive manufacturing, are applicable, optimization results of commercial finite element analysis software can be directly used by applying post processing.

6. CONCLUSION

In this study, by using the finite element method, design of a bracket plate was done. According to the finite element method results, a bracket plate having Hardox 450 tool steel material with 14 mm thickness, 9 mounting side holes and 5 fixed constraints is mechanically safer than a bracket plate having 7050-T7451 Aluminum material with 10 mm thickness, 6 mounting side holes and 6 fixed constraints. In the first iteration, it was seen that the elemental Von-Mises stress values accumulated near the side holes. Increasing the side hole number with increased plate thickness and decreased fixed hole number decreased the elemental Von-Mises stress values significantly. In addition, the results of Hardox 450 tool steel are quite enough to be safe for the given working conditions. The tensile yield strength and the ultimate tensile strength values of Hardox 450 tool steel is adequately higher than the maximum elemental Von-Mises stress value obtained in the figure 9. So, the topology optimization process was achieved.

ACKNOWLEDGMENT

REFERENCES

[1] Herbst, J., (2006), The History of Weapons (1st ed.), Minneapolis: Twenty-First Century Books, 5-7.

[2] Williams, G. A. and Gustin, E., (2004), Flying Guns of the Modern Era (1st ed.), Marlborough: The Crowood Press Ltd., 100-120.

[3] Williams, G. A., (2003), Rapid Fire: The Development of Automatic Cannon, Heavy Machine Guns and Their Ammunition for Armies, Navies and Air Forces (1st ed.), Marlborough: The Crowood Press Ltd., 50-60.

[4] Reddy, J. N., (2019), Introduction to the Finite Element Method (4th ed.), New York: McGraw Hill Education, 1-2.

[5]   Rao, S. S., (2018), The Finite Element Method in Engineering (6th ed.), Oxford: Butterworth-Heinemann, 3.

[6]   Babuska, I. and Strouboulis, T., (2001), The Finite Element Method and its Reliability (1st ed.), Oxford: Oxford University Press, 5.

[7]   Dhatt, G., Touzot, G. and Lefrançois, E., (2012), Finite Element Method (1st ed.), London: ISTE Ltd., Hoboken, NJ: John Wiley and Sons, Inc., 1.

[8]   Liu, G. R. and Quek, S. S., (2014), The Finite Element Method a Practical Course (2nd ed.), Oxford: Butterworth-Heinemann, 3.

[9]   Bendsoe, M. P. and Sigmund, O., (2003), Topology Optimization Theory, Methods, and Applications (2nd ed.), Berlin: Springer-Verlag, 1.

[10] Zhou, M., Fleury, R., Shyy, Y. K., Thomas, H. and Brennan, J. M., (2002), Progress in topology optimization with manufacturing constraints, 9th AIAA/ISSMO Symposium on Multidisciplinary Analysis and Optimization, AIAA 2002-5614.

[11] Jikai, L. and Yongsheng, M., (2016), A survey of manufacturing oriented topology optimization methods, Advances in Engineering Software, 100, 161-175.

RESEARCH ARTICLE

DEVELOPMENT of an ANFIS BASED CONTROL ALGORITHM for MAXIMUM POWER POINT TRACKING in ON-GRID DOUBLE STAGE SINGLE PHASE PV INVERTER

Yasemin ÖNAL[1,*], Ümit Çiğdem TURHAL[2]

[1,*]Bilecik Şeyh Edebali University, Engineering Faculty, Electric and Electronics Department, Bilecik,
yasemin.onal@bilecik.edu.tr, ORCID: 0000-0003-0173-0948
[2] Bilecik Şeyh Edebali University, Engineering Faculty, Electric and Electronics Department, Bilecik,
ucigdem.turhal@bilecik.edu.tr, ORCID: 0000-0003-2387-1637

ABSTRACT

In recent years, interest in solar energy has increased due to the increase in power consumption, the inadequacy of fossil resources and the damage it causes to the environment, as it is a natural energy source and is sustainable. Electricity is generated from solar energy using photovoltaic (PV) panel systems, and PV systems can be easily installed anywhere. In the PV panel systems, the power obtained at the panel output decreases and the efficiency decreases due to geographical conditions, environmental factors and system design. Maximum Power Point (MPP) tracking algorithm is used to obtain maximum output power from the PV panel system and to increase system efficiency. In this study, an Adaptive Network Based Fuzzy Inference System (ANFIS) based MPP tracking algorithm has been developed to obtain maximum power continuously from on-grid double stage 2 kW single phase PV inverter. The ANFIS algorithm uses an adaptive neural network to optimize the parameters of the membership function, and is a combination of artificial intelligence and fuzzy logic. In the algorithm, Direct Quadrant (dq) synchronous reference frame transform is used to generate PWM signals of active switches in on-grid single phase PV inverter. In this algorithm, dq control is performed by converting the grid current and its component obtained by 90° time delay from the stationary axis to the synchronous rotating axis. The algorithm developed based on dq and ANFIS provides the power demanded by the AC grid in a stable and continuous, while following the MPP, increasing the power obtained from the PV panel and inverter, providing maximum efficiency. The validity of the developed algorithm was tested using the Matlab/Simulink simulation program. The comparison simulation results with the PandO algorithm confirm the superiority of the developed ANFIS algorithm.

Keywords: *Adaptive Neuro-Fuzzy Inference System Controller ANFIS, Maximum Power Point Tracking, DC/DC Boost Converter, On-Grid Single Phase PV Inverter*

1. INTRODUCTION

With the depletion of fossil fuels from conventional energy sources, the development of renewable energy systems (RES) and energy management has attracted the attention of researchers due to its clean and renewable features [1]. RES contain different types of energy. Compared to fossil based energy systems, it is safer, reduces gas emissions that harm nature, increases efficiency, and reduces

production costs [2]. With the development of new energy technologies in recent years, research on grid-connected photovoltaic (PV) panel systems, PV power generation and modeling has increased rapidly in the field of RES. PV power generation is discontinuous and unstable. Therefore, higher requirements are put forward regarding the control of the on-grid PV inverter [3].

The control of a conventional two-stage on-grid single phase PV inverter consists of maximum power point tracking (MPPT) algoritm and DC/AC inverter algoritm. Some of the conventional MPPT methods proposed in the literature consist of the Perturb-and-observe (PandO) [4], the hill climbing [5], the incremental conductance (IC) [6,7] and the incremental resistance [8]. In conventional methods, a reference signal is produced by comparing the new output power value calculated with the previous panel output power value. These methods are suitable for the MPPT algorithm where there is only one MPP under uniform solar irradiation.

In recent years, MPPT methods based on meta-heuristic optimization algorithms have been proposed [9]. These optimization methods are genetic algorithm [10], cuckoo search [11], particle swarm optimization [12], and ant colony optimization [13]. Optimization based methods usually determine the operating point at which maximum power is obtained from the PV panel system based on some biological properties. In these methods, the accuracy of the algorithms is variable according to the starting point of the algorithm and the selected parameters.

It is necessary to have more detailed information about the PV panel system in advance and to measure the parameters of the panel such as irradiation, temperature, open circuit and short circuit online. Some intelligent algorithms such as artificial neural networks (ANN) and fuzzy logic controller (FLC) are used in online methods. Adaptive neuro-fuzzy inference system (ANFIS) is a hybrid between ANN and FLC. ANFIS combines the advantages of both of the techniques in making itself the most powerful artificial intelligence technique [14,15]. It utilizes the learning capabilities of ANN with the ability of FLC to treat inaccurate data and this suits well for PV applications [16]. ANFIS is used as an MPP tracking algorithm that is applied both off-line and on-line. A buck-boost converter controlled by an adaptive neuro fuzzy inference system (ANFIS) MPPT algorithm is developed in [17].

In this study, an ANFIS-based MPPT control algorithm has been developed to continuously obtain maximum power from a on-grid double stage single phase PV inverter. Sugeno inference with three inputs and one output is used in the ANFIS algorithm, and irradiation and temperature data are chosen as input training data. In the algorithm, 3 membership functions (MF) are defined for each input. Accordingly, 9 output functions are defined for the ANFIS algorithm output. dq synchronous reference frame conversion is used to generate PWM signals of active switches in a single-phase inverter. The current control in the proposed algorithm is performed by the transformation at the fundamental grid frequency of an orthogonal pair which is the grid current and its time delayed component to a synchronous rotating frame from a stationary frame. Using the control algorithm developed based on dq and ANFIS, the PWM signal of the active switch used in the DC/DC boost converter is adjusted and a voltage of 400 V is obtained at the output. The obtained PV voltage is applied to the 2 kW single phase inverter and 220V 50Hz AC is obtained from inverter output. The control algorithm developed based on dq and ANFIS, while following MPP, provides maximum efficiency by increasing the power obtained from the PV panel and inverter, and provides the power demanded by the load in a stable and continuously.

2. ON-GRID DOUBLE STAGE SINGLE PHASE PV INVERTER

The system model of a 2 kW on-grid double stage single phase PV inverter is shown in Figure 1. It basically consists of two parts. The first part is the DC/DC boost and the second part is the DC/AC inverter. The output voltage obtained from the PV panel system is increased by using the MPPT control algorithm in the DC/DC boost converter. In a DC/AC inverter, DC power is converted to AC power in the same phase and frequency with the grid voltage. MATLAB Simulink R2019a is used for the circuit simulation. The parameters of the system are given in Table 1.
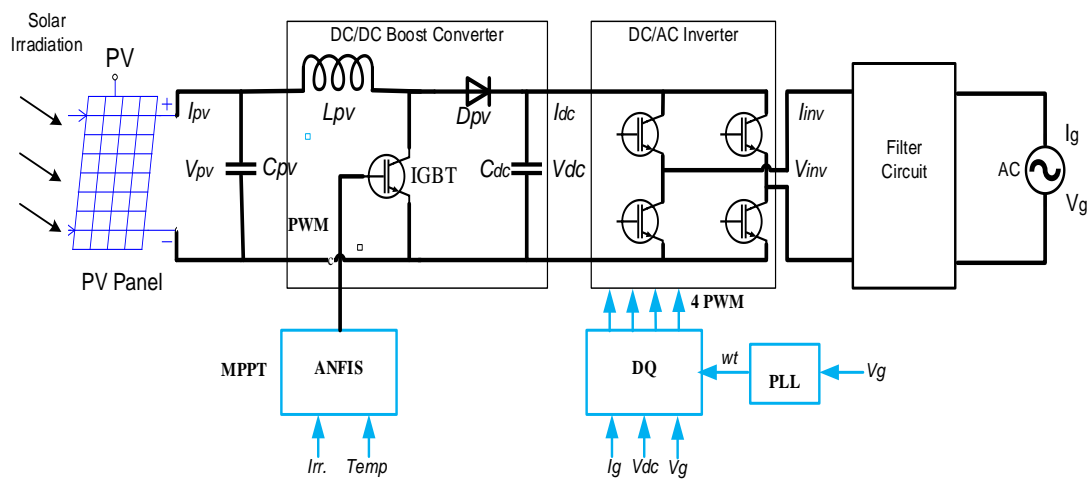
Figure 1. On-grid double stage single phase PV inverter with LCL filter.

Table 1. Parameters of the 2 kW on-grid double stage single phase PV inverter.

Parameters	Symbols	Values
Grid rms voltage	V_g	220 V
Grid operating frequency	f_g	50Hz
Boost DC/DC converter switching frequency	f_{pv}	10 kHz
Boost Inductance	L_{pv}	20 mH
Reference DC voltage	V_{ref}	400V
DC link capacitance	C_{dc}	500 μF
LCL filter	L_1	4.06 mH
	C_f	6.23 μF
	L_2	4.06 mH

Inverter switching frequency	f_{inv}	20 kHz

2.1. PV Panel and DC/DC Boost Converter

They are devices that can convert the irradiation falling on PV panels into direct voltage. PV panels are formed by connecting panels in series or parallel. By connecting the panels in series, the voltage value of the PV system is increased, and by connecting the PV panels in parallel, the current value of the PV system is increased. Thus, it is possible to increase the nominal power of the PV system to the desired level [18]. The PV panel equivalent circuit is as given in Figure 2.
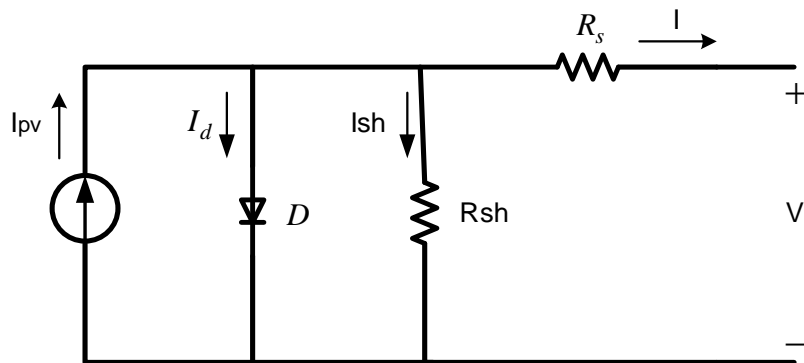
Figure 2. The PV panel equivalent circuit.

It is characterized with a current source and a diode connected in parallel to it. The series resistance R_s is used to define the contact resistance between the PV cell and its terminals, and it represents the resistance of the semiconductor that causes the voltage drop in the PV cell. The parallel resistance R_{sh} is used to show the leakage resistance in the PV panel. Current, voltage and temperature expressions describing the physical model of a PV panel are given in Eq. 1, Eq. 2, Eq. 3, Eq. 4 and Eq. 5 [19].

$$I = I_{ph} - I_d - V_d/R_{sh} \tag{1}$$

$$I_{ph} = I_{sc0}\frac{S}{S_0} + C_t(T - T_{ref}) \tag{2}$$

$$I_d = I_{s0}(\frac{T}{T_{ref}})^3 \exp\left(\frac{qE_g}{Ak}\left(\frac{1}{T_{ref}} - \frac{1}{T}\right)\right)\left[\exp\left(\frac{qV_d}{AkT}\right) - 1\right] \tag{3}$$

$$T = T_a + k_s S \tag{4}$$

$$V_d = V - IR_s \tag{5}$$

Here, q electron charge value is 1.6022e-19, k Boltzmann constant value is 1.3806e-23, S is light intensity, T_a is ambient temperature, I is the output current of the PV panel, V is the output voltage between the ends of the PV panel, I_d is the average current through the diode, V_d is on the diode voltage, I_0 is diode saturation current, and n is the ideal diode factor. The parameters of the PV panel are given in Table 2.

Table 2. PV panel parametparameters.

Model parameters	
Panel current I (A)	9.4447
Diode saturation current I_0 (A)	3.2328e-10
Ideal diode factor A	1.045
Parallel resistance R_{sh} (Ω)	47.9694
Series resistance R_s (Ω)	0.22828
Maximum power (W)	350
Number of cells (N_s)	80
Open circuit voltage V_{oc} (V)	51.5
Short-circuit current I_{sc} (A)	9.4
Voltage at maximum power V_{mpp} (V)	43
Current at maximum power I_{mpp} (A)	8.13
Temperature coefficient in V_{oc} (%/deg.C)	-0.36
Temperature coefficient in I_{sc} (%/deg.C)	0.09

In Figure 3, it is observed that the power obtained at the PV panel output changes with the solar irradiation. Maximum power can be obtained from the PV panel at a maximum voltage. This voltage is called the MPP voltage. For the simulated PV panel system, one panel is connected in parallel and six panels are connected in series, and the maximum power value is 2000 W, the voltage and current values at the MPP point are 258V and 8.13A, respectively.

In low power applications, the output voltage ratio of PV panels is limited. This affects the overall efficiency of the single stage inverter and is its main disadvantage. This problem is solved with the double stage inverter circuit. The PV panel voltage is increased to the desired level for the inverter by the DC/DC boost converter [20].

The DC/DC boost converter consists of a controllable active switch, inductor, capacitor and diode. The PV panel system can be operated in MPP by adjusting the duty cycle of the active switch. ANFIS was used in this study. The MPPT control structure for a boost converter is presented in Figure 4. ANFIS block generates reference voltage V_{ref} from PV panels at MPP. The V_{ref} signal obtained at the output of the ANFIS block is compared with the PV voltage signal and sent to the PI block. The proportional and integral values of the PI block are 9 and 0.009, respectively. PWM signals for IGBT active switches are obtained from the PI and PWM block.

The minimum input inductor and output capacitor values used in the DC/DC boost converter are calculated using Eq. 6, Eq. 7 and Eq. 8 [21].

$$I = I_L - I_d - V_{pv}/R_{shd} \tag{6}$$

$$L_{min} = \frac{D(1-D)^2 R}{2} \tag{7}$$

$$C \geq \frac{D}{R(\Delta V_0/V_0)f_s} \tag{8}$$
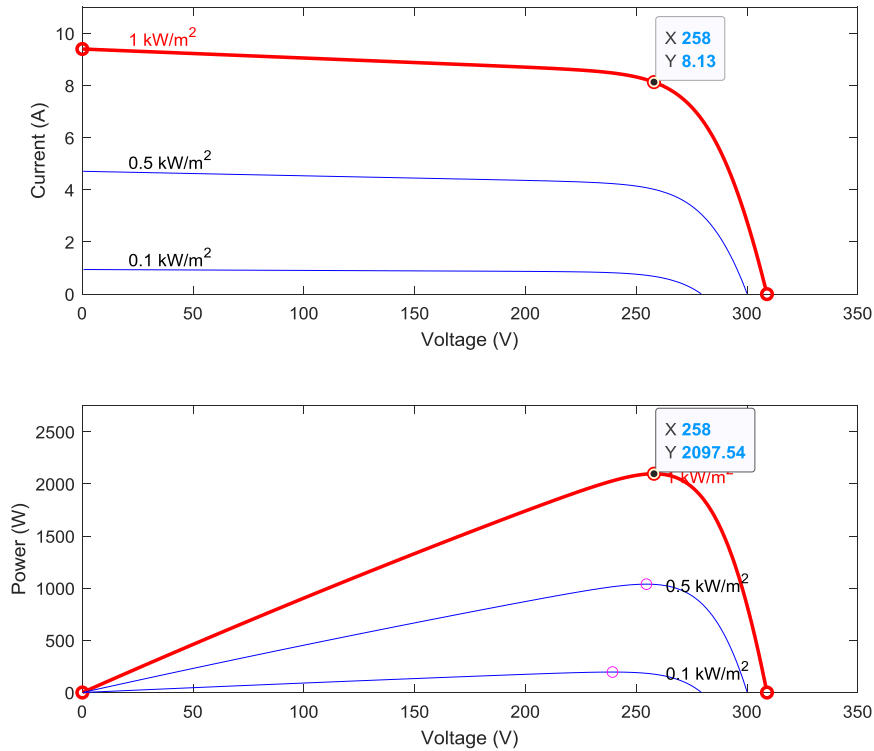
Figure 3. Current-voltage and power-voltage characteristics of the PV panel at 25°C for different solar irradiations.
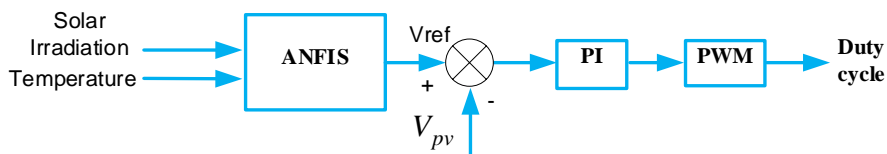
Figure 4. DC/DC boost converter control scheme based on ANFIS.

Here, V_0 is output voltage, V_{pv} is boost circuit input voltage, D is duty cycle, f_s is switching frequency, $\Delta V_0/V_0$ is voltage fluctuation ratio. Since the output resistance is not directly connected to the boost circuit output, it is expressed as $\frac{(V_0)^2}{P}$.

2.2. DC/AC Inverter

DC/AC inverter is used to transfer the DC produced in the PV system to the AC grid voltage. Bridge type DC/AC inverter consists of four controllable active power switches. Switches form two groups of branches and AC voltage is obtained by controlling the duty cycle of the switches.

Grid side control can be performed in a stationary frame $\alpha\beta$ or rotating dq reference frame [22]. Therefore, in this study, the grid part control is done in the dq reference frame. The αβ space to dq

space transformation can be achieved by rotating the $\alpha\beta$ frame at the fundamental frequency effectively. For sinusoidal signals at fundamental frequency, the d and q vectors obtained in the rotating frame are fixed. Similar to the three-phase systems two orthogonal components that are similar to the $\alpha\beta$ components are required for the process of conversion to a synchronous frame. In the generation of the missing orthogonal vector the signal's quarter-period delayed version is used.

V_g is the grid voltage, I_g is grid current. The single phase grid voltage is represented in the $\alpha\beta$ axis system with $\pi/2$ lead in Eq.9 [23,24].

$$V_\alpha = V_g(t) = V_m sin(t)$$
$$V_\beta = V_g(t + \frac{\pi}{2}) = V_m cos(t) \qquad (9)$$

The $\alpha\beta$ components of the grid current are defined 90 degrees lead of the current, as in the Eq. 10.

$$I_\alpha = I_g(t) = I_m sin(t)$$
$$I_\beta = I_g(t + \frac{\pi}{2}) = I_m cos(t) \qquad (10)$$

The linear transformation dq corresponding to the transformation of the $\alpha\beta$ components of the grid current and voltage is given in Eq. 11 [25].

$$I_{dq} = \begin{bmatrix} I_d \\ I_q \end{bmatrix} = \begin{bmatrix} sin(t) & -cos(t) \\ cos(t) & sin(t) \end{bmatrix} \begin{bmatrix} I_\alpha \\ I_\beta \end{bmatrix}$$

$$V_{dq} = \begin{bmatrix} V_d \\ V_q \end{bmatrix} = \begin{bmatrix} sin(t) & -cos(t) \\ cos(t) & sin(t) \end{bmatrix} \begin{bmatrix} V_\alpha \\ V_\beta \end{bmatrix} \qquad (11)$$

The block diagram of the single phase dq transformation is shown in Figure 5. First, the $\alpha\beta$ components are obtained by measuring the voltage V_g and the current I_g. Using the $\alpha\beta/dq$ transform, the dq components of the current and voltage are obtained. The V_q component is implemented as an input to the PLL circuit. In the PLL block, the phase of the new generated sinus signal is adjusted to be the same as the phase of the grid voltage. The V_q is compared with the q component of V_{ref} signal and sent to PI block. The proportional and integral values of the PI block are 10 and 50000, respectively. The signal obtained at the PI is sent to the integrator block. The ωt signal is obtained at the same frequency as the grid at the output of the PLL block.

The block diagram of the dq current control is shown in Figure 6. The V_{dc} obtained at the boost circuit output is compared with the V_{ref}. At the PI block output, the steady state voltage error is reset and the d component signal of the reference current is obtained. I_d and I_q currents are compared with reference values and steady state current errors are reset at the PI controller output. It provides the gain separation terms and the d and q components of the voltage are added. When $\alpha\beta$ is transformed to a stationary reference frame, the α signal and the sawtooth signal are compared to obtain the PWM signals of the single phase PV inverter.
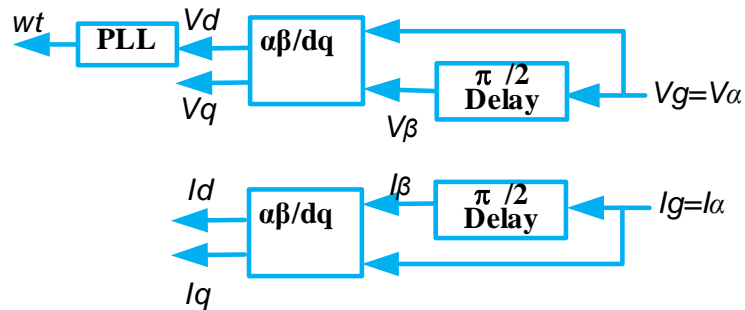
Figure 5. Single phase dq transform block diagram.
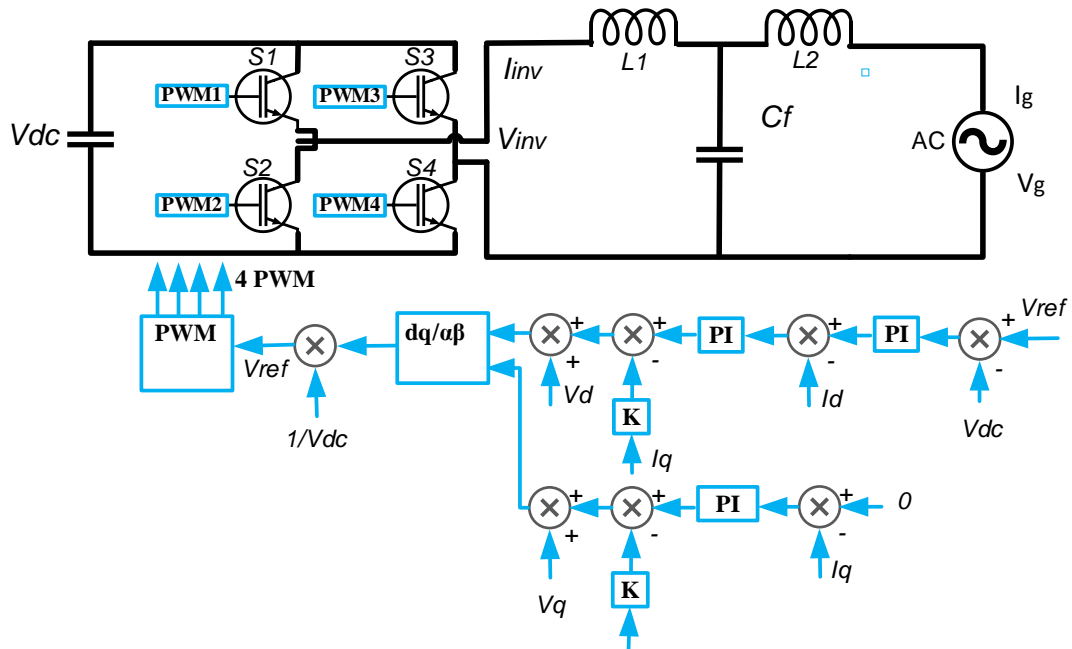
Figure 6. Single phase dq current control block diagram.

3. DEVELOPED ADAPTIVE NETWORK BASED FUZZY INFERENCE SYSTEM (ANFIS) BASED MPPT CONTROL ALGORITHM

ANFIS is a hybrid artificial intelligence method that uses the parallel computation and learning capability of artificial neural networks and the inference feature of fuzzy logic [26,27]. The ANFIS model uses the sugeno type fuzzy inference system and the Hybrid learning algorithm. Adaptive networks consist of directly connected nodes. Each node represents a processing unit. The connections between the nodes show a weight between them whose value is not clear. A few of the nodes are not adaptive. Non-adaptive nodes can be made adaptive using variable parameters[28].

MPPT is obtained using ANFIS. ANFIS is trained to obtain the output voltage that provides the maximum power output from the PV panel system. Solar irradiation and temperature are given as inputs to ANFIS. In the developed ANFIS based MPPT algorithm, voltage control is performed by comparing the V_{ref} obtained at the ANFIS output with the PV voltage. Error signal is obtained with feed forward PI controller and PWM signal of DC/DC boost converter is adjusted. At constant temperature the solar radiation variations results in a large change in the output of PV panel current in the MPP. The MPPT controller provides a non-variable voltage at the output when the temperature does not change. Otherwise, the temperature variance causes a large change in the PV panel output voltage in the MPP, which greatly changes the DC voltage.

The simulation circuit of the developed ANFIS based MPPT algorithm has been confirmed using Matlab/Simulink. The PV panel temperature ranges from 15 °C to 40 °C and the solar irradiation varies between 0 and 1000 W/m. Using these temperature and irradiance values, data is obtained at the output of the simulation circuit, and some of the irradiation and temperature data is used off-line to train the ANFIS. Figure 7 shows the ANFIS structure. In the five-layer network structure, two inputs with solar irradiation and panel temperature are used.
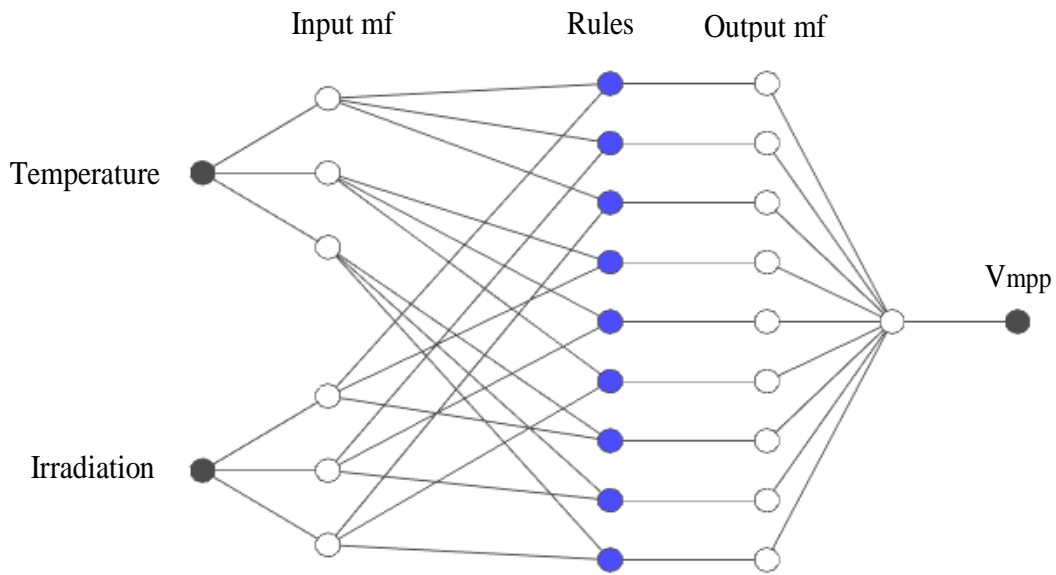
Figure 7. MPPT controller structure based on ANFIS.

The structure converts solar irradiation and temperature into three suitable MF as shown in Figure 8 and Figure 9.
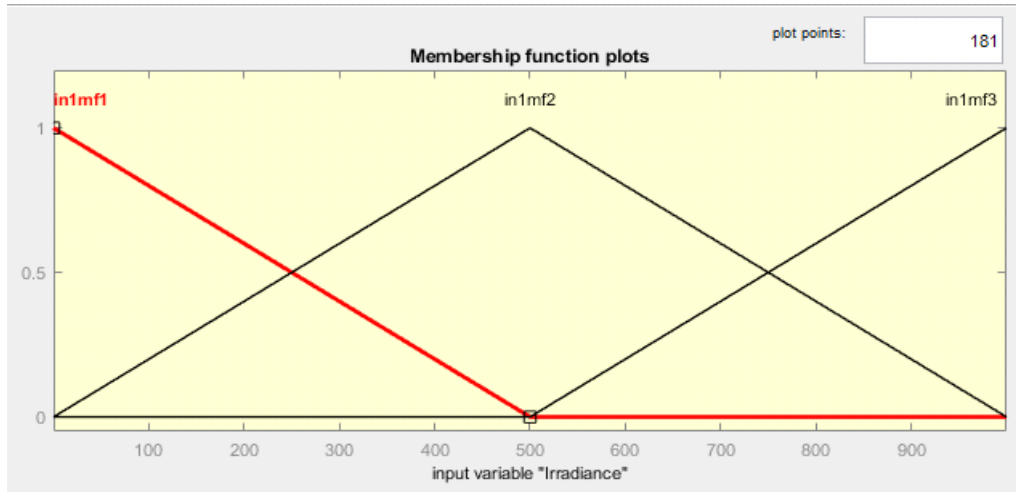
Figure 8. Solar irradiation MF.
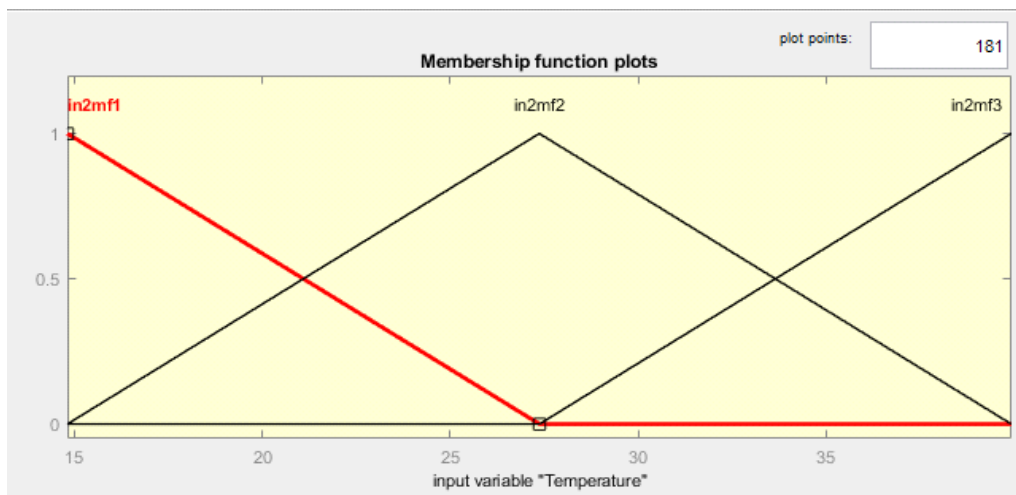
Figure 9. Temperature MF.

The form of these MF generated by the ANFIS controller varies during the training phase. The form of the MF obtained both during the training phase and at the end of the training phase are as given in Figures 8 and 9. The fuzzy rules for a temperature of 22.5 °C and solar irradiation of 500 W/m are shown graphically in Figure 10. The rules show the connection and matching between the variables. All conditions can be accessed by changing the slider on the shape. As shown in the last column, it is seen that the temperature varies between 5 °C and 40 °C, the solar irradiation varies between 0 and 1000W/m and the MPP voltage changes accordingly.
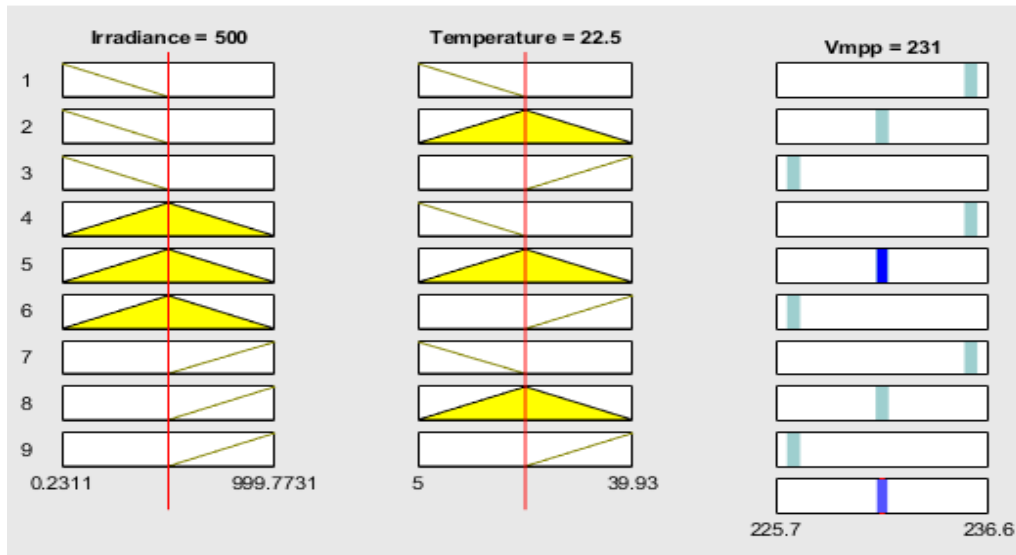
Figure 10. The rules of the ANFIS controller.

4. SIMULATION RESULTS

Considering the solar irradiation in a day, it changes at certain times of the day. Figure 11 shows the time-dependent variation of solar irradiance and temperature values. Initially, the solar irradiation starts with 1000W/m, then decreases to 600W/m between 0.5 s and 1.25 s. Increases to 800W/m between 1.25 s and 2 s and increases again to 1000 W/m irradiance between 2 s and 2.5 s. The temperature starts at 25 °C, then decreases to 5 °C between 0.5s and 1s. Increases to 40 °C between 1 s and 1.5 s and rises again to 25 °C between 1.5 s and 2.5 s. The simulation time interval was taken as 2.5 s.

To test the validity of the developed MPPT controller, system given in Figure 1 was simulated in MATLAB/Simulink. For the simulation of the system, the desired value of PV voltage is obtained by combining 6 serial and 1 parallel panels. For simulation, single phase grid voltage and frequency is simulated as 220V 50Hz. The parameters used for the system are given in Table 1 and section 2. The simulation is done for the different solar irradiation and the panel temperature values in Figure 11.

In the first simulation study, environmental conditions such as panel temperature and irradiation were changed and applied to the PV panel input, and the developed MPPT algorithm is compared with the conventional PandO algorithm. The voltage from the boost converter, PV panel power, reference power and algorithm efficiency signals were obtained from a result of the simulation.

(a)

(b)
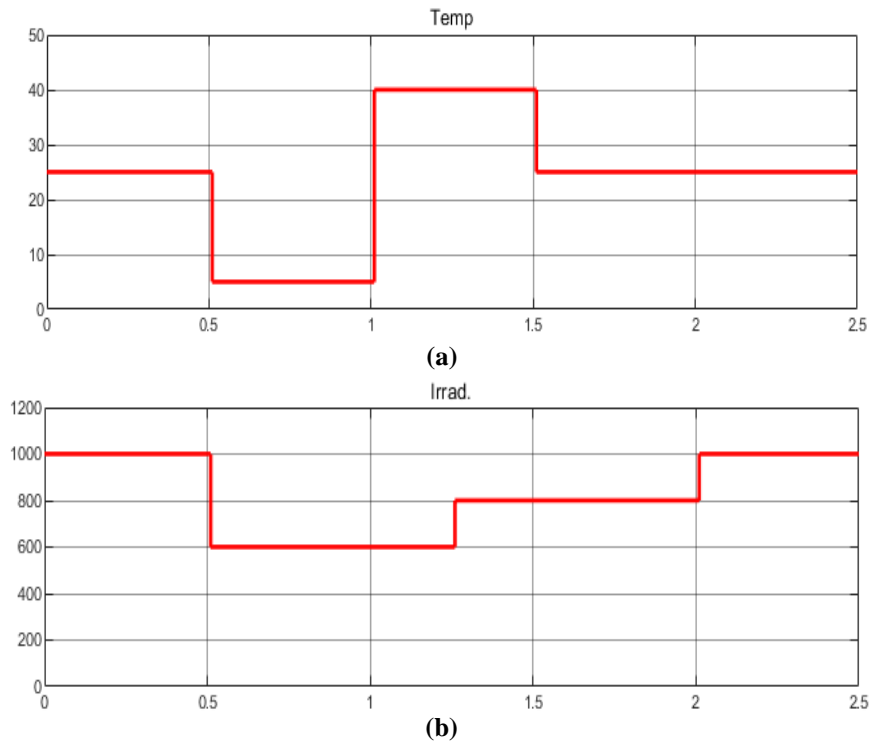
Figure 11. Variation curves of solar irradiation and panel temperature.

In Figure 12, boost converter output voltage, PV panel power, reference power and algorithm efficiency obtained using PandO based MPPT algorithm are shown.

(a)

(b)

(c)
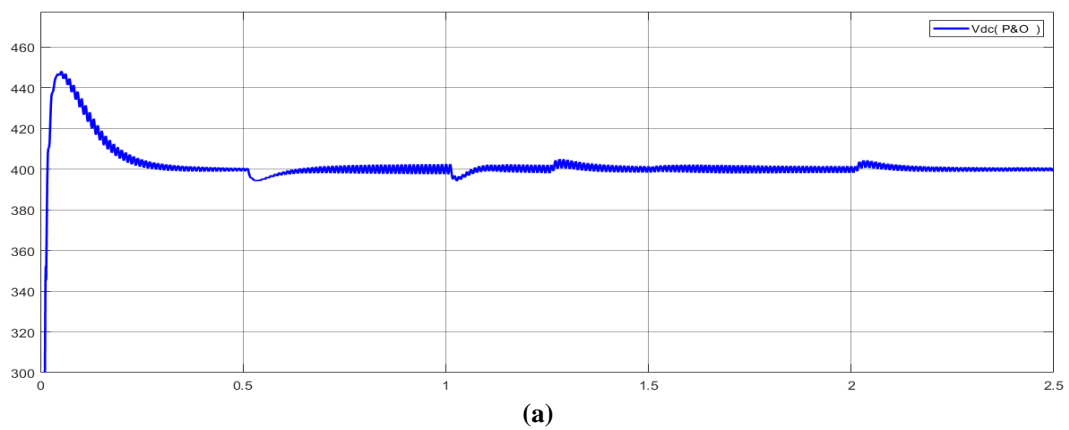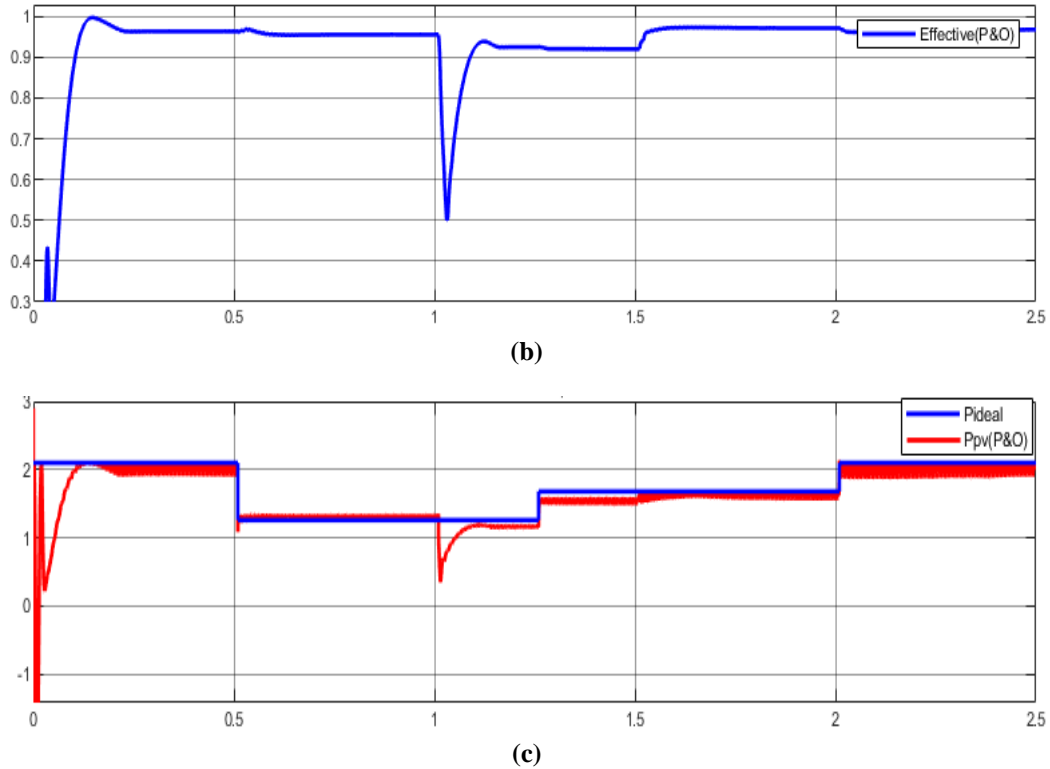
Figure 12. a) The output voltage of boost converter, b) the algorithm efficiency c) the PV panel power, reference power and obtained using PandO based MPPT algorithm.

In Figure 13, the boost converter output voltage, PV panel power, reference power and algorithm efficiency signals obtained using the ANFIS based MPPT algorithm are shown. The comparison results of the PandO algorithm and the ANFIS based MPPT algorithm are given in Table 2. The efficiency of the ANFIS based MPPT algorithm and the PandO algorithm efficiency are obtained as 0.8887 and 0.5079 at t=1.033s respectively. It can be seen from Figure 13 that the maximum power of the PV panel is particularly sensitive to solar irradiation and panel temperature, and the tendency of the power to change is consistent with the ideal power. In addition, the developed ANFIS based MPPT algorithm, when compared to the PandO algorithm, adapts to these changes faster and can follow the MPP power with less change. A reliable inverter control algorithm should be able to keep DC voltage and AC grid voltage constant when environmental conditions change.

Table 2. The comparison results of the PandO algorithm and the ANFIS based MPPT algorithm.

	Algorithm efficiency at t=1.033s
PandO algorithm	0.5079
ANFIS based MPPT algorithm	0.8887

162
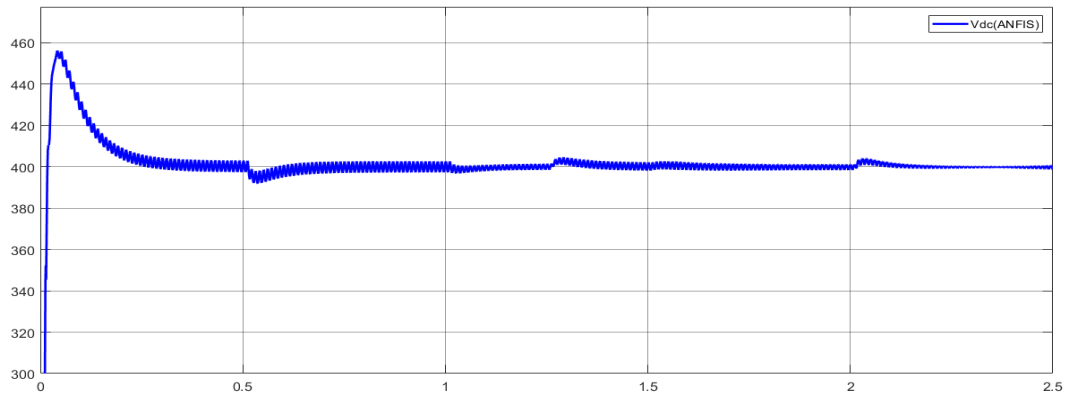
(a)
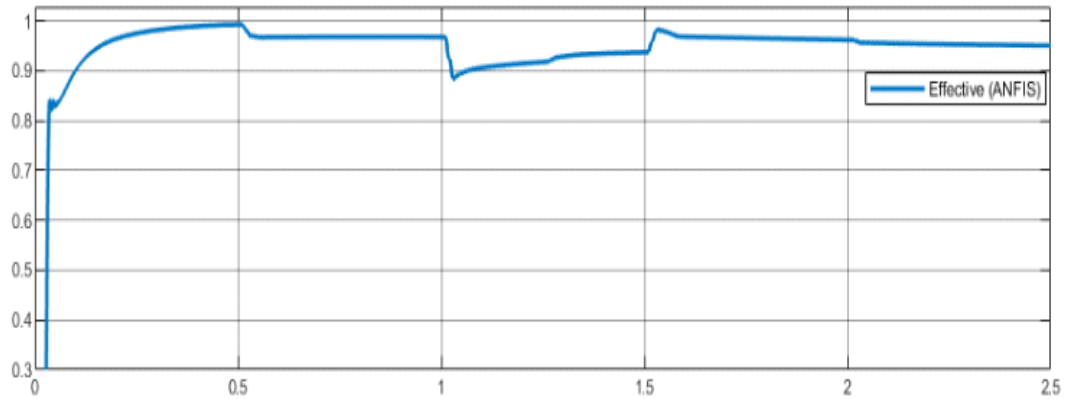
(b)
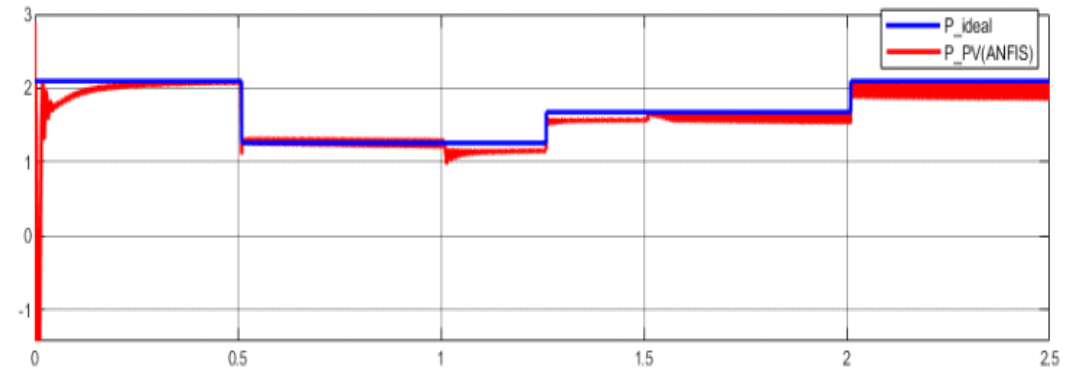
(c)

Figure 13. a) The output voltage of boost converter, b) the algorithm efficiency c) the PV panel power, reference power and obtained using ANFIS based MPPT algorithm.

Figures 14 and Figure 15 show the reference current, grid current and PV panel current obtained using the PandO algorithm and the ANFIS-based MPPT algorithm respectively. From the Figures 14 and 15, when the developed MPPT algorithm is compared with the PandO algorithm, the AC output current of the inverter can follow the grid reference current with less fluctuation.

(a)

(b)
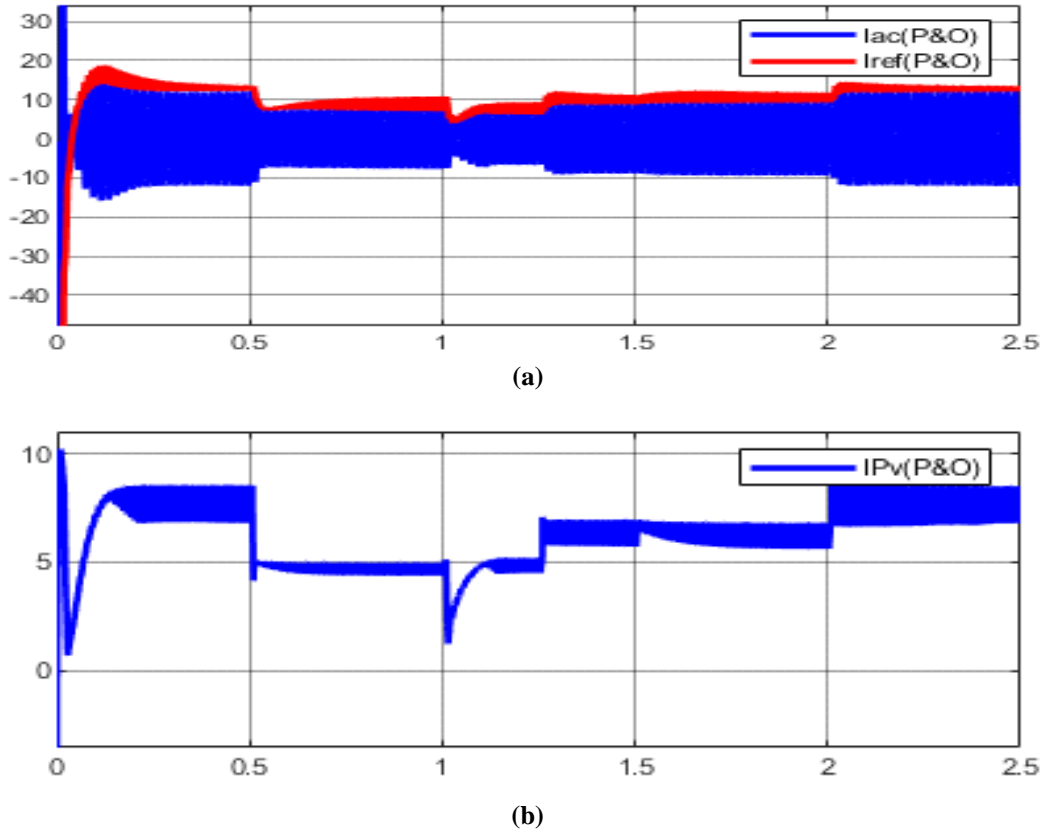
Figure 14. a) The reference current, the grid current and b) the PV panel current obtained using the PandO algorithm.

(a)

(b)
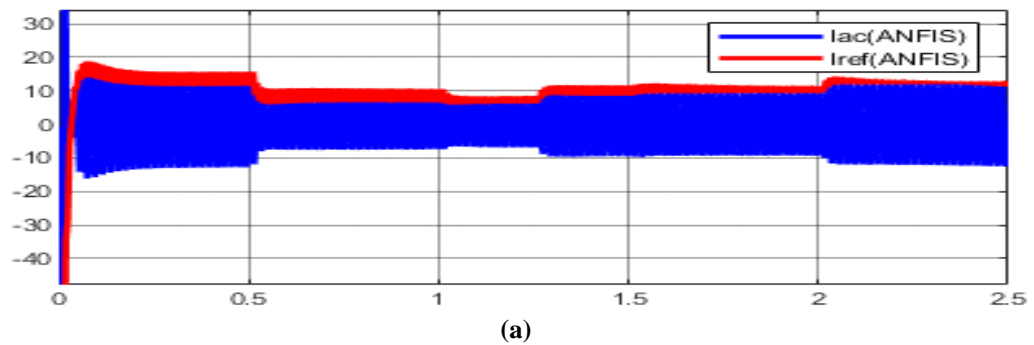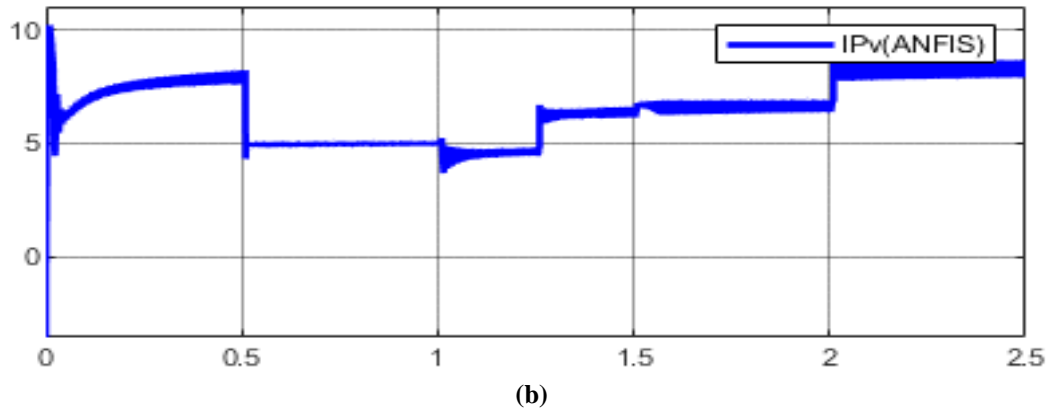
Figure 15. a) The reference current, the grid current and b) the PV panel current obtained using ANFIS based MPPT algorithm.

5. RESULTS

In this study, the ANFIS based MPPT control algorithm is development for a on-grid double stage 2KW single phase PV inverter. The voltage balancing between the PV panel system and the AC grid is performed by a DC/DC boost converter. The duty ratio of active switch is adjusted using the ANFIS based MPPT algorithm to track the MPP of the PV panel system. In the developed ANFIS algorithm, Sugeno inference with three inputs and one output was used and irradiation and temperature data were chosen as input training data. 400V constant MPPT voltage obtained from the DC/DC converter output was applied to input of the single phase inverter and 220V 50Hz AC voltage was obtained by using the dq algorithm. The voltage and frequency on the grid side are regulated by adjusting the PWM signal by the dq controller . Thus, simultaneous control in the PV panel system and the inverter ensures that the control aims are achieved. The validity of the developed algorithm was tested using the Matlab/Simulink simulation program.

ANFIS based MPPT algorithm and PandO algorithm were compared in simulation studies and algorithm efficiency was obtained as 0.8887 and 0.5079 at t=1.033s respectively. The simulation results show that the proposed ANFIS based control algorithm is adaptable to environmental changes and can quickly track MPP. The grid current tracking performance shows that the PV inverter is sensitive to irradiation and temperature changes and the reliability of the developed ANFIS algorithm. The comparison results with the PandO algorithm confirm the superiority of the developed ANFIS algorithm.

ACKNOWLEDGEMENT

REFERENCES

[1] Hu X., Zou Y., Yang Y., (2016), Greener plug-in hybrid electric vehicles incorporating renewable energy and rapid system optimization, Energy, 111: 971-980.

[2] Xue Y., Chang L., Kjær S.B., Bordonau J., and Shimizu T., (2004), Topologies of Single-Phase Inverters for Small Distributed Power Generators: An Overview, IEEE Transactions on Power Electronics,19, 1305-1314.

[3] Fei, J., and Zhu, Y., (2017), Adaptive fuzzy sliding control of single-phase PV grid-connected inverter, Plos one, 12(8), e0182916.

[4] Jubaer, A., and Zainal, S., (2015), An improved perturb and observe (PandO) maximum power point tracking (MPPT) algorithm for higher efficiency, Appl. Energy, 150, 97–108. doi:10.1016/j.apenergy.2015.04.006

[5] Saharia, B. J., and Saharia, K. K., (2016), Simulated study on nonisolated DC-DC converters for MPP tracking for photovoltaic power systems, Journal of Energy Engineering, 142(1), 04015001. doi: 10.1061/(ASCE)EY.1943-7897.0000261

[6] Safari, A., and Mekhilef, S., (2010), Simulation and hardware implementation of incremental conductance MPPT with direct control method using cuk converter, IEEE T. Ind. Electr., 58(4), 1154-1161. doi:10.1109/TIE.2010.2048834

[7] Tey, K.S. and Mekhilef, S. (2014), Modified Incremental Conductance Algorithm for Photovoltaic System Under Partial Shading Conditions and Load Variation, IEEE Trans. Ind. Electron., 61, 5384–5392. doi:10.1109/TIE.2014.2304921

[8] Mei, Q., Shan, M., Liu, L., and Guerrero, J. M., (2010), A novel improved variable step-size incremental-resistance MPPT method for PV systems, IEEE T. Ind. Electr., 58(6), 2427-2434. doi:10.1109/TIE.2010.2064275

[9] Rezk, H., Fathy, A., and Abdelaziz, A. Y., (2017), A comparison of different global MPPT techniques based on meta-heuristic algorithms for photovoltaic system subjected to partial shading conditions. Renew. Sust. Energy Rev., 74, 377-386. doi:10.1016/j.rser.2017.02.051

[10] Daraban, S., Petreus, D., and Morel, C., (2014), A novel MPPT (maximum power point tracking) algorithm based on a modified genetic algorithm specialized on tracking the global maximum power point in photovoltaic systems affected by partial shading, Energy, 74, 374-388. doi:10.1016/j.energy.2014.07.001

[11] Ahmed, J., and Salam, Z. A., (2014), Maximum Power Point Tracking (MPPT) for PV system using Cuckoo Search with partial shading capability, Appl. Energy, 119, 118-130. doi:10.1016/j.apenergy.2013.12.062

[12] Babu, T. S., Ram, J. P., Dragičević, T., Miyatake, M., Blaabjerg, F., and Rajasekar, N., (2017), Particle swarm optimization based solar PV array reconfiguration of the maximum power

extraction under partial shading conditions, IEEE T. Sust. Energy., 9(1), 74-85, doi:10.1109/TSTE.2017.2714905

[13] Titri, S., Larbes, C., Toumi, K. Y., and Benatchba, K., (2017), A new MPPT controller based on the Ant colony optimization algorithm for Photovoltaic systems under partial shading conditions, Appl. Soft Comput., 58, 465-479. doi:10.1016/j.asoc.2017.05.017

[14] Demirel, Ö., Kakilli, A. and Tektaş, M., (2010), Anfis Ve Arma Modelleri İle Elektrik Enerjisi Yük Tahmini. Gazi Üniv. Müh. Mim. Fak. Der., 25, 601-610.

[15] Kharb, R. K., Shimi, S. L., Chatterji, S., and Ansari, M. F. (2014), Modeling of solar PV module and maximum power point tracking using ANFIS, Renewable and Sustainable Energy Reviews, 33, 602-612. doi:10.1016/j.rser.2014.02.014

[16] Chikh, A., and Chandra, A. (2015), An optimal maximum power point tracking algorithm for PV systems with climatic parameters estimation. IEEE Transactions on Sustainable Energy, 6(2), 644-652. doi:10.1109/TSTE.2015.2403845

[17] Lasheen, M., and Abdel-Salam, M. (2018), Maximum power point tracking using Hill Climbing and ANFIS techniques for PV applications: A review and a novel hybrid approach. Energy conversion and management, 171, 1002-1019. doi:10.1016/j.enconman.2018.06.003

[18] Li-Qun, L., and Zhi-xin, W. (2008), A rapid MPPT algorithm based on the research of solar cell's diode factor and reverse saturation current. *WSEAS Trans. System*, *7*(5), 568-579.

[19] Manual, P. U. (2010), Powersim Technol. Rockville, MD, USA.

[20] Dutta, S.; Debnath, D.; Chatterjee, K. A. (2018), Grid-connected single-phase transformerless inverter controlling two solar PV arrays operating under di_erent atmospheric conditions. IEEE Trans. Ind. Electron., 65, 374–385.

[21] Hart, D. W., 2010 Hart, D. W., (2010),Power Electronics. New York, McGraw-Hill.

[22] Zeb, K., Islam, S. U., Din, W. U., Khan, I., Ishfaq, M., Busarello, T. D. C., and Kim, H. J. (2019), Design of fuzzy-PI and fuzzy-sliding mode controllers for single-phase two-stages grid-connected transformerless photovoltaic inverter. *Electronics*, *8*(5), 520.

[23] Da Silva, S. A. O., Novochadlo, R., and Modesto, R. A. (2008, June), Single-phase PLL structure using modified pq theory for utility connected systems. In *2008 IEEE Power Electronics Specialists Conference* (pp. 4706-4711), IEEE.

[24] Onal, Y. (2021), Analysis of a new SEPIC AC–DC PFC converter for light emitting diode applications. *Emerging Materials Research*, *11(1)*, 51-59.

[25] Miranda, U. D. A., Rolim, L. G. B., and Aredes, M. (2005, June), A DQ synchronous reference frame current control for single-phase converters. In *2005 IEEE 36th power electronics specialists conference* (pp. 1377-1381), IEEE.

[26] Jha, R. R., and Srivastava, S. C. (2016, March), Fuzzy Logic and ANFIS controller for grid integration of Solar PhotoVoltaic. In *2016 IEEE 6th International conference on Power Systems (ICPS)* (pp. 1-6), IEEE.

[27] Abu-Rub, H., Iqbal, A., Ahmed, S. M., Peng, F. Z., Li, Y., and Baoming, G. (2012), Quasi-Z-source inverter-based photovoltaic generation system with maximum power tracking control using ANFIS. *IEEE Transactions on Sustainable Energy*, *4*(1), 11-20.

[28] Mahmud, N., Zahedi, A., and Mahmud, A. (2017), A cooperative operation of novel PV inverter control scheme and storage energy management system based on ANFIS for voltage regulation of grid-tied PV system. *IEEE Transactions on Industrial Informatics*, *13*(5), 2657-2668.

RESEARCH ARTICLE

OPTIMIZATION of MACHINING PARAMETERS for BORON ALLOY STEEL by PLUNGE ELECTRO EROSION by TAGUCHI TECHNIQUE

İbrahim Baki ŞAHİN[1*], Asım GENÇ[2], Levent URTEKİN[3] and H. Bekir ÖZERKAN[4]

[1]Ahi Evran University, Department of Mechanical Engineering,Kırşehir, ibrahim.sahin@ahievran.edu.tr,
ORCID:0000-0001-8090-9748
[2]Gazi University, Department of Machinery and Metal Technology, Ankara, asimgenc@gazi.edu.tr,
ORCID:0000-0002-1900-1009
[3]Ahi Evran University, Department of Mechanical Engineering, Kırşehir, levent.urtekin@ahievran.edu.tr,
ORCID:0000-0003-4348-4749
[4]Gazi University, Department of Mechanical Engineering, Ankara, ozerkan@gazi.edu.tr,
ORCID:0000-0002-7214-9985

ABSTRACT

In this study, the machinability of Boron Alloy Steel by electrical discharge machining (EDM) method was investigated. Taguchi L27 vertical knee test set was used in the experimental study. Discharge current, pulse on time, and pulse of time were selected as processing parameters. As a result of the experiments, average surface roughness, material removal rate, electrode wear rate values were investigated. The Taguchi method was used to decide on the optimal machining parameters. The effect of control factors on experimental results was calculated using analysis of variance. In the results of the experimental studies, the discharge current was found to be the most effective parameter on the electrode wear rate (EWR), average surface roughness (Ra) and material removal rate (MRR), It has been shown that increasing the discharge current (I) value will have a negative effect on Ra. The factors affecting the average surface roughness after calculation are 86.51% discharge current, 6.17% pulse on time and 0.2% pulse off time. It was concluded that the effects of the impact time and the impact waiting time on the average surface roughness were insignificant. For MRR, the discharge current is 75.56%, the pulse on time is 9.54%, and the pulse off time is 2.03%. For EWR, the discharge current is 52.87%, toff with 6.25%, and ton with 3.25%

Keywords: *Electrical discharge machining, boron alloy steel, material removal rate, surface roughness, Taguchi analysis*

1. INTRODUCTION

Electro erosion machining (EDM) is one of the most widely used non-traditional manufacturing processes for materials that are difficult to cut (carbides, ceramics, hardened steels), EDM is a thermo-electric process in which material is removed from the workpiece by the erosion effect of a series of electrical discharges known as sparks between the tool and the workpiece immersed in a dielectric fluid. Electro-erosion machining is primarily used in pressure casting dies, forging dies, cold forming dies, pressing dies, cutting and crushing dies, powder compression dies, and mould making [1].

Unlike traditional machining methods, the basic machining principle in these methods is shaping with heat energy produced by electrical sparks that occur in a dielectric fluid without contact between the tool and the workpiece [2].

Recently, research on perforation in difficult-to-machine materials has been influential. Due to their excellent mechanical properties, efficient processing will make them widely used. EDM is an unconventional machining process used for efficient and economical machining difficult-to-machine conductive materials [3]. The most crucial advantage of EDM machining is that there is no cutting force because the tool-workpiece pair does not come into physical contact with each other [4]. Also in addition, low production, and material costs, choosing the appropriate electrode material has an important role in reducing processing costs with EDM [5].

EDM is a metal material forming technique with a complex thermal energy discharge technique in which melting, and solidification events co-occur. Discharge current, pulse on time, pulse off time, dielectric fluid pressure, electrode type, and material properties determine the shape of the pits formed on the machined surfaces. Overlapping craters directly determine the surface structure and machining efficiency [6, 7].

Optimization methods have been created to establish the effective values of the parameters employed by the manufacturing sector during product processing [8]. Factorial designs are used to evaluate all level combinations of each test parameter when there are several test parameters. In other words, a factorial test design combines at least two or more parameters examined and levels in an experiment with at least two or more of these parameters. When a fully factorial experimental design is paired with statistical methodologies, it makes the analysis process much easier for researchers. Complete factorial trials were analyzed using variance (ANOVA) and regression analysis. ANOVA revealed which test parameters were statistically significant [9]. The purpose of regression analysis is to see if there is a precise mathematical relationship between the cause (independent input variable) and the consequence (independent output variable) [10]. Without modifying the order of procedures, these methods can be used to calculate the influence of a factor on the experiment and identify sources of variance [11, 12]. Taguchi test design is a proven strategy for boosting process performance with few tests and a low cost. The number of tests significantly decreases because of Taguchi's vertical index, which saves time and money. Taguchi's technique has the advantage of being able to forecast the outcome. The Taguchi technique yields a solution with the fewest possible experiments and promotes the development of high-quality processes and products. Production circumstances or uncontrolled factors have the most negligible impact on the process or product. By minimizing the total loss generated by the product due to the loss function, the Taguchi approach establishes a new concept of quality cost [13, 14]. Many surface roughness experiments use the Taguchi experimental design extensively. Experimental design is a powerful statistical tool for identifying unknown aspects of threshold parameters and assessing and modelling interactions between variables during the experiment [15].

In a study using the Taguchi method, Lin and colleagues, combining their research with an analysis of variance, argued that I and tone values increased MRR but negatively affected Ra [16]. Raghuraman et al. In their research, optimization techniques to determine the processing parameters for optimum Ra and MRR [17]. In another study using optimization techniques, it was stated that the dwell time and discharge current had a significant effect on the processing parameters [18]. For Lee and Li, the EWR increases with increasing discharge current, but the discharge current negatively affects the

roughness of the surface [19]. Urtekin et al. the machining performance outputs (the machining current, the machining rate, the average surface roughness, and surface topography) were found for the varying process parameters pulse time, pulse-off time, dielectric flushing pressure, and wire speed [20].

This research processed boron alloy steel with high wear resistance and hardness with the EDM method. Since boron atoms alloyed to these steels make the material very hard, they are difficult to shape by machining techniques. The datasheet for statistical analysis was prepared using Taguchi L27. Three separate parameters were used as variables in the experiments: discharge current, pulse time, and pulse waiting time. Workpiece material removal rate (MRR), electrode wear rate (EWR), and average surface roughness (Ra) were studied as a function of machining parameters. To find optimal parameters, the results were examined experimentally and statistically using ANOVA and regression analysis.

2. EXPERIMENTAL METHOD

2.1. Material Selection (Workpiece/Electrode)
The experimental study used 30x20x10 mm boron alloy steel as the workpiece material. The elements in boron added steel are given by weight in the tables below, and their physical properties are indicated. In Table 1, the element distribution according to the workpiece material weight ratio. In Table 2 and 3, the physical properties of the electrode and the workpiece are given. As the electrode, copper electrodes in prismatic form (20x10 mm and 99.99% purity) were used.

Table 1. Element distribution according to weight ratio of Workpiece Material (Çemaş Döküm A.Ş.),

C	Si	Mn	Ni	P	S	Cr	Mo	V	Nb	Ti	B
0,1	0,3	1,2	0,01-0,03	0,05-0,01	<0,001	0,18	0,01	0.002	0.04	0,1	0,0001

Table 2. Electrode and workpiece physical properties.

Specifactions	Value
Tensile Strenght (MPa)	290,28
Elongation at Break (%)	14,31
Hardness (HB)	99,64
Electrical Conductive (MS/m)	57,61

Table 3. Work Piece Material.

Hardness (HRc)	Yield Strenght (MPa)	Tensile Strenght (MPa)	Thermal (W/m-k)
42,7	1350	172-1450	11.3–53.3

2.2. Electric Discharge process
Experimental studies were carried out at room temperature using FURKAN brand, 50 A "K1 Z-NC" type industrial electro-erosion workbench. Using a universal lathe, the machined surface was cleaned of electrode material after each experiment was completed.

2.3. Surface Roughness Measurements

Mitutoyo SJ 210 surface roughness measuring device was used to determine the average surface roughness. Thanks to this device, the measurement of channels up to 0.5 mm are easily achieved. The average surface roughness values of the machined surface were measured in triplicate at room temperature. Surface roughness values are calculated by measuring them at three separate sites on the machined surfaces and calculating their average roughness (Ra) values.

2.4. EDM Experiment Parameters

Experiments full factorial design method was applied according to the Taguchi vertical array. The experimental design was designed as L_{27}. The parameters used were determined as pulse on time, pulse of time and discharge current (Amper), The parameters and levels used in the experiments are shown in Table 2.

Table 4. Control factors and levels used in experiments.

Experımental Parameter	Value
Dıscharge Peak Current (AMPRES) (A)	6 12 24
Pulse On Time (μs)	50 100 200
Pulse Off Time (μs)	6 24 48
Stay On Materıal (SN)	5
Electrode Polarıty	-

3. RESULTS and DISCUSSION

The highest Ra value was measured as 0.49, t_{on}=200 μs, current=24A, and the lowest Ra value was measured as 0.01 t_{on}= 50 μs, I=6A. The lowest MRR value was 6 A, at 50 μs ton values of approximately 0.01 g/min, and the highest MRR was calculated as approximately 0.49 g/min at 24 A and 200 μs percussion times. The lowest EWR was calculated as approximately 0.000326 g/min at 12 A and 200 μs ton time, and the highest EWR was approximately 2.58 g/min at 6 A and 50 μs ton time. The Ra, MRR and EWR values obtained from the experimental work performed by electro-erosion machining are shown in Figure 1.
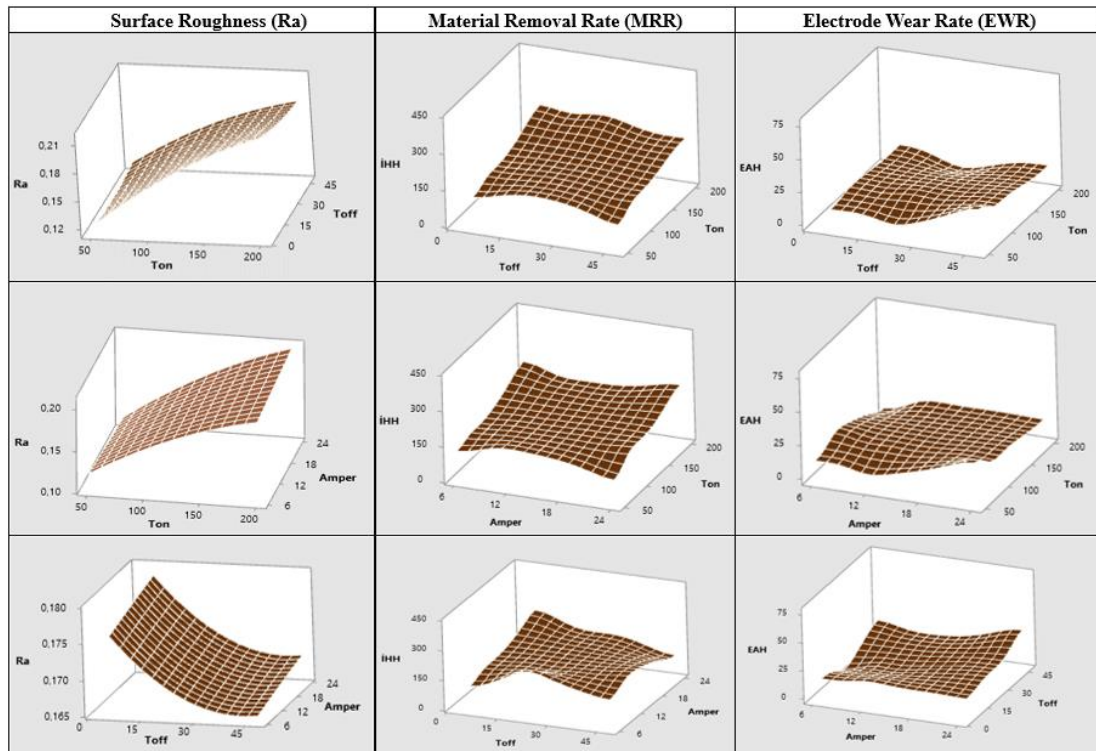
Figure 2. Graphical display of Ra, MRR and EWR values according to amper, t_{on} and t_{off}.

In experimental studies, spark density (energy density) and discharge power are higher when I and ton are high. This caused Figure 1. Graphical display of Ra, IHH and EAH values according to Amper, t_{on} and t_{off}. The surface of the workpiece becomes rougher by removing the amount of material that would cause the formation of a more deep and broader crater on the workpiece surface. As a result of the experimental study, it has been observed that the impact of waiting time has little effect on the surface roughness value of the workpiece. In the graph for the workpiece machining speed in Figure 1, it is seen that the discharge current and the pulse time (t_{on}) increase with the increase and decrease with the increase in the pulse of time (t_{off}), Looking at the graph for EAH in Figure 1, it is observed that as the discharge current increases, the electrode wear rate increases with the discharge current, and the electrode wear rate increases and then decreases with the increase of the pulse duration.

3.1. Signal Noise(S/N) Ratio Analysis

The Taguchi Method allows the user to control variables that are affected by uncontrollable factors that aren't taken into account in standard experimental design. Taguchi measures the performance qualities of the control factor against the level of these factors by converting the goal function's value into a signal-to-noise ratio (S/N), The needed signal ratio of the undesired random noise value is the Signal/Noise ratio, which reflects the quality qualities of the experimental results [21].

There are some methods for using Taguchi to evaluate experimental results. One of these methods, "the smallest is better", was the first choice for surface roughness in this research. This is because the

surface roughness is expected to be at low levels during the electro-erosion process. Equation 2 below is derived from the "smallest best" logic used in the Taguchi method. In order to complete the production process in a short time, it is hoped to obtain a higher UTL value, so the "biggest best" method is adopted in the UTL optimization. Equations 1 and 2 calculations are shown [22].

$$\text{The smallest best:} \left(\frac{S}{N}\right) = -10\log\left(\frac{1}{n}\sum_{i=1}^{n} y_i^2\right) \tag{1}$$

$$\text{The biggest best:} \left(\frac{S}{N}\right) = -10\log\left(\frac{1}{n}\sum_{i=1}^{n} \frac{1}{y_i^2}\right) \tag{2}$$

The effect of the parameters (T_{on}, T_{off} and Ampere) on the surface roughness is given in Tables 5, 6 and 7 to show the control factors and their levels better. The S/N response table created by the Taguchi method was used to determine the optimal level of control factors. These values, given in the table below, show the effect of each level of factors on the change in mean surface roughness, IIH, and EAH. The maximum S/N values in this table represent the ideal level of the control coefficient and are shown in bold. As a result of the Taguchi method, it is understood that the most influential factors and levels found for average surface roughness, MRR, and EWR are discharge current (1), pulse on time (2), and pulse off time (3), Looking at the table, the parameters that have the most significant effect on the surface roughness are determined as Amper, ton, and toff, in the order in which they affect.

Table 5. Surface Roughness S/N ratio table (db),

Levels	t_{on}	t_{off}	Amper
Level 1	**-26,30**	**-25,64**	**-21,25**
Level 2	-28,63	-19,93	-24,49
Level 3	-19,50	-28,85	-28,68
Delta	9,13	8,92	7,43

Table 6. S/N ratio table for IHH (db),

Levels	t_{on}	t_{off}	Amper
Level 1	**35,23**	**35,56**	**38,56**
Level 2	36,95	38,25	36,46
Level 3	38,67	37,03	35,82
Delta	3,44	2,69	2,74

Table 7. Table of S/N ratios for EAH (db),

Levels	t_{on}	t_{off}	Amper
Level 1	**-26,30**	**-25,64**	**-21,25**
Level 2	-28,63	-19,93	-24,49
Level 3	-19,50	-28,85	-28,68
Delta	9,13	8,92	7,43

When the main effects graph (Figure 2) for the average surface roughness is examined, the parameters affecting the surface roughness value are determined as Level 1 (50 μs) for the ton, and Current (6A) according to the smallest best case.
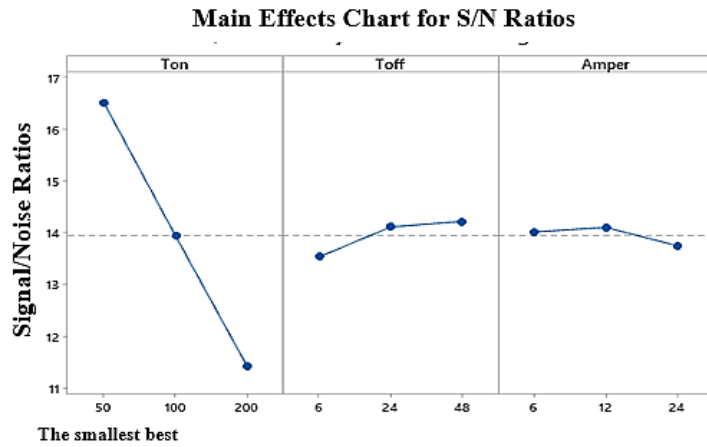
Figure 3. S/N effect plot for surface roughness by ampere, ton and toff.
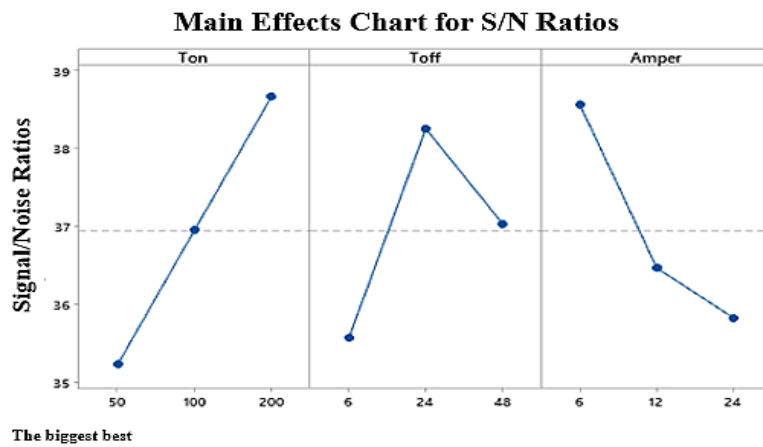
Figure 4. S/N effect graph for IHH according to ampere, ton and toff.
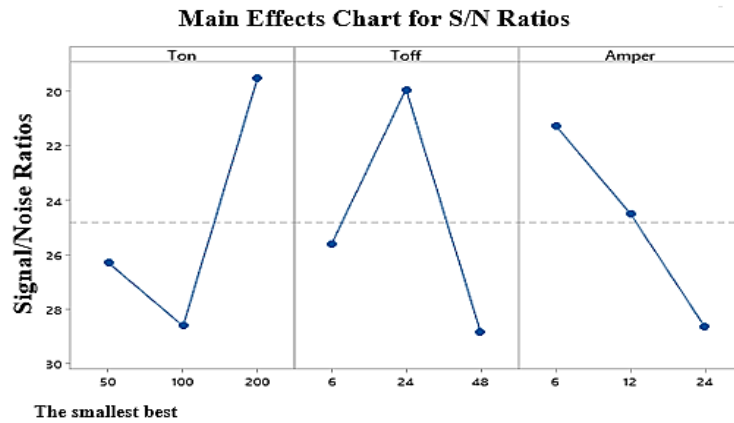
Figure 5. S/N effect plot for EAH according to amps, tones and toffs

3.2. Anova

Statistical analysis of variance (ANOVA) is used to interpret the experimental data and determine the effect ratio of the parameters. ANOVA is a statistical tool used to reveal the average performance difference between applied test sample groups. With the analysis of variance, it is possible to determine which factors are influential in which processes and how. ANOVA aims to determine how the factors examined affect the selected output value to measure the quality and type of variation caused by different levels [23]. The results of the ANOVA analysis performed to determine the effect of processing parameters on Ra, EWR and MRR are presented in Tables 8, 9 and 10. The table shows that the most influential factor for Average Surface Roughness, MRR and EWR is discharge current. The significance level, degrees of freedom (DF), the sum of squares (SS), root mean square (RS), F-number, contribution ratio, and P-value for each variable in the result are displayed here. In the analysis of the variance table, when $P<0.05$, the effects of the parameters on Ra, MRR, and EWR are statistically plausible. As we can see from the tables below, the effect of each of the parameters on Ra, EWR and MRR is seen.

Table 8. Anova Analysis Results for Workpiece Machining Speed.

Control Factor	DF	SS	RS	F	% Contribution
t_{on}	2	38667	19333	7,42	9,54
t_{off}	2	8240	4120	1,58	2,03
Amper	2	306258	153129	58,73	75,56
Error	20	52143	2607	-	-
Total	26	405306	-	-	-
R-sq:87,14% R-sq(adj):83,28					

Table 9. Anova Analysis Results for EAH Processing Speed.

Control Factor	DF	SS	RS	F	% Contribution
t_{on}	2	326,8	163,4	0,86	3,25

t$_{off}$	2	628,3	314,2	1,66	6,25
Amper	2	5312,5	2656,3	14,05	52,87
Error	20	3780,1	189,0	-	**-**
Total	26	10047,8	-	-	**-**
R-sq:62,38% R-sq(adj):51,09%					

Table 10. Anova Analysis Results for Surface Roughness.

Control Factor	DF	SS	RS	F	% Contribution
t$_{on}$	2	0,032872	0,016436	8,44	6,17
t$_{off}$	2	0,001063	0,000532	0,27	0,2
Amper	2	0,461926	0,230963	118,63	86,51
Error	20	0,038937	0,001947	-	-
Total	26	0,534797	-	-	-
R-sq: 92,72% R-sq(adj):90,54%					

The effect ratios of the parameters on the variables Ra, EAH and IHH were calculated. In Table 8, the effective ratio of the discharge current on Ra was 86.51%. It was observed that the effective rate of the impact time on the surface roughness was 6.17%. Table 6 shows the effect coefficients of the parameters on the MRR. The effective discharge flow rate on the MRR was high and was found to be 75.56%. The impact rates of the impact time and the impact waiting time material were 9.54% and 2.03%, respectively. The impact waiting time has little effect on the MRR. The effect ratio of the discharge current was found to be 52.87%, with an expected value on the EWR. The impact rates of the impact time and the impact waiting time on the material were 3.25% and 6.25%, respectively, and it was seen that they had little effect on the EWR.

3.3. Regression analysis
Regression analysis is used in experimental research to find the relationship between controls and experimental factors. In this study, I, ton, and toff were chosen as modifiers. Ra, MRR, and EWR are the result of the experimental process. A linear regression model was set up to find the Ra, MRR, and EWR values. Equations 3,4, and 5 show the linear regression models generated for Ra's rendering performance outputs, MRR, and EWR.

$$MRR = -82,7 + 0,606 ton - 0,689 toff + 14,21 I \tag{3}$$

$$EWR = -10,95 - 0,0502 ton + 0,190 toff + 1,860 I \tag{4}$$

$$Ra = -0,1414 + 0,000556 ton - 0,000322 toff + 0,01747 I \tag{5}$$

4. CONCLUSION

The results of the research, in which the machinability of the boron alloy steel material by using copper electrodes on the EDM machine and statistical analyses were carried out, are presented below.

• It was observed that the increase in discharge current and impact time affected the surface roughness negatively.

• High discharge current has increased the machining speed of the part.

• It was revealed that the parameter that most affected the results on Ra, MRR, and EWR was discharge flow.

• ton and toff turned out to have little effect on Ra, MRR, and EWR.

• The optimum machining parameters for the average surface roughness were measured at ton=200 μs I=24A, and the lowest Ra was 0.01 ton= 50 μs I=6A.

• The best machining parameters for the MRR were 50 μs tons at the lowest 6A current and the highest MRR at 24A current and 200 μs tons.

• According to the analysis of variance's outputs, the discharge current's percentage effect on the surface roughness is 86.51%. The effective discharge flow rate for MRR was determined as 75.14%, and the effective rate on EWR was determined as 52.87%.

• According to the results of the Anova analysis, the hit waiting time is the parameter that has a minor effect on the machining.

Accurate experiments results show that Taguchi's optimization studies can successfully apply to EDM.

ACKNOWLEDGEMENT

REFERENCES

[1] Ho, K. H., and Newman, S. T. (2003), State of the art electrical discharge machining (EDM), International Journal of Machine Tools and Manufacture, 43(13), 1287-1300.

[2] Yue, X., Li, Q., and Yang, X. (2020), Influence of thermal stress on material removal of Cf_SiC composite in EDM. Ceramics International, 46(6), 7998-8009.

[3] Jahan, M. P., Wong, Y. S., and Rahman, M. (2010), A comparative experimental investigation of deep-hole micro-EDM drilling capability for cemented carbide (WC-Co) against austenitic stainless steel (SUS 304), The International Journal of Advanced Manufacturing Technology, 46(9), 1145-1160.

[4] Çaydaş, U. (2008), Ti6Al4V alaşımının elektro erozyon ve elektro kimyasal işleme yöntemleriyle işlenebilirliğinin araştırılması/Investigation of the machinability of Ti6Al4V alloy by electrical discharge and electrochemical machining processes.

[5] Urtekin, L., Bozkurt, F., Özerkan, H., Çoğun, C., and Uslan, İ. (2021), Ti6Al4V Alaşımının Elektro Erozyon ile İşlemesinde Elektrolitik Cu ve CuBe Takım Elektrotlarının Performansının Karşılaştırılması. El-Cezeri, 8(3), 1455-1461.

[6] Abbas, N. M., Solomon, D. G., and Bahari, M. F. (2007), A review on current research trends in electrical discharge machining (EDM), International Journal of machine tools and Manufacture, 47(7-8), 1214-1228.

[7] Kiyak, M., and Çakır, O. (2007), Examination of machining parameters on surface roughness in EDM of tool steel. Journal of Materials Processing Technology, 191(1-3), 141-144.

[8] Masmiati, N., and Sarhan, A. A. (2015), Optimizing cutting parameters in inclined end milling for minimum surface residual stress–Taguchi approach. Measurement, 60, 267-275.

[9] Yang, W. P., and Tarng, Y. S. (1998), Design optimization of cutting parameters for turning operations based on the Taguchi method. Journal of materials processing technology, 84(1-3), 122-129.

[10] Hamzaçebı, C., and Kutay, F. (2003), TAGUCHİ METODU: BİR UYGULAMA. Teknoloji, 6.

[11] Nas, E., Özbek, O., Bayraktar, F., and Kara, F. (2021), Experimental and statistical investigation of machinability of AISI D2 steel using electroerosion machining method in different machining parameters. Advances in Materials Science and Engineering, 2021.

[12] Shetty, N., Herbert, M. A., Shetty, D. S., Shetty, R., and Shivamurthy, B. (2013), Effect of process parameters on delamination, thrust force and torque in drilling of carbon fiber epoxy composite. Research Journal of Recent Sciences, 2(8), 47-51.

[13] Nas, E., and Gökkaya, H. (2017), Experimental and statistical study on machinability of the composite materials with metal matrix Al/B4C/Graphite. Metallurgical and Materials Transactions A, 48(10), 5059-5067.

[14] Taguchi, G., Chowdhury, S., and Wu, Y. (2005), Taguchi's Quality Engineering Handbook, John Willey and Sons. Inc., Hoboken, New Jersey, USA, 134.

[15] Akıncıoğlu, S., Gökkaya, H., and Uygur, İ. (2016), The effects of cryogenic-treated carbide tools on tool wear and surface roughness of turning of Hastelloy C22 based on Taguchi method. The International Journal of Advanced Manufacturing Technology, 82(1), 303-314.

[16] Lin, Y. C., Wang, A. C., Wang, D. A., and Chen, C. C. (2009), Machining performance and optimizing machining parameters of Al2O3–TiC ceramics using EDM based on the Taguchi method. Materials and manufacturing processes, 24(6), 667-674.

[17] Seelan, K. J., and Rajesh, R. (2014), Optimization of EDM Parameters Using Taguchi Method And Grey Relational Analysis For Aluminium Titanium Diboride (Al-TiB2), International Journal of Applied Engineering Research, 9(26), 9358-9361.

[18] Gopalakannan, S., Senthilvelan, T., and Ranganathan, S. (2013), Statistical optimization of EDM parameters on machining of aluminium hybrid metal matrix composite by applying taguchi based grey analysis.

[19] Lee, S. H., and Li, X. P. (2001), Study of the effect of machining parameters on the machining characteristics in electrical discharge machining of tungsten carbide. Journal of materials processing Technology, 115(3), 344-358.

[20] Urtekin, L., Özerkan, H. B., Cogun, C., Genc, A., Esen, Z., and Bozkurt, F. (2021), Experimental investigation on wire electric discharge machining of biodegradable AZ91 Mg alloy. Journal of Materials Engineering and Performance, 30(10), 7752-7761.

[21] Chowdhury, S., Wu, Y., Taguchi, S., and Yano, H. (2005), Taguchi's quality engineering handbook [electronic resource]. John Wiley and Sons.

[22] Erdem, V., Belevi, M., and Koçhan, C. (2010), Taguchi metodu ile plastik enjeksiyon parçalarda çarpilmanin en aza indirilmesi. Dokuz Eylül Üniversitesi Mühendislik Fakültesi Fen ve Mühendislik Dergisi, 12(2), 17-29.

[23] Yıldız, Y. (2017), Biyomedikal Uygulamalar İçin Magnezyum-Kalsiyum (Mg-0.8 Ca) Alaşımının Dalma Elektro Erozyon ile İşlenmesi. Dokuz Eylül Üniversitesi Mühendislik Fakültesi Fen ve Mühendislik Dergisi, 20(59), 336-346.

RESEARCH ARTICLE

THE EFFECT of the USE of DIFFERENT NANOFLUIDS on the HEAT TRANSFER PERFORMANCE of a HEAT EXCHANGER

Ferhat KILINÇ[1*]

[*1]Sivas Cumhuriyet University, Mechanical Engineering Dept., fkilinc@cumhuriyet.edu.tr, ORCID: 0000-0003-2707-6438

ABSTRACT

The most important problem of heating and cooling systems is the removal of heat from the system. Heat exchangers are the most critical equipment of such systems. However, the use of nanofluids has increased significantly in recent years due to the design limitation of heat exchangers. In this study, the effect of using different nanofluids on the heat transfer performance of a heat exchanger was numerically investigated. A 3D heat exchanger model was created and the thermal performance of the system was analyzed by using different types of fluids at different fluid velocities. Analyzes were performed using the ANSYS Fluent program. According to the results obtained, the highest heat transfer increase was obtained in MgO-TiO_2 nanofluid with 33.4% at 0.05 m/s compared to water. The highest and lowest heat transfer rates were calculated with 202.73 W for MgO-TiO_2 nanofluid and 121.59 W for PGW (propylene glycol-water mixture) fluid, respectively.

Keywords: *Heat Transfer, Hybrid Nanofluids, Heat Exchanger, Nanofluids*

1. INTRODUCTION

The need for a more efficient heat exchanger system has become increasingly important because of global warming, greenhouse gas emissions, and energy concerns. Heat exchanger performance is determined by the thermal and physical properties of heat transfer fluids. Fins, microchannels, and increasing the heat transfer area can all be used to enhance the performance of the heat exchanger. In addition, increasing the thermophysical properties of the heat transfer fluid is an important parameter in increasing the performance of heat exchangers [1-4]. For this purpose, the use of nanofluids [5-8] and hybrid nanofluids has recently increased.

In recent years, many engineering applications have been investigated with different nanofluids. Das et al. [9] investigated exergetic characteristics of a heat exchanger (shell and tube) and heat transfer using PGW (propylene glycol-water mixture)-based ZnO nanofluids varying nanoparticle volume concentration and nanofluid (shell side) flow rates in their study. The experimental results show that the heat transfer rate has been enhanced by increasing the concentration of nanoparticles and the flow rate of nanofluids. The efficiency of the heat exchanger was increased with the increase in the concentration of the volume of nanoparticles at a certain amount of nanofluid flow. In their experimental study, Sundar et al. [10] evaluated the friction factor and convective heat transfer coefficient. MWCNT-Fe_3O_4/water hybrid nanofluid was used in the experiments. And a circular tube

is used at constant heat flux. Flow conditions are fully developed turbulent flow. In comparison to base fluid data, the results reveal a maximum increase in Nusselt number of 31.10% with a penalty of 1.18 times increased pumping power for particle loading of 0.3% at 22,000 Reynolds number. In another study, the use of corrugated pipes in a heat exchanger (shell and tube) was investigated using the ε-NTU method, energy/exergy analysis. The effect of using corrugated pipes on energy/exergy efficiency was investigated for different operating conditions. The results revealed that the difference between fluid outlet temperatures could be reduced instead of smooth surfaces due to fluid mixing and secondary flows obtained using corrugated surfaces [11]. Huang et al. [12] examined the pressure drop and heat transfer properties of a hybrid nanofluid mixture incorporating multi walled carbon nanotubes (MWCNTs) and alumina nanoparticles in a heat exchanger (chevron corrugated-plate), When comparing the hybrid nanofluid mixture with water and Al_2O_3/water nanofluid, results show that the hybrid nanofluid mixture has a slightly larger heat transfer coefficient. In addition, hybrid nanofluid mixtures exhibit the highest heat transfer coefficients. A Diamond-water nanofluid's (biologically friendly) heat transfer efficiency, thermophysical characteristics, and pumping power assessment were experimentally studied by Alshayji et al. [13]. The nanofluid was discovered to be an efficient heat transfer fluid in a fully developed internal laminar flow regime at all studied solid concentrations and temperatures.

This numerical study investigated the effect of using different nanofluids on heat transfer performance and pressure drop. Common metallic nanofluids and metallic and metal-carbon hybrid nanofluids were preferred. In this manner, it was aimed to determine what kind of fluid used in a heat exchanger will be more efficient for heating/cooling systems.

2. MATERIALS and METHODS

In this study, a one-tube and one-pass heat exchanger model was used for the analysis. The model of the heat exchanger is given in Figure 1. The tube section has a total length of 2184 mm and is made of copper material. The diameter of the tube is 10 mm and the wall has a thickness of 1 mm. There are 36 aluminum fins with 1mm thickness and placed with a space of 5 mm around the tube. For copper and aluminum, the properties in the Fluent database were used. The numerical studies were conducted by using commercially available software ANSYS FLUENT 18.2 [14]. It was used for pressure-based and steady-state conditions, and energy and laminar viscous models. The analyses were performed at 4 different fluid velocities (0.5, 0.6, 0.7 and 0.8 m/s) and using 5 different fluids (water, propylene glycol-water mixture/PGW [9], ZnO/PGW [9], MgO-TiO_2 [15] and multi-walled carbon nanotubes/MWCNT-Fe_3O_4 [10] hybrid nanofluids), Thermophysical properties of the materials and fluids used in the study are given in Table 1.
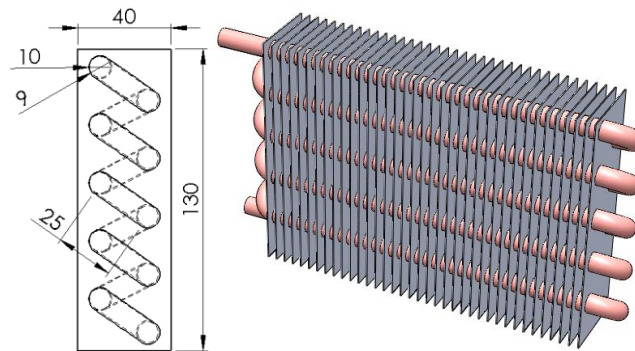
Figure 1. The schematic representation and 3-D model of heat exchanger.

The constant temperature for the tube inlet (60 ^{o}C) and constant heat transfer coefficient (h=20 W/m^{2}K) for the ambient were applied as boundary conditions. The computational domain was divided into 3.112.704 quadratic, uniform, and fine mesh. The mesh structure for the numerical model is shown in Figure 2. The average skewness for the model is 0.244.

Table 1. Thermophysical properties of materials and fluids.

Material	ρ (kg/m^3)	c_p (J/kg·K)	k (W/m·K)	μ (Pa·s)
Aluminum	2719	871	202.4	-
Copper	8978	381	387.6	-
Water	998.2	4820	0.6	0.001003
PGW(40:60)	1026.5	3747.186	0.388	0.58
ZnO/PGW	2247.8	1612.055	0.6752	1.01384
MgO-TiO$_2$	2870	8420	4.768	0.98
MWCNT-Fe$_3$O$_4$	1002.3	4182.66	0.6734	0.91

The calculations are based on the assumptions expressed as follows: materials and fluids have constant and uniform properties, fluids have been incompressible, and the inlet temperature of fluids has been constant.
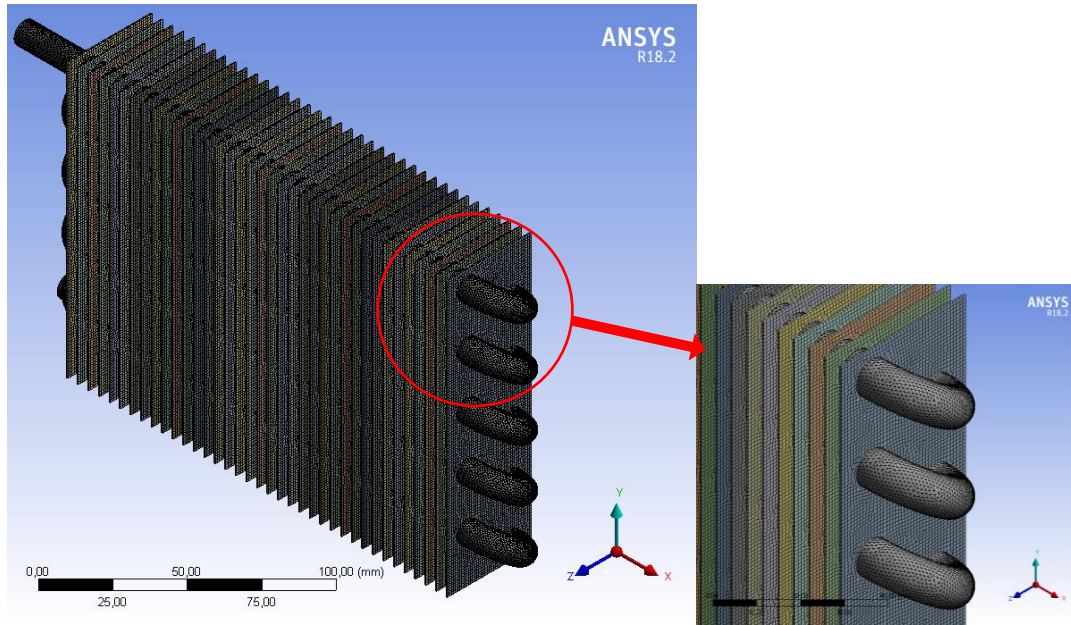
Figure 2. The mesh structure of 3-D numerical model of heat exchanger.

With the CFD (computational fluid dynamics) commercial package program (ANSYS Fluent 18.2), the heat transfer and flow through the geometry have been analyzed using partial derivative equations obtained from the conservation laws of continuity, momentum, and energy. Since the single phase approach is used in the study, the equations can be used for all fluids (nanofluids and hybrid nanofluids), Continuity, momentum, and energy equations, respectively [16];

$$\nabla(V_m) = 0 \tag{1}$$

$$\nabla\rho(V_m V_m) = -\nabla P + \nabla\mu(\nabla V_m) \tag{2}$$

$$\nabla\rho c_p(V_m T) = \nabla k(\nabla T) \tag{3}$$

where ρ is the density (kg/m^3), c_p is the specific heat (J/kgK), μ is the dynamic viscosity (Pas), k is the thermal conductivity (W/mK), P is the pressure (Pa), V is the velocity (m/s) and T is the temperature (^{o}C),

3. RESULTS and DISCUSSION

In this study, the heat transfer performance of 5 different fluids for 4 different flow rates (0.5, 0.6, 0.7 and 0.8 m/s) at constant inlet temperature was analyzed. For this purpose, firstly, numerical analysis of water and PGW fluids, which are widely used as base fluids, were made. Afterward, heat transfer analysis of different nanofluids was performed and water was compared with the base fluid. The temperature contours of the results obtained are given in Figures from 3 to 7 at different fluid flows for all fluids (water, propylene glycol-water mixture/PGW, ZnO/PGW, MgO-TiO$_2$ and multi-walled

carbon nanotubes/MWCNT-Fe_3O_4 hybrid nanofluids), respectively. As seen from the temperature contours in the figures, the outlet temperatures decreased as the fluid velocity increased. In other words, the temperature difference between the inlet and outlet temperatures decreased with increasing fluid velocity.

As the fluid velocity increases, it was seen that more uniform temperature distribution is obtained. It was thought that the distribution of temperature contours of water, ZnO/PGW, and MWCNT-Fe_3O_4 fluids exhibit similar characteristics, and this is due to the fact that the thermal conductivity coefficients are close to each other. It was observed that PGW with the lowest thermal conductivity coefficient is also the fluid with the lowest temperature value (41.9 ^{o}C) in terms of temperature contours. In MgO-TiO_2 nanofluid, the situation is the opposite, and when the thermal conductivity value is the highest, the highest temperature values (55.2 ^{o}C) were seen in this fluid. When the temperature contours are examined in detail, it can be seen starting from the second elbow that other fluids have higher temperature values except for water. This can be explained by the fact that water has the lowest viscosity value.

V1

V2

V3

V4
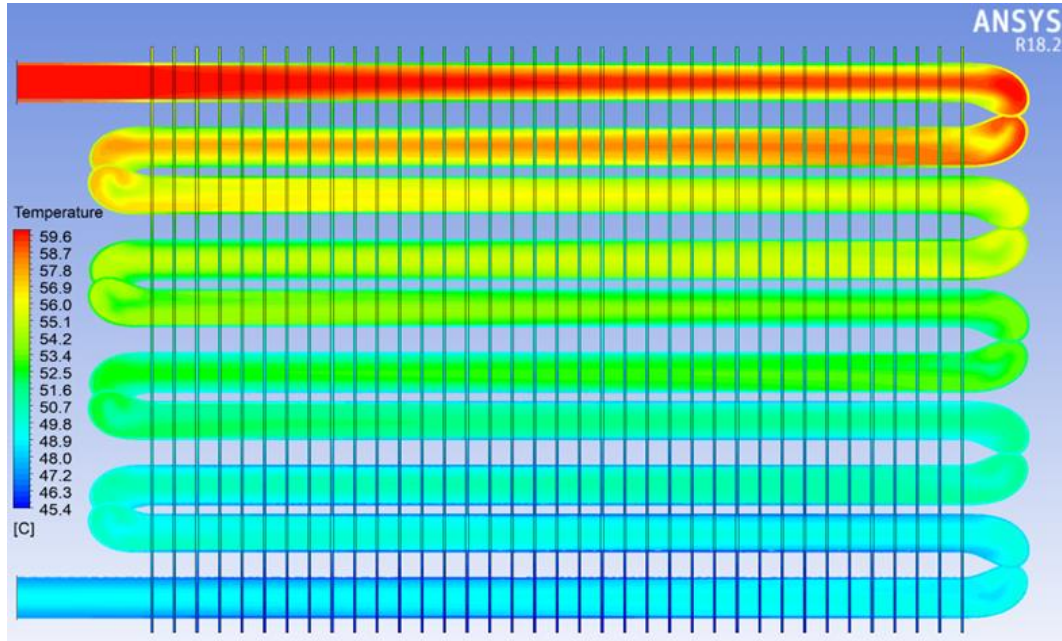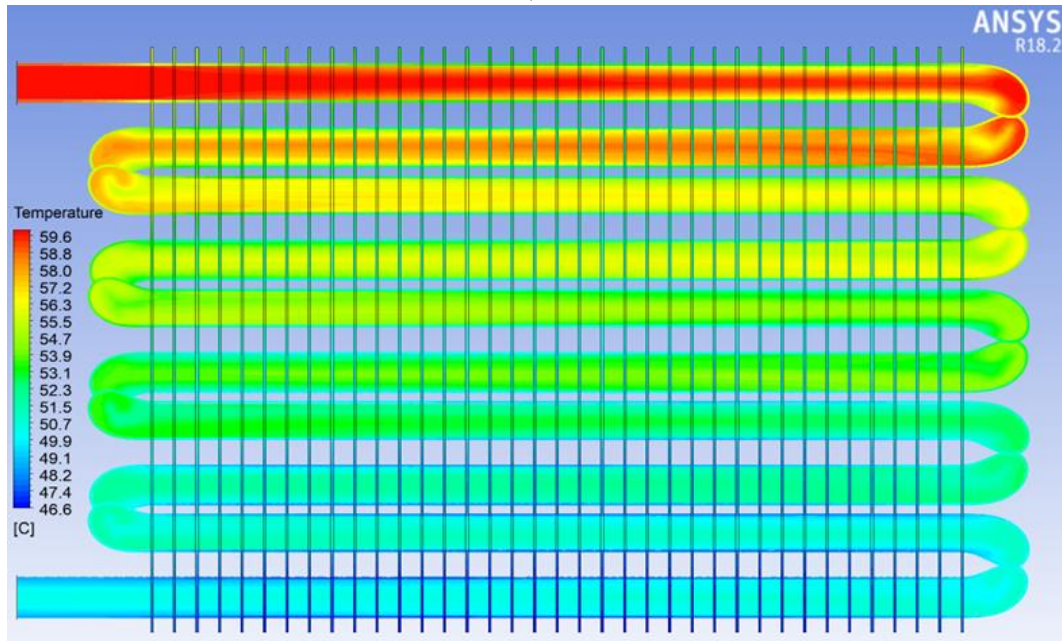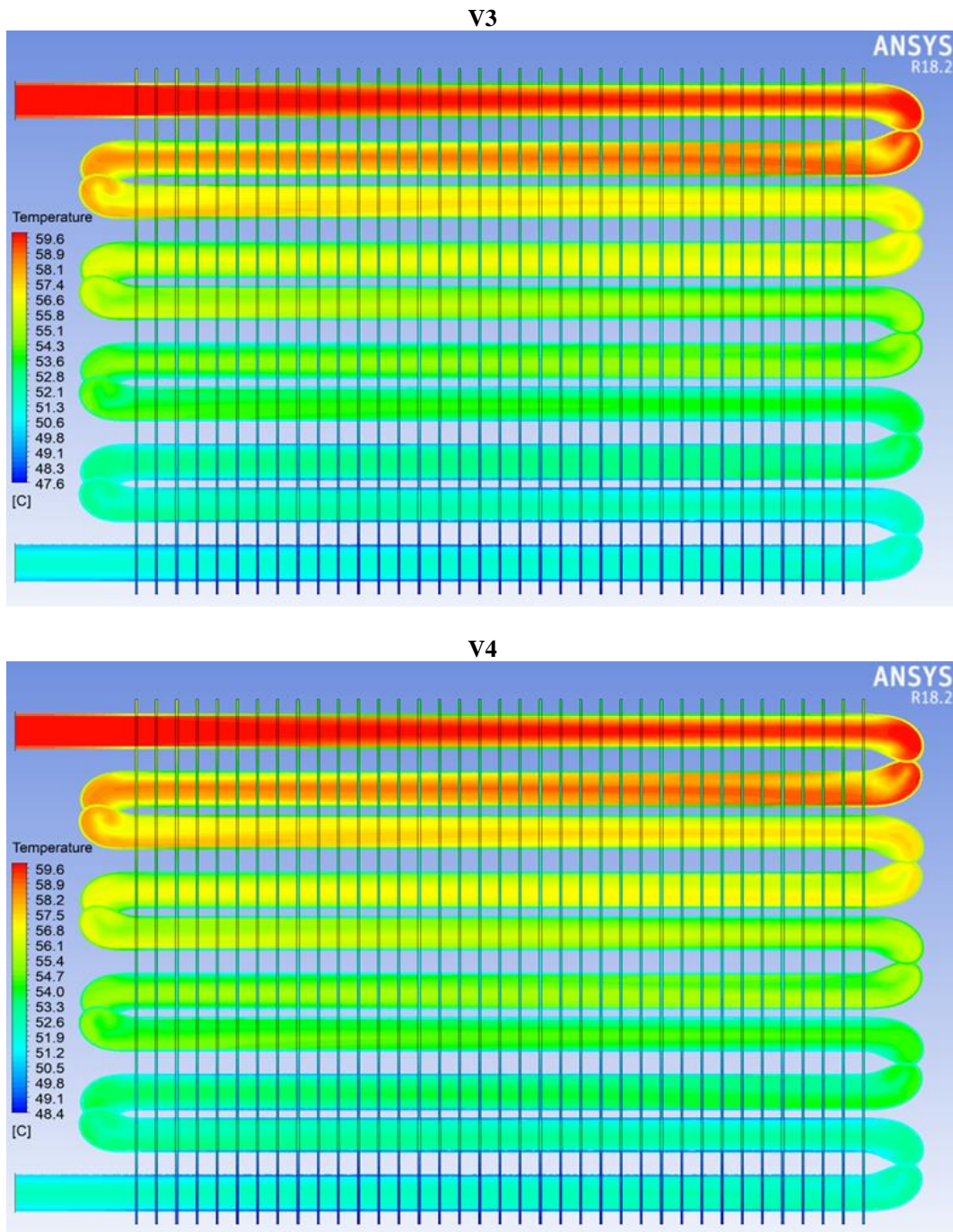
Figure 3. Temperature contours of water at different fluid velocities.

V1

V2

V3

V4
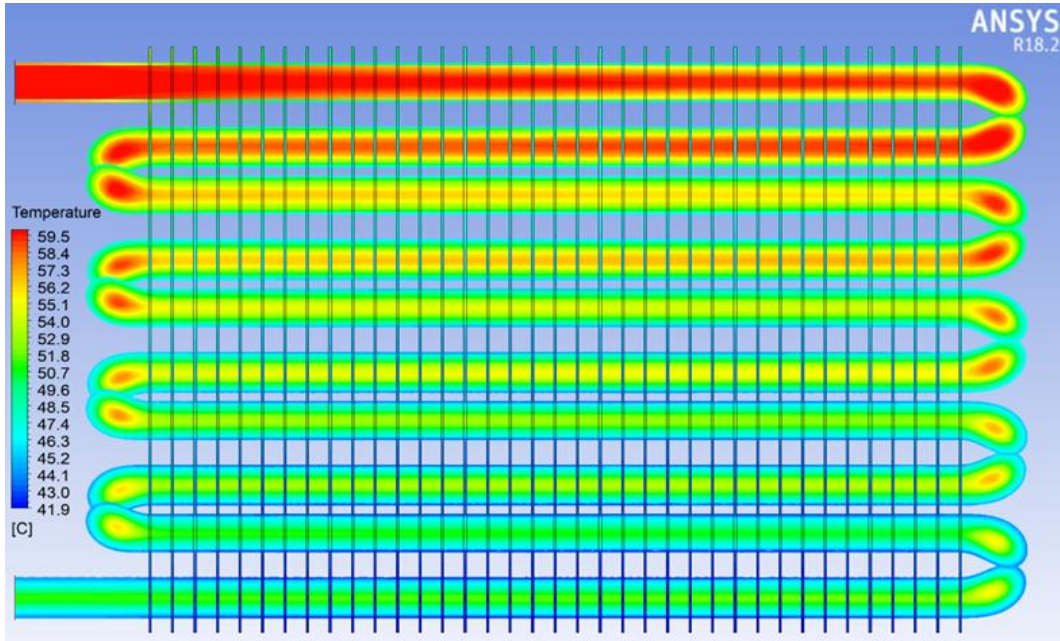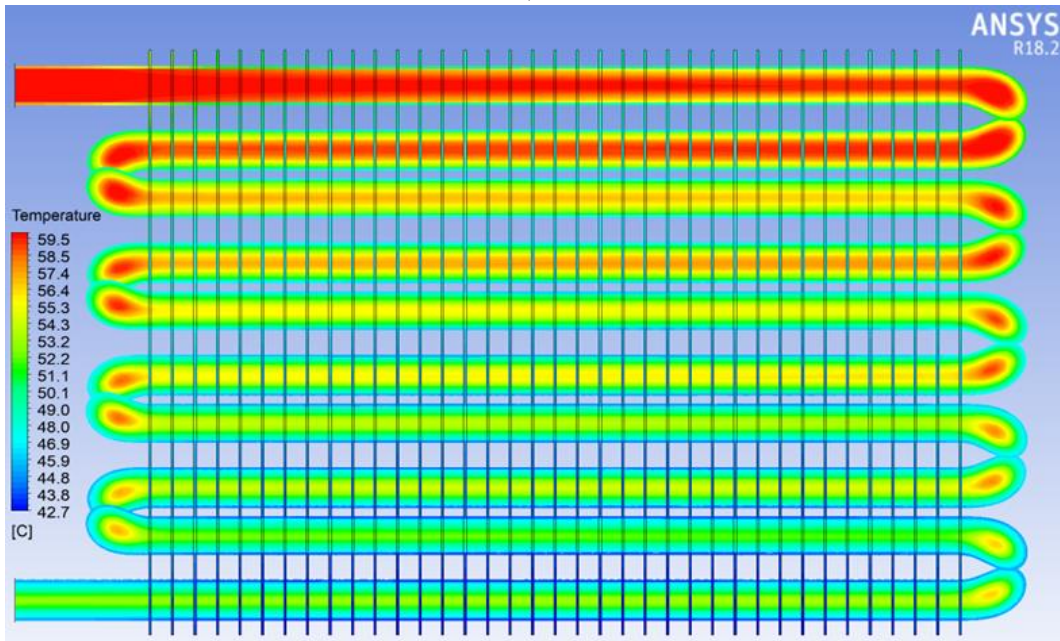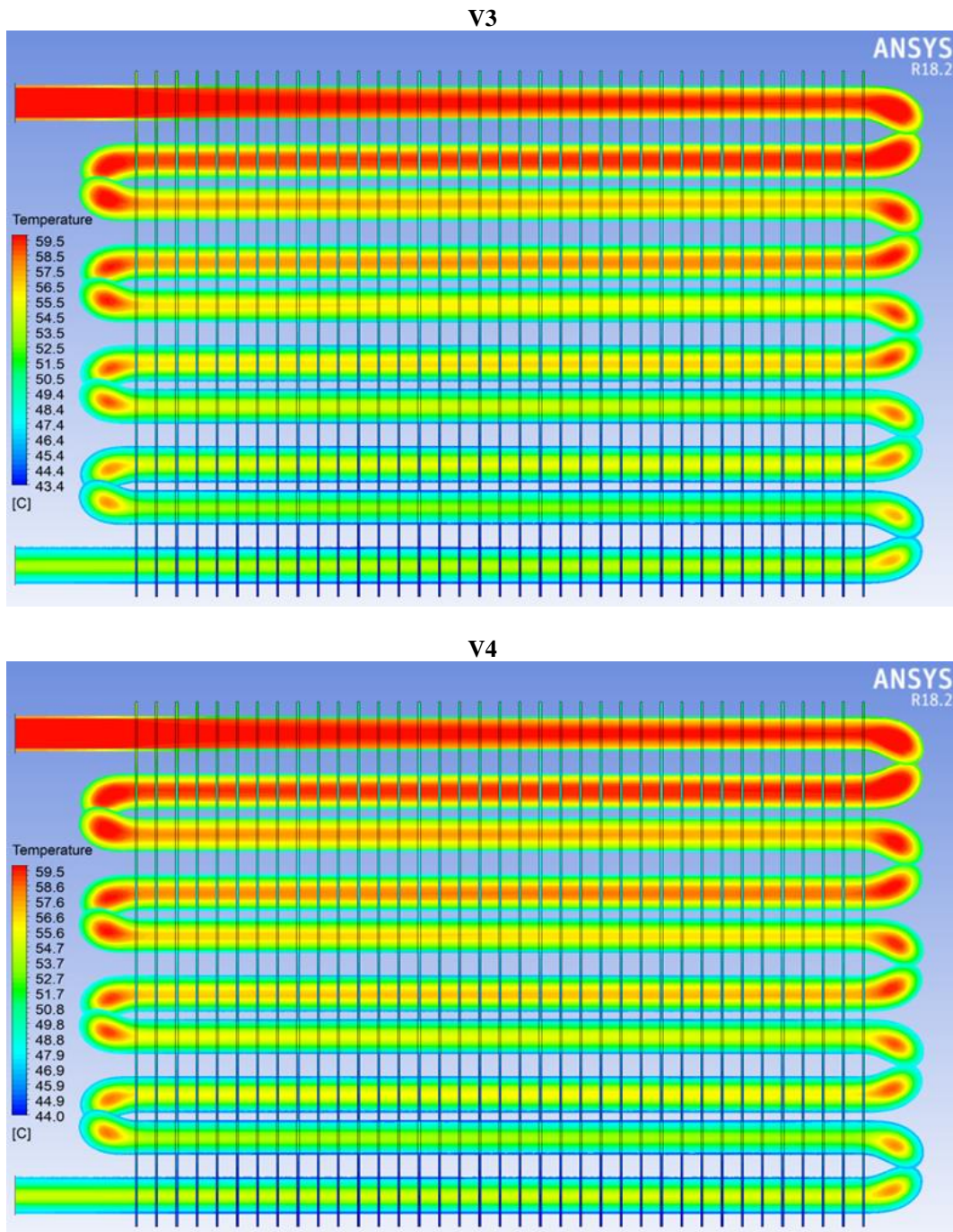
Figure 4. Temperature contours of PGW at different fluid velocities.

V1
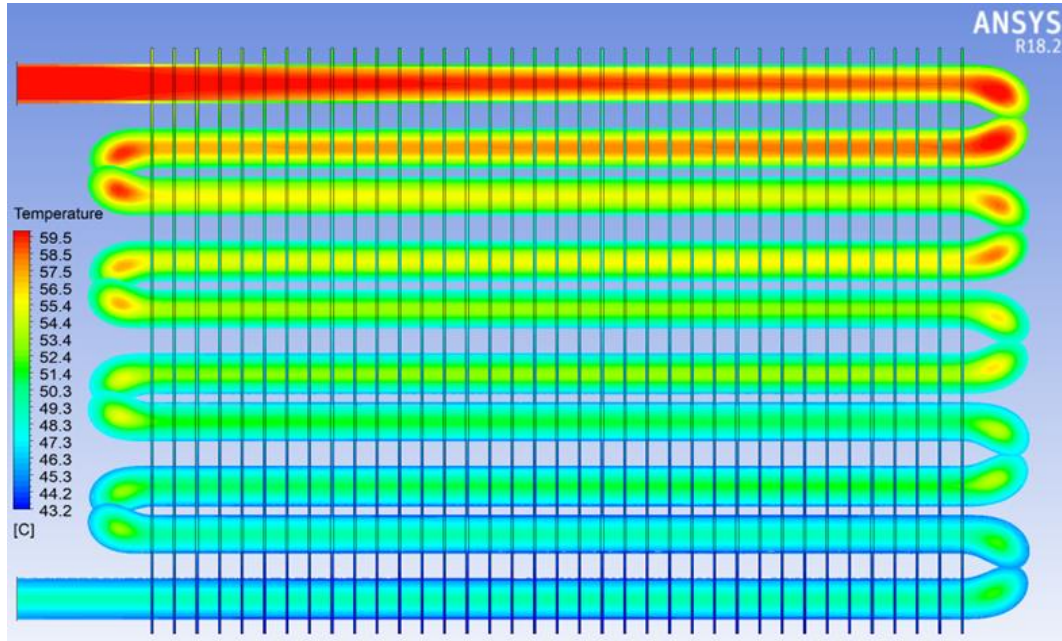
V2
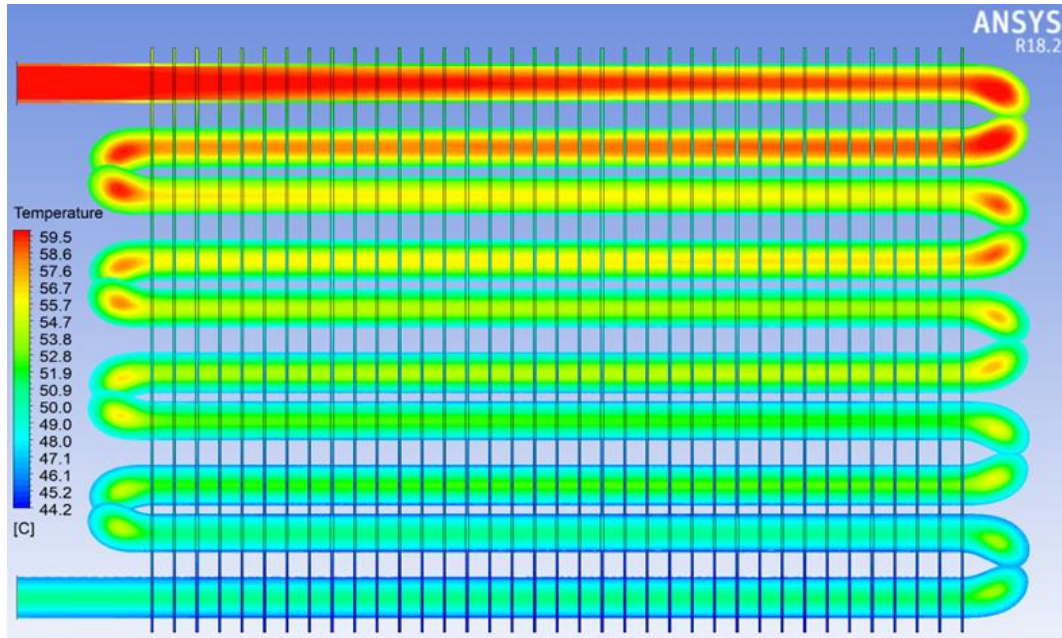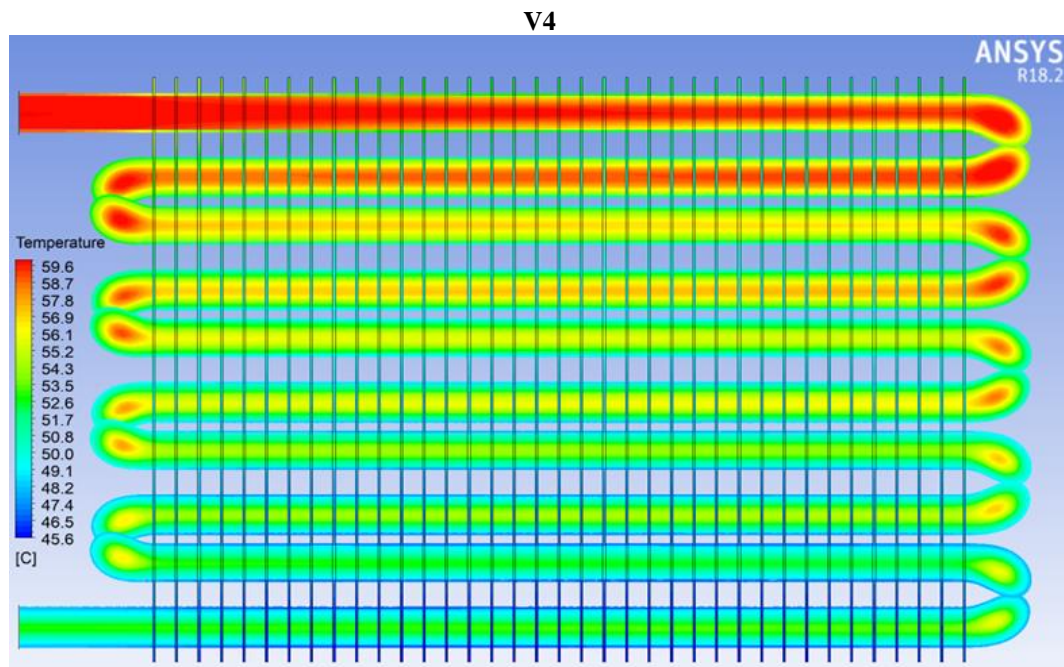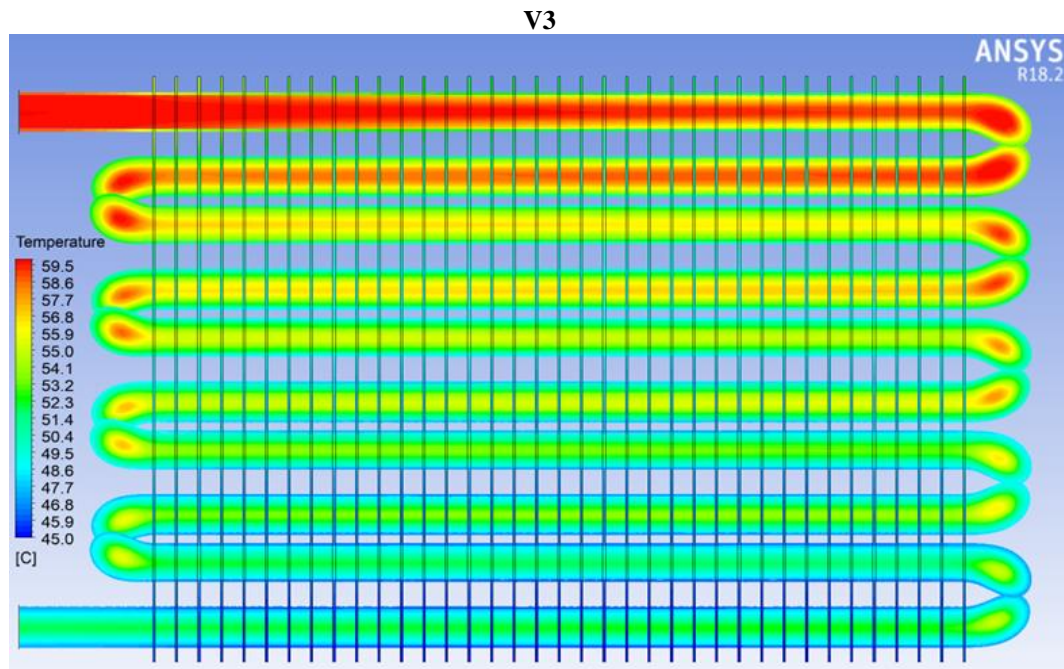
Figure 5. Temperature contours of ZnO/PGW at different fluid velocities.

V1

V2

V3

V4
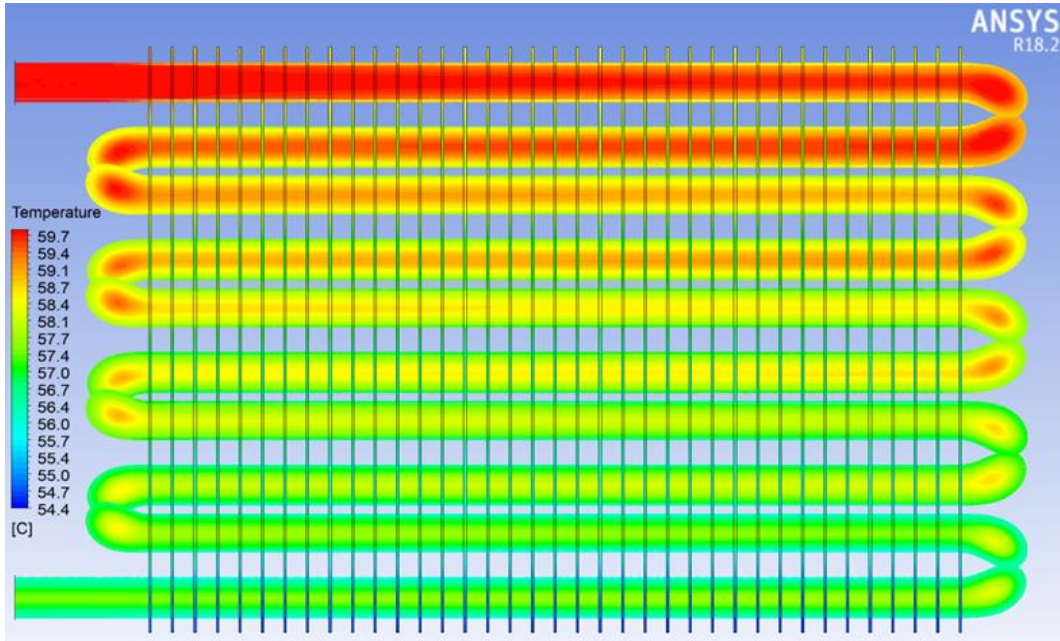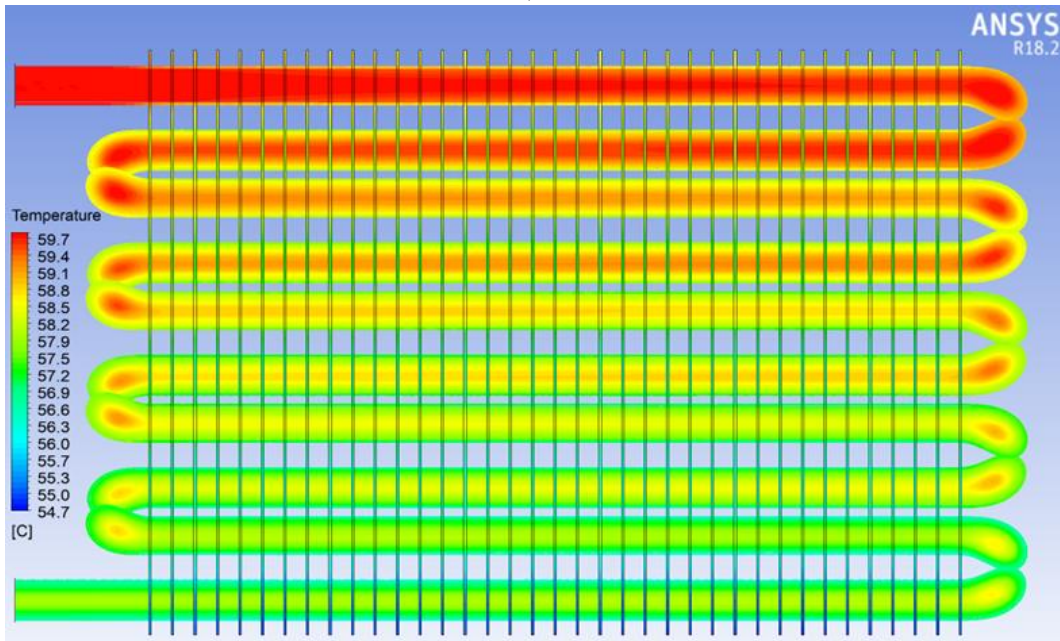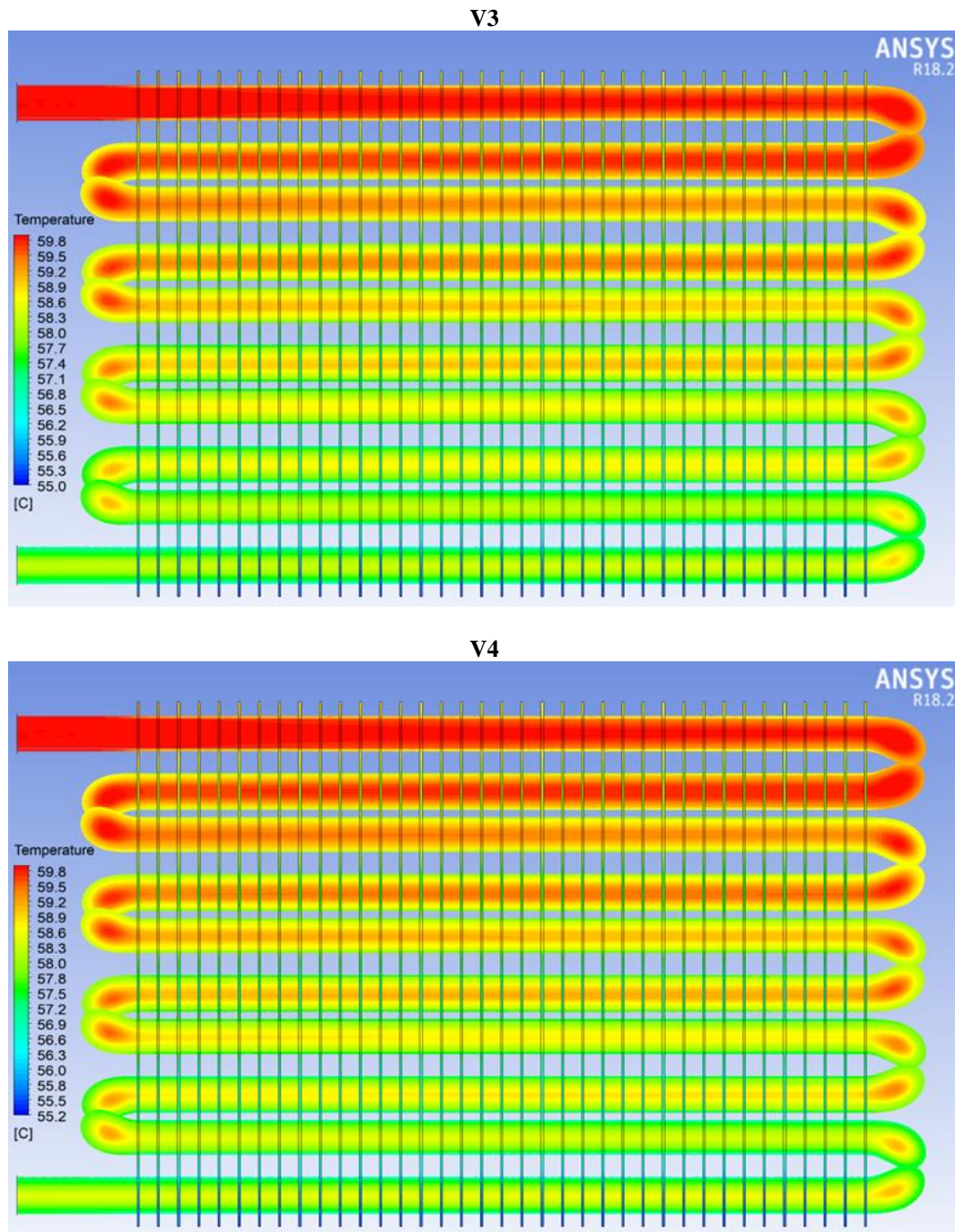
Figure 6. Temperature contours of MgO-TiO$_2$ at different fluid velocities.

V1

V2

V3

V4
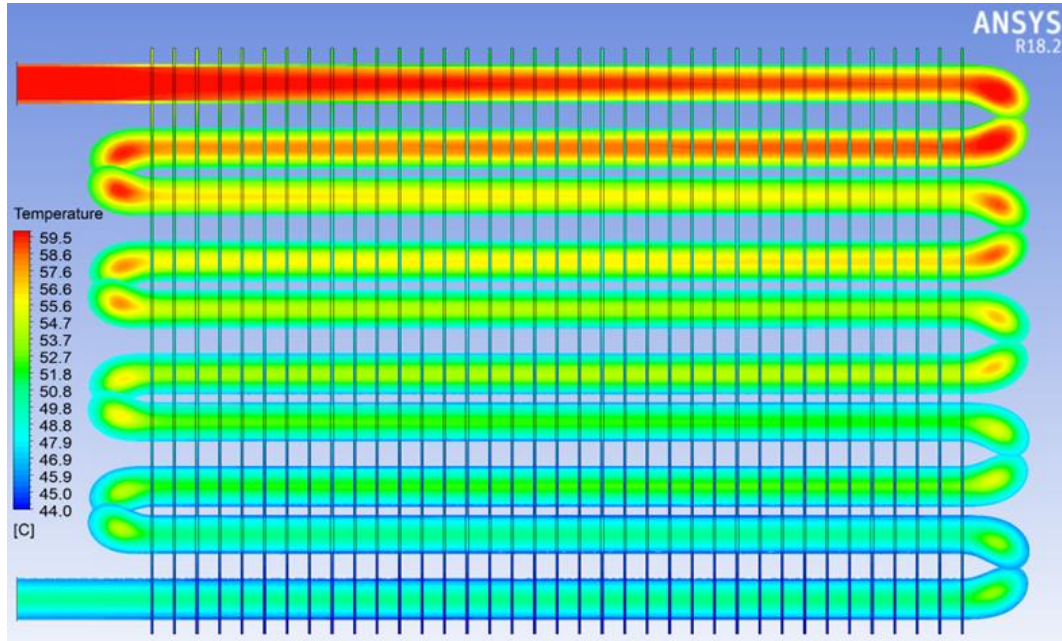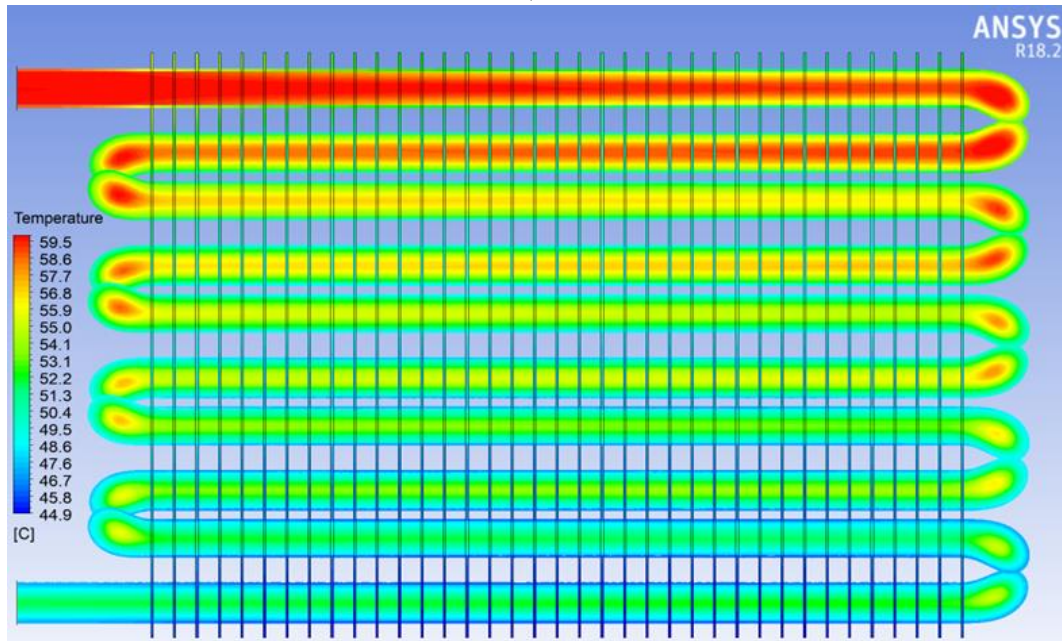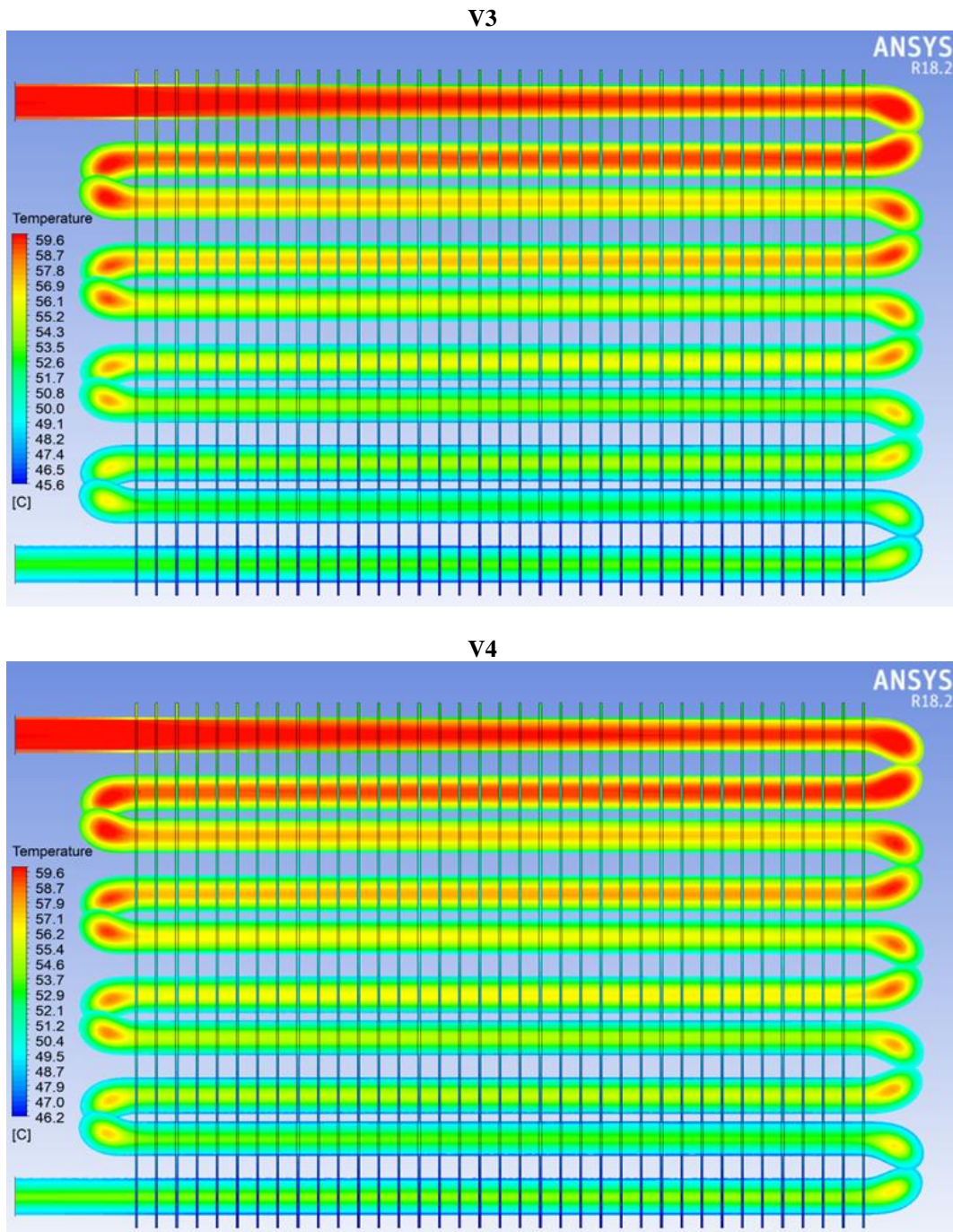
Figure 7. Temperature contours of MWCNT-Fe$_3$O$_4$ at different fluid velocities.

According to the results obtained, the heat transfer rates of all fluids were given at different fluid velocities in Figure 8. It was observed that the heat transfer rate increased for all fluids with increasing fluid velocity. The highest and lowest heat transfer rates were calculated with 202.73 W for MgO-TiO_2 nanofluid and 121.59 W for PGW fluid, respectively. Compared to water, the highest heat transfer increase was obtained in MgO-TiO_2 nanofluid with 33.4% at 0.05 m/s. When this value is compared with PGW, the increase rate was calculated as 63.6%. The second highest heat transfer coefficient values were obtained in water fluid. This situation can be explained by thermal conductivity and heat capacity values.
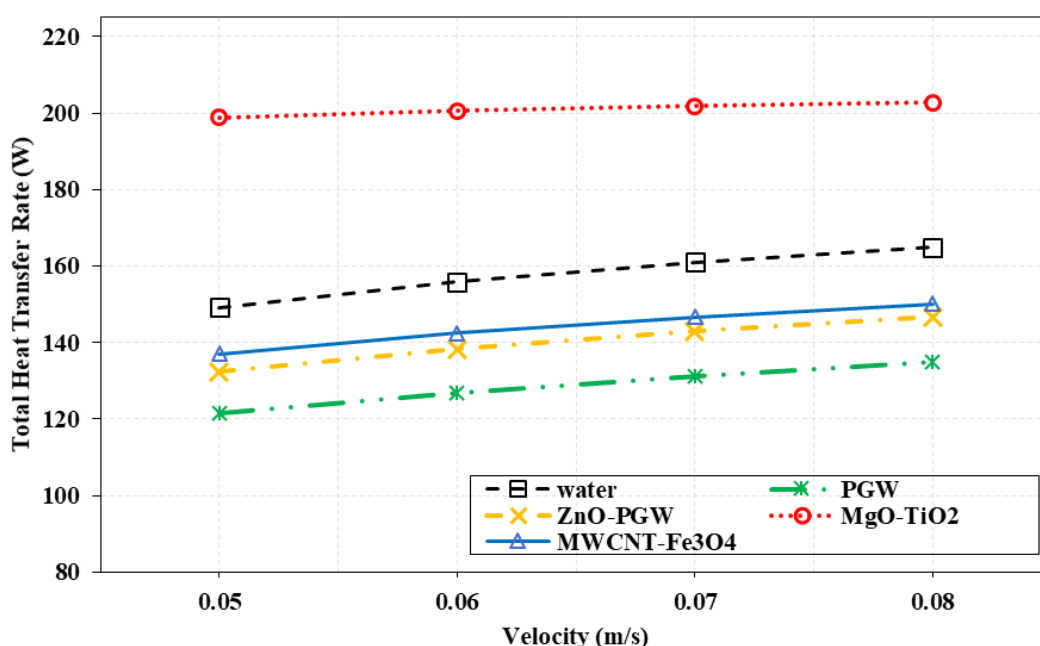
Figure 8. Total heat transfer rates of all fluids at different fluid velocities.

In figure 9, pressure difference values of all fluids are given. It has been calculated that the differences between the inlet/outlet pressure values of all fluids except water are very high. It is also seen that the increase in fluid velocity causes the pressure difference values to increase. The highest pressure difference value was calculated in ZnO/PGW nanofluid. This can be explained by the fluid viscosity. Higher viscosity causes more pressure loss.

The values of the outlet temperatures of all fluids for different fluid velocities are given in Figure 10. It was calculated that when the fluid velocity increased, the temperature values also increased. When the fluids were compared, it was calculated that the most significant temperature values were in MgO-TiO_2 nanofluid. It is seen that other fluids have close values. The highest outlet temperature was obtained at 58.07 $^{\circ}$C in MgO-TiO_2 nanofluid and the lowest at 57.48 $^{\circ}$C in ZnO/PGW nanofluid.
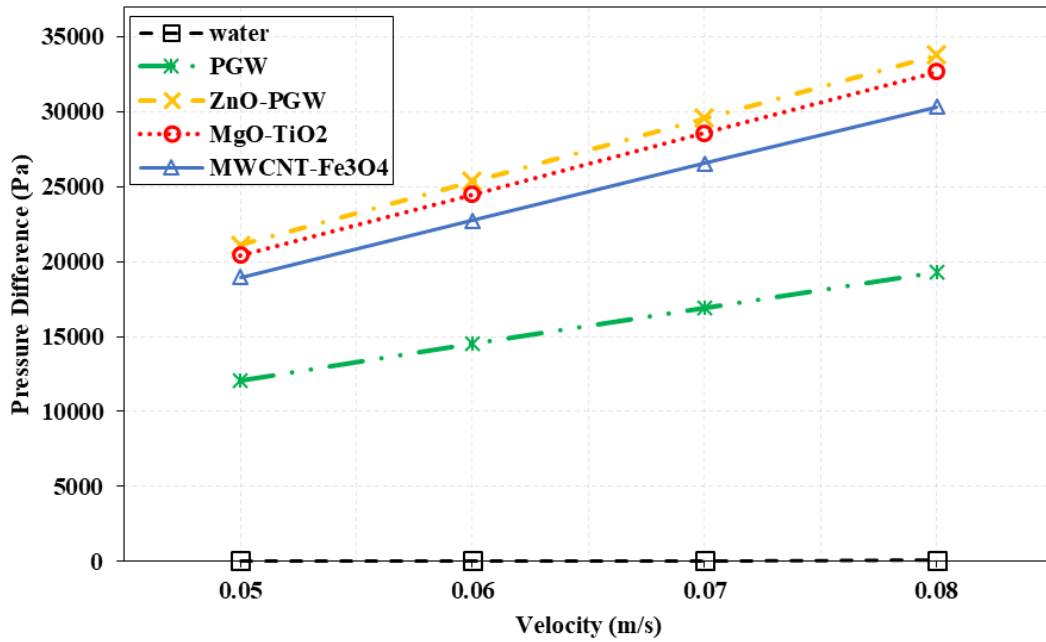
Figure 9. Pressure difference values of all fluids at different fluid velocities.
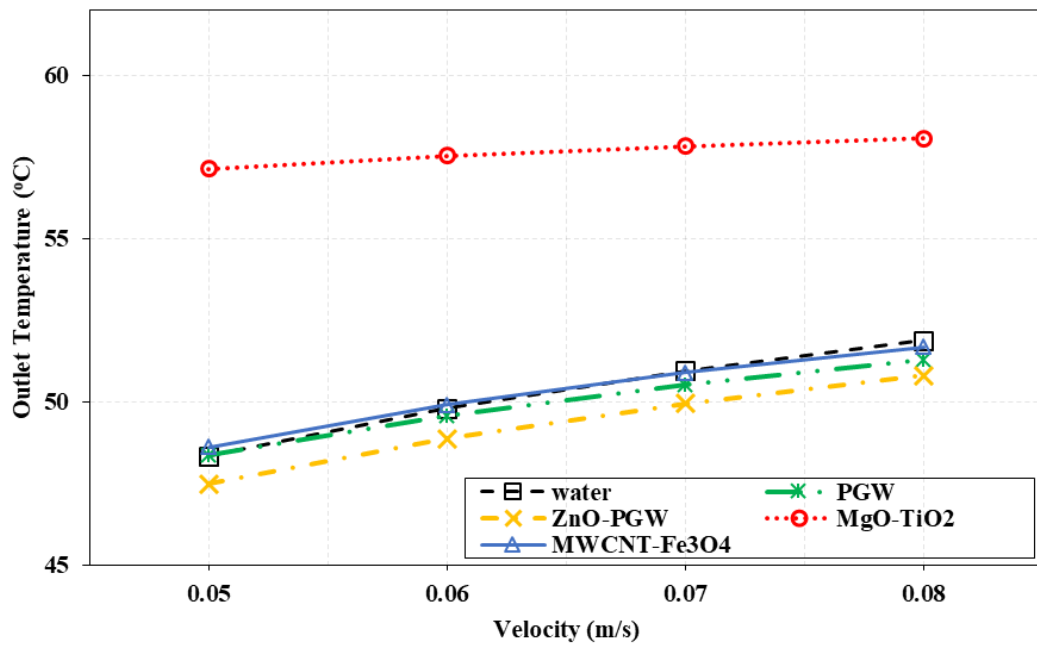
Figure 10. Outlet temperature values of all fluids at different fluid velocities.

4. CONCLUSION

In this study, the effect of using different nanofluids on the heat transfer performance of a heat exchanger was numerically investigated. A 3D heat exchanger model was created and the thermal performance of the system was analyzed by using different types of fluids at different fluid velocities. The following results were obtained as a result of the analysis:

It was observed that the heat transfer rate increased for all fluids with increasing fluid velocity. The highest heat transfer increase was obtained in MgO-TiO$_2$ nanofluid with 33.4% (202.73 W) at 0.05 m/s fluid velocity compared to water. The most important parameter causing this is the thermal conductivity value. When this value is compared with PGW, the increase rate was calculated as 63.6%. The highest pressure difference value was calculated in ZnO/PGW nanofluid. This can be explained by the fluid viscosity. Higher viscosity causes more pressure loss.

In the numerical analysis, it was seen that the thermal properties of the fluids affect the results very much due to the single-phase assumption. When the results were examined, it was seen that the single-phase analysis is not sufficient, especially compared to the experimental results.

ACKNOWLEDGMENT

REFERENCES

[1] Narrein, K. and Mohammed, H. A. (2014), Heat transfer and fluid flow characteristics in helically coiled tube heat exchanger (HCTHE) using nanofluids: A review. Journal of Computational and Theoretical Nanoscience, 11 (4), 911-927.

[2] Etghani, M. M. and Baboli, S. A. H. (2017), Numerical investigation and optimization of heat transfer and exergy loss in shell and helical tube heat exchanger. Applied Thermal Engineering, 121, 294-301.

[3] Shahrul, I. M., Mahbubul, I. M., Saidur, R., Khaleduzzaman, S. S., Sabri, M. F. M. and Rahman, M. M. (2014), Effectiveness study of a shell and tube heat exchanger operated with nanofluids at different mass flow rates. Numerical Heat Transfer, Part A: Applications, 65 (7), 699-713.

[4] Caner, M., Duman, N., Buyruk, E. and Kılınç, F. (2019), Yatay toprak kaynaklı ısı pompası sisteminin sivas şartlarında performans analizi. Journal of Science and Technology of Dumlupınar University, (042), 47-53.

[5] Kılınç, F., Buyruk, E. and Karabulut, K. (2019), Grafen tabanlı nanoakışkanların araç radyatörü soğutma performansı üzerindeki etkisinin deneysel analizi. Journal of the Institute of Science and Technology, 9 (2), 1046-1056.

[6] Kılınç, F., Buyruk, E. and Caner, M. (2019), Sivas ili şartlarinda yatay toprak kaynaklı ısı pompasının ısıtma ve soğutma için performans analizi. Politeknik Dergisi, 22 (4), 1039-1044.

[7] Kılınç, F. and Başcıl, D. (2020), Soğutma sezonu için yatay toprak kaynaklı ısı pompası ekserji analizi: Sivas ili örneği. Bitlis Eren Üniversitesi Fen Bilimleri Dergisi, 9 (2), 797-806.

[8] Kılınç, F. and Uygun, C. Z. (2022), Exergy analysis of graphene-based nanofluids in a compact heat exchanger. Isı Bilimi ve Tekniği Dergisi, 42 (1), 101-112.

[9] Das, U. D., Hossain, M. A. M., Ahamed, J.U. and Razzaq, M. E. A. (2022), Heat transfer and exergy analysis of a shell and tube heat exchanger using PGW based ZnO nanofluids. International Journal of Automotive and Mechanical Engineering, 19 (2), 9773-9789.

[10] Sundar, L.S., Singh, M. K. and Sousa, A. C. M. (2014), Enhanced heat transfer and friction factor of MWCNT–Fe3O4/water hybrid nanofluids. International Communications in Heat and Mass Transfer, 52, 73-83.

[11] Celen, A. (2022), Energy and exergy analysis of a shell and tube heat exchangers having smooth and corrugated inner tubes. Süleyman Demirel Üniversitesi Fen Bilimleri Enstitüsü Dergisi , 26 (1), 171-181.

[12] Huang, D., Wu, Z. and Sunden, B. (2016), Effects of hybrid nanofluid mixture in plate heat exchangers. Experimental Thermal and Fluid Science, 72, 190-196.

[13] Alshayji, A., Asadi, A. and Alarifi, I. M. (2020), On the heat transfer effectiveness and pumping power assessment of a diamond-water nanofluid based on thermophysical properties: An experimental study. Powder Technology, 373, 397-410.

[14] ANSYS. (2016), ANSYS Fluent 18.2, ANSYS Inc.

[15] Mousavi, S.M., Esmaeilzadeh, F. and Wang, X.P.. (2019), A detailed investigation on the thermo-physical and rheological behavior of MgO/TiO$_2$ aqueous dual hybrid nanofluid. Journal of Molecular Liquids, 282, 323-339.

[16] Izadi, M., Behzadmehr, A. and Jalali-Vahid, D. (2009), Numerical study of developing laminar forced convection of a nanofluid in an annulus. International Journal of Thermal Science, 48, 2119-2129.

RESEARCH ARTICLE

ECONOMIC FEASIBILITY ANALYSIS of a GRID-CONNECTED PV ENERGY SYSTEM: A CASE STUDY of KUTAHYA DUMLUPINAR UNIVERSITY, TÜRKİYE

Kerim KARABACAK[1*]

[1]Kütahya Dumlupınar Üniversity, Kutahya Technical Sci. Vocational School, Dept. of Electronics and Automation, Kütahya, kerim.karabacak@dpu.edu.tr, ORCID: 0000-0002-9724-4612

ABSTRACT

Due to their clean energy generation process, PV energy systems are an important alternative energy production system against fossil fuel-based energy production systems. However, it is important to make a clear and brief economic feasibility analysis before the installation of a PV energy system. The return time of the investment should have been calculated carefully. So, this paper presents an economic feasibility analysis of a grid-connected PV energy system. The system is planned to locate on the campus of Kutahya Dumlupinar University, Türkiye. The proposed system is planned to establish approximately 3000 m^2 of an unused field near a pond on the campus. The DC side power plant installed power capacity has been determined as 150kWp. The network side power of the system is determined as 125kW$_e$. The total cost of the system is determined and the monthly energy production of the proposed PV energy system in years is calculated according to solar radiation data. The overall profit of the system is calculated by years. It is found that the system will start to make profits at the middle of the 5th year of the investment.

Keywords: *Renewable energy systems, photovoltaic energy systems, feasibility analysis*

1. INTRODUCTION

These days, the usage of renewable energy sources for electricity production is increasing due to fossil fuels and coal-based electricity production having enormous pollution effects on the atmosphere. In the year 2019, renewable energy production is 11.41% of total energy production in the world (includes hydropower, solar, wind, geothermal, bioenergy, wave, and tidal), In the year 2019, without hydropower, the total renewable energy production in the world is 3137.47 TWh. In the year 2020, this production increased up to 3322.94 TWh. The change ratio of renewable energy production without hydropower for one year is 5.9%. The yearly representation of the world's electrical energy production based on hydroelectric, solar energy, wind energy, and other renewable energy sources is given in Figure 1 [1].

On the other hand, photovoltaic (PV) energy systems are one of the most common renewable energy-based electric production systems. In the year 2011, the total installed solar capacity in the world was 72.04 GW. In the year 2021, the world's total installed PV energy capacity is 707.5 GW and PV

energy systems constitute 3.27% of total renewable energy in the world's electricity production. So, the world's renewable energy installed power capacity has increased 9.82 times in a decade [1].
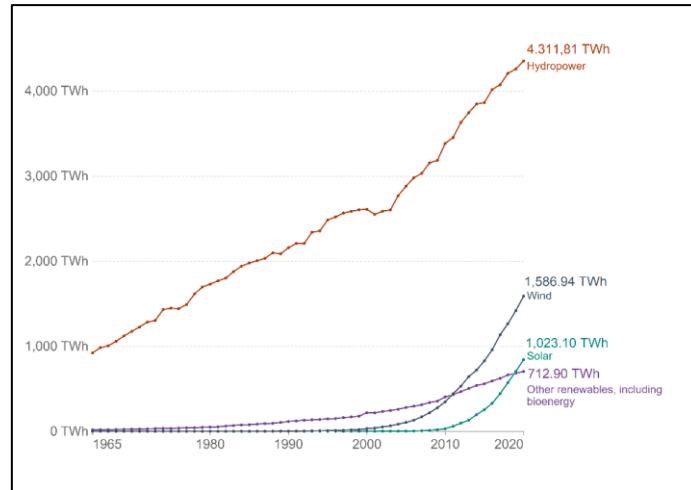
Figure 1. World renewable energy generation by years [1].

In Türkiye, renewable energy sources-based electricity production (without hydropower) was 5.75 TWh in 2011. In 2021, this value reached 61.3 TWh. It is seen that renewable energy production without hydropower is increased 5 times in one decade. In 2014, Türkiye's total installed PV power capacity was 0.07 GW. From the beginning of 2015, PV energy system investments have increased exponentially. In 2020, the total installed PV power capacity is increased to 6.67 GW. This shows that solar energy system investments are increased 95.28 times in 6 years. The total installed PV power capacity in Türkiye by years is shown in Figure 2 [1].
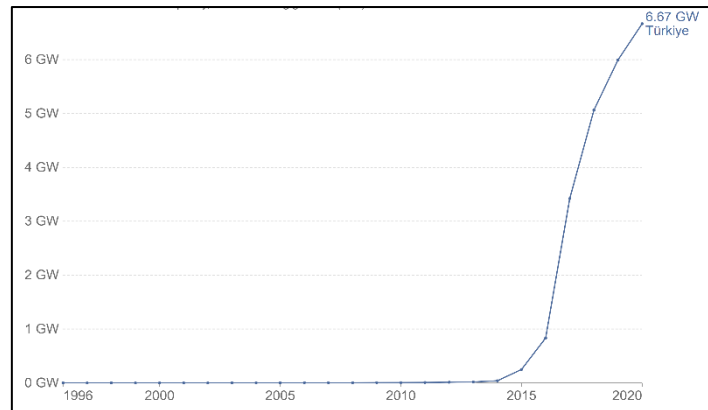
Figure 2. Total installed PV power capacity in Türkiye by years [1].

In the year 2011, PV energy systems constituted less than 0.01% of the total electricity production in Türkiye. In 2021, PV energy systems constitute 3.91% of the total electricity production of Türkiye.

The share of solar energy in total energy production in Türkiye is increased 391 times higher in one decade. Since the year 2018, the share of the PV electricity production of Türkiye is over the share of the PV electricity production of the world. The share of solar energy in electricity production in Türkiye and the world by years is illustrated in Figure 3 [1].
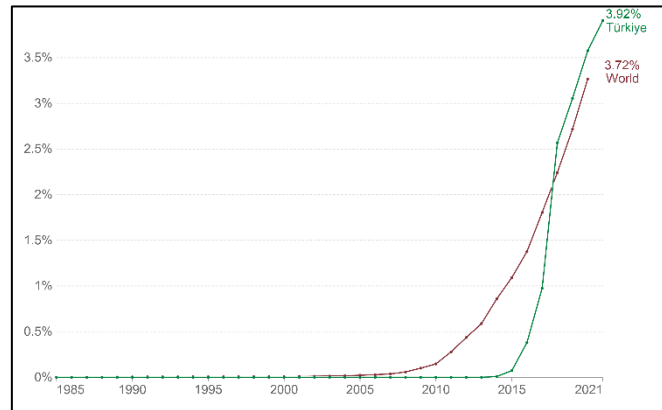
Figure 3. Share of the solar energy world and Türkiye by years [1].

In 2015, Türkiye's total electricity generation from solar energy was 0.19 TWh. In 2021, this production increased to 12.91 TWh. The change in the solar energy-based electricity generation in 6 years is 67.9 times. Figure 4 illustrates the total electricity generation from solar energy in Türkiye by years [1].
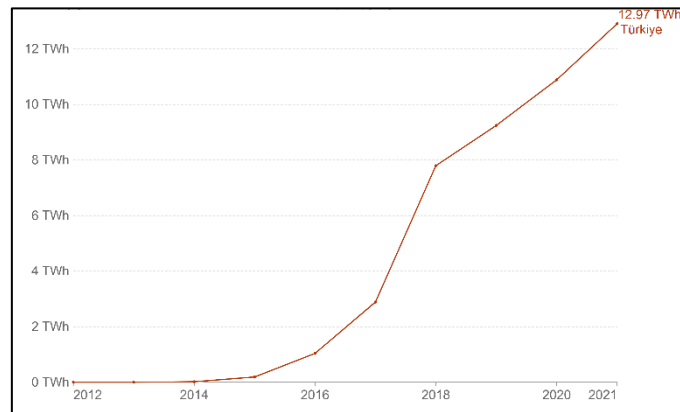
Figure 4. Total PV electricity generation in Türkiye by years [1].

In the literature, there are some studies about the economic feasibility analysis of PV systems in Türkiye and its neighbors. Celik [2] proposed a photovoltaic house concept that uses PV energy as the main energy source to assess the techno-economic feasibility of grid-connected photovoltaic systems in Türkiye. Abbasoglu et al. [3] examined economically and environmentally feasible places in Türkiye to build a 10 MW PV-grid connected solar photovoltaic power plant. Duman and Guler [4]

presented the economic analysis of grid-connected residential rooftop PV systems in nine locations in Türkiye.

Kalinci [5] investigated a PV array feasibility analysis for Bozcaada island, Istanbul. Akpolat et al. [6] presented a simulation study for the Rooftop Solar Photovoltaic System (RSPS) design and calculation for the faculty building at Marmara University in Istanbul. Aykut et al. [7] presented a techno-economic and environmental feasibility study of a hybrid grid-connected wind/PV/biomass energy system for Marmara University Goztepe Campus in Istanbul. Batman et al. [8] presented a feasibility study of grid-connected photovoltaic systems in Istanbul, Türkiye. In their study, power output and temperature data collected from PV modules in Istanbul, Türkiye in 2009. This data have been analyzed to determine solar power generation potential.

Caglayan [9] examined the technical and financial viability of a grid-connected 1 MW photovoltaic PV power plant in the province of Antalya, Türkiye. Karaveli et al. [10] presented the differences in the feasibilities of Photo Voltaic Solar Power Plant (PV SPP) installments in two Turkish cities (Antalya and Ordu) by using the Economic Feasibility Concept (EFC), Kirbas et al. [11] evaluated a feasibility of grid-connected PV SPP for the vicinity of Lake Burdur, Burdur, Türkiye. Their proposed PV SPP system is 1220 MW.

Cetinbas et al. [12] explained a design, performance analysis, and optimization of a hybrid microgrid that includes a PV energy plant for the hospital complex located on the Eskisehir Osmangazi University (ESOGU) campus. Taner [13] presented a techno-economic feasibility analysis of a PV SPP for Yapilcan village, Aksaray city, Türkiye. Adan et al. [14] determined the technical and economic evaluation of a standalone and on-grid hybrid system to supply power to the Department of Electrical and Electronics Engineering at Eskisehir Technical University. Ates and Salmanoglu [15] proposed an economic feasibility study for the installation of an on-grid PV plant was planned on the roof of Manisa Celal Bayar University Koprubasi Vocational School. Ayran and Aslan [16] presented a feasibility analysis for an unlicensed on-grid 336 kWh PV SPP at Sehzade Park in Kutahya, Türkiye. Akpinar et al. [17] proposed an economic feasibility analysis of a PV SPP for a house in Türkiye with a program that created a simulation model in the MATLAB GUI environment. Gurturk [18] presented a cost analysis of a PV SPP, which is located in Elazığ, Türkiye is calculated according to Levelized Cost Analysis (LCA) method. In that study, the payback period of investing in the solar power plant was calculated as 13 years.

Atikol et al. [19] demonstrated an economic feasibility assessment of a PV energy system in North Cyprus. Turjman et al. [20] proposed a 6 kW PV SPP with a wind energy system for Northern Cyprus. Sadati et al. [21] presented a microgrid of a PV array for a university campus-scale community on a Mediterranean island. Abujubbeh et al. [22] presented a techno-economic feasibility assessment for an on-grid PV-Wind hybrid system to cover a typical household annual energy demand in Amman, Jordan. Kassem et al. [23] examined the economic and financial assessments of solar and wind power potential for nine selected regions in Libya.

The main objective of this paper is to make an economic feasibility analysis of a grid-connected PV SPP, which is planned to be established in order to reduce the cost of electricity expenditure at Kütahya Dumlupinar University. The total PV SPP system cost, amount of electricity production, and the investment return time is examined. For optimal sizing of the proposed system, cost per watt comparison of various rated-power types of PV panels are investigated.

The study also aims to reduce the amount of carbon dioxide emitted from the generation of electrical energy using fossil fuels. With the publication of the study, awareness in the society about the use of renewable energy resources and the prevention of carbon emissions will be raised.

There are many other studies about the economic feasibility analysis of PV power systems. Although, the difference in this paper includes the calculation of the shadow distance of PV panels according to the sun's path. The worst-case scenario for the shading effect of PV panels in the year is calculated. The distance between PV panel strings is calculated accurately. So, the optimal sizing of the proposed PV SPP is achieved for economic feasibility analysis.

The remainder of this paper is organized as follows: In introduction part, Türkiye's renewable energy production change in years is given. Also, Türkiye's solar energy installed capacity change by years is interpreted. Then, a literature review is given about economic feasibility analysis of on-grid PV power systems. Then, the purpose of the study is given. In Materials and Methods section, the methodology is explained for the calculation of the sizing of the proposed PV SPP. In results section, the solar radiation falling on the panel surface, total possible energy production of the proposed PV SPP, monthly expected energy from the system is investigated. Then, PV SPP average turnkey installation cost is determined and cash flow statement of the investment in equity is examined. In Conclusion section, the benefits of the proposed system are explained. The planned improvements of the proposed system in the future are expressed.

2. MATERIALS and METHODS

In the investigation, it is seen that the five-years average annual total electricity consumption of Kutahya Dumlupinar University campus is 90.369.725 kWh [24]. In this study, it is planned to establish a grid-connected PV SPP on Kutahya Dumlupinar University Campus area in Kutahya, Türkiye. The electrical energy produced in the system will be sold to the electricity distribution company. Thus, it is planned less electricity bills will be paid as the amount of income to be obtained from the electrical energy produced by the installed system. The system is planned to run on-grid. There isn't any energy storage part is proposed to reduce the total cost of the system.

The selected PV SPP installation area is an empty area near the pond on the campus is a south-facing sloping land. The area is approximately 3000 m^2 (200m x 15m), The planned PV system location is given in Figure 5.

Figure 5. Planned installation place (in yellow rectangle),

2.1. Selection of PV Panels

Today, the most widely used PV technology is slice-based Crystalline Silicon (c-Si) technology and its market share is around 85%. So, within the scope of this project, it is planned to use c-Si based PV modules. In the market, it can be found c-Si structured PV panels in various rated-power values with various prices. So, for the proposed system, PV panels with at various rated-power values are investigated for cost per watt. (450 watts, 400 watts, 350 watts, 285 watts, 250 watts, 175 watts, ...etc.) In the investigation, it is seen that the PV panel with the lowest cost per watt is the monocrystalline panels with a rated-power of 285 watts. Figure 6 shows the comparison of different c-Si structured PV panels with cost per watt.
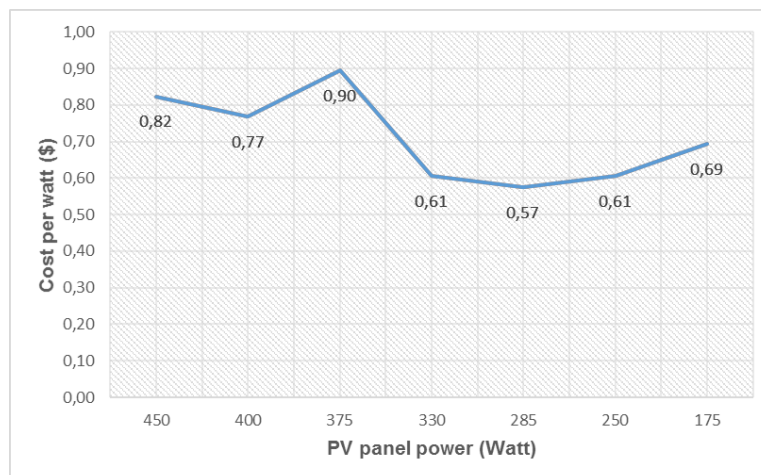
Figure 6. Cost-per-watt comparison of PV panels in the market.

2.2. Determining the Distance Between PV Panel Strings

For determination of the distance between PV panel strings, the shading distances of PV panels has to be calculated. For this reason, sun path chart of the proposed PV SPP location is examined. Figure 7 shows one-year sun path chart for 39.29° North Latitude and 29.54° East Longitude. According to the sun path chart, the system is planned to start produce energy from 9:00 AM to 3:00 PM efficiently.
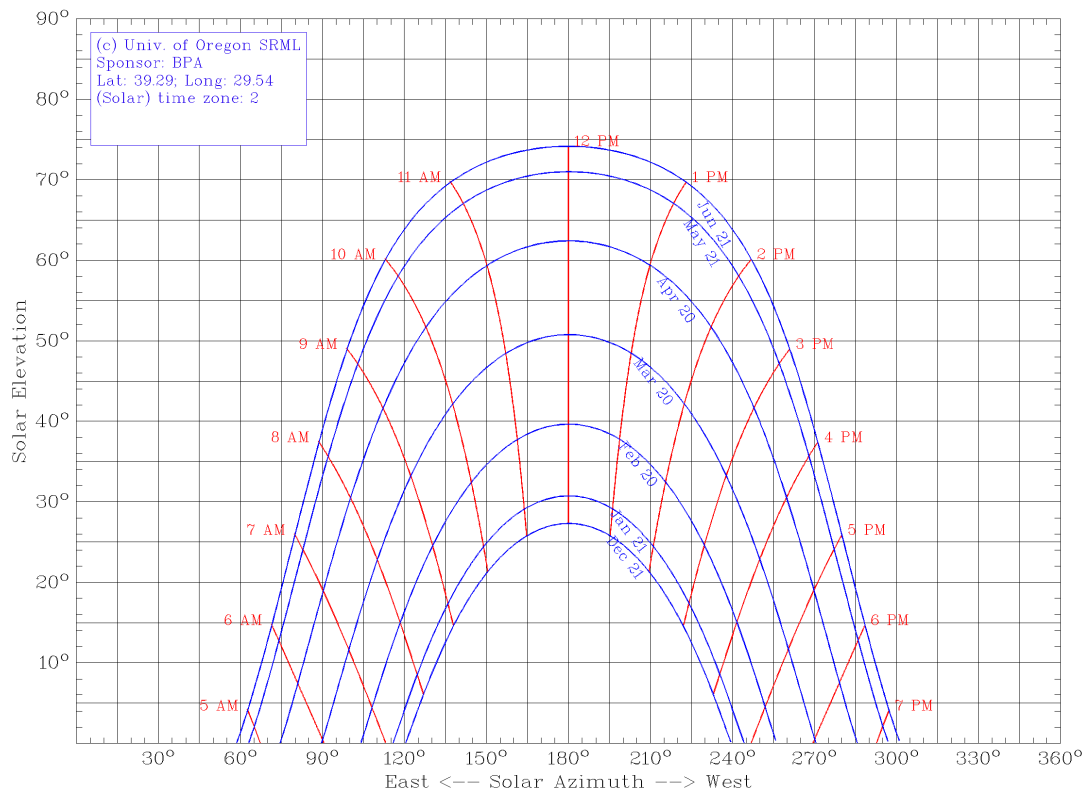
Figure 7. Sun path chart for 39.29° North, 29.54° East [25].

The worst scenario for the shading effect, is 21th of December due to solar elevation angle (α) reaches the minimum value in the year. So, the shadow length of the PV panels become maximum. In Figure 7, it is seen that the solar altitude angle on 21th of December at 9:00 AM is 15°. Symmetrically, in the same day, the solar altitude angle at 3:00 PM is 15°. So, maximum shading distance calculation can be made for 21th of December at 9:00 AM.

Figure 8 illustrates the calculation method of maximum shading distance. The black lines indicate the shadow area of one PV panel. In the proposed system, PV panel dimensions are 1 m width and 1.63 m length. The PV panel tilt angle (denoted as β) is chosen 31° for the proposed location, according to similar studies made neighborhood of Kutahya [26]. The length of the panel is denoted as *l*. So, the height of the panel (denoted as *h*) can be found from the blue triangle in the figure by Equation 1.
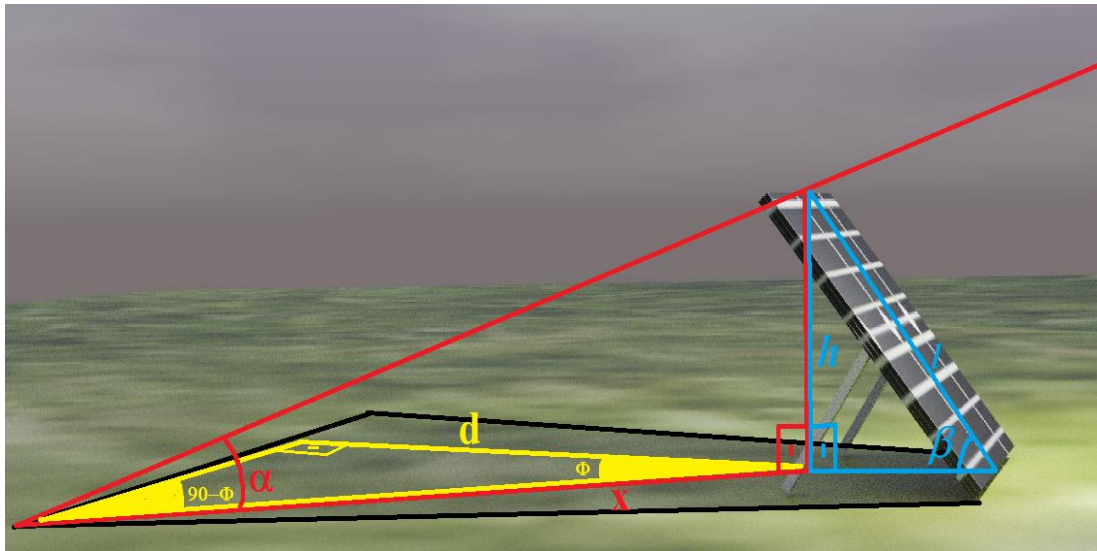
Figure 8. Calculation of maximum shadow distance

$$h = l.sin\beta \tag{1}$$
$$h = 1.63.\sin(31°)$$
$$h = 0.839 \text{ meter}$$

When the worst case scenario is considered, the sun elevation angle (denoted as α) is 15°. Thus, from the red triangle, the distance between the edge of the shadow and the projection of the upper edge of the panel to the ground can be found (denoted as *x*) by Equation 2.

$$x = h/tan(\alpha) \tag{2}$$
$$x = 0.839/0.267$$
$$x = 3.142 \text{ meter}$$

From the sun path chart, the azimuth angle (denoted as Φ) on 21th o December at 9:00 AM is 52.5° (180°-127.5°), So, the shadow length (denoted as d) can be calculated by Equation 3.

$$d = x.sin(90 - 52.5) \tag{3}$$
$$d = 1.91 \text{ meter}$$

In practice, the calculated shadow length value can be round up to 2 meters.

2.3. The System Overall Properties
The length of proposed field of the PV SPP is measured as 200 m. In order for the carrier vehicles to be used for the installation to maneuver easily, it is foreseen that there will be 12m of space at the beginning and end of each PV panel string. The surface area of a 285 watts-rated monocrystalline PV panel is 1.63 m^2 (1 m x 1.63 m), So, the length of one PV panel string is considered as 176 meters. Thus, one PV panel string is considered as have 176 PV panels in series. The width of the planned

installation field is 20 m. In order to prevent shading lost for the proposed PV SPP, the shading distance between two panel string must be at least 2 meter in the 39th North latitude as mentioned in section 2.2. So, when walking ways between the PV panel strings and shadowing spaces are considered, it is decided 3 PV panel strings are suitable for the proposed PV SPP field. Thus, the total PV panels in the proposed PV system is determined as 528 (176x3) pieces.

Table 1. General information for the planned PV system.

City	Kutahya
Location	Kutahya Dumlupinar University Campus Area
Geographical location	39.474762°N- 29.903181°E
Considered Radiation Data	European Union Photovoltaic Geographical Information System (PVGIS)
Planned PV SPP Installed Power	125kW$_e$ (150 kW$_p$)
Number of Inverters	5 x 25kW Grid Connect Inverters
PV Panel Surface Area (Including Shadow Spaces)	~ 3000 m^2
The number of PV Modules:	528 pcs (PV Module with 285Wp Power and c-Si Technology each)
Panel efficiency	16.3 %
Inverter efficiency	98 %
Cable losses	1 %
Other losses (Temperature, shading, dust, etc.)	10 %
Total system efficiency	14.23 %

The overall summary of the proposed PV SPP and important system parameters are given in Table 1. On the DC side, 528 pieces of 285-watt rated-power PV panels are planned to be used. So, the planned DC side power is calculated as 150 kWp. The selected PV panels are mono-crystalline type and their efficiency is 16.3%. The inverter side power is proposed as 125 kW. There are five 25kW rated power three-phase on-grid string inverters in the proposed system. Each inverter is connected to 106 PV panels on the DC power side. On the AC power side, each inverter is connected to the national power network in parallel. Considering inverter losses, panel losses, cable losses, temperature losses, etc., total system efficiency is determined as 14.23%.

3. RESULTS

Considering the solar energy potential of the project installation region, the amount of radiation per unit area on a photovoltaic module placed at a fixed angle at the optimum tilt angle (31 degrees) is 4847.00 Wh/m^2/day [27]. This value is approximately 1.5 times Türkiye's average of 3600 Wh/m^2/day. Therefore, a PV SPP to be established in the examined site location is in a more advantageous position than the average of Türkiye in terms of both the electricity generation potential and the return time of the initial investment cost.

In Table 2, solar radiation coming to the horizontal surface at the installation site and solar radiation coming to the panel surface placed at the best tilt angle (31°) is compared. As the tilt angle of the panel approaches horizontal in summer, it is understood that more solar radiation reaches the panel

surface. On the other hand, in other months, much more solar radiation comes to the surface of the panel placed at the best tilt angle.

Table 2. Radiation coming to the horizontal surface at the installation site (H_h, Wh/[m^2.d]) and radiation coming to the panel surface placed at the best tilt angle (H_{opt}, Wh/[m^2.d]),

Month	H_h Wh/[m^2.d]	H_{opt}, Wh/[m^2.d]
January	1.680,32	2.412,58
February	2.399,64	3.137,86
March	3.562,90	4.189,68
April	4.871,67	5.161,00
May	5.809,68	5.680,00
June	6.779,00	6.349,00
July	7.544,84	7.228,06
August	6.844,19	7.168,06
September	5.037,33	5.904,33
October	3.311,94	4.376,13
November	2.413,67	3.781,67
December	1.700,65	2.669,68
Annual average	4.329,65	4.838,17

The daily and monthly energy production values for the 150kWp PV SPP to be placed at the optimum angle (31°) on Kutahya Dumlupinar University Campus are shown in Table 3. The average production in winter is 10332 kWh. The average monthly production in spring is 18580 kWh. The average monthly production in summer months is 23900 kWh. The average monthly production in autumn months is 16778 kWh. The installation site's expected annual electrical energy generation will be approximately 208781.38 kWh.

Table 3. Daily and monthly average electricity generation of proposed PV SPP.

Months	kWh/150kWp-day	kWh/150kWp-Month
January	309,10	9.582,00
February	393,46	11.016,89
March	526,40	16.318,39
April	627,45	18.823,61
May	664,50	20.599,48
June	723,70	21.710,98
July	809,74	25.101,86

August	802,94		24.891,07
September	677,72		20.331,67
October	519,25		16.096,78
November	463,61		13.908,21
December	335,50		10.400,44
Total kWh/year			208 781,38

The total investment cost of the proposed PV SPP is calculated as 145000$ + Tax. In the investment costs, 285W mono c-Si PV panels, 25kW on-grid string inverters, remote monitoring system, DC and AC electric panels, Solar DC cables, AC cables, panel carrier constructions, grounding materials, infrastructure and construction works, cable trays, etc. are considered. The investment costs of the proposed PV SPP that specified in Section 2 are given in Table 4 below.

Table 4. PV SPP Average Turnkey Installation Cost.

System Equipment	Quantity	Unit	Total cost ($)
285Wp Mono c-Si PV Panel	528	Number	
25kW On-grid String Inverter	5	Number	
Remote Monitoring System	1	Set	
DC and AC Electric Panels	1	Set	
Solar DC cable 1x4mm^2	6.000	meter	
AC Cable	1	Set	
Panel Carrier Construction	1	Set	
Grounding Materials and Apparatus	1	Set	145.000 $+Tax
Infrastructure and Construction Works	1	Set	
Cable Trays	1	Set	
Lightning, Fire, and Electrical Protection Components and Warning Signs	1	Set	
Process Management, Consulting, Installation, Assembly, Cabling, Labor, and other related costs	1	Set	

According to the calculations, it is predicted that the investment made with equity will pay back its entire cost at the middle of the 5th year of the investment. The expected cumulative return from the system at the end of the 25th year is calculated as 1 030 482.54 $. Repayment and cash flow details are presented in Table 5. In all calculations, it is assumed that the energy production performance of the system decreases by 1% every year. In addition, it has been taken into account that the energy obtained from the system is deducted from the current consumption, the price of purchasing energy from the current grid is 0.1333 $ cents, and the sales prices of the grid have increased by 5% on an

annual basis. In addition, since all of the electrical energy produced will be offset against the current consumption, no network usage fee has been taken into account.

Table 5. Cash Flow Statement of Investment in Equity.

	1. year	2. year	3. year	4. year	5. year
Investment Cost ($)	-$171.100,00	$0,00	$0,00	$0,00	$0,00
Annual Energy Production (kWh)	208.781,38	207.319,91	205.868,67	204.427,59	202.996,60
Network Price ($)	$0,1333	$0,1400	$0,1469	$0,1543	$0,1620
Annual Cash Flow ($)	$27.837,52	$29.024,79	$30.262,69	$31.553,40	$32.899,15
Cumulative Cash Flow ($)	-$143.262,48	-$114.237,70	-$83.975,00	-$52.421,60	-$19.522,45

	6. year	7. year	8. year	9. year	10. year
Investment Cost ($)	$0,00	$0,00	$0,00	$0,00	$0,00
Annual Energy Production (kWh)	201.575,62	200.164,59	198.763,44	197.372,10	195.990,49
Network Price ($)	$0,1701	$0,1786	$0,1876	$0,1969	$0,2068
Annual Cash Flow ($)	$34.302,30	$35.765,29	$37.290,68	$38.881,13	$40.539,41
Cumulative Cash Flow ($)	$14.779,85	$50.545,14	$87.835,82	$126.716,95	$167.256,36

	11. year	12. year	13. year	14. year	15. year
Investment Cost ($)	$0,00	$0,00	$0,00	$0,00	$0,00
Annual Energy Production (kWh)	194.618,56	193.256,23	191.903,43	190.560,11	189.226,19
Network Price ($)	$0,2171	$0,2280	$0,2394	$0,2514	$0,2639
Annual Cash Flow ($)	$42.268,42	$44.071,16	$45.950,80	$47.910,60	$49.953,99
Cumulative Cash Flow ($)	$209.524,78	$253.595,95	$299.546,74	$347.457,35	$397.411,33

	16. year	17. year	18. year	19. year	20. year
Investment Cost ($)	$0,00	$0,00	$0,00	$0,00	$0,00
Annual Energy Production (kWh)	187.901,61	186.586,29	185.280,19	183.983,23	182.695,35
Network Price ($)	$0,2771	$0,2910	$0,3056	$0,3208	$0,3369
Annual Cash Flow ($)	$52.084,53	$54.305,93	$56.622,08	$59.037,01	$61.554,94
Cumulative Cash Flow ($)	$449.495,86	$503.801,79	$560.423,87	$619.460,88	$681.015,82

	21. year	22. year	23. year	24. year	25. year
Investment Cost ($)	$0,00	$0,00	$0,00	$0,00	$0,00

Annual Energy Production (kWh)	181.416,48	180.146,56	178.885,54	177.633,34	176.389,91
Network Price ($)	$0,3537	$0,3714	$0,3900	$0,4095	$0,4300
Annual Cash Flow ($)	$64.180,26	$66.917,54	$69.771,58	$72.747,34	$75.850,01
Cumulative Cash Flow ($)	$745.196,08	$812.113,62	$881.885,20	$954.632,53	$1.030.482,54

As it is shown in Figure 9, the proposed system starts to gain profit in the middle of the 5th year of the investment. At the end of the 6th year of the investment, the cumulative cash flow will be 14.779,85 $. At the end of the 10th year of the investment, the cumulative cash flow reaches 167.256,36 $. In a 25 years of perspective, the total profit of the system is calculated as 1.030.482,54 $.
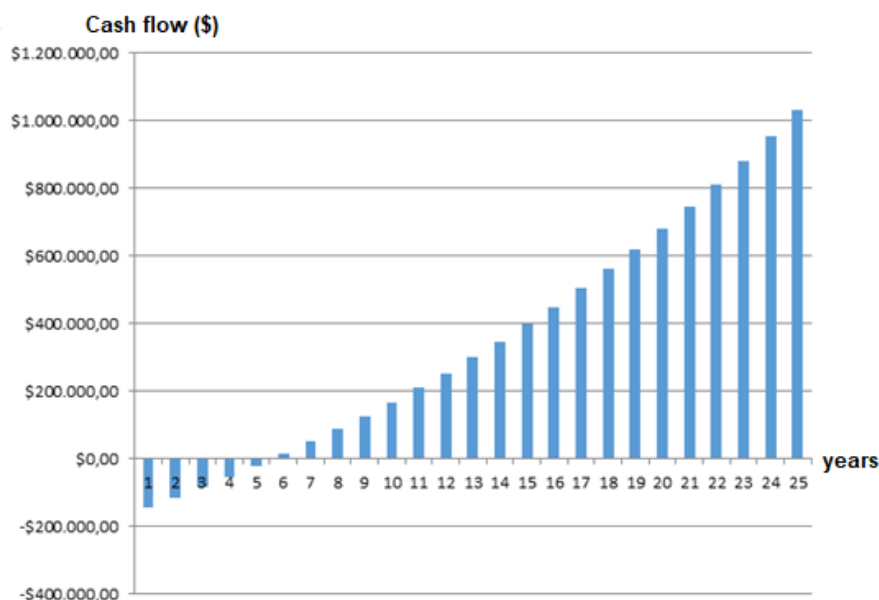
Figure 9. Cash Flow Balance of Investment with Equity.

With the establishment of the proposed system, the electrical energy transferred to the electricity grid will be a renewable energy-based energy, and it will also have an impact on the CO_2 footprint. According to the International Energy Agency (IEA) data, Türkiye's average grid emission intensity is 459.6 g/kWh. In return, the amount of CO_2 emission in the current grid of 208781.38 kWh energy, which is expected to be produced from the proposed system, is approximately 95.96 tons/year. On the other hand, lifetime emission values of silicon solar panels are in the range of 22-46 g/kWh. In this case, the CO_2 footprint in the proposed system is expected to be 7.30 tons/year (by taking an average value of 35 g/kWh), With the system going into production, 88.65 tons of CO_2 emissions per year will be avoided.

4. CONCLUSION

In this study, an economic feasibility analysis is made for a PV SPP which is planned to locate in the campus area of Kutahya Dumlupinar University. First, renewable energy production in the world and Türkiye's situation is investigated. The PV energy-based renewable energy production of Türkiye is interpreted by years.

Then, the area where the PV SPP will be installed on the Kütahya Dumlupınar University campus was examined. A 3000 m^2 area where face to south is selected for PV SPP installment. Different rated-power PV panels are compared by cost per watt. Contrary to popular belief, despite the increase in PV panel rated power, it has been observed that the cost per watt has not decreased. The minimum cost per watt value is achieved for 285 watt c-Si monocrystalline PV panels.

Shading distance of PV panels is calculated. Shading distance of PV panels are calculated not only by using solar altitute angle, but olso used combination of solar azimuth angle and solar altitude angle together. The distance between two PV panel string is determined as 2 meters. When longer distances between two PV panel strings cause less installed power capacity, shorter distances cause decrease in power generation during the day.

After the shading distance is calculated, the dimensions of the proposed PV SPP were determined. The proposed PV SPP is considered as 3 PV panel strings and each string has 176 PV panels in series. So, in the proposed system, there are 528 pieces of 285-watt power-rated PV panels, and the total installed capacity of the proposed PV SPP is considered 150 kWp. On the AC power side, it is considered that 5 pieces of 25kW power-rated three phase on-grid string inverter are used that each inverter connected to 106 pieces of 285-watt power-rated PV panels.

The solar radiation coming to the horizontal surface at the installation site are investigated. Grid-connected crystalline silicon-based PV SPP basic efficiency parameters are presented. Then, the daily and monthly energy production of the planned PV SPP is examined. In the results, the system total cost is calculated as 145000$ and the annual energy production of the planned system is calculated as approximately 208000.00 kWh/year. It's found that the system will start to make profits at the middle of the fifth year of investment.

The future workflow for further studies can be as follows:

- Comparision of an on-grid PV SPP and an autonomous (off-grid) PV SPP for the campus can be made.

- Distrubuted PV SPPs for top roof applications of some faculty buildings in the campus can be planned.

- Feasibility analysis can be made with considering using wind-PV hybrid systems.

ACKNOWLEDGEMENT

REFERENCES

[1] *Our world in data - How much of our primary energy comes from renewables*. [cited 2022 10.03.2022]; Available from: https://ourworldindata.org/renewable-energy.

[2] Celik, A. N. (2006), Present status of photovoltaic energy in Turkey and life cycle techno-economic analysis of a grid-connected photovoltaic-house. *Renewable and Sustainable Energy Reviews, 10*(4), 370-387.

[3] Abbasoglu, S., Nakipoglu, E., and Kelesoglu, B. (2011), Viability analysis of 10 MW PV plant in Turkey. *Energy Education Science and Technology Part a-Energy Science and Research, 27*(2), 435-446.

[4] Duman, A. C., and Guler, O. (2020), Economic analysis of grid-connected residential rooftop PV systems in Turkey. *Renewable Energy, 148*, 697-711. doi:10.1016/j.renene.2019.10.157

[5] Kalinci, Y. (2015), Alternative energy scenarios for Bozcaada island, Turkey. *Renewable and Sustainable Energy Reviews, 45*, 468-480. doi:10.1016/j.rser.2015.02.001

[6] Akpolat, A. N., Dursun, E., Kuzucuoglu, A. E., Yang, Y. H., Blaabjerg, F., and Baba, A. F. (2019), Performance Analysis of a Grid-Connected Rooftop Solar Photovoltaic System. *Electronics, 8*(8), 20. doi:10.3390/electronics8080905

[7] Aykut, E., and Terzi, U. K. (2020), Techno-economic and environmental analysis of grid connected hybrid wind/photovoltaic/biomass system for Marmara University Goztepe campus. *International Journal of Green Energy, 17*(15), 1036-1043. doi:10.1080/15435075.2020.1821691

[8] Batman, A., Bagriyanik, F. G., Aygen, Z. E., Gul, O., and Bagriyanik, M. (2012), A feasibility study of grid-connected photovoltaic systems in Istanbul, Turkey. *Renewable and Sustainable Energy Reviews, 16*(8), 5678-5686.

[9] Caglayan, N. (2020), ENERGY AND ECONOMIC FEASIBILITY OF A GRID-CONNECTED SOLAR PV SYSTEM IN ANTALYA, TURKEY. *Fresenius Environmental Bulletin, 29*(3), 1581-1589.

[10] Karaveli, A. B., Akinoglu, B. G., and Soytas, U. (2018), *Measurement of economic feasibility of photovoltaic power plants-application to Turkey*. Paper presented at the 2018 International Conference on Photovoltaic Science and Technologies (PVCon),

[11] Kirbas, İ., and ÇİFCİ, A. (2019), Feasibility study of a solar power plant installation: a case study of lake Burdur, Turkey. *El-Cezerî Journal of Science, 6*(3), 830-835.

[12] Cetinbas, I., Tamyurek, B., and Demirtas, M. (2019), Design, Analysis and Optimization of a Hybrid Microgrid System Using HOMER Software: Eskisehir Osmangazi University Example. *International Journal of Renewable Energy Development-Ijred, 8*(1), 65-79. doi:10.14710/ijred.8.1.65-79

[13] Taner, T. (2019), A feasibility study of solar energy-techno economic analysis from Aksaray city, Turkey. *J Journal of Thermal Engineering, 3*(5), 1-1.

[14] Adan, H. K., and Basaran Filik, U. (2021), Technical and economic evaluation of a standalone and on grid hybrid renewable energy: A case study at Eskisehir Technical University. *Sigma Journal of Engineering and Natural Sciences-Sigma Muhendislik Ve Fen Bilimleri Dergisi, 39*(2), 184-194. doi:10.14744/sigma.2021.00008

[15] Ates, A. M., and Salmanoğlu, F. (2017), *A Project That Provides Electricity from Solar Energy for Vocational School Campus.* Paper presented at the Solaris 2017 Conference Proceedings.

[16] Ayran, Z. A., and Aslan, Y. KÜTAHYA İLİ GÜNEŞ ENERJİ POTANSİYELİNİN ARAŞTIRILMASI VE ÖRNEK BİR GÜNEŞ ENERJİ SANTRALİNİN EKONOMİK ANALİZİ. *Journal of Scientific Reports-C, 1*(June 2020), 17-37.

[17] Akpinar, K. N., Bilu, A. C., and Kekezoglu, B. (2019), MATLAB GUI Model for PV System Feasibility of a House Electricity Consumption in Turkey. *European Journal of Engineering and Natural Sciences, 3*(2), 27-31.

[18] Gurturk, M. (2019), Economic feasibility of solar power plants based on PV module with levelized cost analysis. *Energy and Buildings, 171*, 866-878.

[19] Atikol, U., Abbasoglu, S., and Nowzari, R. (2013), A feasibility integrated approach in the promotion of solar house design. *International Journal of Energy Research, 37*(5), 378-388. doi:10.1002/er.3025

[20] Al-Turjman, F., Qadir, Z., Abujubbeh, M., and Batunlu, C. (2020), Feasibility analysis of solar photovoltaic-wind hybrid energy system for household applications. *Computers and Electrical Engineering, 86*, 106743.

[21] Sadati, S. M. S., Jahani, E., Taylan, O., and Baker, D. K. (2018), Sizing of Photovoltaic-Wind-Battery Hybrid System for a Mediterranean Island Community Based on Estimated and Measured Meteorological Data. *Journal of Solar Energy Engineering-Transactions of the Asme, 140*(1), 12. doi:10.1115/1.4038466

[22] Abujubbeh, M., Marazanye, V. T., Qadir, Z., Fahrioglu, M., and Batunlu, C. (2019), *Techno-economic feasibility analysis of grid-tied PV-wind hybrid system to meet a typical household demand: Case study-amman, Jordan.* Paper presented at the 2019 1st Global Power, Energy and Communication Conference (GPECOM),

[23] Kassem, Y., Camur, H., and Aateg, R. A. F. (2020), Exploring Solar and Wind Energy as a Power Generation Source for Solving the Electricity Crisis in Libya. *Energies, 13*(14), 28. doi:10.3390/en13143708

[24] *Greenmetric Detail Rankings 2021 - Kutahya Dumlupinar University*. [cited 07.06.2022]; Available from: https://greenmetric.ui.ac.id/rankings/overall-rankings-2021/dpu.edu.tr.

[25] *Sun path chart of 39.29 North, 29.54 East*. [cited 2022 09.06.2022]; Available from: http://solardat.uoregon.edu/SunChartProgram.html.

[26] Karafil, A., Ozbay, H., Kesler, M., and Parmaksiz, H. (2015), *Calculation of optimum fixed tilt angle of PV panels depending on solar angles and comparison of the results with experimental study conducted in summer in Bilecik, Turkey*. Paper presented at the 2015 9th International Conference on Electrical and Electronics Engineering (ELECO),

[27] *European Union Photovoltaic Geographical Information System (PVGIS)*, 10.06.2022]; Available from: https://re.jrc.ec.europa.eu/pvg_tools/en/.

RESEARCH ARTICLE

ROLE of Pt, Cu, Au and Cr UNDERLAYERS on EXCHANGE BIAS PROPERTIES in Pt/Py/IrMn THIN FILMS

Mustafa ÖZTÜRK[1*]

[*1]Gebze Technical University, Department of Physics, Gebze, mozturk@gtu.edu.tr, ORCID: 0000-0002-4564-3435

ABSTRACT

Herein, the structural and magnetic properties of polycrystalline UL-X/Pt/Py/IrMn thin films were studied to observe the role of an underlayer on the exchange bias properties. Thin films with Pt, Cu, Au or Cr underlayers (UL-X) were deposited at room temperature by magnetron sputtering. The structural properties of the samples were investigated to analyze the layer thicknesses, material densities, interface roughnesses, and crystal structures of the samples. Magnetic characterization measurements were performed to obtain the sign and the value of exchange bias properties in the samples. The differences in the sign and the value of exchange bias effect in the samples with different underlayers are mainly explained by discussing the effects of lattice parameters and growth conditions. On this basis, one would expect that these results will help in designing new spintronic devices.

Keywords: *Magnetic multilayers, exchange bias, buffer layer, underlayer*

1. INTRODUCTION

Ultrathin magnetic multilayers are elementary units in spintronics applications such as magnetic random-access memories (MRAM), magnetic data storage devices, and magnetic sensors [1, 2]. For these spintronic applications, the need for reliable, energy-efficient, robust, faster, versatile, rugged, smaller, and non-volatile devices makes the wise design of multilayers more important.

Exchange bias (EB) is defined as the shift of hysteresis loops of a ferromagnetic (FM) layer when it is in close contact with an antiferromagnetic (AF) layer [3]. In the research field of magnetic multilayers, exchange-biased thin films with FM/AF layers have recently taken much notice [4-10]. Because the coercive field (H_C) values and the shift of hysteresis loops in FM layers can easily be adjusted with structural changes [11, 12] with the help of the EB effect. In recent years, several works have reported the interaction between the electrical current and the exchange-biased multilayers [4-7]. The value and the direction of the EB effect are very important for such kinds of work. Current or voltage interaction with EB is remarkable because the magnetization can be controlled with low energy consumption for highly efficient new generation devices through the current or voltage instead of the external magnetic field [6]. Particularly, spin-orbit torque (SOT) is a promising method for switching the magnetic properties in exchange-biased multilayers since SOT is generated simply by passing an electric current through a heavy metal (HM) [5-7, 13-20]. The SOT method can be applied

in EB structures as HM/FM/AF multilayers [6, 7, 21]. In such methods, the effective field can strongly depend on the chosen HM layer, e.g., the usage of Ta or Pt can differ the sign of spin Hall angle in the multilayers [22]. Apart from the HM, when creating a sample stack for such studies, a layer that is called an underlayer (UL) (or seed layer or buffer layer) can be placed between the substrate and the HM. The underlayers are used for reasons such as strengthening the crystal structure of the system, ensuring good adhesion of the thin film to the substrate, or reducing the roughness between the subsequent surfaces [12, 23]. Indeed, a UL can play a vital role in the stack by strongly affecting not only the structural properties but also the magnetic properties [23-26].

In this paper, we analyze how the H_C and exchange bias field (H_{EB}) parameters can be adjusted in principle by varying the UL material under the HM/FM/AF stacks. The contribution of UL to the magnetic properties was investigated by growing Pt, Cu, Au or Cr ULs under the sample systems consisting of exchange-biased Pt/Py/IrMn multilayers. The first Pt in the stack is designed as an HM but its usage as a UL is also analyzed. Our results with different ULs suggest that exchange bias properties at the interface of FM/AF can be modified considerably through UL engineering, which has a not to be underestimated indirect effect of UL on the interface of FM and AF layers.

2. EXPERIMENTAL DETAIL

In this article, four polycrystalline thin films with UL-X (5 nm)/ Pt (8 nm)/ Py(6 nm)/ IrMn(12 nm)/ Pt(3 nm) layers were grown on top of Si/SiO$_2$ substrates, as given in figure 1a, by using a six-gun sputtering chamber. The dimensions of the used substrates were $5 \times 10 \times 0.5$ mm. The difference between the four samples was their ULs which were used between the substrates and HM. A 5nm of Pt, Au, Cu or Cr layer was chosen as a UL-x in the stacks. It is aimed to make comparisons between their functionalities as a UL for an exchange-biased magnetic multilayer. To define the samples in the article easily, they are shortly named by using their UL types as UL-Pt, UL-Au, UL-Cu and UL-Cr. The additional presence of 8 nm Pt after the UL-Xs in all samples is because Pt typically promotes in-plane anisotropy during the growth of the FM layer [22]. The top Pt capping layers are used in the stacks to protect the stacks from outer oxidation.

Ferromagnetic Py and antiferromagnetic IrMn in the study were grown from Ni$_{80}$Fe$_{20}$ and Ir$_{22}$Mn$_{78}$ alloyed targets, respectively. The thickness values of both Py and IrMn were chosen after several preliminary trials until a significant EB effect was observed at RT. Then the samples of this study were grown with these nominal values. IrMn has a Néel temperature much higher than the RT [27, 28]. This helps to provide good magnetic and thermal stability during the exchange interaction of FM/ AF.

The top schematic view drawing of the substrate position and the relative target gun positions in the sputter chamber was given in figure 1b. During the depositions, the substrate positions to the targets has been kept constant, and their long sides were perpendicular to the projection of the growth direction of Py.

The base pressure of the chamber was about 10^{-8} mbar before the depositions of each sample. During the sputtering, Ar pressure was kept around 10^{-3} mbar. To avoid any thermal interdiffusion at the FM/AF interface, samples were deposited at RT.

For the structural characterization of the samples, X-Ray Reflectivity (XRR) and X-ray diffraction (XRD) measurements have been performed by Rigaku Smartlab and Bruker D8 Advance X-Ray diffractometers, respectively. The magnetic properties of the samples were recorded by using a homemade magnetooptical Kerr effect (MOKE) measurement setup [29]. This homemade MOKE system consists of a He-Ne laser with a wavelength of 632.8 nm and an electromagnet that applies magnetic fields up to 1.6 Tesla. During MOKE measurements, the applied magnetic field angle was varied along the film plane. The azimuthal angle (Φ_H) given in figure 1c has been varied but the polar angle (Θ_H) has always been kept constant. This measurement geometry corresponds to the so-called longitudinal MOKE (LMOKE) geometry. Here, the angle $\Phi_H=0°$ was determined before the sample growth with the expectation that the easy axis of the ferromagnetic layer is parallel to the long side of the samples. All magnetic measurements of this article are performed at RT.

Layer thicknesses of the samples were controlled by the deposition time after having a careful growth rate calibration. The growth rate was determined as a result of the analysis of the XRR measurements of thick preliminary samples prepared before this study.
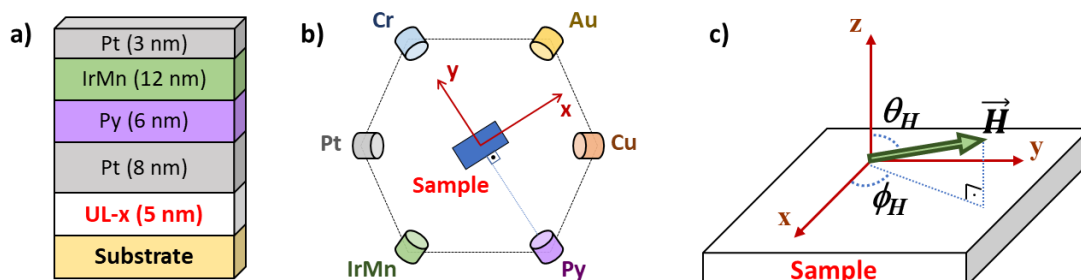
Figure 1. Schematic drawing of (a) the grown sample stack, (b) the gun positions in the sputter chamber and (c) magnetic property measurement geometry of samples. Here in (c), $\vec{H}$ defines the applied magnetic field to the sample and Φ_H defines the angle that the *xy* projection of the applied magnetic field makes with the *x*-axis.

3. RESULTS AND DISCUSSION

Figure 2a shows the XRD patterns of the polycrystalline samples. From the XRD patterns, the peaks at $2\Theta = 39.8°$ and $38.1°$ can be attributed to Pt (111) and Au (111) textures, respectively. From the XRD patterns in figure 2a, it can be seen that all the samples show a remarkable fcc Pt (111) texture. Almost all Pt (111) peaks are shifted compared to the bulk materials, which are thought to result from mechanically induced strain during deposition. The lattice constant of a bulk Pt (111) reflection is known as 3.92 Å. The calculated lattice constant from the Pt (111) layers is found 3.90 ± 0.01 Å, 3.92 ± 0.01 Å, 3.87 ± 0.01 Å and 3.88 ± 0.01 Å for UL-Pt, UL-Au, UL-Cu and UL-Cr samples, respectively. XRD measurements have been performed between $2\Theta = 20°$ and $2\Theta = 85°$. No crystalline peaks for NiFe, IrMn, Cu and Cr textures are observable in the samples. Additionally, XRR measurements have been performed for the samples to characterize their thicknesses and interface roughnesses. The XRR data and theoretical simulation results for the samples are shown in figure 2b. Simulations were made by using Commercial Rigaku GlobalFit software. The data obtained by the simulations are compatible with the nominal values of the films and are given in Table I. Since the thicknesses of all layers in the samples are the same, the peak positions in the graphs seemed very similar especially up to $2\Theta=2°$. It shows a consistency between the growth processes of all samples.

From the simulation data, it is calculated that the roughness values in the sample are relatively large. Since all elements used in sputtering systems can form alloys, these roughness values can be attributed to the interdiffusion of sputtered materials [30].
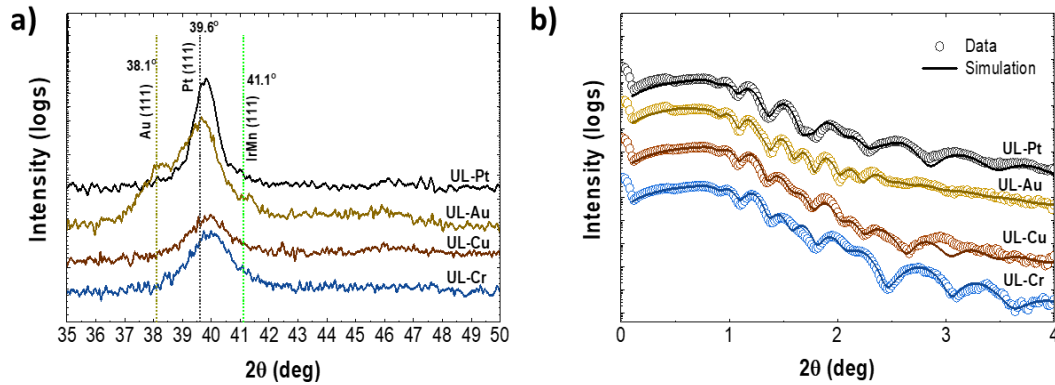
Figure 2. XRD patterns for the samples (a). The XRR data and theoretical simulation of the samples (b). Here in (b), open circles represent reflectivity data and lines indicate the fit of simulation data.

Table I. XRR simulation parameters for the samples.

Layer	Density [g/cm3]	Thickness [nm]				Roughness [nm]			
		UL-Pt	UL-Au	UL-Cr	UL-Cu	UL-Pt	UL-Au	UL-Cr	UL-Cu
Si <100>	2.33	-	-	-	-	-	-	-	-
SiO$_2$	2.64	500	500	500	500	0.81	0.393	0.92	1.046
UL-x	Au:19.30 / Cr:7.19 / Cu:8.96	-	5.51	5.76	5.235	-	1.47	0.94	1.78
Pt	21.10	13.48	8.59	7.84	8.16	0.25	1.75	1.64	1.71
Ni$_{80}$Fe$_{20}$	8.69	6.33	6.26	5.97	6.375	0.96	0.87	0.36	0.23
Ir$_{22}$Mn$_{78}$	10.79	11.97	12.09	11.86	11.93	1.52	1.48	1.82	1.88
Pt	21.10	3.21	2.98	2.88	3.235	1.42	1.59	1.79	1.83

Figure 3a-d shows the LMOKE hysteresis loops measurements at angles Φ_H= 0°, 90° and 180° for UL-Pt, UL-Au, UL-Cu and UL-Cr samples, respectively. As expected, Φ_H= 0° and 180° seem to be the easy axis for all samples from their square-like hysteresis loops and Φ_H= 90° seem to be the hard axis for all samples from their S-shaped hysteresis loops at that angle.
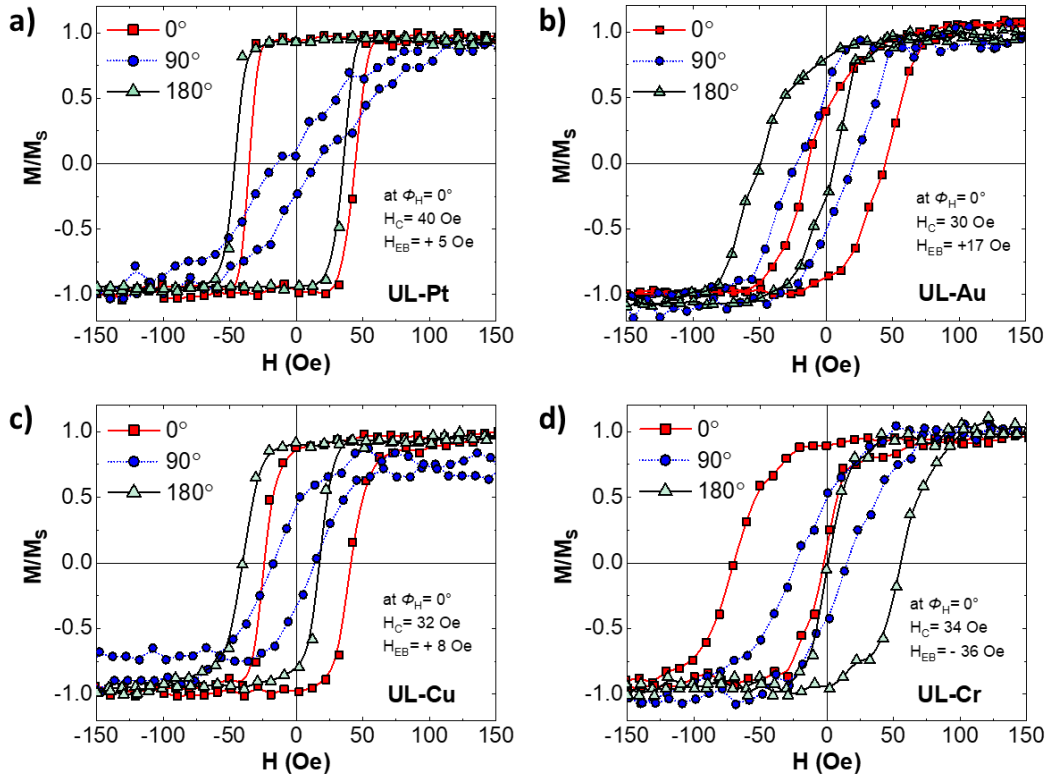
Figure 3. L-MOKE measurement results of (a) UL-Pt sample, (b) UL-Au sample, (b) UL-Cu sample and (c) UL-Cr sample.

It is noticeable from the $\Phi_H = 0°$ angle measurements (solid squared dots) of figure 3a-d that the hysteresis loop shift value, which means H_{EB}, is larger in the UL-Cr sample than in the other samples. Moreover, the shift direction is to the negative values in the UL-Cr sample while the shift directions of UL-Pt, UL-Au and UL-Cu samples are to the positive values. These values were drawn in figure 4a to make a comparison between them. The coercive field (H_C) values varied from 40 Oe to 30 Oe depending on the type of UL. Exchange bias values (H_{EB}) are very low for the UL-Pt, UL-Au and UL-Cu which are +5, +17 and + 8 Oe, respectively. However, UL-Cr has a larger H_{EB} value of -36 Oe and indicates a negative shift. Positive or negative values of H_{EB} in these results indicate a positive or a negative shift with respect to the reference axis ($\Phi_H = 0°$) used in the measurements.
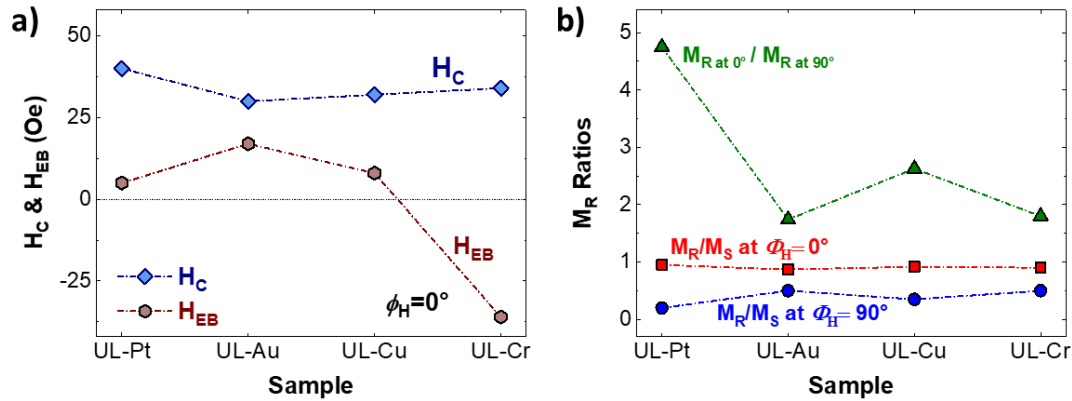
Figure 4. The comparisons of (a) H_C & H_{EB} values and (b) M_R ratios of the samples.

A UL can alter the crystal orientation, texture, microstructure, stress, or roughness in the layers of the stack. All these changes affect the total anisotropy of the ferromagnetic layer. Figure 4b is given to discuss the anisotropic behavior of samples. In the figure, M_R defines the remanent magnetization value and M_S defines the saturation magnetization value. M_R/M_S values at $\Phi_H = 0°$ are very close to each other for all samples and numerically the values are 0.95, 0.87, 0.90 and 0.92 for UL-Pt, UL-Au, UL-Cr and UL-Cu, respectively. At $\Phi_H = 90°$, M_R/M_S values are very different. They are 0.20, 0.51, 0.50 and 0.35 for UL-Pt, UL-Au, UL-Cr and UL-Cu, respectively. M_R/M_S values were also measured at other intermediate angles (not presented in the figures), and their results were found between these values. It can be concluded that all samples have easy axes at $\Phi_H = 0°$ and 180° and hard axes at $\Phi_H = 90°$ and 270° as expected. $M_{R-0°}/ M_{R-90°}$ gives the remanent values rates of samples between their easy and hard axis. Among the samples, the UL-Pt sample has the highest value (4.75) which means that the UL-Pt sample is highly anisotropic compared to the other samples. The UL-Au sample has the lowest rate (1.74).

From the magnetic measurements, four distinct results of UL can be discussed. The varying ULs caused variations in (i) coercive field values, (ii) exchange bias values, (iii) exchange bias sign and (iv) magnetic anisotropies. The reasons for these differences in this study can be attributed to two main factors related to ULs. The first one is the UL's lattice parameters and crystalline structures, and the second one is the growth conditions. Bulk Pt (111) has a lattice parameter of 3.92 Å with a cubic close-packed (ccp) structure. Similarly, bulk Cu (111) and Au (111) have lattice parameters of 3.61 Å and 4.08 Å, respectively, with again ccp structures. However, Cr has a smaller lattice parameter of 2.91 Å with a body-centered cubic (bcc) structure. FM Py layer of the samples has the face-centered cubic (fcc) crystal structure with a lattice parameter of approximately 3.55 Å (for $Ni_{80}Fe_{20}$ [31]). After 5 nm ULs, the samples have 8 nm Pt layers. When the UL and Pt layer consistency of the samples are compared numerically in terms of lattice constants, it can be calculated that this ratio is 92% in the UL-Cu sample, 96% in the UL-Au sample and 75% in the UL-Cr sample. Cu, Au and Pt have similar kinds of crystal structures and have good lattice matches with high rates. UL-Cr sample has a lattice match with a lower rate, and it revealed significant differences in H_C and H_{EB} values. UL-Cr sample also caused a change in the direction of the EB effect and reduced the anisotropic character of the sample. For the UL-Pt and UL-Cu samples, the lattice match may be considered to explain the observation of similar magnetic properties. The only significant difference between the magnetic

properties of UL-Pt and UL-Cu samples was the presence of the highly anisotropic character of the UL-Pt sample. One can attribute this slight difference to their slight lattice mismatch. However, the results of the UL-Au sample do not have an agreement with this approach. Because, although there was a much better lattice match between UL-Pt and UL-Au samples (96%), they did not present similar results in terms of magnetic anisotropies, and H_C and H_{EB} values.
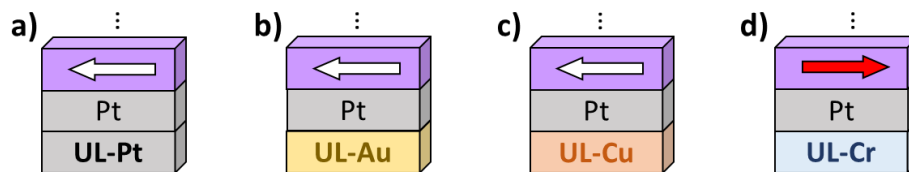
Figure 5. Magnetic moment orientation of (a) UL-Pt, (b) UL-Au, c) UL-Cu and (c) UL-Cr samples.

The second approach to define the differences between the magnetic properties of samples is their growth conditions. Figure 5 illustrates the assumed initial positions of the magnetic moment (spin) directions of the samples which are responsible for the sign of EB. The figure means that the initial magnetic moment direction of the UL-Cr sample is in the opposite direction of UL-Pt, UL-Au and UL-Cu samples according to their initial measurement (and growth) position ($\Phi_H = 0°$). The magnetic anisotropies should play a decisive role for these structures for their magnetic moment directions. It is previously found that the insertion of a buffer layer can change the morphology of the FM surface and the magneto crystalline anisotropy of the FM layer [25]. The MOKE data of the samples at 0, 90 and 180° indicates that samples have in-plane uniaxial magnetic anisotropy. This behavior of polycrystalline samples is explained by growth conditions. This type of anisotropy is called growth-induced or geometric (oblique) anisotropy [32, 33]. The growth conditions, i.e. the growth position of the target guns of the ULs, can alter growth-induced anisotropy and magnetoelastic energy. The total magnetic anisotropy differences in the samples can be the possible reason for the change in the EB direction. The gun positions were mentioned previously while defining figure 1b. From figure 1b, it can be said that all growth angles in the samples, except the growth angles of the ULs, are the same. The subsequent layer after the UL is non-magnetic Pt for each sample. Since Pt layers were deposited under the same conditions, the Pt layers in the samples must have indirect effects on the magnetic properties of the FM layers inherited from the growth conditions of ULs. The gun positions for Pt and Cu targets have almost the same orientation to the substrate (figure 1b), they are geometrically on the same line with the substrate, whereas the gun positions for Au and Cr are significantly different. This can explain why both UL-Pt and UL-Cu samples have higher anisotropic behavior than UL-Au and UL-Cr samples. However, despite these explanations, one question regarding the sign of EB still remains unanswered. In an exchange-biased system with a uniaxial FM anisotropy, two exchange coupling terms play important role in the total energy of an exchange coupled FM/AF bilayer [34]. These terms are called bilinear and biquadratic coupling energies. Normally, bilinear (direct) coupling between FM/AF layers has a dominating role in the exchange bias effect. On the other hand, the presence of 90° coupling between the magnetization of the FM/AF interface can be achieved in the samples with the help of biquadratic (or spin-flop) coupling. Both coupling energies can contribute to the EB effect in an FM/AF bilayer, and the value of their rate changes the value and sign of EB. These energy terms are strongly related to the grain size of the layer and the interdiffusions between the FM/AF layers. Here, the gun position of the Cr target is located at the opposite side of Py during the sample depositions. The position of Cr with the help of growth-induced anisotropy can give a rise to

changes in biquadratic and bilinear coupling energy terms. Additionally, the effect of the interface roughness cannot be excluded here. Roughness contributes to the observed changes in magnetic anisotropies and coupling energy terms. It also can contribute to the growth mode of the Py layer. The effect of roughness can generally be explained by the well-defined random field model of EB [35].

4. CONCLUSION

In summary, the role of Pt, Au, Cu and Cr underlayers on exchange bias properties in Pt/Py/IrMn thin films has been reported and discussed. It was found that the use of a thin Cr underlayer at the bottom was very effective in increasing the exchange bias field value of Pt/Py/IrMn multilayers and also in changing the direction of the EB effect. In contrast to what has been observed for the sample with the Cr underlayer, a very small EB effect is observed in the samples with Cu and Pt underlayers. The coercivity values in the studied samples slightly varied from 32 Oe to 40 Oe depending on the UL type. On the other hand, the exchange bias field values varied from +8 Oe to -36 Oe depending on UL type. Not the use of Cu or Pt, but the use of Cr as a UL has changed both the value and the sign of the exchange bias significantly.

This study can be extended with new samples by changing the UL target positions during the deposition for further research. The effect of underlayers is sometimes ignored as they were thought to be standardized for the multilayers, but our study once again revealed their importance in the design of magnetic multilayers by giving numerical results in EB value, EB sign and magnetic anisotropies. On this basis, one would expect that these results can play a significant role in designing new spintronic devices. This indirect effect of the underlayers on the magnetic properties may be potentially useful for further applications in technological devices since an underlayer can change the H_C values, H_{EB} values, EB sign and magnetic anisotropies to the desired value in the magnetic multilayers.

ACKNOWLEDGMENTS

REFERENCES

[1] Baltz, V., Manchon, A., Tsoi, M., Moriyama, T., Ono, T. and Tserkovnyak, Y., (2018), Antiferromagnetic spintronics, Reviews of Modern Physics, 90, (1), 015005.

[2] Železný, J., Wadley, P., Olejník, K., Hoffmann, A. and Ohno, H., (2018), Spin transport and spin torque in antiferromagnetic devices, Nature Physics, 14, (3), 220-228.

[3] Meiklejohn, W. H. and Bean, C. P., (1956), New Magnetic Anisotropy, Physical Review, 102, (5), 1413-1414.

[4] Demirci, E., Rojas, J. d., Quintana, A., Fina, I., Menéndez, E. and Sort, J., (2022), Voltage-driven strain-mediated modulation of exchange bias in $Ir_{20}Mn_{80}/Fe_{80}Ga_{20}/Ta/\langle 011 \rangle$-oriented PMN-32PT heterostructures, Applied Physics Letters, 120, (14), 142406.

[5] Manchon, A., Železný, J., Miron, I. M., Jungwirth, T., Sinova, J., Thiaville, A., Garello, K. and Gambardella, P., (2019), Current-induced spin-orbit torques in ferromagnetic and antiferromagnetic systems, Reviews of Modern Physics, 91, (3), 035004.

[6] Fang, B., San Jose, L. S. T., Chen, A. T., Li, Y., Zheng, D. X., Ma, Y. C., Algaidi, H., Liu, K., Finocchio, G. and Zhang, X. X., (2022), Electrical Manipulation of Exchange Bias in an Antiferromagnet/Ferromagnet-Based Device via Spin-Orbit Torque, Advanced Functional Materials, 32, (26).

[7] Lin, P.-H., Yang, B.-Y., Tsai, M.-H., Chen, P.-C., Huang, K.-F., Lin, H.-H. and Lai, C.-H., (2019), Manipulating exchange bias by spin–orbit torque, Nature Materials, 18, (4), 335-341.

[8] Zhang, J., Zhou, J., Luo, Z.-L., Chen, Y. B., Zhou, J., Lin, W., Lu, M.-H., Zhang, S.-T., Gao, C., Wu, D. and Chen, Y.-F., (2020), Exchange-biased nanocomposite ferromagnetic insulator, Physical Review B, 101, (1), 014422.

[9] Wu, R., Xue, M., Maity, T., Peng, Y., Giri, S. K., Tian, G., MacManus-Driscoll, J. L. and Yang, J., (2020), Influence of atomic roughness at the uncompensated Fe/CoO(111) interface on the exchange-bias effect, Physical Review B, 101, (1), 014425.

[10] Demirci, E., Öztürk, M., Pişkin, H. and Akdoğan, N., (2020), Angle-Dependent Inverted Hysteresis Loops in an Exchange-Biased $[Co/Pt]_5/IrMn$ Thin Film, Journal of Superconductivity and Novel Magnetism, 33, (3), 721-726.

[11] Dong, Y., Zhao, X., Wang, W., Chen, Y., Bai, L., Yan, S. and Tian, Y., (2022), Room temperature manipulation of exchange bias in magnetic heterojunctions, Journal of Magnetism and Magnetic Materials, 559.

[12] Wu, H., Sudoh, I., Xu, R., Si, W., Vaz, C. A. F., Kim, J.-y., Vallejo-Fernandez, G. and Hirohata, A., (2018), Large exchange bias induced by polycrystalline Mn_3Ga antiferromagnetic films with controlled layer thickness, Journal of Physics D: Applied Physics, 51, (21), 215003.

[13] Wang, R., Xiao, Z., Liu, H., Quan, Z., Zhang, X., Wang, M., Wu, M. and Xu, X., (2019), Enhancement of perpendicular magnetic anisotropy and spin-orbit torque in Ta/Pt/Co/Ta multi-layered heterostructures through interfacial diffusion, Applied Physics Letters, 114, (4), 042404.

[14] Ryu, J., Avci, C. O., Karube, S., Kohda, M., Beach, G. S. D. and Nitta, J., (2019), Crystal orientation dependence of spin-orbit torques in Co/Pt bilayers, Applied Physics Letters, 114, (14), 142402.

[15] Zhu, L., Ralph, D. C. and Buhrman, R. A., (2019), Spin-Orbit Torques in Heavy-Metal--Ferromagnet Bilayers with Varying Strengths of Interfacial Spin-Orbit Coupling, Physical Review Letters, 122, (7), 077201.

[16] Rowan-Robinson, R. M., Hindmarch, A. T. and Atkinson, D., (2018), Efficient current-induced magnetization reversal by spin-orbit torque in Pt/Co/Pt, Journal of Applied Physics, 124, (18), 183901.

[17] Jinnai, B., Zhang, C., Kurenkov, A., Bersweiler, M., Sato, H., Fukami, S. and Ohno, H., (2017), Spin-orbit torque induced magnetization switching in Co/Pt multilayers, Applied Physics Letters, 111, (10), 102402.

[18] Ramaswamy, R., Qiu, X., Dutta, T., Pollard, S. D. and Yang, H., (2016), Hf thickness dependence of spin-orbit torques in Hf/CoFeB/MgO heterostructures, Applied Physics Letters, 108, (20), 202406.

[19] Skowroński, W., Cecot, M., Kanak, J., Ziętek, S., Stobiecki, T., Yao, L., van Dijken, S., Nozaki, T., Yakushiji, K. and Yuasa, S., (2016), Temperature dependence of spin-orbit torques in W/CoFeB bilayers, Applied Physics Letters, 109, (6), 062407.

[20] Akyol, M., Alzate, J. G., Yu, G., Upadhyaya, P., Wong, K. L., Ekicibil, A., Amiri, P. K. and Wang, K. L., (2015), Effect of the oxide layer on current-induced spin-orbit torques in Hf|CoFeB|MgO and Hf|CoFeB|TaOx structures, Applied Physics Letters, 106, (3), 032406.

[21] Engel, C., Goolaup, S., Luo, F. and Lew, W. S., (2017), Characterizing Angular Dependence of Spin-Orbit Torque Effective Fields in Pt/(Co/Ni)$_2$/Co/IrMn Structure, Ieee Transactions on Magnetics, 53, (11), 1-4.

[22] Hayashi, M., Kim, J., Yamanouchi, M. and Ohno, H., (2014), Quantitative characterization of the spin-orbit torque using harmonic Hall voltage measurements, Physical Review B, 89, (14), 144425.

[23] Cavicchia, D. R., D'Orazio, F., Rossi, L., Ricci, F. and Lucari, F., (2013), Influence of Cu seed layer on the magnetization reversal in exchange-biased FeMn/FeCo systems, EPJ Web of Conferences, 40, 13002.

[24] Dunz, M. and Meinert, M., (2020), Role of the Ta buffer layer in Ta/MnN/CoFeB stacks for maximizing exchange bias, Journal of Applied Physics, 128, (15), 153902.

[25] Ashida, T., Sato, Y., Nozaki, T. and Sahashi, M., (2013), Effect of the Pt buffer layer on perpendicular exchange bias based on collinear/non-collinear coupling in a Cr_2O_3/Co_3Pt interface, Journal of Applied Physics, 113, (17), 17D711.

[26] Öksüzoğlu, R. M., Yıldırım, M., Çınar, H., Hildebrandt, E. and Alff, L., (2011), Effect of Ta buffer and NiFe seed layers on pulsed-DC magnetron sputtered $Ir_{20}Mn_{80}$/$Co_{90}Fe_{10}$ exchange bias, Journal of Magnetism and Magnetic Materials, 323, (13), 1827-1834.

[27] Kohn, A., Kovács, A., Fan, R., McIntyre, G. J., Ward, R. C. C. and Goff, J. P., (2013), The antiferromagnetic structures of $IrMn_3$ and their influence on exchange-bias, Sci Rep, 3, 2412.

[28] Nozières, J. P., Jaren, S., Zhang, Y. B., Zeltser, A., Pentek, K. and Speriosu, V. S., (2000), Blocking temperature distribution and long-term stability of spin-valve structures with Mn-based antiferromagnets, Journal of Applied Physics, 87, (8), 3920-3925.

[29] Demirci, E., (2016), "Manyetoelektrik Cr_2O_3 Tabanlı İnce Film Sistemlerinde Dik Exchange Bias Etkisinin İncelenmesi [Investigation of perpendicular exchange bias effect in magnetoelectric Cr_2O_3 based thin films]", PhD Thesis, Written in Turkish, Gebze Technical University, Turkey.

[30] Mokhtari, I. B.-E., Mourkas, A., Ntetsika, P., Panagiotopoulos, I., Roussigné, Y., Cherif, S. M., Stashkevich, A., Kail, F., Chahed, L. and Belmeguenai, M., (2019), Interfacial Dzyaloshinskii-Moriya interaction, interface-induced damping and perpendicular magnetic anisotropy in Pt/Co/W based multilayers, Journal of Applied Physics, 126, (13), 133902.

[31] Li, G., Leung, C. W., Shueh, C., Hsu, H.-F., Huang, H.-R., Lin, K.-W., Lai, P. T. and Pong, P. W. T., (2013), Exchange bias effects of NiFe/NiO bilayers through ion-beam bombardment on the NiO surface, Surface and Coatings Technology, 228, S437-S441.

[32] Knorr, T. G. and Hoffman, R. W., (1959), Dependence of Geometric Magnetic Anisotropy in Thin Iron Films, Physical Review, 113, (4), 1039-1046.

[33] Özdemir, M., Aktaş, B., Öner, Y., Sato, T. and Ando, T., (1997), Anomalous anisotropy of reentrant Ni77Mn23 film, J. Phys. Condens. Matter., 9, 6433–6445.

[34] Hu, J.-g., Jin, G., Hu, A. and Ma, Y.-q., (2004), Temperature dependence of exchange bias and coercivity in ferromagnetic/antiferromagnetic bilayers, The European Physical Journal B - Condensed Matter and Complex Systems, 40, (3), 265-271.

[35] Malozemoff, A. P., (1987), Random-field model of exchange anisotropy at rough ferromagnetic-antiferromagnetic interfaces, Phys Rev B Condens Matter, 35, (7), 3679-3682.

RESEARCH ARTICLE

ENGINEERING of a NOVEL SCREEN-PRINTED ELECTRODE MODIFIED by Pt DECORATED SINGLE WALLED CARBON NANOTUBE NANOHYBRID for MONITORING SULFITE in REAL SAMPLES: A NEW APPROACH to a SUSTAINABLE ENVIRONMENT and HEALTH

Ceren KARAMAN[1*]

[1]Akdeniz University, Vocational School of Technical Sciences, Department of Electricity and Energy, Antalya, cerenkaraman@akdeniz.edu.tr, ORCID: 0000-0001-9148-7253

ABSTRACT

Sensitive and selective monitoring of sulfite anions, a food additive, in real-time applications is still a challenging issue to be solved. It is crucial to engineering highly selective and sensitive, facile, and low-cost analytical tools for monitoring trace levels of sulfite anions in real samples. In light of this, the goal of this work was to tailor a Pt-decorated single-walled carbon nanotubes (Pt@SWCNTs) nanohybrid to be utilized in the engineering of an electrochemical sensor to monitor sulfite anions in real samples. The microstructural features of the fabricated nanocatalysts were assessed via transmission electron microscope (TEM), whereas the electrochemical characteristics were enlightened via differential pulse voltammetry (DPV), linear sweep voltammetry (LSV), and electrochemical impedance spectroscopy (EIS) methods. The screen-printed electrode (SPE), as an electrochemical sensor, was modified via Pt@SWCNTs nanocatalysts and the resultant electrochemical sensor (Pt@SWCNTs/SPE) was employed as a powerful electroanalytical tool for monitoring sulfite in the concentration range of 0.1 - 250 μM with a limit of detection value of 10 nM. The optimal catalyst concentration was determined as 9.0mg Pt@SWCNTs, and the pH 5.0 was selected as the optimal pH. At the optimal operating conditions, it was observed that the oxidation current of sulfite was enhanced almost 2.53-fold, and the oxidation potential of it diminished *ca.50* mV at the surface of Pt@SWCNTs/SPE in comparison to bare SPE. The sulfite anions monitoring ability of proposed Pt@SWCNTs/SPE was further confirmed in red wine and tap water samples by the standard addition method, and the recovery range was determined as 98.5 – 102.3%. The enhanced electrochemical performance of the fabricated electrochemical sensor compared to bare SPE was directly ascribed to the coupled effects of co-existing Pt nanoparticles and SWCNTs architecture, which facilitated both the electron transfer and mass transfer. This works paws the way for tailoring of hybrid nanocatalysts to be utilized in electrochemical engineering applications for sustaining the environment and health.

Keywords: *Sulfite, Electrochemical Sensor, Monitoring, Pt@SWCNTs, Screen Printed Electrode*

1. INTRODUCTION

Sulfite anion (SO_3^{2-}) is frequently served as a preserving agent in beverages, foodstuffs, and pharmaceutical products for avoiding spoilage as a result of oxidation and browning reactions and to prevent the reproduction of microorganisms [1, 2]. Despite being used as a food preservative all over the world and having numerous advantages, SO_3^{2-} concentrations above 0.7 mg.kg^{-1} are not permitted in foodstuffs due to potential toxicity [3]. Moreover, SO_3^{2-} is a forerunner to the formation of acid rain caused by the resulted sulfur dioxide, which damages crops, residences, landmarks, aquatic life, and plants by acidifying the soil [4]. The threshold concentration of SO_3^{2-} anion in beverages and food products has been declared as 10 ppm by the United States Food and Drug Administration [5, 6]. Since high concentrations of sulfite anions can lead to health issues including skin irritation, allergic reactions, asthma, nausea, and diarrhea, as well as can deplete the dissolved oxygen in aquatic media, the products that contain more sulfide than the threshold level should be properly labeled [7, 8]. Therefore, it is vital to engineer and design analytical methods that are sensitive, precise, straightforward to use, selective, and reasonably priced to monitor the trace amount of SO_3^{2-} in actual samples.

Among the various available analytical techniques for the monitoring of SO_3^{2-}, spectrofluorometry [9], chemiluminescence [10], spectrophotometry [11], flow injection technique [12], high-performance liquid chromatography [13], and enzymatic methods [14] can be highlighted as the most preferred ones. The effectiveness and mechanism of the substance to be examined in real sample analysis can also be determined using electrochemical analysis methods since they are analogous to biological redox processes and are unaffected by the formulation's interfering chemicals. Electroanalytical methods allow the determination of analytes at very low concentrations and provide information about the degree and speed of adsorption and chemisorption at interfaces, the stoichiometry of charge transfer, mass transfer rate, equilibrium and rate constants of chemical reactions in systems where electrochemical techniques are applied. However, despite the advantages of these techniques, most of these methods still suffer from some obstacles that limit their widespread and real-time employment such as high cost, low sensitivity, time-consuming and complex sample preparation steps, low throughput, and high cost [15]. On the other side, electrochemical techniques have recently garnered exceptional attention due to their benefits such as being easy to apply, superior selectivity and sensitivity, swift analysis times, on-site application possibilities, being customizable portable devices, and comparatively cheapness [16, 17]. For boosting the sensitivity and precision of the electroanalytical techniques, electrode modification has been considered a prosperous approach [18, 19]. Among the various traditional electrode types, screen-printed electrodes (SPEs) have benefits such as small dimensions, lightweight, low cost, and being disposable [20]. Disposable sensors provide some advantages, including the elimination of issues with biofouling or contaminant spillover and the design flexibility provided by the simplicity of chemical modifications through coating with various nanomaterials[21].

Nanomaterials have received a great deal of interest due to their unique characteristics that allow them to be utilized in various areas including environmental application [22-24], pharmaceuticals [25], energy [26-28], catalyst [29, 30], biotechnology [31, 32], etc. Nanomaterials are also used in the design of electrochemical sensors. Nanostructured materials are of a huge specific surface area resulting in more electrochemically active sites, which allows decreasing overpotential of various analytes and facilitates the electron/ion transport between the electrode surface and analyte, thereby boosting the voltammetric responses [33]. So far, numerous metal and metal oxide nanoparticles,

including Pt, Pd, Au, Ag, Zn, Cu, Ni, NiO, Co_3O_4, etc. have been substantially employed in electrochemical sensor fabrication [34-40]. Amongst, Pt nanoparticles have gained great attention thanks to their unique features including high conductivity, and superior electrocatalytic activity [41]. However, its practical application is still restricted due to its high-cost, and limited reserves, as well as the problem of aggregation. Hence, the decoration of Pt nanoparticles onto suitable supporting nanoarchitecture is one of the suitable ways to enhance its potential application in electrochemical sensor fabrication [42]. These drawbacks of Pt-based electrochemical sensors prevent their widespread adoption. Carbon-based nanomaterials can fulfill the limit of detection level, and operating temperature criteria in addition to having higher selectivity and faster response times than other types of nanomaterials-based sensors, showing great promise for use in electrochemical sensors [43]. Among the various carbonaceous nanomaterials, single-walled carbon nanotubes (SWCNTs) are one of the promising ones which have garnered a lot of interest due to their global importance in nanotechnology and their prospective application in designing electrochemical sensors [44, 45]. According to recent studies, hybrid nanoarchitectures can enhance actual electrocatalytic activity, which may be related to the synergistic interaction between the two elements [46]. Regarding the outstanding individual characteristics of Pt nanoparticles and SWCNTs, it can be expected that a hybrid might yield boosted electrochemical performance of the ultimate sensor.

Although there are some valuable works that investigate various electrochemical sensors for sulfide monitoring, as per the best knowledge of the researcher, this is the first effort that has aimed to synthesize a Pt nanoparticle decorated SWCNTs (Pt@SWCNTs) modified SPE for highly sensitive monitoring of sulfite anions in real samples. Superior limit of detection (LOD), ease of application, acceptable recovery data, swift response time, and being available for miniaturization can be listed as the primary benefits of the proposed Pt@SWCNTs/SPE electrochemical sensor for monitoring trace amount of sulfite anions.

2. EXPERIMENTAL

2.1. Materials and Apparatus
NaOH, HNO_3, H_2PtCl_6, SWCNTs, $NaHCO_3$, H_3PO_4, $NaBH_4$, NaCl, SWCNTs (average diameter: 0.78 nm, median length: 1 μm, purity: ≥95% as carbon nanotubes, specific surface area: ≥700 $m^2.g^{-1}$), dimethylformamide (DMF), ethanol, and isopropyl alcohol (IPA) were directly employed in experiments without any extra purification. Deionized (DI) water was utilized to make ready all of the reagent solutions.

The microstructural investigation of fabricated nanostructures was conducted by JEOL 2100 TEM. For pH measurements, a digital pH-meter (METTLER TOLEDO S220-K) was employed.

Electrochemical Workstation Vertex – Ivium linked to a conventional 3-electrode electrochemical cell was employed to implement the electrochemical investigations of the proposed electrochemical sensor. During the electrochemical characterizations, Pt-wire was used as a counter electrode, and Ag/AgCl (3.0 M KCl) as a reference electrode for recording electrochemical signals.

2.2. Synthesis of Pt@SWCNTs Nanostructures
SWCNTs homogenous dispersion (3.0 $mg.mL^{-1}$) was prepared by ultrasonically dispersing a certain amount of SWCNTs in 20 mL IPA over the course of 45 minutes in an ultrasonic bath. Afterward, 100 mg H_2PtCl_6 was ultrasonically dispersed in SWCNTs dispersion for 45 min. Finally, to acquire

Pt@SWCNTs nanostructure, a determined amount of NaBH$_4$ was introduced into as-obtained SWCNTs-H$_2$PtCl$_6$/IPA dispersion, following by ultrasonicated for 1 hour. The acquired black precipitates consisting of Pt@SWCNTs nanostructure were vacuum-filtered and thermally annealed at 500 °C in a tubular furnace over 1 h under the high purity Argon atmosphere. Subsequently, the obtained black powder was labeled as Pt@SWCNTs, and placed in a sealed vial to be used later.

2.3. Fabrication of Modified SPE

The Pt@SWCNTs modified screen printed electrode for sulfite monitoring was fabricated by a simple drop-casting technique. In this regard, 9.0 mg of produced Pt@SWCNTs nanohybrid was ultrasonically dispersed in 1.0 mL of ethanol-DI water solution (1:1, by v:v) for one hour. Afterward, *ca*.5 µL of dispersion was drop-casted onto the SPE surface, and the solvent was evaporated at the ambient temperature. Subsequently, the resultant electrode was denoted as Pt@SWCNTs/SPE electrode and stored at 4 °C for forthcoming use.

2.4. Real Sample Preparation

The performance of the fabricated electrochemical sensor to monitor SO$_3^{2-}$ anions in real samples was assessed by using red wine and tap water samples as real samples. In this step, red wine was acquired from a wine cellar in İzmir, Turkey. Just before the real sample analysis, the wine bottle was uncorked. A certain amount of red wine sample was filtered and diluted by phosphate buffer solution (PBS, pH=5.0) whereas tap water was gotten ready to use after centrifuging at 5000 rpm over 15 min, and filtration of the supernatant. The prepared red wine and drinking water samples were separately introduced into the electroctrochemical cell, and sulfide was spiked into the real sample solution and monitored by the standard addition method.

3. RESULTS AND DISCUSSION

3.1. Evaluation of The Electrode Surface

The microstructure of the Pt@SWCNTs nanohybrid was characterized via TEM analysis (Fig.1). The TEM image of the nanohybrid showed the SWCNTs to have a tubular morphology with uniformly distributed Pt nanoparticles on the SWCNT skeleton. Moreover, Fig.1 confirmed the successful decoration of Pt nanoparticles onto SWCNTs supporting material. The uniform dispersion of the Pt nanoparticles without aggregation was also observed in the TEM micrographs of the nanohybrid.

Figure 1. TEM micrograph of Pt@SWCNTs nanohybrid.

The electrochemical impedance spectroscopy technique was implemented in 0.1 M KCl solution containing 5.0 mM $[Fe(CN)_6]^{3-,-4}$ redox probe to evaluate the electrical conductivity of Pt@SWCNTs/SPE. The Nyquist plot of both bare SPE and Pt@SWCNTs/SPE was depicted in Fig.2. The observed smaller semicircle radius of Pt@SWCNTs/SPE compared to bare SPE confirmed the boosting effect of the Pt@SWCNTs modification onto the electrical conductivity. Thanks to the enhanced electrical conductivity, the charge transfer resistance of the resultant modified electrode was decreased, thereby facilitating the detection process of the analyte with high sensitivity.
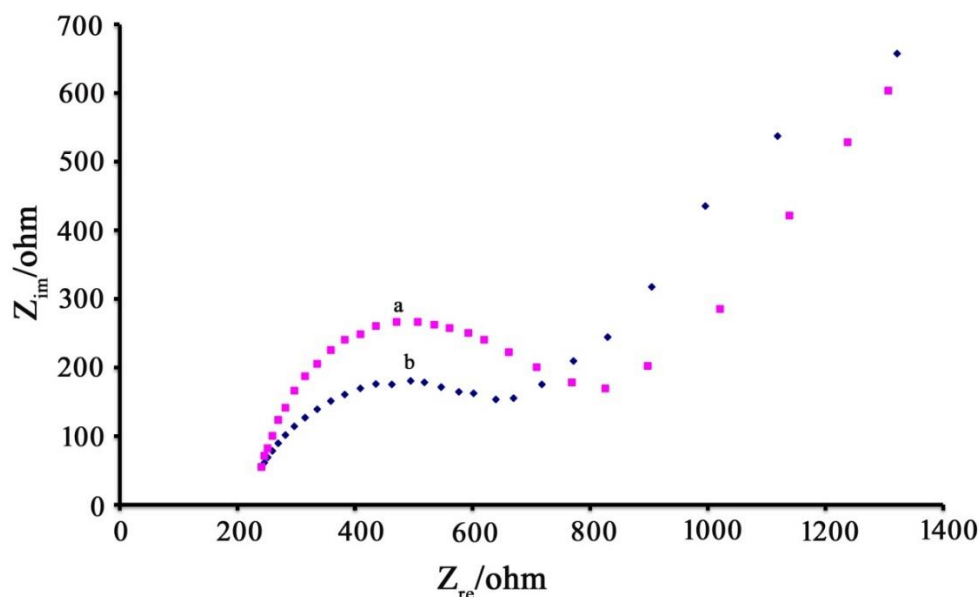
Figure 2. The Nyquist plots of bare SPE (a) and Pt@SWCNTs/SPE (b) in 0.1 M KCl solution containing 5.0 mM $[Fe(CN)_6]^{3-,4-}$.

3.2. Optimization of Catalyst Ratio and pH of the Solution

Firstly, the amount of Pt@SWCNTs catalyst was optimized by investigating various amounts of nanohybrid ranging 2.0 - 8.0 mg dispersed in 1.0 mL DI water-ethanol (1:1, by v:v) solution, and then drop-casted onto SPE to fabricate various Pt@SWCNTs/SPE electrodes. The oxidation signal of 125 µM sulfite was obtained at the surface of the electrode (Fig 3A). The results revealed that the oxidation current of sulfite increased with increasing the concentration of nanohybrid catalyst at the surface of SPE, reaching the maximum value at 9.0 mg Pt@SWCNTs catalyst in 1.0 mL of DI water-ethanol (1:1, by v:v) solution. Hence, this catalyst loading was selected as the optimum catalyst ratio for the fabrication of the modified electrochemical sensor.

The electrochemical features of a fabricated electrochemical sensor can be significantly influenced by the pH of the solution. The adsorbent surface can be affected by the activity of the sulfite anion in real samples due to the pH of the solution in the presence of OH^- and H^+ ions. The pH of the solution was also optimized by evaluating the oxidation signal of the sulfite within the pH range of 3.5-6.0. It was observed that the oxidation signal of sulfite was enhanced by shifting the pH value from acidic to basic (Fig. 3B). The maximum oxidation current was achieved at the alkaline condition of pH 5.0, after this pH value it was observed that the oxidation signal current decreased. Thus, pH 5.0 was shown to be the ideal pH for the electrochemical detection of sulfite anion.

Another parameter that effects the electrochemical performance of the fabricated electrode is type of buffer solution. Thus, three different types of buffer solutions including phosphate buffer, acetate buffer, and Brittion-Robinson buffer solution at the optimal pH value of 5.0 were explored to determine the optimal buffer solution. The recorded oxidation signals (Fig. 3C) revealed that the phosphate buffer solution could be selected as the optimal buffer solution with its superior oxidation

signal value achieved for 125 µM sulfite. As a result, the phosphate buffer solution was selected as the most appropriate buffer solution for the following studies.
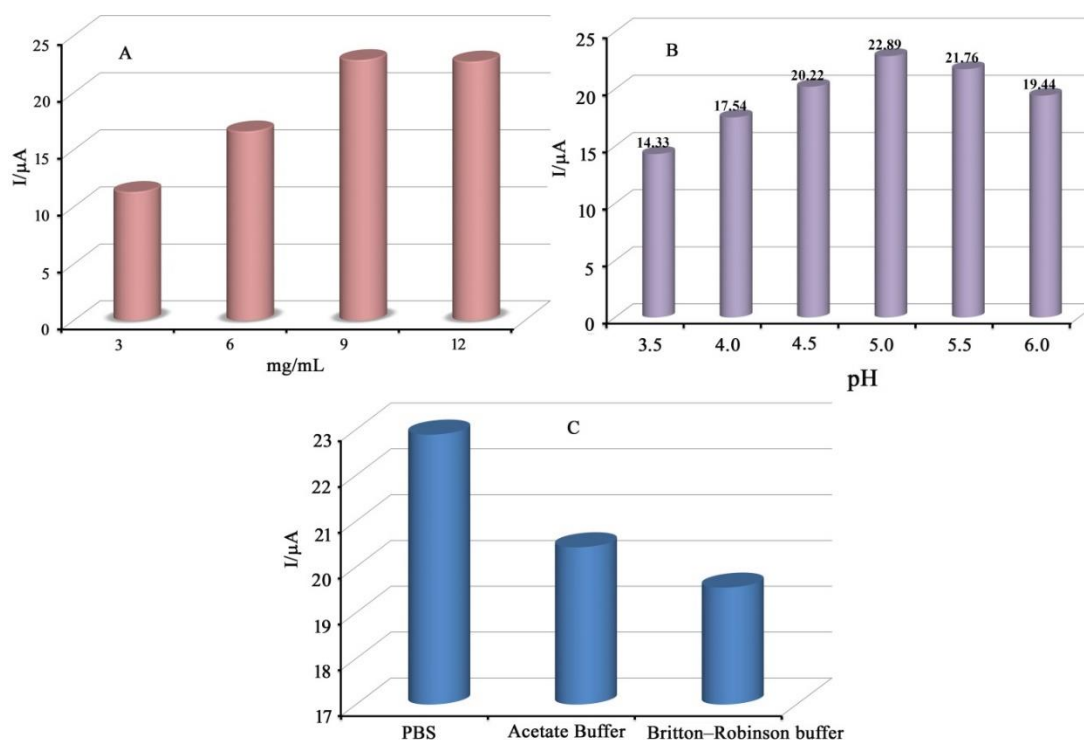
Figure 3. The effect of (A) the Pt@SWCNTs catalyst amount (B) the pH value of the solution ranging between 3.5 to 6.0 (C) type of buffer solution on the voltammetric response of sulfite at a surface of Pt@SWCNTs/SPE.

3.3. Investigation of Catalytic Effect of Pt@SWCNTs Nanohybrid

The electrochemically active surface area (EASE) of bare SPE and Pt@SWCNTs/SPE were evaluated by implementing cyclic voltammetry (CV) measurement in 0.1 M KCl + 1.0 mM $[Fe(CN)_6]^{3-,4-}$ solution at the potential scan rate range of 25-450 mV.s^{-1}. The Randles–Sevcik equation was computed to obtain the EASE values of the electrodes. The EASE values were calculated as 0.143 cm^2, and 0.221 cm^2 for bare SPE and Pt@SWCNTs/SPE, respectively. The results confirmed that the modifying SPE by Pt decorated SWCNTs nanohybrid led to an increase in the EASE value, thereby enhancing the electrocatalytic performance of the ultimate electrochemical sensor.

Differential pulse voltammograms of 125 µM sulfite were recorded at the surface of SPE (Fig.4 curve a) and Pt@SWCNTs/SPE (Fig. 4 curve b), respectively. The findings proved that the oxidation current of sulfite increased from 9.055 µA to 22.89 µA, whereas its oxidation potential of it diminished from 970 mV to 920 mV for bare SPE, and Pt@SWCNTs/SPE, respectively. Thereby, it was concluded that the Pt@SWCNTs nanohybrid modification of SPE successfully amplified the oxidation signal of sulfite thanks to the enhanced EASE and electrical conductivity of nanocatalysts.

The inset of Fig. 4 reflected the current density diagram for oxidation of sulfite at the surface of SPE, and Pt@SWCNTs/SPE, respectively. The Pt@SWCNTs nanohybrid's exceptional electrical conductivity as a novel electrocatalyst to be used in the creation of modified electrochemical sensors was proven by the current density diagram. The boosted performance of Pt@SWCNTs/SPE was ascribed to the coupled effects of the Pt nanoparticles and high surface area SWCNTs which served as carbonaceous supporting material to enhance the electrocatalytic activity of the resultant hybrid.
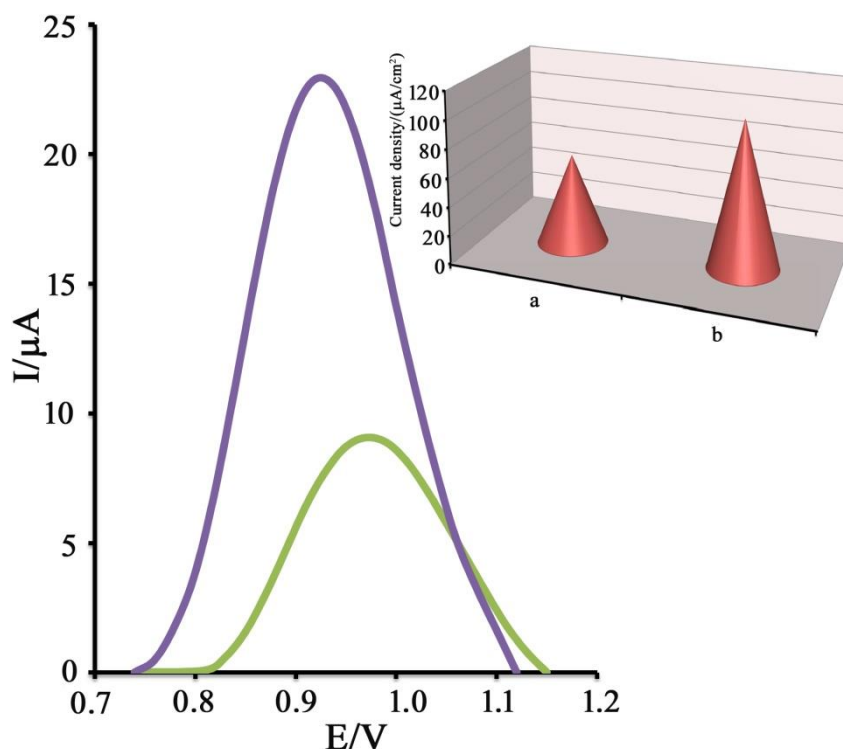
Figure 4. DPV curves recorded at the surface of SPE (curve a) and Pt@SWCNTs/SPE (curve b) (inset; the current density values of sulfite at the surface of SPE and Pt@SWCNTs/SPE electrodes).

3.4. Kinetic Investigations

The kinetic behavior of the fabricated electrochemical sensor towards sulfite monitoring was assessed by linear sweep voltammetry (LSV) measurements. Fig. 5 inset depicted the LSV voltammograms of 700 µM sulfite anions acquired on the surface of Pt@SWCNTs/SPE at a potential scan rate of 10- 150 mV.s^{-1}. The linear relation with an equation of $I = 3.2409 \, \upsilon^{1/2} + 0.3934$ ($r^2 = 0.9967$) was determined between the oxidation current of sulfite and $\upsilon^{1/2}$, thereby revealing the diffusion process for redox reaction of sulfite on the surface of Pt@SWCNTs/SPE (Fig. 5). The Tafel plot for the oxidation of 700 µM sulfite anions on the of Pt@SWCNTs/SPE surface at the scan rate of 40 mV.s^{-1} was depicted in Fig. 6.
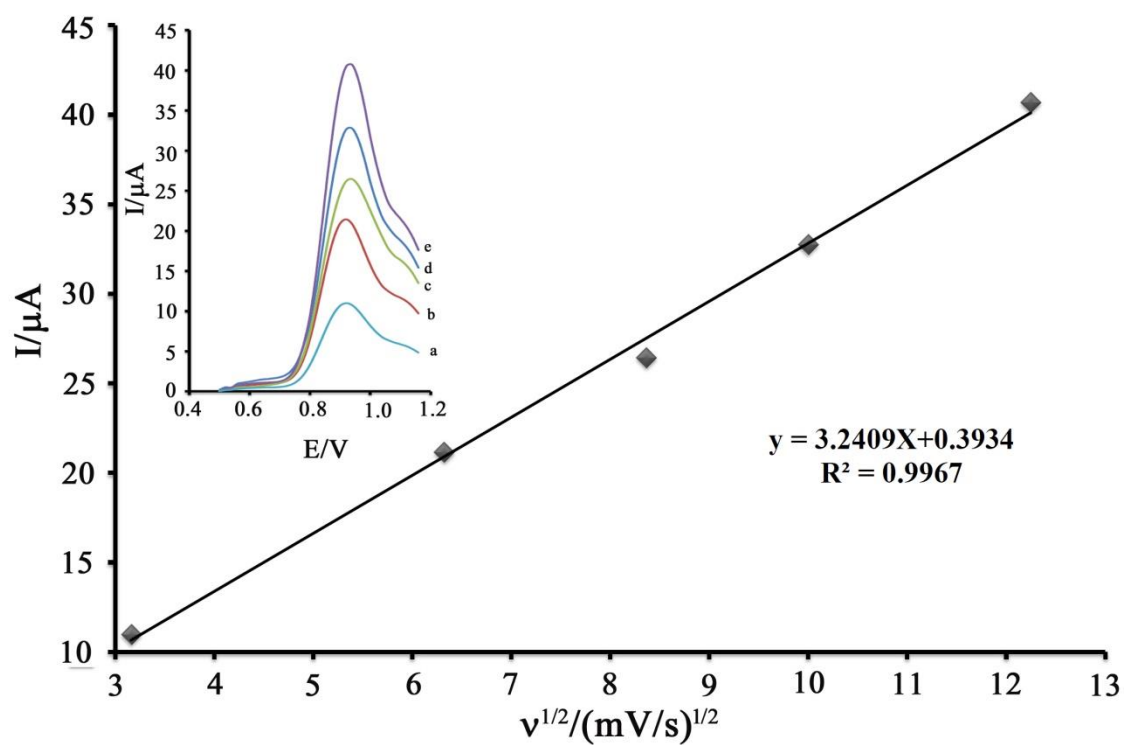
Figure 5. Current- $\upsilon^{1/2}$ plot for redox reaction of 700 µM sulfite at surface of Pt@SWCNTs/SPE. Relative LSV voltammograms of 700 µM sulfite at the surface of Pt@SWCNTs/SPE (scan rates; 10; 40; 70; 100 and 150 mV.s^{-1}).
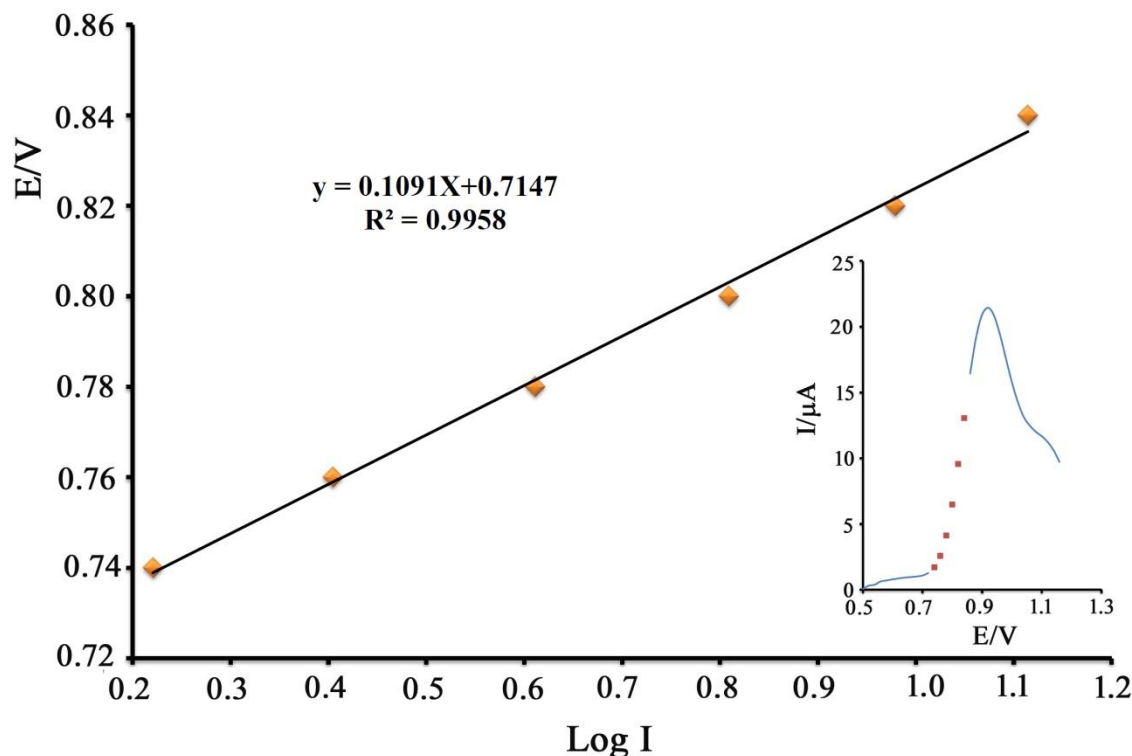
Figure 6. Tafel plot for the oxidation of 700 µM sulfite anions on the of Pt@SWCNTs/SPE surface at the scan rate of 40 mV.s^{-1}

3.5. Repeatability and Analytical Parameters

By fabricating five distinct electrodes under the same conditions and recording voltammograms of 125 µM sulfite on the surface of Pt@SWCNTs/SPE, the reproducibility of the fabricated electrode for monitoring sulfite was evaluated. The obtained results showed and RSD value of 4.3% which is acceptable repeatability of Pt@SWCNTs/SPE to detect sulfite.

The differential pulse voltammetry curves of sulfite in the concentration range of 0.1 to 250 µM were obtained at the surface of Pt@SWCNTs/SPE (Fig. 7). The linear relationship was confirmed with the equation of I = 0.1562 C + 2.8897 (r^2 = 0.9932), was obtained between the oxidation current of sulfite and the concentration at the surface of Pt@SWCNTs/SPE with the limit of detection value of 10 nM.
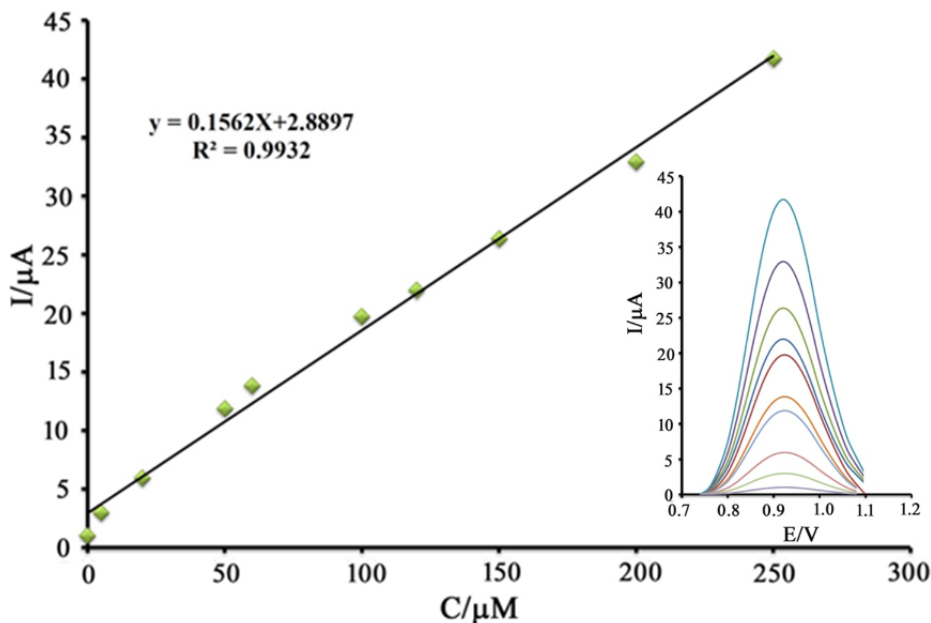
Figure 7. Current-concentration plot for oxidation of sulfite at surface of Pt@SWCNTs/SPE (Inset; Relative DPV curves with the concentrations of 0.01; 5.0; 20.0; 50.0; 60.0; 100; 120; 150; 200 and 250 µM).

3.6. Real sample analysis and interference study

The sulfite monitoring capability of Pt@SWCNTs/SPE was evaluated also in some real samples including red wine and tap water samples. The standard addition method was implemented by using Pt@SWCNTs/SPE to detect sulfite in real samples. The computed results were listed in Table 1. According to acquired data, a recovery range of 98.5-102.3% was determined to monitor sulfite by utilizing Pt@SWCNTs/SPE electrochemical sensor as an analytical tool, proving the outstanding applicability of this novel sensor in real sample analysis with high sensitivity.

Table 1. Real sample analysis data for sensing sulfite using Pt@SWCNTs/SPE.

Sample	Added (µM)	Founded (µM)	Recovery%
Tap water	---	<LOD	---
	10.00	9.85±0.54	98.5
Red wine	---	6.7±0.11	---
	3.3	10.23±0.64	102.3

Moreover, the selectivity metrics of Pt@SWCNTs/SPE towards the detection of 10 µM sulfite were evaluated in the presence of some organic and inorganic pollutants. The results were depicted in Table 2, revealing the excellent selectivity of Pt@SWCNTs/SPE as an electroanalytical sensor for the determination of sulfite thanks to the synergistic features of metal nanoparticles and carbonaceous skeleton as the supporting material.

Table 2. Interference study results for sensing 10 µM sulfite.

Species	Tolerant limits ($W_{Substance}/W_{Analytes}$)
Li^+, Br^-, Ca^{2+}, F^-	1000
Starch	Saturation
Valine, Glycine, Glucose	500

4. CONCLUSION

Herein, the goal was to engineer a novel electrochemical sensor to be implemented in highly sensitive monitoring of trace amounts of sulfide in real samples. In this regard, to take advantage of the coupled effect of Pt nanoparticles and SWCNTs architecture, Pt nanoparticles were decorated onto SWCNTs via a facile fabrication pathway, and the resultant nanohybrid catalyst was implemented as a mediator for the modification of the screen-printed electrode. The synthesized Pt@SWCNTs nanohybrid offered superior electrical conductivity and enhanced electrochemical oxidation signal of sulfite anion thanks to the synergistic effects of each component of the nanohybrid. The boosted electrochemically active surface area also led to improvement in the electrocatalytic performance of the nanomaterial, thereby increasing the sensitivity of the resultant electrochemical sensor towards sulfite monitoring. The optimal catalyst concentration was determined to be 9.0 mg Pt@SWCNTs, while the optimum operating pH and the buffer solution were specified as 5.0 and phosphate buffer solution, respectively. The results confirmed the oxidation of sulfite anion occurred by a diffusion-controlled process on the surface of Pt@SWCNTs/SPE. The boosted sensing performance of the proposed Pt@SWCNTs/SPE sensor was suggested as the basis of the special catalytic behavior of Pt nanoparticles and the SWCNTs providing more active chemical sites, owing to the co-existence of Pt nanoparticles and SWCNT supporting material. In a nutshell, the proposed Pt@SWCNTs/SPE offered superior and outstanding electrochemical performance metrics for monitoring sulfite anions in real samples without any interference, suggesting its potential implementation as a novel analytical tool for determining sulfite levels in real samples.

ACKNOWLEDGMENT

REFERENCES

[1] Maaref, H., Foroughi, M.M., Sheikhhosseini, E., Akhgar, M.R., (2018), Electrocatalytic Oxidation of Sulfite and its Highly Sensitive Determination on Graphite Screen Printed Electrode Modified with New Schiff base Compound, Anal Bioanal Electro, 10, 1080-1092.

[2] Carlos, K.S., Treblin, M., de Jager, L.S., (2019), Comparison and optimization of three commercial methods with an LC-MS/MS method for the determination of sulfites in food and beverages, Food Chem, 286, 537-540.

[3]   Venkatachalam, K., Asaithambi, G., Rajasekaran, D., Periasamy, V., (2020), A novel ratiometric fluorescent probe for "naked-eye" detection of sulfite ion: Applications in detection of biological SO32- ions in food and live cells, Spectrochim Acta A, 228, 117788.

[4]   Malakootian, M., Hamzeh, S., Mahmoudi-Moghaddam, H., (2022), An efficient electrochemical sensor for determination of sulfite in water and soft drinks based on Ce3+-doped CuO nanocomposite, J Food Compos Anal, 113, 104716.

[5]   Zhai, T.T., Li, R., Zhang, N.N., Zhao, L.X., He, M.T., Tan, L., (2022), Simultaneous Detection of Sulfite and Nitrite on Graphene Oxide Nanoribbons-gold Nanoparticles Composite Modified Electrode, Electroanal, 34, 103-110.

[6]   Yang, J., Xu, X.Y., Mao, X.Y., Jiang, L., Wang, X.L., (2020), An Electrochemical Sensor for Determination of Sulfite (SO32-) in Water Based on Molybdenum Disulfide Flakes/Nafion Modified Electrode, Int J Electrochem Sc, 15, 10304-10314.

[7]   Stohs, S.J., Miller, M.J.S., (2014), A case study involving allergic reactions to sulfur-containing compounds including, sulfite, taurine, acesulfame potassium and sulfonamides, Food Chem Toxicol, 63, 240-243.

[8]   Beitollahi, H., Mahmoudi-Moghaddam, H., Tajik, S., Jahani, S., (2019), A modified screen printed electrode based on La3+-doped Co3O4 nanocubes for determination of sulfite in real samples, Microchem J, 147, 590-597.

[9]   Yang, X.F., Guo, X.Q., Zhao, Y.B., (2002), Novel spectrofluorimetric method for the determination of sulfite with rhodamine B hydrazide in a micellar medium, Anal Chim Acta, 456, 121-128.

[10] Bonifacio, R.L., Coichev, N., (2004), Chemiluminescent determination of sulfite traces based on the induced oxidation of Ni(II)/tetraglycine complex by oxygen in the presence of luminol: mechanistic considerations, Anal Chim Acta, 517, 125-130.

[11] Segundo, M.A., Rangel, A.O.S.S., Cladera, A., Cerda, V., (2000), Multisyringe flow system: determination of sulfur dioxide in wines, Analyst, 125, 1501-1505.

[12] Su, X.L., Wei, W.Z., Nie, L.H., Yao, S.Z., (1998), Flow injection determination of sulfite in wines and fruit juices by using a bulk acoustic wave impedance sensor coupled to a membrane separation technique, Analyst, 123, 221-224.

[13] Robbins, K.S., Shah, R., MacMahon, S., de Jager, L.S., (2015), Development of a Liquid Chromatography-Tandem Mass Spectrometry Method for the Determination of Sulfite in Food, J Agr Food Chem, 63, 5126-5132.

[14] Situmorang, M., Hibbert, D.B., Gooding, J.J., Barnett, D., (1999), A sulfite biosensor fabricated using electrodeposited polytyramine: application to wine analysis, Analyst, 124, 1775-1779.

[15] Wang, R.R., Mao, Y., Qu, H., Chen, W., Ma, A.J., Zheng, L., (2019), Highly sensitive and selective sulfite sensors based on solution-gated graphene transistors with multi-walled carbon nanotube functionalized gate electrodes, Food Chem, 290, 101-106.

[16] Karimi-Maleh, H., Khataee, A., Karimi, F., Baghayeri, M., Fu, L., Rouhi, J., Karaman, C., Karaman, O., Boukherroub, R., (2022), A green and sensitive guanine-based DNA biosensor for idarubicin anticancer monitoring in biological samples: A simple and fast strategy for control of health quality in chemotherapy procedure confirmed by docking investigation, Chemosphere, 291, 132928.

[17] Karimi-Maleh, H., Darabi, R., Shabani-Nooshabadi, M., Baghayeri, M., Karimi, F., Rouhi, J., Alizadeh, M., Karaman, O., Vasseghian, Y., Karaman, C., (2022), Determination of D&C Red 33 and Patent Blue V Azo dyes using an impressive electrochemical sensor based on carbon paste electrode modified with ZIF-8/g-C3N4/Co and ionic liquid in mouthwash and toothpaste as real samples, Food Chem Toxicol, 162, 112907.

[18] Cheraghi, S., Taher, M.A., Karimi-Maleh, H., Karimi, F., Shabani-Nooshabadi, M., Alizadeh, M., Al-Othman, A., Erk, N., Raman, P.K.Y., Karaman, C., (2022), Novel enzymatic graphene oxide based biosensor for the detection of glutathione in biological body fluids, Chemosphere, 287, 132187.

[19] Karimi-Maleh, H., Karimi, F., Fu, L., Sanati, A.L., Alizadeh, M., Karaman, C., Orooji, Y., (2022), Cyanazine herbicide monitoring as a hazardous substance by a DNA nanostructure biosensor, J Hazard Mater, 423, 127058.

[20] Wang, Y.T., Wang, S., Tao, L., Min, Q., Xiang, J., Wang, Q.M., Xie, J.M., Yue, Y., Wu, S.C., Li, X.F., Ding, H., (2015), A disposable electrochemical sensor for simultaneous determination of norepinephrine and serotonin in rat cerebrospinal fluid based on MWNTs-ZnO/chitosan composites modified screen-printed electrode, Biosens Bioelectron, 65, 31-38.

[21] Carbone, M., Nestico, A., Bellucci, N., Micheli, L., Palleschi, G., (2017), Enhanced performances of sensors based on screen printed electrodes modified with nanosized NiO particles, Electrochim Acta, 246, 580-587.

[22] Mousavi, S.E., Younesi, H., Bahramifar, N., Tamunaidu, P., Karimi-Maleh, H., (2022), A novel route to the synthesis of alpha-Fe2O3@C@SiO2/TiO2 nanocomposite from the metal-organic framework as a photocatalyst for water treatment, Chemosphere, 297, 133992.

[23] Liang, Y.Y., Demir, H., Wu, Y.J., Aygun, A., Tiri, R.N.E., Gur, T., Yuan, Y., Xia, C.L., Demir, C., Sen, F., Vasseghian, Y., (2022), Facile synthesis of biogenic palladium nanoparticles using biomass strategy and application as photocatalyst degradation for textile dye pollutants and their in-vitro antimicrobial activity, Chemosphere, 306, 135518.

[24] Recber, Z.B., Burhan, H., Bayat, R., Nas, M.S., Calimli, M.H., Demirbas, O., Sen, F., Hassan, K.M., (2022), Fabrication of activated carbon supported modified with bimetallic-platin ruthenium nano sorbent for removal of azo dye from aqueous media using enhanced ultrasonic wave, Environ Pollut, 302, 119033.

[25] Kocak, Y., Oto, G., Meydan, I., Seckin, H., Gur, T., Aygun, A., Sen, F., (2022), Assessment of therapeutic potential of silver nanoparticles synthesized by Ferula Pseudalliacea rech. F. plant, Inorg Chem Commun, 140, 109417.

[26] Karaman, O., (2022), Three-dimensional graphene network supported nickel-cobalt bimetallic alloy nanocatalyst for hydrogen production by hydrolysis of sodium borohydride and developing of an artificial neural network modeling to forecast hydrogen production rate, Chem Eng Res Des, 181, 321-330.

[27] Wu, Y., Altuner, E.E., Tiri, R.N.E.H., Bekmezci, M., Gulbagca, F., Aygun, A., ., Xia, C., Van Le, Q., Sen, F., Karimi-Maleh, H., (2022), Hydrogen generation from methanolysis of sodium borohydride using waste coffee oil modified zinc oxide nanoparticles and their photocatalytic activities., International Journal of Hydrogen Energy.

[28] Karimi-Maleh, H., Karaman, C., Karaman, O., Karimi, F., Vasseghian, Y., Fu, L., Baghayeri, M., Rouhi, J., Kumar, P.S., Show, P.L., Rajendran, S., Sanati, A.L., Mirabi, A., (2022), Nanochemistry approach for the fabrication of Fe and N co-decorated biomass-derived activated carbon frameworks: a promising oxygen reduction reaction electrocatalyst in neutral media, J Nanostructure Chem, 12, 429-439.

[29] Akca, A., Karaman, O., (2022), Electrocatalytic Decomposition of Formic Acid Catalyzed by M-Embedded Graphene (M = Ni and Cu): A DFT Study, Top Catal, 65, 643-655.

[30] Karaman, O., (2021), Oxygen Reduction Reaction Performance Boosting Effect of Nitrogen/Sulfur Co-Doped Graphene Supported Cobalt Phosphide Nanoelectrocatalyst: pH-Universal Electrocatalyst, Ecs J Solid State Sc, 10, 061003.

[31] Bostanci, M.T., Bulbul, A.S., Celik, I.S., Kocabas, Y.Z., Burhan, H., Bayat, R., Sen, F., Zakariae, N., Esmaeili, R., Jafari, H., Karimi, F., Karimi-Maleh, H., (2022), Investigation of antibacterial, antifungal, antibiofilm, antioxidant and anticancer properties of methanol extracts of Salvia marashica Ilcim, Celep & Dogan and Salvia caespitosa Montbret & Aucher ex Benth plants with medicinal importance, Chemosphere, 288, 132602.

[32] Khoshkho, S.M., Mahdavian, M., Karimi, F., Karimi-Maleh, H., Razaghi, P., (2022), Production of bioethanol from carrot pulp in the presence of Saccharomyces cerevisiae and beet molasses inoculum; A biomass based investigation, Chemosphere, 286, 131688.

[33] Beitollahi, H., Tajik, S., Maleh, H.K., Hosseinzadeh, R., (2013), Application of a 1-benzyl-4-ferrocenyl-1H-[1,2,3]-triazole/carbon nanotube modified glassy carbon electrode for voltammetric determination of hydrazine in water samples, Appl Organomet Chem, 27, 444-450.

[34] Kianfar, S., Golikand, A.N., ZareNezhad, B., (2021), Bimetallic-metal oxide nanoparticles of Pt-M (M: W, Mo, and V) supported on reduced graphene oxide (rGO): radiolytic synthesis and methanol oxidation electrocatalysis, J Nanostructure Chem, 11, 287-299.

[35] Jahani, P.M., Beitollahi, H., Nejad, F.G., Dourandish, Z., Di Bartolomeo, A., (2022), Screen-printed graphite electrode modified with Co3O4 nanoparticles and 2D graphitic carbon nitride as an effective electrochemical sensor for 4-aminophenol detection, Nanotechnology, 33, 395702.

[36] Qian, T., Yu, C.F., Zhou, X., Wu, S.S., Shen, J., (2014), Au nanoparticles decorated polypyrrole/reduced graphene oxide hybrid sheets for ultrasensitiye dopamine detection, Sensor Actuat B-Chem, 193, 759-763.

[37] Hashemi, P., Bagheri, H., Afkhami, A., Amidi, S., Madrakian, T., (2018), Graphene nanoribbon/FePt bimetallic nanoparticles/uric acid as a novel magnetic sensing layer of screen printed electrode for sensitive determination of ampyra, Talanta, 176, 350-359.

[38] Zuo, Y.X., Xu, J.K., Jiang, F.X., Duan, X.M., Lu, L.M., Xing, H.K., Yang, T.T., Zhang, Y.S., Ye, G., Yu, Y.F., (2017), Voltammetric sensing of Pb(II) using a glassy carbon electrode modified with composites consisting of Co3O4 nanoparticles, reduced graphene oxide and chitosan, J Electroanal Chem, 801, 146-152.

[39] Bagheri, H., Hajian, A., Rezaei, M., Shirzadmehr, A., (2017), Composite of Cu metal nanoparticles-multiwall carbon nanotubes-reduced graphene oxide as a novel and high performance platform of the electrochemical sensor for simultaneous determination of nitrite and nitrate, J Hazard Mater, 324, 762-772.

[40] Ganjali, M.R., Beitollahi, H., Zaimbashi, R., Tajik, S., Rezapour, M., Larijani, B., (2018), Voltammetric Determination of Dopamine Using Glassy Carbon Electrode Modified with ZnO/Al2O3 Nanocomposite, Int J Electrochem Sc, 13, 2519-2529.

[41] Jiang, C.J., Elliott, J.M., Cardin, D.J., Tsang, S.C., (2009), An Electrochemical Study of 4-Aminothiophenol/Pt Nanoparticle Multilayers on Gold Electrodes, Langmuir, 25, 534-541.

[42] Yu, H., Yu, J.B., Li, L.L., Zhang, Y.J., Xin, S.Q., Ni, X.Z., Sun, Y., Song, K., (2021), Recent Progress of the Practical Applications of the Platinum Nanoparticle-Based Electrochemistry Biosensors, Front Chem, 9, 282.

[43] Karimi-Maleh, H., Beitollahi, H., Kumar, P.S., Tajik, S., Jahani, P.M., Karimi, F., Karaman, C., Vasseghian, Y., Baghayeri, M., Rouhi, J., Show, P.L., Rajendran, S., Fu, L., Zare, N., (2022), Recent advances in carbon nanomaterials-based electrochemical sensors for food azo dyes detection, Food Chem Toxicol, 164, 112961.

[44] Barsan, M.M., Ghica, M.E., Brett, C.M.A., (2015), Electrochemical sensors and biosensors based on redox polymer/carbon nanotube modified electrodes: A review, Anal Chim Acta, 881, 1-23.

[45] Wang, J., (2005), Carbon-nanotube based electrochemical biosensors: A review, Electroanal, 17, 7-14.

[46] Neravathu, D., Paloly, A.R., Sajan, P., Satheesh, M., Bushiri, M.J., (2020), Hybrid nanomaterial of ZnFe2O4/alpha-Fe2O3 implanted graphene for electrochemical glucose sensing application, Diam Relat Mater, 106, 107852.

RESEARCH ARTICLE

INFLUENCE of SPINNING TOPOLOGICAL DEFECT on the LANDAU LEVELS ofRELATIVISTIC SPIN-0 PARTICLES

Abdullah GUVENDİ[1*]

[*1]Erzurum Technical University, Faculty of Science, Erzurum, abdullah.guvendi@erzurum.edu.tr,
ORCID: 0000-0003-0564-9899

ABSTRACT

We investigate relativistic Landau quantization of spinless particle in three dimensional space-time induced by topological defect with spin through acquiring non-perturbative solution of the corresponding Klein-Gordon equation. The obtained results allow us to analyze the alterations stemming from the background geometry on the spectrum. We observe that the background geometry can be responsible not only for shifts on the relativistic Landau levels but also for symmetry breaking of the particle-antiparticle states provided that the defect possesses non-zero spin.

Keywords: *Landau Quantization,Relativistis Quantum Mechanics,Topological Defect,Cosmic String*

1. INTRODUCTION

The history of investigations for quantum fields in curved spaces goes long way back [1-5] and analysis of the influences of curved spaces on the relativistic dynamics of physical systems has great importance in the modern physics due to the fact that these kinds of investigations have provided very interesting results [6-28]. One of the most important results of such studies is that they provide an opportunity us to see what the dependence of relativistic dynamics of a single particle or a composite system on the topological properties of the geometric background [6]. This allows us to discuss also the effect of gravity on the quantum mechanical systems [6,12]. In general, in the theoretical framework, in order to analyze the effects of curved spaces or non-trivial topologies on the quantum mechanical systems, relativistic equations such as Klein-Gordon ($\mathcal{KG}$) [10], Dirac [9], Duffin-Kemmer-Petiau [13], Vector Boson [14,15] and fully-covariant many-body equations [15,16] are used. In the literature, there exists numerous announced results for relativistic dynamics of spinning and spin-less particles in curved spaces [6-19]. The $\mathcal{KG}$ equation is used to describe the dynamics of spin-less relativistic particles [17-19] and the effects of topological defect-induced space-time backgrounds such as cosmic string space-time [19], spiral dislocation space-time [20], screw dislocation space-time [21], global monopole space-time [22] on the relativistic spin-less particles were investigated by solving the generalized $\mathcal{KG}$ equation.

On the other hand, the cosmic strings [23-25] which are stable linear topological defects were introduced first through general solutions in three dimensions [6,23-25] and background geometry

spanned by a static or spinning cosmic string has non-trivial topology [6,23-25]. This is because of such space-time structures are not flat when viewed globally even though they are locally flat [23-25]. Due to this interesting feature, the cosmic string induced background geometry may cause for several interesting phenomena in the universe [6,23-26]. Further, the spatial part of the metric representing to cosmic string space-time (see Ref. [6]) describes also the topological defect that can appear in condensed matter mediums [15,27]. Therefore, the influence of topological defect-induced background geometries on the dynamics of physical systems has been widely studied [6,8,10-22,26,27]. In these works, the well-known quantum systems, such as quantum oscillators [8,11,13,15-22,26], single particle test fields [10,20,21,27,28], positronium or hydrogen-like low energy bound-state systems [6,12] in quantum electrodynamics are preferred to investigate the effects of space-time structures. It is also clear that analysis the effects of external magnetic field on the evolution of quantum systems is of high importance in the modern physics since such fields are exist at almost each point in the universe [9,29,30]. Hence, non-perturbative results obtained for quantum systems exposed to an external magnetic field in curved spaces are very important. In this contribution, we deal with a scalar field under the effect of external magnetic field (uniform) in the geometric background spanned by a spinning cosmic string [6,25].

This article is structured as the following. In Sec. 2, we introduce the generalized $\mathcal{KG}$ equation and then we obtain a wave equation for a scalar relativistic particle (charged) exposed to external uniform magnetic field in the background geometry induced by a spinning string source. In Sec. 3, we acquire non-perturbative results and show the dependence of spectrum on the parameters of background geometry. Then, we summarize the results and discuss to the findings in detail. Here we declare that we will prefer to use the units $\hbar = c = 1$.

2. GENERALIZED KLEIN-GORDON EQUATION

In this part, we write the generalized $\mathcal{KG}$ equation for a charged spinless particle in three-dimensional spacetime spanned by a spinning string source and obtain second order wave equation. The generalized $\mathcal{KG}$ equation is written as follows [5]

$$\frac{1}{\sqrt{|-g|}} \mathfrak{D}_\mu \left(\sqrt{|-g|} g^{\mu\nu} \mathfrak{D}_\nu \Psi \right) = m^2 \Psi, \quad \mathfrak{D}_\mu = \partial_\mu + ieA_\mu, \quad (\mu, \nu = 0,1,2.), \tag{1}$$

where g stands for the determinant of the covariant metric tensor, $g^{\mu\nu}$ is the contravariant metric tensor, the letter e represents to the elementary electrical charge, A_μ is the electromagnetic 3-vector potential and Ψ is the scalar field with mass of m. It is known that the external magnetic field (uniform) is taken into account through the angular component of the 3-vector potential [29,30]. The spacetime background spanned by an idealized spinning string source is described by the following metric with signature $+, -, -$ [6,25]

$$ds^2 = dt^2 + 2\varpi dt d\vartheta - dr^2 - (\alpha^2 r^2 - \varpi^2) d\vartheta^2, \tag{2}$$

for which covariant ($g_{\mu\nu}$) and contravariant ($g^{\mu\nu}$) form of the metric tensor can be written as the following

$$g_{\mu\nu} = \begin{pmatrix} 1 & 0 & \varpi \\ 0 & -1 & 0 \\ \varpi & 0 & -\alpha^2 r^2 + \varpi^2 \end{pmatrix}, \qquad g^{\mu\nu} = \begin{pmatrix} 1 - \frac{\varpi^2}{\alpha^2 r^2} & 0 & \frac{\varpi}{\alpha^2 r^2} \\ 0 & -1 & 0 \\ \frac{\varpi}{\alpha^2 r^2} & 0 & -\frac{1}{\alpha^2 r^2} \end{pmatrix}. \tag{3}$$

In Eq. (2), α relates with the angular deficit in the background and it depends on the linear mass density of the string, ϖ is the spin of the string. The Eq. (3) leads that $det(g_{\mu\nu}) = \alpha^2 r^2$. Now we can write explicit form of the generalized $\mathcal{KG}$ equation for a spinless relativistic particle (charged) exposed to a uniform external magnetic field in the background geometry induced by the spinning string as follows

$$\frac{1}{\sqrt{|-g|}} \partial_t [\sqrt{|-g|} g^{tt} \partial_t \Psi] + \frac{1}{\sqrt{|-g|}} \partial_t [\sqrt{|-g|} g^{t\vartheta} (\partial_\vartheta + ieA_\vartheta) \Psi] + \frac{1}{\sqrt{|-g|}} \partial_r [\sqrt{|-g|} g^{rr} \partial_r \Psi] +$$
$$\frac{1}{\sqrt{|-g|}} (\partial_\vartheta + ieA_\vartheta) [\sqrt{|-g|} g^{\vartheta t} \partial_t \Psi] + \frac{1}{\sqrt{|-g|}} (\partial_\vartheta + ieA_\vartheta) [\sqrt{|-g|} g^{\vartheta\vartheta} (\partial_\vartheta + ieA_\vartheta) \Psi] - m^2 \Psi = 0, \tag{4}$$

where $A_\vartheta = \frac{\alpha \mathfrak{B}_0 r^2}{2}$ [31]. With respect to the Eq. (2), we can factorize the wave function Ψ as follows

$$\Psi = e^{-i\omega t} e^{i\ell\vartheta} \psi(r), \tag{5}$$

in which ω and ℓ are the relativistic frequency and orbital quantum number, respectively. For the considered system, by inserting Eq. (3) and Eq. (5) into the Eq. (4), we obtain a wave equation

$$\partial_r^2 \psi(r) + \frac{1}{r} \partial_r \psi(r) + \left[\omega^2 \left(1 - \frac{\varpi^2}{\alpha^2 r^2} \right) - \frac{2\omega\varpi\ell}{\alpha^2 r^2} - \frac{\omega\varpi B}{\alpha} - \frac{\ell^2}{\alpha^2 r^2} - \frac{B\ell}{\alpha} - \frac{B^2 r^2}{4} - m^2 \right] \psi(r), \tag{6}$$

where $B = e\mathfrak{B}_0$. This second order differential equation can be reduced into a familiar form by means of a new variable, $\varrho = \frac{B}{2} r^2$,

$$\partial_\varrho^2 \psi(r) + \frac{1}{\varrho} \partial_\varrho \psi(\varrho) - \left[\frac{B\varrho + 2m^2 - 2\omega^2}{4B\varrho} + \frac{(\omega\varpi + \ell)}{2\alpha\varrho} + \frac{(\omega\varpi + \ell)^2}{2\alpha\varrho^2} \right] \psi(\varrho). \tag{7}$$

3. ALTERED SPECTRUM

Here, we obtain non-perturbative spectra for the charged scalar relativistic particle exposed to an external uniform magnetic field in the space-time background induced by the spinning cosmic string. To acquire exact result, we will deal with the Eq. (7). By considering an ansatz function, $\psi(\varrho) = \varrho^{-\frac{1}{2}} \chi(\varrho)$, the wave equation in Eq. (7) can be reduced into a familiar form (see also [30])

$$\left[\partial_\varrho^2 + \frac{\zeta}{\varrho} + \frac{\frac{1}{4} - \epsilon^2}{\varrho^2} - \frac{1}{4} \right] \chi(\varrho) = 0, \quad \zeta = \frac{\alpha(\omega^2 - m^2) - B(\omega\varpi + \ell)}{2B\alpha}, \quad \epsilon = \frac{\omega\varpi + \ell}{2\alpha}. \tag{8}$$

It can be verified that solution function of the Eq. (8) is given in terms of the Whittaker function, which can also be expressed in terms of Confluent Hypergeometric function [8], as $\chi(\varrho) = \mathcal{Q} \mathcal{W}_{\zeta,\epsilon}(\varrho)$. Here, $\mathcal{Q}$ is an arbitrary constant and the $\mathcal{W}_{\zeta,\epsilon}(\varrho)$ is the Whittaker function [24,25]. To be polynomial

condition of the solution function is given as the following $\frac{1}{2} + \epsilon - \zeta = -n$, $(n = 0,1,2..)$ [8,29,30] in which n is the radial quantum number. Through this termination, one can acquire the following spectrum of frequency

$$\omega_{n\ell} = \pm m \left\{ \sqrt{1 - \frac{w_c}{m}\left(2n + 1 + \frac{2\ell}{\alpha}\right) + \frac{w_c{}^2\varpi^2}{m^2\alpha^2}} \mp \frac{w_c\varpi}{m\alpha} \right\}, \quad \alpha = 1 - 4\mu_s, \tag{9}$$

where $w_c = \frac{e\mathcal{B}_0}{m}$ is the relativistic cyclotron frequency [29-33]. Here, we should underline that the ϖ(positive) is spin parameter of the cosmic string [6], α relates with angular deficit in the background geometry, $\alpha \in (0,1]$, μ_s is the linear mass density of the cosmic string [6] and orbital quantum number ℓ can take the following values: $\ell = 0, \pm 1 \pm 2..$ [10,18] in 2+1dimensions. In Eq. (9) we see that the obtained spectrum depends on the parameters of the geometric background and allows us to analyze the effects of background geometry on the relativistic Landau levels of the considered scalar particle (see Figures. 1, 2, 3, 4 and Figure 5). Here, we observe that the information about the string tension (see Ref. [6]) is carried also by the orbital quantum number ℓ. But, we lose this information if the string source is static ($\varpi = 0$) for the $\ell = 0$ levels.
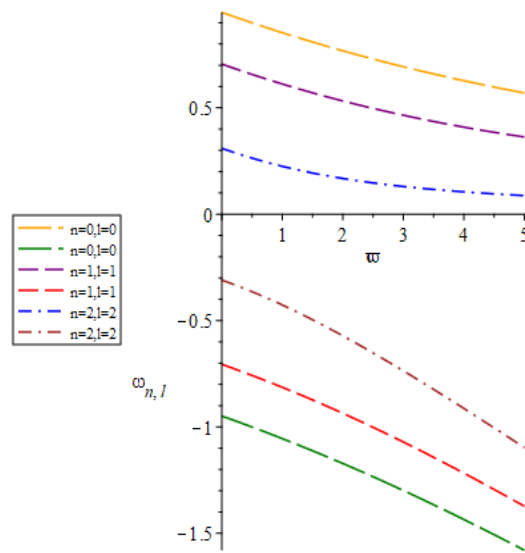
Figure 1. Effect of the spin of the string ($\propto \varpi$) on the Landau levels for $\alpha = 0.99$, $m = 1$, $e = 1, \mathcal{B}_0 = 0.1$.
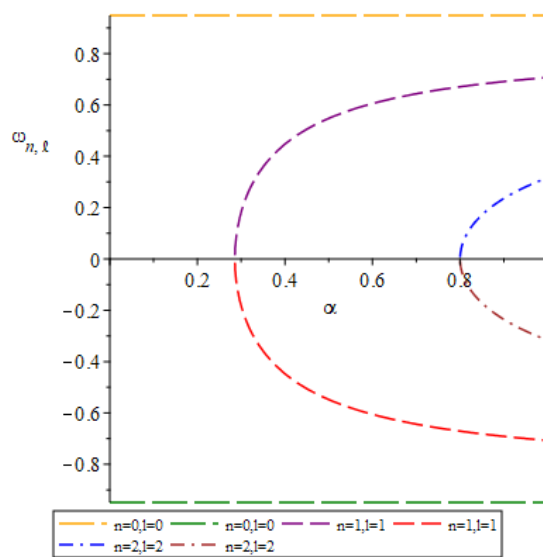
Figure 2. Influence of the α parameter on the Landau levels for $\varpi = 0$, $m = 1$, $e = 1, \mathcal{B}_0 = 0.1$.
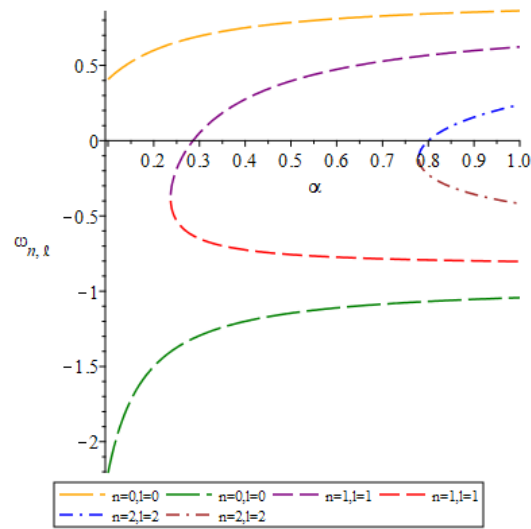
Figure 3. Effect of the parameter α on the Landau levels for $\varpi = 0.9, m = 1, \; e = 1, \mathcal{B}_0 = 0.1$.
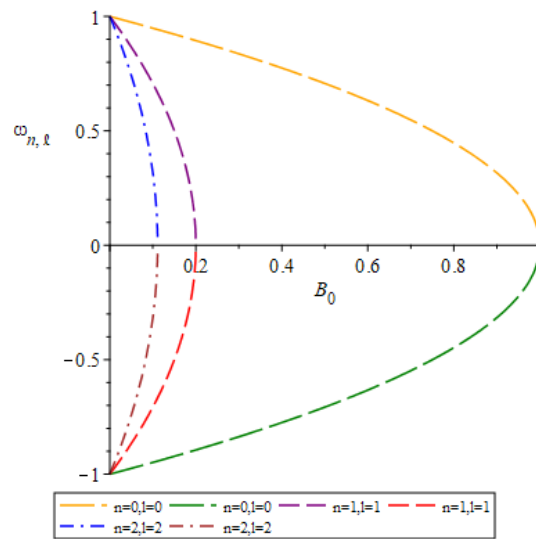
Figure 4. Effect of external magnetic field on the total frequency for $\varpi = 0, \; \alpha = 1, \; m = 1, \; e = 1$.
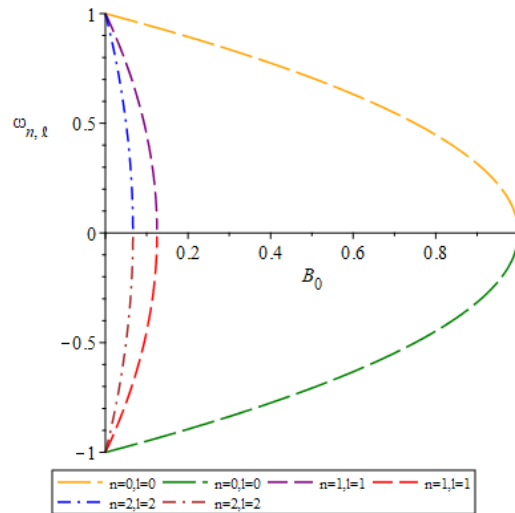
Figure 5. Effect of angular deficit parameter on the Landau levels for $\varpi = 0, \alpha = 0.4, m = 1, e = 1$.

4. CONCLUSION and DISCUSSIONS

In this contribution, we have analyzed the effects of a background geometry induced by a spinning topological defect on the relativistic Landau levels of a scalar relativistic particle exposed to an external uniform magnetic field through obtaining non-perturbative solution of the corresponding Klein-Gordon equation. The obtained spectrum of frequency (or energy) expression is given by the Eq. (9) and shows that the energy levels depend on both the spin parameter (ϖ) of the string and angular deficit ($\propto \alpha$) in the background geometry. The result in Eq. (9) can be reduced for such a flat planar system when $\varpi = 0$ and $\alpha = 1$. The Figure 4 shows that magnitude of the total energy decreases as strength of the external uniform magnetic field increases. In Figure 2 and in Figure 5, we see that the presence of angular deficit in the geometric background can affect the magnitude of the energy levels and can cause shifts in these levels. The Figure 1 and Figure 3 clearly show the string source-spanned geometric background can be responsible for symmetry breaking in the context of the energy for particle-antiparticle states provided that the cosmic string possesses non-vanishing spin.

ACKNOWLEDGEMENTS

REFERENCES

[1] Birrell, N.D. and Davies, P.C.W., (1884), Quantum fields in curved space, Cambridge university press, Reprint edition, p 352.

[2] Brandenberger, R.H., (1985), Quantum field theory methods and inflationary universe models, Reviews of Modern Physics, 57, 1.

[3] DeWitt, B.S., (1975), Quantum field theory in curved spacetime, Physics Reports, 19, 295--357.

[4] DeWitt, B.S., (1957), Dynamical theory in curved spaces. I. A review of the classical and quantum action principles, Reviews of modern physics, 29, 377.

[5] Davies, P.C.W., (1976), Quantum field theory in curved space-time, Nature, 263, 377--380.

[6] Guvendi, A. and Sucu, Y., (2020), An interacting fermion-antifermion pair in the spacetime background generated by static cosmic string, Physics Letters B, 811, 135960.

[7] Anandan, J., (1981), Sagnac effect in relativistic and nonrelativistic physics, Physical Review D, 24, 338.

[8] Guvendi, A. and Hassanabadi, H., (2021), Relativistic Vector Bosons with Non-minimal Coupling in the Spinning Cosmic String Spacetime, Few-Body Systems, 62, 1—8.

[9] Dogan, S.G. and Sucu, Y., (2019), Quasinormal modes of Dirac field in 2+ 1 dimensional gravitational wave background, Physics Letters B, 797, 134839.

[10] Ahmed, F., (2019), Linear confinement of a scalar and spin-0 particle in a topologically trivial flat Gödel-type space-time, European Physical Journal C, 79, 1--13.

[11] Guvendi, A., (2021), Effects of Rotating Frame on a Vector Boson Oscillator, Sakarya University Journal of Science, 25, 847--853.

[12] Parker, L., (1980), One-electron atom in curved space-time, Physical Review Letters, 44, 1559.

[13] Zare, S., Hassanabadi, H. and Montigny, M., (2020), Non-inertial effects on a generalized DKP oscillator in a cosmic string space-time, General Relativity and Gravitation, 52, 1—20.

[14] Guvendi, A., Zare, S. and Hassanabadi, H., (2021), Vector boson oscillator in the spiral dislocation spacetime, European Physical Journal A, 57, 1--6.

[15] Guvendi, A. and Hassanabadi, H., (2021), Noninertial effects on a composite system, International Journal of Modern Physics A, 36, 2150253.

[16] Guvendi, A., (2021), Dynamics of a composite system in a point source-induced space-time, International Journal of modern Physics A, 36, 2150144.

[17] Figueiredo, M.E.R. and Bezerra de Mello, E.R., (2012), Relativistic quantum dynamics of a charged particle in cosmic string spacetime in the presence of magnetic field and scalar potential, European Physical Journal C, 72, 1--14.

[18] Ahmed, F., (2019), The generalized Klein-Gordon oscillator with Coulomb-type potential in (1+ 2)-dimensions Gürses space-time, General Relativity and Gravitation, 51, 1--16.

[19] Hosseini, M., Hassanabadi, H., Hassanabadi, S. and Sedaghatnia, P., (2019), Klein-Gordon oscillator in the presence of a Cornell potential in the cosmic string space-time, International Journal of Geometric Methods in Modern Physics, 16, 1950054.

[20] Vitoria, R.L.L. and Bakke, K., (2018), Rotating effects on the scalar field in the cosmic string spacetime, in the spacetime with space-like dislocation and in the spacetime with a spiral dislocation, European Physical Journal C, 78, 1--6.

[21] Vitoria, R.L.L., (2019), Noninertial effects on a scalar field in a spacetime with a magnetic screw dislocation, European Physical Journal C, 79, 1--7.

[22] Montigny, M., Hassanabadi, H., Pinfold, J. and Zare, S., (2021), Exact solutions of the generalized Klein--Gordon oscillator in a global monopole space-time, European Physical Journal Plus, 136, 1--14.

[23] Vilenkin, A., (1985), Cosmic strings and domain walls, Physics reports, 121, 263--315.

[24] Deser, S., Jackiv, R. and Hooft, G., (1984), Three-dimensional Einstein gravity: dynamics of flat space, Annals of Physics, 152, 220--235.

[25] Clement, G., (1990), Rotating string sources in three-dimensional gravity, Annals of Physics, 201, 241–257.

[26] Linet, B., (1986), Force on a charge in the space-time of a cosmic string, Physical Review D, 33, 1833.

[27] Bakke, K. and Furtado, C., (2010), Bound states for neutral particles in a rotating frame in the cosmic string spacetime, Physical Review D, 82, 084025.

[28] Bezerra, V.B., Lobo, I.P., Mota, H.F. and Muniz, C.R., (2019), Landau levels in the presence of a cosmic string in rainbow gravity, Annals of Physics, 401, 163--173.

[29] Guvendi, A. and Dogan, S.G., (2021), Relativistic dynamics of oppositely charged two fermions interacting with external uniform magnetic field, Few-Body Systems, 62, 1--8.

[30] Guvendi, A., (2021), Relativistic Landau levels for a fermion-antifermion pair interacting through Dirac oscillator interaction, European Physical Journal C, 81, 1--7.

[31] Cunha, M.M., Dias, H.S. and Silva, E.O., (2020), Dirac oscillator in a spinning cosmic string spacetime in external magnetic fields: Investigation of the energy spectrum and the connection with condensed matter physics, Physical Review D, 102, 105020.

[32] [32] Dogan, S.G., (2022), Landau Quantization for Relativistic Vector Bosons in a Gödel-Type Geometric Background, Few-Body Systems, 63, 1--10.

[33] Zare, S., Hassanabadi, H. and Guvendi, A., (2022), Relativistic Landau quantization for a composite system in the spiral dislocation spacetime, European Physical Journal Plus, 137, 1—8.

RESEARCH ARTICLE

PD CONTROLLER DESIGN and STABILITY ANALYSIS for SYSTEMS HAVING FRACTIONAL ORDER DELAY

Münevver Mine ÖZYETKİN[1*]

[1]Aydın Adnan Menderes University, Faculty of Engineering, Department of Electrical and Electronics Engineering, Aydın,
m.ozyetkin@adu.edu.tr, ORCID: 0000-0002-3819-5240

ABSTRACT

Fractional order systems (FOS) are one of the subjects that have been studied extensively. Such systems are difficult and complex structures to be analyzed mathematically. The degree of difficulty is even greater when the system has time delay. Considering the studies on FOS, either the transfer function of the system is of fractional order, or the controller has a fractional order structure. Time delay is common in practical systems. Studies mostly focused on classical time delay term. However, time delay can be of a fractional order. Studies for such systems are quite limited as the mathematical analysis part is complex.

In this study, systems having fractional order delay, are examined. By using the stability boundary locus (SBL) method, the necessary equations for calculating all stable PD controller parameters for such systems are obtained. It is necessary to test whether the parameters selected from the obtained stability region provide stability. However, stability analysis of such systems is very problematic. For this reason, an approximation method previously proposed by the author is used. Thus, the system is transformed to a fractional order structure. Then, the stability analysis of the FOS can be easily done. It is seen that the obtained equations and the approximation method proposed by the author for the stability test provide quite reasonable results.

Keywords: *Fractional Order System, Time Delay, PD Controller, Stability Region*

1. INTRODUCTION

FOS have transfer functions expressed by fractional order derivatives and/or fractional order integrals. Although this is a very old topic, it has been mostly studied by the mathematicians [1]. With the development of modern physics, the application research of fractional order operators has increased [1]. The memory feature of such systems and the emergence of solution techniques also have an effect on this. The voltage-current relation of a semi-infinite lossy RC line is given as an example of FOS [2].

A control system can have both fractional order dynamics and be controlled by a fractional order controller. Many important studies have been done on the fractional order PID (Proportional Integral Derivative) controllers. Some important examples can be found in [3–5]. Since the PID controller is a

widely known controller structure, there are many studies on this subject, and it is still being studied. In this regard, [6–9] can be examined for some important studies based on the stability region concept. Despite its performance limitations, the PD (Proportional Derivative) controller is widely used for robot position control due to simplicity [10]. Position controllers often include PD control. Robot force control systems are commonly included PD or PID controllers [10]. The adaptive PD controller for robot manipulators were studied in [11]. The PD controller design for the active suspension system was made in [12]. However, studies on PD in the literature are still limited.

Time delays are frequently encountered in industrial applications such as heat exchanges, distillation units, mining processes, and steel production, etc. [13]. Time-delay processes range from biological systems to mechanical systems, including economic or electric fields [13]. The classical time delay is known as $\exp(-s\tau)$ in the s domain. However, there are cases where the time delay is fractional order.

For example, the transfer function of the terminated resistance-capacitance line is $\exp(-\sqrt{sT})$ [14]. Here, T is distributed lag. For simplicity, the normalized form $\exp(-\sqrt{s})$ is often used [14]. In addition to the electrical transmission line, certain types of delays in servo mechanisms and other mechanical and thermal phenomena also appear to have transfer functions of interest [14]. Studies have mainly focused on the stability of a class of distributed systems. Transfer functions of such systems involve $\sqrt{s}$ and/or $\exp(-\sqrt{s})$. As noted in [15], many circuits, processes, or systems such as thermal processes, hole diffusion of transistors, electromagnetic devices, and transmission lines have distributed parameters and/or delay elements. Stability analysis of linear distributed parameter systems (DBS) is complex since the Laplace domain representation of these systems include either the square root sign of s or other irrational or transcendental functions [15,16]. Mathematical descriptions of linear DBS with a distributed lag include double valued functions of s in the form of $\sqrt{s}$ and $\exp(\sqrt{s})$. Although it is a very interesting subject, studies in the literature are quite limited. Some of these studies can be summarized as follows. In [17], Pontryagin's stability criterion is extended to systems with distributed delay. In [15], the algebraic stability test procedures are extended to a certain class of DBS with multiple delays. An algebraic stability test procedure such as the Routh is extended to a certain class of DBS with a distributed lag in [16]. When both studies are examined, it is seen that the $\sqrt{s}$ plane is considered. The basis on which it is based is the Riemann surface, and it is seen that the stability in this regard is defined by the Brin criterion [16]. The Brin criterion is an important step in the stability definition of the FOS. In [18], analytical stability bound has been obtained using the Lambert function W for a class of delayed fractional-order differential equations with constant coefficients. A numerical algorithm for testing the BIBO stability of fractional delay systems (FDS) is presented in [19]. BIBO stability of a class of FDS with commensurate orders and multiple commensurate delays of retarded type is studied in [20]. A study was carried out on FOS of retarded type with two independent delays, and the stability regions in spaces of delays were determined in [21]. Recently, a method using frequency domain data to obtain time response of FOS has been reported in [22]. Thanks to this method computation of time responses of FOS is possible. These studies involve very complex procedures and are not easy to understand. Also, these studies do not provide universally acceptable practical algebraic criteria or algorithms. In [23], the author proposed an approximation method to investigate stability of the systems having integer order and non-integer order delay. Using this approximation, the time delay in fractional structure can be converted into a fractional order transfer function (FOTF) and the procedures applied for FOTFs can be applied to these systems. In addition, in this study, PID design has been made for systems with fractional order

time delay (FOTD), As stated before, the studies related on this topic is very restricted. Therefore, there is a need for new research on this subject. This study is the first application of the approximation method presented in [23] for PD controllers. The equations obtained here are completely original.

This study is aimed to calculate all stable PD controller parameters for FOTD processes using the stability region method. In addition, an approximation method previously proposed by the author is briefly presented to test whether the parameters selected from the obtained stability region provide stability.

2. MATERIALS and METHODS

In this section, PD controller is designed for systems with FOTD. The necessary equations have been obtained based on the SBL method. There is extensive literature information about this method. For some of them [6,8,9,24–27] can be examined. To the best of the author's knowledge, there are no studies on PD controller design and stability regions for systems with FOTD. The author's work on PID design on this subject can be seen in [23]. This section also presents an approximation method required for stability test.

2.1. Obtaining PD Parameters Using Stability Region Method

Let the transfer function (TF) of the system given in Figure 1 be defined as follows.

$$G_p(s) = G(s)e^{-(\tau s)^{\alpha}} = \frac{N(s)}{D(s)}e^{-\tau^{\alpha}s^{\alpha}} \tag{1}$$

The TF of the PD controller is defined by Eq. (2),

$$C(s) = k_p + k_d s \tag{2}$$

The characteristic equation (CE) of the system is obtained as follows.

$$\Delta(s) = 1 + C(s)G_p(s) = 1 + (k_p + k_d s)\frac{N(s)}{D(s)}e^{-\tau^{\alpha}s^{\alpha}} = D(s) + (k_p + k_d\,s)N(s)e^{-\tau^{\alpha}s^{\alpha}} \tag{3}$$

Let us express the TF of the system as follows.

$$G(j\omega) = \frac{N_e(-\omega^2) + j\omega N_o(-\omega^2)}{D_e(-\omega^2) + j\omega D_o(-\omega^2)} = \frac{N_e + j\omega N_o}{D_e + j\omega D_o} \tag{4}$$

For simple notation, the expression $(-\omega^2)$ will not be written in the next equations. In this case, the CE is obtained as follows.

$$\Delta(j\omega) = (D_e + j\omega D_o) + (k_p + j\omega k_d)(N_e + j\omega N_o)\left(e^{-\tau^\alpha(j\omega)^\alpha}\right)$$

$$= (D_e + j\omega D_o) + [(k_p + j\omega k_d)(N_e + j\omega N_o)](e^{-\left[(\cos\frac{\pi}{2}\alpha + j\sin\frac{\pi}{2}\alpha)\omega^\alpha\tau^\alpha\right]})$$

$$= (D_e + j\omega D_o) + (k_p + j\omega k_d)(N_e + j\omega N_o)e^{-(\cos\frac{\pi}{2}\alpha)\omega^\alpha\tau^\alpha}e^{-j(\sin\frac{\pi}{2}\alpha)\omega^\alpha\tau^\alpha}$$

$$= (D_e + j\omega D_o) + (k_p + j\omega k_d)(N_e + j\omega N_o)e^{-(\cos\frac{\pi}{2}\alpha)\omega^\alpha\tau^\alpha} \tag{5}$$

$$\times[\cos(\omega^\alpha\tau^\alpha(\sin\frac{\pi}{2}\alpha)) - j\sin(\omega^\alpha\tau^\alpha(\sin\frac{\pi}{2}\alpha))]$$

Let Eqs. (6) and (7) be expressed as follows.

$$e^{-(\cos\frac{\pi}{2}\alpha)\omega^\alpha\tau^\alpha} = e^{-m} \tag{6}$$

$$\omega^\alpha(\sin\frac{\pi}{2}\alpha)\tau^\alpha = n \tag{7}$$

Using these equations, the CE is rearranged as follows.

$$\Delta(j\omega) = (D_e + j\omega D_o) + (k_p + j\omega k_d)(N_e + j\omega N_o)e^{-m}[\cos(n) - j\sin(n)]$$

$$= D_e + k_p N_e e^{-m}\cos(n) - \omega^2 k_d N_o e^{-m}\cos(n) + \omega k_p N_o e^{-m}\sin(n) + \omega k_d N_e e^{-m}\sin(n) \tag{8}$$

$$+ j[\omega D_o + \omega k_p N_o e^{-m}\cos(n) + \omega k_d N_e e^{-m}\cos(n) - k_p N_e e^{-m}\sin(n) + \omega^2 k_d N_o e^{-m}\sin(n)]$$

If Eq. (8) is set to zero, the real and imaginary parts are obtained as follows.

Real Part:

$$\text{Re}\,\Delta(j\omega) = k_p[N_e e^{-m}\cos(n) + \omega N_o e^{-m}\sin(n)] + k_d[\omega N_e e^{-m}\sin(n) - \omega^2 N_o e^{-m}\cos(n)] = -D_e \tag{9}$$

Imaginary Part:

$$\text{Im}\,\Delta(j\omega) = k_p[\omega N_o e^{-m}\cos(n) - N_e e^{-m}\sin(n)] + k_d[\omega^2 N_o e^{-m}\sin(n) + \omega N_e e^{-m}\cos(n)] = -\omega D_o \tag{10}$$

Eqs. (11) and (12) are obtained using Eqs. (9) and (10), The solution of these equations gives Eqs. (13) and (14),

$$k_p A(\omega) + k_d\,B(\omega) = X(\omega) \tag{11}$$

$$k_p\,C(\omega) + k_d\,D(\omega) = Y(\omega) \tag{12}$$

$$k_p = \frac{X(\omega)D(\omega) - Y(\omega)B(\omega)}{A(\omega)D(\omega) - C(\omega)B(\omega)} \tag{13}$$

$$k_d = \frac{Y(\omega)A(\omega) - X(\omega)C(\omega)}{A(\omega)D(\omega) - C(\omega)B(\omega)} \tag{14}$$

Here, the parameters are as follows.

$$
\begin{aligned}
X(\omega) &= -D_e \\
Y(\omega) &= -\omega D_o \\
A(\omega) &= N_e e^{-m}\cos(n) + \omega N_o e^{-m}\sin(n) \\
B(\omega) &= \omega N_e e^{-m}\sin(n) - \omega^2 N_o e^{-m}\cos(n) \\
C(\omega) &= \omega N_o e^{-m}\cos(n) - N_e e^{-m}\sin(n) \\
D(\omega) &= \omega^2 N_o e^{-m}\sin(n) + \omega N_e e^{-m}\cos(n)
\end{aligned}
\tag{15}
$$

By using these equations into Eqs. (13) and (14), k_p and k_d parameters are obtained as follows, respectively.

$$k_p = \frac{(\omega^2 N_o D_o + N_e D_e)\cos(n) + \omega(N_o D_e - N_e D_o)\sin(n)}{-e^{-m}(N_e^{\ 2} + \omega^2 N_o^{\ 2})} \tag{16}$$

$$k_d = \frac{\omega^2(N_o D_e - N_e D_o)\cos(n) - \omega(N_e D_e + \omega^2 N_o D_o)\sin(n)}{\omega^2 e^{-m}(N_e^{\ 2} + \omega^2 N_o^{\ 2})} \tag{17}$$

If Eqs. (6) and (7) are substituted in Eqs. (16) and (17), one obtains Eqs. (18) and (19) .

$$k_p = \frac{(\omega^2 N_o D_o + N_e D_e)\cos(\omega^\alpha(\sin\frac{\pi}{2}\alpha)\tau^\alpha) + \omega(N_o D_e - N_e D_o)\sin(\omega^\alpha(\sin\frac{\pi}{2}\alpha)\tau^\alpha)}{-e^{-(\cos\frac{\pi}{2}\alpha)\omega^\alpha\tau^\alpha}(N_e^{\ 2} + \omega^2 N_o^{\ 2})} \tag{18}$$

$$k_d = \frac{\omega^2(N_o D_e - N_e D_o)\cos(\omega^\alpha(\sin\frac{\pi}{2}\alpha)\tau^\alpha) - \omega(N_e D_e + \omega^2 N_o D_o)\sin(\omega^\alpha(\sin\frac{\pi}{2}\alpha)\tau^\alpha)}{\omega^2 e^{-(\cos\frac{\pi}{2}\alpha)\omega^\alpha\tau^\alpha}(N_e^{\ 2} + \omega^2 N_o^{\ 2})} \tag{19}$$

2.2. An Approximation Method for Systems Having Fractional Order Delay

The exponential transcendental representation brings infinitely many isolated roots [19]. Thus, stability analysis of time delay systems is complicated. The analysis becomes much more complex when the time delay is fractional order. An approximation method is proposed here to simplify operations. One of the aims of the approximations is to reduce the difficulties in theoretical or

numerical analysis by replacing a complex function with a less complex one. Another goal is to find a relatively uncomplicated approximation function that is a valid model for a physical system or device [14]. For this purpose, an approximation method has been proposed to perform stability analysis for systems with FOTD [23]. Necessary details about the method can be found in [23]. The approximations are given in Table 1. Here, α is considered to be in the range of $0 \leq \alpha \leq 1$.

Table 1. Approximations for FOTD term [23].

Delay	First order approximation	Second order approximation	Third order approximation
$e^{-(s\tau)^{\alpha}}$	$\dfrac{-\dfrac{(s\tau)^{\alpha}}{2}+1}{\dfrac{(s\tau)^{\alpha}}{2}+1}$	$\dfrac{\dfrac{(s\tau)^{2\alpha}}{12}-\dfrac{(s\tau)^{\alpha}}{2}+1}{\dfrac{(s\tau)^{2\alpha}}{12}+\dfrac{(s\tau)^{\alpha}}{2}+1}$	$\dfrac{-\dfrac{(s\tau)^{3\alpha}}{120}+\dfrac{(s\tau)^{2\alpha}}{10}-\dfrac{(s\tau)^{\alpha}}{2}+1}{\dfrac{(s\tau)^{3\alpha}}{120}+\dfrac{(s\tau)^{2\alpha}}{10}+\dfrac{(s\tau)^{\alpha}}{2}+1}$

Using these approximations, the FOTD term is converted into a FOTF. Then, the total TF of the system can be obtained. In this way, stability test can be done easily. If the time response of the system is desired to be obtained, the continued fraction expansion (CFE) method can be used, and the TF is converted to an integer order structure and the results can be obtained. Details on the CFE can be found in [28] and [29].

3. SIMULATION RESULTS

In this section, the effects of the obtained equations and the proposed approximation method are investigated. For a better understanding of the subject, let us consider the example given below.

3.1. Example
For a unity feedback control system shown in Figure 1, the TF is given by Eq. (20),

$$G_p(s) = \frac{1.5}{s(0.4s+1)} e^{-\sqrt{s}} \tag{20}$$
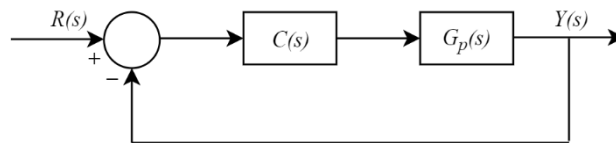
Figure 1. Feedback control system.

By using Eqs. (18) and (19), the stability region of the system is obtained as in Figure 2.
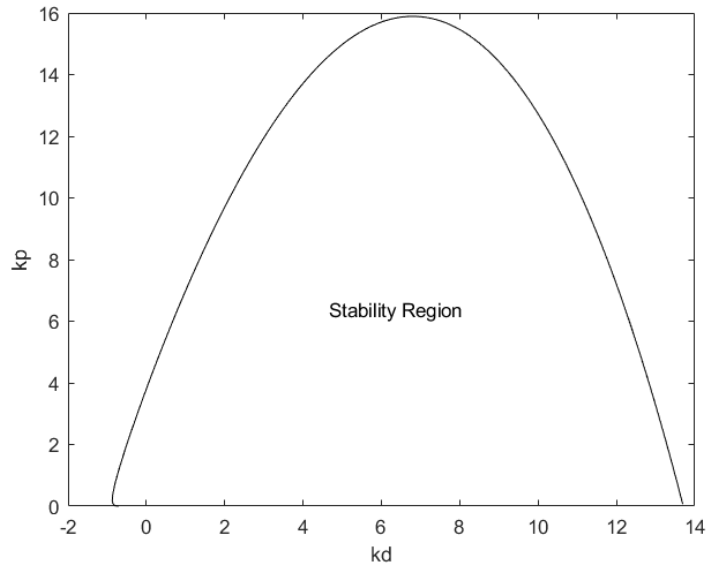
Figure 2. Stability region of the system.

Let $k_p = 4$ and $k_d = 4$ are chosen from the stability region shown in Figure 2. For this case, the CE is found as follows. Here, second order approximation is used.

$$\Delta(s) = 0.4s^3 + 2.4s^{2.5} + (5.8 + 1.5k_d)s^2 + (6 - 9k_d)s^{1.5} + (12 + 1.5k_p + 18k_d)s - 9k_p s^{0.5} + 18k_p$$
$$= 0.4s^3 + 2.4s^{2.5} + 11.8s^2 - 30s^{1.5} + 90s - 36s^{0.5} + 72 \tag{21}$$

If $\sqrt{s} = q$ is taken in this equation, the CE is rearranged as follows.

$$\Delta(q) = 0.4q^6 + 2.4q^5 + 11.8q^4 - 30q^3 + 90q^2 - 36q + 72 \tag{22}$$

As seen from Eq. (22) the CE has been converted to integer order form. The roots of this equation are obtained as follows.

$$q_{1,2} = -4.2773 \pm 5.2687j = 6.7863^{\angle \pm 2.2527}$$
$$q_{3,4} = 1.2348 \pm 1.6191j = 2.0362^{\angle \pm 0.9193} \tag{23}$$
$$q_{5,6} = 0.0425 \pm 0.9700j = 0.9709^{\angle \pm 1.5270}$$

For FOS, the stability condition for the CE $\Delta(q)$ is defined by Eq. (24) in the $\sqrt{s} = q$ plane.

$$|\arg(q_i)| > \frac{\pi}{2}\alpha, \ \forall_i = 1,...,n \tag{24}$$

Where, $0 < \alpha \leq 2$. For this example $\alpha = 1/2$. Thus, argument of q must be greater than 0.7854, $\left| \arg(q) \right| > \dfrac{\pi}{4} = 0.7854$. According to Eq. (24), it is seen that the system satisfies the stability condition. Because the arguments for all roots are greater than $\pi/4 = 0.7854$. The roots of the CE are also shown in Figure 3. Here, second order approximation is used. As seen from Figure 3, the roots lie in the desired region. Therefore, the system is stable. This shows that the approximation method provides a satisfactory result for the stability test. To obtain step responses of the system, the TF is transformed into a classical order TF by using the second order approximation given in Table 1 and the CFE method. Here, 4th order CFE is used. The unit step responses of the system are shown in Figures 4 and 5 for $k_p = 4$ and $k_d = 4$, and for $k_p = 2$ and $k_d = 2$, respectively.
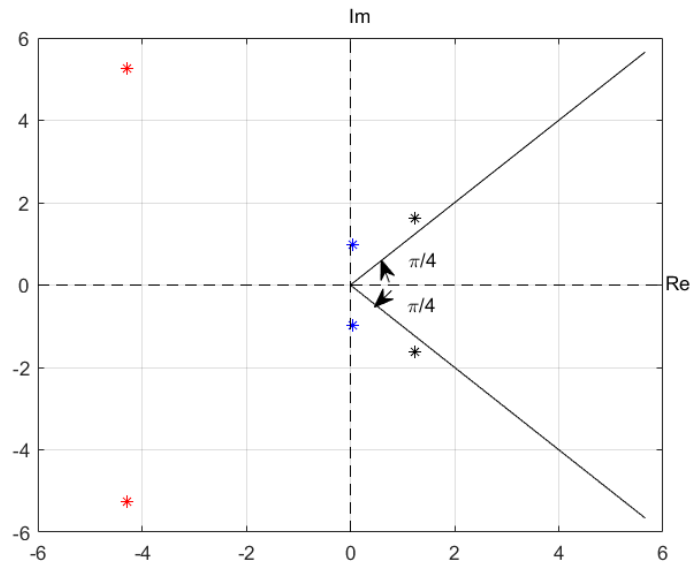
Figure 3. The roots of the CE for the second order approximation.
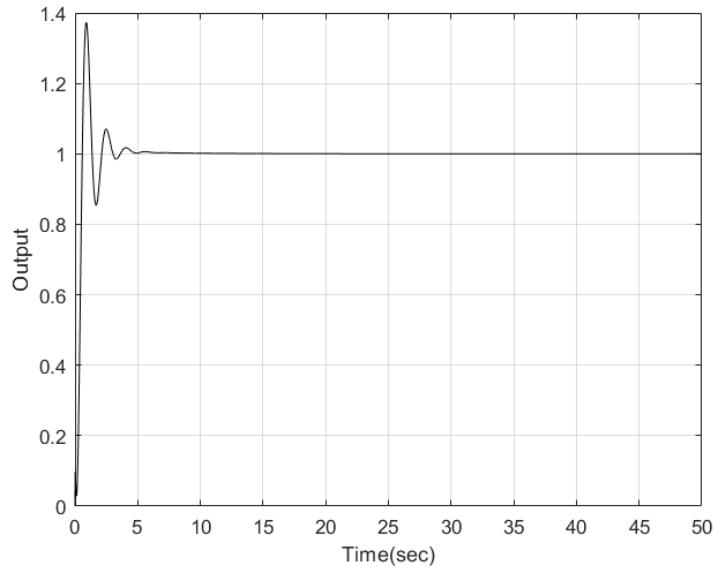
Figure 4. Step response of the system for $k_p = 4$ and $k_d = 4$.
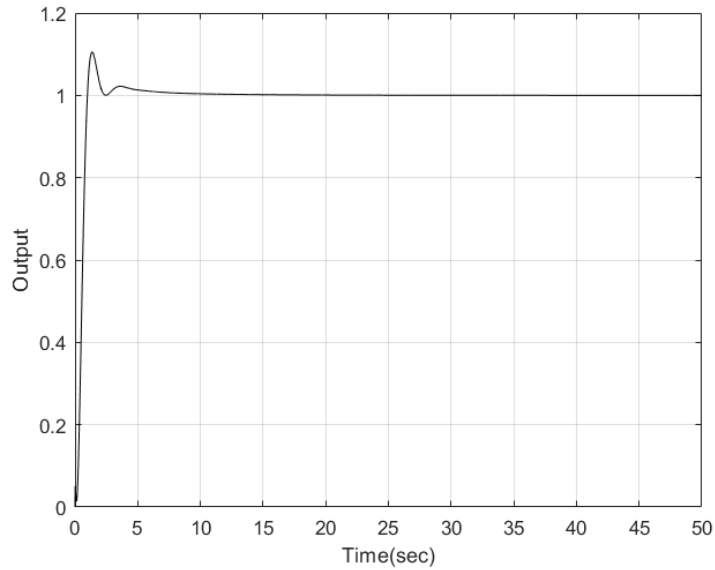
Figure 5. Step response of the system for $k_p = 2$ and $k_d = 2$.

Now let's examine the impact of first and third order approximations for this example. By using the first order approximation given in Table 1, for $k_p = 4$ and $k_d = 4$, the CE is obtained as follows.

$$\Delta(s) = 0.4s^{2.5} + 0.8s^2 + (1-1.5k_d)s^{1.5} + (2+3k_d)s - 1.5k_p s^{0.5} + 3k_p$$
$$= 0.4s^{2.5} + 0.8s^2 - 5s^{1.5} + 14s - 6s^{0.5} + 12 \qquad (25)$$

If $\sqrt{s} = q$ is taken in Eq. (25), the CE is rearranged as follows.

$$\Delta(q) = 0.4q^5 + 0.8q^4 - 5q^3 + 14q^2 - 6q + 12 \qquad (26)$$

The roots of the CE are obtained as follows.

$$q_1 = -5.5277 + 0j = 5.5277^{\angle 3.1416}$$
$$q_{2,3} = 1.7239 \pm 1.6779j = 2.4057^{\angle \pm 0.7719} \qquad (27)$$
$$q_{4,5} = 0.0399 \pm 0.9676j = 0.9684^{\angle \pm 1.5296}$$

The roots of the CE are shown in Figure 6. We know that $\left|\arg(q)\right| > \dfrac{\pi}{4} = 0.7854$. However, for the first order approximation $\left|\arg(q_{2,3})\right| = 0.7719$ and this value is less than 0.7854. So, this approximation does not provide a satisfactory result for this example. However, this does not mean that it will not work well for other systems. But, in general it would be wise not to expect very good performance from first order approximation.

By using the third order approximation, the CE is obtained as follows for $k_p = 4$ and $k_d = 4$.

$$\Delta(s) = 0.4s^{3.5} + 4.8s^3 + (25-1.5k_d)s^{2.5} + (60+18k_d)s^2 + (60-1.5k_p-90k_d)s^{1.5}$$
$$+ (120+18k_p+180k_d)s - 90k_p s^{0.5} + 180k_p \qquad (28)$$
$$= 0.4s^{3.5} + 4.8s^3 + 19s^{2.5} + 132s^2 - 306s^{1.5} + 912s - 360s^{0.5} + 720$$

If $\sqrt{s} = q$ is taken in Eq. (28), the CE is obtained as follows.

$$\Delta(q) = 0.4q^7 + 4.8q^6 + 19q^5 + 132q^4 - 306q^3 + 912q^2 - 360q + 720 \qquad (29)$$

One obtains the roots of the CE as follows.

$$q_1 = -11.1114 + 0j = 11.1114^{\angle 3.1416}$$
$$q_{2,3} = -1.7108 \pm 6.1660j = 6.3989^{\angle \pm 1.8414}$$
$$q_{4,5} = 1.2240 \pm 1.6426j = 2.0485^{\angle \pm 0.9304} \qquad (30)$$
$$q_{6,7} = 0.0425 \pm 0.9700j = 0.9709^{\angle \pm 1.5270}$$

The roots of the CE are shown in Figure 7. It is obvious that the system satisfies stability condition for the third order approximation. However, since this approximation makes solutions more difficult mathematically, it would be better to prefer the second order approximation. Comparison of step

responses of second order and third order approximations is given in Figure 8. As can be seen in Figure 8, the second order and third order approximations give very close results. This shows that the econd order approximation will be sufficient for the stability test.

It is clear that the second and third approximations used for the stability test of the system give good results as expected. The first-order approximation may be sufficient for the stability test, but this issue should be investigated for the different types of systems as first-order approximations generally may not give very good results. In the given example, the first-order approximation did not provide a satisfactory result. But this cannot be a generalization. This issue needs to be investigated in detail. The unit step responses for various points selected within the stability region are stable as expected. This shows the accuracy of the obtained equations and the used approximations.
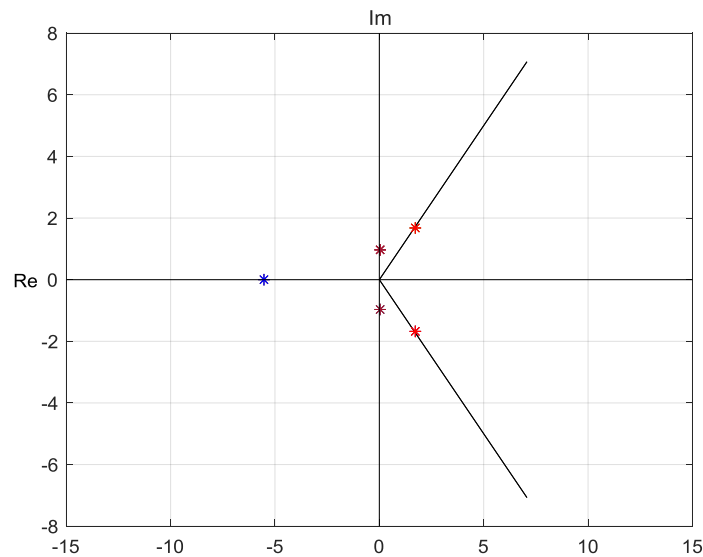
Figure 6. The roots of the CE for the first order approximation.

Figure 7. The roots of the CE for the third order approximation.

Figure 8. Step responses for the second order and third order approximations
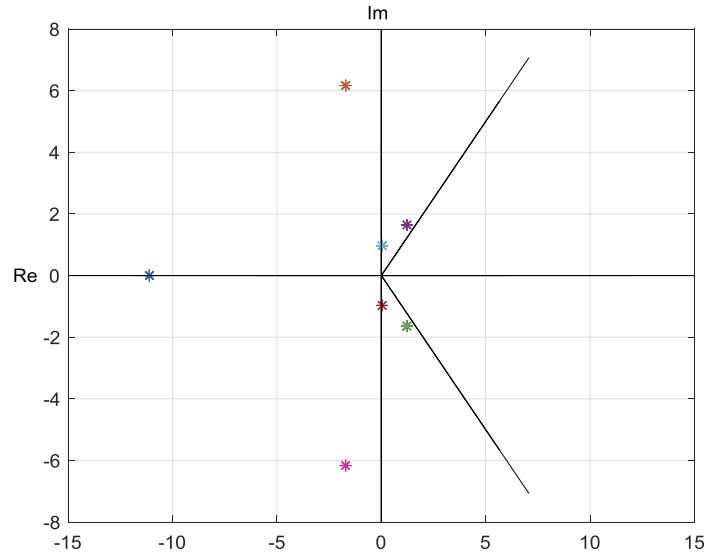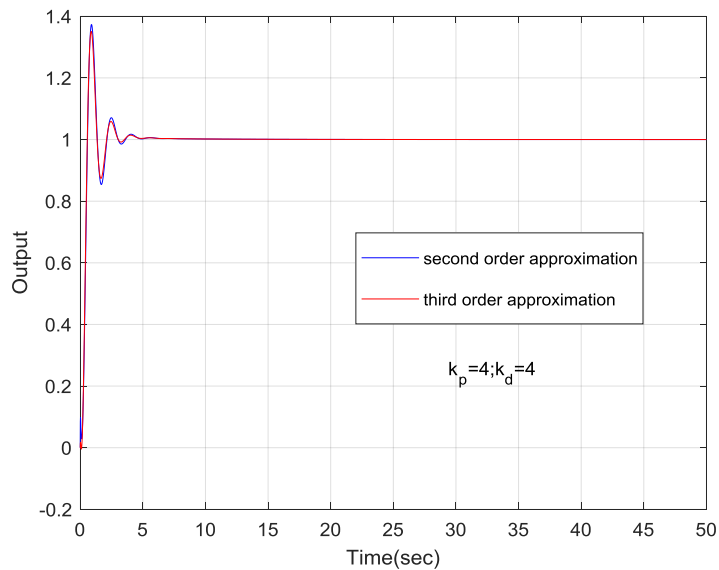
3. CONCLUSION

In this study, all PD controllers providing stability for systems having FOTD are obtained and the approximation method presented in Table 1 is used to test the stability of such systems. The SBL

method is applied to such systems for the first time and the equations are obtained. Here, the results can be summarized as follows.

The first-order approximation may be preferred in the first place for simlicity of the mathematical operation for the stability test, but may not provide the desired performance. This conclusion is obtained depending on one numerical example. Thus, this result cannot be a generalization. This result needs to be investigated in detail for the different types of systems. The second order approximation provides successful results as expected. However, this conclusion should also be reinforced with many numerical examples. The third order approximation also gives good results for the stability test. This result also needs to be supported with many examples. In addition, this approximation makes mathematical operations more complex. For this reason, it will be sufficient to prefer the second order approximation for the stability test.

Using the approximation given in Table 1, FOTD term is transformed into a FOTF. Then the total TF of the system is obtained. This TF is a FOTF. Thus, stability test procedure for FOS can be used. Using the CFE method, FOTF is converted into integer order transfer function to obtain step responses of the system. In the study, it is seen that the second order and third order approximations gave very close results in terms of unit step response.

In the future, studies in which the approximations presented in Table 1 are compared can be conducted to investigate which approximation yields more reasonable and satisfactory results for different control systems. In addition, the necessary equations for different controller types such as classical PI and PID, fractional order PI, PD, and PID can be obtained using the SBL method, and stability analysis can be made. Different techniques can be explored for controller design. In this study, commensurate order systems are considered. It will be important to examine non-commensurate order systems. There is a potential for many different studies on this subject.

4. DISCUSSION

As stated before, studies in which the time delay is fractional order are very limited in the literature. In this study, equations providing all stabilizing PD controller parameters for the given system are obtained using SBL method. To the best of the author's knowledge, stability test of such systems is also an important problem, and satisfactory general solutions are not available in the literature. In this study, an approximation method is used to test the stability of such systems. It is seen that the proposed approximation provides good results for the stability test. The first, second, and third order approximations are compared on the given example. It was seen that the first order approximation did not provide the desired performance in the stability test for the given system. However, this should be investigated in detail for many different systems. Besides, it would be better not to expect first order approximation to perform very well in general. However, extensive studies should be made on this subject. The second and third order approximations yielded successful results as expected. Graphical methods such as Nyquist are also available for stability analysis, but approximation methods are needed to perform stability analysis analytically. The parameters selected from the stability region also give stable responses as expected.

The fractional order structure discussed here is known as commensurate order. However, cases, where the order is non-commensurate, should be investigated in detail, as well. This topic is open to development and needs detailed studies.

Investigating the superior performance of any controller is not the main issue in this study. The main goal is to be able to analyze the stability of FOTD systems and to design a PD controller, which is a subject that has not been studied much in the literature. However, since there are hardly any studies on controller design on this subject, these studies should be increased and the performance analysis of basic controllers such as PI, PD and PID for such systems should be made and compared. Besides, fractional order controller types such as Fractional order PI (FO-PI), FO-PD, FO-PID can be designed for such systems. For this reason, it would be a more correct approach to seek answers to questions such as how the stability analysis of such systems can be made and how the controller design should be, rather than the superiority of any controller for now. Since there are not enough studies on this subject, any study on controller design for such systems will make a significant contribution to the field. When there is a large amount of data on this subject, the issue of superiority among the controllers can be examined more easily.

ACKNOWLEDGEMENT

REFERENCES

[1] Zhe, G., Xiaowu, C., Zhai, L., and Ting, L. (2016), Stabilization criterion of fractional-order PD^mu controllers for interval fractional-order plants with one fractional-order term. Chinese Control Conference, CCC. 2016-Augus (1), 10424–10430.

[2] Dastjerdi, A.A., Vinagre, B.M., Chen, Y.Q., and HosseinNia, S.H. (2019), Linear fractional order controllers; A survey in the frequency domain. Annual Reviews in Control. 47 (2019), 51–70.

[3] Hamamci, S.E. (2008), Stabilization using fractional-order PI and PID controllers. Nonlinear Dynamics. 51 (1–2), 329–343.

[4] Podlubny, I., Petráš, I., O'Leary, P., Dorčák, L., and Vinagre, B.M. (2002), Analogue realizations of fractional order controllers. Nonlinear Dynamics. 29 281–296.

[5] Dimeas, I., Petras, I., and Psychalinos, C. (2017), New analog implementation technique for fractional-order controller: A DC motor control. AEU - International Journal of Electronics and Communications. 78 192–200.

[6] Tan, N. (2005), Computation of stabilizing PI and PID controllers for processes with time delay. ISA Transactions. 44 213–223.

[7] Hohenbichler, N. and Ackermann, J. (2003), Synthesis of robust PID controllers for time delay systems. ECC 2003: Proceedings of the European Control Conference; Cambridge, UK, Sept. 1-4, 2003 / IEE. 0 (5), 1222–1227.

[8] Ackerman, J. and Keasbauer, D. (2003), Stable polyhedra in parameter space. Automatica. 39 937–943.

[9] Tan, N. and Atherton, D.P. (2006), Design of stabilizing PI and PID controllers. International Journal of Systems Science. 37 (8), 543–554.

[10] Xu, Y., Hollerbach, J.M., and Ma, D. (1995), A Nonlinear PD Controller for Force and Contact Transient Control. (February), 15–21.

[11] Tomei, P. (1991), Adaptive PD Controller for Robot Manipulators Patrizio. IEEE Transactions on Robotics and Automation. 7 (4), 565–570.

[12] Haddar, M., Chaari, R., Baslamisli, S.C., Chaari, F., and Haddar, M. (2019), Intelligent PD controller design for active suspension system based on robust model-free control strategy. Proceedings of the Institution of Mechanical Engineers, Part C: Journal of Mechanical Engineering Science. 233 (14), 4863–4880.

[13] Birs, I., Muresan, C., Nascu, I., and Ionescu, C. (2019), A Survey of Recent Advances in Fractional Order Control for Time Delay Systems. IEEE Access. 7 30951–30965.

[14] Stewart, J.L. (1960), Generalized Pade' Approximation. Proceedings of the IRE. 48 (12), 2003–2008.

[15] Ozturk, N. and Uraz, A. (1985), An Analysis Stability Test for a Certain Class of Distributed Parameter Systems with Delays. IEEE Transactions on Circuits and Systems. CAS-32 (4), 393–396.

[16] Ozturk, N. and Uraz, A. (1984), An Analytic Stability Test for a Certain Class of distributed Parameter Systems with a Distributed Lag. IEEE Transactions on Automatic Control. AC-29 (4), 368–370.

[17] Karmarkar, J.S. (1970), Stability analysis of systems with distributed delay. PROC. IEE. 117 (7), 1425–1429.

[18] Chen, Y. and Moore, K.L. (2002), Analytical stability bound for a class of delayed fractional-order dynamic systems. Nonlinear Dynamics. 29 (1–4), 191–200.

[19] Hwang, C. and Cheng, Y.C. (2006) A numerical algorithm for stability testing of fractional delay systems. Automatica. 42 (5), 825–831.

[20] Mesbahi, A. and Haeri, M. (2013), Stability of linear time invariant fractional delay systems of retarded type in the space of delay parameters. Automatica. 49 (5), 1287–1294.

[21] Mesbahi, A. and Haeri, M. (2015), Stable regions in the parameter space of delays for LTI fractional-order systems with two delays. Signal Processing. 107 (2015), 415–424.

[22] Atherton, D.P., Tan, N., and Yuce, A. (2015), Methods for computing the time response of fractional-order systems. Control Theory & Applications, IET. 9 (6), 817–830.

[23] Ozyetkin, M.M. (2022), An approximation method and PID controller tuning for systems having integer order and non-integer order delay. Alexandria Engineering Journal. 61 (12), 11365–11375.

[24] Tan, N., Kaya, I., Yeroglu, C., and Atherton, D.P. (2006), Computation of stabilizing PI and PID controllers using the stability boundary locus. Energy Conversion and Management. 47 (18–19), 3045–3058.

[25] Ho, M., Datta, A., and Bhattacharyya, S.P. (2000), Generalizations of the Hermite ± Biehler theorem: the complex case. 320 (2000), 23–36.

[26] Datta, A., Ho, M.-T., And, and Bhattacharyya, S.P. (2000), Advances in Industrial Control Structure and Synthesis of PID Controllers. Springer-Verlag London Ltd.

[27] Deniz, F.N. and Yüce, A. (2015), SBL Eşleştirme Yöntemi ile Kesir Dereceli PID Kontrolörün Yaklaşık Modellenmesi ve Ters Sarkaç Kontrol Sisteminde Uygulaması. Approximate Modelling of Fractional-Order PID Controller by SBL Matching Method and Application to Inverted Pendulum Control System. TOK'15, 10-12 Eylül, Denizli, 474-479.

[28] Astekin, D. and Özyetkin, M.M. (2021), Sürekli Kesir Açılımı Yöntemi Üzerine Genişletilmiş Bir Çalışma, An Extended Study on the Continued Fraction Expansion Method. in: TOK 2021 Otomatik Kontrol Ulusal Kongresi, Van, Türkiye, 58–62.

[29] Özyetkin, M.M., Yeroğlu, C., Tan, N., and Tağluk, M.E. (2010), Design of PI and PID controllers for fractional order time delay systems. IFAC Proceedings Volumes (IFAC-PapersOnline), 43 (2), 355–360.

RESEARCH ARTICLE

WY-NET: A NEW APPROACH to IMAGE SYNTHESIS with GENERATIVE ADVERSARIAL NETWORKS

Emrullah ŞAHİN[1*], Muhammed Fatih TALU[2]

[*1]Kütahya Dumlupınar University, Faculty of Engineering, Department of Software Engineering, Kütahya,
essahin950@gmail.com, ORCID: 0000-0002-3390-6285
[2]İnönü University, Faculty of Engineering, Department of Computer Engineering , Malatya, fatihtalu@gmail.com,
ORCID: 0000-0003-1166-8404

ABSTRACT

Conditional image synthesis is the translation of images from different domains with the same dimensions into each other. Generative Adversarial Networks (GANs) are commonly used in translation studies in this field. With the classical GAN approach, data are transferred between the encoder and decoder of the generator network in the image translation. While this data transfer increases the quality of the translated image, it also leads to data dependency. This dependence has two negative effects: First, it prevents the understanding of whether the encoder or the decoder causes the error in the translated images, other causes the image synthesis quality to depend on the parameter increment of the network. In this study, two different architectures (dY-Net, uY-Net) are proposed. These architectures are developed on the principle of equalizing high-level feature parameters in cross-domain image translation. The first of these architectures concentrates on the speed of image synthesis, the other on its quality. There is a significant reduction in data dependency and parameter space in the dY-Net architecture, which concentrates on speed performance in image synthesis. The uY-Net architecture, which concentrates on image synthesis quality, attempts to maximize the results of metrics that measure quality like SSIM and PSNR. Three different datasets (Maps, Cityscapes, and Denim2Mustache) were used for performance testing of the proposed architectures and existing image synthesizing approaches. As a result of the tests, it has been seen that the proposed architecture synthesized images with similar accuracy, although it has approximately 66% parameters compared to DiscoGAN, which is one of the existing approaches. The results obtained show that WY-Net architectures, which provide high performance and translation quality, can be used in image synthesis.

Keywords: *Generative adversarial networks, Image synthesis, Deep learning, Image to image translation*

1. INTRODUCTION

Deep learning is a subfield of machine learning where the features that best express data can be learned autonomously. Using this area is increasing gradually, and it is also multiplying in the subareas it branches. Recently, deep learning-based applications have been increasing. For example, it is used in many fields, such as language translation, chatbots, face identification, voice signature, disease diagnosis, data augmentation, autonomous vehicles, and anomaly analysis. Although this field

contains many learning methods, one of the most popular todays is Generative Adversarial Networks (GANs). Goodfellow and his team developed this learning method based on the min-max algorithm in 2014 [1].

GANs are a special type of neural network developed to model relationships between samples in a dataset [1-3]. The network tries to learn the features that best express these samples to model the relationship between the samples [2,3]. The basic structure of these networks is based on the game theory of the famous mathematician John Nash and comprises two convolutional modules that learn by working with each other in an adversarial manner [1]. One of these modules is called the generator network, and the other is called the discriminator network. The generative network tries to simulate a random or special data block (sampler) given to it to the desired data sample. The discriminant network is a classifier that tries to distinguish between the synthesized sample by the generator network and the real data sample. During the training phase, the generator and discriminant network parameters are fed with the similarity cost (loss) of the real and predicted (synthesized) outputs. The working mechanism of these models is shown in Figure 1. In this schema, real data with synthesized data from the generator network are given as input to the discriminator network. Then the cost of similarity between the outputs of the discriminator network is calculated. With this cost, the discriminator and generator network are fed.
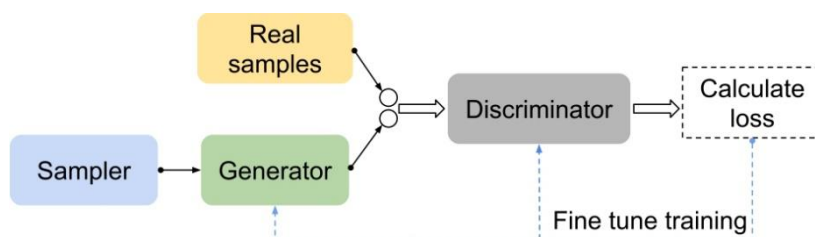
Figure 1. The basic schema of GAN architectures.

Since the development of Generative adversarial networks, multiple types have been developed for use in image generation and manipulation. One of the first examples in this area is the DCGAN [2] architecture developed by Radford et al. in 2015. This architecture can learn the numerical distribution of its features by training with examples in a dataset consisting of images. It is a light and powerful model that can be used in data augmentation. One of the biggest problems in image studies is the low-resolution problem. In solving this problem, the perceptual similarity cost-based SRGAN [3] architecture developed by Ledig et al. has achieved significant success. Convolutional neural networks-based VGG [4] network is used so that the content in the images is not distorted while synthesizing low resolution images in high resolution. The Progressive GAN [5] architecture, which performs progressive learning to reduce distortions in high resolution synthesized images, was developed by Karras et al. in 2017. After learning with 4x4 image scale in the architecture training phase, it continues until it synthesizes 1024x1024 images by increasing the scale step by step. The networks with attention mechanisms have been developed so that GAN architectures focus on the important parts instead of focusing on the whole image. One of these studies, the spatial attention and spectral normalization-based SAGAN [6] architecture, was developed by Zhang et al. in 2018 to reduce the instability of the learning curve due to unbalanced learning in the training phase of the generator and discriminator network in GAN architectures. The StyleGAN [7] architecture fed with content and style image was developed by Karras et al. to transfer any style image to a content image

in 2018. The modulation and reverse modulation-based StyleGAN2 [8] architecture to minimize the distortions on the network sourced image in StyleGAN architecture was developed in 2019. The StyleGAN3 [9] architecture by including Fourier-based features and various changes in this architecture to solve the signal problem from the hidden field caused by translation and rotation in the StyleGAN architectures was developed in 2021. The BigGAN [10] architecture, which can generate class-level images on the ImageNet dataset for high-resolution synthetic image generation, was developed by Brock et al. in 2018. This architecture tries to minimize cosine similarity without restricting the norms between binary filters for quality and diverse image synthesis. This regularization term, added to the parameters of the filters, enables the synthesizing of high-quality images belonging to different classes. The BigGAN-based BigBiGAN [11] architecture to develop a system capable of generating more realistic images was developed by Donahue et al. in 2019. This architecture has an encoder that can convert real images into a random variable, and a discriminator network operating with a binary cost function. For better quality learning, the system tries to bring the values from the encoder network and the values from the hidden field to the same representation.

Image to image translation: A major challenge in image translation is to get a high-dimensional image from a low-dimensional visual space [13,14,16]. An example can be given for a better understanding. Translations such as coloring a black-and-white image [13], getting a semantic label map from an image with an edge map [13,16], converting a real image into an animation image [12] can be given as examples. These translations are difficult to perform with basic image processing algorithms. It is known that GAN architectures are widely used to solve these high-level problems [2-16]. Today, researchers for image-to-image translation have proposed many GAN architectures [12-16]. Although the architectures have differences among themselves, the primary aim is to generate a quality artificial image at an appropriate temporal cost by making an excellent translation between the two domains. One of the first architectures developed in the field of image-to-image translation is Pix2Pix [13]. This architecture was developed by Isola et al. in 2016 to translate between pairs of images in supervised datasets. The architecture includes the L_1 metric in addition to the traditional GAN loss. A new version of this architecture, the Pix2PixHD [14] architecture, was developed by Wang et al. in 2018 to synthesize realistic images from high-resolution semantic image maps. Researchers at Nvidia enhanced the SPADE [15] architecture by adding spatial adaptive normalization on top of the basic structure of the Pix2PixHD architecture to produce realistic nature photographs from unlabeled semantic image maps. The CycleGAN [16] architecture based on double-sided validation was developed by Zhu et al. to perform image-to-image translation in unsupervised datasets. The MixNMatch [17] architecture for various content generation and in-depth image change was developed by Li et al. in 2020. This architecture has a design that takes content, shape, poses, and background images and combines them. To increase the quality of semantic map-based image synthesis, the study called "Panoptic-based Image Synthesis" for panoptic map-based image production was developed by Dundar et al. in 2020 [18]. The GFP-GAN [19] architecture with spatial feature conversion to synthetically generate old or poor-quality images of human faces in high-quality, noiseless, and colorful was developed by Wang et al. in 2021. The Real-ESRGAN [20] architecture, which can reduce effects such as low resolution, blur, compression, and noise in an image and concentrate on over one problem area at the same time for quality image synthesis, was developed by Wang et al. in 2021. The Fourier convolution-based LaMa [21] architecture to remove unwanted objects or regions on the image without disturbing the basic design of the actual image was developed by Suvorov et al. in 2021.

In this study, we proposed a new architecture can translate from image-to-image more efficiently. Performance comparison of this architecture was made with DiscoGAN architecture on three different datasets. In Section 2.1, explanations are given about the similarity metrics used in the study. In Section 2.2, DiscoGAN [22] architecture's basic design is explained. In Section 2.3, the basic design of the proposed (WY-Net) architecture is explained. Information about the datasets used is given in Section 2.4. In Section 3, the results obtained in the study are shared.

2. MATERIAL AND METHODS

2.1. Similarity Metrics
In this section are given the basic similarity methods frequently used in the study.

2.1.1. SSIM
Structural similarity metric (SSIM) is a method that analyzes the perceived change in the image along with important perceptual properties, such as brightness, masking, and contrast. This metric is a statistical measurement built on the mean (μ) and standard deviation (σ) parameters in calculating the similarity between the image pairs, ignoring the positional difference between the pixels in the image [23].

Calculation of structural similarity between real (x) and predicted (y) image statistically is shown in Eq. (1). In this equation, μ_x and μ_y denote the pixel mean of the real and predicted image, the variance of σ_x^2 and σ_y^2, while σxy denotes the covariance between the real and predicted image. In addition, the constant values $c_1 = (k_1 L)^2$ and $c_2 = (k_2 L)^2$ are calculated by taking the L value 255., which specifies the pixel pitch.

$$SSIM(x,y) = \frac{(2\mu_x \mu_y + c_1)(2\sigma_{xy} + c_2)}{(\mu_x{}^2 + \mu_y{}^2 + c_1)(\sigma_x{}^2 + \sigma_y{}^2 + c_2)} \tag{1}$$

2.1.2 MSE
It is a comparison metric where the square of the point difference is taken to calculate the similarity cost between two data samples [24]. The main formula of this metric is shown in Eq. (2). In the equation, each pixel difference between the real (x) and predicted (y) image is squared and summed. Divide the total result by the number of pixels (n).

$$L_2 = MSE(x,y) = \frac{1}{n}\sum_{i=1}^{n}(x_i - y_i)^2 \tag{2}$$

2.1.3. MAE
It is a comparison metric in which the absolute value of the point error is taken to calculate the similarity cost between two data samples [25]. The main formula for this metric is shown in Eq. (3). In the equation, the absolute value of each pixel difference between the real (x) and predicted (y) image is taken and summed. Divided the total result by the number of pixels (n). While measuring, the direction of the error is not considered, it focuses on the absolute difference.

$$L_1 = MAE(x,y) = \frac{1}{n}\sum_{i=1}^{n}|x_i - y_i| \tag{3}$$

2.1.4. PSNR

It is a logarithmic-based metric used for the ratio between the maximum power of a signal and the power of noise that affects the accuracy of its representation [26]. The signal is a real image or data, while noise is the error caused by compression or distortion in the data. This ratio between two images is calculated in decibels. The main formula for this metric is shown in Eq. (4). For the measurement between the real (x) and predicted (y) image in the equation, the $MSE(x, y)$ value and the largest pixel value of the real image (MAX_x^2) are included in the calculation.

$$PSNR\,(x, y) = 10 * log_{10}\left(\frac{MAX_x^2}{MSE(x, y)}\right) \tag{4}$$

The higher the measurement value, the better the signal quality, that is, the lower the cost between the real and the predicted data.

2.1.5. Hinge embedding loss

It is a metric often used to calculate the similarity between nonlinear or semi-supervised data blocks [27]. This metric measures the distance between a real input vector (x) and a label vector (y) (containing 1 or -1). The main formula of the metric is given in Eq. (5). The L value in the equation contains the input and label list. The number of features in the list is expressed as n.

$$L_{HE} = \begin{cases} mean(L), & if\ reduction = 'mean', \\ sum(L), & if\ reduction = 'sum', \end{cases} \tag{5}$$

$$L = \sum_i^n \ell(x_i, y_i) = \begin{cases} L_2(x_i, y_i), & if\ y_i = 1, \\ max(0, m - L_2(x_i, y_i)), & if\ y_i = -1, \end{cases}$$

2.2. DiscoGAN

The DiscoGAN (Learning to discover cross-domain relations with generative adversarial networks) is a conditional GAN architecture developed to explore the relationship between different datasets and synthesize quality images [22]. This architecture has a structure that can work on supervised or unsupervised datasets.

2.2.1. Generator network

The DiscoGAN architecture has two generator networks with the same structure. This architecture learns two separate translation functions: the first network (*G_X2Y*) learns to translate the image in the X-domain (*Real_X*) into the predicted Y-image (*Fake_Y*), while the second network learns to translate the image in the Y-domain (*Real_Y*) into the predicted X-image (*Fake_X*). After the initial processing, the architecture generates the reconstructed *Recons_X* image by passing the predicted *Fake_Y* image through the *G_Y2X* network for complete learning, while passing the *Fake_X* image through the *G_X2Y* network to generate the reconstructed *Recons_Y* image. The basic diagram of the generator networks in the DiscoGAN architecture is shown in Figure. 2. The first translation takes place from *X* to *Y* and the other from *Y* to *X*. Reconstructed images are used for double-sided verification. This validation is calculated between the real and reconstructed images with the L_2 metric.
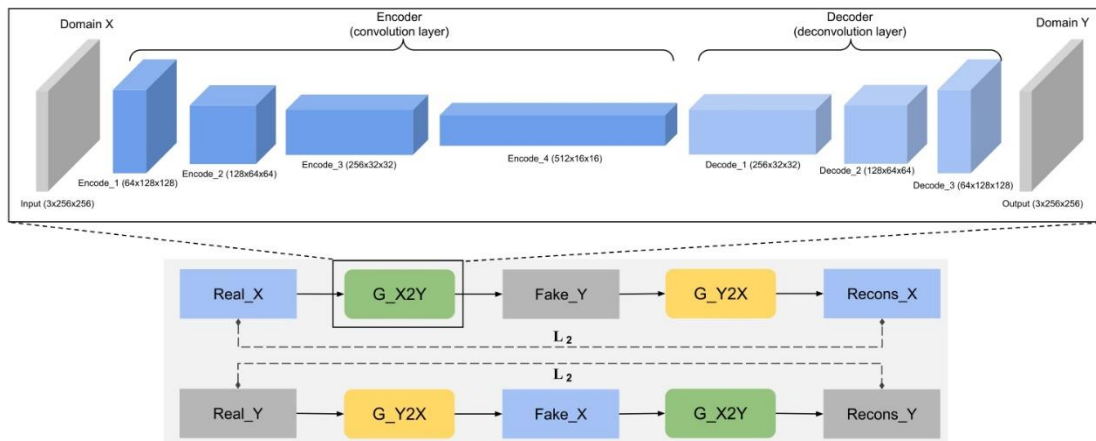
Figure 2. The basic schema of DiscoGAN generator networks. DiscoGAN's generator *G_X2Y* and *G_Y2X* networks learn 2 separate translations.

2.2.2. Discriminator network

The DiscoGAN architecture has two discriminator networks with the same structure. First of these networks (*D_X*) tries to classify the output of the two images as real or fake by trying to learn the properties of *Real_X*, which is the real image in the X-domain, and *Fake_X*, which is the fake image. The other network (*D_Y*) tries to classify the output of the two images as real or fake by trying to learn the properties of *Real_Y*, which is the real image, and *Fake_Y*, which is the fake image, in the Y-domain. The basic schematic of the discriminator networks is given in Figure 3.
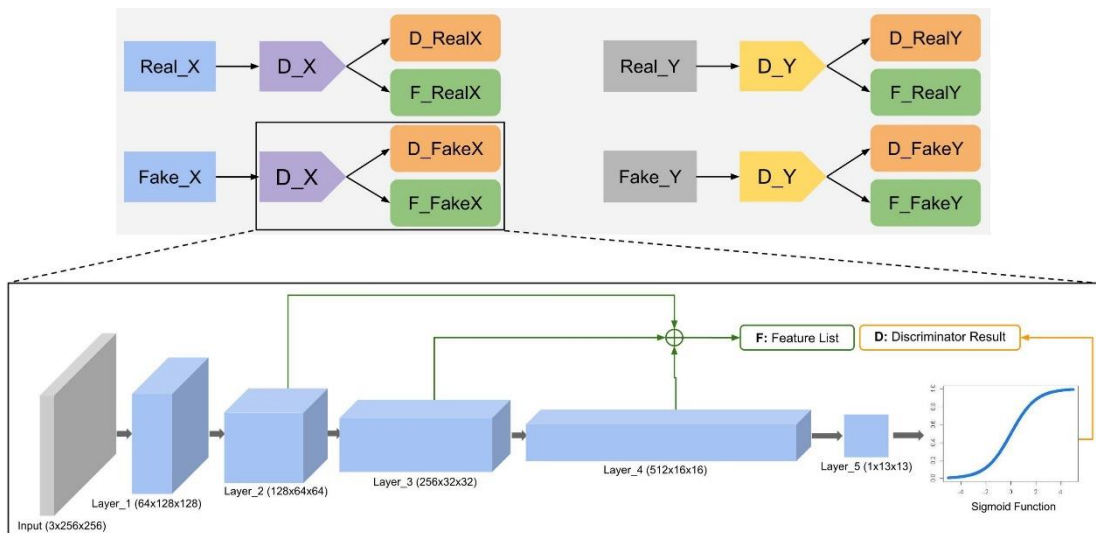

Figure 3. The basic schema schematic of DiscoGAN discriminator networks. DiscoGAN's discriminator *D_X* and *D_Y* networks learn 2 separate classification processes.

The first classification takes place between *Real_X* and *Fake_X* and the other between *Real_Y* and *Fake_Y*. The feature list of each image is extracted so that the generator networks can learn better. Outputs starting with the prefix *D* are used for the cost of discriminator, and *F* for generator. According to this scheme, two outputs are obtained from the image given as input to the discriminator network. The first output is the passed output from the activation function that the discriminator network uses for the adversarial loss. The second output is the feature list obtained from layers 2, 3, and 4 of the networks. This feature list is used for the cost function of the generator network. For example, the *D_RealX* result obtained by giving the *Real_X* image to the *D_X* network represents the output of the discriminator network, while the *F_RealX* value represents the feature list of this image.

2.2.3. Loss functions

The cost function of the generator networks in the DiscoGAN architecture is built on reconstructed, adversarial, and feature losses. The cost of discriminator networks in the architecture is based on the adversarial loss value in traditional GAN architectures.

Generator Loss. In this architecture, the L_2 metric is used for reconstructed loss. This is computed between the *Recons_X* and *Recons_Y* images reconstructed with the input images *Real_X* and *Real_Y*. Its formulation is expressed as Eq. (6).

$$\mathcal{L}_{const_X} = L_2(Real\_X, Recons\_X) \tag{6}$$

The hinge embedding loss function is used for feature cost calculation. This process is calculated between the real (*F_RealX*) and fake (*F_FakeX*) feature list obtained from the discriminator network. It is shown in Eq. (7). It is calculated by taking the λ_1 value in the equation to 0.9.

$$\mathcal{L}_{feature_X} = \lambda_1 * L_{HE}(F\_RealX, F\_FakeX) \tag{7}$$

The adversarial loss value is calculated with the fake (*D_FakeX*) value obtained from the activation function of the discriminator network. This process is shown in Eq. (8). It is calculated by taking the λ_2 value in the equation to 0.1.

$$\mathcal{L}_{adv_X} = \lambda_2 * arg \min_{G\_X2Y}(log(1 - D\_FakeX)) \tag{8}$$

The loss function required for the X-domain of the network is expressed like Eq. (9). The starting ratio in the equation is initially given as $r = 0.01$. This value is changed to $r = 0.5$ after 10000 iterations of training.

$$\mathcal{L}_{G\_X2Y} = r * \mathcal{L}_{const_X} + (1 - r) * \left(\mathcal{L}_{feature_X} + \mathcal{L}_{adv_X}\right) \tag{9}$$

The overall loss of the generator networks is calculated for both areas and then added up. The total loss function is written like Eq. (10).

$$\mathcal{L}_G = \mathcal{L}_{G\_X2Y} + \mathcal{L}_{G\_Y2X} \tag{10}$$

Discriminator Loss. The required loss value for the X-domain of the discriminator networks is calculated between the *D_RealX* blocks of the real data and the *D_FakeY* blocks of the fake data we want to translate. This process is illustrated in Eq. 11.

$$\mathcal{L}_{adv_{D\_X}} = \underset{D\_X}{argmax}(log(D\_RealX) - log(1 - D\_FakeX)) \tag{11}$$

The total loss of the two discriminator networks is calculated like Eq. 12.

$$\mathcal{L}_D = \mathcal{L}_{adv_{D\_X}} + \mathcal{L}_{adv_{D\_Y}} \tag{12}$$

2.3. WY-Net: Proposed Method

When we want to translate from one image domain to another with GAN architectures, unlike Auto-encoders, the encoder and decoder of the generator network are evaluated together. The disadvantage of this is that it cannot be understood that the real error is from the encoder or decoder. The WY-Net architecture proposed in this study allows us to understand this problem by trying to reduce the features of the images in the two domains to the common denominator while translating from one image domain to another image domain. We delegate the feature extraction of images from two domains to a single network. The advantage of this is that it makes the architecture lighter and faster, while also showing how the network will translate between image domains.

2.3.1. Improving generator network

WY-Net architecture has a generator network with one encoder and two decoders. The encoder tries to learn the features of the data of the X and Y-domain. One of the decoders tries to reconstruct the data belonging to this domain from the features of the X-domain, the other does the same for the Y-domain. This architecture learns two separate translation operations, the first translation is from the X-domain to the Y-domain, the second translation is from the Y-domain to the X-domain. The first translation yields three outputs, *Fake_Y*, *Feature_X*, *Recons_X* data respectively. The first output is the image in the X-domain translated to the Y-domain. The second output is the feature map of the data in the X-domain obtained after passing through the encoder. The third output is the reconstructed image of the data in the X-domain, with this image double-sided validation is performed. The same translation process is done for the Y-domain. The WY-Net architecture proposed in this study has two different uses: 1) dY-Net based on DiscoGAN generator network; 2) uY-Net based on U-Net [28] generator network. The dY-Net architecture concentrates on temporal and hyperparameter optimization, while uY-Net architecture concentrates on image quality. Two different design prototypes of the WY-Net architecture are shown in Figure 4. The first translation takes place from *X* to *Y* and the other from *Y* to *X*. Reconstructed images are used for double-sided verification. This validation is calculated between the real and reconstructed images with the L_2 metric. For a better comparison, a similarity calculation is made between the real and fake data with the L_1 metric. Then, the high-level features of the real *X* and *Y* images are compared with the L_{HE} metric and reduced to the common denominator.
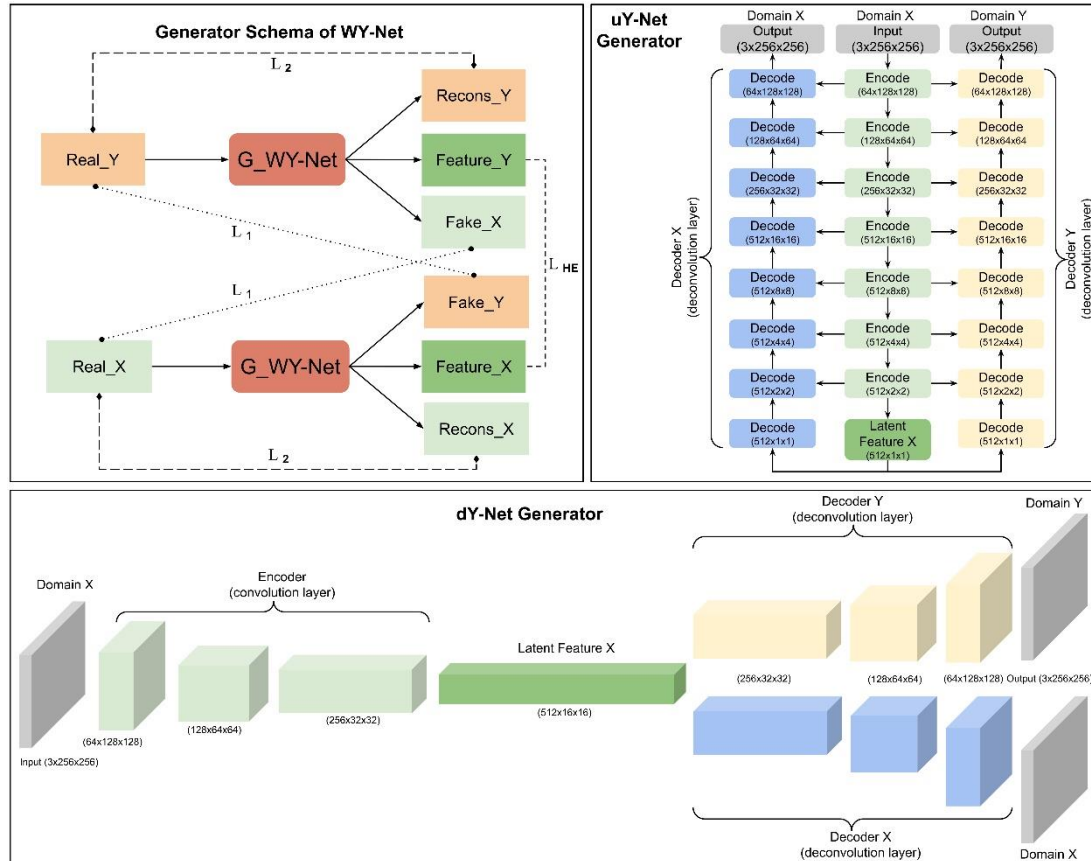
Figure 4. The basic schema of WY-Net generator network. Generator network (G_WY-Net) of WY-Net architectures (dY-Net, uY-Net) learn 2 separate translations.

2.3.2. Improving discriminator network

The WY-Net architecture has a discriminator network that takes real images (*Real_X*, *Real_Y*) and fake images (*Fake_X*, *Fake_Y*) together as input data, unlike traditional GAN architectures. This process is to be compatible with the generator network because, while the generator network tries to reduce the features of the two domains to the same denominator, the discriminator network must also reduce the images of these domains to the same denominator. Thus, the translation process between the two domains is ensured to be balanced. The basic diagram of the discriminator network is given in Figure 5. Discriminator network (D_WY-Net) of WY-Net architectures (dY-Net, uY-Net) tries to reduce real (*Real_X*, *Real_Y*) and fake (*Fake_X*, *Fake_Y*) data to a common denominator for better understand cross-domain image similarity. Outputs starting with the prefix *D* are used for the cost of discriminator, and *F* for generator. In the first stage of this diagram, the output of the discriminator network (*D_Real*) and the feature list (*F_Real*) of the real images are shown, while in the second stage, the *D_Fake* and *F_Fake* data of the synthesized fake images are shown. WY-Net discriminator network architecture was developed based on DiscoGAN.
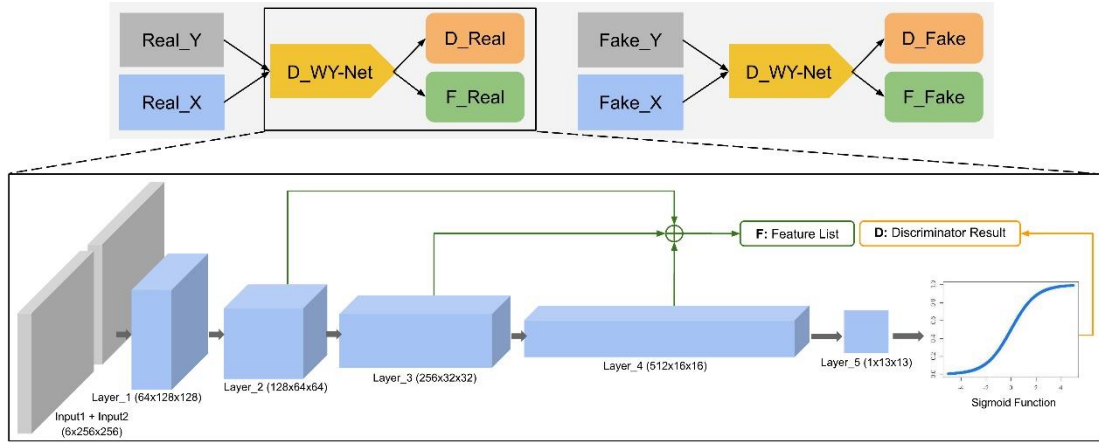
Figure 5. The basic schema of WY-Net discriminator network.

2.3.3. Improving loss functions

The generator network loss function of WY-Net architecture is built on reconstructed, similarity, adversarial, and feature losses. The loss of the discriminator network is based on the traditional adversarial loss value. As the adversarial loss value, the hinge loss [29] technique was used instead of the min-max algorithm.

Generator Loss. In this architecture, the reconstruction loss is calculated using the L_2 metric as in Eq. 8. This is computed between the *Recons_X* and *Recons_Y* images reconstructed with the input images *Real_X* and *Real_Y*.

The similarity loss is calculated using the L_1 metric. This process is calculated between the input images *Real_X* and *Real_Y* and the translated *Fake_Y* and *Fake_X* images to the other domain. It is shown in Eq. 13.

$$\mathcal{L}_{similarity_X} = L_1(Real\_X, Fake\_X) \tag{13}$$

The hinge embedding loss function is used for feature cost calculation. This process is the sum of the result of the real (*F_Real*) and fake (*F_Fake*) feature list obtained from the discriminator network and the result of *Feature_X* of the X-domain and *Feature_Y* of the Y-domain from the generator network. This process is shown in Eq. 14. It is calculated by taking the λ_1 value in the equation to 0.9.

$$\mathcal{L}_{feature} = \lambda_1 * \left(L_{HE}(F\_Real, F\_Fake) + L_{HE}(Feature\_X, Feature\_Y) \right) \tag{14}$$

Adversarial loss: It is calculated on the fake (*D_Fake*) result passed through the activation function of the discriminator network. This process is expressed as Eq. 15. It is calculated by taking the λ_2 value in the equation to 0.1.

$$\mathcal{L}_{adv} = \lambda_2 * mean(-D\_Fake) \tag{15}$$

The overall loss of the generator network is expressed as Eq. 16. The starting ratio in the equation is initially given as $r = 0.01$. This value is changed to $r = 0.5$ after 10000 iterations of training.

$$\mathcal{L}_G = r * \left(\mathcal{L}_{const_X} + \mathcal{L}_{const_Y} + \mathcal{L}_{similarity_X} + \mathcal{L}_{similarity_Y} \right) + (1 - r) * \left(\mathcal{L}_{feature} + \mathcal{L}_{adv} \right) \quad (16)$$

Discriminator Loss. The loss of the discriminator network is calculated between the *D_Real* blocks of the real data and the *D_Fake* blocks of the fake data we want to translate. This process is illustrated in Eq. 17. The result is obtained by passing the averaged data block through the Relu activation function.

$$\mathcal{L}_D = relu\big(mean(1 - D\_Real)\big) + relu\big(mean(1 + D\_Fake)\big) \quad (17)$$

2.4. Datasets
2.4.1. Denim2Mustache
The Denim2Mustache dataset contains 950 image pairs (denim-mustache), 900 of which are training and 50 are tests [30]. The dataset includes front and back photos of different denim products, such as trousers, skirts, and shorts, and the mustache patterns on these denim images. Each image has a size of $256 \times 256 \times 3$. Sample images of this dataset are shown in Figure 6(a).

2.4.2. Cityscapes
The Cityscapes dataset contains various stereo video images from the streets of 50 different cities [31]. It contains semantic segmentation maps belonging to 30 different classes, such as a motor-vehicle, road, building, and human. In this study, 2975 image pairs were used in the training phase and 500 in the testing phase. Sample images of this dataset are shown in Figure 6(b).

2.4.3. Maps
The Maps dataset comprises satellite images around New York and corresponding Google map images [13]. In these satellite images, there are objects and regions such as buildings, parks, roads. In this study, 2095 image pairs were used in the training phase and 98 in the testing phase. Sample images of this dataset are shown in Figure 6(c).
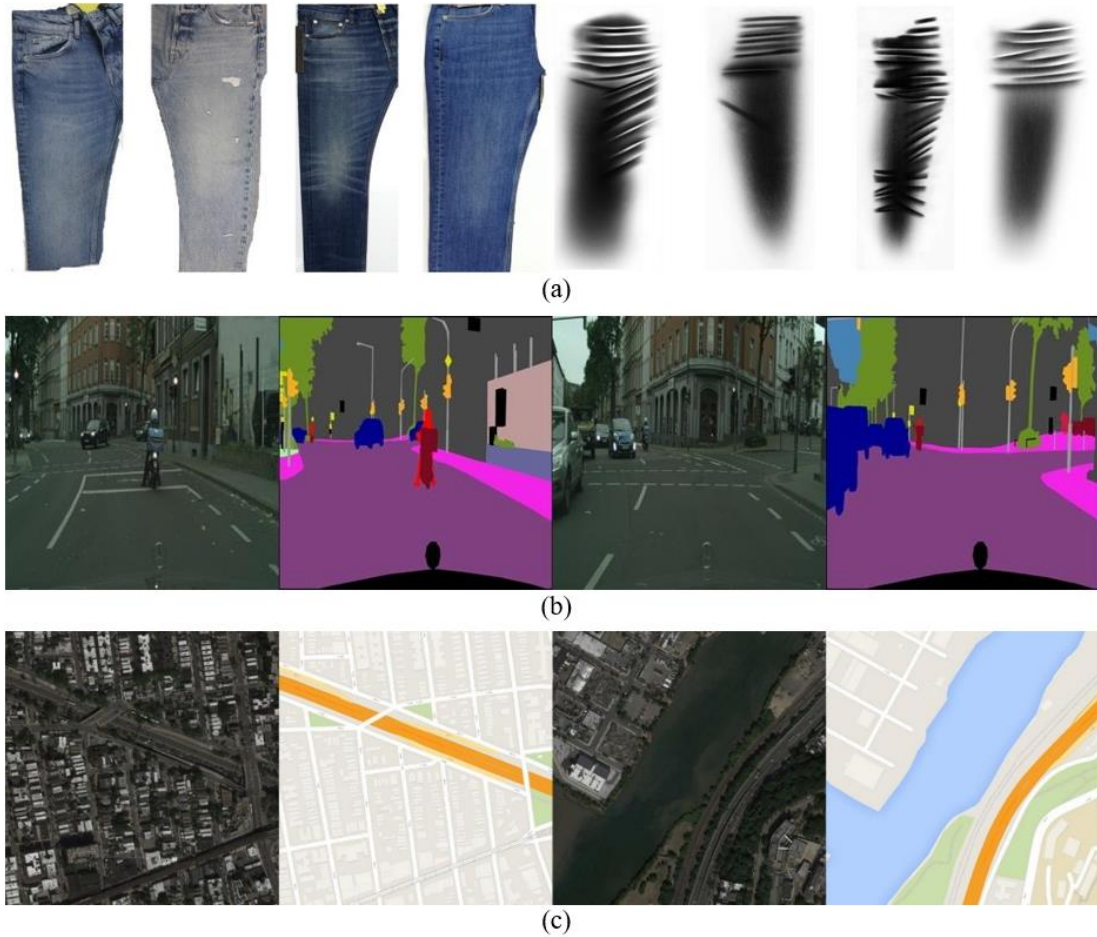
Figure 6. Example images from the Denim2Mustache (a), Cityscapes (b), and Maps (c) datasets.

3. RESULTS

One of the most up-to-date architectures in image synthesis is DiscoGAN. In this section, the performances of the proposed WY-Net architecture and the DiscoGAN architecture in image synthesis are presented comparatively. Table 1. shows the structures and features of the architectures comprehensively.

Table 1. Quantitative property comparison of proposed methods and DiscoGAN.

Network Type	Property Name	Model Name		
		DiscoGAN	**dY-Net**	**uY-Net**
Generator	Number of networks	2	1	1
	Trainable Params	11,022,336	8,266,752	89,283,398
	Forward/backward pass size (MB)	164.00	127.00	135.96
	Params size (MB)	42.04	31.54	340.59
	Estimated total size (MB)	207.54	159.29	477.30
Discriminator	Number of networks	2	1	1
	Trainable Params	5,527,552	2,766,848	2,766,848
	Forward/backward pass size (MB)	74.00	37.00	37.00
	Params size (MB)	21.08	10.55	10.55
	Estimated total size (MB)	96.60	47.56	47.56

In the second stage, training and testing processes were carried out on the Cityscapes, Maps, and Denim2Mustache datasets to compare the architectures. The training and testing processes of the architectures were carried out with the PyTorch deep learning library on a server with an RTX 2080 graphics card, by taking the batch size of 1 for 150 epochs. Adjustments and arrangements such as hyperparameter, epoch, image dimensions have been made on the DiscoGAN architecture. Thus, the necessary environment has been prepared for the performance comparison of these models under appropriate conditions.

Image synthesis quality and the temporal cost of the training process were used as performance criteria. Three different similarity measures (SSIM, PSNR, and MSE) were used to control the synthesis quality of the image pairs in the test set. The performances of the models on the image pairs in the test datasets are shown in Table 2. According to this table, it is seen that dY-Net architecture produces very similar visuals in terms of image quality, although it is approximately 25% more efficient in the generator network structure and 50% more efficient in the discriminator network compared to DiscoGAN. However, it is seen that the uY-Net architecture, which focuses on image quality, produces more successful results in image synthesis than DiscoGAN. The sample outputs of these architectures in the test datasets are shown in Figures. 7 to 9.

Table 2. Performance comparison of proposed methods and DiscoGAN results. This performance comparison was made on the Denim2Mustache, Cityscapes and Maps datasets.

Dataset Name	Model Name	Metric Name	Cross-domain image translation direction	150 epochs training

			X → X	X → Y	Y → Y	Y → X	time (minute)
Cityscapes	DiscoGAN	SSIM ↑	0.451	0.384	0.676	0.676	715
		PSNR ↑	18.85	15.73	19.92	18.22	
		MSE ↓	943.96	2047.1	716.25	1108.1	
	dY-Net	SSIM ↑	0.835	0.397	0.871	0.688	**475**
		PSNR ↑	27.04	16.32	28.01	18.88	
		MSE ↓	143.61	1781.1	109.40	955.9	
	uY-Net	SSIM ↑	0.945	0.437	0.944	0.696	815
		PSNR ↑	32.45	16.43	35.13	18.50	
		MSE ↓	43.32	1744.7	22.21	1051.9	
Maps	DiscoGAN	SSIM ↑	0.268	0.245	0.589	0.516	495
		PSNR ↑	18.02	15.80	28.15	26.48	
		MSE ↓	1093.3	1809.2	129.76	205.5	
	dY-Net	SSIM ↑	0.742	0.255	0.739	0.515	**335**
		PSNR ↑	23.44	16.14	33.25	26.93	
		MSE ↓	320.57	1691.4	34.89	191.1	
	uY-Net	SSIM ↑	0.968	0.252	0.763	0.541	635
		PSNR ↑	28.73	16.13	33.64	26.87	
		MSE ↓	89.60	1676.7	31.63	204.4	
Denim2Mustache	DiscoGAN	SSIM ↑	0.712	0.673	0.922	0.849	210
		PSNR ↑	19.05	19.06	25.26	19.44	
		MSE ↓	956.1	1923.9	235.09	1049.9	
	dY-Net	SSIM ↑	0.814	0.688	0.970	0.819	**145**
		PSNR ↑	28.30	16.53	32.42	19.18	
		MSE ↓	143.8	1735.6	41.73	1166.8	
	uY-Net	SSIM ↑	0.977	0.739	0.983	0.869	265
		PSNR ↑	36.85	16.69	38.08	20.96	
		MSE ↓	27.46	1725.2	12.92	777.9	

Figure 7. Example results of proposed methods and DiscoGAN on image synthesis cityscapes↔segmentation maps, compared to ground truth. Left to right: real *X*, predicted *X*, reconstructed *X*, real *Y*, predicted *Y*, reconstructed *Y* images. Top to bottom for three image pairs: The DiscoGAN, dY-Net, uY-Net architectures.
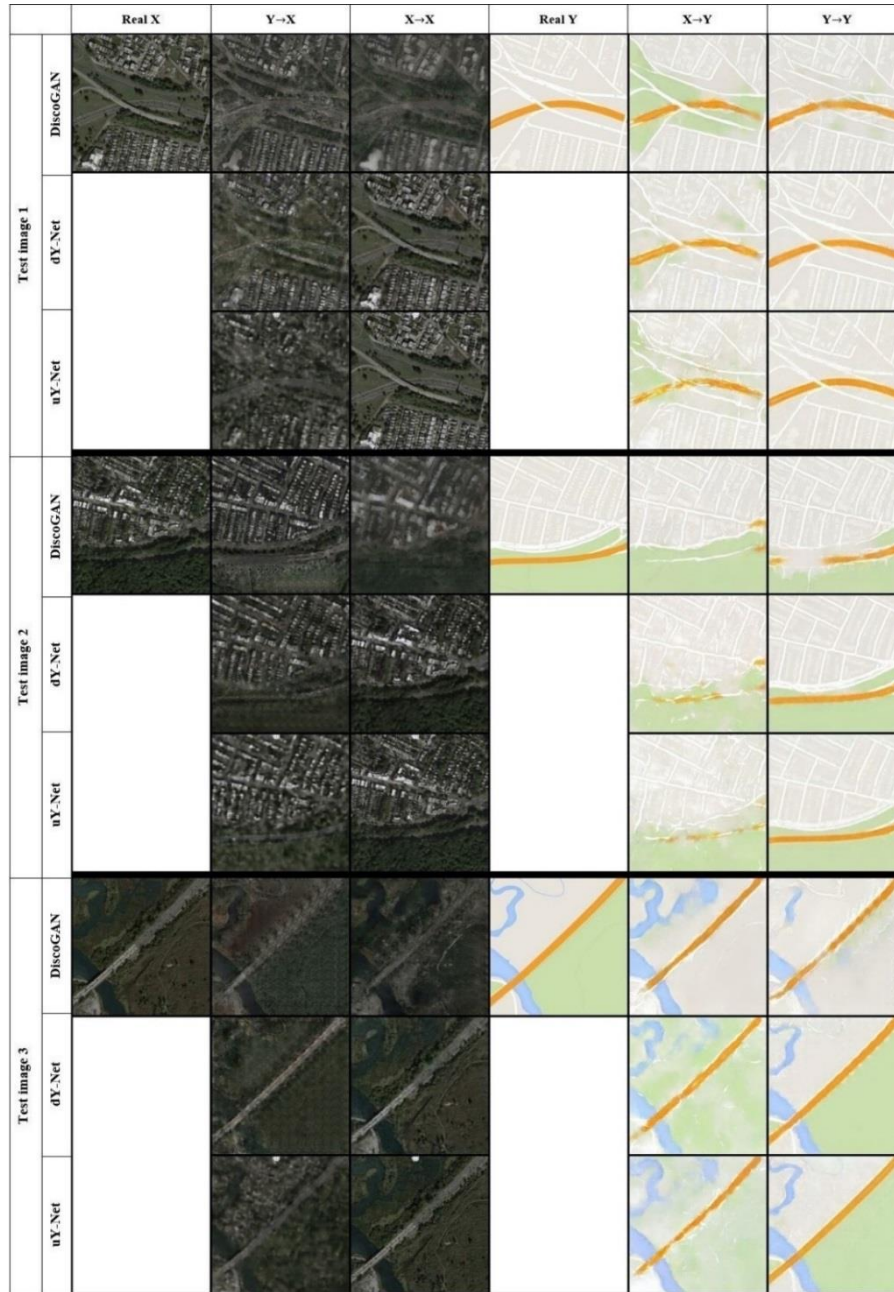
Figure 8. Example results of proposed methods and DiscoGAN on image synthesis satellite images↔Google maps, compared to ground truth. Left to right: real *X*, predicted *X*, reconstructed *X*, real *Y*, predicted *Y*, reconstructed *Y* images. Top to bottom for three image pairs: The DiscoGAN, dY-Net, uY-Net architectures.
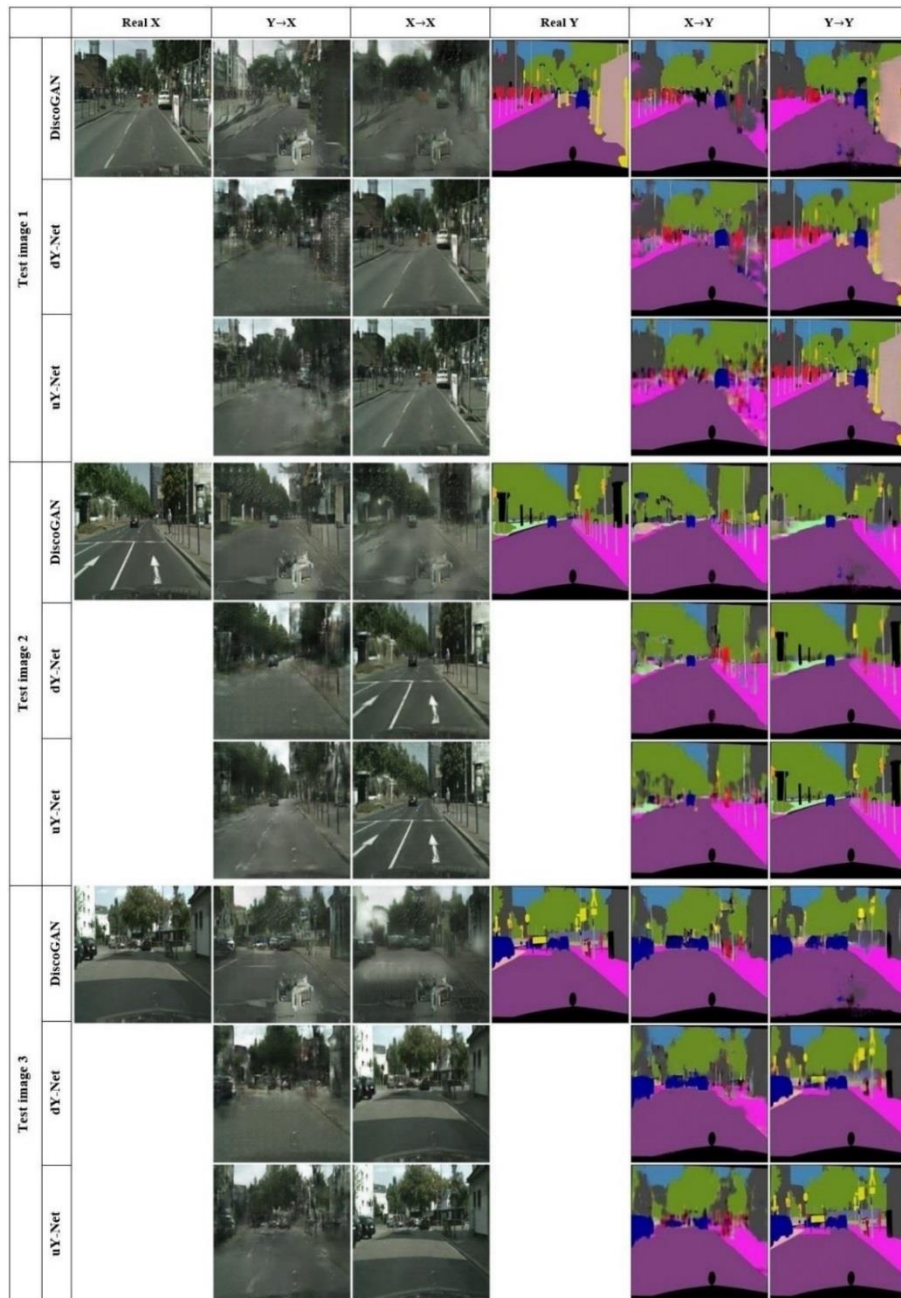
Figure 9. Example results of proposed methods and DiscoGAN on image synthesis denim images↔mustache patterns, compared to ground truth. Left to right: real *X*, predicted *X*, reconstructed *X*, real *Y*, predicted *Y*, reconstructed *Y* images. Top to bottom for three image pairs: The DiscoGAN, dY-Net, uY-Net architectures.
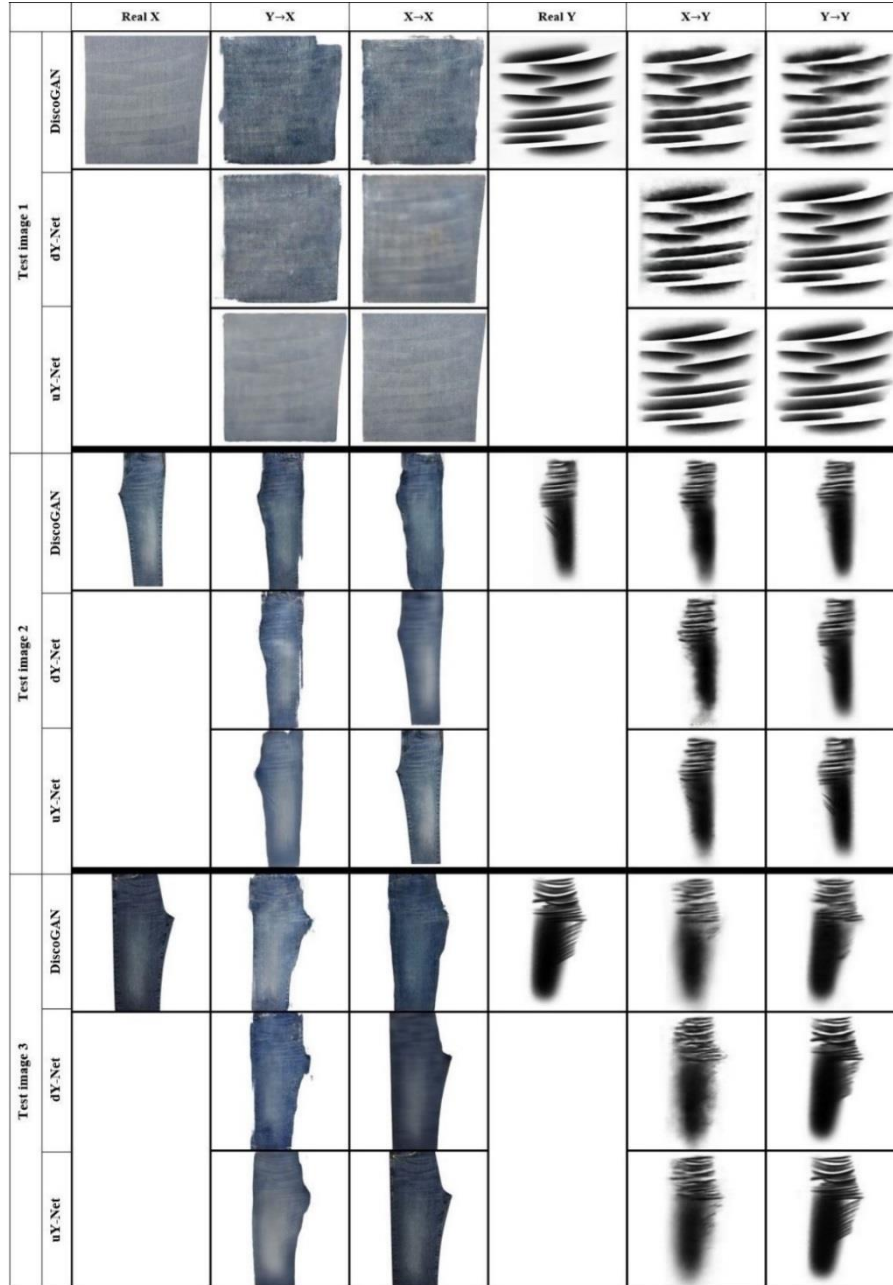
4. DISCUSSION and CONCLUSIONS

In this study, two different architectures, dY-Net, and uY-Net are proposed to be used in the field of image synthesis. The dY-Net architecture has low parameter space and prioritizes performance at image synthesis speed. The uY-Net architecture includes embedding the U-Net structure in WY-Net and prioritizes image synthesis quality. Comparisons of the proposed architectures with existing counterparts are in terms of image synthesis time and accuracy. The basis of WY-Net architectures is the principle of synchronizing the feature spaces of the input and output images. Thus, there is a common use of parameters, and a serious reduction in the number of hyperparameters is realized. Comparisons were made with the DiscoGAN architecture to find out the position of the image synthesizing and speed performances of the proposed architectures in the literature. DiscoGAN architecture, with its bidirectional training structure, is widely used in the field of image synthesis. According to the obtained comparison results, although the number of parameters of dY-Net architecture is 34% lower than DiscoGAN, it can synthesize images of similar quality. It has been observed that uY-Net architecture synthesizes higher quality images than other architectures. Three different datasets (Maps, Cityscapes, and Denim2Mustache) were used in the validation process. These results reveal that two different architectures can be used for applications that prioritize performance or translation quality in image synthesis studies. The next study will be about transferring the feature space synchronization principle used in WY-Net architecture to SSL techniques.

ACKNOWLEDGMENT

REFERENCES

[1]   Goodfellow, I., Pouget-Abadie, J., Mirza, M., Xu, B., Warde-Farley, D., Ozair, S. and Bengio, Y., (2014), Generative adversarial nets. Advances in neural information processing systems, 27.

[2]   Radford, A., Metz, L. and Chintala, S. (2015). Unsupervised representation learning with deep convolutional generative adversarial networks. arXiv preprint arXiv:1511.06434.

[3]   Ledig, C., Theis, L., Huszár, F., Caballero, J., Cunningham, A., Acosta, A. and Shi, W. (2016), Photo-realistic single image super-resolution using a generative adversarial network. In Proceedings of the IEEE conference on computer vision and pattern recognition (pp. 4681-4690).

[4]   Özdemir, D., and Arslan, N. N., (2022) Analysis of Deep Transfer Learning Methods for Early Diagnosis of the Covid-19 Disease with Chest X-ray Images. Düzce Üniversitesi Bilim ve Teknoloji Dergisi, 10(2), 628-640.

[5]   Karras, T., Aila, T., Laine, S. and Lehtinen, J. (2017), Progressive growing of gans for improved quality, stability, and variation. arXiv preprint arXiv:1710.10196.

[6] Zhang, H., Goodfellow, I., Metaxas, D. and Odena, A. (2018), Self-attention generative adversarial networks. In International conference on machine learning (pp. 7354-7363). PMLR.

[7] Karras, T., Laine, S. and Aila, T. (2018), A style-based generator architecture for generative adversarial networks. arXiv preprint arXiv:1812.04948.

[8] Karras, T., Laine, S., Aittala, M., Hellsten, J., Lehtinen, J. and Aila, T. (2019), Analyzing and improving the image quality of stylegan. In Proceedings of the IEEE/CVF Conference on Computer Vision and Pattern Recognition (pp. 8110-8119).

[9] Karras, T., Aittala, M., Laine, S., Härkönen, E., Hellsten, J., Lehtinen, J. and Aila, T. (2021), Alias-free generative adversarial networks. arXiv preprint arXiv:2106.12423.

[10] Brock, A., Donahue, J. and Simonyan, K. (2018), Large scale GAN training for high fidelity natural image synthesis. arXiv preprint arXiv:1809.11096.

[11] Donahue, J. and Simonyan, K. (2019), Large scale adversarial representation learning. arXiv preprint arXiv:1907.02544.

[12] B. Li, Y. Zhu, Y. Wang, C. -W. Lin, B. Ghanem and L. Shen. (2021), AniGAN: Style-Guided Generative Adversarial Networks for Unsupervised Anime Face Generation," in IEEE Transactions on Multimedia, doi: 10.1109/TMM.2021.3113786.

[13] Isola, P., Zhu, J. Y., Zhou, T. and Efros, A. A. (2017), Image-to-image translation with conditional adversarial networks. In Proceedings of the IEEE conference on computer vision and pattern recognition (pp. 1125-1134).

[14] Wang, T. C., Liu, M. Y., Zhu, J. Y., Tao, A., Kautz, J. and Catanzaro, B. (2018), High-resolution image synthesis and semantic manipulation with conditional gans. In Proceedings of the IEEE conference on computer vision and pattern recognition (pp. 8798-8807).

[15] Park, T., Liu, M. Y., Wang, T. C. and Zhu, J. Y. (2019), Semantic image synthesis with spatially-adaptive normalization. In Proceedings of the IEEE/CVF Conference on Computer Vision and Pattern Recognition (pp. 2337-2346).

[16] Zhu, J. Y., Park, T., Isola, P. and Efros, A. A. (2017), Unpaired image-to-image translation using cycle-consistent adversarial networks. In Proceedings of the IEEE international conference on computer vision (pp. 2223-2232).

[17] Li, Y., Singh, K. K., Ojha, U. and Lee, Y. J. (2020), Mixnmatch: Multifactor disentanglement and encoding for conditional image generation. In Proceedings of the IEEE/CVF Conference on Computer Vision and Pattern Recognition (pp. 8039-8048).

[18] Dundar, A., Sapra, K., Liu, G., Tao, A. and Catanzaro, B. (2020), Panoptic-based image synthesis. In Proceedings of the IEEE/CVF Conference on Computer Vision and Pattern Recognition (pp. 8070-8079).

[19] Wang, X., Li, Y., Zhang, H. and Shan, Y. (2021), Towards Real-World Blind Face Restoration with Generative Facial Prior. In Proceedings of the IEEE/CVF Conference on Computer Vision and Pattern Recognition (pp. 9168-9178).

[20] Wang, X., Xie, L., Dong, C. and Shan, Y. (2021), Real-esrgan: Training real-world blind super-resolution with pure synthetic data. In Proceedings of the IEEE/CVF International Conference on Computer Vision (pp. 1905-1914).

[21] Suvorov, R., Logacheva, E., Mashikhin, A., Remizova, A., Ashukha, A., Silvestrov, A. and Lempitsky, V. (2021), Resolution-robust Large Mask Inpainting with Fourier Convolutions. arXiv preprint arXiv:2109.07161.

[22] Kim, T., Cha, M., Kim, H., Lee, J. K., and Kim, J. (2017, July), Learning to discover cross-domain relations with generative adversarial networks. In International Conference on Machine Learning (pp. 1857-1865). PMLR.

[23] Nilsson, J. and Akenine-Möller, T. (2020), Understanding ssim. arXiv preprint arXiv:2006.13846.

[24] Mihelich, M., Dognin, C., Shu, Y., and Blot, M. (2020), A Characterization of Mean Squared Error for Estimator with Bagging. In International Conference on Artificial Intelligence and Statistics (pp. 288-297). PMLR.

[25] Willmott, C. J. and Matsuura, K. (2005), Advantages of the mean absolute error (MAE) over the root mean square error (RMSE) in assessing average model performance. Climate research, 30(1), 79-82.

[26] Fardo, F. A., Conforto, V. H., de Oliveira, F. C. and Rodrigues, P. S. (2016). A formal evaluation of PSNR as quality measurement parameter for image segmentation algorithms. arXiv preprint arXiv:1605.07116.

[27] Bailer, C., Varanasi, K., and Stricker, D. (2017), CNN-based patch matching for optical flow with thresholded hinge embedding loss. In Proceedings of the IEEE Conference on Computer Vision and Pattern Recognition (pp. 3250-3259).

[28] Ronneberger, O., Fischer, P., & Brox, T. (2015, October), U-net: Convolutional networks for biomedical image segmentation. In International Conference on Medical image computing and computer-assisted intervention (pp. 234-241). Springer, Cham.

[29] Lim, J. H., and Ye, J. C. (2017), Geometric gan. arXiv preprint arXiv:1705.02894.

[30] Şahin, E., TALU, M. F., (2021), Bıyık Deseni Üretiminde Çekişmeli Üretici Ağların Performans Karşılaştırması. Bitlis Eren Üniversitesi Fen Bilimleri Dergisi, 10(4), 1575-1589. Doi: 10.17798/bitlisfen.98586.

[31] Cordts, M., Omran, M., Ramos, S., Rehfeld, T., Enzweiler, M., Benenson, R. and Schiele, B. (2016), The cityscapes dataset for semantic urban scene understanding. In Proceedings of the IEEE conference on computer vision and pattern recognition (pp. 3213-3223).

RESEARCH ARTICLE

INVESTIGATION of the CORRELATION BETWEEN POWER CONSUMPTION and SURFACE ROUGHNESS in the TURNING of HARDENED DIN 1.2367 STEEL

Ali Kemal ÇAKIR[1,*]

[1]Adnan Menderes University, Aydın Vocational School, Department of Machinery and Metal Technologies, PK 09100, Central Campus, Aydın, ali.kemal.cakir@adu.edu.tr, ORCID: 0000-0002-2185-8108.

ABSTRACT

Increasing demands in the industrial sector have also increased costs. The share of electricity costs is quite high in these cost increases. Therefore, electricity expenses have become an important phenomenon in the manufacturing sector. On the other hand, brought efficiency to the fore increasing costs in the manufacturing sector. It is tried to give data that will contribute to productivity in manufacturing sectors with this research. The influences of cutting parameters that these are depth of cut, feed rate, and speed of cutting were examined on roughness of surface, power consumption and current of machine through turning of DIN 1.2367 steel using cutting tools are made of coated carbide under dry test case in this study. This study attempts to develop prediction and optimization models to analyze the effect of turning parameters on roughness of surface, power consumption, and ultimately roughness of surface and simultaneous consumption of power. The values of total power consumption were calculated by time of machining and instantaneous current values in the study.
The study results indicated that feed rate has the most important influence on output parameters. The value of surface roughness raised with increasing values of feed rate (56.86 % feed rate). It has been examined that grinding quality surface is obtained, especially at low feed values. The power consumption value increases with rising cutting speed and cut of depth (38.50 % cutting depth) values. Also, the rising in the depth of cut values is effective in the increase in power consumption values.

Keywords: *Hard turning, power consumption, energy, surface roughness.*

1. INTRODUCTION

With the advancement of technology, new equipment and machines are affecting human life. The parts of machine that make up these machines determine the performance of the machine. It is desirable to have a high strength of the machine parts. The high strength of machine parts is provided by heat treatment. Heat treatment increases the strength of the machine part, making it difficult to work. The turning of materials having a hardness above 45 HRC is named hard turning. As the hardness of the materials increases, the resistance to friction increases with the strength. Friction resistance increases the service life of the machine part [1-5].

Increasing the service life is a significant factor in choosing a machine and equipment. It is not desirable that the machines fail, or the service life is short. It is often a waste of raw material when the machine happens inefficient. The raw material, which is limited to raised production amount, should be used more effectually. Further, a shorter machine life reasons more energy sources to be consumed. Another factor in increasing machine life is the surface roughness and cutting parameters. Surface roughness is a sensitive quality criterion that indicates the quality of a product and is effective in the joint surface of two parts. In another saying, the surface roughness is a widely used product quality index in terms of different parameters like aesthetics, resistance of corrosion, considerations of tribological, improvement of the fatigue life, exact fit of crucial mating surfaces. However, achieving a predefined surface roughness and being under certain limits often rises consumption of power and reduces efficiency.

Many studies on the optimization of cutting parameters for roughness of surface, forces, wear of tool, etc. has been done in the last years. But a few studies have been done to optimize the energy productivity of machine tools. Metal cutting processes have been optimized based on economic and technological matters without environmental aspects, formerly [6]. Several studies [7-10] done for optimization of surface roughness and consumption of power for unlike materials indicate opposite results – a small number of researchers have investigated cutting speed is the most important impact by watched by cutting depth in reducing power consumption for CNC machine tools. Moreover, some researchers [11-12] examined that cut of depth is the important factor tracked by cutting speed to decrease the consumption of power. Also, feed rate is the important factor traced by depth of cut to decrease the power consumption was observed in some studies [13-14]. So, more studies are needed to observe the effect of turning parameters on performance features.

Recent review articles on machining indicate that the most mutual turning performances noted by investigators are the machining / manufacturing cost and material removal rate after roughness of surface [15]. Recently, researchers have begun analyzing and optimizing consumption of power in turning progress [16-17]. Savings of energy up to 6-40% can be get based on the best optimal selection of machine tools, parameters of cutting and the suitable optimum tool path design [18]. The impacts of cutting parameters (cutting depth, speed of cutting, and feed rate) on power consumption and roughness of surface were examined on Bhattacharya et al. [8] study. A workpiece considered AISI 1045 steel material was used and using the coated carbide as a cutting tool in their study. Their study results that cutting speed, one of cutting parameters, had a significant impact on surface roughness and power consumption, while other parameters did not significantly affect responses. In the light of the explanations above, the aim of this research is the relationship between inlet parameters like cutting speed, feed rate and cut of depth was decided on output parameters, viz surface roughness, and power consumption, during turning DIN 1.2367 steel using coated carbide insert. In brief, this study is to improve predictive and optimization models for analyzing the effect of turning parameters on roughness of surface, consumption of power, and eventually on surface roughness and power consumption at the same time. Also, in this study, I would like to put forward after I have reflected the result of the surface roughness and power consumption to the researcher studying in this field yet, then how improving surface roughness results in reduced machine power consumption.

2. MATERIALS and METHOD

Appropriate selection of parameter sets of the machining process is important in modelling with optimization and estimation calculation. This is achieved by making sense of the relationship between

parameters affecting the machining process and optimizing the machining conditions. In this part of the study, experiments were carried out on a specific machine tool to understand the effect of different process parameters on the characteristics of performance, namely surface roughness and power consumption.

2.1. Workpiece Material

DIN 1.2367 steel (X38CrMoV5-3 named on EN standard) was utilized as the piece of work in this study. This steel is widely utilized (used in extrusion dies, injection moulds, die cores, punches, etc.). It is a steel resistant to high temperatures in terms of its mechanical properties. Appropriate for heat intervention, it has reach high hardness values, easily. It has peak toughness later the hardening process. It has a high resistance against corrosion and temperature. Therefore, in the mold industry, gear manufacturing, crank-connecting rod manufacturing, and bolt-nut manufacturing has widespread use, such as in manufacturing. DIN 1.2367 tool steel was used in the study. The chemical composition of this tool steel (Ø50.5x250 mm) is shown in Table 1. The high chromium content (5%) in DIN 1.2367 indicates that it is more resistant to abrasion at high temperatures. Hardness of use may be slightly more than estimate (1-2 Rc).

Table 1. Composition of Chemical for DIN 1.2367 Steel [19].

Ingredient	Content (%)					
	C	Si	Cr	Mo	Mn	V
DIN 1.2367	0.38	0.40	5	☐3.00	0.40	0.50

2.2. Process and Parameters of Test and Tooling

In this study, hardening experiments were carried out in Kastamonu University Laboratory. The devices in the laboratory are those that are periodically calibrated. They are devices with high accuracy in experimental studies. It was determined whether there was a temperature drop in the heating furnace. After these stages, the work was started. First of all, the center hole is drilled before the hot work tool steel is heat treated. Vacuum method was used in the heat treatment stage in the study. The reason for using this method is to increase the homogeneity of the part to be used in experimental studies by heat treatment. The DIN 1.2367 steel was first heated (950 C, it was kept in the oven for 1 hour), then cooled (It was cooled in oil after being removed from the oven.) until its hardness value reached 60 HRC . To take away the brittleness of the material, it was cooled in air by standing at 350 °C for 1.5 h. 50 HRC gained after this process. Tempering process was applied to remove the brittle structure of the material. As the hardness of the material increases, corrosion resistance, wear resistance and yield strength increase. Also, because the material was cooled in oil, no martensite structure was formed. In addition, it is seen that no carbon precipitate occurs at the grain boundaries. Thus, the workpiece maintains both hardness and corrosion resistance at high temperatures. This is one of the reasons why the use of DIN 1.2367 steel is so common.

Treatment of heat that is a very process of economical has improved the DIN 1.2367 steel's properties of mechanical. After that, which raised the yield strength of the steel threefold, the 1 mm material was removed. The tests were carried out on peak precision apparatus. Results of test indicating the material features of DIN 1.2367, a hot tool steel, are given below as seen Figure 1 (Fig. 1) and Fig. 2.
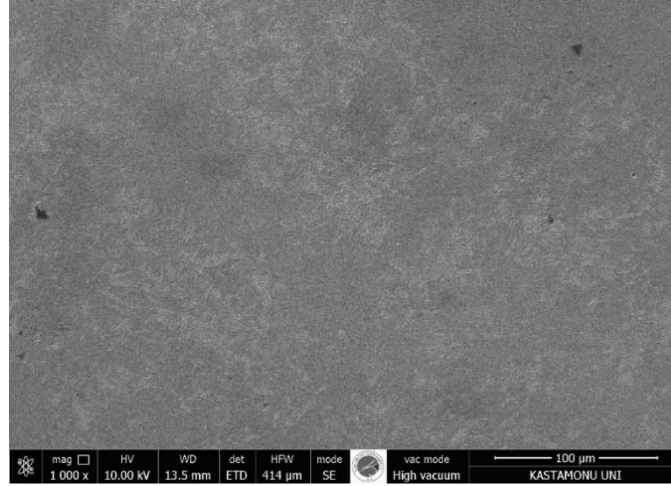
Figure 1. Steel images SEM.

When Fig.1 is examined, cementite grains scattered in martensite blocks are observed. The hardness of steels having martensite structure by giving water decreases while the toughness increases with the tempering process. Microstructures consist of needle-like martensite and plate artensite.
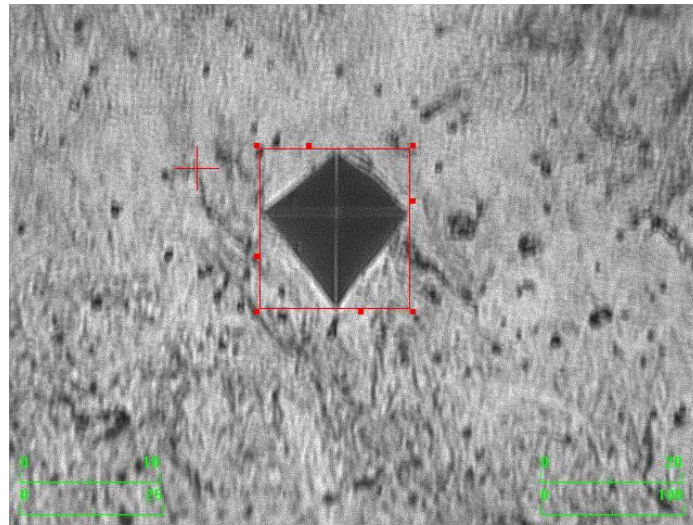
Figure 2. Hardness of the steel.

Micro hardness measurements of the pattern were obtained from 5 different values of hardness and the value of hardness was decided by averaging these data. There has been a high increase in the hardness of the steel and this situation can be seen in Fig. 2. The machining machine used in the study is a model called TTC-630 was used that it was produced by Tezmaksan Co. The high rigidity of this model machine allowed tests of measurement to be carried out in a secure environment. The technical data of lathe machine is seen in the following Table 2.

Table 2. The data of technical for TTC 630.

Special Feature	Value
Diameter of Maximum turning	250 (mm)
Prime power rating	20 (kW)
Max. Speed range	4000 (rpm)
Diameter of chuck	200 (mm)

In order to get efficient and accurate results from the study results, the connections of the equipment in the experimental setup must be made sensitively and securely. In the study, 1.2367 tool steel samples were connected between the chuck center and the cutting tool was connected precisely after the process. Measurement of values of surface roughness was done with Mitutoyo SJ-410 device shown in Figure 3a. Also, the devices shown in Figure 3b were used to measure instantaneous current values. In addition, the measurements of the instantaneous current value were made with the devices indicated in Figure 3b. Both devices were calibrated and verified before the experiment. The environment is isolated so that the devices are not affected by the environment. This situation prevented unnecessary noise from distorting the experimental data.

a)

b)
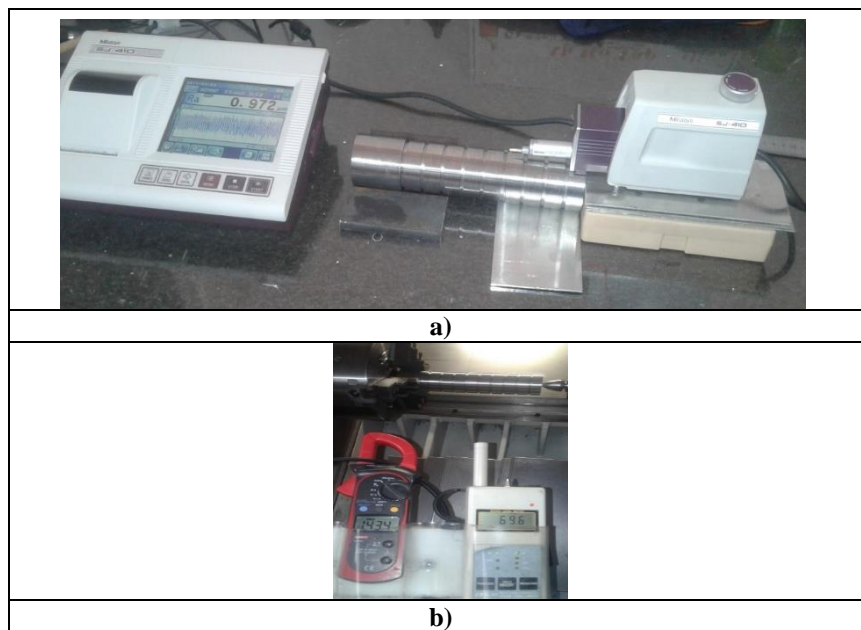
Figure 3. a) Measuring the surface roughness value, **b)** Measurement of instantaneous current value.

LC ISO-16610-21 standards were complied with for surface roughness measurements. Taequtec company's 11T308 model DCMT geometry cutting tools were used for chip. turning operations may vary for each workpiece. For this reason, efficiency can be achieved in the workpiece with the appropriate workpiece and optimum rotational progress. For this reason, the cutting tool has been selected in accordance with the workpiece. Experimental setup is given in Fig. 4a. Also, it is seen schematic diagram in Fig. 4b.

| a | b |
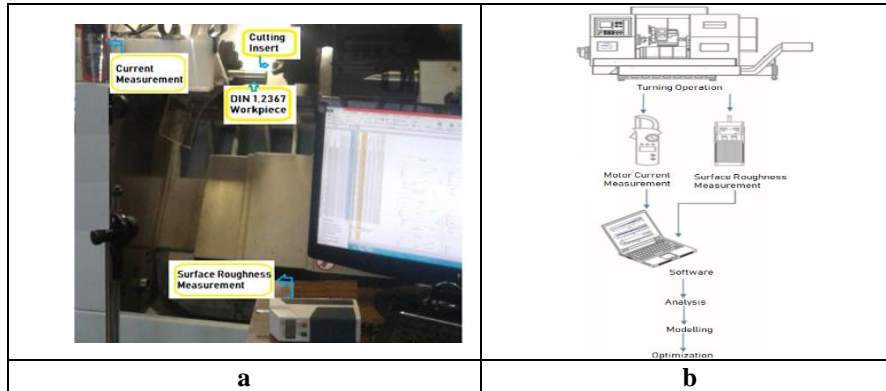
Figure 4. a) Experimental setup, **b)** Schematic diagram in experimental setup.

Parameters of cutting needed to obtain a quality surface of grinding are favoured, while determining for parameters of cutting. Tool holders suited are utilized in the cutting tool. The parameters of cutting for the DIN 1.2367 steel are seen in Table 3. The units are given in the SI unit system.

Table 3. Cutting Parameters for DIN 1.2367.

Parameter Factors	SI Base Units	Factor Levels		
		1	2	3
f- Feedrate	mm/rev	0.06	0.12	0.18
v- Speed of Cutting	m/min	175	200	225
a- Cutting Depth	mm	0.10	0.15	0.20

To see the influences of the cutting parameters, the cutting values are selected over a wide range. By selecting very close values, the effect rate of that parameter was not reduced. By selecting far distant values, the effect rate of that parameter was not increased. The ranges of the cut-off parameters could not go beyond the catalog values [20]. Surface quality is very important in the turning process. A surface quality like grinding quality gives very good results in hard turning processes. Also, hard turning shortens machining times. Therefore, there is no need to grind the material surface. This situation reduces energy consumption. Another reason is that the depth of grinding in the machine has been raised to value of 0.005 while the time of machining has long time. The powder material released during the process shows the energy consumed during the processing time. Thanks to the desired quality of surface, the feed rate has not raised much.

The resulting data were analyzed using R (programming language) software and the Minitab 16 statistics program to run basic statistics including parametric regression and analysis of variance. The distribution curves were omitted. Formulas of regression were calculated. Variance analysis was carried out between the subject variables and unsubjects variables. Finest values for cutting were decided using methods of multiple optimizations for the minimal roughness of surface, consumption of power and time of processing. The best parameters of cutting were defined using the optimization method, weighted according to the importance of dependent variables.

2.3. Methodology of Response Surface

This method (The response surface methodology (RSM)) is utilized to decide a relationship between input and output parameters. It concerns defining parameters for input and output, plan of design in experimental, performing an analysis of regression, calculating variance analysis and examination results for response surface methodology [21].

The influences of cutting parameters on variables of response were examined in dry turning in the study. A complete factorial design that is orthogonal array was chosen for this study which containing three cutting parameters having depth of cut, cutting speeds and feed rate values. This situation is seen in Table 3. Information about the formulas used in the preparation of the test values is given below. The power consumption spent during the process is found according to formula (1).

$$P = \sqrt{3} \ x \ V \ x \ I \ x \ Cos\Phi = \sqrt{3} \ x380x \ I \ x \ 0,95 \tag{1}$$

Experimental feed rate values can be calculated with following formula (2).

$$V = \frac{\pi D n}{1000} \tag{2}$$

The amount of progress in one minute can be calculated following formula (3).

$$F = n \ x \ f \tag{3}$$

The processing time spent during the operation is found according to the formula (4).

$$t = L \ x \ 60 \ / \ F \tag{4}$$

The time spent throughout the process is found by formula (5).

$$T = \frac{\pi.D.60.L.a_{max}}{1000.V.f.a} \tag{5}$$

It has set cutting parameter (a, V, f) being experimental parameters. Values of current were measured by apparatus (trademark is UNI-T UT201) and given in Table 4. The time spent throughout the process is found from formula (5) and displayed in Table 4. Also, Power Consumption Values are found from formula (1) and surface roughness values were taken from the device by machining that they are shown in Table 4.

3. RESULTS and DISCUSSIONS

The obtained results in the light of the knowledge and tests given in Chapter 2 (Material and Method) are reflected as follows.

3.1. Experimental Results

It can be seen experimental results in Table 4.

Table 4. Experimental Conditions and Results.

Numbers of Experiment	a (mm)	V (m/min)	f (mm/rev)	Time (s)	Current (Watt)	Total Power Consumption (Watt)	Ra (μm)
1	0.1	175	0.06	35.89	2.67	1669.47	0.3
2	0.1	175	0.12	17.94	2.81	1757.01	0.53
3	0.1	175	0.18	11.96	2.93	1832.04	1.23
4	0.1	200	0.06	31.40	2.72	1700.73	0.25
5	0.1	200	0.12	15.70	2.84	1775.77	0.54
6	0.1	200	0.18	10.47	2.99	1869.56	1.21
7	0.1	225	0.06	27.91	2.85	1782.02	0.22
8	0.1	225	0.12	13.96	3.04	1900.82	0.64
9	0.1	225	0.18	9.30	3.24	2025.87	1.54
10	0.15	175	0.06	23.92	2.82	1763.26	0.33
11	0.15	175	0.12	11.96	2.96	1850.80	0.66
12	0.15	175	0.18	7.97	3.20	2000.86	1.15
13	0.15	200	0.06	20.93	3.05	1907.07	0.28
14	0.15	200	0.12	10.47	3.24	2025.87	0.6
15	0.15	200	0.18	6.98	3.46	2163.43	0.9
16	0.15	225	0.06	18.61	3.10	1938.34	0.33
17	0.15	225	0.12	9.30	3.36	2100.91	0.36
18	0.15	225	0.18	6.20	3.37	2107.16	1.36
19	0.2	175	0.06	17.94	2.91	1819.54	0.34
20	0.2	175	0.12	8.97	3.12	1950.84	0.67
21	0.2	175	0.18	5.98	3.21	2007.12	1.37
22	0.2	200	0.06	15.70	3.15	1969.60	0.36
23	0.2	200	0.12	7.85	3.39	2119.67	1.02
24	0.2	200	0.18	5.23	3.85	2407.29	1.37
25	0.2	225	0.06	13.96	3.40	2125.92	1.1
26	0.2	225	0.12	6.98	4.26	2663.65	3.66
27	0.2	225	0.18	4.65	4.40	2751.19	4.42

Increasing cutting speed and increasing feed rate caused an excessive increase in surface roughness values. Because, the tool is not appropriate to get good machining with these parameters of cutting. However, with low cutting parameters, very good results were obtained in machining.

3.1.1. Values of surface roughness (Ra)
After each cutting experiment, values of surface roughness (Ra) were measured. The variance analysis values calculated for roughness of surface is seen in Table 5. Roughness of surface has a important impact on all cutting parameters. A p value less than 0.05 shows an important relationship at the 97.27% confidence interval. The value of surface roughness is influenced by the various cutting parameters (12.27 % depth of cut, 12.27 % cutting speed, and 56.86 % feed rate) as seen Table 5. Influences of parameters of cutting on roughness of surface are seen in Fig. 5 and Fig. 6. The slope of

feed rate is large which indicates that has more impact on roughness of surface. The gradient of the cutting speed and depth of cut is no big which indicates that both no have more effect on roughness of surface. The most impact parameter of cutting on the roughness of surface is the feed rate. This reinforces the statement that the impacts of feed rate are more influential than speed of cutting on decreasing the forces and enhancing the surface machining [22]. The rising in cutting speed did not cause an important change in roughness either, because of the increased number of revolutions did not make an important vibration in the machine. So, there was not much deviation in the values of roughness. Thus, the machine does not lose its rigidity with the increasing number of revolutions (cutting speed) due to its rigidity. Also, increasing speed causes the pressure to drop in machining. The decrease in cutting pressure causes the cutting force to decrease. This provides a better cutting. Therefore, low depth of cut and high speed of cutting should be preferential in new machine tools.

As seen in Fig. 5, it is seen that the most efficient parameter on the average roughness value among the cutting parameters is the feed rate. It was observed that the increase of the cutting speed (V) from 175 m/min to 225 m/min and the increase of the cutting depth (a) from 0.10 mm to 0.20 mm did not have a serious effect on the surface roughness, compared to the feed rate. When the feed rate (f) increased from 0.06 mm/rev to 0.18 mm/rev, it was determined that the surface roughness (Ra) value increased 14 times (1400%) on average. The depth of the channels on the cylindrical surface increases with incrementing feed rate. Therefore, the values of surface roughness made parallel to the advancement axis also increase. It is aimed to obtain low surface roughness values in hard turning operations. For this reason, it is preferred that the values of the feed rates are low.

Table 5. Values of Variance Analysis for Roughness of Surface.

The source	The total degrees of freedom (DF)	SS of Seq	SS of Adj	MS of Adj	F	P	Contribution (%)
Defined regression	9	10.6187	10.6187	1.17986	67.42	0.000	97.27
Parameter's Linear	3	8.8856	8.8856	2.96187	169.24	0.000	81.40
Value of a	**1**	**1.3393**	**1.3393**	**1.33934**	**76.53**	**0.000**	**12.27**
Value of V	**1**	**1.3393**	**1.3393**	**1.33934**	**76.53**	**0.000**	**12.27**
Value of f	**1**	**6.2069**	**6.2069**	**6.20694**	**354.66**	**0.000**	**56.86**
Square	3	0.5360	0.5360	0.17867	10.21	0.000	4.91
a *a	1	0.1723	0.1723	0.17227	9.84	0.006	1.58
V *V	1	0.2632	0.2632	0.26320	15.04	0.001	2.41
f *f	1	0.1005	0.1005	0.10054	5.74	0.028	0.92
Interaction	3	1.1971	1.1971	0.39904	22.80	0.000	10.97
a *V	1	0.8640	0.8640	0.86403	49.37	0.000	7.91
a *f	1	0.0631	0.0631	0.06307	3.60	0.075	0.58
V *f	1	0.2700	0.2700	0.27000	15.43	0.001	2.47
Error of residual	17	0.2975	0.2975	0.01750			2.73
Total	26	10.9163					100.00

R^2: Accuracy Value	R^2 = 97.27 %	R^2 (MS of adj) = 95.83 %

While one of the most important indicators of surface quality is the surface roughness value, ovality and the formation of a white layered structure on the surface are undesirable. In addition, the ovality prevents the workpieces from working properly. White layer structure formation causes residual stresses on the surface. This causes the strength of the workpiece to decrease. Hence, it causes a decrease in wear resistance. Speed of cutting and depth of cut have a significant impact on both ovality and white layer formation. For surface quality, only a low surface roughness value will not be sufficient. In such cases, low depth of cut and high cutting speeds should be preferred to improve machinability characteristics.
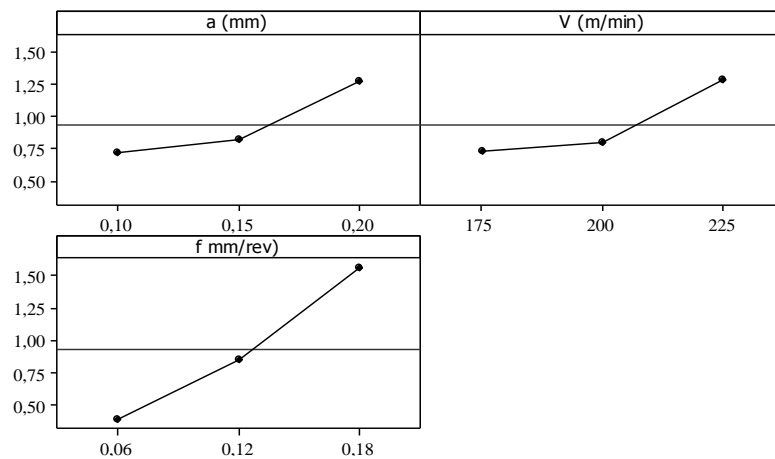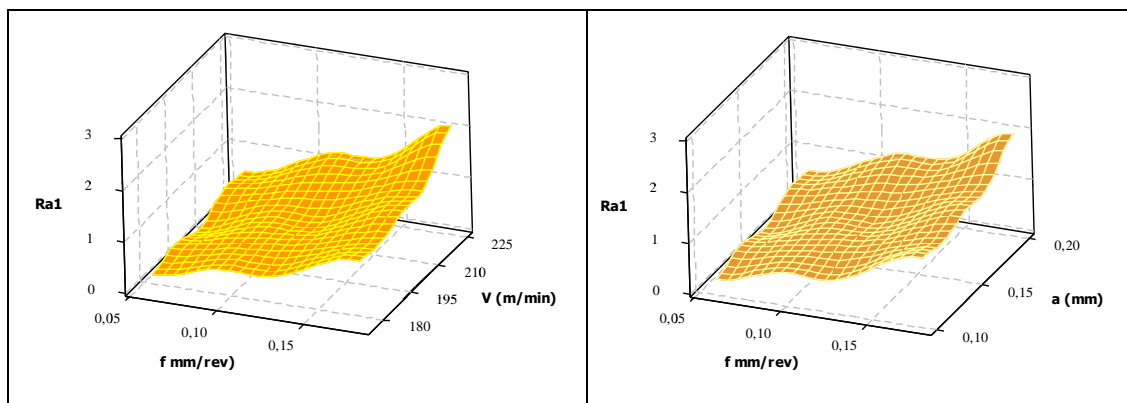

Figure 5. The influence of cutting parameters on means response features for surface roughness.
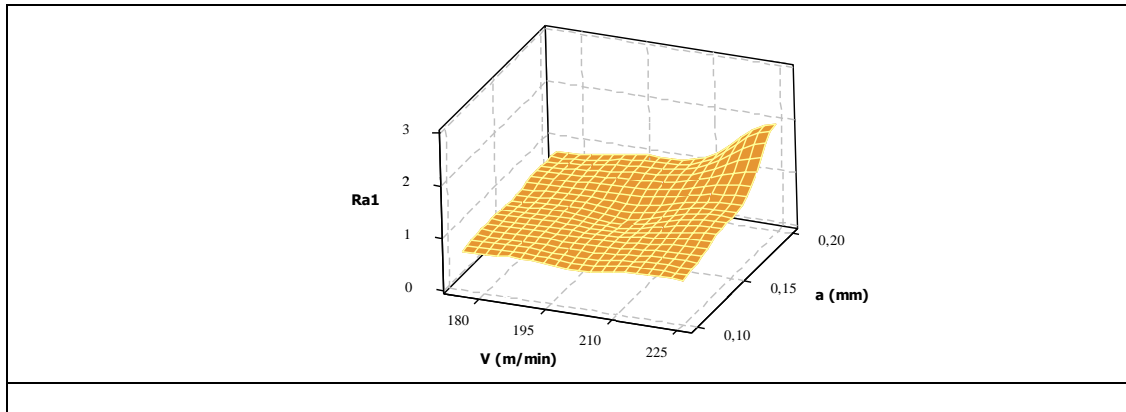
Fig. 6. 3-dimensional representation of the influences of cutting parameters on the surface roughness.

As the feed rate values rise, surface roughness values are also raised as shown in Fig. 5 and Fig. 6. As shown in Fig. 5, due to the mutual effect between the cutting depth and roughness of surface values, while roughness values of 0.75 μm were seen at 0.10 mm the cutting depth, there was no important rise in value of roughness at 0.15 mm. As it can be shown in Fig. 5, it has been tracked that the roughness value from 0.15 to 0.20 mm has suddenly increased. Likewise, while roughness values of 0.75 μm were seen at 175 m/min the cutting speed, there was no significant increase in roughness value at 200 m/min, with the interaction between the cutting speed and surface roughness values. There has been noticeable rise from 200 m/min to 225 m/min. Also, this tendency is reinforced by the percentage additive values in the ANOVA results.

Cakir, A.K. [23] investigated values of surface roughness, sound levels and current of machine in the turning hardened AISI S1 steel material. The most best surface roughness values were found by the most influential cutting factor that is the feed rate, in his study. Asiltürk and Akkuş [2] They used Taguchi method for optimizing turning parameters to down surface roughness. Results indicated that the feed rate was the most impressed factor effecting roughness of surface in their study. However, Cetin et al. [22] showed the influences of depth of cut and feed rate are more influence than cutting speed on decreasing the forces and develop the finish of surface, as mentioned above.

3.1.2. Motor current rating

The motor current values show the instantaneous load and power consumption of the machine, so they are important. In other words, as the amount of strain on the machine tool increases, the current value increases. Cutting parameters affect motor current values in machining processes. That's why it's good to know. The current, power consumption and surface roughness values obtained according to the cutting parameters are indicated in Table 4. Increasing of the feed rate amounts causes the instantaneous current value to increase. Similarly, the increment in the cutting depth caused an increment in the amount of load on the machine tool and an increase in the current value. The instantaneous current value is an indicator instead of the cutting forces, which are expensive and laborious to measure. Choosing a low depth of cut ensures a low load amount in study. Also, the increase in cutting speed provides a slight increase in the current value. Because the increase in the number of revolutions causes an increase in the current consumed by the motor. In addition,

increasing cutting speed causes the cutting forces to decrease. Despite this, although the cutting forces decreased a little, the current value increased a little as the engine speed increased.

We can think of the total power consumption as a function of the value of instantaneous current and the time of processing. Even if the value of instantaneous current rises, the total power consumption is lower because the time of processing is very short. Available current values rise with increasing speed of cutting and depth of cut. Since the load per unit time rises, the motor current value increases as the feed rate increases. Also, it can be seen in the increment in the instant chip section. Choosing the depth of cut in the study provides low load amount. That's way, a small increment in the current value is viewed with rising feedrate.

3.1.3. Power consumption

Energy consumption in machines used in machine tools starts at the preparation stage. Throughout this time, the machine tool not only consumes electrical energy, but also requirements a certain amount of time to be ready for operational progress. While energy consumption directly contributes to power consumption, it affects the operational time during the machine operation. Therefore, the total process time is affected.

The total processing time and the instantaneous current value affect the power consumption, which causes serious costs. Since the electric current used in machining processes is gotten as outcome of burning fuels of fossil, it increases carbon emissions. This situation also harms the ecological balance. The world has limited reserves in underground resources. Therefore, efficient use of energy is important. Machine tool manufacturers, where energy consumption is high in the manufacturing industry, should also take this into account. For these reasons, it is necessary to determine the optimum cutting parameters in machine tools and to work with minimum power consumption. This will reduce energy costs. Linear regression model was used to estimate surface roughness and power consumption. Table 6 shows analysis of variance for power consumption. Confirmation experiments are shown in Table 4.

Table 6. Analysis of Variance for Power Consumption.

Source	DF	SS of Seq	SS of Adj	MS of Adj	Value of F	Value of P	Contribution (%)
Regression	9	1639347	1639347	182150	94.49	0.000	98.04
Linear	3	1470525	1470525	490175	254.28	0.000	87.94
a	**1**	**643746**	**643746**	**643746**	**333.94**	**0.000**	**38.50**
v	**1**	**399719**	**399719**	**399719**	**207.35**	**0.000**	**23.90**
f	**1**	**427060**	**427060**	**427060**	**221.54**	**0.000**	**25.54**
Square	3	2215	2215	738	0.38	0.767	0.13
a*a	1	139	139	139	0.07	0.791	0.01
v*v	1	1373	1373	1373	0.71	0.410	0.08
f*f	1	703	703	703	0.36	0.554	0.04
Interaction	3	166607	166607	55536	28.81	0.000	9.96
a*v	1	91789	91789	91789	47.62	0.000	5.49
a*f	1	47921	47921	47921	24.86	0.000	2.87
v*f	1	26897	26897	26897	13.95	0.002	1.61

Residual Error	17	32771	32771	1928	1.96
Total	26	1672119			100.00

R^2 = 98.04%	R^2(predicted) = 94.52%	R^2 (adj) = 97.00%

The power consumption has an important impact on all three parameters of cutting. Value of P less than 0.05 shows that there is an important correlation in the 94.52 % interval of confidence. Cutting depth (a) was based to be the most important fact on the power consumption which express 38.50% contribution of sum variation. The next additives on the power consumption come from the feed rate and the cutting speed having additive of 25.54% and 23.90% seriatim. The quadratic terms that they are v^2, f^2, a^2 don't have statistical importance on power consumption because of they have less level of additive and p value is also more than the assurance level. The interactions which are (v×f), (a×v) and (a×f) have 1.61%, 5.49% and 2.87% additives, seriatim. Also, residual error has only 1.96% additive. The R^2 is 0.9804 which shows that 98.04% of the sum variations are expressed by the model. The R^2 (Adj.) = 0.97 showing 97% of the sum variability is expressed by the model after regardful the importance facts. R^2 (Pred.) = 0.9452 which indicates that the model is hoped to express 94.52% of the variability in recent data. The increment in the cut-off parameters causes rising of the value of instantaneous current. Likewise, the increment in factors of cutting shortened the time of processing. The increase in the cut-off factors rises the instantaneous current value but decrease the consumption of power as it shortens the processing time. The most useful factor in power consumption is the time of processing. Operating only the machine tool causes a large part of the consumption of energy. In this instance, it is essential to rise the cutting factors to shorten the working time of the machine. However, it is not preferred to increase the feed rate in the cutting parameters as it increases the surface roughness value. So, to reduce energy consumption, shorten the processing time, and avoid to deteriorating the surface quality, while the speed of cutting and cutting depth can be increased, the feed rate must be reduced. This can be seen in Fig. 7 and Fig. 8.
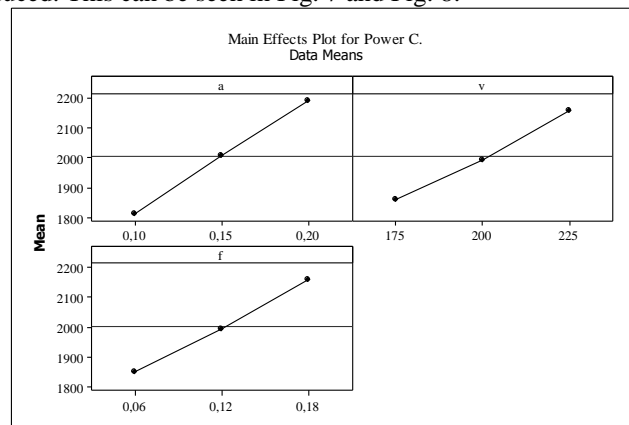

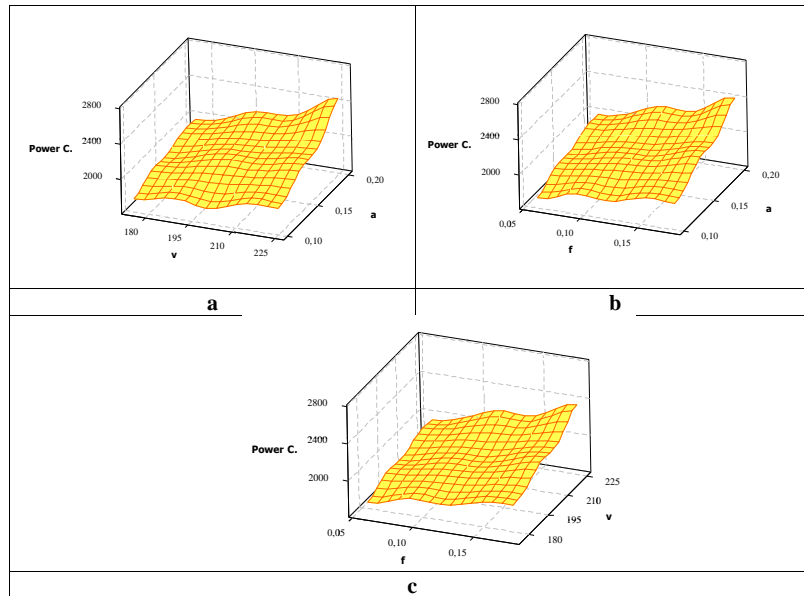**Figure 7.** Main Effects Plot for Power Consumption.

Figure 8. a) Power Consumption with v and a correlation, **b)** Power Consumption with f and a correlation, **c)** Power Consumption with f and v correlation.

The power consumption value rises with the speed of cutting and cutting depth. The increment in the values of depth of cut is more impact in the increment in power consumption value. This situation backings the discussion that the influences of the depth of cut are more efficacious than feed rate and cutting speed to get least consumption of power and best quality of surface in their study by Hanafi et. al. [12].

3.2. Correlation Between Cutting Speed, Feedrate and Power Consumption

Cutting speed and feedrate which have importance value on surface roughness how affect power consumption can be seen in Fig.9. Consumption of power is also low at low feedrate and low cutting speeds. This situation also ensured that the surface roughness was low. However, rising of these values, the generated power consumption values in the processing also increase. However, the rate of this increase decreases at optimum values. The value of surface roughness raised with rising feed rate values that it is 56.86 %. It has been examined that grinding quality surface is obtained, especially at low feed values. The power consumption value increases with rising cutting speed and cut of depth (38.50 % cut of depth) values.
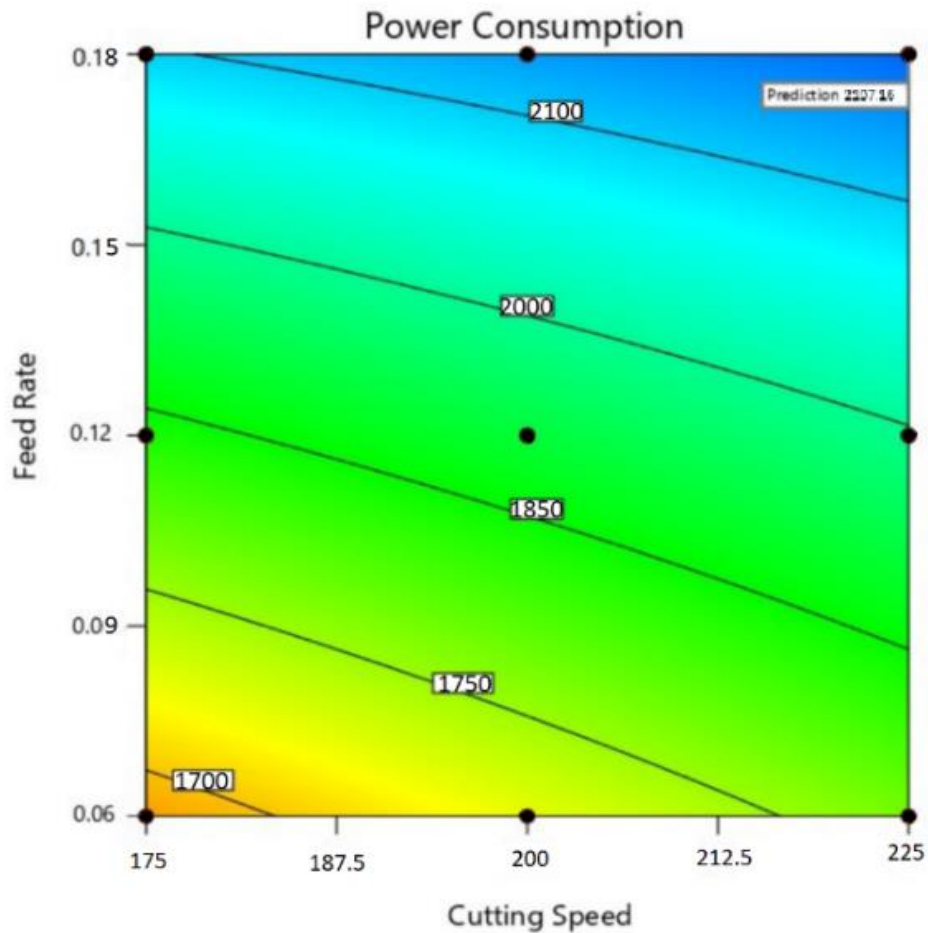
Figure 9. Correlation of between Cutting Speed, Feedrate and Power Consumption.

3.3. Correlation Between Surface Roughness, Power Consumption, and Instantaneous Current

The power consumption value rises with the speed of cutting and depth of cut in the turning process. The increase in depth of cut is more impressive in increasing the power consumption value. Fig. 10. shows the correlation between surface roughness, amount of instantaneous current, and total power consumption. According to Fig. 10, while the surface roughness value increased, the instantaneous current values also increased significantly. Even if the value of instantaneous current rises, the total power consumption reduces as the total time of operation decreases. This is reached by the preference of high cutting speed and high cut of depth. This can be seen in the graphical representation of the numerical data in Figure 10. The increase in current values increased the total power consumption, but with the decrease in the total cutting time, there is a significant decrease in power consumption. Towards the end of the experiment, the rapid increase in surface roughness increased the instantaneous current value and total power consumption rapidly. The final cutting parameter is due to

the bad run-out of the tool combination. This is an acceptable situation. It did not have much of an effect because of considering the overall experimental results.
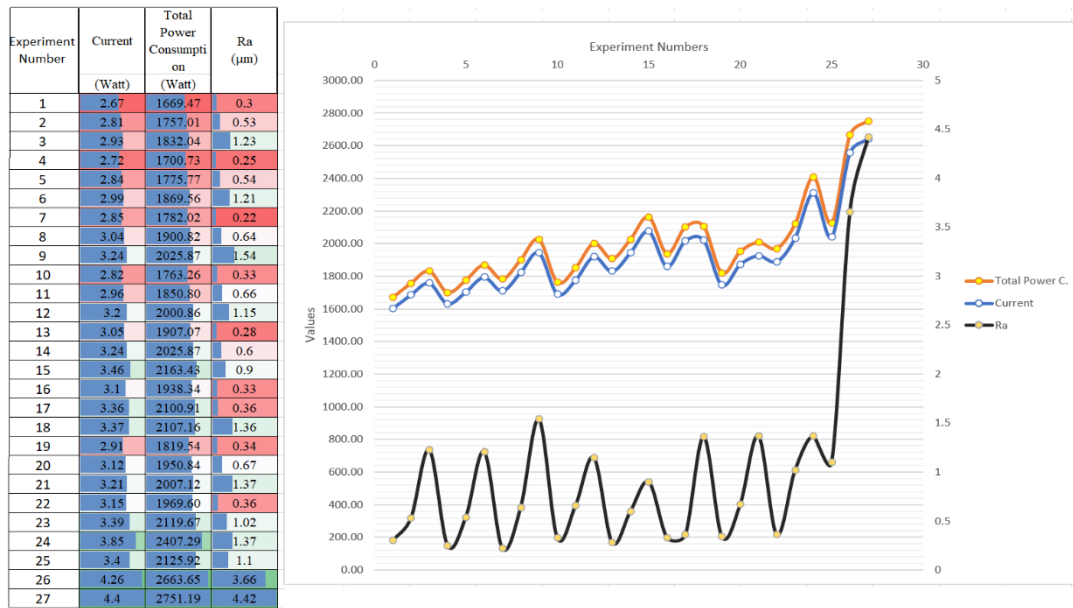
Experiment Number	Current (Watt)	Total Power Consumption (Watt)	Ra (µm)
1	2.67	1669.47	0.3
2	2.81	1757.01	0.53
3	2.93	1832.04	1.23
4	2.72	1700.73	0.25
5	2.84	1775.77	0.54
6	2.99	1869.56	1.21
7	2.85	1782.02	0.22
8	3.04	1900.82	0.64
9	3.24	2025.87	1.54
10	2.82	1763.26	0.33
11	2.96	1850.80	0.66
12	3.2	2000.86	1.15
13	3.05	1907.07	0.28
14	3.24	2025.87	0.6
15	3.46	2163.43	0.9
16	3.1	1938.34	0.33
17	3.36	2100.91	0.36
18	3.37	2107.16	1.36
19	2.91	1819.54	0.34
20	3.12	1950.84	0.67
21	3.21	2007.12	1.37
22	3.15	1969.60	0.36
23	3.39	2119.67	1.02
24	3.85	2407.29	1.37
25	3.4	2125.92	1.1
26	4.26	2663.65	3.66
27	4.4	2751.19	4.42

Figure 10. Correlation Between Surface Roughness, Power Consumption, and Instantaneous Current.

4. CONCLUSIONS

This study presents the corelation between cutting parameters such as cutting speed, feedrate, cut of depth and response parameters, namely surface roughness, and power consumption, during turning DIN 1.2367 steel.

Predictive model was statistically importance using an ANOVA. Analysis of variance shows influence of feedrate on the surface roughness is 56.86 %. Also, the value of surface roughness is modelled with 95.83 % accuracy. It is important using suitable cutting tool to get good surface quality in turning process. It has been traced that value of surface roughness increased with rising feed rate values. By contrast with depth of cut and cutting speed had no significant impact on the surface roughness value. The error of residual contribution is 2.73% for surface roughness. This situation indicates the results of experimental for values of surface roughness was dependable. The low current value range is due to the low depth of cut. However, there is a strong relationship between the current value and the cutting parameters. The value of instantaneous current rises because of rising cutting parameters. Although the instantaneous current value is increased, the total power consumption is also reduced as the total processing time is decreased. Also, the power consumption value increases with rising of cutting depth and cutting speed values (%38.50 cutting depth). The increment in the depth of cut is more impact in the increment in power consumption value. This study can be furthermore extended to analyze the impact of different cutting conditions and cutting tools on power consumption and surface roughness during machining. Response surface methodology and genetic algorithms using cutting

parameters enable to develop optimization of surface roughness and power consumption. In the study, the most effective parameter on the roughness of surface is the feedrate, which provides good surface quality and extends the processing time. To compensate for this loss of time, high depths of cut and high cutting speeds can be preferred. In this way, many workpiece manufacturing is achieved with good surface quality, low current values, and low power consumption.

ACKNOWLEDGEMENT

REFERENCES

[1] Yallese, M. A., Chaoui, K., Zeghib, N., Boulanouar, L. and Rigal, J. F.,(2008), Hard machining of hardened bearing steel using cubic boron nitride tool. J. Mater. Process. Technol(2009).doi:10.1016/j.jmatprotec. 03.014.

[2] Asiltürk, I. & Akkuş, H., (2011), Determining the effect of cutting parameters on surface roughness in hard turning using the Taguchi method. Meas. J. Int. Meas. Confed. doi:10.1016/j.measurement.2011.07.003

[3] Günay, M., Korkmaz, M. E. & Yaşar, N., (2017), Finite element modeling of tool stresses on ceramic tools in hard turning. *Mechanika* doi:10.5755/j01.mech.23.3.14363

[4] Sharma, V. S., Dhiman, S., Sehgal, R. and Sharma, S. K.(2008), Estimation of cutting forces and surface roughness for hard turning using neural networks. *J. Intell. Manuf.* doi:10.1007/s10845-008-0097-1

[5] Chou, Y. K., Evans, C. J. & Barash, M. M. (2003), Experimental investigation on cubic boron nitride turning of hardened AISI 52100 steel. *J. Mater. Process. Technol*doi:10.1016/S0924-0136(02)00070-5.

[6] Yan, J., Li, L., (2013), Multi-objective optimization of milling parameters e the trade-offs between energy , production rate and cutting quality. J. Clean. Prod. 52, 462–471.

[7] Aggarwal, A., Singh, H., Kumar, P., Singh, M., (2008), Optimizing power consumption for CNC turned parts using response surface methodology and Taguchi's technique—A comparative analysis. J. Mater. Process. Technol. 200, 373–384.

[8] Bhattacharya, A., Das, S., Majumder, P.,(2009), Estimating the effect of cutting parameters on surface finish and power consumption during high speed machining of AISI 1045 steel using Taguchi design and ANOVA. Prod. Eng. Res. Devel. 3, 31–40 DOI:10.1007/s11740-008-0132-2.

[9] Bhushan, R.K.,(2013), Optimization of cutting parameters for minimizing power consumption and maximizing tool life during machining of Al alloy SiC particle composites. J. Clean. Prod.39, 242–254.

[10] Chudy, R., Grzesik, W., (2015), Comparıson of Power and Energy Consumptıon for Hard Turnıng and Burnıshıng Operatıons Of 41cr4 Steel. Journal of Machine Engineering, Vol. 15, No. 4, 2015.

[11] Fratila, D., Caizar, C., (2011), Application of Taguchi method to selection of optimal lubrication and cutting conditions in face milling of AlMg 3. J. Clean. Prod. 19, 640–645.

[12] Hanafi, I., Khamlichi, A., Cabrera, F.M., Almansa, E., Jabbouri, A., (2012), Optimization of cutting conditions for sustainable machining of PEEK-CF30 using TiN tools. J. Clean. Prod. 33, 1–9.

[13] Abhang, L.B., Hameedullah, M., (2010), Power prediction model for turning EN-31 steel Using response surface methodology. J. Eng. Sci. Technol. Rev. 3, 116–122.

[14] Camposeco Negrete, C., (2013), Optimization of cutting parameters for minimizing energy consumption in turning of AISI 6061 T6 using Taguchi methodology and ANOVA. J. Clean. Prod. 53, 195–203.

[15] Yusup, N., Mohd, A., Zaiton, S., Hashim, M., (2012), Expert Systems with Applications Evolutionary techniques in optimizing machining parameters: Review and recent applications (2007 – 2011). Expert Syst. Appl. 39, 9909–9927.

[16] Aggarwal, A., Singh, H., Kumar, P., Singh, M., (2008) Optimizing power consumption for CNC turned parts using response surface methodology and Taguchi's technique—A comparative analysis. J. Mater. Process. Technol. 200, 373–384.

[17] Fang, K., Uhan, N., Zhao, F., Sutherland, J.W., (2011), A new approach to scheduling in manufacturing for power consumption and carbon footprint reduction. J. Manuf. Syst. 30, 234–240.

[18] Newman, S.T., Nassehi, A., Imani-Asrai, R., Dhokia, V., (2012), Energy efficient process planning for CNC machining. CIRP J. Manuf. Sci. Technol. 5, 127–136.

[19] Anonymous a, Stherm 2367 Steel, Designation by Standards, https://steelselector.sij.si/steels/UTOPMO7.html, (Last Access Date: 27/05/2020).

[20] Anonymous b, "Item Designation: DCMT 11T308 Tool", https://www.iscar.com/eCatalog/item.aspx?cat=5568588&fnum=739&mapp=IS&app=31&GFS TYP=M, (Last Access Date:25/05/2020).

[21] Şahinoğlu, A., Rafighi, M., (2020), Investigation of Vibration, Sound Intensity, Machine Current and Surface Roughness Values of AISI 4140 During Machining on the Lathe. *Arab* J Sci Eng 45, 765–778

[22] Cetin, M.H., Ozcelik, B., Kuram, E., Demirbas, E., (2011), Evaluation of vegetable based cutting fluids with extreme pressure and cutting parameters in turning of AISI 304L by Taguchi method.

J. Clean. Prod. 19, 2049–2056.

[23] Cakir, A.K., (2021), Analysis of Surface Roughness, Sound Level and Machine Current in the Turning of Hardened AISI S1 Steel. Trans Indian Inst Met (2021). https://doi.org/10.1007/s12666-021-02196-8, 2021.

NOMENCLATURE

P= Power consumption (W),
I= Current (A),
V=Voltage (380 V),
Cos Φ = 0.95
T= Total processing time (s)
F= The amount of progress in one minute (mmmin),
n= speed (rev/min),
f= The amount of progress per revolution (mmdev)
t= processing time(s), L= Total processing length (mm)

Ra (μm)	Surface roughness value
a (mm)	Depth of cut
V (m/min)	Cutting speed
f (mm/rev)	Feed rate
R2	Accuracy value
Pred. R2	Predicted R2
Adj. R2	Adjusted R2
Seq SS	Sequential sum of squares
Adj. SS	Adjusted sum of squares
Adj MS	Adjusted mean squares
DF	The total degrees of freedom
F	An F-value appears for each term in the analysis of variance table
P	The p-value is a probability